

WOFEX 2016

proceedings of the 14th annual workshop

Faculty of Electrical Engineering and Computer Science,
VŠB – Technical University of Ostrava

ISBN 978-80-248-3961-5

WOFEX 2016 wofex

<http://wofex.vsb.cz/2016/>

14th annual workshop,
Ostrava, 6th September 2016
Proceedings of papers

Organized by

VŠB – Technical University of Ostrava
Faculty of Electrical Engineering and Computer Science



WOFEX 2016

© Michal Krátký, Jiří Dvorský, Pavel Moravec, editors

ISBN 978-80-248-3961-5

This work is subject to copyright. All rights reserved. Reproduction or publication of this material, even partial, is allowed only with the editors' permission.

Page count: 575
Impression: 200
Edition: 1st
First published: 2016

This proceedings was typeset by pdfL^AT_EX.

Published by Faculty of Electrical Engineering and Computer Science, VŠB – Technical University of Ostrava

Preface

The workshop WOFEX 2016 (PhD workshop of Faculty of Electrical Engineering and Computer Science) was held on September 6th September 2016 at the VŠB – Technical University of Ostrava. The workshop offers an opportunity for students to meet and share their research experiences, to discover commonalities in research and studentship, and to foster a collaborative environment for joint problem solving. PhD students are encouraged to attend in order to ensure a broad, unconfined discussion. In that view, this workshop is intended for students and researchers of this faculty offering opportunities to meet new colleagues.

This book of proceedings includes 90 papers of faculty PhD students and 4 papers of external authors. The proceedings of WOFEX 2016 are also available at the web site <http://wofex.vsb.cz/2016/>. I would like to thank the authors and the Organizing Committee from Department of Computer Science, namely Jiří Dvorský and Pavel Moravec, for their arduous editing work.

September 2016

Michal Krátký
Program Committee Chair
WOFEX 2016

Organization

Program Committee

Chair:

Michal Krátký (VŠB – Technical University of Ostrava)

Members:

Pavel Brandštetter (VŠB – Technical University of Ostrava)

Radim Briš (VŠB – Technical University of Ostrava)

Zdeněk Dostál (VŠB – Technical University of Ostrava)

Petr Chlebiš (VŠB – Technical University of Ostrava)

Stanislav Rusek (VŠB – Technical University of Ostrava)

Václav Snášel (VŠB – Technical University of Ostrava)

Vladimír Vašínek (VŠB – Technical University of Ostrava)

Organizing Committee

Jiří Dvorský (VŠB – Technical University of Ostrava)

Pavel Moravec (VŠB – Technical University of Ostrava)

Hana Dluhošová (VŠB – Technical University of Ostrava)

Workshop Location:

Campus of VŠB – Technical University of Ostrava

17. listopadu 15, 708 33 Ostrava–Poruba, Czech Republic

6th September 2016

<http://wofex.vsb.cz/2016/>

Table of Contents

Study Programme P2649 Electrical Engineering

Electrical Power Engineering (3907V001)

Correlated Colour Temperature Changes of the LED Sources Depending on the Angle of Their Radiation	1
<i>Petr Bos, Richard Baleja, Tomáš Novák, and Karel Sokanský</i>	
The Geomagnetic Field in the Czech Republic during 23 rd Solar Cycle . . .	7
<i>Jan Fulneček and Veleslav Mach</i>	
Statistical Evaluation of Atmospheric Effects on the Illuminance Caused by Night Sky in Ostrava	13
<i>Tomáš Hanusek</i>	
Creating and Measuring Ultra-Low Voltage Step-Up Converter	19
<i>Petr Hawliczek and Radomír Gono</i>	
Electricity Production by a Small Hydro Power Plant – Statistical Inference	25
<i>Martin Kral and Radomír Gono</i>	
New Concept of Hybrid Off-grid System in Technology Centre of Ostrava	31
<i>Petr Kubalík</i>	
The Impact of Electric Vehicles on Distribution Network	37
<i>Oliver Marcincin</i>	
Simulation of Transfer of Energy by Software EMTP-ATP on Power Converter	43
<i>Tomáš Mozdřeň</i>	
Description of Measurements on Biogas Stations	49
<i>Ladislav Novosád</i>	
Stray Currents Caused by Regenerative Brake in Electric Traction	55
<i>Jiří Plaček</i>	
Influence of Light Sources on Human Circadian Rhythms	61
<i>Karel Sokanský, Richard Baleja, and Tomáš Novák</i>	
Modeling of Cogeneration Units	67
<i>Michal Špaček</i>	

EMTP/ATP Simulation of Power Quality Disturbances in Medium Voltage Grid	73
<i>Dung Vo Tien, Veleslav Mach, Radomir Gono, and Zbigniew Leonowicz</i>	

Electrical Machines, Apparatus and Drives (2642V004)

Simulation of Sliding Mode Control Structure of Induction Motor Drive ..	79
<i>Chau Si Thien Dong</i>	
Induction Motor Parameters Estimation based on Voltage Step Response and Genetic Algorithm	85
<i>Jiri Hajovsky</i>	
Vector Control of Synchronous Motor with Permanent Magnets	91
<i>Petr Chamrád</i>	
Analysis of Motor Data Identification Process of Frequency Converter SINAMICS S120	97
<i>Peter Januška</i>	
Setting up the Optimal Operating Point of the Adams Motor Generator .	103
<i>Martin Koutný</i>	
Ultracapacitors Cooperation with Photovoltaic and Hydrogen Technology in ENET Centre	110
<i>Michal Ney</i>	
The Estimation of Inrush Current for Direct Connection of Induction Generator to Grid	116
<i>Jan Otýpka</i>	
Application of FEM Modeling for Analysis of Asynchronous Motor	122
<i>Pavel Pečínka, Tomáš Hrubý, and Stanislav Kocman</i>	
Experimental Verification of Luenberger Observer in Sensorless Control Structure of Induction Motor Drive	128
<i>Ondrej Petřtyl</i>	
Genetic Algorithm Application for Parameters Optimization of Speed Controller in Induction Motor Drive	134
<i>Thinh Cong Tran</i>	
Direct Torque Control Methods for Speed Sensorless Control of Induction Motor Drive	140
<i>Hau Huu Vo</i>	

Electronics (2612V015)

Battery Management for Electric Vehicle	146
<i>Lukas Cab and Petr Simonik</i>	

Electronic Systems of Remotely Operated Vehicle	152
<i>Jiri Takac</i>	

Technical Cybernetics (2612V045)

Support Vector Machine based Dementia Detection from MRI Scans	158
<i>Radek Hrabuška</i>	
LPC Speech Synthesis in MATLAB	164
<i>Josef Kročil</i>	
Modelling of the Knee Cartilage Morphological Changes on the Base of the Fuzzy Thresholding with the Local Aggregation	170
<i>Jan Kubicek</i>	
Atmospheric Pressure Measurement Proposal	176
<i>Martin Mikolajek</i>	
Modification of Kamada-Kawai Algorithm Using Barzilai-Borwein Method	182
<i>Jana Nowaková</i>	
Automated Image Detection of the Main Bloodstream Stem from CT Angiography Image	188
<i>Tomas Ondraczka</i>	
Measuring and Analysing of Muscle Activity during Shooting with Air Rifle in Standing Position with Surface Electromyography	194
<i>Lucie Švecová</i>	
Environmental Analysis of Emergency Department and Development of Databases Based on IoT	200
<i>Tomas Urbanczyk</i>	
Standalone Data Acquisition Device with NFC Interface	206
<i>Marketa Venclikova</i>	

Study Programme P1807 Computer Science, Communication Technology and Applied Mathematics

Computer Science (1801V001)

Simple Action Recognition Based on Skeleton Detection from Depth Images	212
<i>Martin Barteček</i>	
Evolutionary Algorithms as a Classification Method	218
<i>Petr Buček</i>	
Solar Irradiance Forecasting in the Active Demand Side Management	223
<i>Tomas Burianek</i>	

Flexible Neural Tree and Betweenness Centrality Algorithms	229
<i>Jiří Hanzelka</i>	
Neural Stegoclassifier	235
<i>Jakub Hendrych</i>	
Polar Lines Registration via Functions of Angles in 2D LIDAR Scans	241
<i>Branislav Holý</i>	
Practical NFC Reader Design and the Electromagnetic Interference Measurement	247
<i>Josef Hrabal</i>	
Clustering using Ensemble of GMM	254
<i>Jan Janoušek</i>	
Classification of Astrominformatic Big Data by Means of Analytic Programming	260
<i>Lumír Kojecký</i>	
Basic Cellular Automaton Rule Extractor	266
<i>Lukáš Kroczek</i>	
Statistical Analysis of Steganalytical Method for Steghide Detection	270
<i>Radim Kuncický</i>	
Effort Estimation Supported by Artificial Intelligence and Machine-learning	276
<i>Radoslav Štrba</i>	
Extraction of Abstract Models of Communication from Message-passing Applications	282
<i>Martin Šurkouský</i>	
Complex Network Models of Self Organizing Migrating Algorithms	288
<i>Lukas Tomaszek</i>	
Nearest Neighbors Search Using the Regular Grids and Space Filling Curves	294
<i>Vojtěch Uher</i>	
Complex Network Based Feature Extraction for Fault Detection on Covered Conductors Medium Voltage Overhead Lines	300
<i>Tomas Vantuch</i>	
Data Compression using Delimiters	306
<i>Michal Vašínek and Jan Platoš</i>	
The Malware Analysis based on Static Methods	312
<i>Filip Zatloukal</i>	
Multiple Range Query Processing	319
<i>Martin Zwierzyna and Michal Krátký</i>	

Computational and Applied Mathematics (1103V036)

Global Optimization Using Space Filling Curves	324
<i>Michaela Bailová</i>	
Application of Three-way Contingency Tables	330
<i>Michal Běloch</i>	
Stochastic Galerkin Method for Random Material Problem	336
<i>Michal Bérés</i>	
Parallel Tempering Algorithm in Path Integral Monte Carlo Simulations	342
<i>Rajko Čosić</i>	
A Bayesian Inverse Approach to Material Parameters Estimation in Darcy Flow Problem	347
<i>Šimona Domesová</i>	
Parallel Space-time Discretization Methods	353
<i>Ladislav Foltyn</i>	
Kernel Detection of the Stiffness Matrix in the FETI Methods	357
<i>Pavla Jirůtková and Alexandros Markopoulos</i>	
Discrete Mathematics in Parallel Boundary Element Method	363
<i>Michal Kravčenko</i>	
The Minimization of The Maximal Out-degree in a Simple Graph	368
<i>Matěj Krbeček, Petr Kovář, Michal Kravčenko, and Adam Silber</i>	
Bayesian Formulation of Image Segmentation Problem	373
<i>Daniel Krpelík</i>	
Domain Decomposition for Mixed Finite Elements in Elasticity	379
<i>Lukáš Malý</i>	
Numerical Solution of Hartree-Fock Equations using the Inexact Restoration Method and Tensor Numerical Methods	385
<i>Martin Mrovec</i>	
Proximal Bundle Method for Constraint Nonlinear Optimization Problem	391
<i>Nikola Plívová and Petr Beremlijski</i>	
Time Series Similarity Measure using Dynamic Time Warping	397
<i>Robert Skopal</i>	
Bayes Estimators of the Mixture of Failure Rate Model	402
<i>Tien Thanh Thach and Radim Bris</i>	

Communication Technology (2601V018)

The Influence of Temperature on Chromatic and Polarization-mode Dispersion of the Optical Fiber	408
<i>Lukas Bednarek</i>	
Qualitative Comparison of Video Codec Standards H.264 and H.265/HEVC for 4K Resolution	414
<i>Jaroslav Frnda and Erik Chromy</i>	
Optical Vehicle-to-vehicle (V2V) Communication: Analyze of Photometric Quantities DRL Jaguar XK	420
<i>Peter Hajduk and Vladimír Vasínek</i>	
Classification of Different Turbulent Conditions for Propagation of Optical Laser Light Trough Laboratory Box	426
<i>Lukas Hajek and Vladimír Vasínek</i>	
Utilization of Optical Fibers in Building Structures	433
<i>David Hrubý</i>	
Study of the Colour Correlated Temperature in PDMS Fiber Depending on the Concentration of the Luminophore and on the Distance from the Face of the Fiber	437
<i>Jan Jargus</i>	
Study of the Incidence of External Influences on Optical Fiber Connectors	443
<i>Tomáš Kajnar</i>	
Nondestructive Fiber-optical System for Measurement of Speed in Road Traffic	449
<i>Jan Nedoma</i>	
Measurements of the Attenuation Constant of the Poly-dimethylsiloxane .	455
<i>Martin Novak</i>	
A New Approach to Speech Quality Evaluation	460
<i>Lukas Orcik, Miroslav Voznak, and Erik Chromy</i>	
The Influence of Temperature Loading on the Optical Fiber Passive Componenets	466
<i>Frantisek Perecar</i>	
Aging of Optical Fibers due to Radiation of High Optical Performance ..	472
<i>Radek Pobořil</i>	
Broadband over Visible Light: High Power Wideband Bias-T Solution ...	478
<i>Tomas Stratil, Petr Koudelka, Radek Martinek, and Vladimír Vasínek</i>	

Quality Comparison of Streaming Video and Streaming Encrypted Video using Objective Methods	484
<i>Lukas Sevcik, Miroslav Voznak, and Erik Chromy</i>	
IoT LoRa Gateway on System for Embedded Devices	490
<i>Jiri Slachta and Miroslav Voznak</i>	
Design of Multilayer Neural Network for Speaker Identification	496
<i>Jaromir Tovarek, Miroslav Voznak, and Erik Chromy</i>	
Czech Database of Real Speech Emotions	502
<i>Dominik Uhrin and Erik Chromy</i>	
Common Issues with Simulation of Antenna Systems in COMSOL Multiphysics	508
<i>Zdeněk Urban, Lukáš Wežranowski, and Lubomír Ivánek</i>	
Testing FSO-WDM Communication Systems and Real Measurements Modulation Formats for FSO with using USRP	514
<i>Ales Vanderka</i>	
Path Loss Models in Urban and Rural Terrain for Wireless Communication	520
<i>Yahia Zakaria and Lubomír Ivánek</i>	
Optoelectronic Elements Made from Polydimethylsiloxane	526
<i>Ondřej Zbořil</i>	
External Authors	
Detection of Human Silhouette in Depth Maps using HOG Algorithm . . .	532
<i>Rafal Gasz</i>	
Microsoft Kinect Measurement Accuracy for Different Shapes of Objects .	538
<i>Jakub Osuchowski and Sławomir Szymocha</i>	
The Use of Glass with PDLC Film in Active Dimming Systems	544
<i>Sławomir Szymocha and Jakub Osuchowski</i>	
Renewable Energy Integrated Microgrid for Rural Electrification and Productive use	549
<i>Muhammad Taheruzzaman</i>	

Author Index

Correlated Colour Temperature Changes of the LED Sources Depending on the Angle of Their Radiation

Petr Bos, Richard Baleja, Tomáš Novák, and Karel Sokanský

Department of Electrical Power Engineering, FEECS,
VŠB – Technical University of Ostrava, 17. listopadu 15,
708 33 Ostrava – Poruba, Czech Republic
petr.bos@vsb.cz

Abstract. The aim of the report is a description of an issue connected with subjective perception of colours from the light of the lighting systems stepped by LED. Subjective observation of the colour change on the light of the lighting systems stepped by LED has been mostly related to extensive lighting systems where it was possible to observe identical light source (LED) within various angles. This phenomenon was manifested even more distinctively within lighting systems that made use of optical systems located in luminaries (reflector, diffusers) in a minimal way. Additional optical systems redistribute primary luminous flux coming from light source (LED) and thus there is a blending of luminous flux radiated to a certain angle of the illuminated space from various directions of the luminous flux radiation itself. In case it is not like this and the luminaries are equipped only with LED with a suitable luminous distribution curve, there is no blending of the luminous flux. Thanks to this the observer can also perceive various colours of light within individual luminaries perceived under various angles.

Keywords: LED sources, changes in correlated colour temperature, luminophor, the radiating angle.

1 Introduction

The article is aimed on the issue of dependence of temperature changes within the correlated colour temperature of the LED light sources depending on the angle of their radiation. Each LED source is of various technical characteristics and construction and due to radiation angle some LED sources can have smaller or more extensive changes within correlated colour temperature. These changes cause a change in light colour which can lead to a collision with catalogue of the given LED source and of course induce negative subjective perception of light from lighting systems stepped by these LED sources.

Colour of the light of LED sources depends not only on a type of a luminescent material but also on a length that has to be overcome by a ray coming through the luminophor. The longer the length of the ray coming through the luminophor the wider differences in it's colour.

1.1 LED Construction

LED sources belong among electroluminescent light sources. They are semiconductor components containing PN junction. Through excitation by electric current, on PN junction there is an emission of optical radiation. LED notation comes from the term Light Emitting Diode. These light sources can be very small however they reach relatively high performance. [1] [2]

LED principle implies that they cannot radiate white light directly. That is why in the past an additive blending of radiation of three coloured RGB chips was used. By means of their combination a necessary colour of light was obtained. Another (and most widely used) possibility of getting white light is making use of phosphorescence of a luminophor applied on LED chip, see Figure 1, which transforms a part of emitted blue light from the LED into higher wave lengths with a result of white colour of light in shades varying from cold white (6000 K – 7000 K) up to warm white (2700 K – 3300 K). [3] [5]

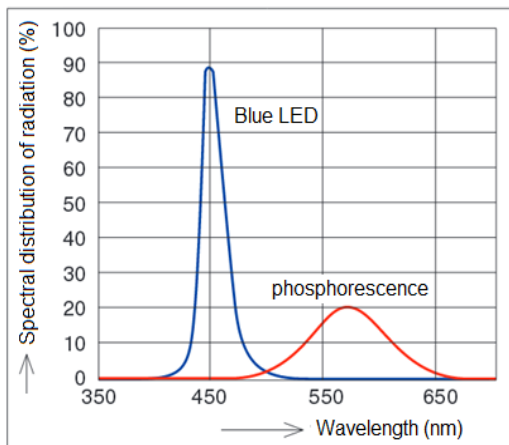


Fig. 1. Sample of emission spectrum of white LED [6]

2 Catalogue data of applied LED

Two various LED sources were used for evaluation of the change in correlated colour temperatures within LED sources depending on an angle of their radiation. The first LED labelled SEUOL SSC Z5 SZW05A0B is used for day light in cars. Second one used LED sources came from Philips Company, i.e. Fortimo LED DLM for interior usage.



Fig. 2. LED SEOUL SSC – Z5 (on the left) and Fortimo LED DLM Module (on the right) [4]

Table 1. Catalogue data for used LED sources

Parameter	Luminous flux [lm]	Correlated colour temperature [K]	Colour rendering index	Power [W]
Type of LED				
SEOUL SSC - Z5 SZW05A0B	124	6000	70	1
Fortimo LED DLM Module	3000	4000	80	44

3 Verification of the prediction model

This chapter points out a principle what changes in colour of light within LED light sources can occur. As mentioned above, there is a various length of the ray transmission through the luminophor ensuring a shift of primary blue radiation into areas of higher wavelengths. Due to increase of the length of the ray transmission through the luminophor there is a transformation of larger content of primary radiation by means of phosphorescence, see Figure 3, and thus there is also decrease of correlated colour temperature within higher angles of radiation. The following relation for calculation of transmission lengths of light ray through the luminophor was used. Its form is:

$$l_n = \frac{l_1}{\cos \alpha_n} [\%] \quad (1)$$

l_1 ... length of light ray transmission through the luminophor in vertical direction

α_n ... angle of LED turning on the photogoniometer

Length l_1 is equal to thickness of the luminophor layer in the right section. As we do not know its precise value, we depict its size as a percentage of thickness of the particular layer, i.e. 100%. We change the angle α_n with a step 5° .

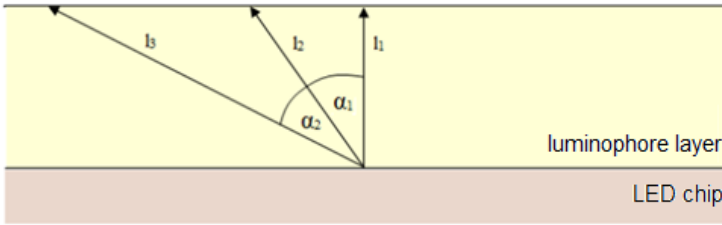


Fig. 3. Light ray transmission through the luminophor layer

The above figure shows a significant relationship between the length of light ray transmission and the angular displacement of the photometric form and it causes change in values of correlated colour temperature. Ideally, there would be constant values of correlated colour temperatures within a change of angular displacement of the LED source.

4 Spectral characteristic of individual LED

The aim of the measurement of the changes in correlated colour temperature depending on the radiating angle is to verify assumed parameters of the mentioned LED. During the measurement the following values were recorded: spectral characteristic of LED, values of luminous flux and correlated colour temperatures.

4.1 The process of changes in correlated colour temperatures depending on the change of the horizontal angle LED SEOUL SSC - Z5 SZW05A0B

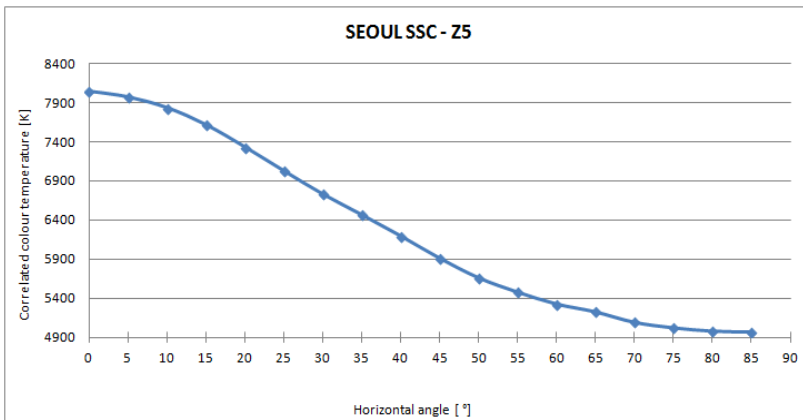


Fig. 4. The changes in correlated colour temperature with regard to the changes of the horizontal angle LED SEOUL SSC - Z5

4.2 The process of changes in correlated colour temperatures depending on the change of the horizontal angle Fortimo LED DLM Module 44W/840

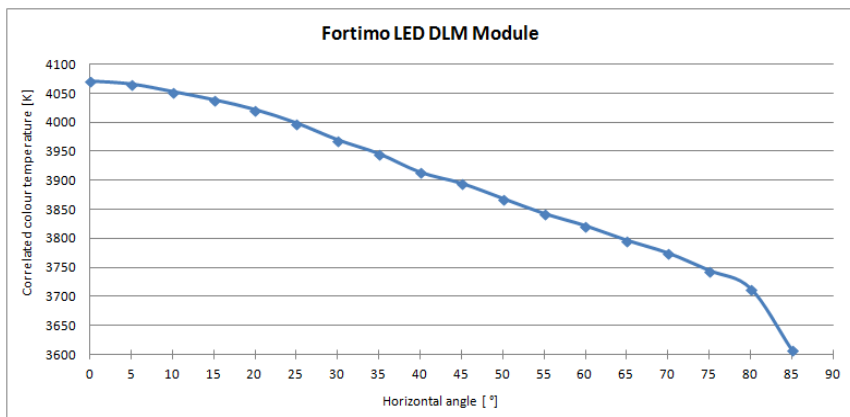


Fig. 5. The changes in correlated colour temperature with regard to the changes of the horizontal angle Fortimo LED DLM Module

As a result of the measured values we can compare the prescribed value of correlated colour temperature within the catalogue data with the measured value of colour temperature of the Ulbricht sphere.

Table 2. Comparison of catalogue and measured values of correlated colour temperature from the LED sources measured by the Ulbricht sphere.

Parameter	Catalogue T_{CP}	Measured T_{CP}
Type of LED	[K]	[K]
SEOUL SSC - Z5 SZW05A0B	6000	6416
Fortimo LED DLM Module	4000	3394

By means of the measurement the parameters of correlated colour temperatures set by the producer for individual LED sources were verified. From the above scheme it is evident that there are higher deviations for the sources LED SEOUL SSC - Z5 SZW05A0B and Fortimo LED DLM Module.

The graphs show that measured correlated colour temperatures for the source by Philips Company are comparable with correlated colour temperatures measured in a straight line at an angle of 0° .

5 Conclusion

The comparison of spectral characteristics of chosen LED sources depending on angular displacement implies, based on executed measurements, a change of correlated colour temperature. In the graphs there are highest step changes of correlated colour temperatures for angular displacement of 0° , 85° and for measurement in the Ulbricht sphere. There is a conclusion for producers of luminaries – to secure a superior immixture of light coming from the luminary.

The LED SEOUL SSC - Z5 SZW05A0B experienced the most significant change in correlated colour temperature – 8043 K was recorded as correlated colour temperature for radiating angle of 0° and 4975 K for the angle of 85° . Thus the difference was up to 3068 K and it caused a change of colour of radiated light. The second type of LED Fortimo DLM Module recorded lower differences in correlated colour temperature, i.e. only 677 K.

A supposed reason for correlated colour temperature is the difference in length within transmission of light ray during vertical and the largest angle of the luminophor. As a result of various lengths of transmission there can be extensive disparity of correlated colour temperature during changes of the radiating angle. This difference caused a change in correlated colour temperature on the order of 3000 K for LED SEOUL SSC - Z5.

6 Acknowledgment

This article was prepared with the support of the project "Intelligent lighting control systems" SP2016/151, by institution of VSB-TU Ostrava.

7 References

1. HABEL, J. et al. Světlo a osvětlování. 2nd ed. Praha: FCC Public. 2013. 622 s. ISBN 978-80-86534-21-3.
2. SOKANSKÝ, K. et al. Světelná technika. 1st ed. Praha: České vysoké učení technické v Praze. 2011. 255 s. ISBN 978-80-01-04941-9.
3. IES Lighting Handbook 10th edition. Illuminating Engineering. New York. Society of North America 2011.
4. SEOUL SEMICONDUCTOR [online]. Specification SSC-Z5 series. 2012 [cit. 2016-01-06]. Available from: http://www.seoulsemicon.com/_upload/Goods_Spec/SZW05A0B.pdf
5. Škoda, J., Baxant, P., Krbal, M., Sumec, S. and Pavelka, T. Photometry of LED sources. Przeglad Elektrotechniczny. 2013. vol. 89. no. 6. pp. 341–344. ISSN 00332097.
6. DVOŘÁČEK, V.: „Světelné zdroje - světelné diody,“ Časopis světlo, 2009, vol. 12, no. 5, pp. 68-71. ISSN 1212-0812.

The Geomagnetic Field in the Czech Republic during 23rd Solar Cycle

Jan Fulneček and Veleoslav Mach

Department of Electrical Power Engineering, FEECS,
VŠB – Technical University of Ostrava, 17. listopadu 15,
708 33 Ostrava – Poruba, Czech Republic
{jan.fulnecek, veleslav.mach}@vsb.cz

Abstract. The activity of the Sun influences the geomagnetic field of the Earth. Solar flare on the Sun can trigger geomagnetic storms on the Earth. These storms have negative influence on power grids. For better understanding of this phenomenon, a computing model was created. This article provides a view on data used for computation.

1 Geomagnetic storms influence on power grids

The geomagnetic field can be simplified into a magnetic dipole-like field with north geomagnetic pole situated on the south hemisphere [1]. Each phase of transmission line acts as a conductive loop. A geomagnetic storm causes variations of the magnetic field intensity B , which leads to creation of electric field E . According to Faraday's law (eq. 1) and Ohm's law, a geomagnetic induced current (GIC) appears in the line [2].

$$\oint_l \vec{E} \cdot d\vec{l} = -\frac{d}{dt} \cdot \int_s \vec{B} \cdot d\vec{S} \quad (1)$$

Frequency of this current is usually below 1 Hz, so it can pass through a winding of a power transformer. This leads to a transformer half cycle saturation [3].

2 Solar cycles

The activity of the Sun is variable in a time. There are several known cycles of the activity [4]. The most significant one is called the Schwabe cycle and it has a period in a length of approximately 11 years. It was discovered by Samuel Heinrich Schwabe in 1843 after a long term observation of sunspots (sunspot is a dark area on the Sun with lower temperature).

At the start of the Schwabe cycle, there are no or just a few sunspots on the Sun. In the middle of this cycle, activity of the Sun reaches its maximum level. High intensity of the magnetic field in some areas makes the plasma flowing impossible. This leads to an appearance of a sunspot. Such sunspots are usually situated in groups. Most of the solar flares are observed around these sunspots [5].

Beside Schwabe cycle, there are another two known cycles with longer periods – magnetic cycle (22 years) and Gleisberg cycle (80 years). Some other cycles with even longer periods are predicted, for example Suess cycle (210 years) or Hallstat cycle (2300 years) [6].

3 Geomagnetic field in the Czech Republic

The history of geomagnetic field measurement in the Czech Republic began in 1830 [7]. In this year, the geomagnetic observatory in Prague was founded. It was the second one in the Europe (the first observatory was founded in London). Since 1958, this observatory is situated in Budkov.

3.1 23rd Solar cycle

The last solar cycle started on May 1996 and ended in January 2008. The total length of this cycle was 11.6 years, which is close to the average. In a past, some shorter (9 years) or longer (13,7 years) periods were observed [8].

Hourly means of the geomagnetic field horizontal components measured at the Budkov observatory (ground measurement) were examined. These data are available for public at the SPIDR database [9]. Horizontal magnetic field intensity B_H (fig. 1) and declination D were calculated. Average value of the horizontal magnetic field intensity component during the whole cycle was 20320 nT. The lowest drop to 19954 nT was recorded during the geomagnetic storm on November 20th at 18:00 local time.

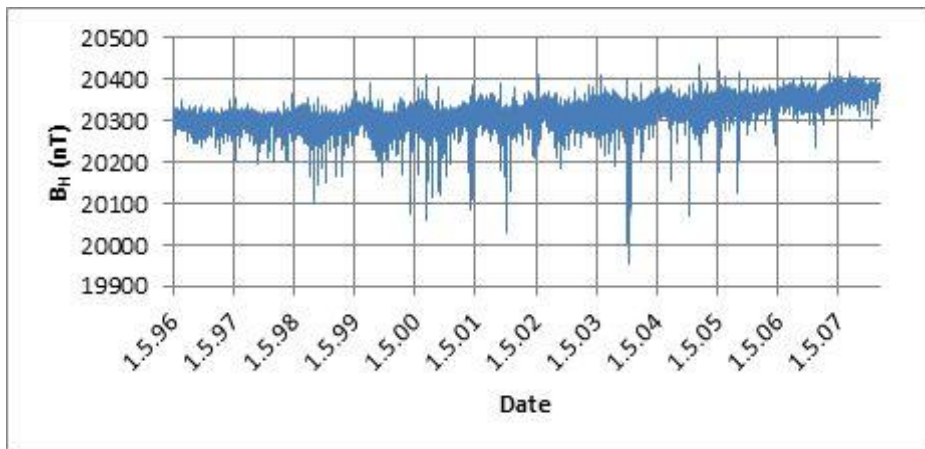


Fig. 1. Horizontal intensity of the geomagnetic field

The average inclination of the cycle was 1.9° . Short time variations of magnetic declination during the cycle are not significant ($<1^\circ$).

3.2 Halloween geomagnetic storms event

During the 23rd cycle, series of eleven high energy solar flares occurred between October 19th and November 7th 2003. One of them (on November 4th) was X28 category - the most powerful flare ever recorded [10]. Luckily, this particular blast was aimed away from the Earth.

During the Halloween geomagnetic storms event, the Solar and Heliospheric Observatory (SOHO) satellite temporarily failed. Another satellite, Advanced Composition Explorer (ACE), was permanently damaged [11]. Also some other satellite based systems and communications were affected. One hour power outage was caused by this event in Malmo (Sweden) [12]. Transmission lines in the Czech Republic were not affected.

In the Czech Republic, the strongest impact of this event was detected on October 29th at 6:00 am local time (fig. 2). In that time, the magnetic field intensity drop from 20303 nT to 20064 nT was recorded at the Budkov observatory. This was also the strongest impact of a geomagnetic storm during the whole examined cycle.

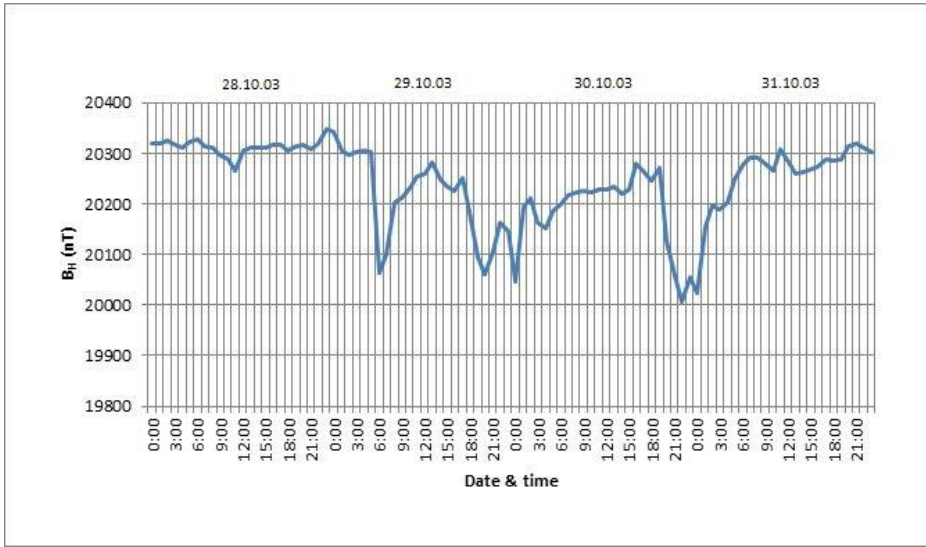


Fig. 2. Halloween geomagnetic storms event

As it shows fig. 3, variations of the magnetic declination during this geomagnetic storm were very small in the Czech Republic. At the same time in the Alaska, declination quickly changed by more than 20° .

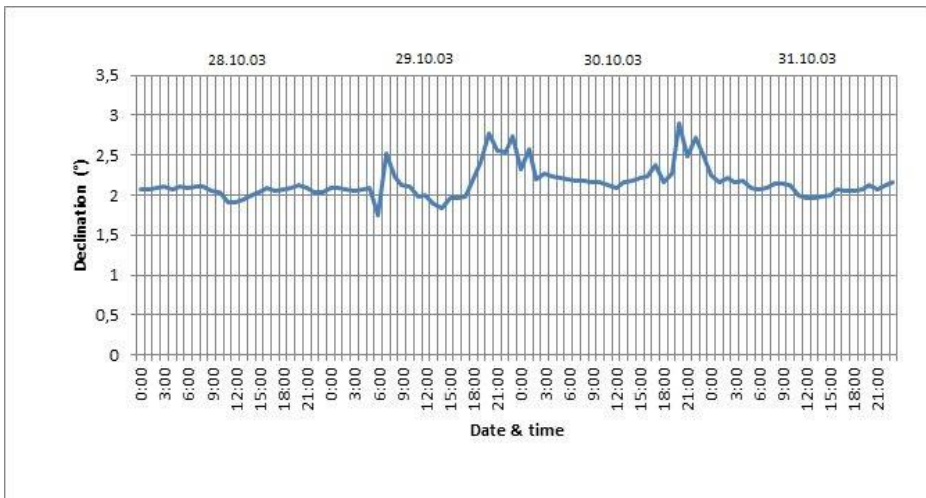


Fig. 3. Declination during the Halloween geomagnetic storms event

4 Conclusion

In the Czech Republic, only magnetic component of the geomagnetic field is measured. For the GIC simulation purposes, the electric component of the field is more important. Calculation of the electric component is not possible without knowledge about physical properties of the Earth up to depth of several hundred kilometers. Because of unachievability of such depth, GIC simulations are very complicated.

The most important result of this work is description of the magnetic declination. Short time changes in the magnetic declination in the Czech Republic can be neglected even during strong geomagnetic storms. This information makes a future risk assessment less complicated.

5 References

- [1] W. Campbell, Introduction to Geomagnetic Fields, Cambridge: Cambridge University Press, 2003. ISBN 0 521 82206 8
- [2] C. Schrijver, F. Bagenal, J. Sojka, „Space Weather and Society,“ in *Heliophysics V.*, 2015.
- [3] D. McMorow, Impacts of Severe Space Weather on the Electric Grid, Virginia: Jason, 2011.
- [4] V. Bothmer, I. Daglis, Space Weather Physics and Effects, Chicchester: Springer, 2007. ISBN 978-3-540-23907-9
- [5] „Coronal Mass Ejections,“ NOAA Space wether prediction center, [Online]. Available: <http://www.swpc.noaa.gov/phenomena/coronal-mass-ejections>. [visited March 2016].
- [6] „The Sunspot Cycle,“ NASA Solar Physics, 6 June 2016. [Online]. Available: <http://solarscience.msfc.nasa.gov/SunspotCycle.shtml>. [visited 10 July 2016].
- [7] J. Štěřstík, „Historie magnetických měření v Čechách a dlouhodobé změny složek geomagnetického pole,“ in *Člověk ve svém pozemském a*

kosmickém prostředí, Úpice, 2010.

- [8] A. Balogh, H. Hudson, K. Petrovay, R. Steiger, *The Solar Activity Cycle: Physical Causes and Consequences*, Springer, 2015. ISBN 1493925849
- [9] „Space Physics Interactive Data Resource,“ NOAA National Geophysical Data Center, [Online]. Available: <http://spidr.ionosonde.net/spidr/>.
- [10] C. Cid, J. Palacios, E. Saiz, A. Guerrero, Y. Cerrato, „On extreme geomagnetic storms,“ *Space Weather Space Clim*, September 2014. ISSN 2115-7251
- [11] „The Sun Goes Haywire,“ NASA, 12 November 2003. [Online]. Available: http://science.nasa.gov/science-news/science-at-nasa/2003/12nov_haywire/. [visited 16 January 2016].
- [12] M. Wik, R. Pirjola, H. Lundstedt, A. Viljanen, P. Wintoft, A. Pulkkinen, „Space weather events in July 1982 and October 2003 and the effects of geomagnetically induced currents on Swedish technical systems,“ *Annales Geophysicae*, April 2009.

6 Publications

Space weather effects on power grids, Electric Power Engineering EPE, 2015 16th International Scientific Conference

Geomagnetic Storms Effects on Power Transformers, Wofex 2015, Ph.D. Workshop of Faculty of Electrical Engineering and Computer Science

Statistical Evaluation of Atmospheric Effects on the Illuminance Caused by Night sky in Ostrava

Tomáš Hanusek

Department of Electrical Power Engineering, FEECS,
VŠB – Technical University of Ostrava, 17. listopadu 15,
708 33 Ostrava – Poruba, Czech Republic
tomas.hanusek.st@vsb.cz

Abstract. This article continues on results of work named “Long-term measurement of obtrusive light in the area of VŠB-TUO”. In article is described statistical evaluation of measured values of illuminance from night sky which were affected by change atmospheric conditions like a snowfall, rainfall, fog and clouds. The light emission depends on three main factors, same like all environments. This includes spectral reflectance factor describing light environment $\rho(\lambda)$, environments absorption $\alpha(\lambda)$ and throughput environment $\tau(\lambda)$. Values of these factors are changes with atmospheric conditions and the result is an increase or decrease in reflection characteristics of the sky. In the paper there are data used from the measuring system, which was located on the roof of the building NK VŠB TU Ostrava and data from the Czech Hydro meteorological Institute, which includes the types and times of ongoing meteorological events and the value of clouds in the required timeframe. They were obtained from the observation station Ostrava - Mošnov, which is remote from the measuring point approximately 15 kilometers as the crow flies.

Keywords: Long-term measurement, horizontal illuminance, cloudiness, statistical processing

1 Measuring system

Measuring equipment must fulfill the requirements for long-term measurement of illuminance from night sky. We expected values of illuminance in the range of tenths to hundredths lux, it is necessary to use mobile devices that are capable of measuring in thousandth of lux. Little problem was that all the types of luxmeters are calibrated for sensitivity curve of human eye for photopic vision $V(\lambda)$ and not on the curve of human eye sensitivity for scotopic vision $V'(\lambda)$. Luxmeter must be equipped with analog output for reading and further processing of measured values. It was used luxmeter MINILUX from German company MX-Electronic for measuring intensity of illumination. It has following parameters:

- Analog output with range 0-200 mV
- Six switchable ranges of measuring from 2lx to 200 klx
- Silicon photodetector with $V(\lambda)$ correction
- D/A converter with display
- Sensitivity 2nA/lx

Further data processing is carried out in application programmed with LabVIEW software and 12-bit, 16-channel measuring card from company National Instruments. This configuration enables great variability within the long-term measuring of other parameters of the sky (not only light parameters), but also to connect the luminaire XENON 1500 W HDG, which will serve as a generator of disturbing light with the known parameters. This luminaire is equipped with a halogen bulb OSRAM HALOLINE 1500 W 10 A; $\Phi = 36$ to lm. It is located close to the measuring device and emits luminous flux directly into the upper hemisphere. 2



Fig. 1. Measuring system on the roof of the building NK.

2 Input data and processing

Illuminance values were recorded continuously and saved every thirty seconds. In this paper values are processed for year 2011, for months January, February, March, April, September, October and November. As an input data were selected values measured from midnight to one o'clock in the morning. It was so definitely eliminated influence of sunset or sunrise. These one hundred and twenty values were divided into eighty values without artificially generated obtrusive light and forty values with generated obtrusive light. The average values of these files, were subsequently deducted from each other, so we obtained average increment illuminance for given hour on each day of the month. The calculated values were used for statistical processing.

2.1 Influence of the season for increment of illuminance

Firstly, there was a statistically verified influence of season on the increment of illuminance for turned on luminaire without the inclusion of meteorological events and cloudiness. It was performed exploratory analysis for the selected months, and then were performed tests of normality and homoscedasticity of selected samples. Based on the results of these tests was elected Kruskal-Wallis test, which compares the medians of selected files. The result of this test was rejected the null hypothesis that there is not a statistically significant difference between the selected months. The Post-hoc analysis suggests that in the file there are two groups between with no statistically significant differences. The first group includes January, February and March. The second group includes April, September and October.

Table 1. Results of a Post-hoc Analysis

tr -ts (critical value)							
	Jan	Feb	Mar	Apr	Sept	Oct	Nov
Jan	-	13,288 (25,24)	10,171 (24,32)	32,369 (24,32)	33,519 (24,75)	32,313 (24,987)	39,44 (25,512)
Feb	13,288 (25,24)	-	2,571 (24,818)	45,657 (24,818)	46,807 (25,24)	45,602 (25,472)	26,152 (25,988)
Mar	10,171 (24,32)	2,571 (24,818)	-	43,086 (23,881)	44,236 (24,32)	43,031 (24,561)	28,723 (25,094)
Apr	32,369 (24,32)	45,657 (24,818)	43,086 (23,881)	-	1,149 (24,32)	0,056 (24,561)	71,809 (25,094)
Sept	33,519 (24,75)	46,807 (25,24)	44,236 (24,32)	1,149 (24,32)	-	1,205 (24,987)	72,958 (25,512)
Oct	32,313 (24,987)	45,602 (25,472)	43,031 (24,561)	0,056 (24,561)	1,205 (24,987)	-	71,753 (25,742)
Nov	39,44 (25,512)	26,152 (25,988)	28,723 (25,094)	71,809 (25,094)	72,958 (25,512)	71,753 (25,742)	-

2.2 Influence of cloudiness on the horizontal illuminance

For calculated values of average illuminance were assigned values of cloudiness, which were measured in the observation station CHMI Ostrava -Mošnov in a time from 0:00h to 1:00h. From these values it is possible to observe the dependence of light emission on the state of the sky. Information about the cloudiness are given in numerical form and moving in a range of 0-9. This value reflects the degree of coverage sky by clouds in eighths and at the base of this value we can differentiate following states of sky: clear, almost clear, partly cloudy, cloudy, almost overcast, overcast and undetectable. During determining cloudiness it does not matter if the clouds overlap or they are in more layers, determining is only relation between clouds and blue sky. Distribution according to numerical values is as follows 4 :

- Cloudiness 0 – clear
- Cloudiness 1 to 2 – almost clear
- Cloudiness 3 to 4 – partly clear
- Cloudiness 5 to 6 – cloudy
- Cloudiness 7 – almost overcast
- Cloudiness 8 – overcast
- Cloudiness 9 – undetectable

Measured values of cloudiness had to be averaged and from data file of illuminance had to be deleted values, which were affected by meteorological event for verify addition and determining the regression model. The result three files contained 172 values fulfilling the required criteria. To search the most accurate regression model software Statgraphics was used and tested three dependencies:

Dependence of average illuminance from turned off luminaire on cloudiness.

The regression curve that best describes the dependence of average illuminance without the contribution of luminaire on cloudiness is a function Logarithmic Y-squared-X:

$$Y = \exp(a + b \cdot X^2)$$

The resulting model is described by equation (1) and its waveform is shown in the graph.

$$E_{\text{turn off}} = \exp(-2.89605 + 0.0219427 * (\text{avg_cloudiness})^2) \tag{1}$$

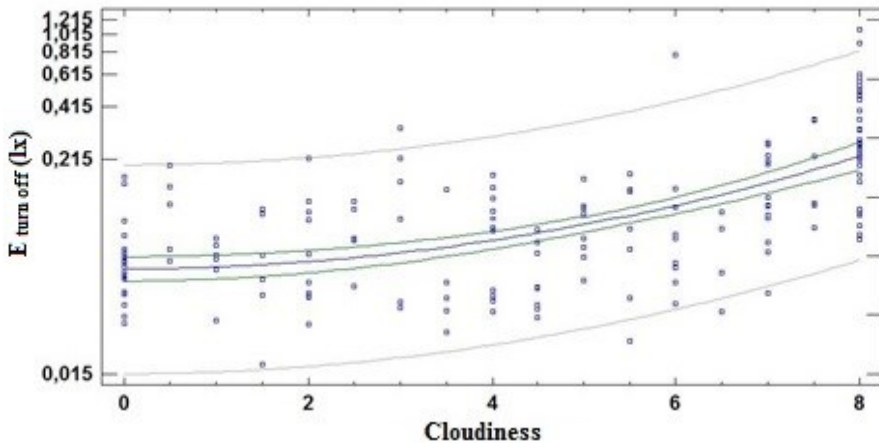


Fig. 2. Graph the regression curve.

The correlation coefficient is 0.64, indicating a moderate relationship between these variables. This model describes 40.8% the variability of average illuminance values.

Dependence of average illuminance from turned on luminaire on cloudiness.

The regression curve that best describes the dependence of average illuminance with turned on luminaire on the cloudiness is again functions Logarithmic Y-squared-X. The resulting model is described by equation (2). The correlation coefficient is 0.578, indicating a moderate relationship between these variables. The model describes 33.2% variability of average illuminance values.

$$E_{\text{turn on}} = \exp(-2.22981 + 0.0158666 * (\text{avg_cloudiness})^2) \quad (2)$$

Dependence of increment the illuminance from source of luminous flux located near the measuring apparatus to the cloudiness.

The correlation coefficient is 0.195, indicating a relatively weak relationship between these variables. The resulting model describes only 3.8% of the variability of the average increment illuminance. From these knowledge we can conclude that the degree of cloudiness has no direct influence on the increment of illumination from the luminaire, which is emits luminous flux directly into the upper hemisphere. 5 , 6

3 Conclusion

It was verified the influence of the average increment of illuminance (ΔE) on season using statistical methods from data file obtained from long-term measurement of illuminance in Ostrava. From the results of exploratory analysis is showed that variability increment illuminance decreases with a transition from winter to summer period and conversely increases with the transition from summer to winter season. The maximum increment of illuminance was 0,216 lx and the minimum value was 0.0042 lx. Null hypothesis was rejected at significance level $\alpha = 0.05$, it means there are statistical significant differences between data from each month. From this we can deduce that the season has effect on the average increment of illuminance caused by the reflection luminous flux from the night sky. Further, the paper describes the dependence between the average values of illuminance (without the contribution of artificially generated light, with the contribution of artificially generated light and increment of illuminance) on average cloudiness. The strongest correlation between these variables was during the time when the luminaire was switched off. Regression model describing the behavior of the illuminance, depending on the cloudiness explains 40.8% of the variability and is described by equation (1). It was also found out that the increment of illuminance caused by installed luminaire is not influenced by the degree of cloudiness. Its size does not depend on the actual cloudiness. In this work it will be continued and it will be expanded by including data of air pollution values which can specify the designed regression model more.

This article was prepared with the support of the project "Intelligent lighting control systems" SP2016/151 by institution of VSB-TU Ostrava.

4 References

1. SOKANSKÝ, Karel. Světelná technika. Praha: České vysoké učení technické v Praze, 2011. ISBN 978-80-01-04941-9.
2. DOSTÁL, František, Karel SOKANSKÝ a Tomáš NOVÁK. Dlouhodobé měření rušivého světla v areálu VŠB-TUO. 2009.
3. Litshmannová, M. *Úvod do statistiky (interaktivní učební text)*, Vysoká škola báňská – Technická univerzita Ostrava Západočeská univerzita v Plzni, 2012. Available from: http://mi21.vsb.cz/sites/mi21.vsb.cz/files/unit/interaktivni_uvod_do_statistiky.pdf
4. Czech Hydrometeorological Institute, Available from: <http://portal.chmi.cz/informace-provas/meteorologicka-terminologie>
5. Šimonová, L. *Průvodce programem Statgraphics, část 1*, VŠB – TU Ostrava, Fakulta elektrotechniky a informatiky, Ostrava, 2006, 36s.
6. Šimonová, L. *Průvodce programem Statgraphics, část 2*, VŠB – TU Ostrava, Fakulta elektrotechniky a informatiky, Ostrava, 2006, 70s.

Creating and Measuring Ultra-Low Voltage Step-Up Converter

Petr Hawliczek and Radomir Gono

Department of Electrical Power Engineering, FEECS,
VŠB – Technical University of Ostrava, 17. listopadu 15,
708 33 Ostrava – Poruba, Czech Republic
{petr.hawliczek.st, radomir.gono}@vsb.cz

Abstract. The paper contemplated the possibility of using the power thermobattery with special converter that operate from voltages in the tens of millivolts. One converter has been developed and characteristics have been measured and documented. The only thermobattery with such a converter is able to supply low-power devices from the temperature difference of one tenth of a degree Celsius.

Keywords: Peltier thermobattery; TEG; ultra-low voltage step-up converter

1 Introduction

The quality and efficiency of thermal energy conversion into electric power using Peltier thermobattery has been rising constantly. The use of Peltier thermobatteries in numerous fields of application is still growing. This paper deals with use of Peltier thermobatteries under conditions with a very small difference of temperature, when the current and voltage generated are very low. Utilization of the low current and voltage by various devices requires development of a converter capable to work with such a low voltage. There has been one converter developed to work with the input voltage of around 20 mV already. For some application is 20 mV still too high that's why I focus to decreasing input voltage of converter. When connected, such boosting converter working from the level represented tens of millivolts can supply power to low-consumption equipment using its thermobattery from the temperature difference as low as 0.1 K only. Lower temperature differences can be accommodated by connecting multiple thermobatteries in series. Such small temperature differences are relatively easy to achieve in practice in order to create a source of power with almost unlimited service life to power measurement or communication equipment using solely the low temperature difference.

2 Supplying and creating converter

Converter which I created with such low voltage input doesn't exist yet.

The selected power source comprised the thermobattery of classic shape TEG 450-200-45 made by the German company THERMALFORCE.DE. This company is the supplier of high efficiency TEG type thermobatteries with a very wide range of products. They supply various types and shapes of thermobatteries, together with thermobatteries already integrated in various devices [1, 2].

The reason for selecting the thermobattery TEG 450-200-45 was its top voltage generated at the particular temperature level, when compared to other thermobatteries. The thermobattery is sized 57x54x3.4 mm. With the temperature difference of $\Delta T = 100$ K, the open circuit voltage generated is 23.70 V, 1.09 A in short circuit run with the optimal load of 6.5 W. The internal resistance of this thermobattery is 14.80 Ω , it generates 0.220 V for the temperature difference of $\Delta T = 1$ K. The thermal conductance of this thermobattery is 1.40 W/K with the maximum permissible temperature of 200 °C [3].

The Ultra-low Voltage Step-Up Converter was built using integrated circuit LTC3108. This is special step-up converter chip capable of raising the voltage from the mere 20 mV fed to the input.

3 Converter with LTC3108

3.1 Default connection of the LTC3108 circuit

The Fig. 1 shows the basic wiring diagram for the LTC3108 circuit designed for building of a step-up converter. Similar integrated circuit is LTC3109 which can work bipolar low input voltage [5]. The LTC3108 is able to operate with the input voltage between 20 mV and 500 mV. Its practical applications concern utilisation of minimum direct voltages to power microchips, communication devices and similar devices [6].

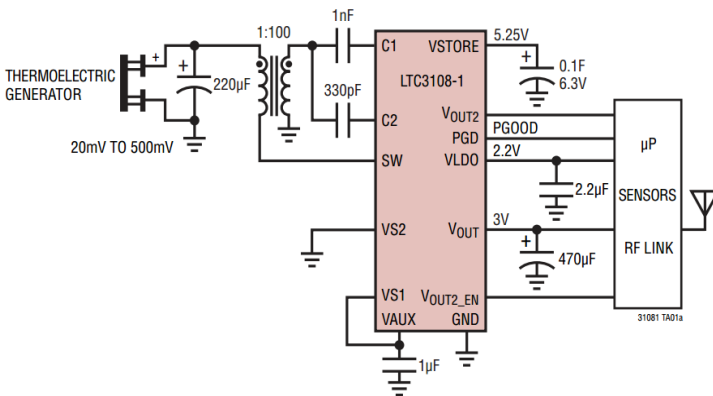


Fig. 1. Basic wiring diagram for the LTC3108 circuit [4]

The most important part to determine the lowest voltage, at which the converter starts working, is the transformer, its turn ratio respectively. The basic wiring diagram shows the transformer with the turn ratio of 1:100, the wiring system subject to measurement then uses 1:125.

The efficiency of LTC3108 converter remains below 40%, the largest losses are incurred on the switching transistor J-FET with the internal resistance of $0.5\ \Omega$ with further losses developing right on the transformer. The top efficiency of this converter is achieved with the power supply of 60 mV and it can range around 40%. It would be used ideally with power supply voltage from 20 mV to 60 mV. The efficiency drops at higher supply voltage levels admittedly, yet there is already enough power, so the output current will still remain sufficient. The use of higher voltages with higher efficiency requires application of a transformer with a different turn ratio (1:50 or 1:20).

The internal wiring shown by Fig. 2 demonstrates the internal structure of wiring in the LTC3108 and connecting the transformer. The most important element within the entire circuit is J-FET transistor between C2, SW and GND and basically just this transistor is used in the measured (modified) wiring.

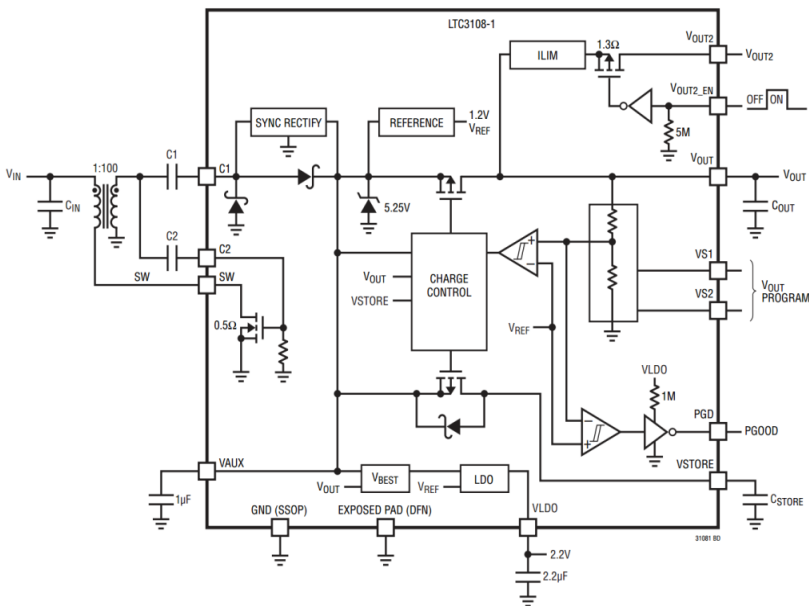


Fig. 2. Internal wiring of LTC3108 circuit [4]

3.2 Modified wiring of the LTC3108 circuit

The diagram of measured (modified) wiring in Fig. 3 still differs with respect to utilization of the output voltage. That is not fed into the circuit, rather used by the external pulse pump formed by the Shottky diodes BAT48 D1 and D2. Shottky diodes D3 and D4 protect the connections against over-voltage and inversion at the input. ZD1 helps avoid over-voltage at the output and stabilizes the output voltage at 12 V.

The light emitting diode LED1 with R1 in the circuit serves to indication of output voltage when the switch is actuated only.

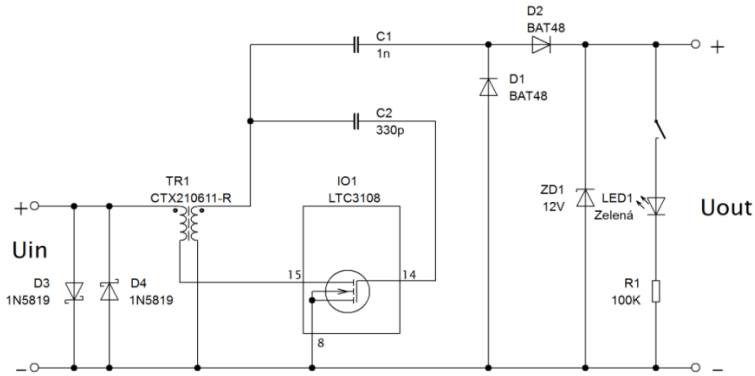


Fig. 3. Wiring diagram for the converter measured with LTC3108

The wiring in transformer employed also differs. The recommended transformer can be sourced either from the company Coilcraft LPR6235-752SML (1:100 Ratio) or from the company Würth S11100034 (1:100 Ratio). The transformer COILTRONICS - CTX210611-R was chosen, designed for powering CCFL luminescent lights in LCD displays with the run ratio of 1:125. The greater number of turns and the lower internal coil resistance makes this transformer ideal for applications in converter with integrated circuit LTC3108.

The measured converter was checked with respect to the dependency of the input voltage on the output current with the output voltage limited to 4V. Measurement, results are in Fig. 4 and Table 1.

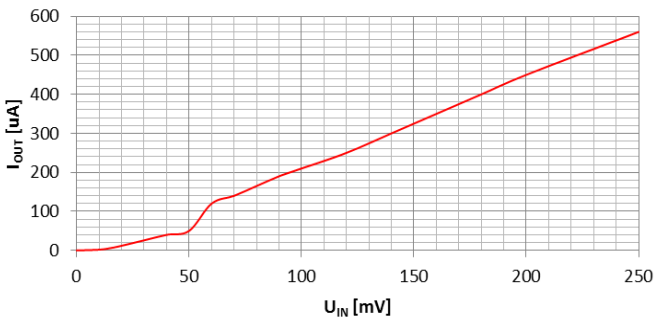


Fig. 4. Graph of input voltage on the output current with the output voltage limited to 4V.

Table 1. Dependency of the input voltage on the output current with the converter output voltage limited to 4V

U_{IN}	I_{IN}	$I_{OUT} (4V)$
[mV]	[mA]	[μ A]
0	0	0
10	2	2
15	4	6
20	6	12
30	12	26
40	16	40
50	20	50
60	30	120
70	33	140
80	40	165
90	50	190
100	60	210
120	70	250
140	80	300
160	100	350
180	110	400
200	130	450
250	170	560

U_{IN} - Converter input voltage

I_{IN} - Converter input current

$I_{OUT} (4V)$ - Converter output current

The current supplied from the converter is little lower, which is probably due to the higher turn ratio in the transformer. Original wiring respect to the turn ratio 1:100 and the turn ratio of the measured circuit is 1:125. The greater turn ratio enables the converter operate from lower voltage levels to ensure stable operation right from the input voltage of 6 mV.

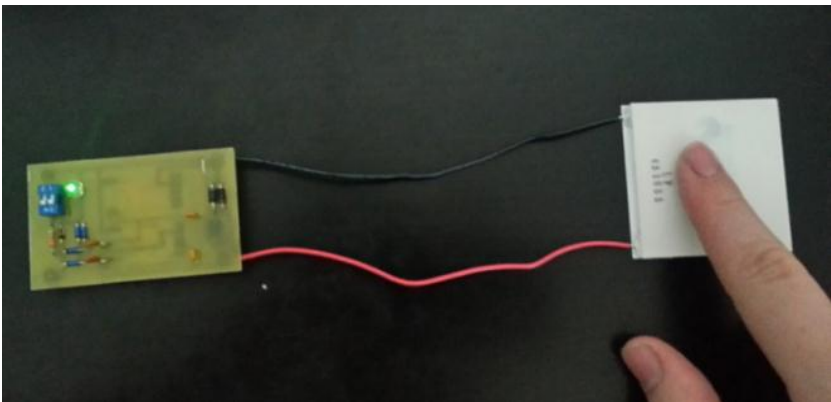


Fig. 5. The measured converter supplied with heat from human finger with the thermobattery TEG 450-200-45

The modified converter enables supplying the green LED using the temperature difference on thermobattery of approximately 0.1 K. Speaking in practical terms, this means that just one human finger set onto the thermobattery generates power sufficient to run the converter and light up the LED.

4 Conclusion

Ultra-Low Voltage Step-Up converter can be used to supply power into various low-consumption devices using thermobatteries from the voltage level of approximately 20 mV. In the converter there was used integrated circuit LTC3108 featuring the special transistor J-FET actuated basically from the voltage level of 6 mV and started about voltage level of under 20 mV. Converter with high quality thermobattery can works from very low difference of temperatures on the thermobattery as 0.1 K. Such low temperatures differences are very easy to achieve in practice in order to develop a power source with almost unlimited lifetime and capable of powering measurement or communication devices, for example, using just this low difference in temperature. Future scope is to develop converters differing by their switching transistors. There will be no more used integrated circuits as LTC3108, but different type transistors in order to create a converter using even lower operating voltage.

The results were published at the functional sample No. 016/27-06-2016_F.

Acknowledgment

This research was partially supported by the SGS grant from VSB – Technical University of Ostrava (No. SP2016/95) and by the project TUCENET (No. LO1404).

References

1. Thermogeneratoren / Seebeckelemente [online, cit. 2016-01-10]. <http://thermalforce.de/de/product/thermogenerator/index.php?uid=e00f7b7cfb2e445b2e399b9c55c3d6b0&ref=>
2. Generatormodule + Accessories [online, cit. 2016-01-10]. <http://thermalforce.de/de/product/module/index.php?uid=e00f7b7cfb2e445b2e399b9c55c3d6b0&ref=>
3. TEG 450-200-45 [online, cit. 2016-01-10]. http://thermoelectrics.de/de/product/thermogenerator/TG450-200-45S_.pdf
4. LTC3108 [online, cit. 2016-01-10]. www.linear.com/docs/28823
5. LTC3109 [online, cit. 2016-01-10]. www.linear.com/docs/29537
6. P. Mullen, J. Siviter, A. Montecucco, A.R. Knox, A Thermoelectric Energy Harvester with a Cold Start of 0.6 °C, 12th European Conference on Thermoelectrics, Volume 2, Issue 2, 2015, Pages 823–832

Electricity Production by a Small Hydro Power Plant – Statistical Inference

Martin Kral and Radomir Gono

Department of Electrical Power Engineering, FEECS,
VŠB – Technical University of Ostrava, 17. listopadu 15,
708 33 Ostrava – Poruba, Czech Republic
{martin.kral.st3, radomir.gono}@vsb.cz

Abstract. This paper deals with the dependencies of electrical energy produced by a small hydro power plant and daily outdoor temperature. Dependence was verified with help of static induction.

Keywords: small hydro power plant, temperature, statistical inference

1 Introduction

The current global trend is an effort to increase the share of renewable sources in power production. Among the most significant renewable resources belongs in this context also the hydroelectric plant. Territory of the Czech Republic, however with respect of its geographical position offers only a limited number of sites where it is possible to technically implement the new small hydroelectric plant for economically efficient use of water power. In the foreground is therefore a request to enhance the efficiency of the use of hydro-energy potential in the existing hydroelectric power stations. An essential basis for considering the possible reconstruction of the small hydroelectric plant (SHP) in economic terms, is the assessment of the amount of power produced.

This paper deals with the analysis of the measured data of produced electrical energy by a small hydro power plant Podhradí, which is located in drink water system. The vast majority of SHP in water systems is used for the utilization of the excess energy of the water, which would have been without the benefit of the "lost". This usage of the excess energy of the water is beneficial for reduction of pressures in the pipeline of water supply systems. Thanks to the measured power produced, thus flow of the water in the water-supply system we can observe the quantity of water used. The measured data are processed for two different seasons. Specifically in terms of the period September 2014 and March 2015, that is, autumn and spring. Thanks to the analysis in the two above mentioned periods, we can monitor the use of water in the different mentioned periods.

This research was partially supported by the SGS grant from VSB - Technical University of Ostrava (No. SP2016/95).

© M. Krátký, J. Dvorský, P. Moravec (Eds.): WOFEX 2016, pp. 25–30.

VŠB – Technical University of Ostrava, FEECS, 2016, ISBN 978-80-248-3961-5.

2 STATISTICAL INDUCTION — LINEAR REGRESSION

As already described above, power production is tied with the consumption of water in the water-supply system of SHP Podhradí. We gathered that this water consumption is associated with outdoor temperatures, and this correlation (regression) we wanted to investigate. We analyzed this regression for the autumn and spring. Outdoor temperatures are available from the archives in a limited sampling. There are only an average daily temperatures available. The average daily temperatures were compared with the average daily power production.

The context between the daily temperature and daily power production in autumn.

An important issue concerning linear regression is investigation, whether the data do not include the influential points. Examination of the influential points we made using X-Y scatter chart (XY scatter plot). The dependent variable (Y) here was made by power, no-dependent variable (X) was the average outdoor temperature.

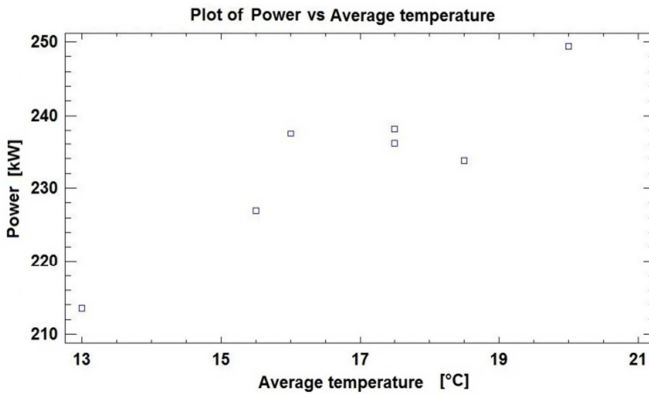


Fig. 1. An XY scatter chart for the autumn term

From the X-Y scatter chart (Fig. 1.) it can be seen that the data used in the linear regression does not contain influential points. Based on the visualization we chosen the linear regression model type.

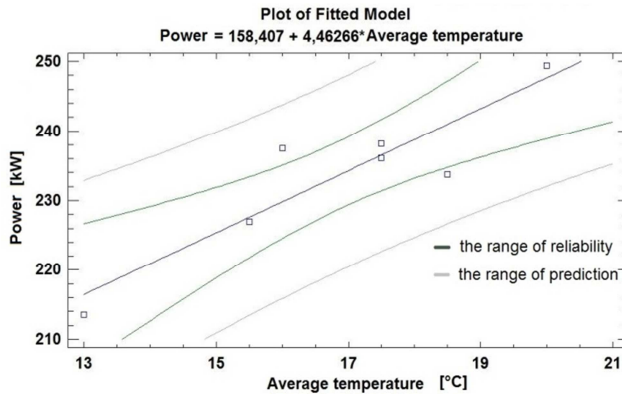


Fig. 2. The range of reliability and the range of prediction, $\alpha=0.95$.

Table 1. Point estimates of the coefficients and standard errors of coefficients of the regression line

Parameter	Estimate	Error	P-Value
Intercept	158.407	15.3801	0.0001
Slope	4.46266	0.905383	0.0044

Numbers described earlier in the Table 1. describe the estimated regression line, so called the balancing line. This linear line is:

$$Y = a + b \cdot X \quad (1)$$

According to the P-values of partial t-tests, we can consider the significance of the regression coefficients, which are for the absolute and also for the linear term $\ll \alpha$, we can not delete from the regression equation any term.

By the Table 2. it is possible to assess the suitability of the selected model.

Table 2. Analysis of Variance

Source	Sum of Squares	Mean Square	P-Value
Model	614.532	614.532	0.0044
Residual	126.471	25.2942	
Total (Corr.)	741.002		

Correlation Coefficient = 0.910673, R squared = 82.93 %

From the values of the test set out above, it is evident that the P-value for the Analysis of Variance is $\ll \alpha$, linear relationship between produced power and outdoor daily temperature exists. Index of determination R^2 (R squared) shows that 82.93 % of the variables is explained by the regression model, the rest of the unexplained remains, this index gives an indication of the suitability of the determination of the model used. Evaluation of assume for use of the linear regression model we did by the assessment of the residues.

Assumptions of the linear regression model:

- the normality of residues,
- zero mean value of residues,
- zero covariance of residues.

Verification of the normality of residues

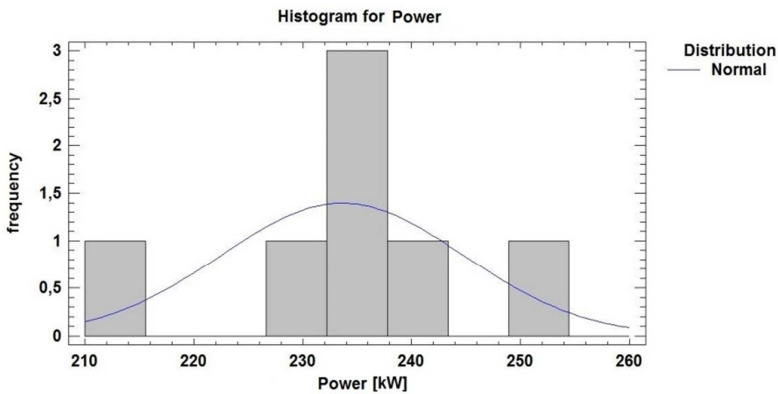


Fig. 3. Histogram of residues

In the Fig. 3. can be seen the histogram of residues.

Table 3. Verification of the normality of residues

Test	Statistic	P-Value
Chi-Square	5.57143	0.350177
Shapiro-Wilk W	0.938068	0.639338

From the values of the test set out above (Table 3.), it is evident that the P-value > 0.05, i.e. do not deny the null hypothesis of normality-residues.

Verification of the zero mean value of residues

Table 4. Verification of the zero mean value of residues

Sample mean	233.635
Sample median	236.159
t-test	
Null hypothesis	0
Alternative	not equal
Computed t statistisc	55.6227
P-Value	2.26769 E-9

This test does not deny that it is a zero mean value of the residues, as you can see (Table 4.).

Verification of zero covariance of residues

We verify zero covariance residues by using only the exploratory chart (Fig. 4.). The chart is showing the correlation field residues towards produced power. If it is not apparent to any functional dependency, remote observation or "alternation of marks" (alternating positive and negative residues), it is considered a zero covariance.

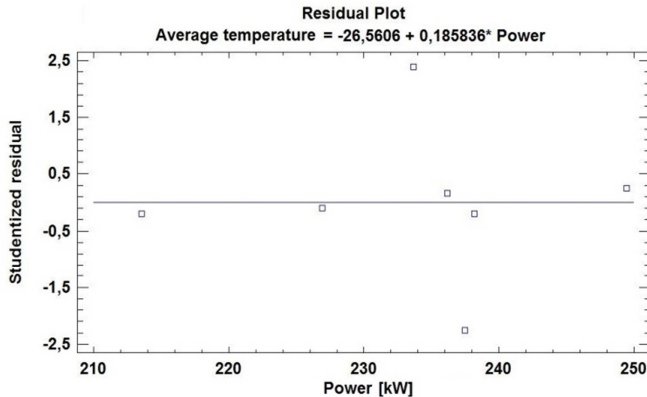


Fig. 4. Verification of zero covariance of residues

In the picture there is no functional dependency, therefore we considered covariance zero residue.

The context between the daily temperature and daily power production in spring.

Relation between the daily temperature and power production in the spring was evaluated using the same procedure that is seen above in the evaluation for the autumn period. The results of both evaluations are listed at the end of this post.

3 Conclusion

In this paper we focused on static induction. We wanted to verify the connectedness (regression) of the electrical energy produced by a small hydroelectric plant on the outdoor temperature. These two quantities are linked together, because power generation of the small hydro power plants located in the water supply system increase with consumption of water during the warmer days. We have carried out both regressions of the annual period. For a successful examination of regression we performed first data examination using the XY (scatter) chart (Fig. 1.), if there are influential points that would disrupt the evaluation.

In autumn we defined dependency of produced electrical energy on the outdoor temperature as: Produced power = $158.407 + 4.46266 * \text{the average temperature}$ (Fig.

2.). This dependency is almost linear, since the correlation coefficient 0.91 came out. It is also seen that it is explained by the relatively large amount of the variance of the dependent variable 83 %. For the test of the linear regressive model data also correspond.

In order to prove a regression in the spring time there are negative assumptions already at the beginning. When we conducted the examination, whether the data do not include the influential points, data were uneven and there were influential data points. These influential points have then influence on the evaluation of regression. We could not delete the influential points because they are in our material, and it was not caused by errors of measurement. The measured data in the spring time are measured during the month of March. Our assumption of influence of outdoor temperature on produced electric power for this cold month does not apply. The most of population is inside their houses and that is why the outdoor temperature do not affect water consumption. Following testing confirmed the assumption. The data from the spring season, therefore, did not satisfy the test for detection of influential Analysis of Variance. Further, these assumptions were not met for the linear regression: the normality of residues and verification of zero covariance of residues. Therefore, it is not possible to express the dependency of the produced power on the outdoor temperature for the spring period.

The results were published at the functional samples No. 017/28-06-2016_F, 018/28-06-2016_F and 019/28-06-2016_F.

Acknowledgment

This research was partially supported by the SGS grant from VSB – Technical University of Ostrava (No. SP2016/95) and by the project TUCENET (No. LO1404).

References

1. Briš, R., Litschmannová, M. Statistika I. (pro kombinované a distanční studium. Ostrava: VŠB – TU Ostrava, 2004, 341 s.
2. Litschmannová, M. Statistika I. (řešené příklady, studijní opora pro výuku Statistiky I.). Ostrava: VŠB – TU Ostrava, 2007, 195 s.
3. Litschmannová, M. Statistika (průběh přednášek). Ostrava: VŠB – TU Ostrava.
4. Šimonová, L. Průvodce programem Statgraphics, část 1. Ostrava: VŠB – TU Ostrava, 2006, 36 s.
5. Šimonová, L. Průvodce programem Statgraphics, část 2. Ostrava: VŠB – TU Ostrava, 2006, 70 s.

New Concept of Hybrid Off-grid System in Technology Centre of Ostrava

Petr Kubalík

Department of Electrical Power Engineering, FEECS,
VŠB – Technical University of Ostrava, 17. listopadu 15,
708 33 Ostrava – Poruba, Czech Republic
petr.kubalik@vsb.cz

Abstract. The off-grid system is a networks without connected to the external grid with possibility of autonomous mode operation. These Off-grid systems use mostly renewable sources which are complemented by the emergency source for case bad weather conditions. Among the most common alternative sources may include for example photovoltaic systems, wind power plants, co-generation units, hydrogen technology and power generators. This combination of individual's sources is possible to called as multisource system with a combination of a storage devices and smart control system.

Keywords: Off-grid, Multisource, Storage Device, Load acid traction battery, LiFePO₄.

1 Introduction

At the moment TCO is supplied predominantly from the grid and the excess electrical energy produced (usually from photovoltaic panels) is fed back into the grid. Our goal is to create a hybrid off-grid system or partial off-grid power supply system for the entire technology center. This system should serve as a power balancer Grid, which will be surplus electricity stored in batteries, and if necessary it will be possible to supply power back to the grid.

2 Energy power sources of TCO

TCO energy mix has many sources of a different character and characteristics. From a direct connection to the distribution network, to cogeneration units burning process gases (produced in TCO), alternative sources of solar energy, hydrogen fuel cell technology, UPS diesel generator and UPS units. A summary of these sources and their power ratings are given in Table 1.

This paper was supported by the project LO1404: Sustainable development of ENET Centre, Students Grant Competition project reg. no. SP2016/128, project LE13011 and project TACR: TH01020426 .

© M. Krátký, J. Dvorský, P. Moravec (Eds.): WOFEX 2016, pp. 31–36.
VŠB – Technical University of Ostrava, FEECS, 2016, ISBN 978-80-248-3961-5.

Table 1. Type and nominal power of energy sources of TCO

Power source	Nominal power
micro cogeneration unit with Stirling engine	11 kW
photovoltaic power plant	22.5 kWp
UPS (only backup)	33 kW
fuel cells	50 kW
diesel generator (only backup)	100 kW
cogeneration unit	100 kW

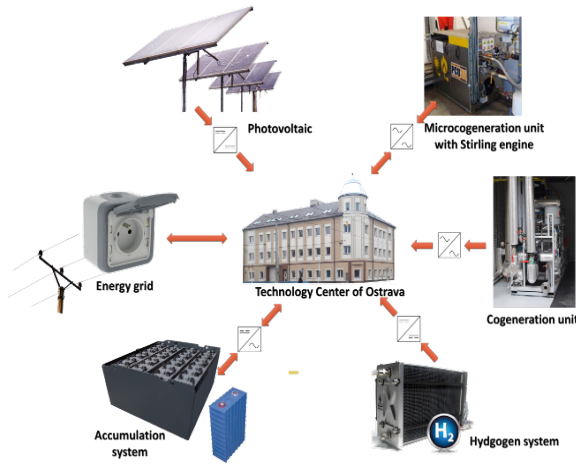


Fig. 1. Energy power source of TCO

The electrical energy produced in energy resources TCO is either used directly in the centre or power is stored in batteries. An alternative method for storing electric energy produced is used in electrolyzers for hydrogen production, storage and re-use in fuel cells for generating electricity. [1,2,3]

Table 2. Specific types of accumulators and their properties

Type	Lead acid traction	LiFePO ₄	Pure lead
title	<i>Hawker water less</i>	<i>Tundersky</i>	<i>Hawker XFC</i>
voltage	2 x 400 V	2 x 360V	408 V
capacity	930 Ah	100 Ah	115 Ah
power	744 kW	72 kW	47 kW
usable power	600 kW	57 kW	28 kW
durability	1000 cycles	3000 cycles	1200 cycles
voltage per cell	2 V	3,2 V	12 V

3 Measuring in the TCO

The aim of my thesis is create a hybrid off-grid system with a power balancer distribution network. Therefore it was necessary to measure the capacity of the batteries and find in what condition they are.

Because the lead-acid batteries don't use for more than two years it was necessary to determine their condition. For charging and discharging of the batteries are nowadays used in parallel converter U10 and U11 about 75 kW. Converter control is performed in LabVIEW when it set the charging or discharging current of the accumulator bank.

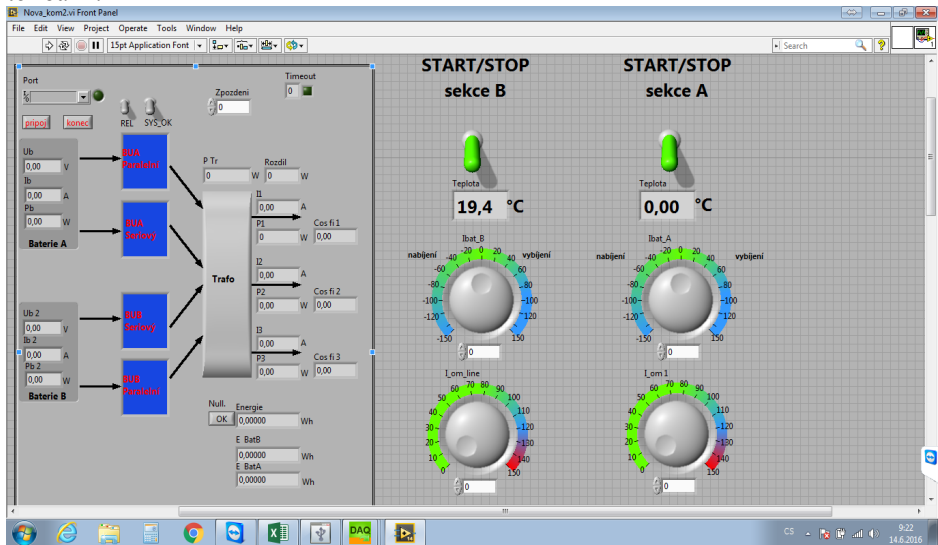


Fig. 2. Control panel for control of power convertors

During measurements charging and discharging characteristics is progressed according to the discharge characteristics provided by the manufacturer. Where it is important to maximize battery life when don't discharge lead-acid battery below 80% depth of discharge (DOD) which corresponds to a 1.82 V per cell, and 364 throughout the storage bank. During our measurements we convertors switch off when reaching 370V. With regard to illegal overflows into the grid were carried cycling accumulators. When a higher power ratings while exterminating one section and the second section reloading. Measurements were performed on fully charged batteries in the steady state.

Charging the batteries was performed on fully discharged batteries with a DOD of 80%. Voltage in vain after stabilization ranged between 385 V and 390 V. The batteries have been recharged always constant stream, which we set LabVIEW. The measurement is repeated for a certain current value in the range from 10 to 70 A.

Since we were interested in and the battery capacity we carry out and discharge cycles. The batteries are fully recharged and the voltage stabilization in vain ranged between 425 V and 427 V. The discharge was performed with a constant current set.

During these measurements were recorded energy used for charging and discharging batteries, power consumed from the grid voltage and currents on the batteries. All this data is stored in a file at one-minute intervals. From our the measured values, we also have compiled charts.

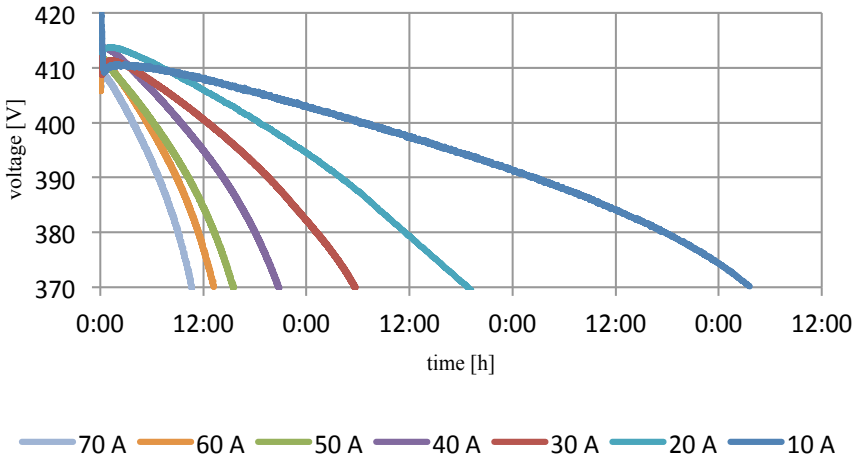


Fig. 3. Discharge characteristics of lead-acid traction batteries

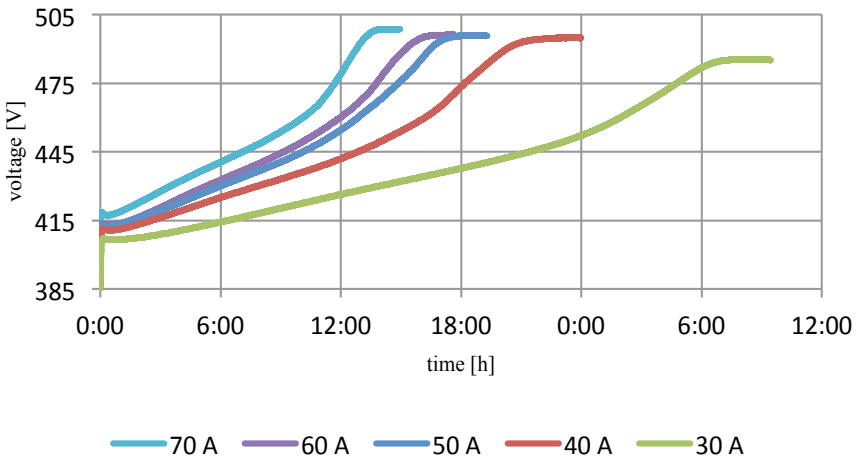


Fig. 4. Charging characteristics of lead-acid traction batteries

The measuring results show that these batteries are still in good condition. When discharging current 10A, when the discharge lasted 73.5 hours, these batteries supplied to the grid 367.5 kWh.

It was also necessary execute the initialization charging LiFePO₄ batteries and execute formatting. These batteries were charged with a constant current to 0.05 C. And then it was through discharged the resistive load to determine their capacity. From the measurement results it is evident that these batteries exceed the declared capacity. The measured capacity of LiFePO₄ battery is in the range from 105 to 110 Ah. After the complete coupling DC / DC convertor U60 testing is performed LiFePO₄ batteries. Setting the parameters of the convertor are in Automatic Control System (ACS). In Figure 5 and 6 are measured charge-discharge characteristics of LiFePO₄ batteries. In testing, we cannot currently continue because we have a problem with ACS.

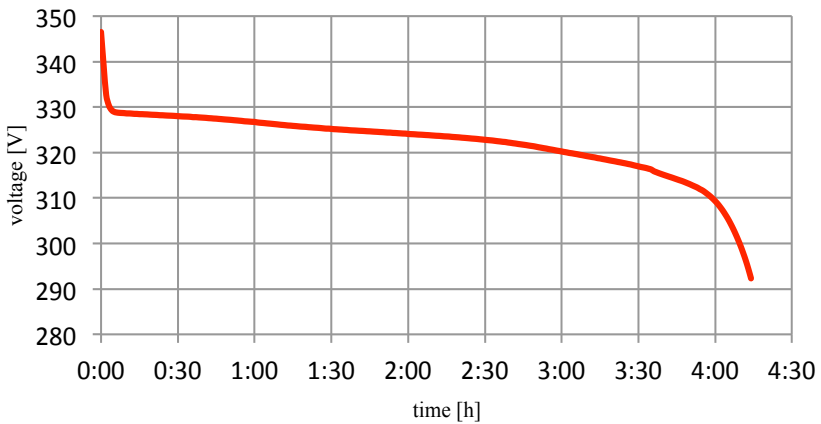


Fig. 5. Discharge characteristics of LiFePO₄ batteries

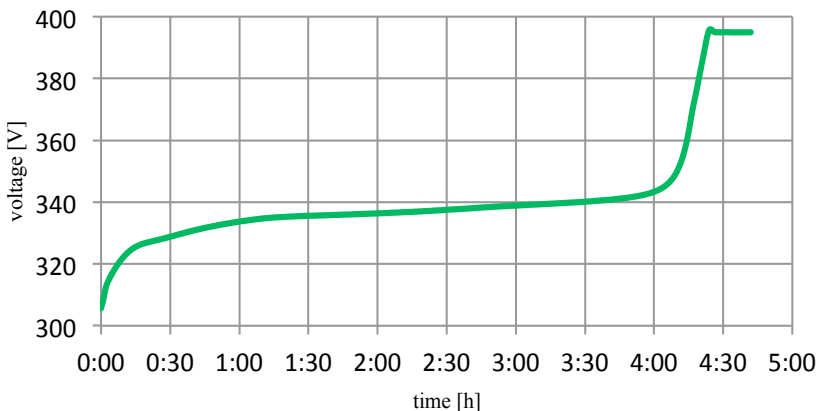


Fig. 6. Charging characteristics of LiFePO₄ batteries

4 Conclusion

The goal of my thesis is research and development of hybrid off-grid system in TCO. Now a day is in TCO experimental measurements and testing of operating conditions. After completion of this testing will be needed to start it and ACS convert the whole system to autonomous operation.

5 References

- [1] Misak S, Prokop L, Bilik P, Krejci P. Evaluation of power quality in off-grid power system. *Komunikacie* 2015;17(1A):71-6.
- [2] Kubalík, P., Misak, S., Stuchlý, J., Vřamba, J., & Uher, M. (2014, May). Suitable energy storage in Off-Grid systems. In *Environment and Electrical Engineering (EEEIC), 2014 14th International Conference on* (pp. 345-349). IEEE.
- [3] Kosmak, J., Misak, S., & Prokop, L. (2015, May). Power quality dependence on connected appliances in an off-grid system. In *Electric Power Engineering (EPE), 2015 16th International Scientific Conference on* (pp. 423-428). IEEE

The Impact of Electric Vehicles on Distribution Network

Oliver Marcincin

Department of Electrical Power Engineering, FEECS,
VŠB – Technical University of Ostrava, 17. listopadu 15,
708 33 Ostrava – Poruba, Czech Republic
oliver.marcincin.st@vsb.cz

Abstract. This paper deal with charging stations for electric cars. It contains estimation of the electrical energy amount needed for charging electric vehicles, connecting of charging stations for electric cars to the distribution network and basic concept of charging stations with minimal impact on the supply network. Also include practical measurement on small charging station in region of Ostrava.

Keywords: Charging station; electric vehicle; distribution network; charging current; stored energy, grid.

1 Introduction

Electromobility is currently perhaps the most commonly discussed terms of automotive technology. Low number of vehicles operated in the Czech Republic is also corresponding to the low density of charging stations, most of which are also operated an amateur way. In case of expansion of electric vehicles will also increase the demands on the construction of an adequate network for charging stations.

For these purposes seems to be very advantageous to combine the emerging system of infrastructure charging stations with renewable power sources. Such as energy produced by the sun with the possibilities of accumulation and its subsequent delivery to the uniform charging infrastructure [3].

2 Connecting of Charging Stations for Electric Cars to the Distribution Network

If the number of electric vehicles operators will increase, it will be necessary to build sufficiently dense network of charging stations, to ensure not only the range of electric cars in its area of operation, but also allows occasional crossing at medium distances up to about 300 km [2]. This requires the deployment of charging stations along major roads within a maximum of 50-60 km.

2.1 Estimation of the Electrical Energy Amount Needed for Charging Vehicles

The amount of electric power consumption is estimated based on expected performance structure of the vehicle and their fail safe distances. The energy needed for an average range 120 km of electric vehicles in three distinctive categories gives us Tab. 1. The three basic categories of electric vehicles, which are characterized by different engine power, were chosen for analysis. Category "A" - a small urban vehicle with traction engine power about 10 kW, category "B" - standard vehicle lower middle class with performance of traction engine about 30 kW and category "C" - a higher class with performance of traction engine about 80 kW. Range is in all three categories averaged 120 km. The energy required for operation of the vehicle was determined simplified calculation based on basic physical equations for calculating the engine performance of engine vehicles (Tab. 1) [3].

Table 1. Energy and Sampling Intensity in Terms of Charging Electric Vehicles in Selected Categories for a Single Driving cycle

Category of Vehicle	Stored Energy of the Vehicle (Range 120 km)	Charging Current		
		t = 8 Hours	t = 4 Hours	t = 0.5 Hour
A	13.3 kWh (Wak(A))	5.1 A	10.2 A	81.6 A
B	30.0 kWh (Wak(B))	10.2 A	20.4 A	163.2 A
C	41.1 kWh (Wak(C))	14.2 A	28.4 A	227.2 A

In a similar way, was calculated charging current for stored energy and expected nominal voltage of 350V battery, for three different charging times. These times are set for probable modes:

- t = 8 hours - long-term (e.g. night) charging electric vehicles by low current at full capacity battery,
- t = 4 hours - charging electric vehicles during the day (e.g. a vehicle parked during working hours around lunch breaks or business meetings),
- t = 0.5 hours - so-called fast charging as during a long journey stops.

2.2 Estimation of the Amount of Electricity Needed to Charge the Vehicles in the Region of Ostrava

The basic premise solutions and designing active networks of charging stations is to create conditions for adequate consumption of electrical energy in repetitive cycles, which can be linked to the cycles of the daily load diagram distribution network.

The second prerequisite for successful application of active power stations in the area, is its positive effect on the network. The solution must be open enough to allow even the use of non-traditional and renewable energy sources [5].

Types of electric vehicles operated in the Ostrava region in accordance with the breakdown (Tab. 1) could look under Tab. 2.

Table 2. Expected Number of Electric Vehicles in the Ostrava Region in the Period 2020 – 2025.

Category of Vehicle	Number of Vehicle (%)	Number of Vehicle (pc)
A	70	17 500 (NA)
B	25	6 250 (NB)
C	5	1 250 (NC)

Based on this distribution is calculated energy stored in vehicles for daily cruising range of 120 km. It correspond to daily charging cycle. Stored energy in all vehicles:

$$\begin{aligned}
 W_{ak(celk)} &= N_{(A)} \cdot W_{ak(A)} + N_{(B)} \cdot W_{ak(B)} + N_{(C)} \cdot W_{ak(C)} = \\
 &= 17500 \cdot 13300 + 6250 \cdot 30000 + 1250 \cdot 41100 = \\
 &= 471.6 (MWh)
 \end{aligned} \tag{1}$$

Actual status of distribution network in Ostrava region is assumed in terms of its design and in terms of possible sources. And it would be not enough to cover the requirements of electromobility in a certain period of time. The solution shows the necessity of using active charging stations.

3 Impact of Small Charging Station in the Ostrava Region

The purpose of this measurement on small charging station is to uncover possible undesirable influences on distribution network. Measure is realized on charging station in campus of VSB Ostrava by analyzer BK-ELCOM ENA 330. All outputs are evaluated by relevant program BK-report. For measure are used vehicles of category “B” with engine power about 30 kW (based on dividing in chapter 2). Electric vehicles are charged in three periods because of BK-ELCOM ENA 330 memory.



Fig. 1. Connected measuring device in distributor.

First period start from 23.11.2015 to 3.12.2015. Results are showed in pictures below (Fig. 6, Fig. 7, Fig. 8). Next periods will be evaluated later on.

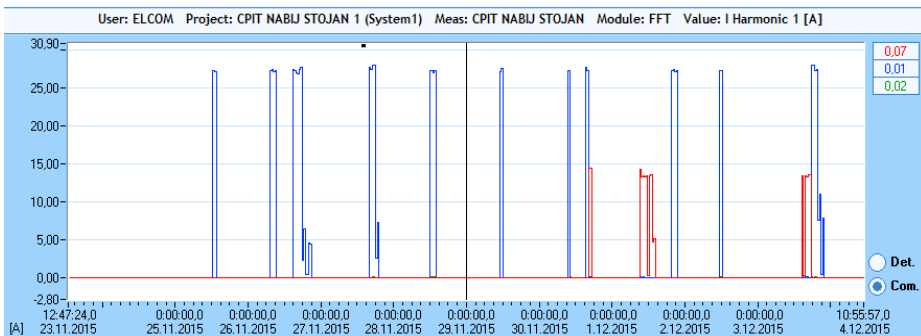


Fig. 2. Load current during charging of electric vehicle.

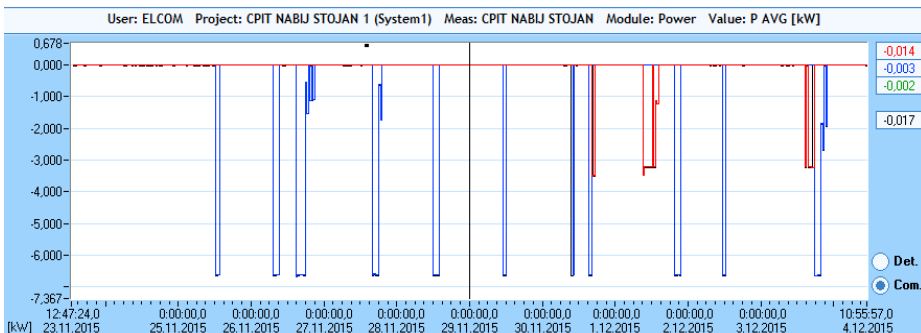


Fig. 3. Power load during charging of electric vehicle.

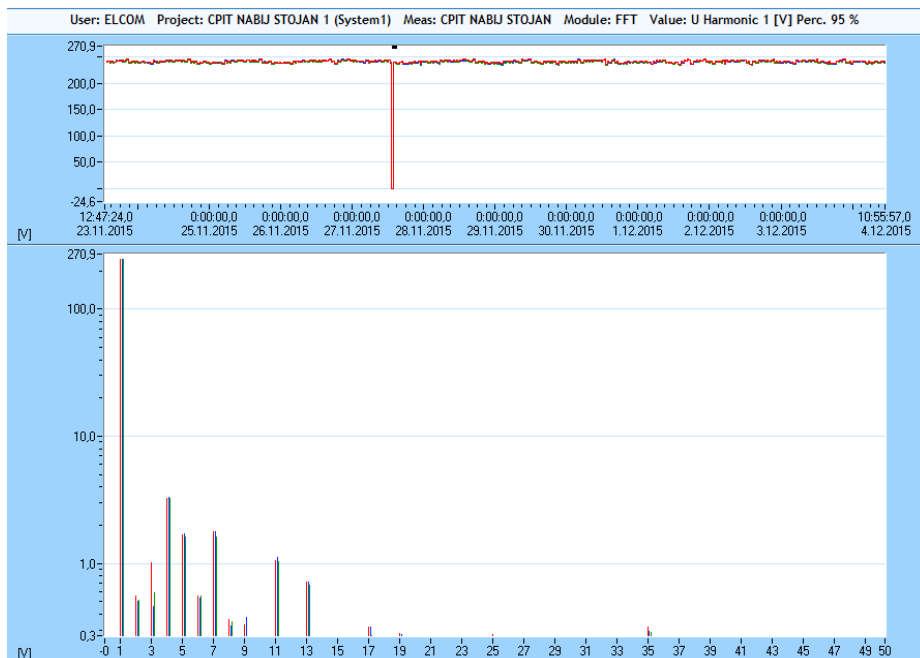


Fig. 4. FFT Analyse of harmonics and interharmonics.

Vehicle with engine power about 30 kW is charged with a charging power approximately 7 kW. For charging of electric vehicle with a low traction power is used "long term" method with low charging currents. As was expected, charging ongoing smoothly without signs of negative effects on the distribution network. It is caused by low power engine of vehicle and low parameters of charging currents.

In future is expected higher density of charging stations and electric vehicles with higher power engine. In this case is also expected higher undesirable influence.

4 Conclusion

The paper deals with charging of electric vehicles and possible undesirable influence on distribution network in the case of massive increase. Also deals with active charging stations, which are not yet used in Ostrava region, so there is no experience with the operation and impact on the local power grid.

The purpose is to create such an active station, which is in equilibrium with the opportunities and needs of daily load diagram at the site. Therefore, the whole calculation is based on the needs for continuous cycling of energy in one day.

Expected higher amount of electric vehicles in future and possible unwanted influence on distribution network, appears necessity to use active charging stations for electric cars. Especially in places with high density such as cities and also in areas that are likely to be implemented in infrastructure between the larger sites, creates

new possibilities for managing the operation of distribution network by active charging stations.

Acknowledgements

This research was partially supported by the SGS grant from VSB - Technical University of Ostrava (No. SP2016/95).

References

1. R. BENGER, R. HEYNE, A. HAUBROCK, and H.P. BECK. Sustainable Fast Charging Stations for Electric Vehicles. In: 5th, International Renewable Energy Storage Conference. Berlin: IRES, 2010, pp. 223-225. ISBN 978-3-00-037648-1.
2. E. CHLEBIŠOVÁ, J. KYZEKOVÁ, AND H. SVOBODOVÁ. Marketing Study of the Electric Vehicles' Diffusion. In: 11th International Scientific Conference on Electric Power Engineering. Brno: EPE, 2010, pp. 807-811, ISBN 978-80-214-4094-4.
3. H. BAREŠOVÁ, Vliv nabíjecích stanic elektromobilů na elektrickou síť. Ostrava, 2011. Diploma thesis. VŠB-TU Ostrava. Z. Medvec.
4. Asociation of Automobile Industry. Mapy nabíjecích stanic, J. Marušinec, 2015. Available at: <http://www.asep.cz/interaktivni-mapa-dobijecich-stanic>
5. The Ministry of the Interior of the Czech Republic. Motor Vehicle Register. MVCR, 2012. Available at: <http://www.mvcr.cz/clanek/centralni-registr-vozidel-865510.aspx?>

Simulation of Transfer of Energy by Software EMTP-ATP on Power Converter

Tomáš Mozdřeň

Department of Electrical Power Engineering, FEECS,
VŠB – Technical University of Ostrava, 17. listopadu 15,
708 33 Ostrava – Poruba, Czech Republic
tomas.mozdren.st1@vsb.cz

Abstract. This paper deals with analysis of power generating units installed within the technological centre laboratories in Ostrava-Vítkovice. These power supply units will help build the dynamic model of the technological centre using the EMTP-ATP software. The current configuration of the simulation is based on the block diagram containing all the unconventional sources of electric power.

Keywords: Simulation; technological centre; software; AC bus; DC bus; power converter

1 Introduction

The current demand for sources of electric power keeps rising and the existing deposits of fossil fuels are unfortunately exhaustible. This is the reason for accelerated efforts towards search and application of new renewable energy sources for mankind. The reasons mentioned above then supported evolution of the ENET project dealing with research on utilisation and application options covering non-traditional sources of energy in the laboratory of the technological centre in Ostrava – Vítkovice ("TCO") since the year 2010.

2 Connections and Technologies at TCO

For a simplified circuit diagram of TCO, refer to the Fig. 1. Individual energy sources have been divided and drawn into technological blocks for legibility purposes; these blocks are formed per basic functioning principles of the sources or with respect to the assumed relevance to other technologies within the TCO. The primary supply of power to TCO and the power outlet from the centre are ensured in terms of connection to the local distribution system. The backbone source of electric output from TCO is the co-generation unit with a synchronous generator with the power output of 100 kW cooperating with a gas piston combustion engine. This unit is supplied with gas fuel in volumes of 250-450 kg per hour (depends on the fuel composition). The topology of electric power distribution system of TCO comprises the main AC bus with the option to connect onto

the backup AC bus. The whole distribution system at the centre has been designed and built as fully subsistent with potential opportunity to switch into island operation mode with $3 \times 230/400\text{V}$ and with the optional power supply to the adjacent industrial buildings. Installation of various accumulation systems forms a vital part of the whole TCO. This accumulation is ensured with various types of batteries that are always linked to the main direct-current bus DC 400V . The bus enables distribution of electric power into the individual parts and components of the system using reversible inverters. The links between direct-current buses and the standard network buses are made of power semi-conductor inverters combined with transformers and chokers $\text{TR1}+\text{TL1}$ and $\text{TR2}+\text{TL2}$ to enable two-way transfer of power between AC and DC buses. If the centre is disconnected from the grid supply and its internal accumulation capacity has been fully depleted, it is still fitted with a diesel generator and the UPS unit to ensure stable supply of power and safe shutdown of all technologies, especially the thermal cracker.[1], [2]

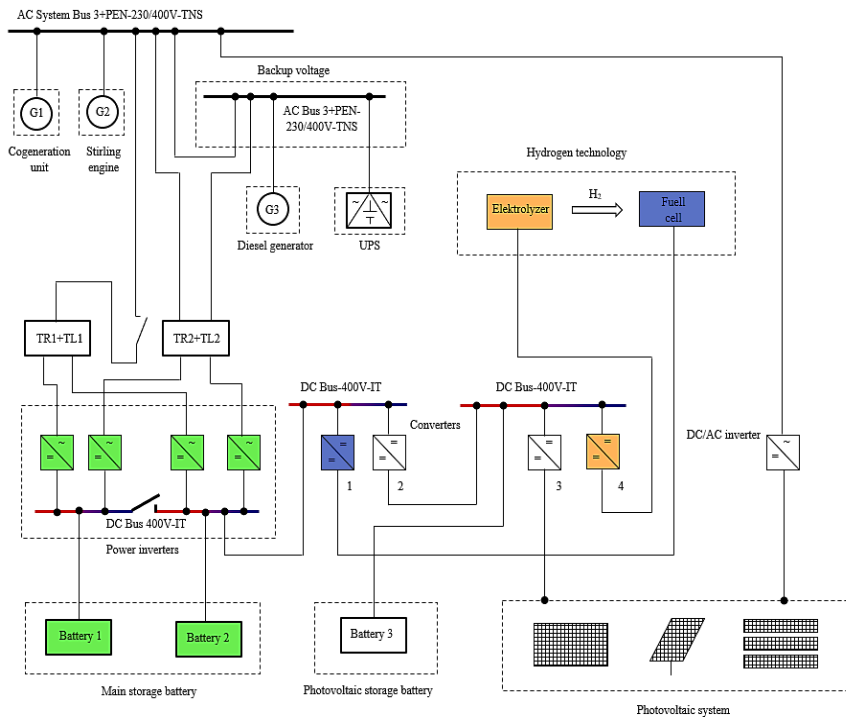


Fig. 1 Connection of individual power sources in TCO to technological blocks

3 Simulation of transfer of energy on power converter

The following simulation of the energy transfer is performed by software EMTP-ATP, wherein the simulation is used connection DC source (battery), controlled DC / DC converter controlled by the DC / AC inverter and then connect to the AC network. In this simulation are monitored flow of power between the AC and DC power source.

The values for the simulation are shown in Table 1.

Table 1 Information about sources for simulation

Information about sources					
DC source		3 phase source		Load 16 kW	
U_{DC}	400 V	U_{fm}	327 V	R	1000 Ω
TRI period	2.5 μ s	PWM period	1 ms		
		Constant	0.6		

$$R = \frac{U^2}{P} = \frac{400^2}{16000} = 1000\Omega \quad (1)$$

Overall scheme sources which has been modified and simplified in blocks shown in Fig. 2.

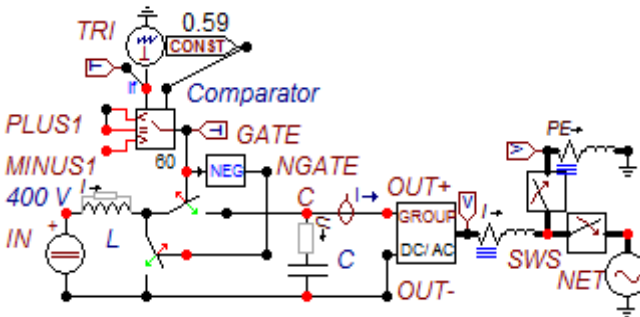


Fig. 2 Adapted schema for transfer of energy

Energy balance of DC power supplies for $t = 50$ ms at 1 microsecond step of the calculation is as follows. Performance DC source is the product of the DC voltage source (400 V) and the current DC power source. For the case is related to the following:

$$P = U_{DC} * I \quad (W) \quad (2)$$

For selected load $R = 1.2 \Omega$ on the side of AC power source is based on approximately $P = 171$ kW. It gives unloaded DC voltage $U_{DC} = 707$ V, and initially oscillates between values of 1,400 V and 0 V.

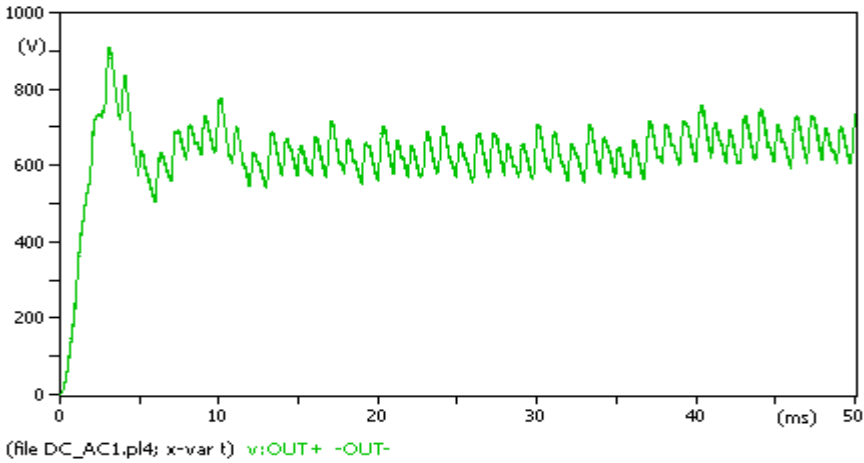


Fig. 3 Voltage waveform on a DC source

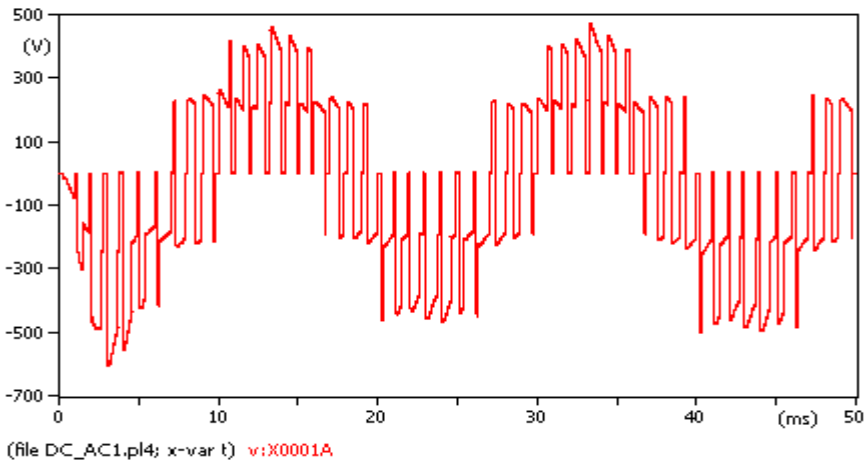


Fig. 4 Voltage waveform on the AC power supply

For zero power transmission is needed to set the values of R and L . In this case the values of $R = 0.01 \Omega$ and $L = 0.1 \text{ mH}$, and also have to debug the DC/AC converter, wherein the required output voltage of the inverter $U_{fm} = 327 \text{ V}$ is required set the value of the DC voltage source to twice the voltage at the output of the inverter, thus $U_{DC} = 655\text{V}$. For input DC voltage of 400 V is fed into the grid power approximately 68 kW and losses on the AC side of the approximately 4 kW .

4 Transient

For the above-mentioned load $R = 1.2 \Omega$ on the AC side is in this case solved transients. Transient arises disconnecting the supply to the network and connect this burden, everything is done in a time of $t = 60$ ms. Thus, the performance drops from 789 kW to 162 kW.

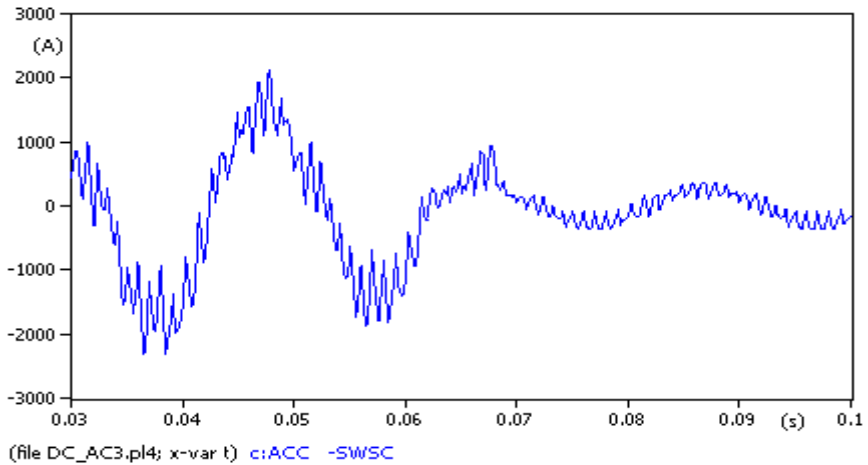


Fig. 5 Current waveform in phase A at the output of the DC/AC inverter

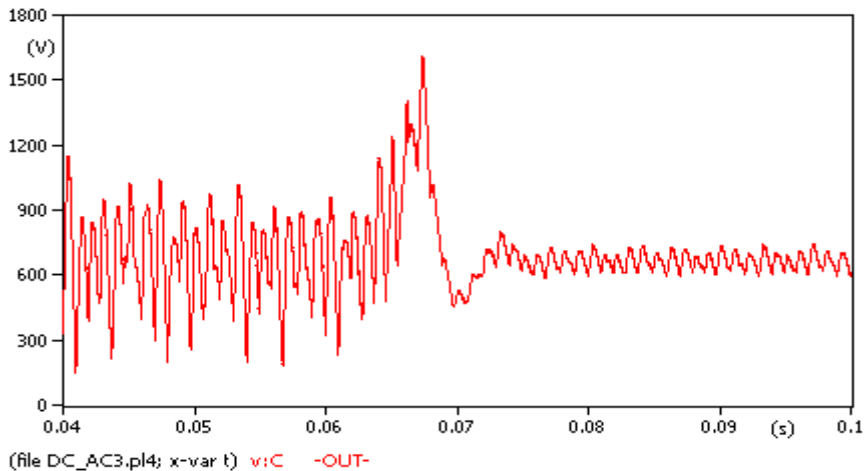


Fig. 6 The output voltage from the DC/DC converter

5 Conclusion

This paper describes connection of the TCO using the block diagram that shows all the power sources within TCO laboratories. The second part of this paper provides a description of the software used for simulation of transfer of energy on connection of components and power converter. The next part shows the existing transient, which occur on output side on converter, after to disconnect supply from network.

Acknowledgements

This research was partially supported by the SGS grant from VSB-TU Ostrava (No. SP2016/95) and by the project TUCENET (No. LO1404).

References

- [1] D. Minarik, S. Rusek and R. Gono: "Implementation of accumulation technologies of electric energy to hybrid energy system", Electric Power Engineering 2012, ISBN 978 - 80 - 214 - 4514 - 7
- [2] T. Mozdren, S. Rusek, R. Gono, D. Minarik, P. Moldrik: "The Input Analysis of Parameters and Expected Operation Modes of Energetic Technologies in Technological Centre ENET", Electric Power Engineering 2015, ISBN 978-1-4673-6787-5
- [3] H. K. Hoidalen: "Introduction to ATPDraw ver. 5.", 2016, [cit. 2015-22-1]. Available at WWW: <<http://atpdraw.net/docs/ATPDraw%20v5%20Presentation.pdf>>
- [4] F. Milano: "Power System Modelling and Scripting", University of Castilla, Spain 2010, ISBN 978-3-642-13669-6
- [5] H. Bluhm: "Pulsed Power Systems-Principles and Applications", Germany 2006, ISBN 978-3-540-26137-7
- [6] T. Degner, A. Engler, O. Osika: "Modelling of Distributed Energy Resources with ATP-EMTP", European ATP-EMTP Users Group Meeting and Conference, 2005, Warsaw, Poland

Description of Measurements on Biogas Stations

Ladislav Novosád

Department of Electrical Power Engineering, FEECS,
VŠB – Technical University of Ostrava, 17. listopadu 15,
708 33 Ostrava – Poruba, Czech Republic
ladislav.novosad.st@vsb.cz

Abstract. This article focuses on the description of the project dealing with the analysis of biogas stations. Its aim is to gain a full picture of the operation of biogas stations and an outline of their possible use in 22kV networks. Within this project, several basic measurements of electrical quantities at BS were carried out. Therefore, the article describes the method of measurement, individual biogas stations and the processing of measured data. The final part of this paper deals with the analysis of course data obtained, with special regard to voltage, current, active power and reactive power data.

Keywords: biogas station; power analysis; measurement database; black out; co-generation units; distribution grid

1 Introduction

The distribution networks (DN) have experienced the rise in volumes of electric power generated by renewable energy sources (RES) over the recent years. Vast majority of these sources work within the distribution network on decentralised basis and this practice brings a lot of new problems. Such problems are due to the very principle employed by certain sources. The dependency on weather conditions among photovoltaic and wind power plants is a typical example. The question is how to ensure safe and stable operation or even development of such systems. That is why it is necessary to know the characteristics of particular RES, also including the biogas stations (BS). The reason above is therefore addressed by this paper with respect to an operation of BS and provision of details referring to the variability of output produced over time. From these results, it is then possible to further explore the possibilities of cooperation between the renewable electrical energy sources which include the aforementioned photovoltaic (PVP) and wind power plants. Or to monitor other options of the use of BS, such as electrical network (EN) support services or sources involved in the renewal of electrical system after a black-out.

Acknowledgement: This research was partially supported by the SGS grant from VSB-TU Ostrava (No. SP2016/95) and by the project TUCENET (No. LO1404).

© M. Krátký, J. Dvorský, P. Moravec (Eds.): WOFEX 2016, pp. 49–54.

VŠB – Technical University of Ostrava, FEECS, 2016, ISBN 978-80-248-3961-5.

2 Description of measurement

These requirements were accommodated by several long-term measurements conducted directly at the biogas stations. These BS are situated at three various locations within the Czech Republic, serving as both sources of electric power and heat

The measurement at each of the three biogas stations was conducted using the automatic digital measurement devices – the network analyser BK ELCOM ENA 330 and monitor distribution grids MDS-U(MDS10). This is a complete system for monitoring and analysing electric power quality. The devices were employed to record effective values of phase voltage and current in one-minute increments. The voltage readings were taken directly from the bus bars inside the BS main distribution board; the monitoring of current was performed using flexible Rogowski coils – AmpFLEX. The device then completed calculations of remaining values, such as the active or reactive power, as well as the apparent power automatically and saved these details in its internal memory.



Fig. 1. Demonstration of connection measurement equipment in the BS 1

The electric power generated by all three BSs is supplied to the main distribution board which is linked with a transformer station rated for 0.4/22kV, further connected to the 22kV distribution grid (DG). The measurement of electric values also involved the assessment of electric power quality in compliance with CSN EN 50160. The characteristic subject to assessment included mainly the magnitude and drops in voltage, the total harmonic distortion of voltage, flicker and voltage unbalance. The network analyser BK ENA 330 used in this case complies with the requirements focused on measurement equipment and the measurement procedure set forth by standards CSN EN 50160, CSN EN 61000-4-7, CSN EN 61000-4-15 and CSN EN 61000-4-30. [4]

2.1 Biogas station Hraničář-Loděnice

The first measurement was conducted at the BS located in Loděnice near Opava (BS1). The biogas station itself is situated within the premises of a piggery farming enterprise. The input raw material for the wet fermentation process is represented mainly by pig slurry and maize silage. This BS provides the installed electrical capacity of 1,090 kW. Transformation of biogas into electric power is handled by four co-

generation units. There are three identical compression ignition units delivering the output of 250 kWe and one spark ignition unit with the output of 340 kWe.

2.2 Biogas station Hodoňovice

Another measured BS was the one in Hodoňovice biogas station (BS2). This station forms a part of the collective farm nearby; this is also the point for supply of the input raw materials for fermentation. The main input raw material for wet fermentation at this BS is grass silage, wheat silage, maize silage and pig or cow slurry. This BS provides the installed electrical capacity of 1,186 kWe. Conversion of biogas into electric power is handled by two co-generation units with the electrical power of 549 kWe and 637 kWe. [1]

2.3 Biogas station Tošanovice

The last measurement was performed at Tošanovice BS (BS3). This BS also forms an immediate part of the collective farm enterprise dealing both with livestock and crops production. The extraction of biogas is also based on wet fermentation with the raw material represented by maize silage and farmyard slurry. These are supplied from the said collective farm enterprise. Electric power and heat are generated using three co-generation units (CGUs). The total installed electrical capacity of the BS is 750kW (2xKGG with the electrical power of 265kW and 1xKGG with the electrical power of 250kW).

3 Evaluation of measured data

The method described above yielded large amounts of data. The initial processing of these data was done using software that comes with the measurement equipment. Comprehensive waveforms of individual variables depending on time were created with this software. Furthermore, the data were exported and processed using MS Office Excel 2007. STATGRAPHICS Centurion XV.II was subsequently used for the statistical evaluation. [3]

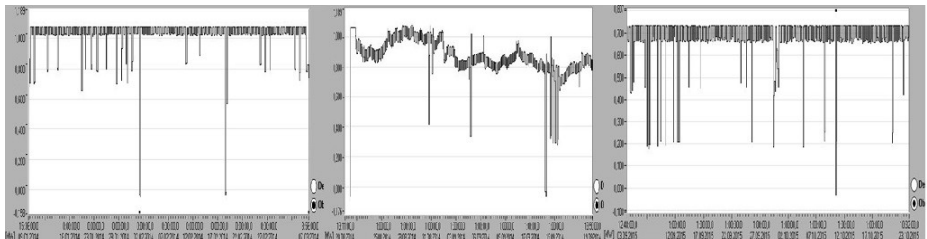


Fig. 2. Course of entire active power over the whole period observed at the location of BS1, BS2 and BS3

Fig. 2 demonstrate the course of the entire active power (P) from the all BSs measured. The total three-phase active power (P) is then equal to the sum of power ratings of individual phases ($P_1+P_2+P_3$).

The graphs of active power and the chart depicted here also show that the operation of all three BSs encountered black outs or drops in power supplied to the grid. All these BSs show basically the same nature of these drops in the power supplied or black outs, as the case may be. The total duration of these black outs or drops is almost negligible with respect to the total operation time, it ranges between approximately 3.5 to 73.7 hours, representing approx. 0.5–5.4 % of the total operation time of CGU in individual BSs (BS1–3). As far as this period is concerned, individual stations would suffer approx. 2.7–69 min of total power black outs (approx. 0.004 – 0.084 % of the total operation time of individual BSs). The stability of CGUs at individual biogas stations implies that the supply of electric power is stable and predictable. This is evident mainly during operation of BS 1 and BS 3. These two BSs operated in a fairly stable manner throughout the majority of measurement period, their active power ranged within values approximating the nominal values. The only unit showing larger fluctuation of the output active power was BS 2. However, this fluctuation was mainly due to the incorrect control of BS, i.e. the failure to obey procedures to feed the fermented material.

Another condition occurring during the operation more frequently than total black outs was the drop in supplied power, as mentioned above. As far as the nature of their course was concerned, these drops showed identical characteristics at all three BSs. These drops were characteristic for a reduction of the active power of around 100–350kW. The apparent major cause of these drops was represented by shutdown of one or more CGUs.

The dependence of produced active power and consumption of biogas also correspond to the above-described waveforms of active power supply. The following chart shows the record of BS1 consumption for a longer period of time. It displays the data from December 2011, when the BS1 was commissioned. The noticeable increases in gas consumption are caused by the gradual connection of other co-generation units. The station was first launched with two CGUs. After approximately two months of operation, the third CGU was connected and the last CGU was connected at the turn of 2012/2013. The shape of the curve shows the direct correlation with actual production of biogas (biogas consumption) and electricity production.

After studying the available operational logs and maintenance records recorded directly by a specific operation of a biogas station, we can conclude that the above power decreases are due to a number of the most common causes which include insufficient speed of biogas creation, unforeseen technical problems, ambient weather and climatic effects, scheduled technological downtime. [1,5]

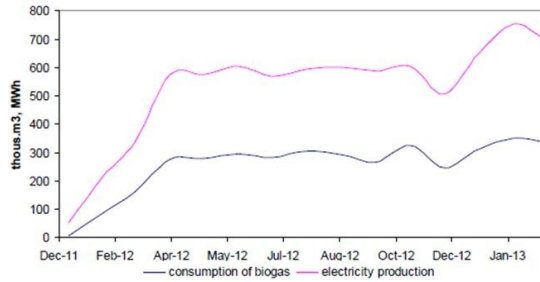


Fig. 3. Course of biogas consumption and electric power production for the whole biogas station

Table 1. Basic information of CGU operation

Basic Information of CGU Operation			
Basic information on power supply	BPS 1	BPS 2	BPS 3
Total measurement period (h)	1,361	693.1	1,197.97
Total period of decreased power supply (h)	73.7	3.5	46
Total period of full power failures (h)	1.15	0.25	0.045
Trouble-free operation (no black outs or power failures)	1,287.3	689.6	1,151.97
Full supply power failure	2	1	1

4 Evaluation of electric power quality

As already mentioned in the introductory part, each measurement conducted on particular BS was accompanied by evaluation of electric power quality in compliance with CSN EN 50160. The outcomes of measurement then imply that the network parameters such as the frequency, flicker and voltage unbalance complied with conditions given by the relevant standard and applicable to all three BSs subject to measurement.

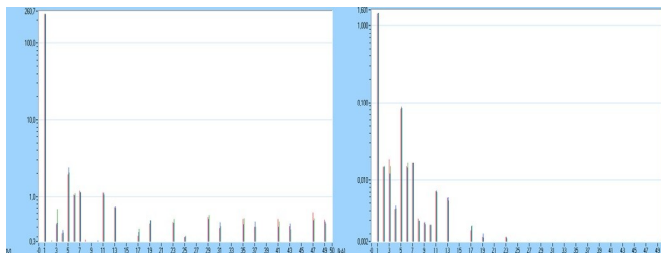


Fig. 3. Spectrum of harmonic voltage and harmonic current of higher levels with designated permitted limits in accordance with CSN EN 50160 – BPS2

The spectra of harmonics of higher degree and currents were almost identical for all the BSs measured. Figures 4 show the sample spectrum of harmonic voltage and spectrum of harmonic current of higher levels with designated permitted limits in

accordance with CSN EN 50160 applicable to BS 2. None of the limits were exceeded.

5 Conclusion

The aim of this paper was to find reminiscence in the course of power supplied from individual BSs or even to explain the causes of black outs with the attempt to suggest a way for their further elimination. The results obtained by measurement show the high reliability of electric power supply to the grid (the duration of black outs per BS is equal to approximately 0.0029 % of the operating hours). The supply of electric power from co-generation unit combusting biogas can be therefore generally described as very stable and also easily predictable as a renewable energy resource. The greatest impact on power supply is seen at quality, that is the lack of biogas supplied (percentage of methane CH₄ in biogas), strongly dependent on the quality of primary (organic) product. This problem is associated with the technical procedures during fermentation but the option to store the biogas produced in particular. Storage of biogas produced, i.e. keeping its stock for periods of insufficient production, relates to the volume of gas tank. The vast majority of existing BSs within the territory of Czech Republic has been designed for uninterrupted operation, i.e. the biogas produced is consumed by CGUs almost immediately

This paper also serves as a source of information about stability of output from co-generation units for further research. The research will deal with cooperation among other renewable resources of electric power (solar or wind power plants) and present an opportunity for stabilisation of the power supplied to 22kV grids. Another continuation of this work will be an attempt to create a virtual model of BS. The model will be built on the data obtained from previous measurements. Thus created model will be then combined with models of renewable energy sources and ES models created within the research of other projects. The aim will be to verify the theoretically possible types of collaboration of various sources with a distribution system.

6 References

1. L. Novosád, Z. Hradílek, "Power Analysis of Co-Generation Units at Biogas Station", Proceedings of the 16th International Scientific Conference on Electric Power Engineering (EPE) 2015 Dlouhá Stráň, 2015, ISBN 978-1-4673-6788-2
2. L. Novosád, Z. Hradílek, P. Moldřík, "Analysis of data measured in Tosanovice biogas station", ELNET 2015: 12th workshop : Ostrava, 24th November 2015, pp. 28-36
3. M. Dummer, M. Litschmannova, "Statistika I.". Statistika I. VSB – Technical university of Ostrava, 1997, 80-7078-496-2
4. Z. Hradílek, "Elektroenergetika průmyslových a distribučních zařízení," 1.vyd. VŠB – TU Ostrava. 2008. ISBN 978-80-7225-291-6.,p.315, 2008.
5. L. Novosád, Z. Hradílek, "Analysis of Energy Balances Three Biogas Stations in Czech Republic", Proceedings of the 16th IEEE International Conference on Environment and Electrical Engineering, 2016

Stray Currents Caused by Regenerative Brake in Electric Traction

Jiří Plaček

Department of Electrical Engineering, FEECS,
VŠB – Technical University of Ostrava, 17. listopadu 15,
708 33 Ostrava – Poruba, Czech Republic
jiri.placek@email.cz

Abstract. This paper describes the effects of currents brought about by electric traction. The main problem in DC electrified railways is electrochemical corrosion. The goal of this paper is to sum up basic theoretical knowledge from the given area. The paper describes the negative effects of regenerative brake in DC railway tracks. The most significant source of stray currents is a DC electrified railway track where rails are used as return conductors. In this case, part of the overall return current leaks into the ground. Stray currents occur especially in places where metal or reinforced concrete structures are insufficiently insulated from the ground. In this case, these devices can lead a significant part of the total current, with an intensity within tens of amperes. It is Based on Faraday's law, it can be deduced that within one year, DC stray current of 1 A causes electrochemical corrosion that leads to the loss of 9.1 kg of iron on each current output. Stray currents are currents which flow through a conductive environment (e.g. soil, water, buried devices). These stray currents come from electric devices which are insufficiently insulated from this environment, or the ground serves as a return conductor. Stray currents can be alternating or direct.

Keywords: Stray current, electrochemical corrosion, devices buried in the ground, ground current fields, anti-corrosion

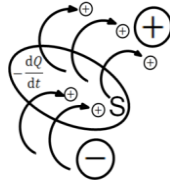
1 Introduction

There is a close link between the occurrence of artificially created ground current fields and the occurrence of stray currents. These are currents which leak into the ground when a conductor is insufficiently insulated from the ground, or when the ground is used by a device as a return conductor. These currents then form ground current fields, which are the most dangerous because they may lead to the corrosion of devices buried in the ground. DC currents always flow through places with the least resistance, spreading within long distances, according to soil conductivity, i.e. hundreds of metres to kilometres from the lines through which current is supposed to flow. This means that when soil conductivity is low, the area where these stray currents propagate is larger. On the other hand, if soil conductivity is good, stray current dispersion is not so significant.

Stationary current field distribution is characterised by the continuity equation. This equation states that the sum of currents flowing in and out through an enclosed

surface around a certain will manifest itself as a time change of the charge contained in this volume.

Just like Maxwell equations, this continuity equation is valid for all spatial points where J stands for a continuously differentiable function of the coordinates in (1) and ρ is a continuously differentiable function of the coordinates and time (2).



$$\oint_S \vec{J} \cdot d\vec{S} = \frac{-dQ}{dt} \quad (1)$$

$$\text{div} J = -\frac{\partial \rho}{\partial t} \quad (2)$$

$$\text{div} J + \frac{\partial \rho}{\partial t} = 0 \quad (3)$$

Fig. 1. Surface representation of the continuity equation [1]

For a stationary current field, it is possible to define $\text{div} J = 0$, because at any time interval, identical charge will flow in and out of any enclosed surface.

$$\oint_S \vec{J} \cdot d\vec{S} = 0 \quad (4)$$

In a stationary current field, the continuity equation may be defined in the form of the First Kirchhoff's Law.

$$\oint_S J \cdot ds = 0 = J_1 S_1 + J_2 S_2 + J_3 S_3 + \dots + J_n S_n = I_1 + I_2 + I_3 + \dots + I_n = \sum I = 0 \quad (5)$$

Equipotential surface

In an equipotential surface, potential has the same value in all of its parts. If charge is moved along any trajectory connecting two points in an equipotential surface, no work is performed by any electric field. This is implied in Relationship (6), which is shown here in its form for voltage.

$$U = \varphi_i - \varphi_f = -\frac{W}{Q} \quad (6)$$

If $\varphi_i = \varphi_f$ then $W=0$.

The equation shows that when a charged particle is moved along an equipotential surface, no work is performed by electric powers. This means that the vector E must be vertical in each point of the equipotential surface.

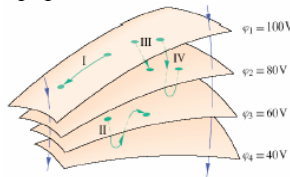


Fig. 2. Parts of four equipotential surfaces [1]

Fig. 2 shows several equipotential surfaces in an electrostatic field. When moving a charged particle from a starting point in Trajectories I or II, work performed by the power of this field is equal to 0, because as shown in the picture, both of these trajectories begin and end on the same equipotential surface. However, this is not the case

for Trajectories III and IV. When moving charged particles from a starting point to a final point along these trajectories, the work which is performed is not equal to 0 and its size is the same in both cases. The reason why it is identical is because at both starting points and both final points of both trajectories the potential has the same value.

2 Regenerative Brake

The process of transforming the kinetic energy of a traction vehicle back into electrical energy in the process of braking is referred to as regenerative brake. In this process, the traction electric motor works as a generator and the obtained electrical energy is used for the operation of traction vehicle. If needed, excess energy goes into the traction network, and the rest which is not used up is thwarted by resistors. Regenerative brake cannot be used in cases when electricity is not immediately consumed. If it was impossible to thwart excess electric energy, voltage in the traction network would rise high above nominal values and insulation would be damaged. On the other hand, if energy storage devices such as flywheels and super-capacitors are used in the traction network, the energy is stored inside them until reaching their capacity.

Since current EU legislation is aimed at encouraging companies to decrease energy consumption, some newly developed systems make it possible to return the energy produced by regenerative brake back into the AC distribution network. Several such projects have been completed so far: Bilbao Underground and ADIF (1500 V) in Spain, Bielefeld, Germany (750 V), as well as a project in Brussels, Belgium. So far, this solution has proved to be highly efficient.

The system makes it possible to return energy obtained by the regenerative brake of electrical vehicles back into the distribution system. It has to be noted, though, that traction substations must be equipped with a DC/AC converter between trolleys and the secondary side of the transformer. Another great disadvantage is that the lifespan of the device is 30 years (i.e. considering the price of electrical energy on the market, the payback period is rather long).

Energy obtained by regenerative brake is considered peak energy and it must comply with network standards and regulations. It leads to network interferences (voltage is increased irregularly). The price for returned electrical energy is a commercial one, i.e. it varies every hour, and if the contracted quantity is not provided, the contractual relationship is subject to electrical energy trading regulations.

3 Measuring Regenerated Energy Thwarted in Resistors of an LF Tram

To evaluate the use of energy obtained by regenerative brake, it was necessary to adjust the process of energy measurement in the Vario LF vehicle. In this way, it was possible to measure thwarted energy in resistors. Data which was obtained from the

recording units is listed in the following table. Measurements from Nov 14-18 2014 show that for a Vario LF2 tram, 60% of all regenerated energy was thwarted in resistors. According to measurements from Dec 8-15 2014, only 25% of regenerated energy were thwarted in resistors.

Table 1. Values recorded by measurement units

Date	2014/11/14-18	2014/12/8-15
Consumed energy	770,714	781,771
Regenerated energy	209,380	213,067
Total energy	561,334	568,704
Average consumption	1.2639	1.2667
Distance	444,138	448,976
I. chassis (thwarted energy)	157.6	683.1
II. chassis	70.6	186.4
III. chassis	133.3	463
Total thwarted energy	346.0	1,317.0
Average thwarted energy/km	0.44	0.23
Total regenerated energy/km	0.30	0.70
Thwarted energy (%)	60%	25%
Regenerated energy (%)	40%	75%

4 Measuring Regenerated energy on a Selected Segment of a Traction System

The segment which was selected for the measurement is part of Ostrava City tramway system. The whole system is 66.7 km long and the chosen segment was located on a one-way track between the Zátíší and Vřesinská loops on the only inter-city tram track in the Ostrava region.. The length of the segment was 9,030 m.

The track segment between the Zátíší and Vřesinská loops is powered by two traction substations, Vřesina and Dolní Lhota. Under normal conditions, the segment is powered in a different way than when the measurement was performed. For this reason, short circuit tests needed to be done first, to ensure good short-circuit conditions on the powered segment, and an alternative power source was used. During the time of the measurement, the segment was powered by a substation.

4.1 Measuring Regenerated Energy on a Selected Track Segment

To ensure maximum efficiency, suitable locations were chosen near the track, on which it was possible to perform the measurement.



Fig. 3. Regenerated energy measuring sites on the Vřesinská - Zátíší tram track

The immediate values of regenerated power supplied into the traction power network by the traction vehicle on different measuring sites are shown in the picture above.

Table 2. Measuring regenerated energy: immediate current values recorded on location A, before the tram reached location C

Measurement	I a	I b	I c
1	-275.16	-213.695	-245.488
2	-266.484	-204.364	-228.546
3	-256.689	-196.357	-220.897

After it reached measuring point C, the tram changed kinetic energy into electrical energy (i.e. it regenerated energy), and then this traction electrical energy was consumed after measuring point A, where a starting tram was located. The regenerated energy was consumed and immediate current values were recorded at individual measuring points.

The recorded current values show that in energy regeneration (i.e. supplying energy) into the traction network, stray currents start spreading. Otherwise all the recorded current values on the individual locations would correspond to current losses and value sequence from location C to A would be kept (i.e. current values would decrease due to resistance).

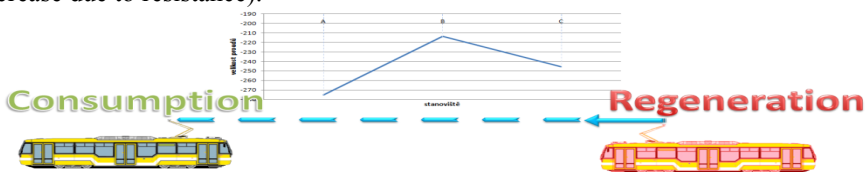


Fig. 4. Recorded current waveforms during tram regenerative brake on the individual measuring points

5 Conclusion

This paper deals with energy regeneration and measuring currents on different locations of the traction system. Recorded current values are then used to demonstrate the effects of electric traction on devices which are buried in the ground.

Measurement was performed and values of current which leaves the traction substation and flows through the individual measuring points were recorded. Current values were recorded for a certain time period. Afterwards, a graph of regenerated energy was created. Both the recorded waveforms and the graphs show a strong influence of stray currents. This is due to the fact that a different source of power supply was used during the measurement (the Dolní Lhota substation was turned off at that time). This resulted in the occurrence of strong stray currents near the powered track segment. It occurred because of the great length of the segment without return cables. The goal of this paper was to sum up and present the most important theoretical information which has to do with this issue, i.e. to briefly introduce the topic of returning regenerated energy into the traction network and to point out that stray currents may occur. In the future, the author is planning to investigate ways in which this regenerated energy can be used. Measurement results are applicable in real life.

6 References

- [1] FEYNMAN R. P., LEINGHTON R. B., SANDS M.: Feynmanovy přednášky z fyziky s řešenými příklady 2/3, 2001 Havlíčkův Brod: Nakladatelství Fragment, 806 s., ISBN 80-7200-420-4
- [2] PALEČEK Josef: Napájení jednofázové vozby Českých drah z hlediska elektromagnetické kompatibility. Vyd. 1. Ostrava: VŠB - Technická univerzita Ostrava, 2000, 98 s. ISBN 80-707-8791-0
- [3] V. KOLÁŘ, J. PALEČEK, T. MLČÁK, “Vliv provozu vodní elektrárny Lipno na kvalitu elektrické energie v souvislosti s trakčním odběrem,” (The Influence of the Lipno Hydro Power Plant Operation on the Quality of Electric Energy in Connection with Traction Consumption) Electric Power Engineering 2012, Brno, 2012
- [4] V. KOLÁŘ, R. HRBÁČ, Measurement of ground currents leaking from DC electric traction, 15th International Scientific Conference on Electric Power Engineering (EPE) 2014, p.p. 613-617, ISBN: 978-147993806-3, Brno, 2014
- [5] ČSN EN 50122-2, Drážní zařízení - Pevná trakční zařízení: Část 2: Ochranná opatření proti účinkům bludných proudů, způsobených DC trakčními proudovými soustavami, Červenec 2001, Praha: Český normalizační institut, 2001.
- [6] ČSN EN 50122-1 ed.2, Drážní zařízení-Pevná trakční zařízení-Elektrická bezpečnost, uzemňování a zpětný obvod: Část 1: Ochranná opatření proti úrazu elektrickým proudem, Listopad 2011, Praha: Úřad pro technickou normalizaci, 2011.

Influence of Light Sources on Human Circadian Rhythms

Karel Sokanský, Richard Baleja, and Tomáš Novák

Department of Electrical Power Engineering, FEECS,
VŠB – Technical University of Ostrava, 17. listopadu 15,
708 33 Ostrava – Poruba, Czech Republic
baleja.richard.st@vsb.cz

Abstract. The article deals with examining light sources used in households from the point of view of their potential influence on circadian rhythms. Nowadays, there are lots of different types of light sources available on the market with different light colours. An inadequate choice of the colour of the light source can result in worsening visual comfort, which can lead to disturbing circadian rhythms. When choosing light sources, it is necessary to take into account the purpose of the room for which the lights are chosen. Especially, it is a question whether LED sources with similar quantitative and qualitative characteristics have stronger influence on circadian rhythms than classical light sources or not.

Keywords: circadian sensitivity, circadian rhythm, luminous flux, correlated colour temperature, LED sources.

1 Introduction

This article was inspired by discussions which have been appearing more and more recently. Their main theme is the question whether LED sources used in households have a greater influence on human circadian rhythms in comparison with other light sources such as compact fluorescent lamps, incandescent and halogen light bulbs. In some media, there were even commentaries that LED sources can cause cancer. So we tried to answer the following question. If we take light sources with approximately the same luminous flux and correlated colour temperature, which are used the most often to light households, and if we multiply their radiance spectra by the curve of the spectral sensitivity of human sight controlling the circadian rhythm C , we should get relevant information about which light sources have the greatest and the least influence on circadian rhythms. This comparison was done for four types of light sources used in housing premises. It is an incandescent light bulb, a halogen bulb, an LED filament and a compact fluorescent bulb.

2 Choice of light sources

Human circadian rhythms are influenced by the spectral composition of the radiance of a light source, the intensity of radiance and the time during which a person is exposed to this radiance. The spectral composition of radiance is defined by the correlated colour temperature of a light source; this means that by changing the correlated colour temperature, it is possible to influence the human circadian rhythm. For example, light in shades from white to blue wakes up human body and so it prevents it from a comfortable sleep. From a long-term perspective, these light sources have a bad influence on production of melatonin – a sleeping hormone.

The choice of the colour temperature is connected with the choice of the level of illuminance. This dependence is described in Kruithof curve which is in the figure 1 and which describes the dependence between the intensity of illuminance and the colour temperature of the source.

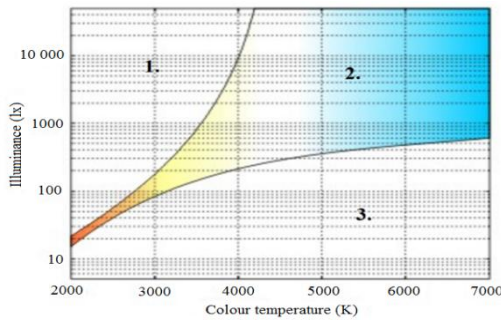


Fig. 1. Kruithof curve – the influence of colour temperature and illuminance on the feeling of visual comfort [6]

The Kruithof curve can be divided into three parts, down from top, there are these areas:

1. Upper part – The area of the feeling of flare and chromatic distortion (happens very early with low colour temperatures)
2. Middle part – The area of a pleasant feeling from the lighting (visual comfort), it is clear that especially cold light but also day light require high intensity of the light.
3. Bottom part – The area of the feeling of insufficient lighting. Because of reasons mentioned above, sources with low colour temperature are compared in this article first of all. [4] [6]

When choosing light sources for comparison, the light sources used in lighting systems in housing premises, where people are the most often, were preferred. They are children's rooms, living rooms and bedrooms. In these rooms, light sources called "warm" are used the most often because consumers prefer visual comfort to visual performance there when using relatively low illuminance. Therefore, light sources with correlated colour temperature from 2700 K to 3000 K, colour rendering index superior to 80 and luminous flux around 400 lm were chosen for comparison.

Table 1. Light and electrical parameters of light sources for testing

Light source	LED lamp	Compact fluorescent lamp	Halogen bulb	Incandescent bulb
Luminous flux [lm]	420	430	405	420
Correlated colour temperature [K]	2800	2700	2700	2700
Colour rendering index [-]	≥80	≥80	100	100
Power input [W]	4	8	30	40
Power factor [-]	0,54	0,57	0,99	0,99

3 Behaviour of circadian receptors

Nowadays, the question of the influence of blue light on human organism has been discussed more and more. The organ of sight not only transmits visual sensations but also influences human circadian rhythm (a biological clock) and provides an organism with information when it is a day and when it is a night. However, scientists thought for a long time that both visual sensations and the distinction of light and darkness are provided by the same retina cells (rods and cones). After a series of experiments, it was discovered that circadian rhythms are controlled by other cells – photosensitive ganglion cells. These cells are connected with hypothalamus which controls the biological clock of the organism what is connected with a excretion of hormone melatonin. The series of experiments proved that these cells are the most sensitive to blue light whereas the visual system of cones is sensitive mainly to yellow-green light.

For illustration, melatonin is a sleeping hormone which influences human day-night cycles. The production of melatonin in the pineal gland is controlled by the biological clock in the brain. The first one to discover this information was the professor Helena Illnerová. Besides that, circadian rhythm influences the cycle of physiologic processes, activity of brain, hormone production, cell regeneration and other physiologic processes. [5]

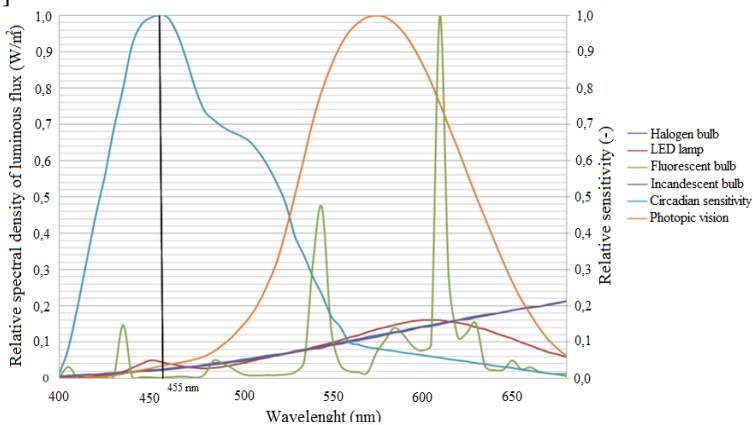


Fig. 2. Spectra of radiation of light sources, spectral sensitivity of human sight controlling circadian rhythm and the curve of sensitivity of photopic vision [3]

The ganglion cells are the most sensitive to the blue light at the wave lengths from 450 nm to 482 nm with the maximum sensitivity at the wave length 455 nm. For a visual image of how individual spectra intervene in the spectral sensitivity curve of human sight controlling circadian rhythm, this curve with measured spectra of assessed light sources was drew into a graph, see figure 2, with highlighting the maximal sensitivity at the wavelength 455 nm. [1] [2]

4 Description of measurement and calculation of the influence of measured spectra on circadian rhythms

To compare the influence of individual light sources on circadian sensitivity, it was necessary to measure spectral radiation of light sources so that they were comparable with each other. The spectra of individual sources were measured in an Ulbricht sphere to ensure the same conditions for all light sources. A spectrophotometer JETI Specbos 1211 was used.

With the help of the programme JETI LiVal, the measured spectra were transferred into the table editor Excel. In Excel, the spectra (curves) were depicted into one graph together with the curve of spectral sensitivity of human sight controlling the circadian rhythm C_λ and the curve of spectral sensitivity of photopic vision V_λ , see figure 2. These curves are displayed from 400 nm to 680 nm, which is the range in which circadian receptors are the most sensitive.

For comparison of the influence of individual light sources on the function of circadian receptors, individual spectra of measured light sources were transferred by the curve of spectral sensitivity controlling the circadian rhythm C_λ . By adding these values according to formula (1), we got the final integral transmission of the chosen light source transferred by circadian sensitivity. The same thing according to formula (2) was used to get the final integral transmission transferred by the sensitivity of photopic vision V_λ . Final transfer functions of chosen light sources, which are transferred by circadian receptors, are in the figure 3. To describe the influence on circadian rhythms, so-called relative transfer of radiant power transferred by circadian sensitivity compared with radiant power transferred by photopic sensitivity of human eye according to formula (3) was used. This assessment was based on assessing so-called S/P ratio, which is used to assess changes of influences of light sources between scotopic and photopic vision.

$$C = \sum \phi_{(\lambda)} \cdot C_{(\lambda)} [W/m^2] \quad (1)$$

C – final transfer function of chosen light source between wavelengths 400 nm and 680 nm transferred by circadian rhythms

$\phi_{(\lambda)}$ - relative spectral density of luminous flux of light source at a given wavelength

$C_{(\lambda)}$ - relative sensitivity of circadian receptors

$$P = \sum \phi_{(\lambda)} \cdot V_{(\lambda)} [W/m^2] \tag{2}$$

P –final transfer function of chosen light source between wavelengths 400 nm and 680 nm transferred by sensitivity of photopic vision

$\phi_{(\lambda)}$ - relative spectral density of luminous flux of light source at a given wavelength

$V_{(\lambda)}$ - relative sensitivity of circadian receptors

$$\frac{C}{P} ratio = \frac{C}{P} \cdot 100 [\%] \tag{3}$$

$\frac{C}{P}$ ratio –Relative transfer of luminous flux transferred by circadian sensitivity to luminous flux transferred by photopic sensitivity of human eye

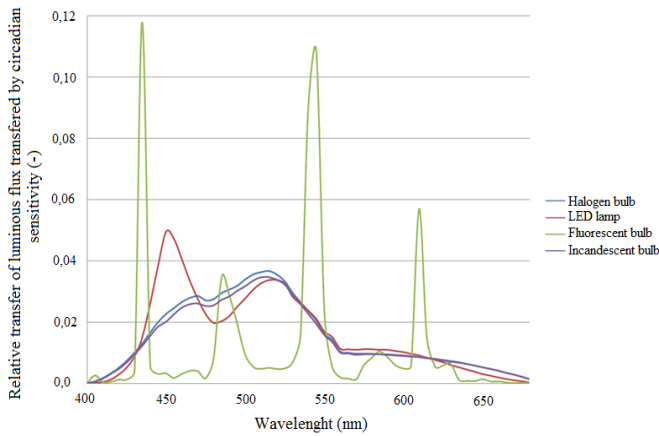


Fig. 3. Final spectral transfer of chosen light source transferred by circadian sensitivity

The Tab. 2 shows counted values of the final relative transfer of luminous flux transferred by circadian sensitivity to luminous flux transferred by photopic sensitivity of human eye. Final transfer values differ only slightly although it is necessary to draw attention to the fact that if sources with different correlated colour temperature were used, final values would differ more.

As it was mentioned, ganglion cells are the most sensitive to the wavelength 455 nm. Because of that, spectral density of luminous flux at this wavelength was also compared for each light source. The values are shown in the Tab. 3.

Table 2. Final relative transfer of luminous flux transferred by circadian sensitivity to luminous flux transferred by photopic sensitivity of human eye

Light source	$\frac{C}{P}$ ratio
LED lamp	35,11%
Halogen bulb	33,66%
Incandescent bulb	32,67 %
Compact fluorescent bulb	24,67 %

Table 3. Relative spectral density of luminous flux transferred at the wave length 455 nm

Light source	Relative spectral density of luminous flux transferred at the wavelength 455 nm [W/m ²]
LED lamp	0,047
Halogen bulb	0,025
Incandescent bulb	0,023
Compact fluorescent bulb	0,002

From the point of view of evaluating the influence of the contents of blue light at the wavelength 455 nm, where the effect of light transfer on circadian trains is the highest, it is possible to state that LED diodes have the highest effect, see Tab. 3.

5 Conclusion

On the basis of above mentioned comparison, we came to the conclusion that even though the radiance spectra of light sources used in housing premises are very different, we can expect that their influence on circadian rhythms does not vary too much. The peaks in areas of maximal sensitivity of circadian sensors produced by LED lamps and compact fluorescent lamps are not so energetically important to have a significant influence on exciting circadian receptors, compared to classical warm sources. Our pilot measurement implies that an LED lamp has the greatest influence on circadian rhythms. However, it is not distinctively higher than with light bulbs. The least influence has from this point of view compact fluorescent lamp, see Tab. 2. [2]

6 References

1. T. Novák, B. Socha, Z. Carbol, and K. Sokanský, "Luminance evaluation of LED indoor luminaires for workspaces lighting," 13th International Scientific Conference Electric Power Engineering, Brno, 2012.
2. A. Brüning, F. Hölker, S. Franke, W. Kleiner and W. Kloas. "Impact of different colours of artificial light at night on melatonin rhythm and gene expression of gonadotropins in European perch" *Science of the Environment*, Volume 543, February 01, 2016, pp: 214-222
3. G. Brainard, et al., "Action Spectrum for Melatonin Regulation in Humans," *Journal of Neuroscience* 21, pp. 6405-6412, 2001.
4. D. Gall, "Die Messung circadiener Strahlungsgrößen," Ilmenau.
5. W. van Bommel. "Incandescent replacement lamps and health," *Light and Engineering*, Volume 19, Issue 1, 2011, pp: 8-14.
6. R. G. Davis, and D. N. Ginthner. "Correlated color temperature, illuminance level, and the kruithof curve" *Journal of the Illuminating Engineering Society*, Volume 19, Issue1, 1 January 1990, pp:27-38.

Modeling of Cogeneration Units

Michal Špaček

Department of Electrical Power Engineering, FEECS,
VŠB – Technical University of Ostrava, 17. listopadu 15,
708 33 Ostrava – Poruba, Czech Republic
michal.spacek.st2@vsb.cz

Abstract. This article deals with general modelling of cogeneration units. It provides substantial information about cogeneration units. Development of cogeneration units has experienced an evident boom over the recent years. These are significant sources of both heat and electric power. That is the reason for seeking the fastest and the cheapest method to design a cogeneration unit with optimal performance. The fastest and still the cheapest method is modelling, as described by this article. It shows a model of a cogeneration unit with the electric power of 401kWe and the heating power of 549kWh (401kWe/549kWh).

Keywords: accumulation; cogeneration unit; modeling; regulation; electric power; heating power; electrical efficiency.

1 Introduction

When designing a cogeneration unit for any type of technology requires the electrical efficiency assessment. Another decision shall consider the suitability of particular cogeneration unit for the specific technology.

A cogeneration unit may be operated in the range of thermal power from 100% to 63% of the nominal value. It is appropriate to have each cogeneration unit modelled so as to allow energy balance at each operating state in this range. Modelling of the cogeneration units is also appropriate with respect to altitude. Altitude, depending on the air temperature, affects engine performance and thus the electric and thermal power cogeneration unit.

2 Cogeneration units

Cogeneration units with piston engines comprise the engine itself to drive the power generator, together with a set of heat exchangers using the heat from engine cooling system and lubrication oil (glycol/water or water/water exchanger types) or exhaust gases (exhaust/water exchanger type). Combustion engines are heat machines converting the heat generated by fuel during the combustion process into mechanical energy

using the pressure of exhaust gases exerted on the piston moving inside the cylinder. The exhaust gases produced by combustion of fuel generate a high pressure and temperature ranging within 2 000 – 2 500 °C at the beginning of combustion process and 1 000 – 1 500 °C at the end of expansion. The efficiency of current combustion engines ranges around 45%. Their disadvantages include mainly the top performance threshold (35 MW), low engine overload potential, the inability to actuate the engine when overloaded [1].

Power generators in cogeneration units with lower performance are asynchronous, higher performance if linked with synchronous generators. The fuel, mostly natural gas, is blended with air in the mixing unit to be drawn in and compressed using the supercharger driven by exhaust gases emitted by the combustion engine. The compressed hot mixture passes through the cooler (fuel/glycol exchanger) on its way to the combustion engine. The electrical efficiency of cogeneration unit, depending on its size, will range within approx. 27% - 42% [2] [3].

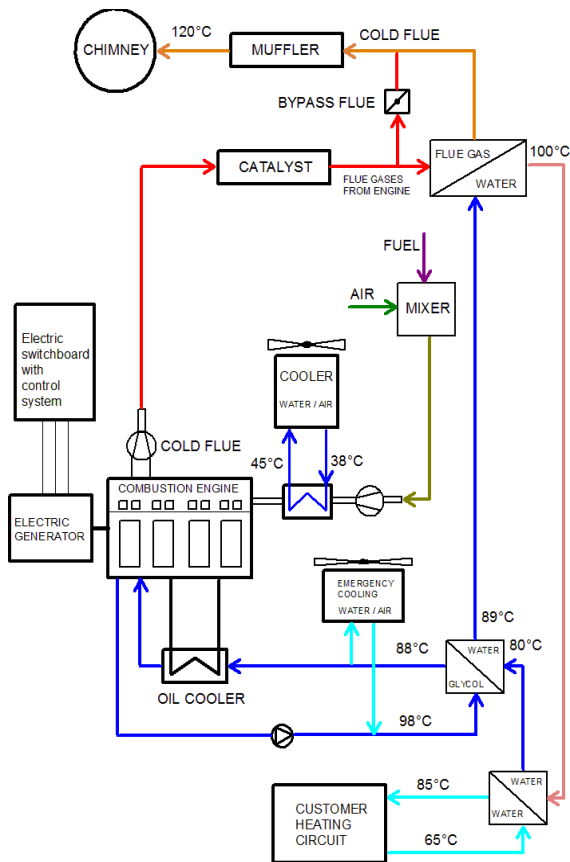


Fig. 1. Basic configuration of a cogeneration unit with combustion engine

3 Cogeneration unit modeling

The input data recorded in type data sheets will be used for retrieval of the basic nominal values necessary for processing of energy balance details as engine performance, generator efficiency, electrical output, heat output, fuel consumption per hour, heating, electrical and overall efficiency.

Determination of operating parameters of cogeneration units depends on the average annual load of cogeneration units, certain manufacturers declare output and efficiency data even for loads as 75 % and 50 %. Polynomial equations of 2nd degree can be then used to enumerate the operating characteristics of cogeneration units within the load range between 100 % and 50 % [4].

The cogeneration unit selected for modelling was the unit with electrical output of 401kWe and the heat output of 549kWt (401kWe/549kWt) Fig. 2. This unit may be operated 24 hours per day, yet this scope may not exceed 3,000 hours per year in order to secure the so called green bonuses.

The functional relation between the generator efficiency and its load expressed as a percentage will be aided by the polynomial equation (1) to calculate the generator efficiency for load range between 100 % and 50 %. The form of this equation for the 401kWe/549kWt cogeneration unit can be seen in the Figure No. 4.

$$-0.0292X^2 + 0.0445X + 0.9462 = Y \tag{1}$$

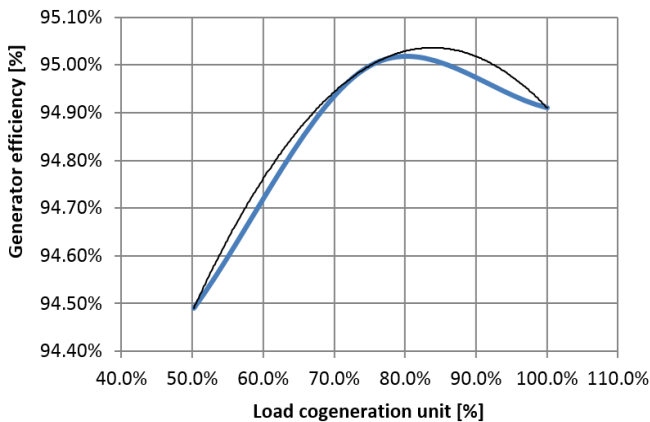


Fig. 2. Relation between the cogeneration efficiency on the load of cogeneration unit and the polynomial equation

The functional relation between ratios of heat and electrical output will help determine the functional relation with the load of cogeneration units as a percentage. The result would be in form of a 2nd degree polynomial equation (2). Such value defined for the

load range between 100 % and 50 % will be used to determine the heat output of cogeneration unit with the known electrical output and vice versa. The form of this equation for the 140kWe/207kWt cogeneration unit can be seen in the Figure No. 5.

$$1.0672X^2 - 2.0151X + 2.317 = Y \quad (2)$$

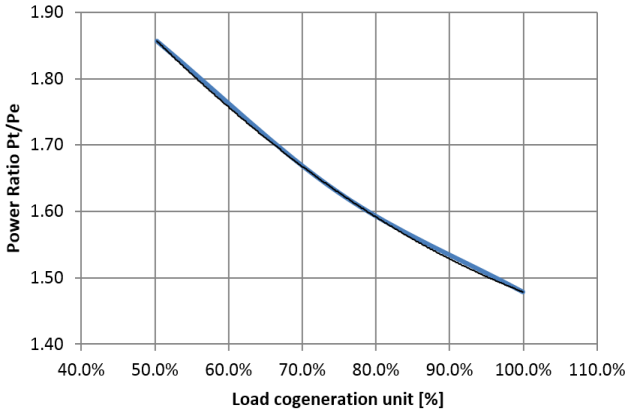


Fig. 3. Relation between the output ratio of PT/PE and the load of cogeneration unit and the polynomial equation

The functional relation between fuel consumption and the load of cogeneration unit expressed as a percentage will be used to create the 2nd polynomial equation (3). The fuel consumption is considered with respect to normal conditions, i.e. the ambient temperature of 0 °C and pressure of 101 325 Pa or under business conditions, that is the temperature of 15 °C and pressure of 101 325 Pa, all within the cogeneration unit load range between 100 % and 50 %. This consumption of natural gas determined in [Nm³/h or m³/h] for any operating load of the 140kWe/207kWt cogeneration unit is expressed with the equation in form shown in the Figure No. 6.

$$-1.9713X^2 + 92.112X + 15.546 = Y \quad (3)$$

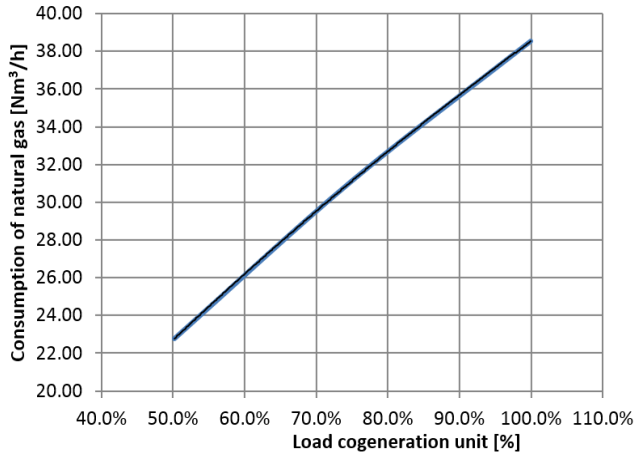


Fig. 4. Relation between fuel consumption and the load of cogeneration unit and the polynomial equation

Pursuant to nominal and estimated operating output and efficiency, as well as the estimated amount of operating hours of cogeneration unit per day or year, the material and energy balances of the cogeneration unit will be determined accordingly. That concerns mainly power generation, heat production, fuel consumption, and inherent power consumption.

The values entered for modelling of cogeneration unit are shown in the Chart I. The balance data calculated for various operation regimes can be found in the Chart II. This chart contains modelled data for cogeneration units within the nominal electrical output of 100%, 75% and 50% respectively. Modelling can be conducted under any load, while it must be done in compliance with the nominal output range from 50% to 100%.

Table 1. Values entered for cogeneration unit modelling

<i>Maximum daily operation (hours/day)</i>	24
<i>Maximum annual operation (hours/year)</i>	3000
<i>Shaft engine power (kW)</i>	147.5
<i>Generator efficiency (%)</i>	94.9
<i>Electrical output (kW)</i>	401
<i>Heat output (kW)</i>	549

Table 2. Values calculated with the cogeneration unit loads at 100%, 75% and 50% levels of the nominal electrical output

Cogeneration unit power loading (%)	100	75	50
<i>Heat and electrical output ratio</i>	1.37	1.41	1.58
<i>Electric power produced per year (MWh)</i>	1 203	903	601
<i>Heat produced per year (GJ)</i>	5 929.2	1,847.9	1,399.5
<i>Natural gas consumption (m³/h)</i>	111.5	88.1	64.5

<i>Cogeneration unit energy input (combustion engine) (MJ/h)</i>	3 790.7	2 995.7	2 191.
<i>Electric efficiency (%)</i>	38.08	36.21	32.92
<i>Heat efficiency (%)</i>	52.14	50.91	51.90
<i>Overall efficiency (%)</i>	90.22	87.12	84.82
<i>Annual fuel consumption (m³/year)</i>	334 473	264 323	193 395
<i>Specific heat consumption to generate 1kWh of electric power (MJ/kWh)</i>	9.453	9.943	10.935
<i>Specific heat consumption to generate 1kWh of heat energy (MJ/kWh)</i>	6.905	7.072	6.937

4 Conclusion

This article deals with modelling of cogeneration units. One of the aspects sought is the cheapest method to find a specific cogeneration unit compliant with the particular technology.

The modelling process enables demonstration of any cogeneration unit with any electrical output.

This article concerns modelling of the cogeneration unit delivering 140kWe/207kWt. The electrical output levels were set at 100%, 75% and 50% of the nominal value. These are clearly entered in the Chart 2 for particular calculations. Operation of cogeneration units was further assessed, considering their location at various altitudes.

Cogeneration units with piston engines are usually used as primary resources of energy for heating and heating of domestic hot water. Sufficient backup of heat output within the maximum heat consumption period is provided by gas boilers to cover consumption peaks, in parallel connection to the cogeneration unit. The cogeneration unit can be controlled together with the electrical output. That is mainly linked with a storage reservoir gathering the excess heat obtained during generation of electrical power.

References

1. James L. Kirtley, *Electric Power Principles*, Massachusetts Institute of Technology, ISBN: 978-0-470-68636-2, Hardcover, 404 pages, 2010
2. Ibrahim Dincer, Marc A. Rosen, *Thermal Energy Storage*, ISBN: 978-0-470-74706-3, Hardcover, 620 pages, 2010
3. James Momoh, Lamine Mili, *Operation and Electric Energy Processing Systems*, ISBN: 978-0-470-47209-5, 200 pages, 2010
4. M. Špaček, Z. Hradílek, P. Moldřík, "Cooperation between Photovoltaic and Biogas Power Plants within 22kV Network", *Electric Power Engineering 2015*, Czech Republic, 2015

EMTP/ATP Simulation of Power Quality Disturbances in Medium Voltage Grid

Dung Vo Tien¹, Veleslav Mach¹, Radomir Gono¹, and Zbigniew Leonowicz²

¹Department of Electrical Power Engineering, FEECS,
VŠB – Technical University of Ostrava, 17. listopadu 15,
708 33 Ostrava – Poruba, Czech Republic
{dung.vo.tien, veleslav.mach, radomir.gono}@vsb.cz
²Wroclaw University of Science and Technology
zbigniew.leonowicz@pwr.edu.pl

Abstract. Power system simulation programs are powerful tools to study electrical power systems quality. It gives an insight on how power quality disturbance occurring within the simulated power system model. This paper presents techniques to simulate various power quality disturbances in medium voltage grid such as voltage sag, voltage swell, transient, harmonic, distortion by using ATP/EMTP software. The results of simulations explain the cause of power quality disturbance.

Keywords: Power quality, voltage disturbances, power system, simulation model, EMTP/ATP software.

1 Introduction

Nowaday the quality of electric power has become an important issue for electric utilities and its customers. The development of modern industrial devices requires ensure the quality of power because the electric devices are very sensitive to disturbances. Power Quality (PQ) events such as sag, swell, transients, harmonics, notch, fluctuation and flicker are the most common types of disturbances that occur in a power system. There are many misunderstandings regarding the cause of power quality problems. Improving the quality of power system is necessary to determine the cause of the power quality disturbance phenomenon. With the development of computer technology and software, it can be simulated power quality disturbance to estimate the presence and cause of the disturbance and apply the mitigating action.

There are many power system simulation tools available, such as PSCAD/EMTDC [2], EMTP/ATP [3], MATLAB with Power System Toolbox [4], [14]. In this paper, ATP/EMTP is chosen as the simulation platform because because the simulation results from EMTP are very close to the experimental results [12],

[13]. Some cases of basic models developed to simulate voltage sag, swell, transient, harmonic, power quality disturbance are presented in this paper.

ATP is a universal program system for digital simulation of transient phenomena of electromagnetic as well as electromechanical nature. With this digital program, complex networks and control systems of arbitrary structure can be simulated [11], [12]. In this paper, various practical power disturbances are considered such as sag, swell, interruption, harmonic, transient and simulations performed with the help of EMTP/ATP. The distribution voltage level used in the models is based on the Viet Nam grid code.

2 Medium voltage grid description

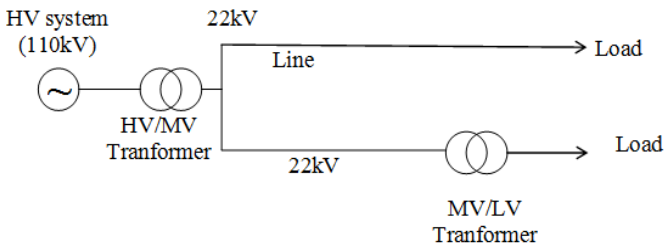


Fig. 1. One phase diagram of the MV network

Fig. 1 shows the one-phase diagram of the MV network to which the industrial user is connected, it is used in this paper. The loads include low voltage (LV) loads and medium voltage (MV) loads. The parameters of this network are set as follows:

- Source frequency: 50Hz.
- Short circuit power of the HV System at the 110kV busbar: 250MVA.
- HV/MV transformer: Three phases, 25MVA rated power, two winding 110/22kV, D/Y11 connection.
- MV/HV transformer: Three phases, 2 MVA rated power, two winding 22/0.4 kV, Y/Y0 connection.
- Overhead line AC70.
- Load: Load 1 at 22 kV voltage: Active power 1.58 MW, Reactive power 1.02 MVA. Load 2 at 0.4 kV voltage: Active power 1.67 MW, Reactive power 0.45 MVA.

3 Cases study

3.1 Induction motor starting model

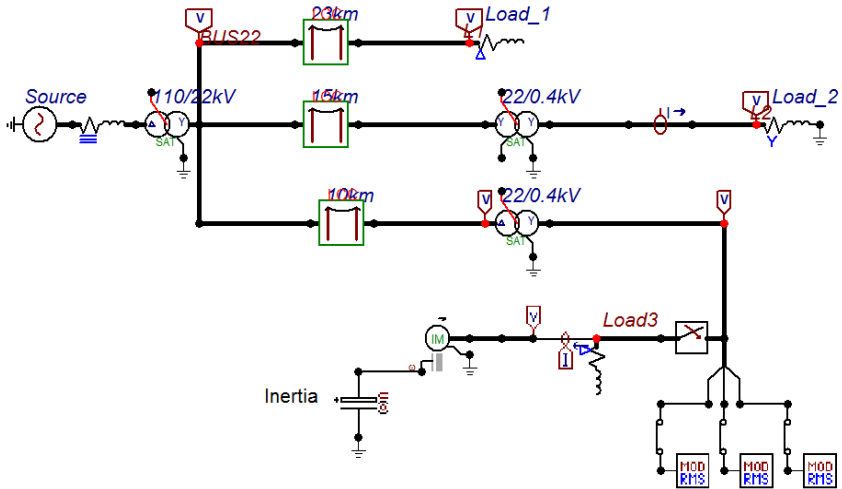


Fig. 2. Induction motor starting/load ATPDraw model

Motors have undesirable effects of drawing several times their full load current while starting. The induction motor starting model [5], [6], [14] is used to simulate voltage sag caused by starting a high power industry induction motor. The induction motor starting model developed in EMTP/ATP is shown in Fig. 2.

The model used diagram in Fig. 1, adding a three phase breaker as motor starting contactor, a three-phase induction motor, and 120 kW resistive, 90 kvar inductive load through 22/0.4kV, 250kVA transformer. The power of induction motor is 37.5 kW and its parameters are the follow table

Parameters	Voltage (V)	Current (A)	$R_1(\Omega)$	$X_{l1}(\Omega)$	$X_m(\Omega)$	$R_2(\Omega)$	$X_{l2}(\Omega)$
	380	57	0.322	0.657	12.5	0.196	0.510

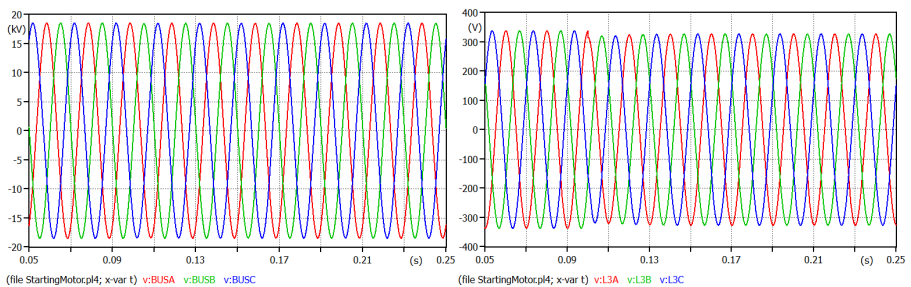


Fig. 3. Voltage sag instantaneous waveform of 22 kV feeder voltage and 0.4 kV load voltage caused by the starting of 37.5 kW induction motor at 0.4 kV feeder.

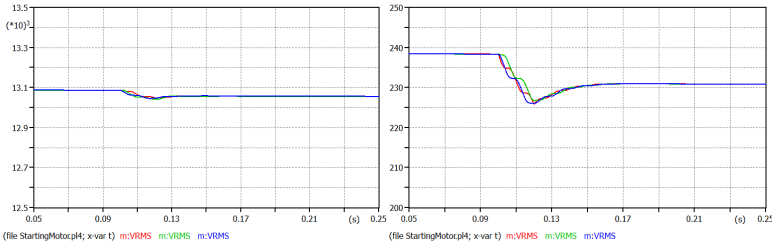


Fig. 4. Voltage sag RMS waveform of 22 kV feeder voltage and 0.4 kV load voltage caused by the starting of 37.5 kW induction motor at 0.4 kV feeder

Fig. 3 shows a three-phase voltage sag instantaneous waveform caused by an induction motor starting upon closing of motor starting contactor at 0.1 second. The sag magnitude of the induction motor voltage sag is dependent on the induction motor and transformer power rating. The voltage sag at 22 kV feeder is not noticeable because power of transformer is much large than the power of load and induction motor. It is very difficult to recognize voltage sag because voltage drops out very small. In this case, using RMS analysis is better (Fig. 4).

3.2 Capacitor bank energizing model

A capacitor switching transient is normal system event that can occur whenever a capacitor energized. The capacitor bank energizing model developed in EMT/ATP is shown in Fig. 5. It is used to simulate voltage oscillatory transient caused by capacitor banking energizing for improve power factor in the power system. The model used diagram in Fig. 1. A capacitor bank connected to feeder through three-phase breaker as a switching contactor. The capacitor bank at 22 kV bus or at 0.4 kV bus has a capacity of 300 kvar which can compensate power factor for load 2, 450 kvar inductive load. Simulation voltage transient caused by energizing of capacitor bank at 22 kV bus or at 0.4 kV bus at 0.1 second.

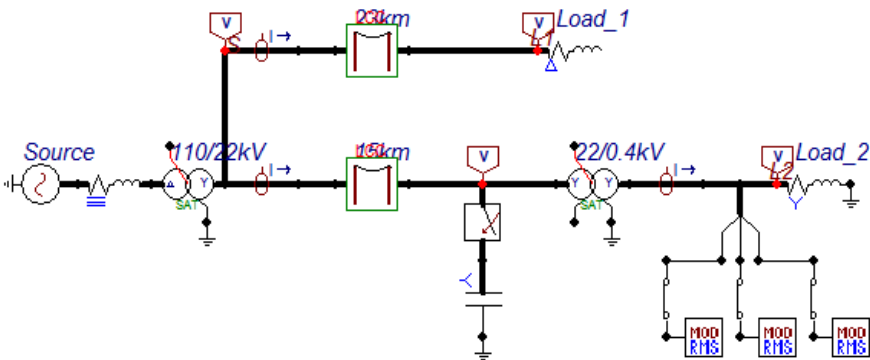


Fig. 5. Capacitor bank energizing at 22kV voltage model

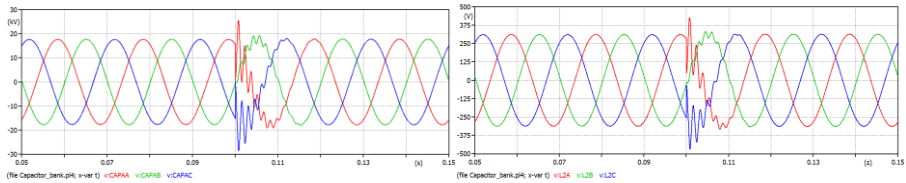
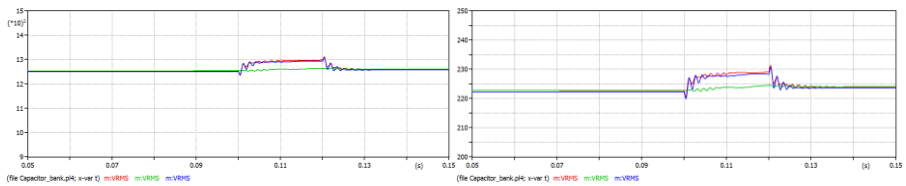
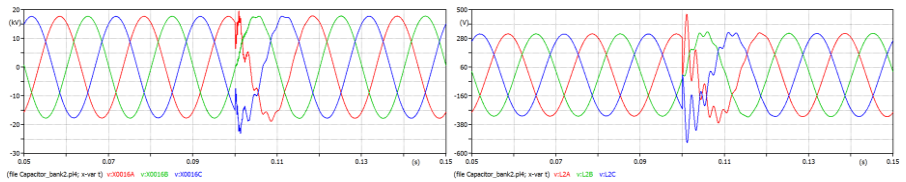
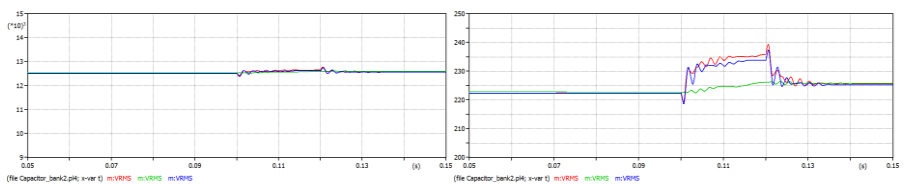
Fig. 6a. Instantaneous waveform of 22 kV feeder voltage and 0.4 kV load voltage**Fig. 6b.** RMS waveform of feeder voltage and 0.4 kV load voltage**Fig. 7a.** Instantaneous waveform of 22 kV feeder voltage and 0.4 kV load voltage**Fig. 7b.** RMS waveform of feeder voltage and 0.4 kV load voltage**Fig. 7.** Oscillatory transient caused by capacitor bank energizing at 22 kV feeder line.**Fig. 8.** Oscillatory transient caused by capacitor bank energizing at 0.4 kV bus

Fig. 7 and 8 shows the energizing of capacitor bank upon closing of three-phase breaker at 22 kV feeder line and at 0.4 kV bus causing voltage transient at 0.4 kV and 22 kV bus. It can also be clearly seen that the voltage load when set capacitor bank at 0.4 kV bus is higher than at 22 kV feeder line.

4 Conclusion

This paper presents technique to simulate various power quality disturbances in medium voltage grid by using ATP/EMTP software. Five study cases are conducted, the results shown that EMTP/ATP very flexible to deal with various network configurations in steady as well as in transient state. The cause of power quality disturbance was recognized.

Acknowledgement: This research was partially supported by the SGS grant from VSB-TU Ostrava (No. SP2016/95) and by the project TUCENET (No. LO1404).

The results were published at the conference IEEEIC2016 Florence, Italy.

References

1. Mohamed A. Ibrahim, *Disturbance Analysis For Power Systems*, IEEE press, 2012.
2. Patne N.R, Thakre K.L, *Stochastic Estimation of voltage Sag Due to Faults in the Power System by Using PSCAD/EMTDC Software as a Tool for Simulation*, Journal of Electrical Power Quality and Utilisation 13, p59-63, 2007.
3. Filho J.M.C, Leborgne R.C, Abreu J.P.G, Novaes E.G.C, Bollen M.H.J, *Validation of Voltage Sag Simulation Tools: ATP and Short Circuit Calculation Versus Field Measurements*. IEEE Transactions on Power Delivery 23, p. 1472-1480, 2008.
4. Hadi Saadat, *Power System Analysis*, 2nd edn, McGraw Hill, 2004.
5. P.Pillay, S.M.A. Sabur, M.M. Haq, *A model for induction motor aggregation for power system studies*, Electric Power Systems Research 42, p. 225-228, 1997.
6. Dr Morris Lockwood, *Issues in Modelling Transformers, Machines and their Controllers Using ATPDraw*, EEUG course, August 2010, Finland.
7. Durbak W.D.: *Zinc-Oxide Arrester Model for Fast Surges*, *EMTP Newsletter*, Vol. 5, No. 1, January 1985.
8. Pinceti P., Giannettoni M.: *A Simplified Model for Zinc Oxide Surge Arresters*, IEEE Trans. On Power Delivery, Vol. 14, No. 2, p. 393-397, April 1999.
9. M. Popov, *ATPDraw-based Models: Nonlinear Elements, Surge Arresters and Circuit Breakers*, EEUG meeting 2008, European EMTP- ATP Conference, p.15-28.
10. Mack Grady, *Understanding Power System Harmonics*, IEEE Power Engineering Review, April 2012.
11. Löszlú prikler, Hans Kristian Hoidalén, *ATPDRAW version 5.6*, 2009.
12. *ATP Theory book, EMTP-ATP Programs*, 2004.
13. Jorge Blanes, *Low voltage model for the study of slow disturbances in medium voltage grids*, Electric Power Systems Research 99 (2013),p 64–70.
14. Rodney H.G. Tan and Vigna K. Ramachandaramurthy, *A Comprehensive Modeling and Simulation of Power Quality Disturbances Using MATLAB/SIMULINK*, InTech 2015

Simulation of Sliding Mode Control Structure of Induction Motor Drive

Chau Si Thien Dong

Faculty of Electrical and Electronics Engineering, Ton Duc Thang University, Nguyen
Huu Tho Street, Tan Phong Ward, District 7, Ho Chi Minh City, Vietnam
dongsithienchau@tdt.edu.vn

Abstract. The control of induction motor drives constitutes a vast subject, and the technology has further advanced in recent years. There are many types of controllers, such as scalar control, vector control, direct torque and flux control, intelligent control, etc. In practical, vector control is one of most popular control methods because of its good dynamic behaviors in wide speed range. Moreover, by using vector control, control AC motor is similar to control process of separately excited DC motor. Traditionally, PI controllers are usually used to control torque and flux. In this paper, a sliding mode controller is used to control induction motor drives. The mathematical description and simulation results are presented in the paper.

Keywords: induction motor, vector control, sliding mode control, sensorless control, sliding mode observer.

1 Introduction

Induction machines are used widely in practice. These machines are very economical, rugged and reliable. For the control of the induction motor, it is required rotor magnetic flux and rotor speed of the induction motor. However, the control and estimation of important quantities of AC drives with induction motors is difficult because of variable frequency of a supply stator phase voltages realized by frequency converters, complex dynamics of AC machines, machine parameters variations, and signal processing of feedback signals [1], [2]. Control methods can be listed as scalar control, vector control, direct torque and flux control (DTC), intelligent control, etc. Scalar control is very simple but it disregards the coupling effects so it has inferior performance. As the result, this method disappears in real world. The DTC is an advance of scalar method. It is simple but it does not work well at low speed. The intelligent control methods do not require model but it is very complicated. Among these control methods, vector control is one of the most popular methods. It has high efficiency in wide range speed [1], [2].

Vector control consists of controlling the stator currents represented by a vector. This control is based on projections which transform a three phase time and speed dependent system into a two co – ordinate time variant system, torque current compo-

ment and flux current component. So there are two control loops: torque control loop and flux control loop. In this research, sliding mode controllers are used for torque and flux control loop because sliding mode controllers are robust to the change of parameters [3], [4], [5].

In this paper, firstly, mathematical model of induction motor is presented. The sliding mode controller will be developed in the next part. The third part shows some simulation results. Finally, some conclusions are in the fourth part.

2 Mathematical model of the induction motor

State space equations which describe of the induction motor are written as follows:

$$\frac{d}{dt} \mathbf{x} = \mathbf{A} \cdot \mathbf{x} + \mathbf{B} \cdot \mathbf{v} \quad (1)$$

$$\mathbf{y} = \mathbf{C} \cdot \mathbf{x} \quad (2)$$

$$\mathbf{x} = \begin{bmatrix} i_{S\alpha} & i_{S\beta} & \Psi_{R\alpha} & \Psi_{R\beta} \end{bmatrix}^T, \quad \mathbf{v} = \begin{bmatrix} v_{S\alpha} & v_{S\beta} \end{bmatrix}^T \quad (3)$$

$$\mathbf{A} = \begin{bmatrix} a_{11} & a_{12} & a_{13} & a_{14} \\ a_{21} & a_{22} & a_{23} & a_{24} \\ a_{31} & a_{32} & a_{33} & a_{34} \\ a_{41} & a_{42} & a_{43} & a_{44} \end{bmatrix}, \quad \mathbf{B} = \frac{1}{\sigma L_S} \begin{bmatrix} 1 & 0 \\ 0 & 1 \\ 0 & 0 \\ 0 & 0 \end{bmatrix}, \quad \mathbf{C} = \begin{bmatrix} 1 & 0 & 0 & 0 \\ 0 & 1 & 0 & 0 \end{bmatrix}. \quad (4)$$

$$a_{11} = -\frac{L_h^2 R_R + L_R^2 R_S}{\sigma L_S L_R^2}, \quad a_{12} = 0, \quad a_{13} = \frac{L_h R_R}{\sigma L_S L_R^2}, \quad a_{14} = \frac{L_h}{\sigma L_S L_R} \omega_r \quad (5)$$

$$a_{21} = 0, \quad a_{22} = -\frac{L_h^2 R_R + L_R^2 R_S}{\sigma L_S L_R^2}, \quad a_{23} = -\frac{L_h}{\sigma L_S L_R} \omega_r, \quad a_{24} = \frac{L_h R_R}{\sigma L_S L_R^2} \quad (6)$$

$$a_{31} = \frac{L_h R_R}{L_R}, \quad a_{32} = 0, \quad a_{33} = -\frac{R_R}{L_R}, \quad a_{34} = -\omega_r \quad (7)$$

$$a_{41} = 0, \quad a_{42} = \frac{L_h R_R}{L_R}, \quad a_{43} = \omega_r, \quad a_{44} = -\frac{R_R}{L_R}, \quad \sigma = 1 - \frac{L_h^2}{L_S L_R}. \quad (8)$$

where $i_{S\alpha}$, $i_{S\beta}$ – stator current vector components in $[\alpha, \beta]$ stator coordinate system; $v_{S\alpha}$, $v_{S\beta}$ – stator voltage vector components in $[\alpha, \beta]$ stator coordinate system; $\Psi_{R\alpha}$, $\Psi_{R\beta}$ – rotor magnetic flux in $[\alpha, \beta]$ stator coordinate system; L_h – magnetizing inductance; L_R – rotor inductance; L_S – stator inductance; R_R – rotor phase resistance; R_S – stator

phase resistance; σ – total leakage constant; ω_r – rotor angular speed, $\omega_m = \frac{2}{p} \omega_R$ – mechanical speed.

3 Sliding mode control.

For the speed control of an induction motor, let $y = \omega_m$, $y_{ref} = \omega_{mref}$, and $n = 3$. Due to $n = 3$, the first and the second order derivatives of the rotor speed are the feedback signals for the SMC algorithm. The sliding mode surface is defined as:

$$S_\omega = \omega_{mref} - \omega_m - \left(\frac{4}{9} T_{s\omega} \frac{d\omega_m}{dt} + \frac{4}{81} T_{s\omega}^2 \frac{d^2\omega_m}{dt^2} \right) \quad (9)$$

The orders of the derivative feedback can be reduced by using a smoothing integrator and the output control variable T_{eref} can be written as:

$$T_{eref} = K_{SM\omega} \int (\omega_{mref} - \omega_m) dt - K_{SM\omega} \left(\frac{4}{9} T_{s\omega} \omega_m + \frac{4}{81} T_{s\omega}^2 \frac{d\omega_m}{dt} \right) \quad (10)$$

where $T_e = \frac{3}{2} \frac{p}{2} (\psi_{R\alpha} i_{S\beta} - \psi_{R\beta} i_{S\alpha})$ is the motor torque.

To control the stator flux and torque of the induction motor, we define $y = \psi_S$ or $y = T_e$ and $y_{ref} = \psi_{Sref}$ or $y_{ref} = T_{eref}$, $n = 2$. Hence, the sliding mode surface is defined as follows.

$$S_\psi = \psi_{Sref} - \psi_S - \frac{1}{3} T_{s\psi} \frac{d\psi_S}{dt} \quad (11)$$

$$S_T = T_{eref} - T_e - \frac{1}{3} T_{sT} \frac{dT_e}{dt} \quad (12)$$

Where $T_{s\psi}$ - settling time for the stator flux control loop and T_{sT} - settling time for the stator torque control loop.

The output control variables u_{Sx} and u_{Sy} are defined by:

$$u_{Sx}^* = K_{SM\psi} \left(\int (\psi_{Sref} - \psi_S) dt - \frac{1}{3} T_{s\psi} \psi_S \right) \quad (13)$$

$$u_{Sy}^* = K_{SMT} \left(\int (T_{eref} - T_e) dt - \frac{1}{3} T_{sT} T_e \right) \quad (14)$$

The schematic of sliding mode control of induction motor

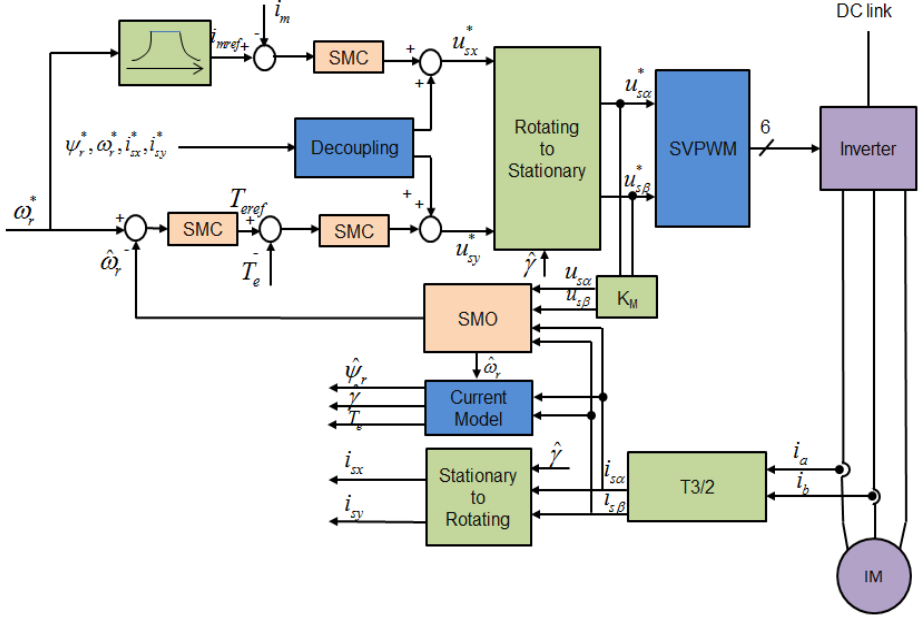


Fig. 1. Block diagram of the sliding mode control of induction motor

4 Simulation results

The described sliding mode observer was simulated by MATLAB-SIMULINK on a vector controlled AC drive with the induction motor (see Fig. 1). The controllers of quantities in control structure of AC drive with vector control were adjusted accordance with the following parameters of the induction motor (type 1LA7106-4AA10):

- $P_n = 2.2$ kW, $T_n = 14.8$ Nm
- $\omega_{mn} = 1420$ rpm, $p_p = 2$
- $I_{Sn} = 8.43$ A, $I_{Rn} = 17$ A
- $I_{Sxn} = 6.8$ A, $I_{Syn} = 8.16$ A
- $U_{Sn} = 400/230$ V, $\Psi_{Sn} = 0.877$ Wb
- $R_S = 1.28$ Ω , $R_R = 1.52$ Ω
- $L_S = 0.137$ H, $L_R = 0.137$ H
- $L_m = 0.129$ H, $T_R = 0.09$ s

The time courses of the actual rotor speed (see Fig. 2) were obtained from the speed control structure at the jump of the load torque $T_L = 5$ Nm (see Fig 5).

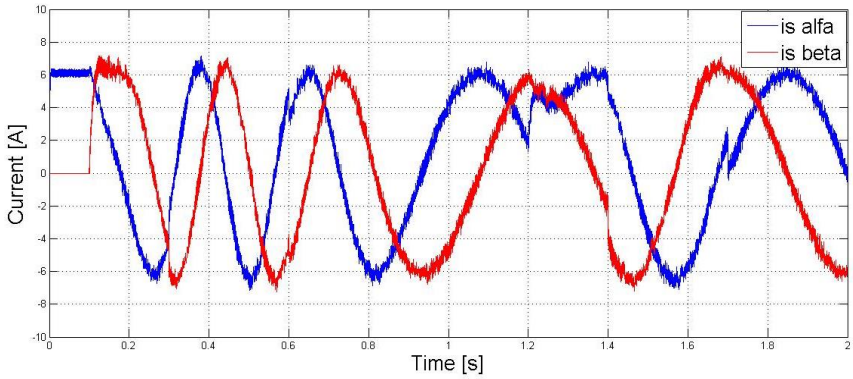


Fig. 2. The stator current components $i_{S\alpha}$ (blue), $i_{S\beta}$ (red)

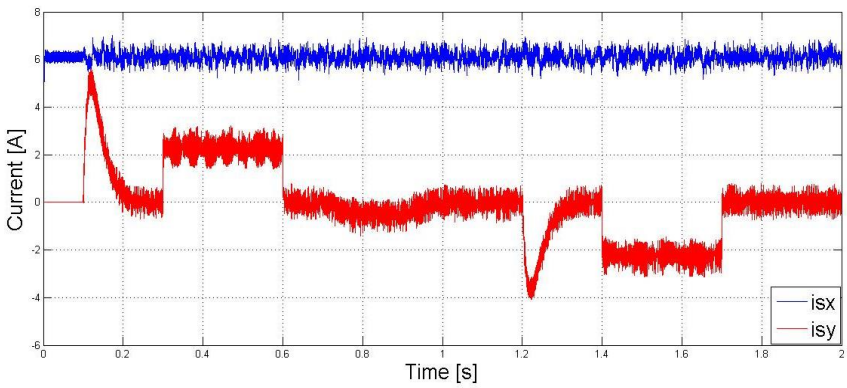


Fig. 3. The magnetizing current component i_{Sx} and torque current component i_{Sy}

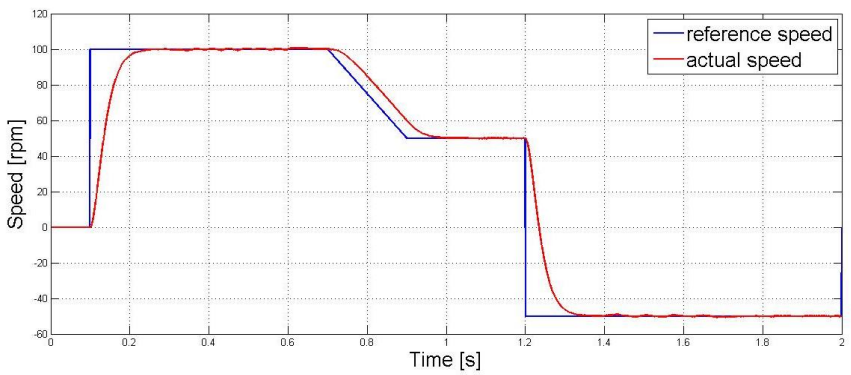


Fig. 4. Reference rotor speed (blue) and actual rotor speed (blue) of the induction motor

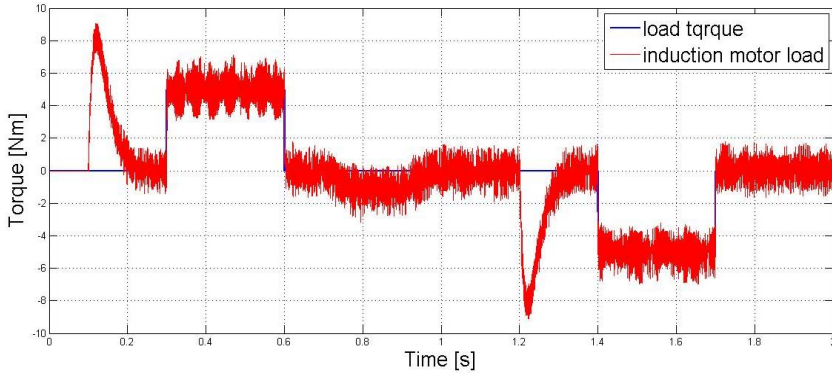


Fig. 3. Load torque (blue) and induction motor torque (red)

5 Conclusion

The sliding mode control of induction motor drives was presented in the paper. The induction motor drive gives good dynamic responses in steady state and also in transient state. However, there are oscillations in dynamic responses of stator current components, magnetizing current component, flux current component and the torque. This results from choosing parameters of sliding mode controller. In future work, advance sliding mode control as well as parameter estimators will be added to reduce these oscillations.

Acknowledgement

In the paper, there are the results of the project reg. no. SP2016/83 funded by the Student Grant Competition of VSB-Technical University of Ostrava. This research was supervised by Prof. Ing. Pavel Brandstetter, CSc.

References

1. K. B. Bose, *Power Electronics and Modern Electric Drives*. N. Jersey: Prentice Hall, 2002.
2. P. Brandstetter, *AC Controlled Drives – Modern Control Methods*. Ostrava, VSB-Technical University of Ostrava, 177 p., 1999.
3. V. I. Utkin, *Sliding Mode Control Design Principles and Applications to Electric Drives*, *IEEE Transactions on Industrial Electronics*, Vol. 40, No. 1, pp. 23-36, 1993.
4. J. Vittek, S. J. Dodds, P. Bris, M. Stulrajter, P. Makys, *Experimental Verification of Chattering Free Sliding Mode Control of the Drive Position Employing PMSM*, *Journal of Electrical Engineering*, Vol. 59, No. 3, pp. 139–145, 2008.
5. I. Bendass, F. Naceri, *A New Method to Minimize the Chattering Phenomenon in Alisinf Mode Control Based on Intelligent Control for Induction Motor Drives*, *Serbian Journal of Electrical Engineering*, Vol. 10, No. 2, pp. 149 – 156, 2013.

Induction Motor Parameters Estimation based on Voltage Step Response and Genetic Algorithm

Jiri Hajovsky

Department of Electronics, FEECS,
VŠB – Technical University of Ostrava, 17. listopadu 15,
708 33 Ostrava – Poruba, Czech Republic
jiri.hajovsky@vsb.cz

Abstract. The paper presents experimental results of induction motor parameters estimation using genetic algorithm. Method is based on voltage step current response to one phase of induction motor. Mathematical model of induction motor is presented. Simulated and measured results are shown and discussed.

Keywords: genetic algorithm, induction motor, voltage step response

1 Introduction

Most of industrial application use induction squirrel cage motors. The trend is development of speed or position is obtained from the waveforms of stator voltages and currents. To design and implementation of vector control is necessary to know the parameters that this procedure is dependent on the motor parameter changes. This is particularly important in applications where there are high demands on precision and to change the parameters of induction motors [1] - [7].

2 Mathematical model of induction motor

Assuming the initial conditions of currents i_1^S and i_2^R following equations are given [8] - [12].

$$\frac{u_1^S}{s} = R_S i_1^S(s) + s \cdot L_S i_1^S(s) + s \cdot L_h i_2^R(s) \quad (1)$$

$$0 = R_R i_2^R(s) + s \cdot L_R i_2^R(s) + s \cdot L_h i_1^S(s) \quad (2)$$

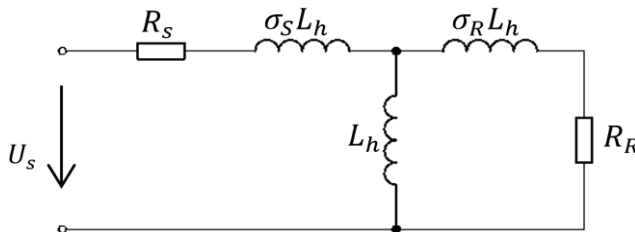


Fig. 1. Equivalent circuit connection of one phase of induction motor

Stator current equation (3) in Laplace transform is given by substituting and modifying the equations (1) and (2)

$$\mathbf{i}_1^S(s) = \frac{u_1^S}{R_S} \cdot \frac{T_{RS}+1}{s[\sigma T_R T_S s^2 + (T_R + T_S)s + 1]} \quad (3)$$

Inverse Laplace transform to equation (3) were applied. Equation (4) presents current response in time domain after applied voltage step to one phase.

$$i_{1a}(t) = \frac{U_{1a}}{R_S} \left\{ 1 + \frac{1}{2\xi} \left[(T_S - T_R - \xi) e^{-t \frac{T_R + T_S + \xi}{2\sigma T_R T_S}} - (T_S - T_R + \xi) e^{-t \frac{T_R + T_S - \xi}{2\sigma T_R T_S}} \right] \right\} \quad (4)$$

Parameter ξ is used as a substitution of the equation (5).

$$\xi = T_R + T_S \sqrt{1 - \frac{4\sigma T_R T_S}{(T_R + T_S)^2}} \quad (5)$$

3 Simulation Results

Matlab was used to simulate the current response of one phase to voltage step. As an induction motor parameters were inserted parameters of real innduction motor Siemens 7AA100L04K. Parameters of the simulated motor are displayed in table 1.

Table 1. Induction motor 7AA100L04K parameters

Parameter	Value	Unit
P_n	2,2	kW
n_n	1420	min ⁻¹
f_n	50	Hz
J_m	0,05	kgm ²
p	2	-
U_{sn}	400	V
I_{sn}	4,7	A
R_s	3.71	Ω
R_r	3.06	Ω
L_h	0.317	H
$L_{s\sigma}$	0,013	H
$L_{r\sigma}$	0,013	H
U_d	640	V

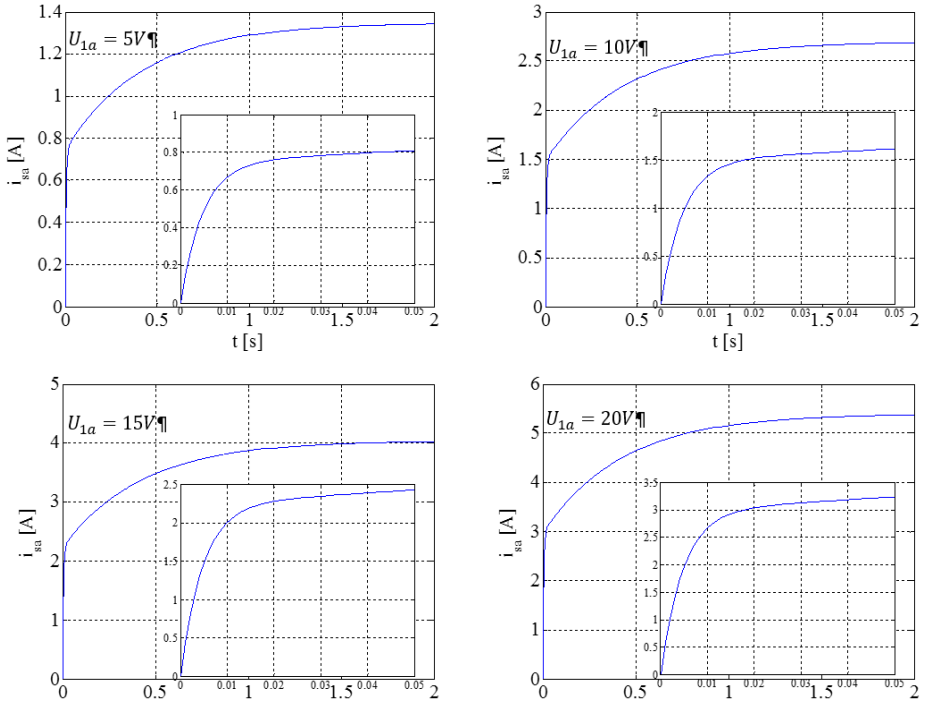


Fig. 2. Simulated phase current response after dc voltage excitation

4 Experimental Results

Figure Fig. 3. shows circuit connection during experimental measurement. Digital oscilloscope was used for data acquisition.

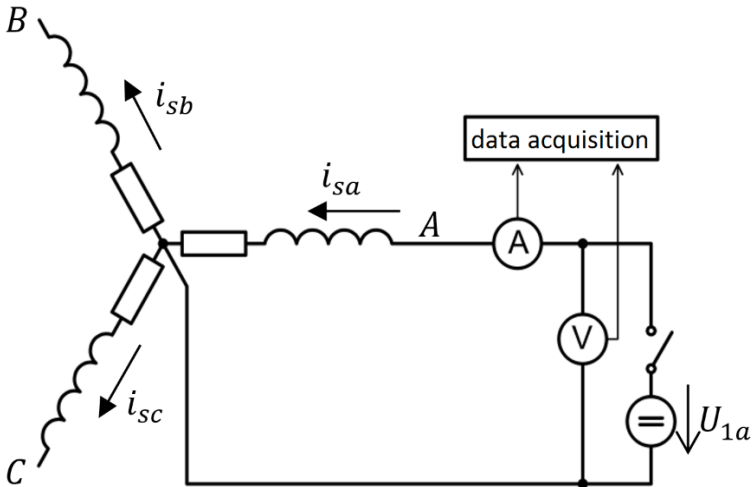


Fig. 3. Circuit connection for experimental measurements

Waveforms of measured phase current response after dc voltage excitation are shown at figure Fig. 4.

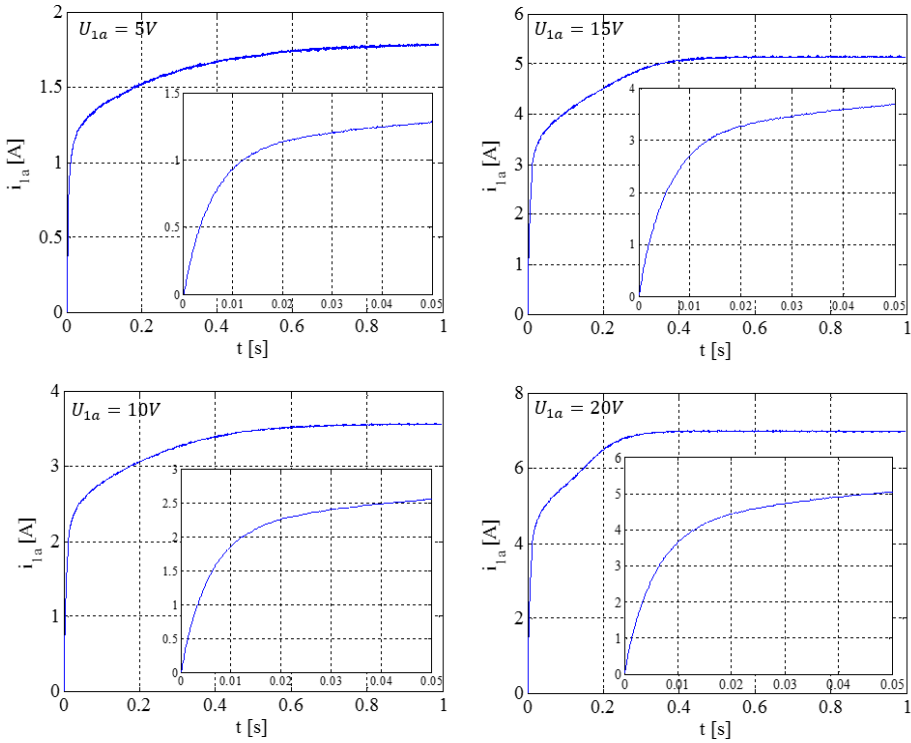


Fig. 4. Measured phase current response after dc voltage excitation

Selected values current at that time were inserted into developed interpolation algorithm based on genetic algorithm. The results of interpolation are shown in Fig. 5. At table 2 are shown estimated parameters developed by interpolation algorithm based on genetic algorithm. The greatest consensus of estimated values can be observed in the excitation voltage of 5 and 10V. During excitation voltage 15V and 20V estimated parameters are relatively greater error. Measured current waveform during excitation voltage of 15 to 20V in Fig. 4. lose their characteristic shape according to simulated waveform at figure Fig. 2. While excitation voltage of 15 to 20V leads to higher currents and thus the earlier saturation of inductances, which issues non-linearity.

Table 2. Estimated parameters

U_{1a} [V]	T_R [s]	T_S [s]	R_S [Ω]	σ [-]
5	0,0517	0,0300	2,8137	0,3172
10	0,0515	0,0314	2,8034	0,3064
15	0,0474	0,0313	2,8910	0,2975
20	0,0365	0,0273	2,8242	0,3334

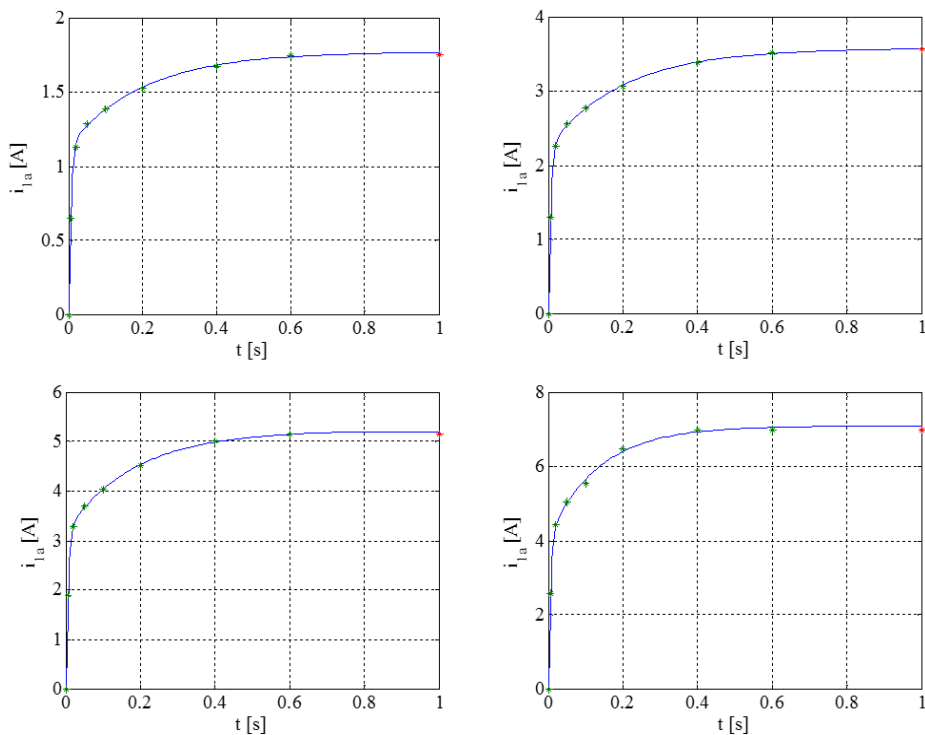


Fig. 5. Interpolation of selected points based on genetic algorithm

5 Conclusions

The results presented above shows off-line induction motor estimation with acceptable level of accuracy. Higher accuracy achieved excitations of lower voltage 5V and 10V. Higher voltage 15V and 20V caused higher current and thus the earlier saturation of inductances, which issues non-linearity and higher error of estimated values.

6 Acknowledgement

The paper was supported by the projects: Center for Intelligent Drives and Advanced Machine Control (CIDAM) project, reg. no. TE02000103 funded by the Technology Agency of the Czech Republic, project reg. no. SP2016/83 funded by the Student Grant Competition of VSB-Technical University of Ostrava.

7 References

1. Brandštetter, P. Střídavé regulační pohony - Moderní způsoby řízení. Monografie, VŠB-Technická univerzita Ostrava, 177 s., 1999, ISBN 80-7078-668-X.

2. Čermák, T. Elektrické regulační pohony. 1. vyd. Ostrava: Vysoká škola báňská, 1986, 328 s.
3. Vas, P. Sensorless Vector and Direct Torque Control. Oxford Univ. Press, Oxford, UK, 1998, 729 p. ISBN: 9780198564652.
4. Neborák I.: Modelování a simulace elektrických pohonů. Monografie, VŠB- Technická univerzita Ostrava, 168 s., 2002, ISBN 80-248-0083-7.
5. Bose, B. K. Modern power electronics and AC drives. Upper Saddle River, NJ : Prentice Hall PTR, 711 p., 2002, ISBN 0-13-016743-6.
6. Finch, J.W. - Giaouris, D. Controlled AC Electrical Drives. Industrial Electronics, IEEE Transactions on vol. 55, no. 2, pp. 481-491, 2008. DOI: 10.1109/TIE.2007.911209, ISSN: 0278-0046.
7. Bojoi, R.n - Guglielmi, P. - Pellegrino, G.-M. Sensorless Direct Field-Oriented Control of Three-Phase Induction Motor Drives for Low-Cost Applications. Industry Applications, IEEE Transactions on vol. 44, no. 2, pp. 475-481, 2008. DOI: 10.1109/TIA.2008.916735, ISSN: 0093-9994.
8. Couto, E. B. - de Aguiar, M. L. Parameter identification of induction motors using DC step excitation at standstill." In IEEE International Symposium on Industrial Electronics, vol. 2, pp. 468–471.
9. MOON, S.I - Keyhani, A. Estimation of Induction Machine Parameters from Standstill Time Domain Data, The Ohio State University Columbus, OH 43210 U.S.A. 1993, IEEE-IAS Annual Meeting, 1993, Toronto, Canada, 0-7803-1462-x/9303.00
10. Ambrožič, V. - Cajhen, R. – Nastran. A. A Step Voltage Method for Determination of an Induction Motor Rotor Time Constant in a Cold State, Faculty of Electrical Engineering and Computer Science, Ljubljana, SLOVENIA, IEEE 0-7803-1227-9/93/3.
11. Evandro, B.C. - Manoel, I.A. Parameter Identification of Induction Motors Using DC Step Excitation at Standstill, Department of Electrical Engineering, University of Silo Paulo, Brazil, IEEE 0-7803-4756-0/98
12. Belloc, C. - Zhang, H. - Vagapov, Y. - Moreno, P A Step Voltage Response Method for Identification of Induction Motor Parameters at Stand Still, North East Wales Institute of Higher Education, Wrexham, LL 11 2AW, UK
13. Juhamatti, N. Induction Motor Parameter Identification in Elevator Drive Modernization, diploma thesis, Helsinki University of Technology, Faculty of Electronics, Communications and Automation, 2009, 78 stran, vedoucí práce: Prof. Jorma Luomi.
14. Brandstetter, P. - Dobrovsky, M. – Kuchar, M. Implementation of Genetic Algorithm in Control Structure of Induction Motor A.C. Drive, Advances in Electrical and Computer Engineering, vol. 14, November 2014.
15. Brandstetter, P. - kuchar, M. – palacky, P. Estimation an adaptation of selected parameters of induction motor drive, Center of Intelligent Drives and Advanced Machine Control, VŠB- Technická univerzita Ostrava, December 2015.
16. Buja, G. S. - Menis, R. - Valla, M. I. MRAS identification of the induction motor parameters in PWM inverter drives at standstill, In Proceedings of the 1995 IEEE IECON 21st International Conference on Industrial Electronics, Control and Instrumentation, vol. 2, pp. 1041–1047.
17. Boltz, J.-Thimm, T. Identification of the machine parameters in a vector-controlled induction motor drive, IEEE Trans. on Industry Applications, vol. 27, no. 6, pp. 1111-1118, November/December 1991.

Vector Control of Synchronous Motor with Permanent Magnets

Petr Chamrad

Department of Electronics, FEECS,
VŠB – Technical University of Ostrava, 17. listopadu 15,
708 33 Ostrava – Poruba, Czech Republic
petr.chamrad@vsb.cz

Abstract. This article describes a problems of the vector control of the synchronous motor with permanent magnets (SMPM). In the introduction there is description of the properties of the drives with the synchronous motors and their utilization in practice. As another thing there is a description of the principle of the vector control that is explained on the mathematical model of the SMPM. Based on the theoretical analysis the algorithm of the vector was realised and it was implemented into micro computer control system with the digital signal processor. Then the experimental measurement in the laboratory was executed with the results than can be found in the conclusion.

Keywords: Synchronous motor with permanent magnets, vector control, digital signal processor, algorithm of the vector control, vector diagram.

1 Introduction

The electrical drives are the part of many branches of industry. In most cases they are used in heavy industry. Currently the AC motors are applied in the structure of drives and these motors are the followers of the DC motors that were used earlier. The AC drives in the contrast to the DC drives are characterized by simpler construction.

One of the modern methods of the regulation of AC machines is the vector control. It is characterized by good dynamics in the temporary as well as in the steady situations. Relatively perspective type of drives are synchronous motors with permanent magnets that are characterized by compactness, robustness and large torque overloading. Due to these characteristics they are used as servo-motors. Service of synchronous motors with permanent magnets is economical in many ways. The efficiency of this type of drives is more than 98%.

2 Mathematical model of SMPM

For realization of the vector control is necessary to separate torque component of current and flux component of current from the current vector of the stator \mathbf{i}_1 , both components (flux and torque components of current) are orthogonal. The torque com-

ponent of the current has influence on torque of the motor. The flux component of the stator current together with the vector of the magnetic field of the rotor determine the magnetization and forms the idle performance. The vector of stator current can be calculated from single phase currents according to equation (1). The equation (1) can be simplified to (2) providing symmetry of phase currents i_{1a} , i_{1b} and i_{1c}

$$\mathbf{i}_1^S = i_{1\alpha} + j i_{1\beta} = \frac{1}{3}(2i_{1a} - i_{1b} - i_{1c}) + j \frac{\sqrt{3}}{3}(i_{1b} - i_{1c}) \quad (1)$$

$$\mathbf{i}_1^S = i_{1\alpha} + j i_{1\beta} = i_{1a} + j \left(\frac{1}{\sqrt{3}} i_{1a} + \frac{2}{\sqrt{3}} i_{1b} \right) \quad (2)$$

For better understanding of how the SMPM is working there is the equation describing the mathematical model of motor.

$$\mathbf{u}_1^S = R_S \mathbf{i}_1^S + L_S \frac{d\mathbf{i}_1^S}{dt} + \mathbf{u}_i^S \quad (3)$$

If the current vector of the stator \mathbf{i}_1 rotates into suitable axis system we will obtain the equation simplification (4). The current vector of the stator can be oriented from stationary axis system (SSS) with $[\alpha, \beta]$ axis into the rotor axis system (RSS) with $[d, q]$ axis that rotate with angular speed ω_e . It is preferable to situated the flux component of current i_{1d} of stator current \mathbf{i}_1 to the vector of magnetic field of rotor. This forms the permanent magnets field Ψ_{PM} located on the rotor. The angle of the rotation between booth axis system ε is directly proportional to the to the angle of the rotation of the rotor. After the modification we get the equation describing the actions into the motor in the rotor axis system.

$$\mathbf{u}_1^R = R_S \mathbf{i}_1^R + L_S \frac{d\mathbf{i}_1^R}{dt} + j\omega_e L_S \mathbf{i}_1^R + \mathbf{u}_i^R \quad (4)$$

By the decomposition (4) into the component parts we get the view about space position of the single vectors of current and voltage in the rotor axis system. The vector diagram SMPM is illustrated on Figure 1.

$$\tau_S \frac{di_{1d}}{dt} + i_{1d} = \frac{u_{1d}}{R_S} + u_{de} \quad (5)$$

$$\tau_S \frac{di_{1q}}{dt} + i_{1q} = \frac{u_{1q}}{R_S} + u_{qe} \quad (6)$$

$$u_{de} = \omega_e \tau_S i_{1q} \quad (7)$$

$$u_{qe} = -\omega_e \tau_S i_{1d} - \frac{u_i}{R_S} \quad (8)$$

$$\omega_e = p_p \Omega_m, \quad \Omega_m = \frac{d\varepsilon}{dt}, \quad \tau_S = \frac{L_S}{R_S}, \quad u_i = \omega_e \Psi_{PM} \quad (9)$$

$$J \frac{d\omega}{dt} = \frac{3}{2} \Psi_{PM} \operatorname{Im}[\mathbf{i}_1^S e^{-j\varepsilon}] - M_{mech} \quad (10)$$

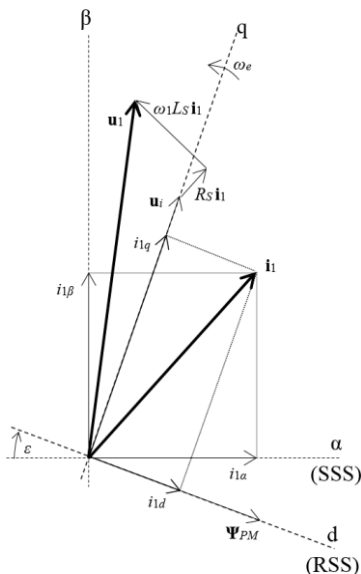


Fig. 1 The space position of single vectors in vector control of the SMPM

2.1 Synchronous motor with permanent magnets in field weakening

If we need to work into the area of higher speed than nominal we must cause field weakening. We obtain this by changing flux component of current i_{1d} and this makes the reduction of the vector of the induced voltage \mathbf{u}_p . The equation for the calculation of induced voltage \mathbf{u}_p is introduced below.

$$\mathbf{u}_p = j\omega(L_S i_{1d} + jL_S i_{1q}) + j\omega_e \Psi_{PM} \quad (11)$$

During the field weakening of the motor is necessary to respect the maximum value of the stator current. Next decrease of the negative value of the flux component of current i_{1d} leads to the increasing of the value of the vector of the stator current \mathbf{i}_1 (see Figure 2). There is the equation to limit the torque component of the stator current i_{1qmax} .

$$i_{1qmax} = \pm \sqrt{i_{1max}^2 - i_{1d}^2} \quad (12)$$

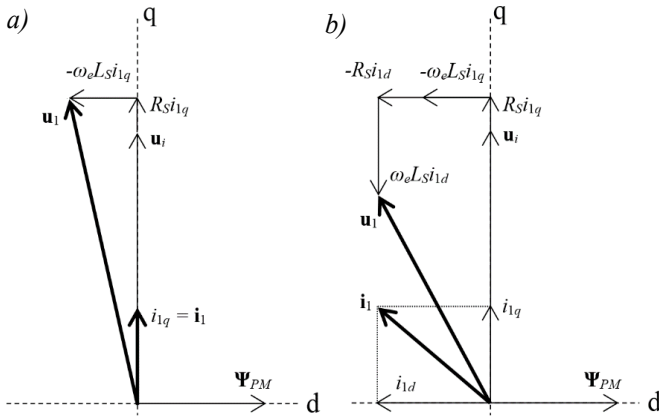


Fig. 2. The space position of single vectors in the rotor axis system in the vector control of the SMPM in the area of: a) nominal speed b) field weakening

3 Regulatory algorithm of vector control SMPM

The block diagram of the regulatory loop of the vector control of the SMPM is introduced on Figure 3.

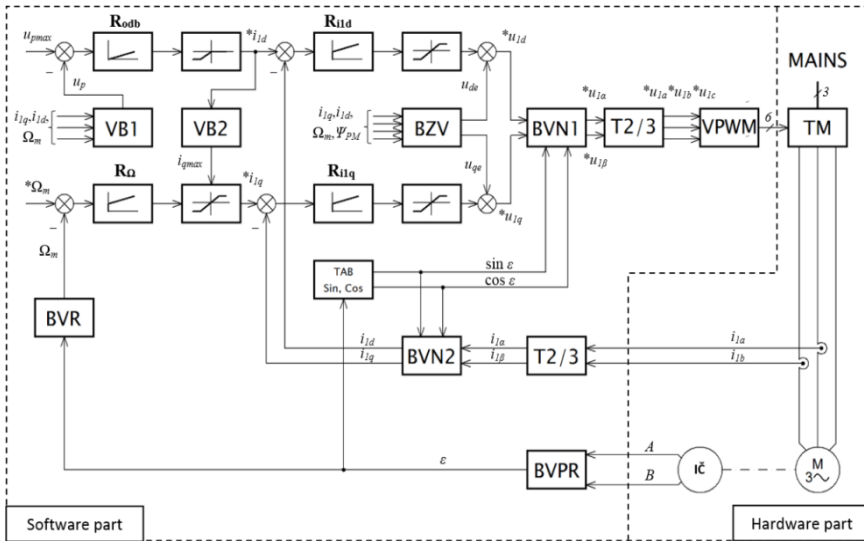


Fig. 3 Block diagram of regulatory structure in the vector control of the SMPM

VB1– computing block 1, **VB2** – computing block 2, **BVR** – block speed evaluation, **BZV** – decoupling block, **sin cos** – table of sinus and cosinus values angle, **BVPR** – evaluation block of the rotor, **T3/2** – Park transformation, **T2/3** – inverse Park transformation, **BVN1** – evaluation block rotation 1, **BVN2** – evaluation block rotation 2, **VPWM** – (method) comparison **PWM**, **TM** – semiconductor converter, **IC** – incremental sensor

The stator phase currents i_{1a} and i_{1b} are measured by the current sensor. Then the signal is lead into the block of transformation T3/2 where the stator current vector \mathbf{i}_1 is converted into the biaxial axis system and happen to be current $i_{1\alpha}$ and $i_{1\beta}$. At the same time we measure the position of the rotor by incremental sensor and its signals are converted by the blocks BVPR and TAB to the functions of angle of arbor rotation $\sin\varepsilon$ and $\cos\varepsilon$. Based on the rotor position the block BVN1 makes conversion of the stator currents $i_{1\alpha}$ and $i_{1\beta}$ to the stator currents i_{1d} and i_{1q} into the rotor axis system. The regulators R_{i1d} and R_{i1q} keep flux and torque component of current i_{1d} and i_{1q} on required values according to required quantity $*i_{1d}$ a $*i_{1q}$. The information about required values are coming from high-level regulators of the speed R_Ω (for R_{i1q}) and regulator of the field weakening R_{odb} (for R_{i1d}). The absolute value of the induced voltage vector u_p is calculated in the block VB1 according the equation (11). According to absolute value of the induced voltage vector u_p occurs the field weakening of the motor. The output of the regulator R_{odb} allows the decrease of the flux component of current into negative values only. The block VB2 provides the calculation (12) for variable limitation. On the output of the regulators R_{i1d} and R_{i1q} occurs the elimination of the cross coupling (components u_{de} and u_{qe}) according the equations (7) and (8). The calculation takes place in the block BZV. In the block BVN2 the control voltage $*u_{1d}$ and $*u_{1q}$ is converted from the rotor axis system into the stator axis system as voltage $*u_{1\alpha}$ and $*u_{1\beta}$. Than with the help of Park transformation (T2/3) the voltage is converted into three phases control voltage $*u_{Sa}$, $*u_{Sb}$ and $*u_{Sc}$. After that it is modulated in the block VPWM and sent to the frequency converter.

4 Experimental results

The measurement has been proceeded in laboratory on measurement station with SMPM – machine type 1FK7063-5AF71 made by Siemens. The control system with digital signal processor TMS320F28335 has been used for the vector control with the speed regulation.

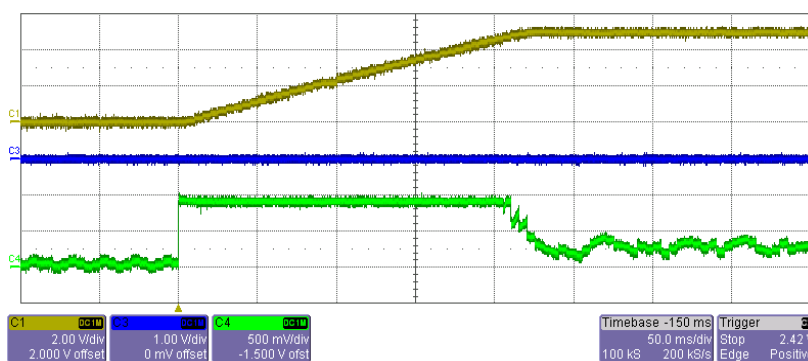


Fig. 4. Start of drive from 0rpm to 1000rpm in the unloaded conduction without field weakening

C1 – real rotation speed of rotor (1V = 1000rpm), C3 – flux component of current i_{1d} (1V = 1A), C4 – torque component of current i_{1q} (1V = 1A)

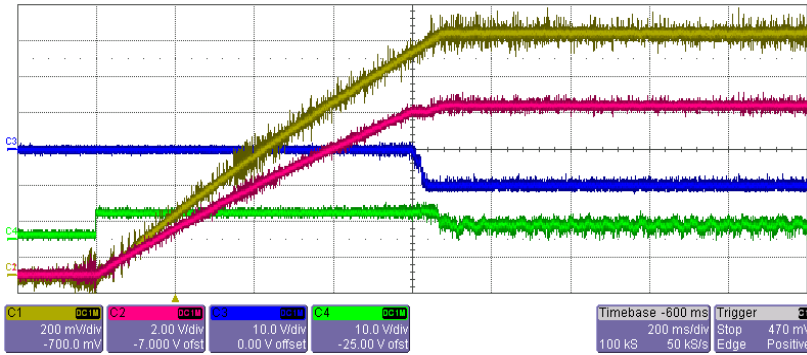


Fig. 5. Start of drive from 0rpm to 1430rpm in the unloaded conduction with field weakening

C1 – real rotation speed of rotor (1V = 1000rpm), C2 – induced voltage u_p (1V = 100V), C3 – flux component of current i_{1d} (1V = 1A), C4 – torque component of current i_{1q} (1V = 1A)

At first the waveforms were measured in the area of nominal speed when the motor starts from zero speeds to 1000rpm (see Figure 4). On the waveforms can see the angular speed of the rotor, the flux component of current and torque component of current. As next step of the measurement of the waveforms took place in area of the field weakening with angular speed under 1430rpm (see Figure 5). On the waveform we can see the decrease of the induced voltage with the increasing negative part of flux component of current.

5 Conclusion

The algorithm of the vector control of the SMPM has been developed and tested on the real drive with good results in static and dynamics areas (the starting, the breaking, the reversing and the stable operation). Measured waveforms see in Figure 4 and Figure 5 demonstrate the function of drive in the vector control of the speed regulation. Nowadays the measure station is used for teaching and for experimental purposes in laboratories of VŠB-TUO.

6 References

1. Brandstetter, P.: *Electric Controlled Drives III*, VSB – Technical University of Ostrava, Ostrava 2012.
2. Platnic, M. (2016, 6. 8.). *Implementation of Vector Control for PMSM Using the TMS320F240 DSP*. Retrieved from Texas Instruments: www.ti.com/lit/an/spra494/spra949.pdf
3. *Digital Signal Processing Solution for Permanent Magnet Synchronous Motor*. (2016, 8. 6.). Retrieved from Texas Instruments: www.ti.com/lit/an/bpra044/bpra044.pdf

Analysis of Motor Data Identification Process of Frequency Converter SINAMICS S120

Peter Januška

Department of Electronics, FEECS,
VŠB – Technical University of Ostrava, 17. listopadu 15,
708 33 Ostrava – Poruba, Czech Republic
peter.januska.st@vsb.cz

Abstract. Manufacturers of frequency converters provide for their products a lot of software applications, which can be used not only for commissioning. They include for example advanced functions for automatic parameter identification of connected asynchronous motor, tools for drive optimization, communication configuration and many other options. This paper describes functions and integrated processes for automatic parameter identification of asynchronous motor which is connected to commercially distributed frequency converter Sinamics S120 from Siemens. It offers a description of practical procedure of identification complemented with graphical illustrations of measured signals.

Keywords: motor data identification, standstill measurement, rotating measurement, speed control tuning.

1 Introduction

An identification process should start immediately after connecting of frequency converter with 3-phase asynchronous motor to the power grid, when it is necessary to enter a set of some basic parameters before you can run automatic identification itself. Normally, the basic information from the manufacturers rating plate of the motor is sufficient. In that case, when only one motor module of the frequency converter operates with many of different asynchronous motors, it is necessary to go through an identification process for each motor separately. In this case, each motor corresponds to one set of parameters, called MDS (Motor Data Set). For motors, which are equipped with speed sensor, connected via Siemens Drive-Cliq interface, the necessity of initial parameters entering is suppressed. All parameters are automatically read from the electronic rating plate of the motor. It is convenient to put the motor for a sufficient long time to environment where it will run, before starting an identification process. The reason is equalization of the motor temperature with an ambient temperature. The value of ambient temperature should be entered into converter before identifying the motor. For successful identification, it is also useful to connect motor with appropriate motor cables. During the automatic identification of motor parameters, the motor shaft may turn slightly, it is therefore necessary to ensure safe operation of the free end of the motor shaft.

After successful automatic identification of the motor parameters, it is possible to continue with optimization of the speed controller parameters. During this process, the moment of inertia of the connected load is taken into account. Therefore it is necessary to ensure good connection with load. After performing static identification and subsequently optimization of the speed controller, the drive is ready for operation.

2 Motor data identification (standstill measurement)

Static identification is used to determine the parameters of equivalent circuit diagram without rotating of the motor shaft. The motor cable resistance is one part of the diagram, therefore it is not sufficient to use a provisional motor cable. In case of using long motor cables, it is appropriate to specify the value of their resistance, which can then be subtracted from the measured resistance and thus the value of the stator resistance can be determined more accurately. Incorrectly entered rating plate parameters may also affect the value of stator resistance, which greatly affects the stability of SLVC (Sensorless Vector Control) and also the voltage boost for the V/f control. Conversely, correct estimation of the motor cable resistance improves the accuracy of thermal resistance adaptation, which has a significant impact in low speed operation, mainly in SLVC mode. Correctly entered value of ambient temperature is taken as a reference point for the thermal motor model and thermal R_S/R_R adaptation. [1]

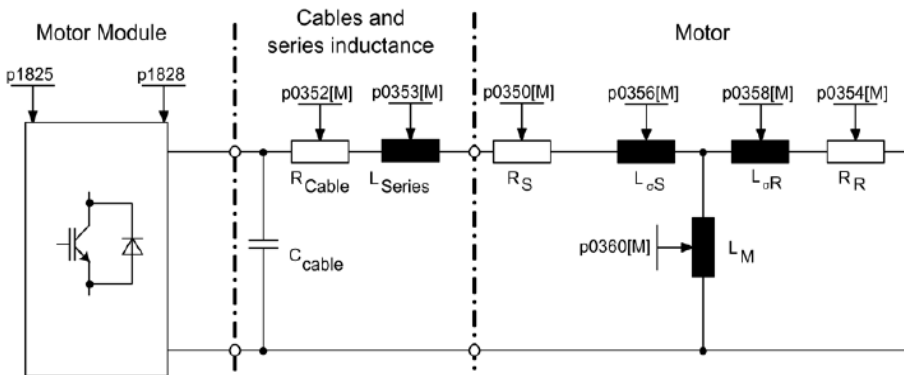


Fig. 1. Equivalent circuit diagram for induction motor and cable [1]

If the output filter or another series inductance is used on the output side of the frequency converter, it is also necessary to enter their parameters before starting the identification process. With this inductance value is calculated during leakage measurement.

The rating plate parameters are used as initial values for static identification algorithms. Great emphasis is placed on the correct determining of circuit (star/delta). The result of the calculations is to determine the following parameters:

- Rotor and stator resistance
- Magnetizing inductance

- Rated magnetization current
- Rotor and stator leakage inductance
- Drive converter valve threshold voltage
- Converter valve interlocking times

If sine-wave filters are used, only the stator resistance, drive converter valve threshold voltage and converter valve interlocking times are measured. [1]

3 Rotating measurement

After static motor data identification, the optimization of speed controller parameters should be performed. Rotating measurement should be executed in two steps: before connecting the load and after the load is connected. First step is recommended because of the rated magnetization current and the magnetization characteristic calculation. Magnetization characteristic is used to determine the field generating current in the field weakening mode. This is used to increase torque accuracy. During rotating measurement are this values determined much more accurately. The second rotating measurement with connected load has automatically deactivated recording of the saturation characteristic. The total moment of inertia is calculated and speed controller parameters are tuned. For this purpose, it is necessary to ensure good connection of motor and load. The rotational measurement comprises following steps:

- Encoder test – the direction of rotation and the number of pulses are checked
- Measurement of the saturation characteristic and magnetizing current
- Measurement of the saturation of the leakage inductance and current controller adaptation
- Speed controller tuning
- Setting of acceleration precontrol
- Determining of ratio between the total moment of inertia and shaft moment of inertia

For the purpose of good estimation of total moment of inertia it is recommended to realize rotating measurement with highest possible motor shaft speed. It is necessary to take into account the kind of load. This value and the value of speed for calculating of saturation characteristic or encoder test should be coherently set.

Tuned parameters of speed controller are during optimization set to the symmetrical optimum in accordance with dynamic factor. Value of dynamic factor must be set before rotating measurement. The value 100% means speed controller optimization according to a symmetric optimum. The value higher than 100% means optimization with a higher dynamic response (higher K_p , lower T_n). Actual dynamic response can be reduced as a result of mechanical load oscillations or large torque ripples. It is possible to realize rotating measurement without the oscillation test, but it is not recommended. The drive must be checked, that it is stable across the entire control range. [1]

4 Results

For analysis of identification process was used Device Trace tool included in software tool for parametrizing of frequency converters Siemens – STARTER. For identification was selected star connected 4-pole asynchronous motor with nominal power 1,57kW.

4.1 Standstill measurement

Below mentioned parameters was used from rating plate:

- Nominal voltage: 400V
- Nominal current: 3,15A
- Nominal power: 1,57kW
- Cos φ : 0,8
- Nominal frequency: 50Hz
- Nominal speed: 1445rpm
- Cooling: forced ventilation

The next picture shows these curves:

- Blue: steps of identification process
- Black: motor temperature
- Green: absolute current actual value
- Orange: phase U current actual value
- Red: phase V current actual value
- Pink: phase W current actual value

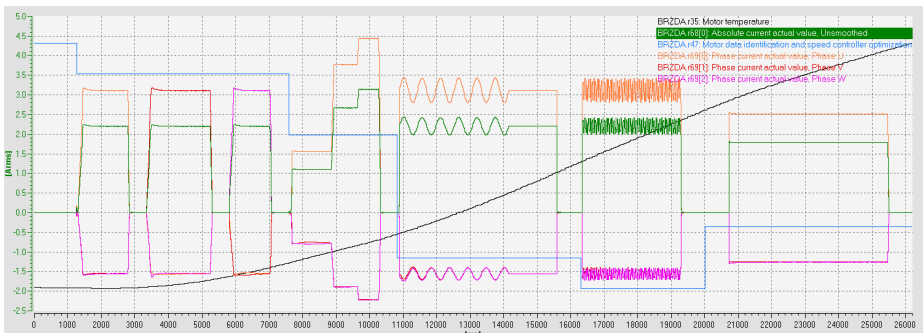


Fig. 2. : Curves of stator currents

The identification process consists of these sections:

- 300 – Start of stationary identification process
- 290 – Specifying of converter valve interlocking times
- 270 – Measurement of stator resistance
- 230 – Identification of rotor time constant
- 220 – Identification of leakage inductance

240 – Identification of stator inductance
 0 – End of identification

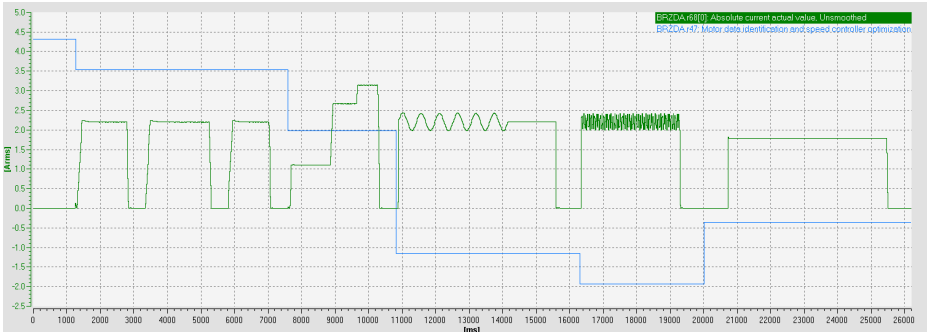


Fig. 3 : Absolute current actual value

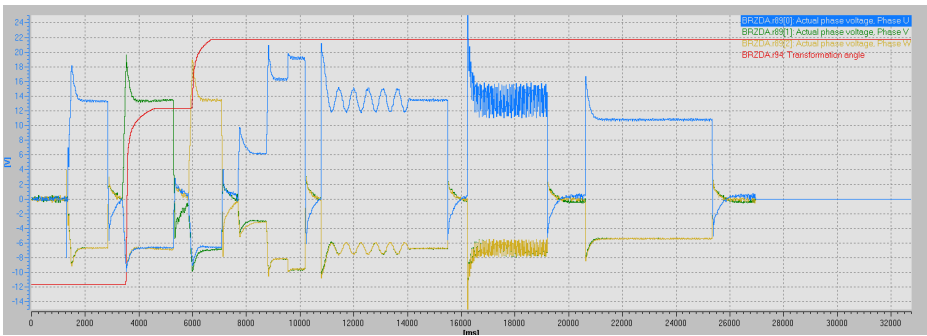


Fig. 4 : Phase U, V, W actual voltage

4.2 Rotating measurement

Next picture shows steps of rotating measurements, absolute current actual value, actual speed and an increase of motor temperature.

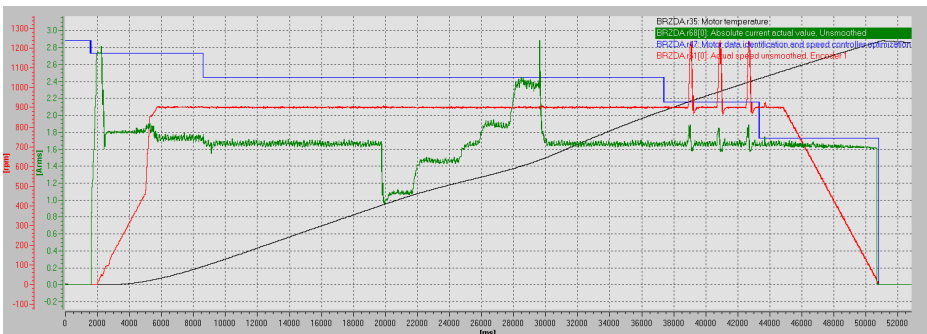


Fig. 5. Stator current actual value, actual speed

The optimization process consists of these steps (blue curve on Fig.5):

- 200 – Rotating measurement selected
- 190 – Speed encoder test
- 170 – Measurement magnetizing current and saturation characteristic
- 150 – Measurement moment of inertia
- 120 – Speed controller optimization
- 0 – End of measurement

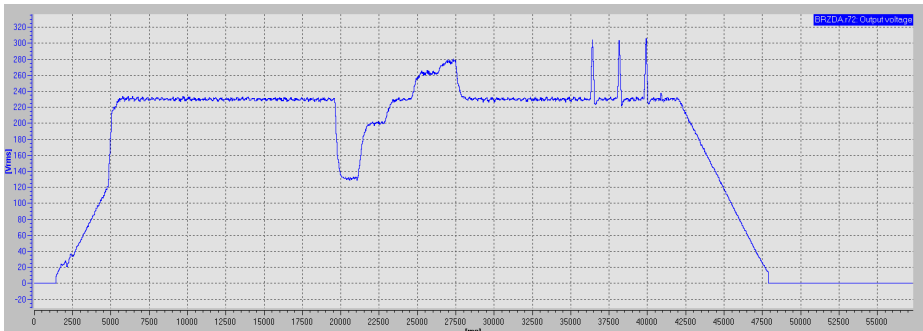


Fig. 6. Output voltage

5 Conclusion

After successful motor data identification process, important parameters of equivalent circuit diagram for induction motor were obtained:

- Motor rated magnetizing current: 1,607A
- Motor moment of inertia: 0,006062kgm²
- Cable resistance: 0,81295Ω
- Cold stator resistance: 3,25181Ω
- Cold rotor resistance: 2,72254Ω
- Stator leakage inductance: 25,6182mH
- Rotor leakage inductance: 27,5593mH
- Motor magnetizing inductance: 404,983mH

During static motor data identification process, speed controller parameters remain stable at values $P = 3,92$ and $T_i = 96\text{ms}$. After rotating measurement, this parameters was adjusted to $P = 3,73$ and $T_i = 48\text{ms}$.

6 References

1. SIOS: SINAMICS S120 Function Manual Drive Functions. Home - English - Siemens Global Website [online]. NÜRNBERG: Siemens, 2014 [cit. 2016-08-04]. Available: <https://support.industry.siemens.com/cs/mdm/99686093?c=65848063883&lc=en-WW>

Setting up the Optimal Operating Point of the Adams Motor Generator

Martin Koutný

Department of Electrical Power Engineering, FEECS,
VŠB – Technical University of Ostrava, 17. listopadu 15,
708 33 Ostrava – Poruba, Czech Republic
martin.koutny.st3@vsb.cz

Abstract. This paper focuses on description, practical realization and operational testing of the Adams pulsed motor generator with permanent magnets in rotor. In January 1993 Robert Adams released a manual which describes the high efficiency motor generator. The purpose for the machine realization is interesting balance of the input and output battery voltage measured by Adams. The machine described in this paper is realized with a few construction differences in comparison with the original Adams motor generator described in the Adams motor generator manual. The result of the paper is relative comparison of the revolutions of the rotor represented by current switching frequency for several degree position of the feet-back coil in stator. There is a significant increase speed of the rotor and decrease of current supplying the stator coil.

Keywords: motor, Adams motor generator, vacuum, vacuum fluctuation, zero-point energy field, aether, efficiency, back-electro motive force, energy conversion, permanent magnet, electric power generation, magnetic repulsion motor, ferromagnetic core.

1 Introduction

In January 1992-1993 Robert G. Adams from New Zealand has published The Adams pulsed motor generator manual. Nowadays the Australian Nexus New Times Magazine offers this manual for buy. Very interesting results of measurement on Adams machines are presented in the manual. Adams shows a many graphs of voltage trace measured on an input battery and on an output battery connected to the Adams motor generator. [1]

Robert Adams and Harold Aspden from the University of Cambridge are authors of UK patent 2,282,708 named Adams motor generator with a date of filling at 30.9.1993. The patent describing the principles utilized in upgraded Adams motor generator construction for reducing a magnetic flux leakage in the machine. [2]

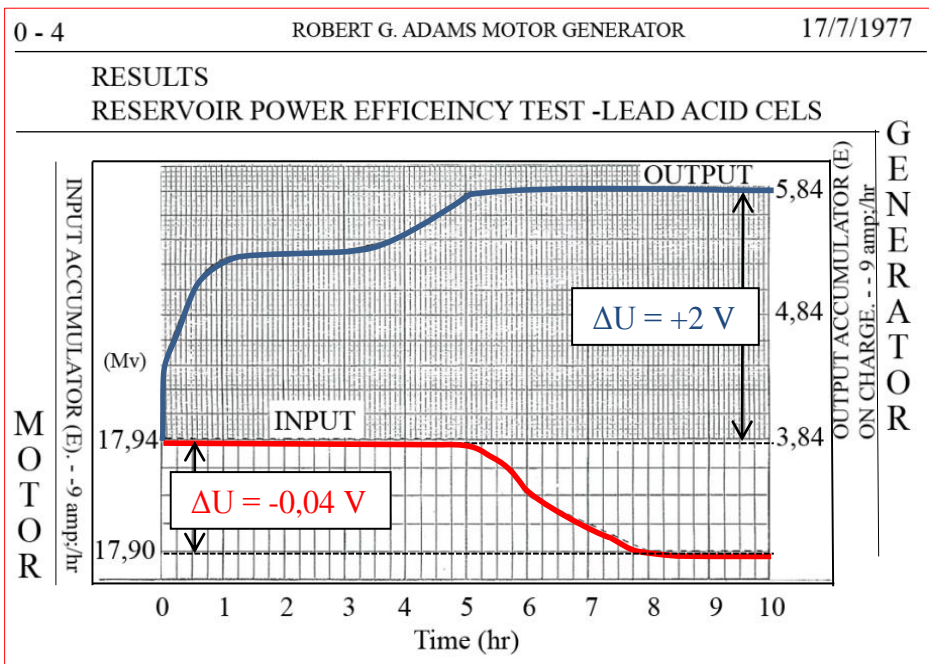
Many writers refer about a zero-point energy (ZPE) field pervading all space and about a possibility of conversion the ZPE to usable electric energy, for example in publications [3] and [4]. About the vacuum features dissertate the publication [5].

Harold Aspden have written about the ZPE in relationship with the equivalent term “aether” or quantum vacuum electromagnetic field fluctuations. [6]

Electromagnetic energy fluctuation activity in the vacuum is often connected with a Casimir effect, where is a non-symmetric state of quantum electromagnetic fluctuation in vacuum between two parallel metal plates and state of background. It is asymmetric state where attractive force between plates is presented. [3]

2 Energy conversion in Adams motor generator

In Fig.1. there is a measurement of an old car batteries voltage for determine the Adams machine efficiency during the test running for 10 hours. For this time the input battery voltage dropped from 17.94 V to 17.9 V and the secondary battery was charged from 3.84 V to 5.84 V. There is a relative low voltage drop 0.4 V on input battery and on the other hand, the output battery was charged about 2 V. [1]



3 The principles and structure of the Adams motor generator

The Adams motor generator is assembled using four permanent magnets in rotor, four permanent magnets in stator and three kinds of magnetic stator cores fitted with a coils.

In Fig. 2 is a sketch of the Adams motor generator coils and magnet configuration for demonstration the principles of the machine. The stator permanent magnets are represented by blue cylinders. These magnets were not used in realized machine.

1. A drive coils - $L_{D1,2}$ are mounted on a “drive cores” and are used to repulse the salient poles of the rotor by demagnetization the drive core by current pulse.
2. A feet-back coils - $L_{BMF1,2}$ (or the equivalent coils named L_{FB} in Fig. 3) are excited by back-electromotoric force produced by the drive coil after a voltage supply is switched off by a mechanic or an electronic commutator.
3. A generator coils - $L_{G1,2}$ are used to generate electric power and it can be used for the measure the efficiency.

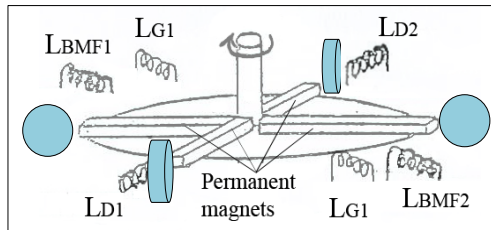


Fig. 2. Adams drawings of the stator coils and magnets configuration [1]

We can use different number of the stator coil pairs for any type of coil. There is wide capability of configuration the Adams model for set up the optimal operation point. The Adams motor generator utilize the physical phenomenon called back electromotive force (B-EMF). In the Adams motor generator, the B-EMF is produced in the drive coils when the voltage supply is switched off. The same principle is used in voltage converters for reach efficiency.

In Fig. 3, the drive coils are connected to the battery by mechanic or electronic commutator S_D . The output voltage U_2 can be used as an alternator output. Adams didn't mention where the output battery was connected for charging during the tests.

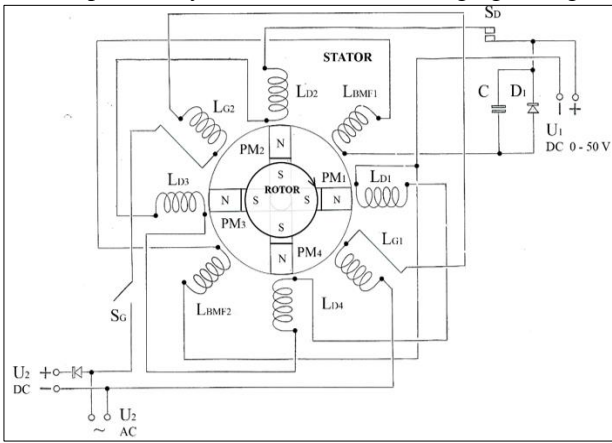


Fig. 3. The one of the scheme of the Adams motor generator

4 Realization of the Adams motor generator

4.1 Electronic control circuit

The benefits based on use Arduino Nano programmable module allows periodically switching the current supply supplying the drive coil. In Fig. 4. is the electronic circuit of the machine. A sensor Hall A detects the switch on supply position and a Hall B sensor detects the switch off position.

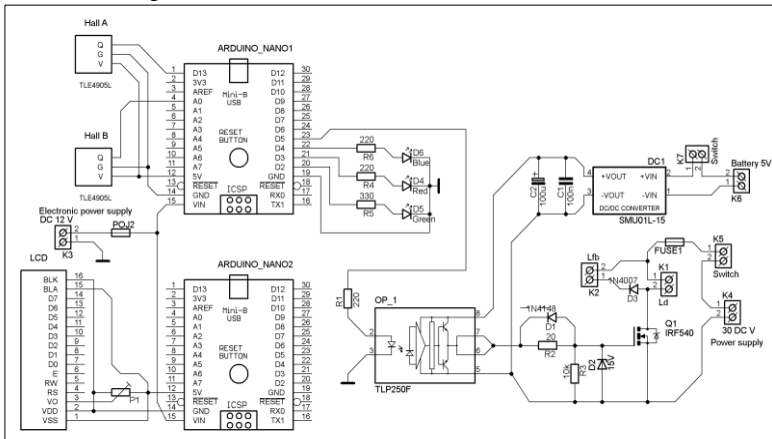


Fig. 4. Electronic circuit for switching the current in the drive coil L_D

Switching time is determined by position of sensors, actual speed of the rotor and switching delay. Arduino Nano 1 producing a switching pulses in dependence on relative position between the stator and rotor poles. The Arduino Nano 2 is counting the time for the drive coil is switched on and switched off, counting a frequency of the current and shows the actual values on LCD. The layout of realized machine is described in Fig. 5.

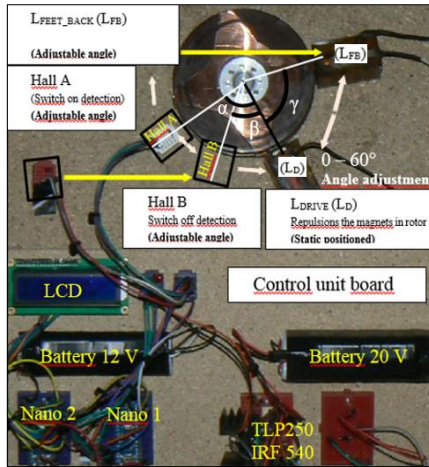


Fig. 5. The side view of the Adams motor generator structure (without generator stator coil L_G).

4.2 The magnetic parts of Adams motor generator

There are four NdFeB permanent magnets $PM_1 - PM_4$ in the rotor with the same polarity and ahead to the perimeter of the rotor. Remanent flux density B_r is 1.21 T, coercivity of -980 kA/m and dimensions of 8 x 8 x 32 mm. Adams didn't describe the parameters, and polarity of stator magnets. The magnetic stator cores are made of electric sheets with thickness of 0.1 mm. There are the parameters of the L_D and L_{FB} coil in Table 1. and the Table 2. presents the maximum value of measured remanent flux density of the rotor permanent magnet, flux density measured on the surface of cores during supplying the coils at 5 V and 30 V.

Table 1. Parameters of the coils and cores

	\varnothing_{Cu}	N	L	R	Core
L_D	0,2 mm	900	21,46 mH	19,83 Ω	10x6x36 mm
L_{FB}	0,2 mm	440	6,34 mH	14,68 Ω	5x6x36 mm

Table 2. The values of flux density on the surface of the magnet and of the stator cores.

Measured on the face	Magnet	Coil 1		Coil 2	
		(5 V) *	(30 V) *	(5 V) *	(30 V) *
Conditions:	B_{TMAX}				
Maximum flux density	0,522 T	0,021	0,041	0,023	0,031
DC current in coil [A]	-	0,13	0,66	0,27	0,33

5 Conclusion

For comparison the relative efficiency of the following configuration of the machine serves Fig. 6, where L_{FB} is unconnected to L_D (on the left) and the coil L_{FB} is connected to the L_D (on the right). The operational test in Fig 6. shows dependence of frequency and current on the angle adjusted between L_D and L_{FB} at 30 V DC power supply.

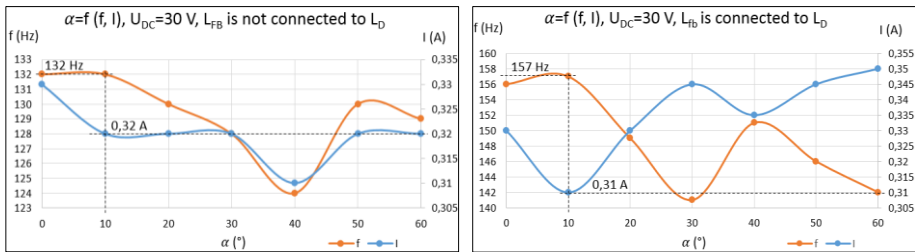


Fig. 6. The current and frequency dependence of the angle adjustment between the L_D and the L_{FB} . The left part is without the connection between the L_{FB} and the L_D and on the right part is the L_{FB} connected to the L_D .

On the left part of Fig. 6 the magnetic energy stored by the drive coil was not used for creating additional tongue in the Adams motor generator. The frequency and current was 132 Hz and 0,32 A at the most optimal angle 10° between the L_D and L_{FB} . The higher efficiency was indicated in the case on the right part of the Fig. 6. There was the feet-back coil connected with drive coil and supplied by the energy of collapsing magnetic field in the drive coil at the 157 Hz, 0,31 A and 10° .

The results of measurement of an upgraded construction of the Adams motor generator was presented at conference Electro 2016 in Slovakia under paper named FEM electromagnetic simulation and Operational Testing of the Adams Electric D.C. Motor-Generator. The device for presentation the principle of the Adams motor generator was realized and named Storing magnetic energy in air gap. There is a difference between results of Adams and Aspden air gap experiment [6] and experiment on realized device. The relative drop of the current measured for difference air gap dimension was not appeared at the level of magnetic flux in linear part of the BH characteristic of the ferromagnetic transformer core.

6 Acknowledgement

Acknowledgement: This research was partially supported by the SGS grant from VSB-TU Ostrava (No. SP2016/95) and by the project TUCENET (No. LO1404).

7 References

[1] ADAMS, Robert. The Adams pulsed motor generator manual. 46 Landing Roat,

- Whakanate, New Zealand: Nexus magazine, 1992.
- [2] ADAMS, Robert George a Harold ASPDEN. Electrical motor-generator. Patent, GB2282708, 1993.
 - [3] VALONE, Thomas. Zero Point Energy: The Fuel of the Future. United States: Integrity Research Institute, 2007, 228 s. ISBN 9780964107021.
 - [4] KING, Moray B. Quest for Zero Point Energy: Engineering Principles for Free Energy: Engineering Principles for Free Energy. United States: Integrity Research Institute, 2001, 224 s. ISBN 9780932813947.
 - [5] RAFELSKI, Johann a Berndt MÜLLER. The structured vacuum: Thinking about nothing. Published electrically, 2006. ISBN 3-97144-889-3.
 - [6] ASPDEN, Harold. Power from magnetism. Sabberton Publications, 1996. ISBN 0850560179.

Ultracapacitors Cooperation with Photovoltaic and Hydrogen Technology in ENET Centre

Michal Ney

Department of Electrical Power Engineering, FEECS,
VŠB – Technical University of Ostrava, 17. listopadu 15,
708 33 Ostrava – Poruba, Czech Republic
michal.ney.st@vsb.cz

Abstract. This paper deals with utilisation of ultracapacitors in cooperation with a photovoltaic power plant and the hydrogen technology for accumulation of electric power. All these technologies are situated within the ENET centre for research of renewable resources and accumulation of power.

Keywords accumulation; fuel cell; hydrogen; photovoltaic plant; ultracapacitor

1 Introduction

The ENET technology centre is fitted with several systems for generation and accumulation of electric power. Power is generated by the photovoltaic plant, fuel cells integrated within the hydrogen technology for accumulation, together with two synchronous generators that are included in co-generations units one of which is driven by the Stirling engine. The fuel for this system is natural or pyrolyzed gas produced by the inherent thermal cracker processing basically any combustible solid waste.

The accumulation system comprises a set of lead and lithium batteries, four ultracapacitors and the above-mentioned hydrogen technology used for production of hydrogen through electrolysis of de-mineralised water, storage of the hydrogen produced in pressure vessels and its subsequent use as fuel in fuel cells. All these technologies serve exclusively for accumulation of energy supplied from the photovoltaic plant. For a detailed description of the said technologies, refer to further chapters below.

2 Photovoltaic plant

The photovoltaic plant is formed by three sections installed on the centre building. The first section is installed on the southern side of the inclined roof and it is made of polycrystalline panels Trina Solar TSM PC05. The second section is located on the straight part of the roof and made of polycrystalline panels EcoDuoAUO PM220P00. This section is fitted with an automatic adjustment device to achieve maximum exposure of panels during the day. The third section is fitted on the roof above the adjacent auditorium and it is formed by non-crystalline photovoltaic foils Fatrasol Model 576. The total installed power from this plant is 22.5 kWp, the detailed parameters of panels and sections can be found in Table I.

TABLE I. PHOTOVOLTAIC PLANT PARAMETERS

Section	1	2	3
Number of panels	60	18	10
Power of panel [Wp]	210	230	576
Number of strings	6	2	5
Number of panels in string	10	9	2
Power of section [kWp]	12.6	4.14	5.76
No load voltage of section [V]	364	336	370
Nominal current of section [A]	47.2	16	26.5

3 Accumulators

The centre is equipped with an accumulator room using a set of lead traction batteries with the total capacity of 930 Ah and a set of batteries type LiFePO with the total capacity of 200 Ah. The distribution plant is further fitted with lead gel-based batteries with the total capacity of 200 Ah. The resultant voltage of LiFePO assembly is 400 V and both Pb sets are rated for 480 V.

TABLE II. ULTRACAPACITOR MODULE PARAMETERS [1]

Rated Capacitance	63 F
Maximum Capacitance (initial)	76 F
Number of Cells	48
Capacitance of Individual Cells	3000 F
Rated Voltage	125 V
Maximum Voltage	136 V
Maximum Current	1900 A
Short Circuit Current	6900 A
Maximum Leakage Current	10 mA
Maximum ESR (initial)	18 mΩ
Stored Energy	140 Wh
Stored Energy of Individual Cells	3 Wh
Mass (without fan)	61 kg

4 Ultracapacitors

The distribution plant is installed with four modules of ultracapacitors Maxwell BMOD0063 P125s with parameters defined in the Table II.

5 Hydrogen Technology

The hydrogen technology lab is provided with eight electrolyzers Acta AES500 and five modules of fuel cells Nedstack FCS 8-XXL. The detailed parameters of these devices can be found in Table III. and Table IV.

TABLE III. ELECTROLYZER PARAMETERS [2]

Cell number:	38 (2 blocks x 19 cells)
Maximum H₂ production:	504 NI/h
Operating current:	30 A
Operating voltage:	34.6 – 35.5 V (each block)
Power consumption:	2075 – 2132 W
Efficiency:	85 %

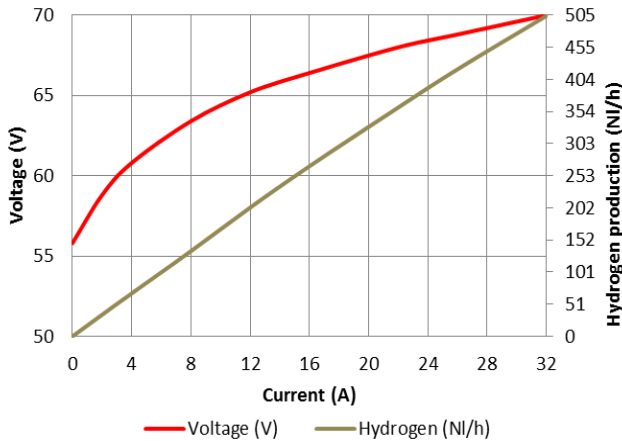


Fig. 1. Electrolyzers AES500 characteristics

TABLE IV. FUEL CELL MODULE PARAMETERS [3]

Cell number:	64
Maximum power:	8 kW
Maximum current:	230 A
Operating voltage:	61.9 – 34.8 V
Maximum H₂ consumpti-	102 NI/min

6 Centre Operation with Ultracapacitors

The daytime operation with the photovoltaic plant in full pace delivering sufficient power also includes electrolyzers and the hydrogen produced is collected into pressure vessels. Fluctuation of power delivered by the photovoltaic plant due to overcast condition is balanced by a set of Lithium batteries in order to ensure reliable operation of electrolyzers. Photovoltaic panels and and electrolyzers are linked with the direct-current bus bar with the nominal voltage of 400 V via the DC/DC binding converters [4].

When the fuel cells are in operation, the power supplied is consumed within the centre, any unused power can be then supplied to the grid. The load characteristics of fuel cells is significantly soft, full load reduces their voltage to the half of open-circuit voltage. This event is not desired for the load condition and it can be oobviously eliminated by a sufficiently broad range of the input voltage in the inverter or the binding DC/DC converter employed. However, there is also the option to use ultracapacitors for stabilisation of fuel cells, especially to smoothen the current spikes during load actuation in order to limit voltage drops.

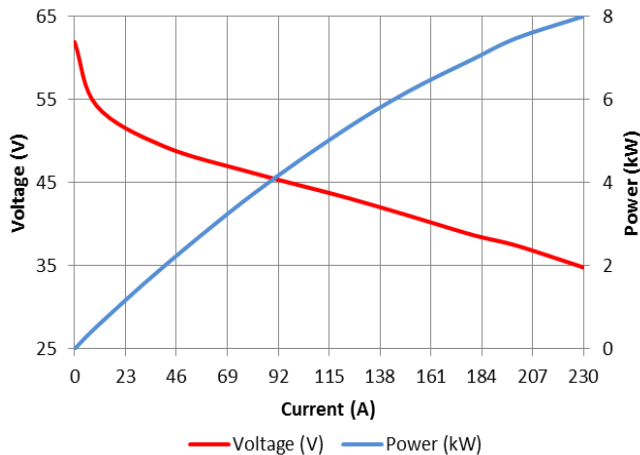


Fig. 2. Fuel cell module Nedstack FCS 8-XXL load characteristics

Cooperation of ultracapacitors with fuel cells is also fit for parallel operation of fuel cells, when these are connected in successive order with respect to the power drawn. When linking a not loaded cell with open-circuit voltage and a loaded cell with the ever lower voltage results in the transition effect to level the voltage in both cells accompanied by a current spike absorbed by the cell with lower voltage and its power is not used in any way. Such current spike can be also absorbed by the linked ultracapacitor [5].

See the simplified block diagram of the technology centre above. There are two isolated direct-current systems with the nominal voltage of 400 V and 480 V. The system rated for 400 V is connected to photovoltaic panels, electrolyzers and lithium batteries, the 480 V system is linked with fuel cells, ultracapacitors and lead batteries.

Both direct-current systems are in mutual linkage in terms of the binding converter. The system rated for 480 V is then further provided with an inverter linked to the regular three-phase grid (3x 230/400 V) connected to both co-generation units [6, 7].

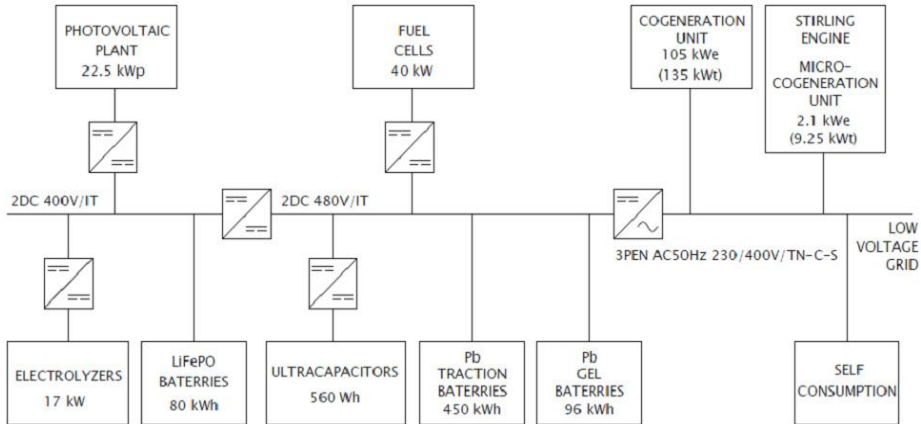


Fig. 3. Simplified block diagram of technological centre

7 Conclusion

The paper describes individual parts of the technological centre, including their parameters and the options for their mutual cooperation. The photovoltaic plant with polycrystalline panels and the non-crystalline foil deliver the output of 22.5 kWp. The accumulation with lead batteries enables storage of almost 550 kWh of power, with further 80 kWh that can be stored in lithium batteries. The accumulation capacity of ultracapacitors rated for 560 Wh is negligible when compared to these batteries, yet the ultracapacitors can be charged promptly and these are able to supply a very strong current over a short time interval, the manufacturer declares the supply of up to 1 900 A. This parameter is suitable to cover current spikes during actuation of loads and during cooperation with fuel cells significant for fairly soft load characteristic. Fuel cells are integrated in the hydrogen technology for accumulation offering the power of 40 kW.

Hydrogen is produced using electrolyzers with the installed capacity of 17 kW and these are supplied solely by the photovoltaic plant. The installed power sources include the co-generation unit with the power output of 105 kW and the heat output of 135 kW; that is supplemented with another micro co-generation unit based on Stirling engine with the power output of approx. 2 kW and the heat output of almost 10 kW. Both co-generation units may be fuelled using the natural or pyrolyzed gas from the internal thermal cracker. The energy obtained from all the sources installed is mainly consumed internally, with potential surplus available for supply to the distribution

grid. The aim of further research in the technological centre is to optimise cooperation among renewable energy resources, especially by means of photovoltaic plants and accumulation technologies.

Acknowledgement

This research was partially supported by the SGS grant from VSB – Technical University of Ostrava (No. SP2016/95) and by the project LO1404: Sustainable development of ENET Centre.

References

- [1] Heavy Transportation Module, Datasheet, [online], [2016-02-08] <http://www.maxwell.com/images/documents/125vmodule_ds_1014696-7.pdf>
- [2] AES500-1000, Datasheet, [online], [2016-01-29] <<http://www.acta-spa.com/wp-content/uploads/2013/08/AES500-1000.pdf>>
- [3] Product Specifications of XXL stacks, [online], [2016-01-29] <<http://www.nedstack.com/products/product-specifications-of-xxl-stacks>>
- [4] J. Vaculik, P. Moldrik and Z. Hradilek, “Laboratory Research of Hydrogen Production at VSB-Technical University of Ostrava,” *Advances in Electrical and Electronic Engineering*, vol. 11, Issue 1, pp. 10-15, March 2013.
- [5] D. Minarik, B. Horak, P. Moldrik and Z. Slanina, “An Experimental Study of Laboratory Hybrid Power System with the Hydrogen Technologies,” *Advances in Electrical and Electronic Engineering*, vol. 12, Issue 5, pp. 518-528, December 2014.
- [6] P. Vaculik and J. Frantik, “Mix of Energy Sources in Technology Centre of Ostrava,” *Proceedings of the 2015 16th International Scientific Conference on Electric Power Engineering*, Eds. S. Rusek and R. Gono, Ostrava: IEEE, pp. 448-452, May 2015.
- [7] P. Vaculik and P. Kanovsky, “Research on Modern Semiconductor Converters and the Usage of SiC Devices in the Technology Centre of Ostrava,” *World Academy of Science, Engineering and Technology, International Journal of Computer, Electrical, Automation, Control and Information Engineering*, pp. 1016-1021, 2015.

The Estimation of Inrush Current for Direct Connection of Induction Generator to Grid

Jan Otýpka

Department of Electrical Engineering, FEECS,
VŠB – Technical University of Ostrava, 17. listopadu 15,
708 33 Ostrava – Poruba, Czech Republic
jan.otypka@vsb.cz

Abstract. This paper is focused on the estimation the size and the time waveform by the inrush current for the direct connection of induction generator to grid. The simulation of this system has been provided by Matlab Simulink environment, where main aim is focused on observation of initial conditions induction generator direct connection. The simulation solutions are summary in end of this paper, when the gear importance is placed to the time point of induction generator direct connection.

Keywords: Induction motor, generator, inrush current, direct connection, grid.

1 Introduction

This paper is focused on using of the induction generator (further referred as IG) for electric energy production at a hydro – power plant and which effects during the direct connection to MVG. The generally lower price is a great advantage of such IG's operation in comparison with synchronous generator (excitation circuit). Hence, the IG is designed for small hydro – power plants rated to 10MW.

These conditions must be ensured for operation of the induction motor as the generator state:

- The shaft speed must be higher than synchronous speed.
- The IG must have source of reactive power for creating of magnetic field.

The reactive power could be supplied by the capacitor battery or directly form mains. The examined 2,65MW engine is operated at the small hydro-power plant Slezská Harta. The main aim of this paper is determined the inrush current value by models and simulations for direct connection of IG to mains. This evaluation of inrush current is necessary for power engineering, because the voltage dip created on the mains and transformer impedances results in the supply voltage dip.

The direct connection analysis is undertaken by using the d-q coordinate frame model with the parameters, which are given by the manufacturer Končar Generators

and Motors Inc. This analysis is based on the operating state when the IG is operated with shaft speed close to synchronous speed for a low values of slip (less than 1%) in the generator and motor state. The task is to determine the inrush current value for the worst state of connecting the IG. Furthermore, the paper is focused on the analysis of the connection IG for the different immediate value of terminal voltage. This fact has great impact on the inrush current value respectively the DC component of this current.

2 The Problems of Direct Connection of Induction Generator at UN Slezská Harta

In this paper describes the concerned case, when the IG with terminal voltage 6.3kV is connected by the switch to the 22kV MVG through a transformer, as shown at fig. 1. The IG is rotated by the water turbine to over-synchronous speed and is connected subsequently to the grid. The generator is not excited by the external source of reactive power, which is required for creating of magnetic field.

The reactive power consumption is accompanied by the current inrush impact, which can achieve the values of starting current from zero speed. This inrush current creates the voltage dip on the impedances of the grid and the transformer. The supply voltage dip is defined by standard [1], which does not suit the measured voltage dip on the output of hydro – power plant Slezská Harta.

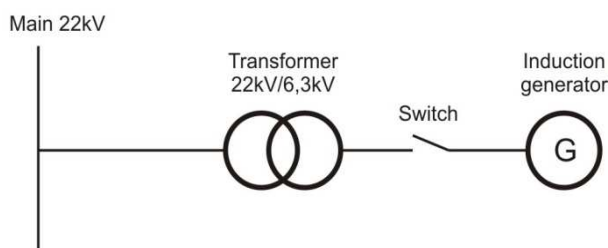


Fig.1. The layout of the direct connection of IG to 22kV mains through a transformer.

2 The Matlab Simulink Analysis of Inrush Current

The Matlab Simulink environment is used for the design of the IG – transformer – grid system and simulation of the inrush current. The great advantage of this environment is the using of the function blocks, which are important for the realization of the complicated mathematical functions. The described model was created by using of a toolbox SimPower System for designing the completed blocks for the electrical engines, transformers, electronics and switching elements etc.

The system model is shown on fig. 2 for the direct connection of IG to grid. The mechanical shaft angle speed Ω_m is forced to model of IG. The simulations could be performed for the generator or motor states by choosing the shaft angle speed. Then the rotating IG is connected to the grid through the transformer. The main task of this simulation is the obtaining of the waveforms of inrush current and voltage dip for each phase before and behind the transformer.

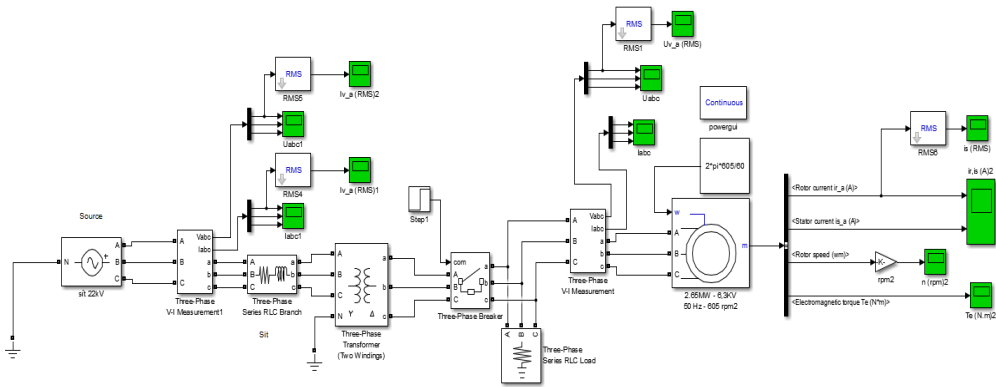


Fig.2. The layout of the direct connection of IG to 22kV mains through a transformer.

The model of generator based on [4], which describes the asynchronous starting process of hydro-generator, another models of IG are also described in [5] and [6]. The model of IG is based on the following voltage equations for the stationary d-q- coordinate frame:

$$u_{ds} = R_S i_{ds} + \frac{d\Psi_{ds}}{dt}, \tag{1}$$

$$u_{qs} = R_S i_{qs} + \frac{d\Psi_{ds}}{dt}, \tag{2}$$

$$u_{dr} = 0 = R_R i_{dr} + \frac{d\Psi_{dr}}{dt} + \omega_r \Psi_{qr}, \tag{3}$$

$$u_{qr} = 0 = R_R i_{qr} + \frac{d\Psi_{qr}}{dt} - \omega_r \Psi_{dr}, \tag{4}$$

where the magnetic stator and rotor fluxes are given by equations set for d and q axis:

$$\Psi_{ds} = L_S i_{ds} + L_m i_{dr}, \tag{5}$$

$$\Psi_{qs} = L_S i_{qs} + L_m i_{qr}, \tag{6}$$

$$\Psi_{dr} = L_R i_{dr} + L_m i_{ds}, \tag{7}$$

$$\Psi_{qr} = L_R i_{qr} + L_m i_{qs}, \tag{8}$$

The internal electromagnetic torque and rotor angle speed are calculated as follows:

$$T_e = \frac{3}{2} p_p L_m (i_{qs} i_{dr} - i_{ds} i_{qr}), \tag{9}$$

$$\omega_r = p_p \Omega_m, \tag{10}$$

where p_p is number of pole pairs and ω_r is the electrical rotor angle speed. The parameters of examined IG at the hydro – power plant Slezská Harta are listed in tab. 1. These parameters were given by the manufacturer - Končar Generators and Motors Inc.

Table 1. The table of identified parameters for specific type of induction motor

<i>Parameter</i>	<i>Sign</i>	<i>Value</i>
Nominal power	P_N	2.65 MW
Nominal voltage	U_N	6 300 V
Nominal current	I_N	280 A
Nominal frequency of grid	f_N	50 Hz
Nominal speed	n_n	605 rpm
$\cos \varphi$	$\cos \varphi$	0.87
Stator resistance	R_S	0.085 Ω
Stator leakage inductance	$L_{1\sigma}$	4.8 mH
Rotor resistance	R_R	0.075 Ω
Rotor leakage inductance	$L_{2\sigma}$	4.3 mH
Magnetizing inductance	L_m	136.9 mH
Equivalent resistance for core loos	R_{Fe}	2390 Ω
Winding connection		Star

Firstly, the IG is rotated by the turbine to the nominal speed $n_n = 605$ rpm for simulation. The rotated and unexcited generator is connected to mains by 3-phase switch with internal resistance $R_{on} = 0.1$ m Ω . The grid is represented by the distribution transformer, the 22 kV source and the impedance Z_a , which is given by serial connection of mains resistance R_a and mains inductance L_a (the identified main parameters recalculated to 6.3kV are $R_a = 0.609$ Ω and $L_a = 5.12$ mH). The connection is performed at the immediate voltage value $u(t) = 0V$ and $\varphi_0 = 0$ rad for the first phase.

The simulated inrush current waveforms in each phase are shown on fig. 3 for direct connection of IG to grid on the secondary site of transformer. The voltage dips waveforms are shown on fig. 4. Furthermore, the paper is also focused on the research of moment φ_0 of the connection of IG to the mains. The simulations were performed for the accurately defined connection moment φ_0 , which was defined by the angle in

range 0 to $\pi/2$ rad. Hence, this fact has great impact on the inrush current value especially the DC component of this current.

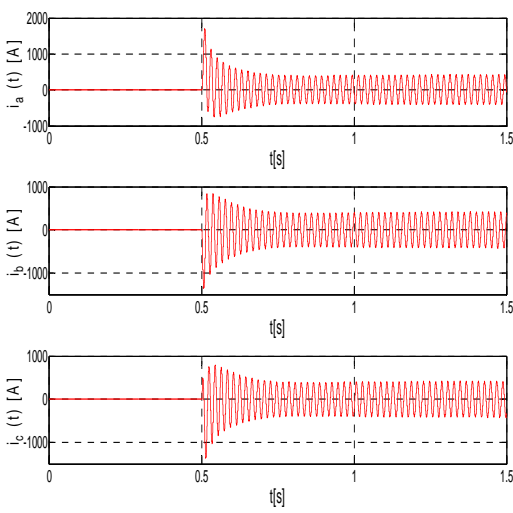


Fig. 3. The inrush current waveforms in each phase for direct connection of IG at $n = 605$ rpm.

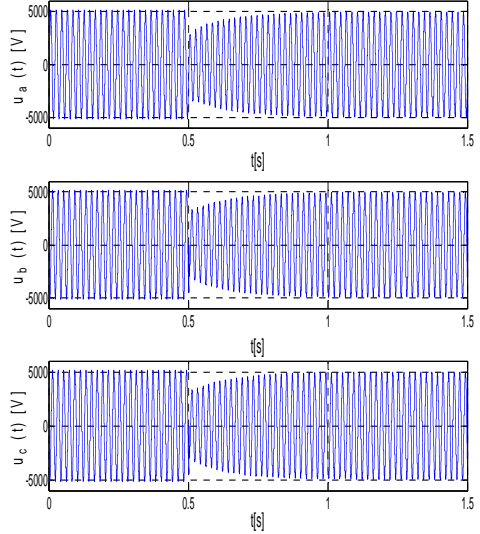


Fig. 4. The dip voltage waveforms on secondary transformer site at $n = 605$ rpm.

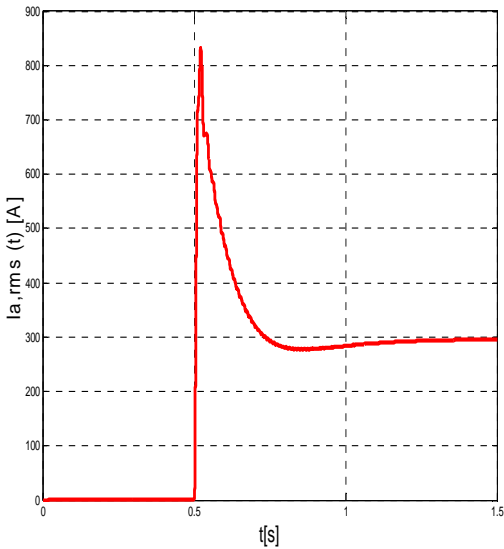


Fig. 5. The effective value of inrush current in first phase for $n = 605$ rpm and connection moment $\varphi_0 = \pi/3$

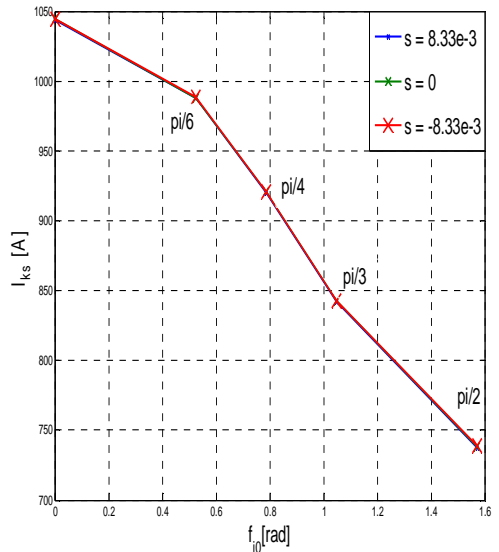


Fig. 6. The dependence of maximal inrush current value for different connection moments and slips

3 Conclusion

The inrush current and dip voltage waveforms could be precisely simulated by the software environment Matlab Simulink for the direct connection of IG to grid for the different operation states (generator, motor and synchronous state). The value of grid impedance Z_a has the main effect on maximal value of inrush current reducing by this impedance and the voltage drop created by this current, which results in the voltage dip in the grid.

Furthermore, the stator and rotor resistance have rather small the influence on the maximal value of inrush current, because both resistance values could be negated by the stator and rotor leakage reactance values for the 3MW IG ($R_S \ll \omega L_{\sigma 1}$ and $R_R \ll \omega L'_{\sigma 2}$). This fact is confirmed by simulation. Hence, the maximal inrush current values are identical for the generator, motor and synchronous state.

The IG was simulated for the different time-points of direct connection, when the effect of transient DC component was observed at the maximal inrush current level for different time points and confirmed in [6].

Acknowledgment

The work is partially supported by Grant of SGS N°. SP2016/143, VŠB - Technical University of Ostrava, Czech Republic.

References

1. ČSN EN 50160
2. J. Bašta, J. Chládek, I. Mayer, "Teorie elektrických strojů", SNTL, Praha 1968.
3. T. J. Hammonts, "Voltage dips due to direct connection of induction generator in low head hydro electric scheme", IEEE Transaction on Energy Conversion, 1994.
4. Z. Maljkovic, M. Šundrica, B. Tomičić, "Asynchronous Starting Proces of Hydro-generator". IEEE, ISBN 978-1-4244-1736-0, 2008.
5. M. Vlasák, "Reduction of Exciting Current of Induction Machine During Connection to Electrical Grid". IEEE, ISBN 978-1-4799-3720-2, 2014.
6. J. Otýpka, V. Stýskala, D. Kolosov, S. Mišák, "The Simulation of Connection of the Induction Generator to Grid Using the d-q Coordinate Frame Model". Proceedings Of The 8th International Scientific Symposium On Electrical Power Engineering (Elektroenergetika 2015), TECHNICAL UNIV KOSICE, FAC ELECTRICAL ENGRG & INFORMATICS, 2015, s. 460-464, ISBN 978-80-553-2187-5

Application of FEM Modeling for Analysis of Asynchronous Motor

Pavel Pečínka, Tomáš Hrubý, and Stanislav Kocman

Department of Electrical Engineering, FEECS,
VŠB – Technical University of Ostrava, 17. listopadu 15,
708 33 Ostrava – Poruba, Czech Republic
{pavel.pecinka.st, tomas.hruby.st1, stanislav.kocman}@vsb.cz

Abstract. This paper presents a time-dependent simulation of three-phase squirrel cage asynchronous motor using COMSOL Multiphysics software. Simulation was made for constant rotational velocity adjusted to the nominal one of the tested motor. The work describes finite element method model, external electrical circuits and meshing. The course of stator currents, currents in rotor bars and in rotor ring and course of motor torque are also shown. The values of stator current and motor torque are compared to their values from motor catalogue. As will be seen, the simulation results from COMSOL match the catalogue values rather well.

Keywords: COMSOL, asynchronous motor, model, simulation, motor parameters, simulation.

1 Introduction

Three-phase squirrel cage asynchronous motors are the most widespread types of electrical motors used in electrical drives in various technical applications in industrial plants. Asynchronous motor is an electromagnetic device with complex geometry and several phenomena, such as magnetic field, electrical circuits and mechanical rotation. To help of better understanding of these phenomena it is important to develop their models. To design and calculate asynchronous motors, respectively the numerical electromagnetic field calculation is used as an important tool. Finite element method (FEM) which uses subdivision of a whole problem domain into simpler parts called finite elements and variant methods to solve the problem by minimizing an associated error function is used for analyses of electrical machines [1]-[6]. In this case COMSOL Multiphysics is used for an analysis of asynchronous motor with catalogue parameters in Table 1.

Table 1. The catalogue parameters of the motor

Selected motor parameters			
Rated power	4 kW	Nominal speed	1440 rpm
Nominal voltage	400 V	Nominal power factor	0.83
Nominal current	8,4 A	Nominal torque	27 N·m
Nominal frequency	50 Hz	Nominal efficiency	83,1 %

2 FEM Model Description

The electromagnetic field in asynchronous motor is described by the set of Maxwell's equations stated as:

$$\operatorname{div} \underline{B} = 0, \quad (1)$$

where \underline{B} is the magnetic flux density,

$$\operatorname{rot} \underline{E} = -\frac{\partial \underline{B}}{\partial t}, \quad (2)$$

where \underline{E} is the electric field,

$$\operatorname{rot} \underline{H} = \underline{J}, \quad (3)$$

where \underline{H} is the magnetic field, \underline{J} is the current density. Combination of (1)-(3) with constitutive relations for material properties following equations are given, which are solved in the Rotating Machinery physic of COMSOL [7]:

$$\sigma \frac{\partial \underline{A}}{\partial t} + \operatorname{rot} \underline{H} - \sigma \underline{v} \times \underline{B} = \underline{J}_e, \quad (4)$$

$$\operatorname{rot} \underline{A} = \underline{B}, \quad (5)$$

where \underline{A} is the magnetic vector potential, σ is the electric conductivity, \underline{v} is the velocity of conductors, \underline{J}_e is the externally generated current density.

Externally generated current density \underline{J}_e for stator slot in the model of asynchronous motor with multi-turn coil is formulated as:

$$\underline{J}_e = \frac{NI}{A} \underline{e}, \quad (6)$$

where N is the number of turns of the stator coil, I is the stator phase current, A is the total cross-section area of the coil domain, \underline{e} is the vector field representing the direction of the wires in the slot. Externally generated current density \underline{J}_e for rotor slot in the model of asynchronous motor with single-turn coil is formulated as:

$$\underline{J}_e = \sigma \frac{V}{d} \underline{e}, \quad (7)$$

where V is the electrical potential applied on the turn of the coil, i.e. on the rotor bar, d is the physics interface's thickness.

3 External Electrical Circuits

Some parameters and conditions which cannot be included into FEM model are incorporated into external electrical circuits in COMSOL. Three-phase sinusoidal voltage source is connected to the stator in the FEM model through end-winding impedances representing overhang effects as it can be seen in Fig.1. Rotor bars are interconnected through external impedances representing end-ring impedances and resistors for the part of bar which is outside of the iron sheets, but in the ring as seen in Fig. 2.

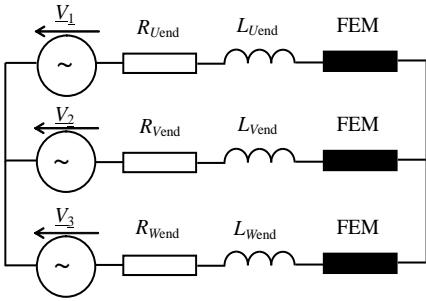


Fig. 1. Coupling external stator electrical circuit and FEM model.

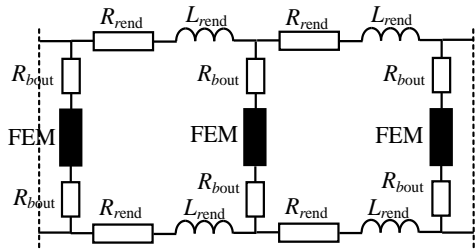


Fig. 2. Part of rotor circuit

4 Asynchronous Motor Model Meshing

The asynchronous motor geometry is shown in Fig. 3. The mesh of it was carried out as user-controlled mesh in COMSOL. A detail of the air gap meshing is shown in Fig. 4.

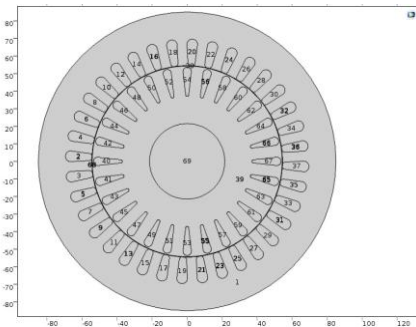


Fig. 3. Asynchronous motor geometry.

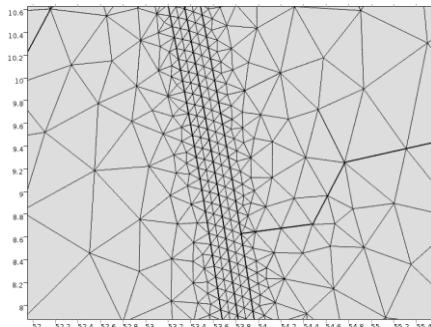


Fig. 4. Detail of the mesh in the airgap

The very small air gap of asynchronous motors requires a special attention to obtain a proper meshing of domains in this region. A free triangular node was used to

create unstructured triangular meshes in domains. Statistics of the mesh is given in Table 2.

Table 2. The statistics results of the mesh

Selected parameters	
Triangular elements	80056
Edge elements	15858
Vertex elements	552
Minimum element quality	0.359
Average element quality	0,8977
Element area ratio	2,002 E-5
Maximum growth rate	4,375
Average growth rate	1,552

5 Results of the simulation

Simulation was made for constant rotational velocity adjusted to the nominal one of the induction motor to detect stator currents, bar and ring currents and motor torque, and to compare values of stator current and motor torque to the catalogue values, respectively. In Fig. 5, magnetic flux density and equipotencial lines of magnetic vector potential is shown after reaching a steady state. As seen the magnetic field in the machine creates four magnetic poles.

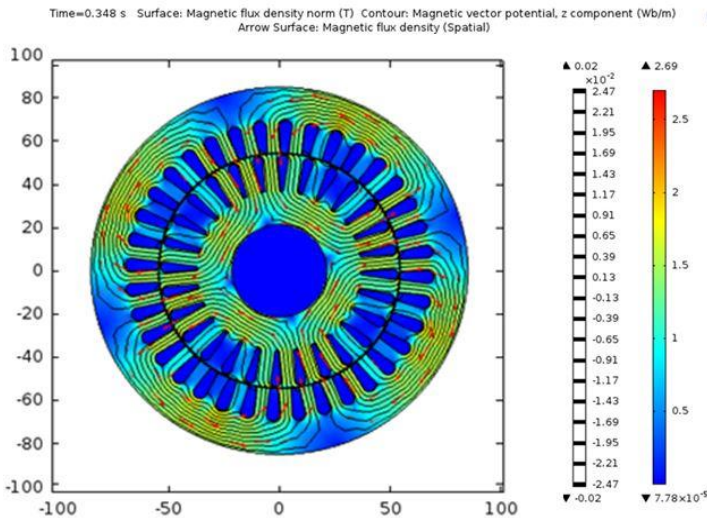


Fig. 5. Magnetic flux density and equipotencial lines of magnetic vector potential.

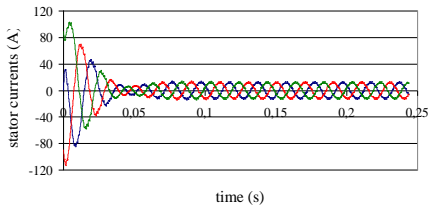


Fig. 6. Waveforms of stator currents for constant rotational

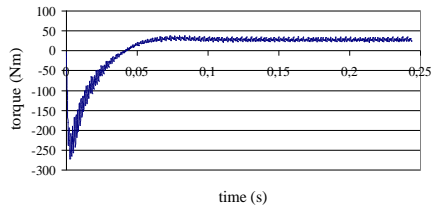


Fig. 7. Waveforms of motor torque for constant rotational velocity

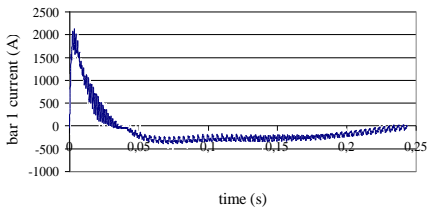


Fig. 8. Waveform of current of the first rotor bar.

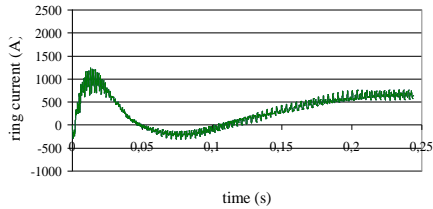


Fig. 9. Waveform of current in rotor ring.

In Table 3, a comparison of values of the stator current and motor torque from the induction motor simulation in COMSOL under the motor nominal speed to motor catalogue values is shown. As seen, there are some minor differences between values obtained from the simulation and motor catalogue ones. It should be mentioned that relatively longer time steps can be used for the calculation of the stator currents whereas for the calculation of the motor torque is necessary to use shorter ones to acquire more precise value.

Table 3. Comparison of selected parameters of the asynchronous motor

Parameter	Catalogue value	Measurement	Simulation
Speed	1440 rpm	1440 rpm	1440 rpm
Torque	27 N·m	26,5 N·m	27,9 N·m
Current	8,4 A	8,8 A	8,6 A

6 Conclusion

The model of three-phase squirrel cage asynchronous motor was carried out in COMSOL Multiphysics. To reduce three-dimensional model a quasi-3D model was

modeled coupling physic interfaces like Electrical Circuit and Rotating Machinery. Interconnection of external impedances in the electrical circuits to the FEM as it can be seen in Fig. 1 and in Fig. 2, respectively, is important to avoid inaccuracies in the tested motor parameters. A corresponding attention should be devoted to their correct identification and calculation. As shown above, the simulation results match the motor catalogue values rather well. The simulated values of stator current and torque exceed the catalogue ones only moderately, as it can be seen from their comparison in the Table 3. Their values depend on the accuracy of identification and calculation of induction motor parameters, geometry and material properties, and especially in the case of the inner motor torque on proper meshing of the motor air-gap and on the time step of simulation. The two-dimensional model in the COMSOL Multiphysics software is a good tool for study of induction motor behavior under various conditions of tested motor both electrical and mechanical. Further analyses will be carried out for next studies.

Acknowledgment

This work was supported by the SGS FEI, VŠB – TU under Grant SP 2016/143

References

- [1] M. Bose, A. Bhattacharjee, and R. Sudha, "Calculation of induction motor model parameters using finite element method," *International Journal of Soft Computing and Engineering (IJSCE)*, vol. 2, issue 3, pp. 41-43, July 2012.
- [2] A. Arkkio, *Analysis of Induction Motors Based on the Numerical Solution of the Magnetic Field and Circuit Equations*, Ph.D. thesis, ActaPolytechnicaScandinavica, Series No. 59, Helsinki, 1987.
- [3] E. Vassent, G. Meunier, A. Foggia, and G. Reyne, "Simulation of induction machine operation using a step by step finite element method coupled with circuits and mechanical equations," *IEEE Transactions on Magnetics*, vol. 27, No. 6, pp. 5232-5234, November 1991.
- [4] H. De Gersem, K. Hameyer, and T. Weiland, "Field-circuit coupled models in electromagnetic simulation," *Journal of Computational and Applied Mathematics*, No. 168, pp. 125-133, 2004.
- [5] R. Escarela-Perez, E. Melgoza, J. Alvarez-Ramirez, and A.-L. Laureano-Cruces, "Nonlinear time-harmonic finite-element analysis of coupled circuits and fields in low frequency electromagnetic devices," *Finite Elements in Analysis and Design*, No. 46, pp. 829-837, 2010.
- [6] P. Zhou, D. Lin, W. N. Fu, B. Ionescu, and Z. J. Cendes, "A general cosimulation approach for coupled field-circuit problems," *IEEE Transactions on Magnetics*, vol. 42, No. 4, pp. 1051-1054, April 2006.
- [7] COMSOL Multiphysics Reference Manual, November 2013.

Experimental Verification of Luenberger Observer in Sensorless Control Structure of Induction Motor Drive

Ondrej Petrtyl

Department of Electronics, FEECS,
VŠB – Technical University of Ostrava, 17. listopadu 15,
708 33 Ostrava – Poruba, Czech Republic
ondrej.petrtyl@vsb.cz

Abstract. The paper presents experimental results for a sensorless vector control of a three-phase induction motor with the Luenberger observer. Measured results are shown and differences between reference, measured and estimated values are discussed. An experimental rig - a hardware construction and a software implementation are described as well.

Keywords: sensorless control, induction motor, luenberger observer

1 Introduction

Induction motors (IM) are widespread in an industry nowadays. Especially with intelligent control methods and a sensorless realization. Modern microprocessor systems provide a sufficient power for a computation of all necessary variables in real-time. The aim of this paper is a sensorless vector control of a three-phase induction motor with the Luenberger observer (LO). A theory background has been presented previously [1], [2] based on these references [3] - [10].

2 Experimental Rig

The experimental rig has been done with a focus to a development of modern control methods for sensorless control drives, namely induction motors. A block diagram is presented bellow (Fig. 1). Results shown in this paper have been done for a control of one IM without a load. Main IM is coloured black. Second IM (load) and devices related with this motor are coloured gray.

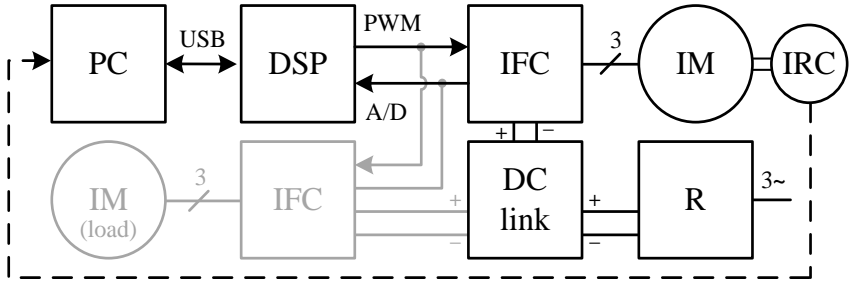


Fig. 1 Experimental rig - block diagram

The present realization is shown at the Fig. 2. The experimental rig contains two IMs with shafts connected by a flexible coupling. An IRC sensor is mounted on the shaft of the main motor and this signal is used for a comparison of a real (measured) and estimated speed. Both IMs are supplied by two indirect frequency converters (IFC) which are controlled by a digital signal processors (DSP). The control software is developed in a personal computer (PC) and connected with the DSP by USB.



Fig. 2 Experimental rig - realization

Left - PC, Converters and Control system (DSP). *Right* - IM with IRC, couple and IM (load).

3 Experimental Results

During an experimental measuring the vector control structure is implemented to the DSP which controls the IM via expansion modules and modules for a voltages and currents transformation as well as a galvanic isolation. A user interface on PC send data to the DSP, measured data are saved in an expansion memory of the DSP. From this memory are downloaded to PC and converted to plots in MATLAB.

The observers parameters have been set as follows, a parameter of observer matrix $k = 1.1$, a proportional constant $K_P = 0.1$, a constant of integration

$K_I = 1000$ and a voltage of DC link $U_{DC} = 250$ V. Figures below show three different types of results. First are referenced values provided by the control structure (blue colour), second are experimentally measured values (red) and finally estimated values from the observer (green). The reference speed has been set as step function, an initial value is 0 rpm and until 0.1 s, then has been changed to 200 rpm.

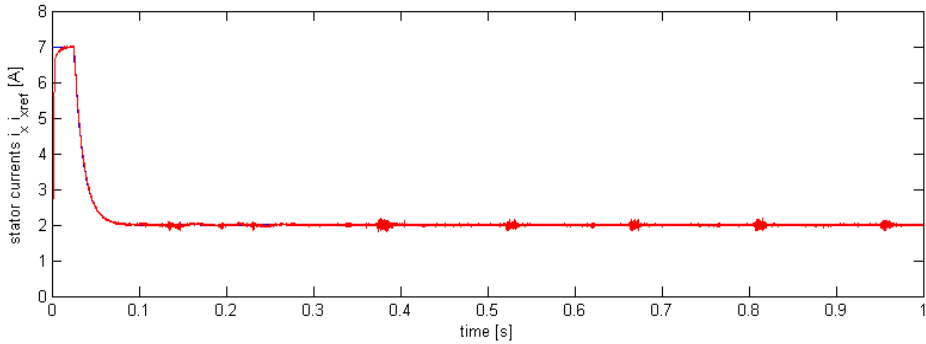


Fig. 3 Component of stator current i_{xref} (blue) and i_x (red) in magnetic field coordinate system

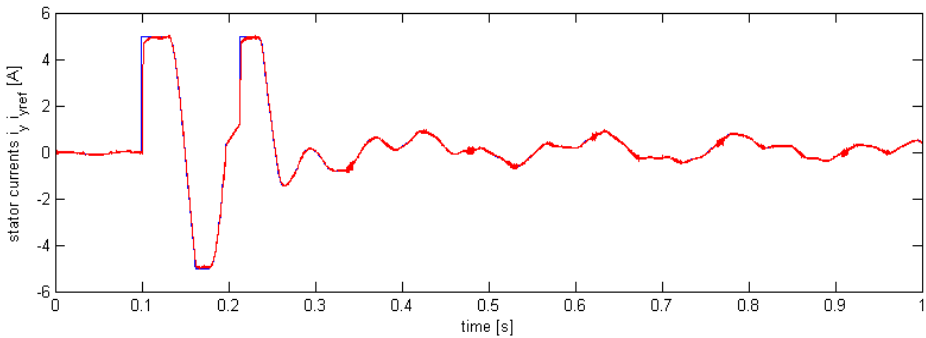


Fig. 4 Component of stator current i_{yref} (blue) and i_y (red) in magnetic field coordinate system

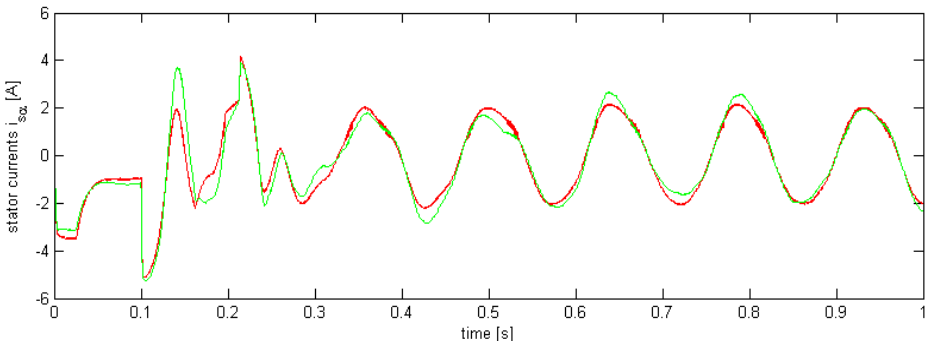


Fig. 5 Component of stator current $i_{s\alpha}$ (red) and $i_{s\alpha st}$ (green) in stator coordinate system

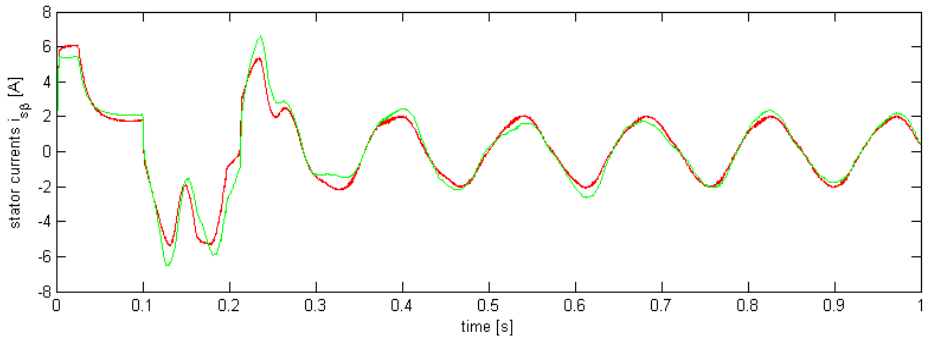


Fig. 6 Component of stator current $i_{s\beta}$ (red) and $i_{s\beta est}$ (green) in stator coordinate system

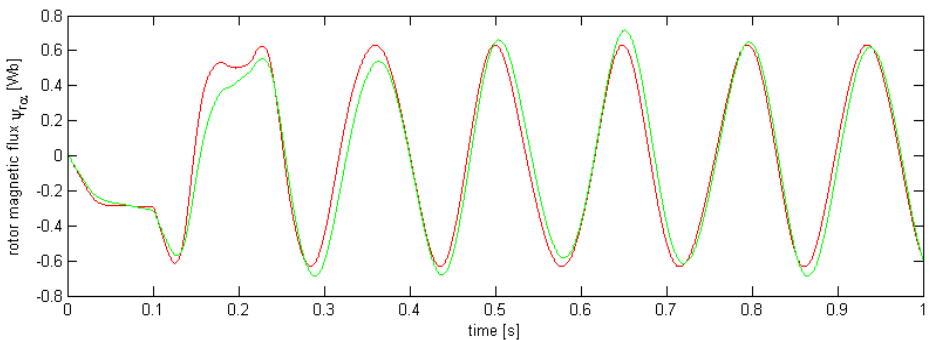


Fig. 7 Component of rotor magnetic flux $\psi_{r\alpha}$ (red) and $\psi_{r\alpha est}$ (green) in stator coordinate system

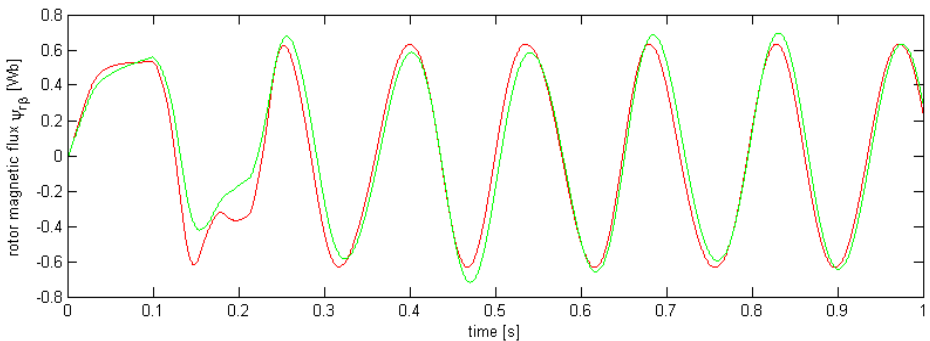


Fig. 8 Component of rotor magnetic flux $\psi_{r\beta}$ (red) and $\psi_{r\beta est}$ (green) in stator coordinate system

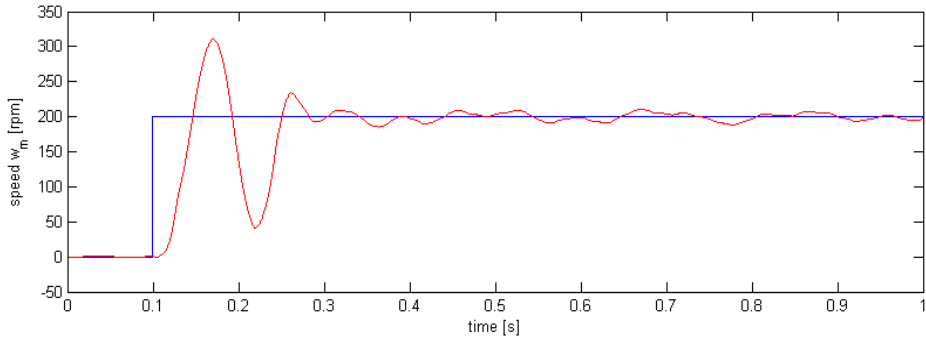


Fig. 9 Response to step function of speed ω_{mref} (blue) and ω_m (red)

4 Conclusions

The results presented above shows acceptable level of accuracy. Differences between measured and estimated values are generally lower than 5 %. Results prove observer is designed well, without rough inaccuracy. Of course tuning of parameters has to be done for lower differences, especially a dynamic response needs improvement.

5 Acknowledgement

The paper was supported by the projects: Center for Intelligent Drives and Advanced Machine Control (CIDAM) project, reg. no. TE02000103 funded by the Technology Agency of the Czech Republic, project reg. no. SP2016/83 funded by the Student Grant Competition of VSB-Technical University of Ostrava.

6 References

- [1] Petřtyl, O. *Design of Luenberger Observer for Sensorless Control of Induction Motor*. In 12th Annual Workshop of FEECS WOFEX, VSB-TU Ostrava, pp. 114-119, 2014, ISBN 978-80-248-3458-0.
- [2] Petřtyl, O. *Implementation of Luenberger Observer to Sensorless Vector Control Structure of Induction Motor Drive*. In 13th Annual Workshop of FEECS WOFEX, VSB-TU Ostrava, pp. 114-119, 2015, ISBN 978-80-248-3787-1.
- [3] Brandstetter, P. *AC Control Drives - Modern Control Methods*. VSB-Technical University of Ostrava, 1999. ISBN> 80-7078-668.

- [4] Brandstetter P. - Friedrich, J. *Speed Estimation of Induction Motor Using Luenberger Observer*. In Proceedings of the Acta Technica CSAV. vol. 57, pp. 113-126, 2012. ISSN 0001-7043.
- [5] Holtz, J. *Sensorless control of induction motor drives*. Proceedings of the IEEE vol. 90, no. 8, pp. 1359-1394, 2002. DOI: 10.1109/JPROC.2002.800726, ISSN: 0018-9219.
- [6] Bose, B. K. *Modern power electronics and AC drives*. Upper Saddle River, NJ : Prentice Hall PTR, 711 p., 2002, ISBN 0-13-016743-6.
- [7] Luenberger, D. G. *An introduction to observers*. *Automatic Control*. IEEE Transactions on, 1971, vol. 16, no. 6, pp. 596602. ISSN: 0018-9286.
- [8] Cuzner, R.M. - Lorenz, R.D. - Novotny, D.W. *Application of nonlinear observers for rotor position detection on an induction motor using machine voltages and currents*. Industry Applications Society Annual Meeting, 1990., Conference Record of the 1990 IEEE, vol. 1, pp. 416-421, 1990. DOI: 10.1109/IAS.1990.152219, ISBN: 0-87942-553-9.
- [9] Zalman, M. - Gacho, J. *IM Based Speed Servodrive with Luenberger Observer*. Journal of ELECTRICAL ENGINEERING, vol. 61, no. 3, pp. 149-156, 2010. ISSN: 1335-3632.
- [10] Pana, T.C. - Stoicuta, O. *Small speed asymptotic stability study of an induction motor sensorless speed control system with extended Luenberger estimator*. In Optimization of Electrical and Electronic Equipment, 2008. OPTIM 2008. 11th International Conference, pp. 175 - 180, 22 - 24 May 2008. doi: 10.1109/OPTIM.2008.4602406.

Genetic Algorithm Application for Parameters Optimization of Speed Controller in Induction Motor Drive

Think Cong Tran

Faculty of Electrical and Electronics Engineering, Ton Duc Thang University, 19
Nguyen Huu Tho street, Dist. 7, Ho Chi Minh City, Vietnam
trancongthink@tdt.edu.vn

Abstract- The paper presents a genetic algorithm application for parameter settings of a speed controller in the control structure of the induction motor drive. An induction motor model with the PI speed controller is described in the first part. The second part presents how to determine the parameters of PI speed controller using the genetic algorithm. Important simulations with the traditional PI speed controller and the PI speed controller using the genetic algorithm together with change of parameters and variable disturbances were performed in the Matlab-Simulink environment.

Keywords: induction motor, vector control, speed controller, genetic algorithm, parameter optimization.

1 Introduction

The vector controlled induction motor drives are widely used in high performance motion control. Because of torque/flux decoupling, the vector control achieves a good dynamic response and an accurate motion control as the control of separately excited DC motors. However, in real-time implementation, precise decoupling which requires accurate motor parameters cannot be completely achieved due to significant plant uncertainties. These uncertainties include external disturbances, unpredictable parameter variations, and plant nonlinear dynamics. Consequently this deteriorates the dynamic performance of the drive significantly. Generally speaking, the performance of this control system depends on the accuracy of the mathematical model of induction motor [1]-[3].

Genetic Algorithm (GA) based search and optimization techniques have recently found increasing use in machine learning, drive systems, robot motion planning, scheduling, pattern recognition, image sensing and many other engineering applications. GA is search algorithm based on mechanics of natural selection and natural genetics [2], [3].

In a closed loop, speed control system the speed error is proposed through PI controllers. With the elapse of time, the error varies and full effectiveness of the control aspect cannot be achieved. Sometimes, the conventional controllers produce unwanted oscillations or slow response.

2 Mathematical model of the vector controlled induction motor

The voltage equations of the induction motor (IM) model in x - y coordinates are expressed as follows:

$$v_{sx} = R_s i_{sx} + \frac{L_s}{L_m} \frac{d\psi_{rx}}{dt} - L_m \sigma \frac{di_{rx}}{dt} - \omega_e \frac{L_m}{L_r} \psi_{ry} - \omega_e \sigma L_s i_{sy} \quad (1)$$

$$v_{sy} = R_s i_{sy} + L_s \sigma \frac{di_{sy}}{dt} + \omega_e L_s i_{sx} + \frac{L_m^2}{L_r} \frac{di_{sy}}{dt} + \omega_e L_m i_{rx} + L_m \frac{di_{ry}}{dt} \quad (2)$$

Where $\sigma = 1 - \frac{L_m^2}{L_s L}$ is the leakage coefficient.

If the vector control is established such that y -axis component of the rotor flux vector is set zero, and x -axis rotor flux is maintained constant, then we have following equations:

$$\psi_{rx} = L_m i_{sx} \quad (3)$$

The slip frequency is calculated from the reference torque producing component of stator current vector i_{sy_ref} and the motor parameters:

$$\omega_{sl} = \omega_e - \omega_r = \frac{L_m}{T_r} \frac{i_{sy_ref}}{\psi_{rx}} \quad (4)$$

Where $T_r = L_r / R_r$ is the rotor time constant.

For the coordinates transformation, the rotor flux position θ_e is necessary. It is calculated from the rotor speed ω_r and slip frequency ω_{sl} as follows:

$$\theta_e = \int (\omega_r + \omega_{sl}) dt \quad (5)$$

The electromagnetic torque of the IM is given by:

$$T_e = \frac{3}{2} p_p \frac{L_m}{L_r} \psi_{rx} i_{sy} \quad (6)$$

The Fig. 1 shows the speed control structure of the induction motor drive that was implemented in Matlab-Simulink environment.

3 Classical PI speed controller

The quality of the control is assessed according to the response of the control loop to step changes of input variables. From a practical point of view, four factors are the most important for the assessment of the control quality: rise time t_r , settling time t_s ,

overshoot y_m and steady state error Δ . The classical PID speed controller for the induction motor drive can be expressed as follows:

$$i_{sy_ref} = K_p (\omega_{m_ref} - \omega_m) + K_i \int (\omega_{m_ref} - \omega_m) dt \tag{7}$$

where i_{sy_ref} is the reference value of the torque producing component, ω_{m_ref} and ω_m are the reference and actual value of the rotor angular speed, K_p is the proportional gain, and K_i is the integral gain.

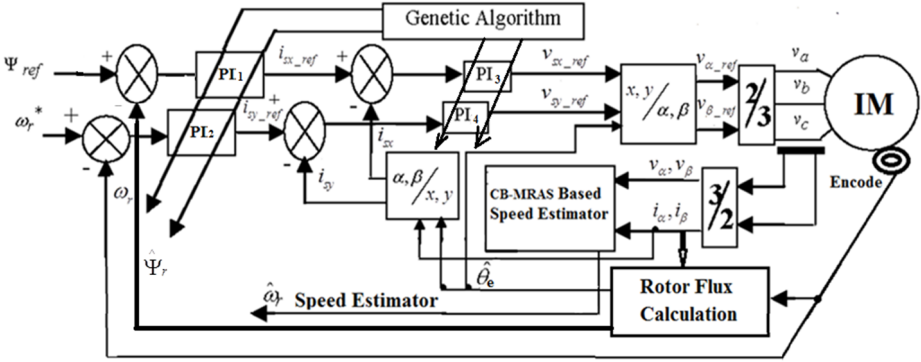


Fig. 1. Speed control structure of the induction motor drive

The actual speed is measured by the speed sensor then is compared with the reference value of the rotor angular speed. Difference between reference and actual value e_ω is processed by PI speed controller whose parameters determine a behavior of the electrical drive [3].

At the start of control process, the conventional PI-controller should have large proportional gain either for a fast motor acceleration or deceleration. The integral gain should be small to avoid overshoots. When the motor reaches the reference speed, a small proportional gain and large integral gain are required to maintain the motor speed at desired value. Based on this, K_p is varied between K_{pmin} and K_{pmax} , K_i is varied between K_{imin} and K_{imax} to get satisfactory control performance.

4 Determining parameters of PI speed controller using genetic algorithm

The genetic algorithms are finding important applications in optimization of technical systems [2], [3]. The GA part of the controller performs parameter setting, which the genetic algorithm attempts to optimize by using simulation based fitness evaluation of the controllers in the closed-loop systems. The block scheme of the algorithm is shown in the Fig. 2. The search the coefficients K_p , K_i of classical PI speed controller by experimentation takes a lot of time but the response has just as good. If we find the coefficients using genetic algorithms, it will be faster, much better results. In the control scheme (see Fig. 1), we have 4 the PI-controllers, we need a response of the

best speed. Each PI-controller has 2 coefficients (K_p , K_i). The PI₃ and PI₄ are the same, so we need to find 6 parameters (K_{p1} , K_{i1} , K_{p2} , K_{i2} , K_{p3} , K_{i3}).

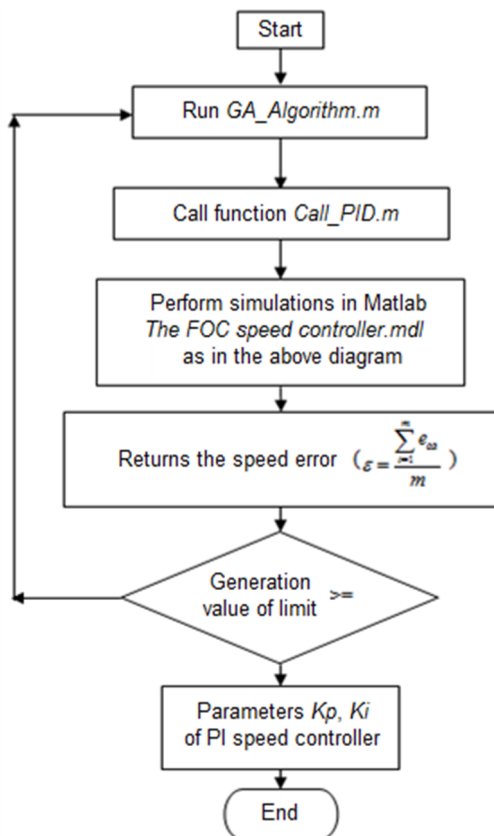


Fig. 2. The flowchart of the search algorithm for parameters K_p , K_i

The GA speed controller differs from the classical PI controller. Modifications and tuning of these constants ensures Genetic Algorithm block that evaluates the input variables based on the speed error e_{ω} according to a specified algorithm best suited values of the proportional gain K_p and the integral gain K_i which then sends to the conventional part of the speed controller. The GA has these parameters: probability of mutation 0.05, number of generations 5, number of pairs K_p and K_i in population 8.

5 Simulation results

The described induction motor drive was simulated in MATLAB-SIMULINK. The basic parameters of the induction motor $P=0.75\text{kW}$, $U_{dc}=270\text{V}$, $P_p=2$, $R_S=2.1\Omega$, $R_r=1.51\Omega$, $L_m=0.129\text{H}$, $L_S=0.137\text{H}$, $J=0.043\text{ Kg.m}^2$. Parameters of the speed controllers are listed in the Table 1. The Fig. 3 – Fig. 6 show time courses of the important quantities of the induction motor drive with the different speed controllers.

Table 1. Parameters of the speed controllers

Parameter	Classical PI controller	GA speed controller
Proportional gain K_{p1} (T_R_Im)	0.03 A/rad/s	2.4301 A/rad/s
Integral gain K_{i1} (K_Rm)	50 A/rad	35.4057 A/rad
Proportional gain K_{p2} (T_R_omega)	0.05 A/rad/s	12.1937 A/rad/s
Integral gain K_{i2} (K_R_omega)	0.6 A/rad	35.7321 A/rad
Proportional gain K_{p3} (T_R_is)	0.005 A/rad/s	25.2275 A/rad/s
Integral gain K_{i3} (K_Ri)	0.5 A/rad	43.1532 A/rad

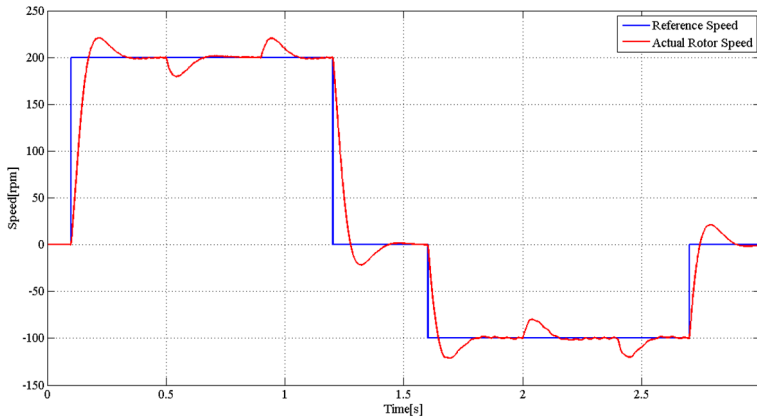


Fig. 3. Reference speed ω_{m_ref} (blue) and actual rotor speed ω_m (red) – classical PI controller

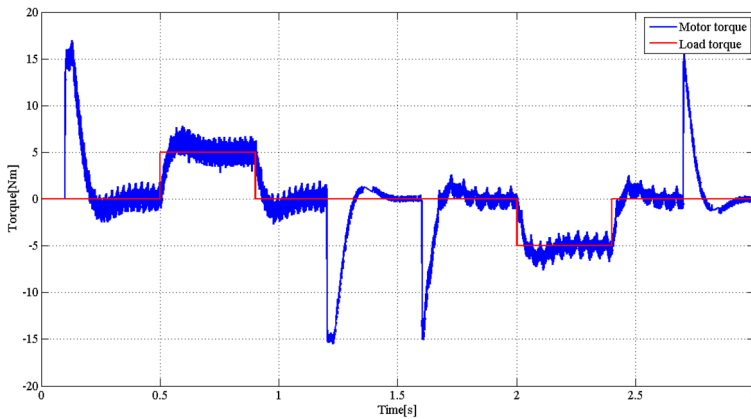


Fig. 4. Load torque (red) and induction motor torque (blue) – classical PI controller

6 Conclusion

The paper demonstrates how to find the parameters for the PI controller using the genetic algorithm offline. The parameters K_p , K_i can be obtained using classical methods such as Ziegler-Nichols method. These methods take longer. Meanwhile applications of the genetic algorithms find parameters quickly and have better time response.

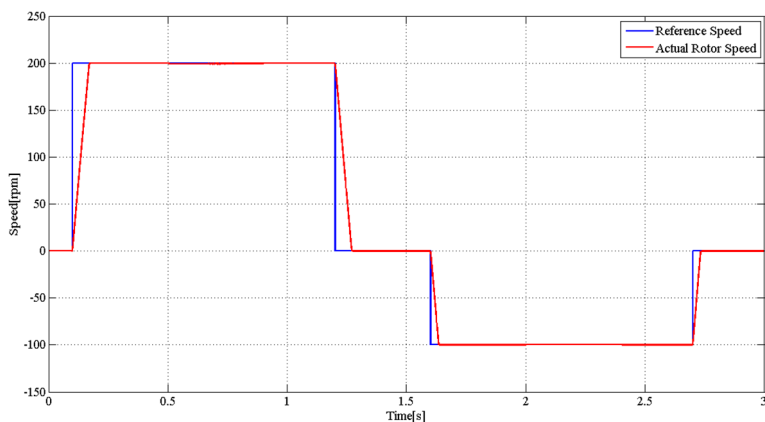


Fig. 5. Reference speed $\omega_{m\ ref}$ (blue) and actual rotor speed ω_m (red) – PI controller using GA

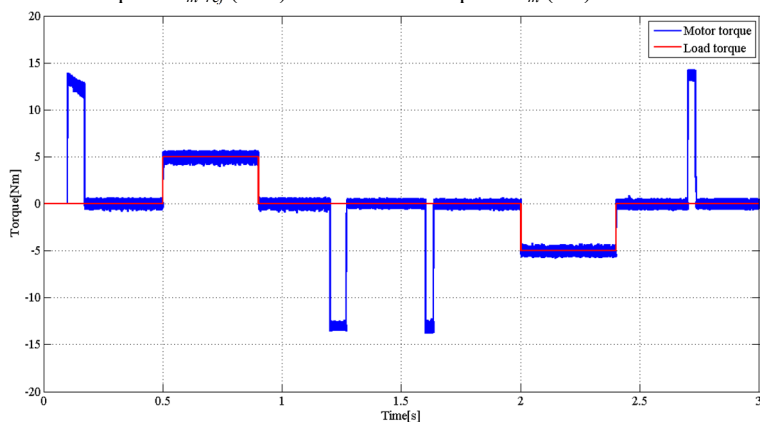


Fig. 6. Load torque (red) and induction motor torque (blue) – PI controller using GA

Acknowledgement

The paper was supported by the projects: Center for Intelligent Drives and Advanced Machine Control (CIDAM) project, reg. no. TE02000103 funded by the Technology Agency of the Czech Republic, project reg. no. SP2016/83 funded by the Student Grant Competition of VSB-Technical University of Ostrava.

References

- [1] J. Holtz, Sensorless Control of Induction Motor Drives, *Proceedings of the IEEE*, vol. 90, n. 8, pp. 1359-1394, 2002.
- [2] Manoj Datta, Md. Abdur Rafiq, and B. C. Ghosh, Genetic Algorithm Based Fast Speed Response Induction Motor Drive without Speed Encoder, *Conference Proceedings of POWERENG 2007*, April 12-14, 2007, Setubal, Portugal.
- [3] P. Brandstetter, M. Dobrovsky, M. Kuchar, Implementation of Genetic Algorithm in Control Structure of Induction Motor A.C. Drive, *Advances in Electrical and Computer Engineering*, vol. 14, n. 4, pp. 15-20, 2014.

Direct Torque Control Methods for Speed Sensorless Control of Induction Motor Drive

Hau Huu Vo

Faculty of Electrical and Electronics Engineering, Ton Duc Thang University, 19
Nguyen Huu Tho Street, Tan Phong Ward, District 7, Ho Chi Minh City, Vietnam
vohuuhaus@tdt.edu.vn

Abstract. The paper describes current-based model reference adaptive system speed observer for a speed sensorless induction motor drive with the direct torque and flux control methods. The sensorless control structures of the induction motor drive were implemented in Matlab-Simulink environment. The simulation results confirm that speed estimator in control structures are simple to simulate and experiment. By comparison of control structures, the current based model reference adaptive system observer with vector pulse-width modulator gives higher accuracy of the speed estimation, and smaller ripple of the motor torque.

Keywords: induction motor, direct torque control, vector pulse-width modulator, speed control, sensorless control, MRAS observer.

1 Introduction

The induction motor drive with a cage type of machine has many applications in industry. These applications often require adjustable speed and wide power range [1], [2]. The direct torque and flux control (DTC) method may be applied for obtaining good dynamic performance. DTC methods has some advantages such as high robustness and ability of quick changes of motor torque. However, classical DTC methods produce converters with variable switching frequency. Implementation of vector pulse-width modulator (VPWM) into the control structure gave high performance and constant switching frequency [3].

2 Direct torque control methods

The basic principle of DTC methods are: a rotating magnetic field in the stator is created on the basis of a calculating algorithm with the help of voltage vectors V_1 to V_6 (Figure 2), where the rotation speed of the magnetic field, and subsequently the amount of motor torque, can be controlled by the switching of zero vectors or the

switching of active vectors working in the opposite direction of the magnetic field. Signal Calculation block computes motor torque and magnetic flux:

$$\begin{aligned} \psi_{s\alpha} &= \int (u_{s\alpha} - R_s i_{s\alpha}) dt, & \psi_{s\beta} &= \int (u_{s\beta} - R_s i_{s\beta}) dt, & \gamma &= \tan^{-1}(\psi_{s\alpha} / \psi_{s\beta}), \\ \psi_s &= \sqrt{\psi_{s\alpha}^2 + \psi_{s\beta}^2}, & T_e &= \frac{3}{2} p (\psi_{s\alpha} i_{s\beta} - \psi_{s\beta} i_{s\alpha}). \end{aligned} \tag{1}$$

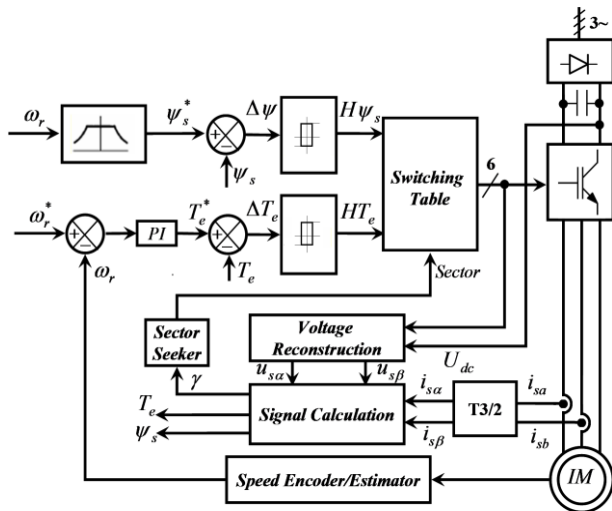


Fig. 1. Block scheme of the direct torque and flux control

In classical DTC method or Takahashi DTC method (T_DTC), the stator flux is controlled so that the final point of the stator flux vector moves within a circular ring, whereby its trajectory in a simplified case approaches a circle. The errors between the command torque and stator flux with their estimated values will be processed by two hysteresis-band (HB) controllers.

Tab. 1. The influences of the switching of individual vectors in first sector for two DTC methods.

Voltage vector	T_DTC (-30°, +30°)	M_DTC (0°, +60°)
V ₁	Ambiguous torque	IF, DT
V ₂	IF, IT	IF, IT
V ₃	DF, IT	Ambiguous flux
V ₄	Ambiguous torque	DF, IT
V ₅	DF, DT	DF, DT
V ₆	IF, DT	Ambiguous flux

A modification of T_DTC (M_DTC), is described as in Fig. 2. The differences between M_DTC and T_DTC are the shifting of the sectors (first sector is shifted from range (-30°, +30°) to range (0°, +60°)) and the switching table as shown in Figure 2 and

Table 1. The content of the switching table does not contain vectors which cause an unclear increase or decrease of flux or torque. The four abbreviations DF, IF, DT, IT denote the decrease, increase of flux and torque respectively. An unclear increase or decrease of torque by V_1 and V_4 with T_DTC is changed into an unclear increase or decrease of flux by V_3 and V_6 with M_DTC.

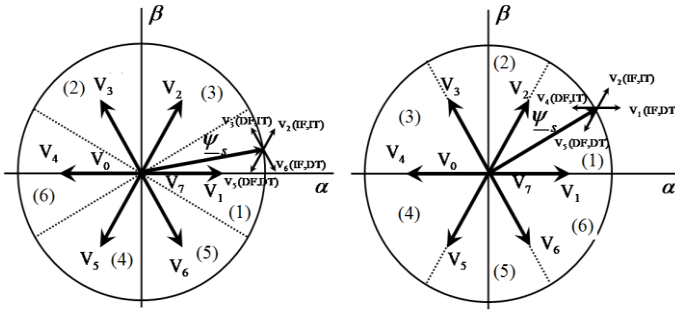


Fig. 2. Principle of selection of voltage vector in the first sector of the plane α, β according to T_DTC (left) and M_DTC (right).

The DTC method with a direct calculation of voltage vector (DVC_DTC) has no requirements in using HB controllers or dividing the plane α, β into sectors. Vector sum of g_1 component, determines motor excitation, and g_2 component, determines size of the torque determines the resultant vector g . The Sector Seeker, two HB controllers, Switching Table blocks in Fig. 1 are replaced with Switching Pulse Calculation block in Figure 3. Since the voltage inverter is able to provide only 6 active vectors is the next part of the program calculated the vector, which is ideal vector g comes closest. This rough selection of voltage vector causes during the control period greater flux and torque deviation. These deviations are compensated by another voltage vector in the next control period.

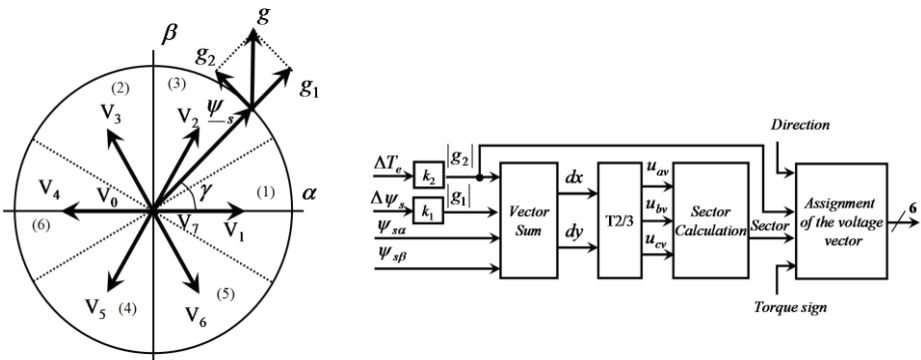


Fig. 3. Trajectory of stator flux vector according to DVC_DTC (left) and Switching Pulse Calculation block for DVC_DTC (right).

The above DTC methods produce converters with variable switching frequency. With VPWM modulator, the vector g is approximated accurately, it means that ripples of stator flux and torque are minimized.

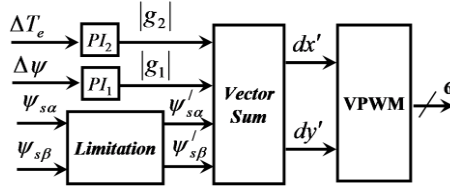


Fig. 4. DTC method with VPWM.

3 Current-Based MRAS observer

Figure 5 shows the structure of a current-based model reference adaptive system (CB-MRAS). This MRAS observer uses stator currents as output quantities of the reference model. The scheme has one reference model and two adaptive models.

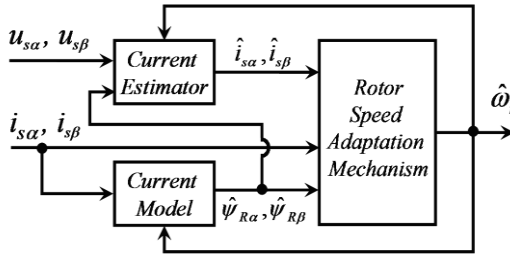


Fig. 5. Block scheme of the speed estimation using CB-MRAS

The outputs of current model are also described with Equation (14); the outputs of the current observer are calculated:

$$\begin{aligned} \hat{i}_{s\alpha} &= \left[\int (K_1 u_{s\alpha} + K_2 \hat{\psi}_{R\alpha} + K_3 \hat{\omega}_R \hat{\psi}_{R\beta} - \hat{i}_{s\alpha}) dt \right] / T_i, \\ \hat{i}_{s\beta} &= \left[\int (K_1 u_{s\beta} + K_2 \hat{\psi}_{R\beta} - K_3 \hat{\omega}_R \hat{\psi}_{R\alpha} - \hat{i}_{s\beta}) dt \right] / T_i, \end{aligned} \tag{2}$$

where:

$$K_1 = \frac{L_r}{C_1 L_m}, K_2 = \frac{L_m}{C_1 (L_r \hat{R}_s T_r + L_m^2)}, K_3 = \frac{1}{C_1}, T_i = \frac{L_s L_r - L_m^2}{C_1 L_m}, C_1 = \frac{L_r \hat{R}_s}{L_m} + \frac{L_m}{T_r} \tag{3}$$

The following equation is used for obtaining the rotor speed ([4], [5]):

$$\xi = (i_{s\alpha} - \hat{i}_{s\alpha}) \hat{\psi}_{R\beta} - (i_{s\beta} - \hat{i}_{s\beta}) \hat{\psi}_{R\alpha}, \quad \hat{\omega}_r = K_p \xi + K_I \int_0^t \xi dt \quad (4)$$

where $K_p > 0, K_I > 0$.

4 Simulation results

The described induction motor drive with the DTC methods was simulated using MATLAB-SIMULINK. The basic parameters of the induction motor (type P 112 M04) are: $P_n = 2.7$ kW, $T_n = 19$ Nm, $\omega_{mn} = 1360$ rpm, $p_p = 2$, $I_{Sn} = 7.51$ A, $I_{Rn} = 17$ A, $U_{Sn} = 400/230$ V, $\Psi_{Sn} = 0.877$ Wb

The time courses of important quantities (see Fig. 7 - Fig. 9) were obtained from the speed control structure at the jump of the load torque $T_L = 5$ Nm (see Fig. 6).

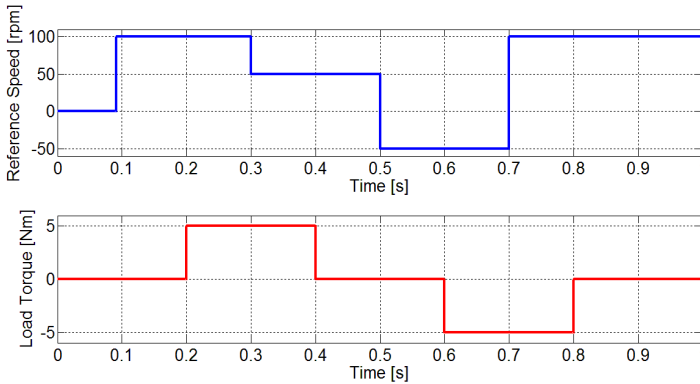


Fig. 6. Reference speed (blue) and load torque (red).

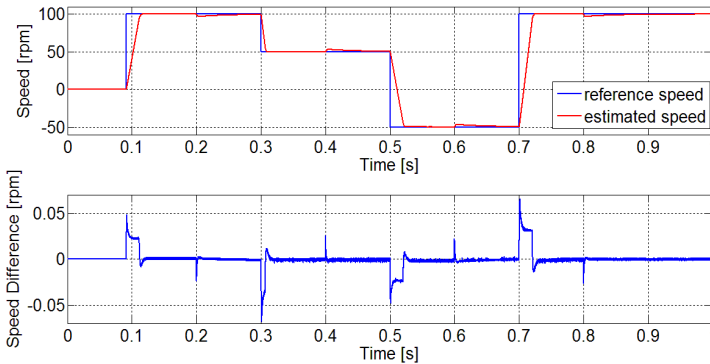


Fig. 7. Reference speed and estimated rotor speed (upper), and speed difference between real speed and estimated rotor speed (lower).

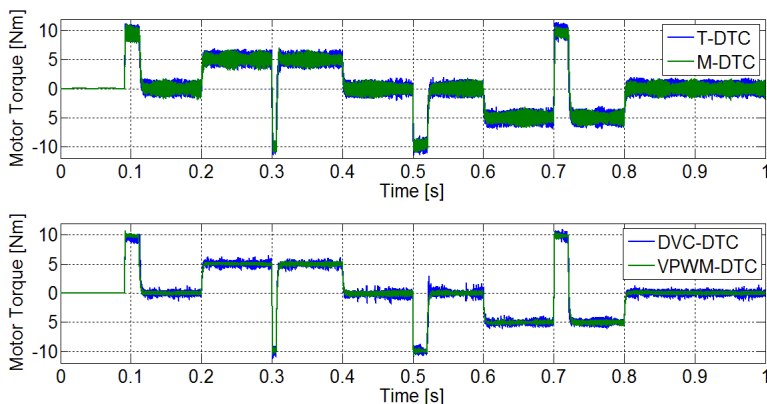


Fig. 1. Motor torque with different DTC methods.

5 Conclusion

The estimation technique for sensorless induction motor drive with the direct torque control was presented in the paper. The speed estimator is based on application of the current-based MRAS observer. The DTC with Vector Pulse Width Modulator induction motor drive with the presented speed estimator gives good dynamic responses and the estimation of the mechanical speed is good in steady state and also in transient state.

Acknowledgement

In the paper, there are the results of the project reg. no. SP2016/83 funded by the Student Grant Competition of VSB-Technical University of Ostrava. This research was supervised by Prof. Ing. Pavel Brandstetter, CSc.

References

1. P. Vas, *Sensorless Vector and Direct Torque Control*, Oxford University Press, 1998.
2. J. Holtz, *Sensorless Control of Induction Motor Drives*, Proceedings of the IEEE, vol. 90, n. 8, pp. 1359-1394, 2002.
3. P. Brandstetter, P. Chlebis, P. Palacky, *Direct Torque Control of Induction Motor with Direct Calculation of Voltage Vector*. Advances in Electrical and Computer Engineering, vol. 10, no. 4, pp. 17-22, 2010.
4. T. Orłowska-Kowalska, M. Dybkowski, *Stator-Current-Based MRAS Estimator for a Wide Range Speed-Sensorless Induction-Motor Drive*, IEEE Transactions on Industrial Electronics, vol. 57, n. 4, pp. 1296-1308, 2010.
5. P. Brandstetter, *Sensorless Control of Induction Motor Using Modified MRAS*. International Review of Electrical Engineering - IREE, Vol. 7, N. 3, pp. 4404-4411, 2012.

Battery Management for Electric Vehicle

Lukas Cab and Petr Simonik

Department of Electronics, FEECS,
VŠB – Technical University of Ostrava, 17. listopadu 15,
708 33 Ostrava – Poruba, Czech Republic
{lukas.cab.st, petr.simonik}@vsb.cz

Abstract. This paper describes the development and implementation of a battery pack for an electric vehicle. In the introduction to approach the issue of Management of electric energy. The following describes the use of batteries, their basic properties. The main part is described in detail Battery Management System, including the topology and protective elements. One section is devoted to the control unit developed by BMS.

Keywords: battery management system (BMS), LiFePO₄, electric vehicle, control unit

1 Introduction.

Electrically powered vehicles are often referred to as the vehicles of the future, because they offer the possibility of very ecologic and low-cost operation, together with low maintenance requirements. Recently there is a relatively large expansion of purely electric drives in the automotive industry. It is very likely that electric vehicles will sooner or later dominate the automotive industry, and certainly not only automotive. At this moment, one of the biggest problems is lobby of the oil companies and the relatively high cost of batteries that highly increases cost of manufacture of electric vehicles.

Power electric vehicles is currently one of the most discussed topics. Especially energy storage for power drive units, lighting, and other vehicle systems. There are obviously great demands on energy density, that is the ratio of stored energy to weight and volume of the battery, as well as resistance to relatively unfavorable operating conditions such as a temperature changes, vibrations, greatly fluctuating load or need of regenerative braking and associated requirements for very fast charging. It is also necessary that the batteries in the vehicles are safe, in order to avoid fire, as is the case with Li-ion batteries.

The current trend in electrically driven vehicles is the use of LiFePO₄ batteries that have very convenient properties, both in terms of energy density and safety of operation even in case of accident.

For the reasons discussed above, this type of battery was used for the construction of battery modules for powering demonstration vehicle "Democar".

2 Used Batteries

Lithium iron phosphate (LiFePO₄) battery sometimes called LFP battery is a kind of lithium-ion battery, which uses a compound LiFePO₄ cathode material

Table 1. Basic parameters LiFePO₄ cell

energy / size	220 Wh / L
energy / weight	90-110 Wh / kg
power / weight	> 3000 W / Kg
the lifespan	> 2000 cycles
time stability	> 10 years
nominal voltage	3.3 V

2.1 Advantages and Disadvantages LiFePO₄

The main disadvantages of LiFePO₄ batteries include a slightly lower energy density compared to LiCoO₂ (Li-ion) batteries, but this disadvantage disappears in time due to faster aging of Li-ion cells so after about a year of use have both types of cells about the same energy density. Another major drawback of this technology are relatively small reserves of lithium in the earth's crust. These are estimated at 30,000 tons in 2015.

In terms of safety LiFePO₄ cells are significantly better than Li-ion cells. It's caused by the stronger bond Fe-P-O than the Co-O in Li-ion cells. In case of improper use (overheating, short circuit, overcharge, etc.) in LiFePO₄ cells occurs crash at temperatures around 800 ° C and above. In case of damage due to overcharging there is no risk of fire as with the Li-ion cells. LiFePO₄ batteries only gets inflated, some gas leak can occur through emergency valve and life of a battery will shorten. It is known that the battery voltage should not exceed the maximum limit of charge and should not fall below a minimum discharge level, which can cause irreversible damage to a battery, which may cause the inability to re-charge. Therefore, it is recommended to keep the battery in a charged state, because in charged state, there is significantly lower risk of discharge of cell below the safe level by self-discharge when cell is not in use.

3 Battery Management System

Standard battery management system (BMS) can be divided into two basic parts. These are balancing modules (on each battery cell) and a control unit.

In order to limit the risks when using the battery charging and discharging, it is necessary to set the parameters of the BMS system for the actual battery. This is com-

posed of multiple cells of various parameters connected in series, where each of the cells in series has the same threshold values for use. These are especially the upper limit of the charge and the discharge lower limit. These must not be exceeded.

One of the ways to charge those cells is the "CC-CV" (Constant Current - Constant Voltage). In this method, battery is normally charged using constant current until it reach a nearly full charge and then maintaining a constant voltage to match potentials. However, this method would reduce battery life due to uneven charging of individual cells.

When using LiFePO4 cells it is necessary to include the balancing state intocharge cycle which eliminates the possibility of overcharging or incomplete charging of individual cells in the battery.

Basic Properties of BSM:

- control of the charging and discharging,
- control and management of cell heat,
- protection of cell,
- predicting or estimation of future cell status,
- collecting data of cell or battery status,
- communication with other units (control unit),
- extending life of battery and its cells.

BMS used in demonstration vehicle “Democar” is distributed type which is shown on figure 1.

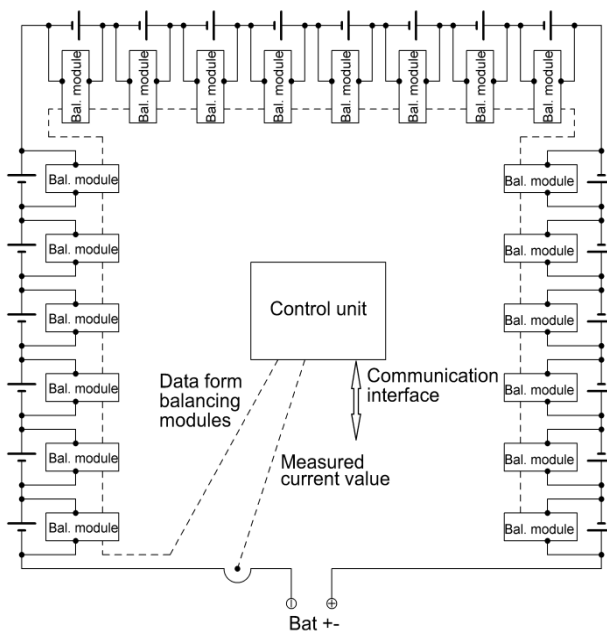


Fig. 1. Distributed type of BSM

This type of topology has balancing module placed on each battery. These modules are monitoring actual status of battery like a voltage, balancing current, temperature, etc. These balancing modules are connected to control unit, that evaluates and processes data gathered from balancing modules.

These data are send via communication interface to energy management control unit (EMCU) which process data from BMS and provide some of them to the other control units on “Democar” via CAN bus.

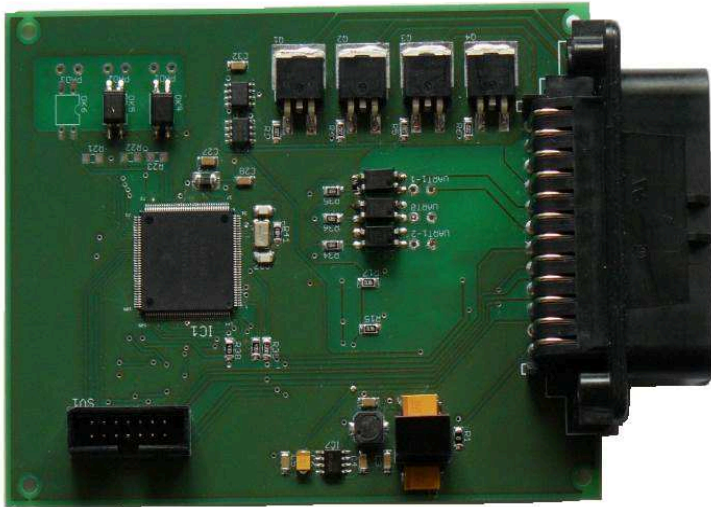


Fig. 2. Photo final version of EMCU

4 Conception of Battery Management System

The overall concept of "energy management" Democar vehicle system consists of three separate battery modules, which are placed in three boxes made of aluminum alloy sheets. Each module has its own control unit called “unit X” which monitors the status of the battery and controls the peripherals that regulates charging and can detach the battery module from the appliance. These units are connected to an Energy Management Control Unit called EMCU, which is connected with sub-units X linked via UART interface and takes valuable information about the state of the individual battery modules, processes it and sends to the CAN bus vehicle. From CAN bus, other units of the vehicle can use data provided by EMCU. The picture below shows a block diagram of this concept.

EMCU provides information about status of batteries in “Democar” vehicle. This is very important because some safety systems in this vehicle need continuous power supply and it can be dangerous in case of battery failure. Because of that, EMCU deliver information that battery is near to dangerous voltage level before that happens.

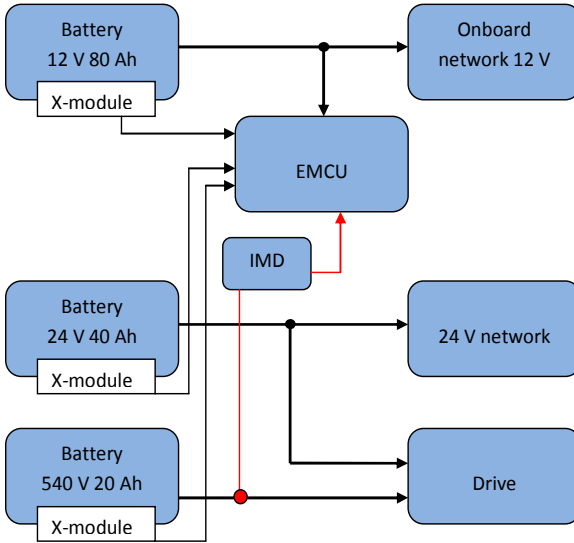


Fig. 3.Block diagram of energy management of “Democar”

Battery power unit is composed of 162 cells with a nominal voltage of about 540 V / 20 Ah and battery for powering the control circuitry and servo drives composed of 16 cells with a nominal voltage of 24 V / 40 Ah are placed in boxes 1 and 2 on the vehicle chassis under the seating area. Battery for powering on-board network composed of 16 cells with a nominal voltage of 12 V / 80 Ah is mounted on the chassis of the vehicle behind the front bumper. On-board network is galvanic isolated from the other two. All networks in the vehicle are isolated networks (IT) and therefore when normal operation even when an accident threatens only a very small risk of electric shock. Nevertheless, it is advisable to include a network isolation monitoring device called IMD, which provides information signal when the insulation resistance drops below the selected value. This information may result of disconnection of the main battery 540V. Concept of such protection is shown in the figure 4.

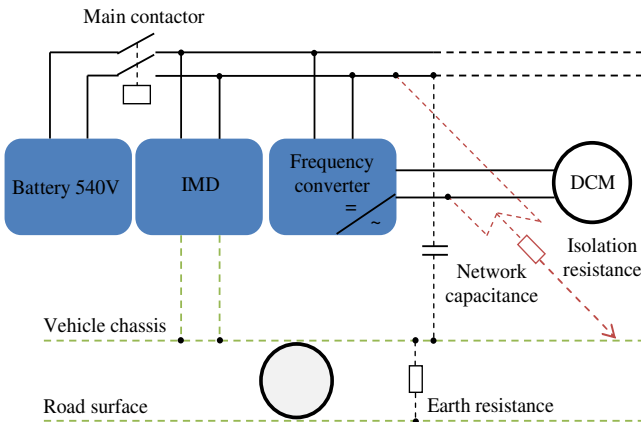


Fig. 4. Principles schematics of IMD connection

The high voltage system in a vehicle should be throughout its operation including phase of charging monitored by IMD. This ensures that if the insulation resistance drops under the critical limit, IMD will report this state by OK_{HS} signal. The lower isolation impedance state itself does not mean immediate threat for operator, because IT network used on “Democar” has a neutral potential against ground potential. However this fault still has to be locate and removed as soon as possible. This is to prevent eventual negative effect on the vehicle, which could occur eg. by another fault of line with opposite polarity at another place of chassis or another cable. Limit values of insulation resistance according to standards are: $100 \Omega / V$ for DC network and $500 \Omega / V$ for AC network. Because in case of “Democar” vehicle there is a combined network (when charging), limit values must be based on the value for the AC network. So the critical resistance value should be set to a value of about $300 k\Omega$.

5 Conclusion

In this paper presents the results of the development of energy management of electric vehicle Democar. Described was also developed functionality of the control unit of the system. It is a platform for further development of algorithms for energy managing.

Acknowledgement

This research and development is carried out within the SGS project no. SP2016 / 181 on the Faculty of Electrical Engineering and Computer Science, VSB – Technical University of Ostrava.

References

- [1] Neborak, I., Simonik, P., and Odlevak, P.: “Electric Vehicle Modelling and Simulation” In: 14th International Scientific Conference on Electric Power Engineering 2013, pp. 693-696, 2013.
- [2] Przcetek, S.: Sestavení funkční koncepce a vývoj aplikačního software elektrohydraulického systému brzd elektromobilu Democar. Ostrava, 2016, Diploma Work. VSB – Technical University of Ostrava. Supervised by Petr Simonik.
- [3] Jarolim, A.: Návrh a praktická realizace koncepce managementu napájení vozidla s elektrickým pohonem Democar. Ostrava, 2016, Diploma Work. VSB – Technical University of Ostrava. Supervised by Petr Simonik.

Electronic Systems of Remotely Operated Vehicle

Jiri Takac

Department of Electronics, FEECS,
VŠB – Technical University of Ostrava, 17. listopadu 15,
708 33 Ostrava – Poruba, Czech Republic
jiri.takac@vsb.cz

Abstract: This article describes concept and design of electronic units of remotely navigated vehicle Democar. Article is mainly focused on hardware part of this vehicle. Described are systems of this vehicle and their main functions. Also is included cooperation between systems. In last part are shown results of communication between systems and functional results.

Keywords: Control Unit, Democar, CAN bus, controller, electric vehicle, electronic system

1 INTRODUCTION

In these days are widely developed vehicles or moving robots to operate in long distances or in unsafety environments. This vehicles are mostly navigated with some sort of remote control units, most often by using radio waves. This vehicles are designed to work at areas hard to reach for humans, or in areas where is big danger of some sort of explosion or is unhostile for people.

The most important part of these vehicles are theirs chassis and types of movement abilities and how they are able to move in certain areas. Next important part is their purpose, for example if they should look for objects (mostly by using camera to see what is around the vehicle for operator) and pick them up, or to rescue people, or in army and security forces to disassembly bombs.

In basis these vehicles have electric motors for movement powered by batteries. That means they need some electronic units for regulations, measuring systems, motor control and other parts. Mostly, each system has its own electronic control unit (ECU). That require good cooperation between these ECUs. They need to share lot of information about current state of each ECU if there are no errors or values from theirs sensors.

2 DESCRIPTION OF REMOTELY NAVIGATED VEHICLE

Our vehicle is remotely controlled electric vehicle with several systems, in the text it will be called Democar. It is built on ATV chassis. Each system has its own control unit and they are changing information over CAN bus. Democar has totally seven systems for drive control, steering system, brakes, lightning system, battery management, sensor system and communication unit with radio transmitter.

It is equipped with four synchronous motors with permanent magnets, wireless transmitter to operate, because it is designed to operate only remotely. Communication unit (CCU) receives demands from user over radio communication, transform this information and pass it through CAN bus to other units.

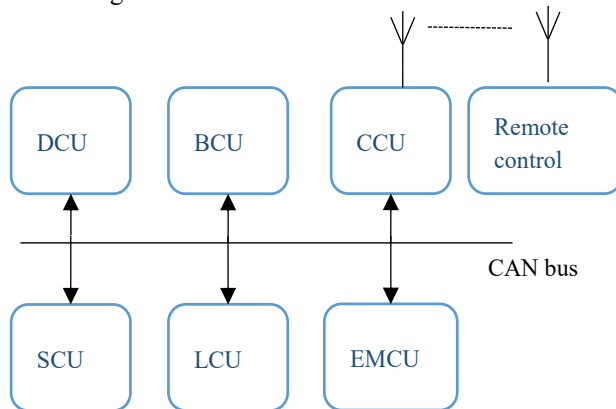


Fig. 1. Units block diagram of Democar

3 FUNCTIONAL REQUIREMENTS

To develop this vehicle and its units we need to set up requirements for each system and their cooperation. It is important to know how fast the vehicle will be moving, his maximum weight and environment where it should operate. We decided that we won't be moving faster than 30 kmph and we want to be able to operate in areas with potentially explosive atmosphere. That means we can't use any sparkling devices, that's why we are using permanent magnet synchronous magnets.

3.1 Drive control

Drive system consist of four permanent magnets synchronous motors, one for each wheel. Each motor has its own inverter. Important part is control unit to control vehicle trajectory. And to this system also belongs batteries to power up inverters, control unit and motors.

Drive control unit (DCU) has to control four synchronous motor over inverters and control vehicle's traction. Parametrization inverters is done over CAN bus too using

CANopen protocol. Through this bus we are able to drive motors and get information about each wheel speed and motor states.

DCU from received coded information about want torque from CCU, computes right value for each motor and transform it to known parameter for inverter. Also it need information about angle of direction front wheels to correct wheels speed to simulate differential.

Basically this unit need two CAN buses, one for communication with other units and second to drive inverters. Unit also includes switches for turning on and off power to inverters and motors.

3.2 Steering system

To steer vehicle remotely we need to equip it with some electromechanical system to operate original steering column. To turn with steering rod we are using linear system with stepper motor and special rod to transfer the linear movement to rotary movement. To use smaller stepper motor we added to steering column electric power steering system from Hyundai to increase power and also this system includes information about angle of front wheels.

Control unit of steering system SCU from user's commands calculates right value for stepper motor, which is driven by stepper motor controller. Controller is able to communicate over RS485 bus. To correct regulation of steer angle unit need information about actual position. This information is get from power steering. That has CAN bus and provide over it position, torque value and state off operation.

Thanks to those information SCU need two CAN buses to communicate with other units and power steering and RS485 bus to operate stepper motor and also battery system to power up unit, and motors.

3.3 Energy management and batteries

Energy management controlling batteries health and their charge level. If battery capacity is low it need to tell to other system to shut down or to lower somehow energy consumption. Batteries need to power up all system from control units to electric motors for drive. Power steering and ABS unit is taken from conventional car, so it operate on 12 volts. Using this voltage level we decided to power up units from this level too. Also from 12 volts are powered up lights.

Another voltage level is required by inverters for motors. Those need 24 volts, because they are designed for industry and there is 24 V standard level. This voltage is also used to power up stepper motor for his better performance in higher speeds. Last voltage level is 540 V for power up synchronous motors. This level is isolated from other so we need to watch this isolation value.

3.4 Central electronic

Task for central electronic (CCU) is to receive commands from user over radio control, transform this information and send them to CAN bus, where other units take these

information and make some steps based on it. Also CCU has data logger, saving actual values of speed, steering angle, wheels rews, voltages, currents and information about 3-axes accelerations. Some of these values are used to autonomous moving when connection is lost, to get back same way, when connection will be again established. Other values are for back analysis of vehicle's state during operation.

4 STRUCTURE OF ECU

Each ECU (electric control unit) consist of microcontroller (MCU) and peripheral devices to communicate over buses or measure voltages, currents or for switching other loads. Microcontroller structure is based on Freescale's MPC5643L. We are using this chip on each unit because it is easier to design new unit based on others because platform is the same. Also this is the automotive industry chip with some safety features and other on-chip hardware peripherals to faster program operations.

To power up ECU's is used 12 voltage level which is transform to 5 V and 3.3 V using on board step down switching supply converter. This converter monitor currents and voltages and is able to disconnect load if there is some error. Every unit have also two CAN drivers to transform signal from MCU to ISO 11898-2 standard. Also to be units universal is used same input/output connector with enough pins for each unit. To this connector is wired power, CAN and programing pins on every unit on same positions. Next picture shows example of steering system structure.

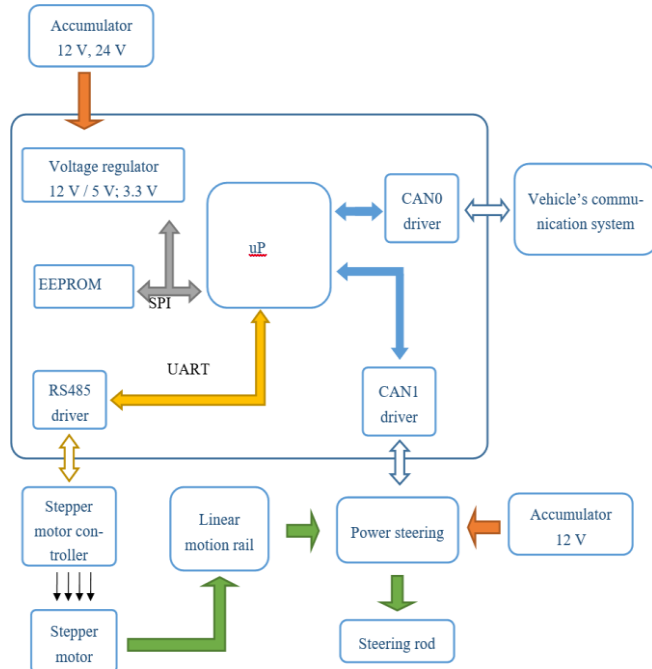


Fig. 2. Block structure of steering system

5 COMMUNICATION AND FUNCTIONAL TESTS

For most communication test were used oscilloscope with bus analysis from Lecroy. This was used mostly for SPI and UART analysis and for CAN bus you can see clearly bus load. For analysis of the CAN bus were used USB-CAN converter with PC application PP2CAN to easy monitor what data is on the bus.

Functional testing of drive system was done using PP2CAN, were we monitor communication between units and communication of drive unit with inverters and with Pro-Drive application for inverter, were we could see actual and wanted parameters for motors. On the graph below is shown torque (M) and velocity (v) of one motor in time.

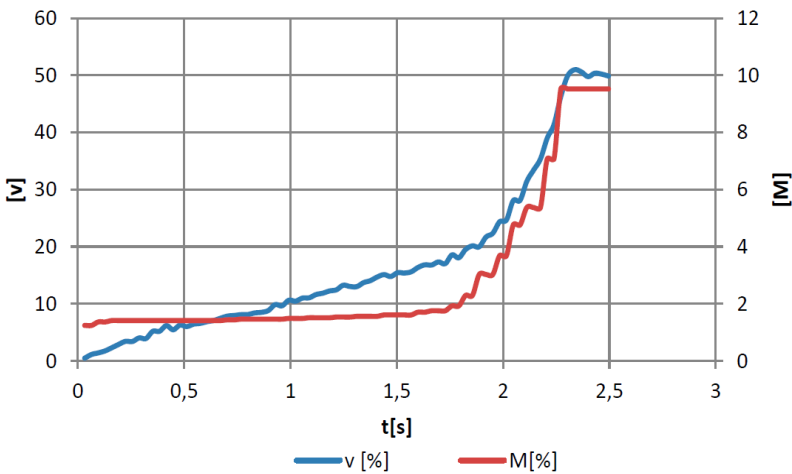


Fig. 3. Torque and velocity of one motor

Next picture shows example of communication between DCU and inverters. Marked area demonstrates sent command to inverter and its response.

Nu...	Received time	Type	Id 1	Id 2	Bytes	B0	B1	B2	B3	B4	B5	B6	B7	Port
3924	16:41:7.637:0.00	St	1541		8	35	148	68	0	20	0	0	0	1
3923	16:41:7.615:0.00	St	1539		8	64	97	65	0	0	0	0	0	1
3922	16:41:7.602:0.00	St	1540		8	64	97	65	0	0	0	0	0	1
3921	16:41:7.584:0.00	St	1414		8	67	97	65	0	176	176	234	295	1
3920	16:41:7.592:0.00	St	1542		8	64	97	65	0	0	0	0	0	1
3919	16:41:7.584:0.00	St	1413		8	67	97	65	0	136	79	10	0	1
3918	16:41:7.582:0.00	St	1541		8	64	97	65	0	0	0	0	0	1
3917	16:41:7.575:0.00	St	1539		8	35	12	68	0	0	0	0	0	1
3916	16:41:7.562:0.00	St	1540		8	35	12	68	0	1	0	0	0	1
3915	16:41:7.554:0.00	St	1414		8	96	12	68	0	0	0	0	0	1
3914	16:41:7.552:0.00	St	1542		8	35	12	68	0	1	0	0	0	1
3913	16:41:7.544:0.00	St	1413		8	96	12	68	0	0	0	0	0	1
3912	16:41:7.542:0.00	St	1541		8	35	12	68	0	0	0	0	0	1

Fig. 4. Communication between DCU and inverters

Also is shown tests of ASR system. This was simulated with bigger load on one motor. Results are shown on next graph. When velocity of second motor rise up, the torque is reduced and by that wheel will turn slowly, with almost same speed as first motor.

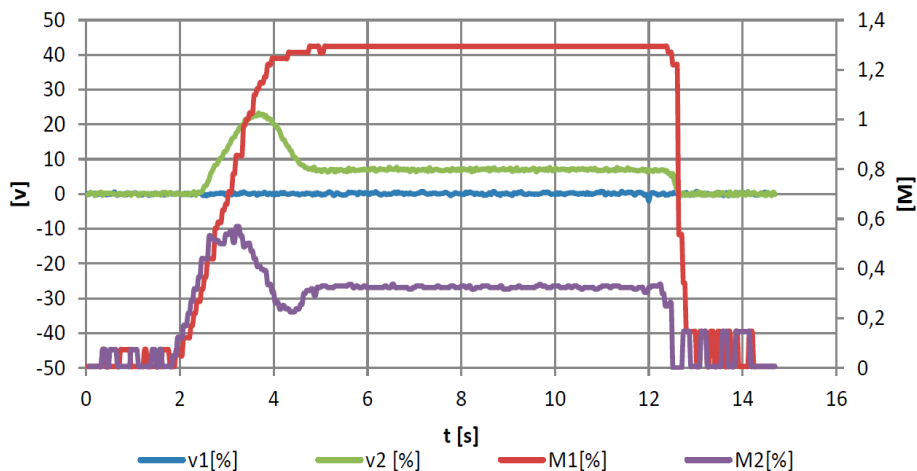


Fig. 5. ASR system testing

5.1 CONCLUSION

This paper presents results of development electric systems and their cooperation of electric vehicle Democar. Described was also structure of vehicle's electronic units. Also is described cooperation between systems and is shown results of communication a functional tests. This research and development is carried out within the SGS project number SP2016/181 on the Faculty of Electrical Engineering and Computer Science, VSB-Technical University of Ostrava.

6 REFERENCES

1. Wolf, O.: "Assembling of Functional Conception and Development of the Application Software for 4WD Powertrain Electronics System of the Electric Vehicle Democar". Ostrava, 2016, Diploma Work. VSB – Technical University of Ostrava.
2. Palacky, P., Slivka, D., Hudecek, P., Sobek M.: "Synerga of Control Units in Electric Vehicle." In International Scientific Conference EPE 2011, Kouty nad Desnou, 2011, vol. 12., ISBN 978-80-248-2393-5.
3. Oplustil, J., Sprlak, R., Kalvar, D., Uchoc, M., Palacky, P., Sladeczek, V.: "Measuring and control central based on digital signal controller." In International Conference on Advanced Engineering Theory and Applications 2013, Minh City; Viet Nam, ISBN 978-3-642-41967-6.
4. Slivka, D., Palacky, P., Vaculik, P., Havel, A.: "Electric vehicle control units communication" Advances in Electrical and Electronic Engineering, Department of Electronics, Faculty of Electrical Engineering and Computer Science, VSB-Technical University of Ostrava, ISSN: 13361376.
5. Chan, C.C.; Chau, K.T.: "An overview of power electronics in electric vehicles" IEEE Transactions on Industrial Electronics (Volume: 44, Issue: 1, Feb 1997), ISSN: 0278-0046.

Support Vector Machine based Dementia Detection from MRI Scans

Radek Hrabuška

Department of Cybernetics and Biomedical Engineering, FEECS,
VŠB – Technical University of Ostrava, 17. listopadu 15,
708 33 Ostrava – Poruba, Czech Republic
radek.hrabuska@vsb.cz

Abstract. MRI (Magnetic Resonance Imaging) of brain studies indicates abnormalities in corpus callosum properties in patients with different types of dementia. Usually patients with dementia tend to have smaller corpus callosum in mid to posterior part. The dataset consisting of 54 elder female patients labelled as demented or non-demented were used during training and testing of the classifier. The Corpus Callosum region is segmented (K-means/Watershed) and the region is cropped with template matching algorithm. Feature vectors consisting Corpus Callosum morphological and texture details are used with the Support Vector Machine classifier. Classification is done using feature vector consisting morphological features of CC, textural features of CC and a combination of both morphological and texture features. This paper reports the classification results with different combinations of feature vectors with an accuracy of 90.00%.

Keywords: Corpus callosum, SVM

1 Introduction

Corpus callosum (CC) is an important part of the human brain responsible for information transfer between hemispheres [1]. The degeneration or underdevelopment of CC leads to decreased ability to solve a complex problem. People suffering from hypoplasia or agenesis of corpus callosum (CC) are often affected by dementia [2-7], seizures, lack of physical coordination and social skills [8]. Dementia covers broad category of brain diseases, making it very difficult to detect from just one symptom. The early recognition of these illnesses is challenging.

Image processing approach to extract CC information from mid sagittal Magnetic Resonance (MR) image scan finds different classes of people may have a normal CC or deformity in CC [2-14]. The studies on classification of CC have shown that the morphological features such as thickness, area, length, curvature of CC as the discriminating factors between normal and abnormal patients[3][8-12]. Previous studies on CC report the division of CC into sub-regions and measurements of its various morphological properties [1]. The textural parameters of CC provide rich visual information to investigate the type of abnormalities and can be used as promising features for the classification of MR images [14-15]. For the segmentation of CC from MR images several

segmentation approaches such as Watershed Segmentation [16], K-Means clustering [17], Multi-scale Segmentation [18], Active contour [19] and Active shape approaches [19] have been proposed. The Support Vector Machine (SVM) technique is used widely as a classifier for classifying various CC abnormalities such as Parkinson's disease [20], Autism [21], Dyslexia [12,22], Multiple Sclerosis [23], Hydrocephalus [4,13], Gender Identity Disorder [24] and Alzheimer's disease [5]. The classification of non-demented and demented MR images using classifiers such as, Multilayer Perceptron [7], SVM [25-26] is reported in the earlier works. It is investigated that there are significant differences between patient groups which are normal and patients with mild or questionable dementia [2-14].

Main purpose of the proposed method is to classify demented patient among the available population. The proposed two class problem uses image based approach for detection of CC and groups it into the pre labelled categories: demented and non-demented.

1.1 METHODOLOGY

Dataset specification.

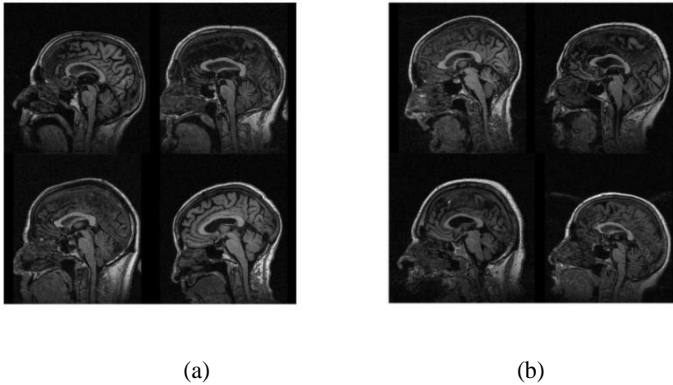


Fig. 1. MRI original data: (a) non-demented (b) demented

Data used for processing are originally in courtesy of longitudinal OASIS database [27], they are free to use with agreed terms. Data from longitudinal database consists of 103 patients divided into two groups (Demented, Non-demented). In addition some of the patients had more than two MRI sessions. In the database are 246 MRI head scans. One properly segmented and measured patient scan was chosen for each female patient. Preliminary study confirmed that there are different sizes of CC based on gender [24]. There were 18 demented and 36 normal patients in the female group. From those patients' data, 10 are used as testing group and rest as training group. Shown in figure 1 (a) and (b) (MRI original data) indicates of the 5 normal and 5 demented female patients, respectively.

Feature extraction.

The feature vector is formed by extracting morphological and textural features. The important morphological details focused here are the area of CC and the length of the CC. The CC region is in turn divided into sub-regions and area features are extracted by measuring the ratio of area of each sub-region to the total area of CC. The approximated 7 sub-regions are found using Witelson's protocol [1] as shown on figure 2.

The textural details are extracted from gray level pixel distribution in CC region using statistical approach. The textural details such as energy, correlation homogeneity, Contrast can be found out by calculating the Gray-Level Co-Occurrence Matrix for different directions and pixel distances [28]. The features are calculated using relations defined by Haralick [15].

The feature vector reported here is designed using the following features: The ratios calculated as lobes' area to total area of the sub-regions of CC (1 - 6), energy of the CC image (7), correlation of the image (8), homogeneity of the image (9), length of the CC (10), and contrast of the image (11). All combinations of 11 features without repeating are tested as classifier. Data are normalised before use.



Fig. 2. The sub-regions of CC with highlighted G and G2 point

Classification of CC images.

Based on extracted features SVM classifier is trained [25]. Its calculated division line or plane is used as division between the groups. It might be possible to get results with better precision by employing more complex classification algorithms [26].

Studies have suggested that for different causes of dementia, there are different smaller regions of CC are responsible [3]. For our test set we were trying all combinations of feature vectors to determine one with the highest accuracy, specificity and sensitivity.

2 RESULTS & DISCUSSION

Studies showed that there are differences between patient groups which are normal and patients with mild or questionable dementia. Figure 3 is comparing variances of both the groups. The variance plot shows that there are significant differences in the areas of 1st, 2nd and 6th CC sub-regions, whereas the rest of the sub-regions do not contribute much variation between the two groups. The textural features energy(7),

correlation(9), homogeneity(10), contrast(11) shows that there are significant differences between the non-demented and demented groups. The length of the CC (10) can also be seen as the parameter of significant variation between the two groups. The SVM classifier is fed with all the possible combinations of features in order to find the best discriminating features between the two groups.

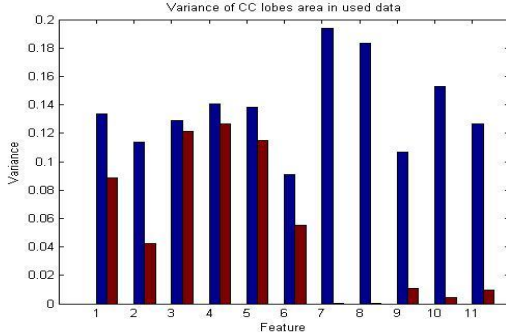


Fig. 3. Variance of normalized data for Non-demented (blue) and Demented patients (red)

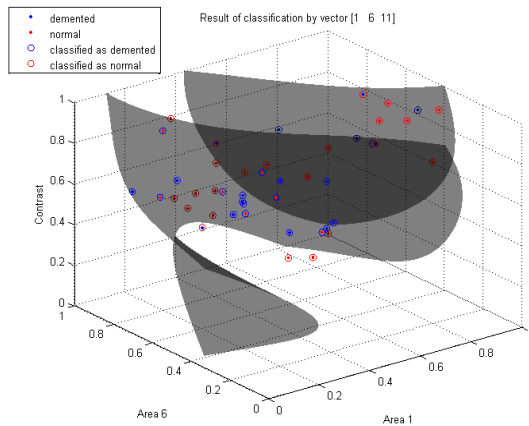


Fig. 4. 3D plot with combined features of area of 1st (Feature 1) and 6th(Feature 6) sub-regions of CC along with contrast texture feature (Feature 11)

The classification is done by considering the extracted features in three important cases: feeding the classifier with, seven morphological features i.e. six area features and length of CC separately, four texture features separately and then the combination of both morphological and texture features. These two cases are used to test classifier performance for different combinations of feature vectors. The 3D scatter plot show the distribution of the three features in the feature space. The 3D plots with SVM classification for all the three cases are shown in figure 4. Figure 4 shows the plot of combined features of area of 1st and 6th CC sub-regions and contrast as a texture feature.

The different combinations of morphological features accounted the 80% accuracy of classification while the texture features provided the accuracy of 60%. The combination

of both the morphological and texture features increased the overall accuracy of classification to 90%. The accuracy of the classifier is increased using different combinations of all the features in higher dimensional feature space. The feature vector combinations and their corresponding accuracy, sensitivity and specificity are enlisted in table 1. Accuracies are in the range from 20.00% to 90.00%. For 3 best results feature vectors' sensitivity (100.00%) and specificity (86%) are among the highest rated.

All the gathered evidence is suggesting that tested method is a promising approach. This paper used presumption that posterior parts of CC can be more likely affected by dementia. In best scored feature vectors sorted by accuracy are more numerous vectors consisting both anterior and posterior features. Methods accuracy is improved by adding set of textural features.

3 CONCLUSION

Paper proposes corpus callosum segmentation method for abnormal cases with promising results and novel head tilt measurement method. Performance can be improved with better G2 point definition and approximation tools. Accuracy of proper segmentation could be improved with optimization.

Classification method using SVM algorithm is showing promising results when anterior region of CC is compared to posterior regions. It is also possible to use improved SVM algorithm to improve classification accuracy. Area oriented features had highest accuracy of 80%. Texture oriented features had highest accuracy of 60%. Combination of both types resulted in increased accuracy to 90%.

REFERENCES

- [1]. S.F. Witelson." Hand and sex differences in the isthmus and genu of the human corpus callosum: a post-mortem morphological study". In *Brain: A Journal of Neurology*, Dimitri M. Kullmann, Oxford, Oxford press, pp. 799 – 835, 1989.
- [2]. A. Hensel, H. Wolf, F. Kruggel, S.G. Riedel-Heller, C. Nikolaus, T. Arendt, H.J. Gertz. "Morphometry of the corpus callosum in patients with questionable and mild dementia". *Journal of Anatomy*, vol. 171, pp. 163 – 167, 1990
- [3]. B.J. Hallam, W.S. Brown, C. Ross, J.G. Buckwalter , E.D. Bigler , J.T. Tschanz ,M.C. Norton, K.A. Welsh-Bohmer , J.C.S. Breitner. "Regional atrophy of the corpus callosum in dementia". *Journal of the International Neuropsychological Society*, vol.14, pp. 414-423, 2008
- [4]. R. Hurley, W.G. Bradley, H.T. Latifi, K.H. Taber." Normal pressure hydrocephalus: Significance of MRI in potentially treatable dementia". *The Journal of Neuropsychiatry and Clinical Neurosciences*, 11, no.3, pp.297-300, 1999.
- [5]. X.Long, C.Wyatt." An Automatic Unsupervised Classification of MR images in Alzheimer's disease". *IEEE conference on Computer Vision and Pattern Recognition*, San Francisco, CA, 2010, pp. 2910-2917.
- [6]. M.G. Preti, M.M. Lagana, L. Griffantny, R. Nemni and G. Baselli." comparison between skeleton-based and atlas-based approach for the assessment of corpus callosum damages in mild cognitive impairment and Alzheimer disease". *IEEE EMBS*, Boston, Massachusetts, USA, 2011, pp.7808-7811
- [7]. M.M. Patil, A.R. Yardi." MLP classifier for Dementia levels ". *International Journal of Modeling and Optimization*, Vol.2, No.5, pp.567-569, 2012

- [8]. M. Moutard, V. Kieffer, J. Feingold, F. Kieffer, F. Lewin, C. Adamsbaum, A. Gélot, J. Campistol I Plana, P. van Bogaert, M. Andre, G. Ponsot, "Agenesis of corpus callosum: prenatal diagnosis and prognosis". *Child's Nervous System, Springer-Verlag*, vol. 19, pp. 471-476, 2003.
- [9]. S.Prabhakar, K.Porkumaran." An investigation of volumetric and corpus callosum dimension to detect brain disorders". *Journal of biomedical science and engineering*, no. 5, pp. 369-377, 2012.
- [10]. T.J.Herron, X. Kang, D.L. Woods." Automated measurement of human corpus callosum using MRI". *Frontiers in Neuroinformatics*, 2012.
- [11]. J.P.Laissy, B. Patruix, C. Duchateau, D.Hannequin, P. Hugonet, H. Yahia, et al. " Mid-sagittal MR measurements of corpus callosum in healthy subjects and diseased patients: A prospective survey". *American society of neuroradiology*, pp.145-154, 1993.
- [12]. A. Elnakib, A. El-baz, M.F. Casanova, G. Gimel and A.E. Switala." Image-based detection of corpus callosum variability for more accurate discrimination between dyslexic and normal brains". *IEEE conference on Image Processing*, 2010, pp.109-112.
- [13]. Y. Segev, Ur. Metsler, L.BeniAdani, C. Elran, I.-I. ReiderGroswasser, S. Constantini," Morpho-metric study of mid-sagittal MR imaging plane in cases of Hydrocephalus and atrophy and in normal brains", *American Journal of Neuroradiology*, 2001.
- [14]. M.S. de Oliveira, M.L.F. Balthazar, A.D' Abreu, C.L. Yasida, B.P. Damasceno, F. Cendes, et.al." MR Imaging Texture Analysis of Corpus Callosum & Thalamus in Amnesic Mild Cognitive Impairment & Mild Alzheimer Disease". *American Journal of Neuroradiology*, pp.60-66, 2011.
- [15]. R.M. Haralick," Statistical and Structural Approaches to Texture", *Proceedings of IEEE*, Vol.67, No. 5, pp.788-804, May 1979.
- [16]. F. Meyer, "Topographic distance and watershed lines", *Signal Processing*, July 1994, vol. 38, pp. 113-125.
- [17]. G.V. Bhalerao, N. Sampathila. "K-Means Clustering Approach for the Segmentation of Corpus Callosum from Brain Magnetic Resonance Images" *International conference on circuits, computing, communication and control*, November 2014, pp.387-390.
- [18]. P.T. Selvy, V. Palanisami, S. Elakkiya." A novel approach for the prediction of epilepsy from 2D medical images using case based reasoning classification model." *WSEAS transactions on computers*, vol.12, pp.2224-2872, 2013.
- [19]. E. Adiya, Y.S. Izmantoko, H.K. Choi." Comparison of active contour and active shape approaches for corpus callosum segmentation". *Journal of Korea multimedia society*, vol.16, pp.1018-1030, 2013.
- [20]. C.Salvatore, A.Cerasa, I.Castiglioni, F.Gallivanone, A.Augimeri, M. Lopez, et al." Machine learning on brain MRI data for differential diagnosis of Parkinson's disease and progressive supranuclear palsy". *Journal of neuroscience methods*.pp.230-237, 2013.
- [21]. A.C.C. Modeling. "Abnormalities in MRI traits of corpus callosum in autism subtypes". *International conference, IEEE EMBS*, Vancouver, British Columbia, Canada, 2008, pp.3900-3903.
- [22]. A. Elnakib, M.F. Casanova, G. Gimel and A.E. Switala," Dyslexia diagnostics by 3D shape analysis of the corpus callosum", *IEEE transactions on Information technology in biomedicine*, vol.16, no.4, pp.700-708, 2014.
- [23]. R. Bakshi, A.J. Thomson, M.A. Rocca, D. Pelletier, V. Dousset, F. Barkhof et al.," MRI in multiple sclerosis: current status and future prospects", *National Institute of Health*,2008,pp.615-625.
- [24]. Y. Yokota, Y. Kawamura, Y. Kameya." Callosal shapes at the mid-sagittal plane: MRI differences of normal males, normal females and GID" *Proceedings of the 2005 IEEE engineering in medicine and biology*,27th annual conference, Shanghai, China,pp.3055-3058,2005.
- [25]. N. Cristianini, J. Shawe-Taylor, "An Introduction to Support Vector Machines and Other Kernel-based Learning Methods", 1st Edition, Cambridge: Cambridge University Press, 2000.
- [26]. S. Ding, X. Hua, J. Yu."An overview on nonparallel hyper plane support vector machine algorithms". *Journal of Neural Computing and Applications*, vol. 25, pp. 975-982, 2014.
- [27]. OASIS brain MRI database, available on: <http://www.oasis-brains.org/>
- [28]. MATLAB and Statistics Toolbox Release 2013a, theMathWorks, Inc., Natick, Massachusetts, United States.

LPC Speech Synthesis in MATLAB

Josef Kročil

Department of Cybernetics and Biomedical Engineering, FEECS,
VŠB – Technical University of Ostrava, 17. listopadu 15,
708 33 Ostrava – Poruba, Czech Republic
josef.krocil@vsb.cz

Abstract. This article is focused on implementation of one of many methods of speech synthesis in MATLAB environment, using GUI (graphical user interface) as a simple TTS system (text to speech system). For the synthesis of speech signal, linear predictive coefficients (LPC coefficients) and transfer function of vocal tract were used. This type of speech synthesis takes place in spectral domain and it is based on source and filter theory. Whole synthetic speech signal is a product of concatenation of smaller short time synthetic speech units. Phonemes and some diphones were chosen as a basic speech units. Although this is the basic method of speech synthesis, requiring previous analysis of speech units, it can be modified by many ways and it can be useful for teaching purposes.

Keywords: Speech, LPC, Synthesis, MATLAB

1 Introduction

Speech synthesis means the artificial generation of human speech in its acoustic form. The first experiments in synthesis were conducted in 1779, when a German professor Kratzenstein constructed mechanical synthesizer, which was capable of using acoustic resonator to produce sounds of five long vowels, similar to the human voice. Mechanical synthesizers were developed and improved until the beginning of 20 th century. In 1939, Homer Dudley presented the first continuous speech synthesizer VODER, which was composed of ten bandpass filters and was driven by a periodic signal (voiced utterance - eg. Vowels) or noise (unvoiced speech - eg. Fricatives). Electronic analog synthesizers were developed until the first half of the sixties, when they were replaced by digital synthesizers. The first experiments with digital concatenative synthesis fall to the late sixties when Rex Dixon and David Maxey developed parametric concatenative synthesizer (1968), which concatenated diphones, which were parameterised via formant frequency. The first TTS system (ie. TTS systems - text to speech) was developed by Noriko Umeda (1968), then, during the seventies by Dennis Klatt at MIT. In the eighties were developed a series of TTS systems, which for parameterisation of speech units used mainly LPC coefficients (linear prediction coefficients). Currently, many other approaches such as e.g. Hidden Markov models and neural networks are tested. Speech synthesis is undoubtedly of great importance, especially in TTS systems, which may allow automated reading books for blind people etc [1].

2 Simplified description of applied principles and methods

2.1 Source and filter theory

The principle of the speech signal production can be described by the theory of the source and filter (Fig. 1), which can be driven by either a periodic impulse signal in the case of voiced speech or random noise in the case of unvoiced speech. The filter, which is described its transfer function $H(z)$ then represents the characteristics of the vocal tract (oral cavity, nasal cavity, etc.). Modifying the transfer function $H(z)$ on the frequency response, we can get the frequency spectrum of the speech tract model. Frequency spectrum of output speech signal can be obtained by multiplying of the frequency spectrum of speech tract with spectrum of input signal. In the time domain, the resulting output signal is the product of convolution of the input signal and the impulse response of the filter. Because speech is a time-variable process, the filter parameters are also variable in time [1].

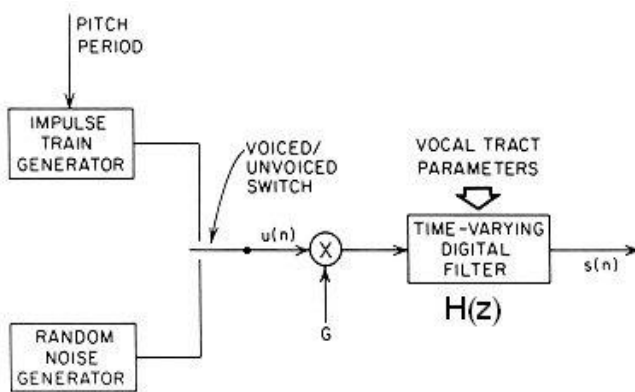


Fig. 1. Block diagram showing source and filter theory [2]

2.2 Speech signal preprocessing

Synthesis by LPC coefficients requires a prior analysis of speech units (phonemes or diphones, etc.) to be synthesized. LPC coefficients are filter parameters, represent the vocal tract, as described in the previous chapter. Discretized speech signal is not processed whole, but it must be divided into short segments (about 10 ms to 32 ms) in order to maintain information about the status change of the speech tract, thus change the filter parameters. Before the segmentation of selected speech unit, mean value subtraction and amplitude normalisation is required. When performing segmentation, it is possible to use various types of window functions (most often Hamming). For each extracted segment it is necessary to analyze voiced/unvoiced character of speech (zero-crossing values etc.) and calculating the LPC coefficients. Voicing information about the segment, along with the LPC coefficients, gain, and the name of speech unit is then the basis for its synthesis [1], [3].

2.3 LPC model of vocal tract

Transfer function $H(z)$ of the vocal tract can be described by the equation

$$H(z) = \frac{G}{1 + \sum_{i=1}^Q a_i z^{-i}} \quad (1)$$

where Q is order of the filter (in practice about 8 to 20), G is the gain and a_i are LPC filter coefficients. Frequency response of this system can be obtained via substitution

$$z = e^{j\omega} \quad (2)$$

Derivation of calculation of the filter parameters would be extensive, so we are satisfied with the explanation that the calculation of unknown parameters is based on minimizing energy of prediction error E . Any interested person can find the derivation in [1]. Values of wanted filter parameters are obtained using Durbin Levinson algorithm, recursively for $i = 1, 2 \dots Q$ as follows:

$$\begin{aligned} E^{(0)} &= R(0), \\ k_i &= - \left[R(i) + \sum_{j=1}^{i-1} a_j^{i-1} R(i-j) \right] \frac{1}{E^{(i-1)}}, \\ a_i^{(i)} &= k_i, \\ a_j^{(i)} &= a_j^{(i-1)} + k_i a_{(i-j)}^{(i-1)}, \quad 1 \leq j \leq i-1, \\ E^{(i)} &= (1 - k_i^2) E^{(i-1)} \end{aligned} \quad (3)$$

Where R are the autocorrelation coefficients of short time signal segment. Value of gain G can be obtained from the following equation

$$E = R(0) + \sum_{i=1}^Q a_i R(i) = G^2 \quad (4)$$

[1], [3]

2.4 Basic principles of parametric concatenative LPC synthesis

Concatenative synthesis is based on the assumption that the sounds from which the speech is composed, can be represented by a finite number of speech units, a specific speech sounds (phonemes, diphones, etc.). Representatives of the units (their name, LPC coefficients, gain, voiced/unvoiced information) are stored in a database, from where they are selected during synthesis. Synthesis takes place in fr. domain, by the theory of source and filter. By applying discrete inverse Fourier transform during synthesis, selected units are synthesised and concatenated to whole speech signal (time domain) [1].

3 LPC concatenative synthesis in MATLAB

Graphical user interface of speech synthesizer consists of two main panels (Fig. 2). Panel "Segmentace řečových jednotek" is used to create speech units, whose parameters are stored and their name is listed in the table "Inventář" (Inventory). Inventory stored content can be loaded at any time and can be updated. Panel "TTS" is used for speech synthesis from text, which is formed by interconnection of names of speech units by separating them by the sign "+". Natural and synthetic signal can be played, or only its selected part, which is especially useful within the creation of speech units. Within the analysis of the speech units, the segment length is 512 samples, sampling frequency is 16 kHz and order of LPC model Q is 20. Voiced/unvoiced analysis of segments is based on the calculation of zerocrossing rate. In synthesis, the filter input signal is either a periodic sequence of unit pulses with adjustable frequency (voiced speech, fundamental frequency of voice), or Gaussian white noise (both from the theory of source and filter).

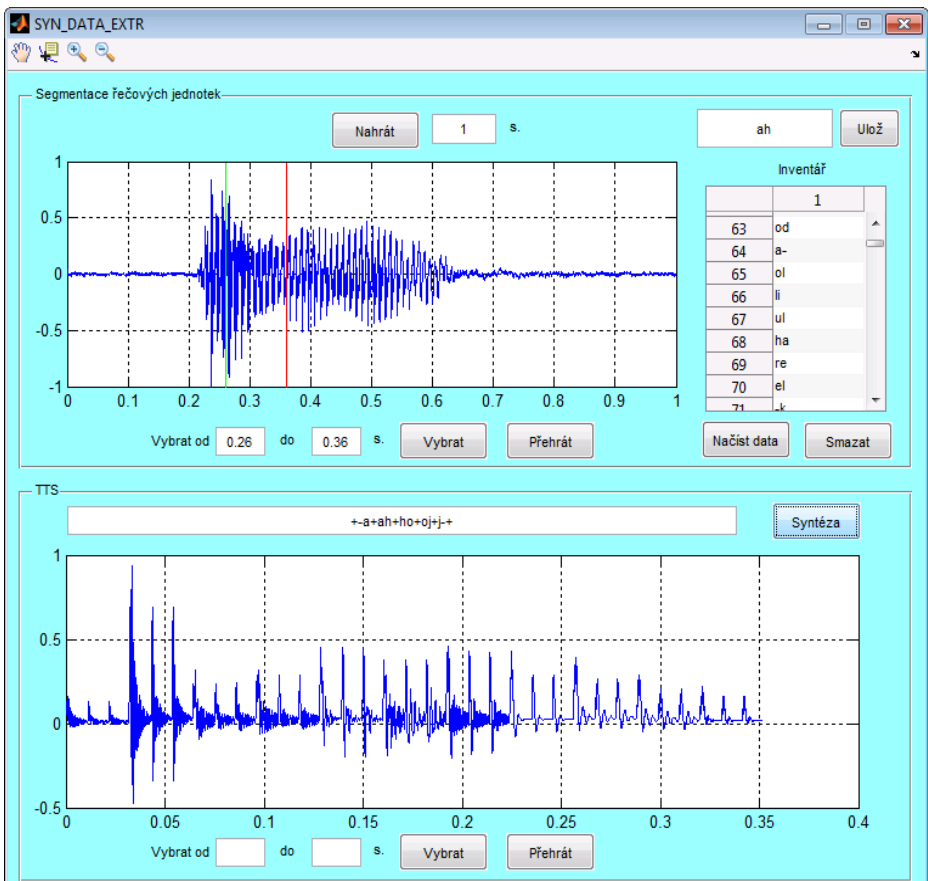


Fig. 2. Speech synthesizer in MATLAB – graphical user interface

3.1 Comparison of speech synthesis using phonemes and diphones

Selecting the type of speech units has a major impact on the accuracy and acoustic quality of synthetic speech. Two types of speech units were chosen, namely phonemes and diphones for Czech language. A Database of all 39 Czech phonemes was created, so it is possible to create any word or entire sentence. Due to the large number of diphones database has been created 77 diphones, which is sufficient to compare the quality of synthetic speech with a few selected words. On the Fig. 3 is a synthetic speech signal of Czech word "ahoj", where phonemes were used as speech units. The interval, indicated by the green and red line represents the transition of two last phonemes /o/ and /j/. This signal in its acoustic form lacks signs of co-articulation, so that speech is not well understandable. The same transition is marked on the Fig. 4, where diphones were used as speech units. In this case, a transition is slow, and signal in its acoustic form is well understandable. Synthesis using diphones is acoustically better, but it has a large amount of data (about 1400 diphones used in Czech language).

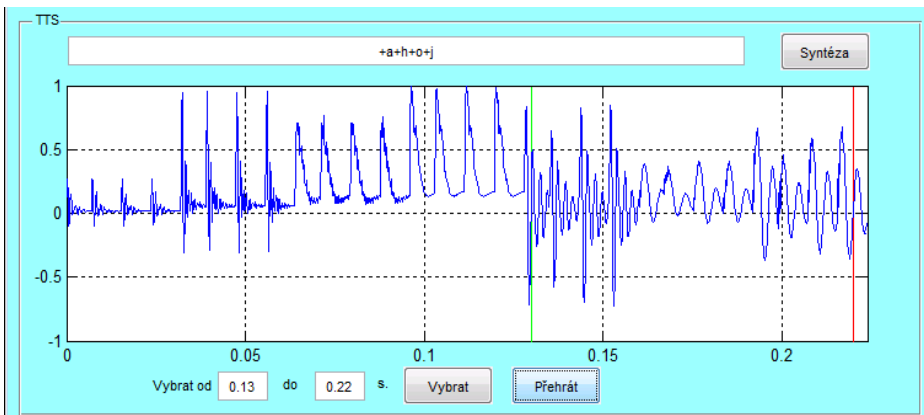


Fig. 3. Synthesis of czech word "ahoj" using phonemes as a speech units

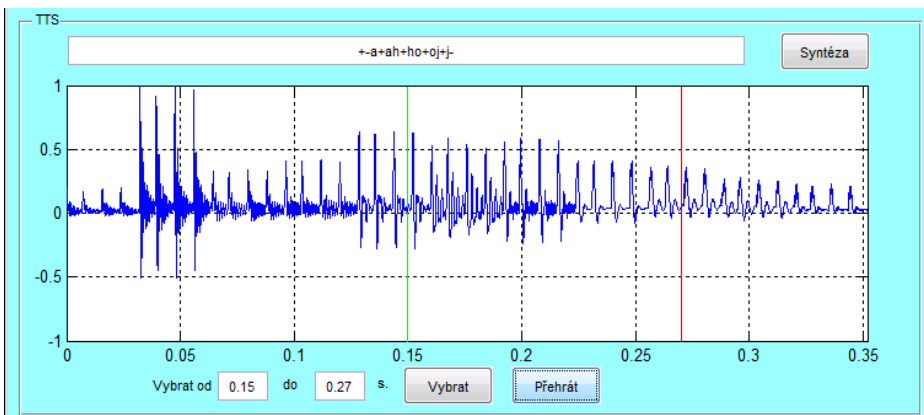


Fig. 4. Synthesis of czech word "ahoj" using diphones as a speech units

4 Conclusion

In this paper, one of the many algorithms of speech synthesis is presented. There are explained basic concepts and principles of LPC concatenative speech synthesis. In Matlab environment, the LPC synthesizer with graphical user interface was created, enabling the collection and analysis of speech units for their synthesis using concatenation. Two speech unit databases were created, namely all of Czech phonemes and limited number of diphones, which can be synthesised using a simple TTS system to generate synthesized speech. It was verified that the choice of speech unit type has a major impact on the quality of speech. Synthesis using diphones generates relatively well understandable speech. Synthesis using phonemes as a speech units produces speech, that lacks coarticulatory phenomena, so it is less understandable. The program can serve as a teaching tool in the study of the fundamental principles of LPC speech synthesis.

References

1. PSUTKA, Josef. *Komunikace s počítačem mluvenou řečí*. Praha: Academia, 1995. 287 p. ISBN 80-200-0203-0.
2. RABINER, L., SCHAFFER R. *Digital Processing of Speech Signals*. Prentice-Hall, 1978. ISBN 978-0132136037.
3. MCLOUGHLIN, Ian. *Applied Speech and Audio Processing*. Leiden: Cambridge University Press, 2009. 216 p. ISBN 978-0-521-51954-0.

Modelling of the Knee Cartilage Morphological Changes on the Base of the Fuzzy Thresholding with the Local Aggregation

Jan Kubicek

Department of Cybernetics and Biomedical Engineering, FEECS,
VŠB – Technical University of Ostrava, 17. listopadu 15,
708 33 Ostrava – Poruba, Czech Republic
jan.kubicek@vsb.cz

Abstract. The paper deals with the design of the soft thresholding multiregional segmentation method completed of the local aggregation procedure applicable on the modelling of the structural changes of the knee cartilage with the target of the identification and detection of the pathological cartilage deterioration, clinically called chondromalacia or chondropathies. This particular cartilage deterioration is badly recognizable from the native MR (magnetic resonance) images therefore modelling in this area is beneficial, furthermore the cartilage mathematical modelling allows the precise differentiation of the individual adjacent structures, this fact causes the knee cartilage selection from the other knee structures. The significant benefit of the proposed soft segmentation method is fact that the segmentation procedure goes into two phases of pixel classification: the brightness and the spatial segmentation. This fact makes the method more robust to noise.

Keywords: Soft thresholding, PTS membership function, spatial aggregation, knee cartilage, MRI, multiregional segmentation

1 Introduction

The analysis is mainly focused on the genesis of the articular cartilage mathematical model which is intended for the precise extraction of the cartilage with the target of the area identification where it is supposed the pathological interruptions badly recognizable from the native image records. It should be noted that the knee cartilage records are acquired in the shade levels where, especially, the early pathological changes are unrecognizable. The mathematical model is sufficiently sensitive in order to even early pathophysiological changes were clearly observable. Furthermore, the cartilage model allows the tissue differentiation in the artificial color map where individual tissues are much better recognizable.

2 The Purpose of the Soft Classification

The soft thresholding method uses the fact that each pixel is transformed into fuzzy space via the PTS membership function, thus each pixel is described by the vector of the fuzzy membership values instead of using the hard classification. Furthermore, membership values are consequently modified by the local aggregation which takes into account the pixel spatial information. This functionality ensures that the method is robust to classifying of the noise pixels which commonly have significantly different level intensity to cartilage structure and they would be incorrectly classified in other class by the thresholding method. The significant benefit of the aggregation part is that does not work in the image space but in the space of the fuzzy membership functions.

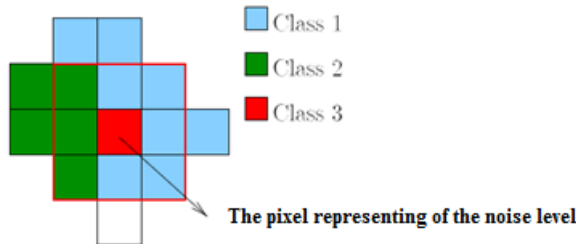


Fig. 1 The example of the noise level classifying on the base of the hard thresholding

3 The Structure of the Soft Multiregional Thresholding Method

It is supposed that $I(r)$ denotes to the image data with structure of L regions which should be extracted by the thresholding so that we obtain the segmented image denoted as $M(r)$ to:

$$M(r) = g_s\{I(r)\} \tag{1}$$

where $g\{.\}$ denotes to the segmentation method which can be considered as function mapping N_I monochromatic image levels into L regions i.e. $g_s: N_I \rightarrow L$ where $L < N_I$. After performing of the segmentation the proposed method supposed that each pixel is described by the fuzzy membership level in each region in each of the L regions. In the following text it is used indication $\mu_l(x), l=1, \dots, L$ for the membership function of the l^{th} region. The spatial aggregation can be applied on the so called membership plane to taking into account the relation among adjacent pixels to obtaining final segmentation.

The methodology is demonstrated in the figure 2 containing the five essential steps. Since it is methodology and not close algorithm within each step the alternative is given of the method implementation. The respective choice is depended on the kind of the image records and particular features of the segmented image.

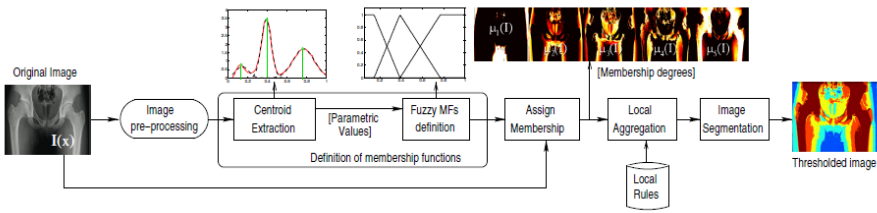


Fig. 2 The flow chart of the soft thresholding method

3.1 The Centroids Extractions

In the initialization step for each image class the centroid is defined characterizing the middle point of the respective class. Number of the centroids can be manually set by user alternatively the algorithm can be set for finding the optimal number of centroids.

For the practical purposes of the soft segmentation methodology the K means method is used for centroid extraction. The algorithm iteratively finds the vector elements that minimize the center deviation between given data set (pixels) and vectors (pixel distance from centroid). In each iteration step the Euclidean distance of each pixel is calculated to every class. The pixel is classified on the base of the minimal distance. Conclusively, the centroid of the respective class is calculated. It should be state that it used just centroid of the respective class.

3.2 Fuzzy Membership Function Definition

The fuzzy membership function $\mu_l(x)$, $l=1, \dots, L$ is associated to each of the classes connected with the defined centroids. This method offers two approaches for histogram approximation by fuzzy membership functions. The image histogram can be approximated by the sequence of Gaussian membership function. Nevertheless, this method is not so appropriate for relevant histogram approximation because must be solved optimization minimization technique so that we achieve as minimal difference as possible between discrete histogram and Gaussian curve. Due to this fact the method is relatively computational demanding. It turns out to better alternative using the triangular membership function (the main part of the PTS function). This method is generated directly on the base of the extracted centroids without necessity of knowledge of brightness level distribution of particular tissues in the analyzed image. It is supposed that each region is approximated by triangular membership function. This situation is depicted in the figure 3.

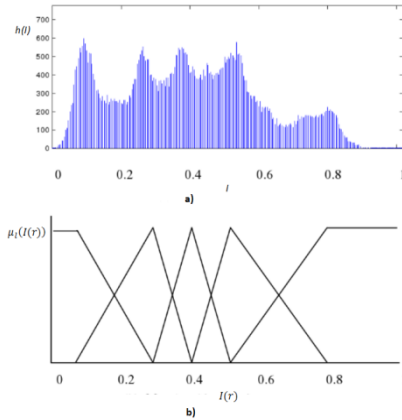


Fig. 3 The image histogram (a), PTS membership functions (b)

Each pixel is described by vector of the membership values:

$$\mu(I(r)) = [\mu_1(I(r)) \ \mu_2(I(r)) \ \dots \ \mu_L(I(r))]$$

In the case of PTS function just two vector elements are non-zero. After taking this segmentation procedure the image thresholding can be done by the following relationship:

$$M(r) = \operatorname{argmax}_l \{\mu_l(I(r))\} \quad (2)$$

where $M(r)$ denotes to the image segmentation output. Nevertheless, this approach does not taking into account spatial information and the result is strongly depended on the noise presence.

3.3 The Spatial Aggregation Definition

The spatial aggregation consist the main contribution in the context of the whole segmentation methodology. The fuzzy logic versatility allows designing of many ways for considering the influence of neighbourhood from $\mu(I(r))$. In the case of the pixel neighborhood $\eta(r)$ centering in the surround of the pixel r we can take advantage the membership values $\mu(I(r))$ of all pixels in $\eta(r)$ for achieving better classification image into regions. The general spatial aggregation is defined by the following expression:

$$\mu^S(I(r)) = \operatorname{agg}_{s \in \eta(r)} \{\mu(I(s))\} \quad (3)$$

where $\operatorname{agg}\{\cdot\}$ denotes to the aggregation in the pixel neighborhood $\eta(r)$. The main task of this segmentation part is the modification of the original membership function

$\mu_l(I(r))$. For this purpose various aggregation functions can be used which take into account spatial information. In the context of the soft segmentation methodology the median aggregation (MedAg) is used. MedAg is described by the following expression:

$$\mu_l^s(I(r)) = \text{median}_{s \in \eta(r)} \{ \mu(I(s)) \} \quad (4)$$

4 The Articular Cartilage Modelling

The main task of the modelling is separation of the physiological cartilage area from the pathological changes. Soft segmentation algorithm has been tested especially in the cases of the badly recognizable early stages of the chondromalacia. The segmentation output is knee cartilage model fully reflecting of the morphological cartilage structure, pathological interruptions are indicated by gaps in the segmentation results. The exemplary results are depicted in the figures 4.

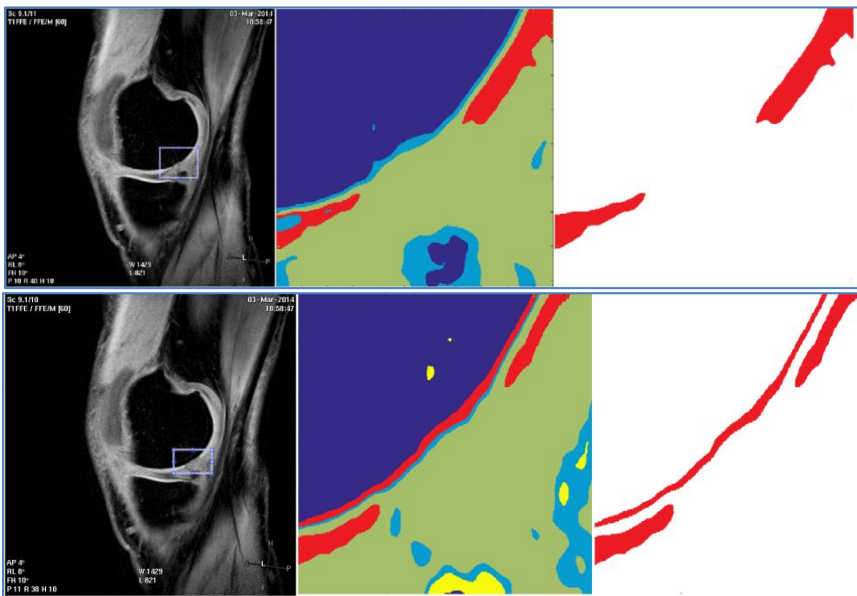


Fig. 4 The original MRI data (left), the segmentation output (middle), the articular cartilage extraction (right)

5 Conclusions

The soft thresholding appears itself as the reliable approach for segmenting medical images which are often corrupted by noise. The noise presence is frequent cause of the incorrect classification. The main benefit of the method is using of the spatial

aggregation taking into account spatial pixel information. It is important, especially, for noise pixel classification. The method has been used for modelling knee cartilage structure. The method allows the precise differentiation of the physiological cartilage from the pathological interruptions which are not clearly observable from the native MR image records.

6 Publications

1. Kubicek, J., Penhaker, M., *Fuzzy algorithm for segmentation of images in extraction of objects from MRI* (2014), Proceedings of the 2014 International Conference on Advances in Computing, Communications and Informatics, ICACCI 2014, art. no. 6968264, pp. 1422-1427.
2. Kubicek, J., Penhaker, M., Bryjova, I., Kodaj, M., *Articular cartilage defect detection based on image segmentation with colour mapping* (2014), Lecture Notes in Computer Science (including subseries Lecture Notes in Artificial Intelligence and Lecture Notes in Bioinformatics), 8733, pp. 214-222.
3. Kubicek, J., Penhaker, M., Pavelova, K., Selamat, A., Majernik, J., Hudak, R., *Segmentation of MRI Data to Extract The Blood Vessels Based on Fuzzy Thresholding* In 7th Asian Conference on Intelligent Information and Database Systems ACIIDS 2015. 23th - 25th March, 2015 Bali, Indonesia
4. Kubicek, J., Penhaker, M., Bryjova, I., Augustynek, M. *Classification method for macular lesions using fuzzy thresholding method* (2016) IFMBE Proceedings, 57, pp. 239-244.
5. Kubicek, J., Bryjova, I., Penhaker, M., Kodaj, M., Augustynek, M. *Surface of articular cartilage extraction using fuzzy C-means segmentation* (2016) Studies in Computational Intelligence, 642, pp. 209-219.
6. Kubicek, J., Bryjova, I., Penhaker, M. *Macular lesions extraction using active appearance method* (2016) Lecture Notes of the Institute for Computer Sciences, Social-Informatics and Telecommunications Engineering, LNICST, 165, pp. 438-447.
7. Kubicek, J., Valosek, J., Penhaker, M., Bryjova, I. *Extraction of chondromalacia knee cartilage using multi slice thresholding method* (2016) Lecture Notes of the Institute for Computer Sciences, Social-Informatics and Telecommunications Engineering, LNICST, 165, pp. 395-403.
8. Kubicek, J., Bryjova, I., Penhaker, M., Kodaj, M., Augustynek, M. *Extraction of myocardial fibrosis using iterative active shape method* (2016) Lecture Notes in Computer Science (including subseries Lecture Notes in Artificial Intelligence and Lecture Notes in Bioinformatics), 9621, pp. 698-707.
9. Kubicek, J., Bryjova, I., Penhaker, M., Javurkova, J., Kolarcik, L. *Segmentation of macular lesions using active shape contour method*, (2016) Advances in Intelligent Systems and Computing, 423, pp. 213-221.
10. Kubicek, J., Valosek, J., Penhaker, M., Bryjova, I., Grepl, J. *Extraction of blood vessels using multilevel thresholding with color coding* (2016) Lecture Notes in Electrical Engineering, 362, pp. 397-406.

Project Investigator

TA ČR GAMA PP1: PRE SEED fond VŠB-Technické univerzity Ostrava

Číslo projektu: TA ČR GAMA PP1: TG01010137. Název dílčího projektu: Segmentace obrazových dat artikulární chrupavky a cévního systému s cílem extrakce patologických nálezů.

Atmospheric Pressure Measurement Proposal

Martin Mikolajek

Department of Cybernetics and Biomedical Engineering, FEECS,
VŠB – Technical University of Ostrava, 17. listopadu 15,
708 33 Ostrava – Poruba, Czech Republic
martin.mikolajek@vsb.cz

Abstract. This article talks about testing and realization device for measurements atmospheric pressure. In this currently exist many simply devices for atmospheric measurement. This contribution contains main information about pressure measurement. The main part of this article contains proposal and realization measurement system for atmospheric pressure. Last part of this article contain practical test of proposed device. This last chapter talks about practical test for wireless data exchange from sensor and recalculation pressure change to altitude.

Keywords: Altitude, C#, Microcontroller, Pressure measurement, RS232, .NET

1 Introduction

This topic writes about atmospheric pressure measurement. Data information with atmospheric pressure is useful in several areas. This data is used in in meteorology, aviation and automotive and automations areas. Measurement pressure in aviation device is calculated to elevation or speed. Measurement is also used for pressure information in pipe. Although in industrial automation are usually used with bigger pressure range. [1] Atmospheric range can be used in situation like controlled burn in boiler or in atmospheric car engine. In these cases controls system need information about amount of air supplied to burn process. Therefore system need pressure and flow measurement. Flow measurement can be realized like one measurement device with flow and pressure sensor. Average atmospheric pressure on sea level is 1013,25 hPa.

The aim of this research is test and using own pressure sensor for next using. Obtained information with sensor measurement is designated for use in aviation area. This article contains information about design and realization electronic device for measurement atmospheric pressure. The sensor measurement test is developed by design own electronic device. System of test realization contains microprocessor, pressure sensor, power supply management, data connection part, personal computer.

2 Main information about pressure measurement

Pressure unit is derived from these equations: First equations derive pressure p is force F acting perpendicular to the surface S . $p = F / S$ Pressure p can be also defined by hydrostatic fluid column. $p = h * \rho * g$ The main unit for pressure in Si system is

Pascal (Pa). That is pressure with are caused by one newton acting to one meter square. Pascal is very small unit, therefore in technical area are practically used multiples of this unit. Usually are used hPa, kPa and MPa. Sometime are also used bar unit. After that 1 bar = 100 kPa. Values of pressure are defined like two related relative worth. Can be talk about absolute and barometric pressure. Barometric pressure is pressure with some condition in defined place. Devices for barometric pressure measurement are called as a barometer and for absolute pressure measurement are use device for absolute pressure measurement. Terminology pressure transmitter is similar designation for pressure sensor. It is electric device for pressure measurement which converts pressure information to electric signal. This signal can be easily transfer and using in other electronic devices. Technical area can contain pressure measurement with measuring ranges from 10^{-12} to 10^{12} Pa. But any sensor does not permit measurement for whole mentioned range. Measurement range is overlap therefore each specific pressure measurement needs own selected sensors. [1]

3 Design of measurement device

First part of design measurement device was about choosing own electric parts and overall electric topology. Measurement device has to contain part with sensor for non-electric variables and electrical parts like power voltage, reference voltage, signal and transfer measurement, data memory, data transfer and human interface. Therefore in first step was chosen pressure sensor. During device research was chosen pressure sensor MPX4115AP. **Fig. 1** It is sensor for atmospheric pressure measurement with measuring range 15 - 115 kPa. Pressure value is distributed by output voltage from sensor. Sensor sensitivity is 46 mV/kPa. [4] Measure device has to contain also next electrical parts like microprocessor, communications transfer voltage levels TTL - RS232, wireless network, PC with developed software. Block scheme of measurement device technology shows **Fig. 2**



Fig. 1. Pressure sensor

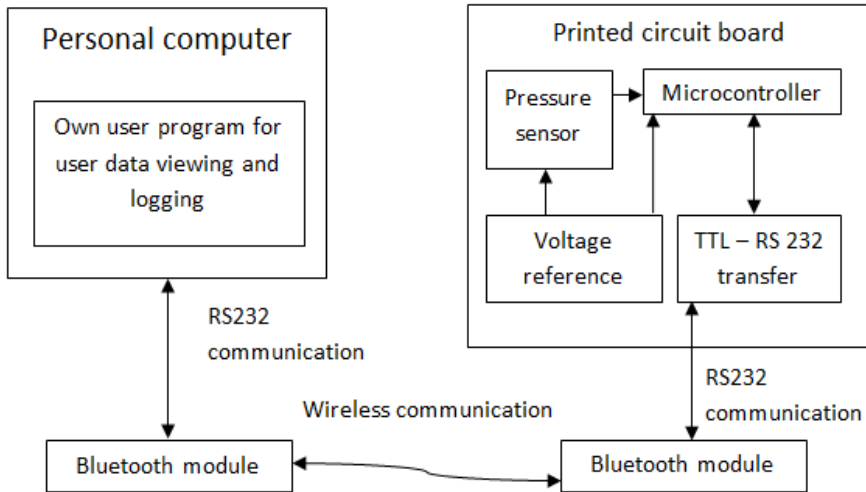


Fig. 2. Block scheme of measurement device technology

4 Measurement device

Measurement electronic device needs own microcontroller with fulfilling several criteria like analog measurement, communication possibility. Measurement device was realized like application for simple testing however during choosing of microcontroller emphasis for future was using. And therefore microcontroller was chosen in automotive execution. In this choice the measurement device is more resistant to electrical noise and etc. For realization was chosen microcontroller Freescale series HCS08 MC9S08DZ60. [2][3] In recent years freescale was renamed to NXP. For realization was chosen microcontroller Freescale HCS08 series MC9S08DZ60. It is 8-Bit HCS08 Central Processor Unit with 60 Kb memory. Next part in realization device is voltage reference ANALOG DEVICES ADR 435. This voltage provides reference to pressure sensor and analog/digital converter contained in microprocessor.

The last parts of device are communication components. Data from microcontroller was distributed by serial communication in TTL voltage logic. For communication with personal computer is needed transfer to RS232 communication. This request is realized by MAXIM MAX 232 CWE. Communication can be realized exactly over cable or via wireless communication module by Adapter RS232 Bluetooth RS-232 blu2i Ezurio. Hardware realization is shown on figure. **Fig. 3**

Microcontrollers program was designed by C language using in CodeWarrior developed software. Microcontroller's software contains those functions: Analog value

from pressure sensor is converted to 16 bits variable. Because serial communication use 8 bits communication therefore 16 bits data are separated to two variables with 8 bits length. Pressure measurement has period 100 ms. Microcontrollers calculate averages from measured values. Personal PC application can data request new data each one second.

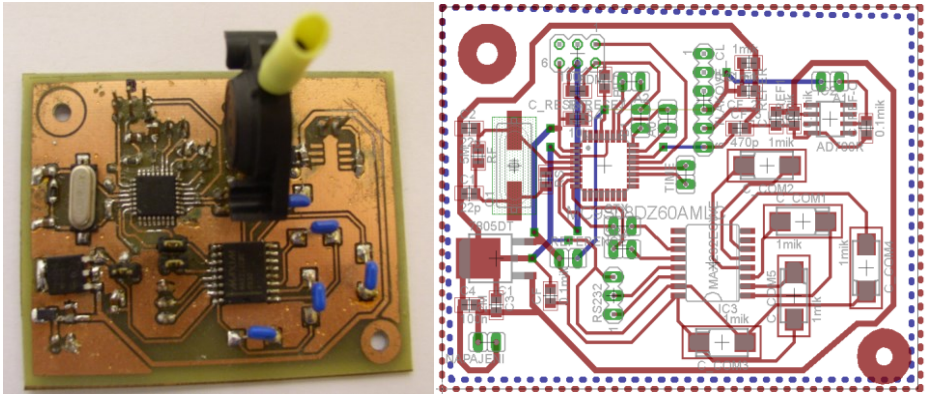


Fig. 3. Tested measurement device

5 Users application for PC

Application PC was designed by C# in Microsoft visual studio. Software uses .NET technology. Fig. 4 Applications communicate with microcontroller by serial communication 9600 kb/s. Data from microcontrollers are only information from analog/digital converter measured on pressure sensor. For valid information with measured voltage and pressure or altitude is calculated by equations. Applications software allows data logging to txt or csv file.

V_{out}	= output voltage from pressure sensors
V_{ref}	= voltage reference
QUA_{NUM}	= number of quantization count microcontrollers convertor
V_{MEAS}	= actual measurement voltage from pressure sensor
P_{ACTUAL}	= actual measured pressure
$ER_{CORECTION}$	= error for calibration (0.4351 during test)
Altitude	= altitude
P_{ref}	= reference pressure (during test actual pressure on the ground)

First equation calculates voltage from pressure sensor.

$$V_{out} = V_{ref} / QUA_{NUM} * V_{MEAS}$$

Next request is recalculation measured voltage to the actual value of pressure.

$$P_{ACTUAL} = (V_{out} + V_{ref} * 0.009 * 0.095 + ER_{CORECTION}) / (V_{ref} * 0.009) \quad [5]$$

Ground altitude can be calculated from pressure by this equation:

$$\text{Altitude} = (1 - (P_{\text{ACTUAL}} / P_{\text{ref}})^{0.19026}) * 44330.7$$

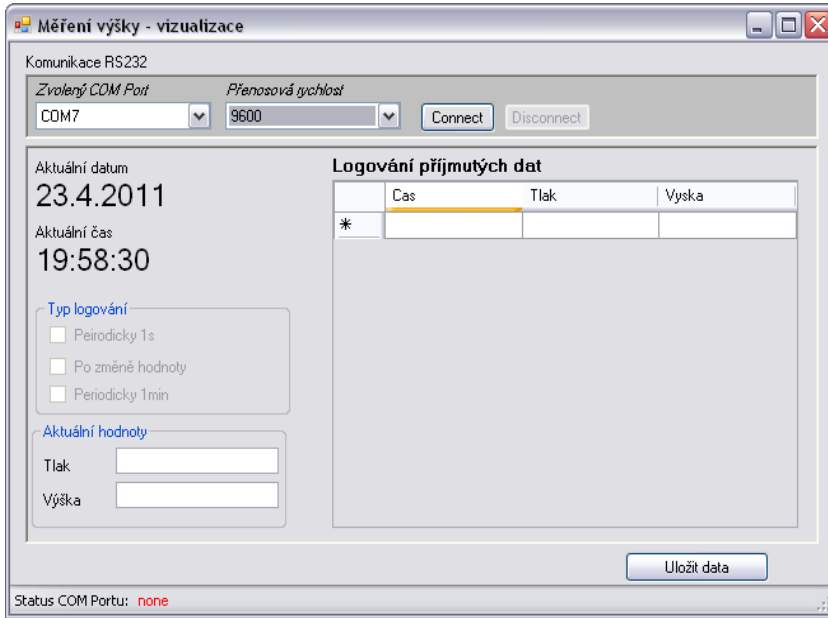


Fig. 4. PC measurement application

6 Tests and result

After realization device was conducted several practical measure tests. First test was general test with calibration and static atmospheric pressure measurement.

Second measure was dynamic measurement with model plane using. This test used wireless data connection. Wireless communication by Adapter RS232 Bluetooth RS232 blu2i Ezurio was commissioned using by supplier datasheet information. [6] Data connection by wireless during flying with RC plane was correct. Bluetooth RS232 supposed connection about 200 meters. Tested communication distance during flying test was similar. Data from test is on figure. **Fig. 5.** . Third test was realized by ultra-light plane using. Aim of this test was compared altitude value from designed measuring device and altimeter in ultra-light plane. This test was also correct.

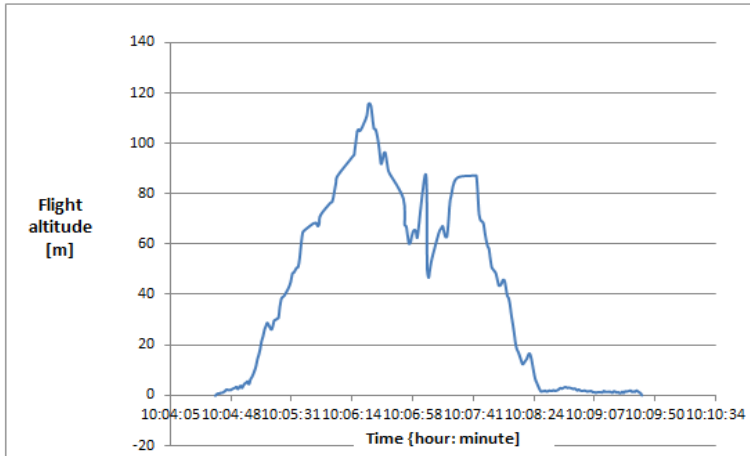


Fig. 5. Graph with measured data

7 Conclusion

Aim of created device was about testing possibility of selected pressure sensor and options for data processing. All tests were realized practically by using RC plane or by ultralight aircraft. Information during creating this device brings new knowledge for next electronic construction using like own autopilot for RC plane or ultralight plane. During device creation was problem with electrical noise. That was resolved by arithmetic averaging.

References

1. KADLEC, K. Snimace tlaku – principy, vlastnosti a pouziti. AUTOMA: AUTOMA 10/2007 [online]. 2017, 2007(2), 4 [cit. 2016-08-06]. From: <http://automa.cz/download/au020728.pdf>
2. MIKOLAJEK, M. LED Based Light controlled by CAN Bus for Electric Car, Bachelor thesis, Technical university Ostrava (2010).
3. MC9S08DZ60 : Technical Data Sheet. Rev. 4. [s.l.] : Freescale Semiconductor, 2008. 416s.
4. MPX4115 SERIES: Technical Data Sheet MPX4115. Rev. 5. : Freescale Semiconductor, 08/2006. 8s.
5. GOLA, Miroslav. *EMGO: BAROMETRICKÉ ČIDLO MOTOROLA MPX4115* [online]. 01.02.2008 [cit. 2016-08-06]. From : http://www.emgo.cz/barometr_mpx4115.htm
6. <http://de.rs-online.com/web/p/bluetooth-adapter/0189201/>

Modification of Kamada-Kawai Algorithm Using Barzilai-Borwein Method

Jana Nowaková

Department of Cybernetics and Biomedical Engineering, FEECS,
VŠB – Technical University of Ostrava, 17. listopadu 15,
708 33 Ostrava – Poruba, Czech Republic
jana.nowakova@vsb.cz

Abstract. Graph type of data may be found all around us and it can help to simplify the description of many very complicated situations as well as it presents a different description of any complex system with respect to mutual relationships between system parts. There is lot of known methods for graph drawing. In the paper it is suggested to use the algorithm presented by Kamada and Kawai. The main idea of the presented work is to present the comparison of classic Kamada-Kawai algorithm with Newton-Raphson method used for the minimization and the Kamada-Kawai algorithm with Barzilai-Borwein method used instead the Newton-Raphson method. For all cases the results are presented in 2D. As it was proved the computation time was rapidly changed using the suggested Barzilai-Borwein.

Key words: Graph layout; optimization; Kamada-Kawai algorithm; Barzilai-Borwein method; convergence.

Graph data is very common. This type of data may be found everywhere and it simplifies the description of many very complicated situations as well as it presents a different description of any complex system with respect to mutual relationships between system parts. Therefore, graph drawing or graph layout is an important task because automatic visualization of the graph data allows users to focus on the system itself instead on the problem how to draw a graph precisely. The quality of graph layout is, therefore, the key aspect of any graph drawing algorithm. The quality of the graph drawing is measured by many different measures, such as minimal number of crossed edges, area needed to draw a graph, symmetry etc. Several algorithm was developed for automatic graph drawing. Orthogonal methods [1] were developed for drawing very-large-scale integration circuits and printed circuit board designing problem. Spectral layout [2] uses coordinates from eigen-vectors of a matrix derived from graph adjacency matrix. However, the most interesting methods belong to the force-directed family of methods [3]. These algorithms use forces between nodes to iteratively move node positions until a certain optimum is reached for defined error function.

The first well known algorithm was published in 1989 by Kamada and Kawai [3]. They introduced a different approach to graph drawing, which is based on the

idea, that graph can be considered as a system of springs. Every pair of nodes, which is connected by edge, is connected by spring. The theory of elastic potential energy says that energy stored in stretched or compressed spring is equal to work W [Joule], which is computed as $W = 1/2kx^2$, where k [N/m] is positive spring constant and x [m] is stretched or compressed distance, i.e. the difference between length to equilibrium state (l), [4]. Energy of the whole system can be computed for n nodes by Equation 1 [4, 5].

$$W_{\text{tot}} = \sum_{i=1}^{n-1} \sum_{j=i+1}^n \frac{1}{2} k_{i,j} \left((x_i - x_j)^2 + (y_i - y_j)^2 - 2l_{i,j} \sqrt{(x_i - x_j)^2 + (y_i - y_j)^2} + (l_{i,j})^2 \right). \tag{1}$$

$$\frac{\partial W_{\text{tot}}}{\partial x_m} = \frac{\partial W_{\text{tot}}}{\partial y_m} = 0, \quad \text{for } 1 \leq m \leq n. \tag{2}$$

$$\frac{\partial W_{\text{tot}}}{\partial x_m} = \sum_{m \neq j=1}^n k_{m,j} \left\{ (x_m - x_j) - \frac{l_{m,j} (x_m - x_j)}{[(x_m - x_j)^2 + (y_m - y_j)^2]^{1/2}} \right\}, \tag{3}$$

$$\frac{\partial W_{\text{tot}}}{\partial y_m} = \sum_{m \neq j=1}^n k_{m,j} \left\{ (y_m - y_j) - \frac{l_{m,j} (y_m - y_j)}{[(x_m - x_j)^2 + (y_m - y_j)^2]^{1/2}} \right\}. \tag{4}$$

$$\Delta_m = \sqrt{\left(\frac{\partial W_{\text{tot}}}{\partial x_m} \right)^2 + \left(\frac{\partial W_{\text{tot}}}{\partial y_m} \right)^2}. \tag{5}$$

The Kamada-Kawai (KK) algorithm is based on the minimization of the energy W_{tot} of the whole system of springs, which represent the graph. The idea is demonstrated in the Figures 1 and right subfigure 3. Figure 1 shows graph at initial state and the right subfigure of Figure 3 shows the same graph after minimization of energy stored in springs, i.e. edges. The necessary condition of optimality is given by Equation 2.

Equation 2 shows that the gradient of W_{tot} is non-zero and the function can increase or decrease in direction of gradient. If the function W_{tot} is in point of a local minimum then every move out increase its value and this point is dynamic state of forces balance. Partial derivations of W_{tot} with respect to spacial coordinates x_m and y_m are given by Equation 3 and Equation 4.

KK minimizes W_{tot} using two-dimensional Newton-Raphson method [3]. However, this method requires set of independent non-linear equation, but the problem produces equations which are dependent on each other. Therefore, it leads to minimization of W_{tot} in each iteration for selected point m with the maximal Δ_m computed from Equation 5. Afterwards, the Newton-Raphson algorithm is used for minimization of W_{tot} of whole system with respect to selected node m .

From computational point of view, the Kamada-Kawai algorithm [3] is not optimal from several reasons. First of all, the initialization of the particles onto

circle (Figure 1) needs $\Theta(n)$. The outer *while* loop consists of the searching algorithm to find the node with the largest Δ_m and afterwards, the change of the position of this node is computed using Newton-Raphson method, see [3]. However, the same node can be chosen again during the next loop. The inner minimization loop is performed using Newton-Raphson method, which has quadratic convergence and it requires $O((\log n)F(n))$, where $F(n)$ is the evaluation cost of $f(x)/f'(x)$.

Due to these reasons, the usage of KK algorithm on large graphs is practically inconvenient and even for small graphs, the computation time is long. Hence this is the motivation to modify the original algorithm.

1 Barzilai-Borwein method

As it was mentioned, the classic KK approach has some failings, so in the presented work it is suggested to replace the Newton-Raphson (NR) method using the Barzilai-Borwein method (BB). From our point of view, the method can be also used to solve the minimization problem of energy W_{tot} , or equivalently, it can be used to solve the system of non-linear equations from the necessary optimality conditions (2). The method generates the sequence of approximations using Newton-like formula

$$x^{k+1} = x^k - \alpha_k \nabla f(x^k), \quad (6)$$

where the step-size $\alpha_k > 0$ approximates the inverse of Hessian matrix using the least-square solution of the secant equation

$$\frac{1}{\alpha_k} = \arg \min_{\alpha \in \mathbb{R}} \|(x^k - x^{k-1})\alpha - (\nabla f(x^k) - \nabla f(x^{k-1}))\|. \quad (7)$$

The BB method for convex quadratic cost function was studied extensively by many authors, see for instance Raydan [6], Dai and Liao [7], or Fletcher [8]. The BB method has been already successfully used for solving optimization problems in graph draws applications, see [9].

2 Numerical experiments

To test the KK with BB method, some standardized graphs¹ were chosen. The results in [10] were published. The same set of graph was used in [11]. In [10] consists of 30 graphs, which summarize standardized graphs with different sizes from 34 to 4824 nodes for planar graphs. All graphs were solved by classic KK with NR and KK with BB algorithm. For both of them Floyd's algorithm [12] was used. Floyd's algorithm is the method for searching the matrix of the shortest paths from one node to another. All results were computed at MATLAB environment (2012a) using i5 Intel Core processor with 16GB of memory with Linux system.

¹ <http://ls11-www.cs.tu-dortmund.de/staff/klein/gdmult10>

2.1 Results

We compared the solution time and number of performed iterations of the classic KK with used NR method and KK with BB algorithm instead of NR method.

Here we present the results for consequently drawing of the *sierpinski.04* graph for given precision, but also describes the 'evolution' process of the graph drawing by KK with BB algorithm.

Also the number of iterations for KK with BB is smaller for all graphs from data-set against KK with NR, compare with [10]. Moreover, KK with NR algorithm has outer and inner iterations. Outer iterations search the node with the highest Δ_m (4) and inner iterations minimize the energy of the whole system, i.e. it moves with this node in the sense of the minimization of W_{tot} . On the other hand, BB algorithm works with all variables of the system at once. The difference in the minimization process of W_{tot} can be seen in [9], where BB algorithm found the required value of W_{tot} in 45 steps, against that KK with NR algorithm just slightly minimized W_{tot} in 45 iterations. We have not observed any difference between graphs drawn with stopping criteria for BB algorithm $\|\nabla W_{tot}(x, y)\| < 1e - 1$ or $\|\nabla W_{tot}(x, y)\| < 1e - 4$, compare subfigures in Figure 3.

It can be seen, that Figure 3 (left) is similar to subfigure in Figure 3 (right). It was given unlimited number of iteration to the KK with NR algorithm and stopping criteria $\Delta_m < 1e - 4$; and the result was the same as drawn KK with BB algorithm in right subfigure of Figure 3.

The results from KK with BB and KK with NR algorithms were compared for thirty different graphs of different nodes (vertices) and edges, here only *sierpinski.04* is depicted .

Both algorithms minimize W_{tot} , hence we are still able to compare the value of W_{tot} in the end of the process. The smaller value of W_{tot} even without the reach of

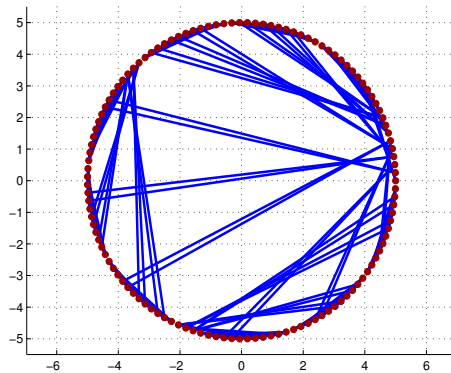


Fig. 1: Initial distribution of *sierpinski.04* graph for both KK with NR and KK with BB algorithm.

the stopping condition denotes the better performance during the minimization process. The truth is that for bigger graphs the differences in W_{tot} between both algorithm are more and more significant, even for graphs with smaller ration between vertices and edges, the difference was higher. Moreover, Figures 3 show that with less strict accuracy the number of the iterations can be smaller with sufficiently good results.

3 Conclusions and future work

In this paper the Barzilai-Borwein modification of Kamada-Kawai algorithm was presented. This modification minimizes graph as unity. Instead of 'classical' Kamada-Kawai algorithm with Newton-Raphson method, which works with Hessian matrices and minimize the one node with highest potential energy against

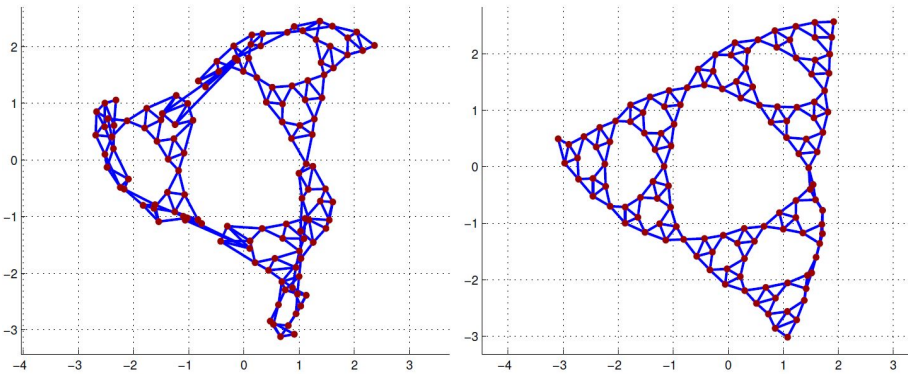


Fig. 2: The visualization of *sierpinski_04* graph by KK with BB algorithm with $\|\nabla W_{tot}(x, y)\| < 1e1$ (left one) and with $\|\nabla W_{tot}(x, y)\| < 1e0$ (right one).

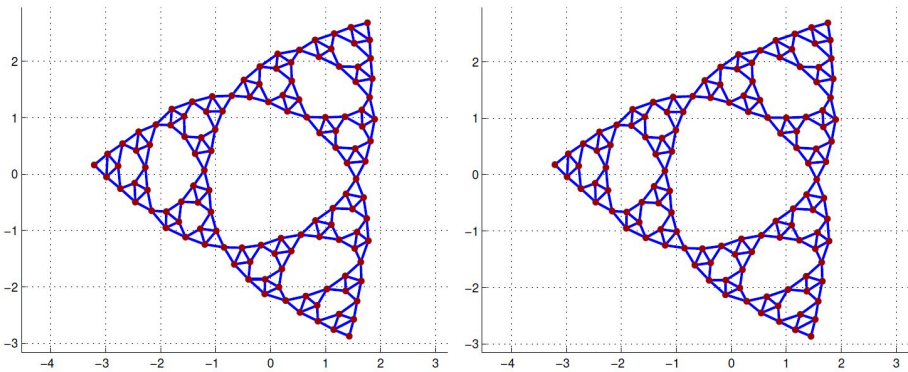


Fig. 3: The visualization of *sierpinski_04* graph by KK with BB algorithm with $\|\nabla W_{tot}(x, y)\| < 1e - 1$ (left one) and with $\|\nabla W_{tot}(x, y)\| < 1e - 4$ (right one).

whole system. The computation requirements of Kamada-Kawai with Barzilai-Borwein are significantly smaller against classic Kamada-Kawai algorithm. It is caused by working only with gradient vector in Barzilai-Borwein method. It takes the less computational time than computation with matrices in classic Kamada-Kawai method. The second advantage is no need to compute the second derivatives of W_{tot} .

The results of presented and connected work are published in two papers. The final results with focus on the practical application of the spring algorithms are going to be published soon in journal with impact factor.

References

1. G. D. Battista, P. Eades, R. Tamassia, and I. G. Tollis, "Algorithms for drawing graphs: an annotated bibliography," *Computational Geometry*, vol. 4, no. 5, pp. 235 – 282, 1994.
2. Y. Koren, "Drawing graphs by eigenvectors: theory and practice," *Computers & Mathematics with Applications*, vol. 49, no. 1112, pp. 1867 – 1888, 2005.
3. T. Kamada and S. Kawai, "An algorithm for drawing general undirected graphs," *Information processing letters*, vol. 31, no. 1, pp. 7–15, 1989.
4. J. R. Taylor, *Classical mechanics*. University Science Books, 2005.
5. S. G. Kobourov, "Spring embedders and force directed graph drawing algorithms," *arXiv preprint arXiv:1201.3011*, 2012.
6. M. M. Raydan, "Convergence properties of the Barzilai and Borwein gradient method," Ph.D. dissertation, Rice University, 1991. [Online]. Available: http://www.caam.rice.edu/tech_reports/1991/TR91-17.pdf
7. Y. Dai and L. Liao, "R-linear convergence of the barzilai and borwein gradient method," *The Institute of Mathematics and its Applications*, 2002.
8. R. Fletcher, "On the barzilai-borwein method," in *Optimization and Control with Applications*, ser. Applied Optimization, L. Qi, K. Teo, and X. Yang, Eds. Springer US, 2005, vol. 96, pp. 235–256.
9. M. Hasal, L. Pospisil, and J. Nowakova, "Barzilai-Borwein Method in Graph Drawing Algorithm Based on Kamada-Kawai Algorithm," in *ICNAAM 2015 proceedings*, Sep 2015.
10. L. Pospisil, M. Hasal, and J. Nowakova, "Computation of Kamada-Kawai algorithm using Barzilai-Borwein method," in *INCOS 2015 proceedings*, Sep 2015.
11. H. Hosobe, "Numerical optimization-based graph drawing revisited," in *Pacific Visualization Symposium (PacificVis), 2012 IEEE*, Feb 2012, pp. 81–88.
12. C. E. Leiserson, R. L. Rivest, C. Stein, and T. H. Cormen, *Introduction to algorithms*. MIT press, 2001.

Automated Image Detection of the Main Bloodstream Stem from CT Angiography Image

Tomas Ondraczka

Department of Cybernetics and Biomedical Engineering, FEECS,
VŠB – Technical University of Ostrava, 17. listopadu 15,
708 33 Ostrava – Poruba, Czech Republic
tomas.ondraczka@vsb.cz

Abstract. Purpose of this paper is to design automatized system for detection of main bloodstream stem and use its output for another processing.

System is design to get image ready for segmentation after using two images, obtained by examination with medical device called computer tomography, using method digital subtraction tomography. The methods for normalization and filtration are used as pre-processing.

The blood vessels are object of interest in images, and this is why the designed system separate them form the background. Segmentation methods are used for display main bloodstream stem from blood vessels. This output can be used for another applications of larger project. Next applications will be finding blood vessels connect on main bloodstream stem and separated them, using outputs for verification of therapy success or output can be used, after connection with database, for comparison of therapy success in time.

Keywords: image processing, segmentation, pre-processing, filtration, angiography, blood vessel.

1 Introduction

Realization of systems for enhance possibilities of software used in medical instruments is very important. It provides upgrades, which will ease diagnostic for medical personal. In case of digital subtraction angiography is necessity to apply new methods for measurement of volume and flow parameters. Methods will provide more possibilities for diagnostic taper of blood vessels. In this times the methods used for this measurements are imperfect and not comply requirements of medical personal. This project will ease diagnostic of level of unblocking blood-stream after removal clots.

One of basic steps for achieve our goal is segmentation of blood vessels from input images.

Before segmentation methods can be used, the input images must go through pre-processing methods. First step is application of normalization and filtration methods.

Normalization will provide better decomposition of brightness in image. Filtration will remove noise from image.

After using methods of pre-processing, the next step is implementation of methods used for thresholding. The adaptive thresholding is used to get the object of interest from input image. The output of segmentation is then adjust by methods of mathematic morphology for separate main bloodstream stem.

The output of algorithm will be used for implementation of measurements methods. Methods will measure volume and flow parameters of bloodstream. The results of measurements, in user marked area of bloodstream, will be display in table. The results will be total volume and flow of bloodstream, volume and flow of main bloodstream stem, volume and flow of blood vessels without main bloodstream stem, volume and flow of blood vessels in marked area.

2 Methods of pre-processing used in system

Before application of segmentation methods the input images must be adjust with methods of pre-processing.

2.1 Normalization

First step is to normalize the input image for better decomposition of brightness. Method is based on extension of brightness values range of the pixels in image. For example from range from 30 to 100, normalization will make new range from 0 to 255. Equation (1) describe method of normalization, where $I_{new}(x, y)$ is output image same size as input image. $I(x, y)$ is input image. Max is maximum of pixel intensity in range of input image. Min is minimum of pixel intensity in range of input image. Results of inputs and outputs of the implemented method of normalization are shown in Fig. 1.

$$I_{new}(x, y) = \frac{(I(x, y) - Min) * 255}{Max - Min} \quad (1)$$

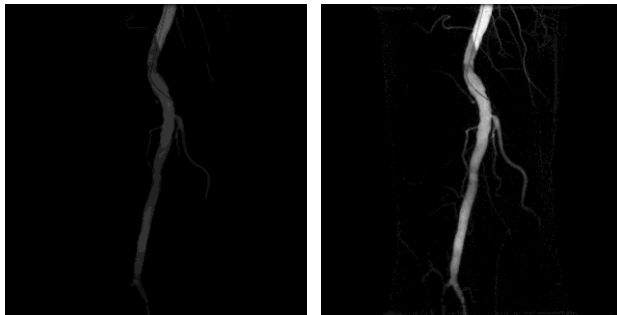


Fig. 1. Normalization: from left input image, output image same size as input images.

2.2 Filtration

Next step is to remove noise from the image. Noise can distort results of segmentation. Gaussian filter is used to remove noise from image. Convolution mask, which goes through input matrix, is size 3x3. Mask gradually goes through input matrix pixel by pixel and edits each pixel value with average value of its neighbors. Equation (2) describes method of Filtration, where $G(x, y)$ is output image same size as input image. σ is standard deviation. x is size of image in horizontal axis. y is size of image in vertical axis.

Results of inputs and outputs of the implemented method of filtration are shown in Fig. 2.

$$G(x, y) = \frac{1}{2\pi\sigma^2} e^{-\frac{x^2+y^2}{2\sigma^2}} \quad (2)$$

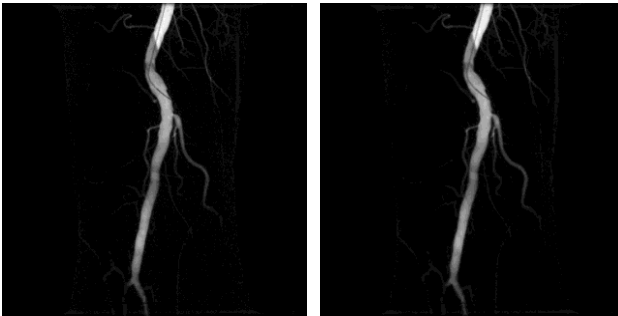


Fig. 2. Filtration: from left input image, output image same size as input images.

3 Design of procedure for segmentation of bloodstream

First method of segmentation used in system is thresholding. Method is based on browsing input matrix pixel by pixel and comparing each pixel value with threshold value. Equation (3) describes method of thresholding, where $I(i, j)$ is output binary image. $p(i, j)$ is pixel value of output binary image. $p(x, y)$ is pixel value of input binary image. [4, 5, 8, 9]

$$I(i, j) = \begin{cases} p(i, j) = 1, & p(x, y) > \text{prah} \\ 0, & \text{jinak} \end{cases} \quad (3)$$

To get threshold value system is using adaptive thresholding method. Threshold value is automatically set from image histogram.

Adaptive threshold method is based on setting a different threshold value for different input images. In some cases same threshold value can not be used for all input images. The adaptive threshold method based on variable threshold is used in this paper. Data in the image are divided to areas with the segmentation window. Window

go through input matrix and setting threshold value for each area. Input image is segmented with more than one threshold. This method can find the blood vessels which are not differ from background. Results of inputs and outputs of the implemented method of adaptive thresholding are shown in Fig. 3.

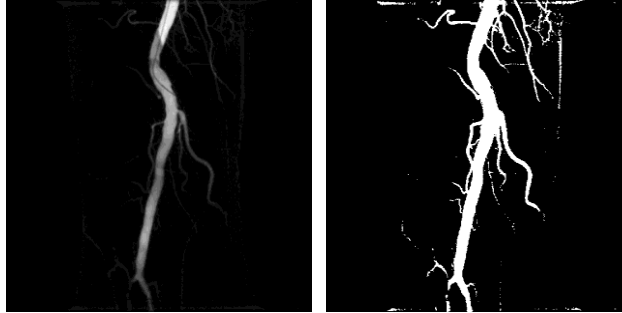


Fig. 3. Adaptive thresholding: from left input image, output image same size as input images.

3.1 Comparison with another threshold methods

Basic threshold method is based on experimental choosing of threshold. Threshold value is set by the user based on knowledge of the fix value. It is called trial and error method.

Threshold method based on experimental choosing of threshold is not ideal for this project, because some of blood vessels has similar brightness level as background so this method cannot be used.

Another method of adaptive thresholding is setting threshold value based on bimodal histogram. Bimodal histogram is histogram, which has to peaks. Value of the threshold is set as minimal value between both peaks. Method is heuristic so it presuppose, that the data has bimodal histogram. It means that the values of pixels for background and for objects are represented with sufficiently great frequency and have very different brightness level.

Adaptive threshold method based on bimodal histogram is not ideal for this project, because pixels have different brightness levels and some pixels of object of interest have similar brightness level as background pixels. So the histogram cannot be bimodal. [1, 2, 3, 6, 7]

4 Methods of mathematical morphology used in system

For finding main bloodstream stem in segmented image it is appropriate to use methods of mathematical morphology. This methods works with binary data. So both input and output image is binary image.

4.1 Opening

Opening is morphological method, which is defined as erosion followed by dilatation with same structural element for both methods. It means the shape of mask is same. Equation (4) describe method of Opening, where B is input binary matrix, M is created dilatation mask.

Results of inputs and outputs of the implemented method of opening are shown in Fig. 4.

$$B \circ M = (B \otimes M) \oplus M \quad (4)$$



Fig. 4. Opening: from left input image, output image same size as input images.

Opening is used in this project, because it will delete smaller objects than the largest object. The largest object is found with indexation and counting of pixels of each object.

5 CONCLUSION

This paper has two main parts on which is focused with basic explanation of whole developed application.

First part of the paper is describe implementaton of normalization method and filtration method. Normalization must be done because it will better decompose brightness in the image. Normalization is followed by filtration. Filtration will remove noise from image which was not remove by subtraction.

In third part of the paper segmentation of bloodstream is done. Adaptive trashold segmentation will do final seperation of object of interes from background of the image. Then methods of mathematical morphology are used for acquiring image just with main bloodstream stem.

Methods of segmentation does not work with 100 % accuracy. Some blood vessels are not shown on image, because their pixels intensity level is similar to pixels intensity level of background. For this application is not necessary to segment very small blood vessels on the end of bloodstream, because main bloodstream stem is visible.

Final output of the system will be used in another part of project. Output will be used as input for measurements algorithms. Volume and blood flow parameters of the bloodstream and main bloodstream stem will be measured.

6 REFERENCE

1. Kubicek, J., Penhaker, M., Bryjova, I., Augustynek, M. Classification method for macular lesions using fuzzy thresholding method (2016) IFMBE Proceedings, 57, pp. 239-244.
2. Kubicek, J., Bryjova, I., Penhaker, M., Kodaj, M., Augustynek, M. Surface of articular cartilage extraction using fuzzy C-means segmentation (2016) Studies in Computational Intelligence, 642, pp. 209-219.
3. Kubicek, J., Bryjova, I., Penhaker, M. Macular lesions extraction using active appearance method (2016) Lecture Notes of the Institute for Computer Sciences, Social-Informatics and Telecommunications Engineering, LNICST, 165, pp. 438-447.
4. Kubicek, J., Valosek, J., Penhaker, M., Bryjova, I. Extraction of chondromalacia knee cartilage using multi slice thresholding method (2016) Lecture Notes of the Institute for Computer Sciences, Social-Informatics and Telecommunications Engineering, LNICST, 165, pp. 395-403.
5. Hercik, R, Slaby, R, Machacek, Z. Image Processing for Low-power Microcontroller Application. (2012) PRZEGLAD ELEKTROTECHNICZNY. Vol 88, 12A pp. 343-346. ISSN 0033-2097.
6. Slaby, R, Hercik, R, Machacek, Z. Compression methods for image processing implementation into the low capacity devices (2013). TEHNICKI VJESNIK-TECHNICAL GAZETTE. Vol. 20, 6, pp 1087-1090. ISSN: 1330-3651
7. Novotny, J. , Dvorak, J. , Krejcar, O. User based intelligent adaptation of five in a row game for android based on the data from the front camera intelligent adaptation of five in a row game for android based on the data from the front camera. Lecture Notes in Computer Science. Vol. 768, 2016, pp 133-149. ISSN: 03029743
8. Machacek, Z.; Slaby, R.; Hercik, R., Koziorek, J. Advanced System for Consumption Meters with Recognition of Video Camera Signal. ELEKTRONIKA IR ELEKTROTECHNIKA. Vol.18,10, pp 57-60. (2012). ISSN: 1392-1215
9. Idzkowski, A., Walendziuk, W., Zygmunt L. Unconventional Double-Current Circuit for Deflection and Temperature Simultaneous Measurement. ELEKTRONIKA IR ELEKTROTECHNIKA Vol.21, 4, pp. 23-26 (2015). ISSN: 1392-1215

Measuring and Analysing of Muscle Activity during Shooting with Air Rifle in Standing Position with Surface Electromyography

Lucie Švecová

Department of Cybernetics and Biomedical Engineering, FEECS,
VŠB – Technical University of Ostrava, 17. listopadu 15,
708 33 Ostrava – Poruba, Czech Republic
lucie.svecova@vsb.cz

Abstract. This article describes measurement of muscle tension during shooting with air rifle in standing position. The SOMNOScreen device with 2 channel surface electromyography was used. The goal of the work was analyzed muscle activity of right upper limb and select muscle groups for next step of work. The main goal is to create a map of muscle activity during shooting for improving training and detection of shooters errors. In this part of work, the muscles of shoulder and scapula, muscles of arm and forearm and spinohumeral and thoracohumeral muscles were researched. Muscle tension of each measurement is explained in relation to shooting.

Keywords: EMG, shooting, muscle tension

1 Introduction

Using of EMG in the training of sport shooting can help detect errors that are currently unable to detect by any commercially available shooting training systems. Electronic training systems usually work on the principle of optical sensors mounted on the barrel of the weapon and the target, which record the trajectory of weapon during a certain time period before and after the shot and the shot. But it is unable to record the shooters "movements" during the crucial phase of aiming and triggering. It is not such a move that would have been possible to record with conventional methods of movement recording, it's the correct muscle tension, which ensures the stability of the shooter and thus the accuracy of fire. Lack of muscle tension causes a large scatter. Too much strong muscle tension causes errors, which occur as a bad shot away from the center of the target. While the lack of muscle tension is in case of untrained shooter aecnd problem will disappear by the time, too much tension in the muscles indicates an error, which should be removed. To use EMG during practice target shooting, it is necessary to analyze which muscles are actively involved in the process of aiming and could be a potential source of errors. This will create a map of muscles, which is important for shooting. It is also necessary to decide which muscle groups

can be measured by surface EMG. Some important muscles for shooting do delicate work - too little change in muscle tone, that it's hard to notice it with this method.

2 Preparing for measurement

In this article measured data of muscles activity of right upper limb during shooting with air rifle in standing position is evaluated. The SOMNOScreen device with two-channel surface EMG was used. The shot was recorded by microphone located on the weapon, which is also part of the SOMNOScreen device (Fig 2). Sampling frequency for measuring EMG was set to 256Hz. Since the surface EMG is not able to record the potential differences in all muscle layers, the deeper layers were not included into the measurement. The measured curves correspond to the summation of electrical potentials of the muscle fibers in the range of the electrode.



Fig. 1. Left: Measurement without complete shooting equipment. Right: Standing position with complete shooting equipment

Measurements were performed on shooter of international level, which is expected to perform correct muscle tension during aiming and triggering. In this measurements weren't used the entire shooting equipment (shooting suit), so it may be some muscle tension muscle groups larger than standard during shooting (Fig. 1). The aim of this measurement was mainly determine, which muscle groups of right arm involved shooting. Measurement of selected muscle groups will be repeated in the next phase of work at the standard shooting training. Measurements were performed on certain muscles of shoupder and scapula, muscles of the arm and forearm and spinohumeral and thoracohumeral muscles, that are evolutionally and functionally also belongs to the upper limb, although usually are described by the muscles of the back and chest muscles.



Fig. 2. Left: SOMNOScreen device and air rifle prepared for measurement. Right: shooter's arm with marks for attaching electrodes

3 Analyze of measurement

As the first was measured deltoid muscle (Fig 3), all of its three parts, clavicular, acromial and spinal. Functions of the deltoid muscle are raising arm forward, sideways and backward, the whole muscle in resting tension keeps the head of the shoulder joint in the hole. From the viewpoint of shooting, clavicular part of the deltoid muscle is interesting, because this muscle is near the point where the butt of the rifle is placed into the shoulder. At figure 3, there is obvious, that the muscles is at a slight tension while aiming. Before raising a rifle into the shoulder, the acromial part of the muscle is completely relaxed, the clavicular portion is only in slight tension. Spinal part of the deltoid muscle is not participates on the shot.

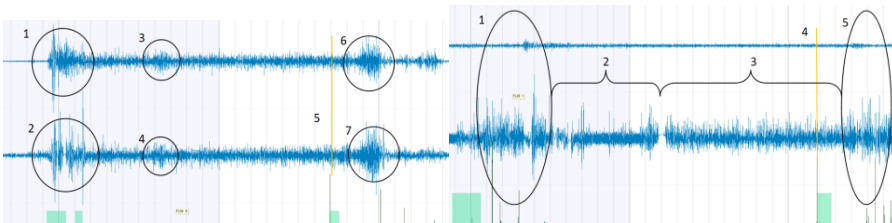


Fig. 3. Left: electromyogram of deltoid during shooting, upper curve – acromial part, bottom curve – clavicular part; 1, 2 – placing rifle into the shoulder, 3, 4 – slightly increased tension in muscles, calming position before aiming, 5 – moment of shot, 6, 7 – putting rifle aside after shot; Right: electromyogram of deltoid and trapezoid during shooting, upper curve: spinal part of deltoid, bottom curve – trapezoid, cranial part; 1 – placing rifle into the shoulder, 2 – calming position, 3 – aiming, 4 – moment of shot, 5 – putting rifle aside after shot

At the next step, the tension in trapezius was investigated. Function of trapezius is, except stabilization of the scapula, raising of shoulder (cranial part), which is inappropriate phenomenon while shooting. It also provides a raising arm above the horizontal. This muscle is often overloaded, and its impact on shooting will also be more closely examined. When measuring cranial part of trapezius muscle (Fig 3), there was repeated pattern. During phase of calming the position was recorded more intense muscular activity, which may be associated with activity of muscle splenius capitis. This muscle is covered with trapezius and its function is to move head. Other parts of the trapezius muscle, caudal and lateral parts, don't involve shooting

significantly. Their activity is increased only while putting rifle into the shoulder. There is no noticeable difference in tension between the aiming and the resting time. Activity is seen only at the end of the calming position phase during attaching the head to the cheek piece (Fig 4).

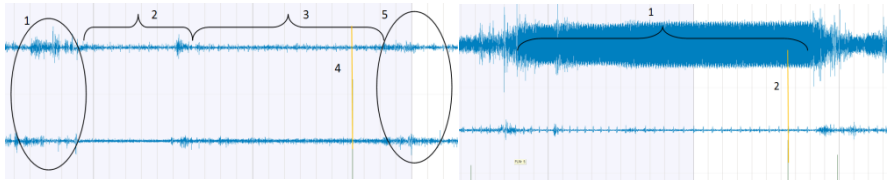


Fig. 4. Left: electromyogram of trapezius during shooting, upper curve – caudal part, bottom curve – lateral part; 1 – placing rifle into the shoulder, 2 calming the position, 3 - aiming, 4 – moment of shot, 5 – putting rifle aside after shot. Right: upper curve: electromyogram of m. latissimus dorsi during shooting: bottom curve – pectoralis major – clavicular part; 1 – calming position and aiming, 2 – moment of shot,

Another measured muscle was m. Pectoralis major. Clavicular part helps the arms raise forward, sternocostal and abdominal adduct arm and rotate from the external. Also m. Latissimus dorsi affects the movement of the upper limb. Its function is adduction and internal rotation of the humerus, and extension of the humerus in a shoulder joint. In place of attaching electrode overlies the muscle m. Teres major, which also adducts and rotates humerus. At this point the most intense muscular activity was measured (Fig 4), which is determined by the size of the muscle - the amount of muscle fibers. Increasing tension in the muscle during an easing position and aiming opposite to manipulating with rifle is caused by rotated arm, what is typical for the standing position rotation upwards. All parts were relaxed in the shooting. A curiosity appears, the cardiac activity was recorded on the electromyogram of m. pectoralis major.

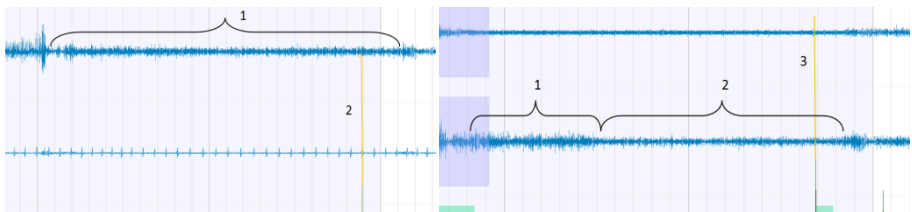


Fig. 5. Left: upper curve – electromyogram of m. biceps brachii, bottom curve: electromyogram of m. pectoralis major, sternocostal and abdominal part; 1 – Calming the position, 2 – moment of shot. Right: upper curve – m. triceps brachii, bottom curve: m. flexor carpi radialis; 1 – calming the position, 2 – aiming, 3 – moment of shot

In the case of m. Biceps brachii a slight muscle tension has been recorded. It is caused by flexion of the elbow while shooting. Muscle activity changes again only when handling weapons. During faultless performance of a shot tension in muscle tension is constant. Increased muscle tension may appear with shooter's error during aiming as shown on Fig 5.

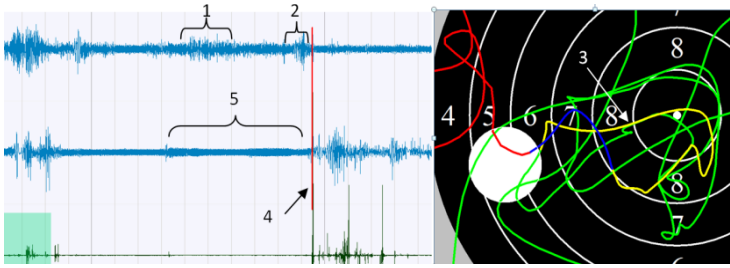


Fig. 6. Electromyogram of left (upper curve) and right (bottom curve) biceps brachii and SCATT record of shot. 1, 2 – increased tension in left biceps brachii in effort to get rifle back to the center of target and stabilize the position, 3 – yellow line record 1s before firing, 4 – moment of shot, 5 slightly increased tension in right biceps brachii in effort to stabilize the position.

Triceps, as extensor of the elbow is relaxed during shooting, as it was supposed. The only change in tension appeared during the handling of weapons (Fig 4).

M. flexor carpi radialis and m. flexor carpi ulnaris flex the hand in wrist. Increased tension in the muscle M. flexor carpi radialis is evident during the handling of weapons and in calming the position phase. During aiming period, there is slight tension based on the position of the hand. Even a small difference in tension was observed in case m. Carpi ulnaris.

The only motion in an otherwise static rifle shooting is the motion of the finger on the trigger. With the proper work, this movement should not be seen with the naked eye. Therefore, it was very interesting to see whether it will be seen on the electromyogram. M. digitorum superficialis and m. Flexor digitorum profundus muscles are located in the second, respectively in the third layer of forearm muscles, and thus they are covered by m. flexor carpi radialis, m. palmaris longus and m. flexor pollicis longus. As a summation of all potentials on the record shows a certain tension in the muscles of the forearm. Unfortunately, the motion of the finger on the trigger is not visible on the record. First, triggering was done properly - slow, smooth motion. But the main reason, why the motion is not visible is very small trigger weight, only about 100 grams, which is common setting of trigger in sport shooting with air rifle or small bore rifle. By repeated the same action with bigger trigger load, muscle tension increased markedly (Fig 7). (Notice: Trigger weight is a term from sport shooting rules, its value is determined in kilograms or grams. It is load, which trigger must hold at least. For example, sport pistol trigger has to hold 1,5 kilograms.)

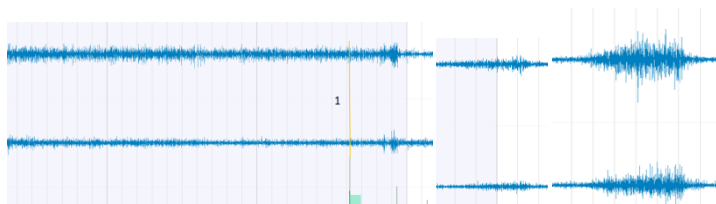


Fig. 7. electromyographs of flexor digitorum superficialis upper graph – muscle belly for fore-finger, lower graph – muscle belly for other fingers, 1 – moment of shot; Left: trigger weight – 100 g, Middle: trigger weight - 1500 g, Right: trigger weight – 5000 g

4 Conclusion

As it apparent from measurement, some muscles of right upper limb have no important influence on shooting. Namely, they are the spinal part of deltios muscle, caudal and lateral parts of trapezoid muscle, m. pectoralis major and m. triceps brachii. Muscles were bigger tension was recorded will be investigated again, especially m. latissimus dorsi. M. biceps brachii, flexors of wrist and fingers, will be investigated more carefully, because, they participate directly on holding grip and triggering.

All measurements described in the article was conducted with a very experienced shooter, with ideal shot performing. The results are a guide to next part of research, where will be decided, which muscle groups have impact on shooting in the standing position. To verify the conclusions, is required to repeat the same measurements on shooters with less experience who are still making mistakes. Only then it will be possible to create a map of points to measure muscle tension of right upper limb. In a similar manner they will be processed and the other muscles in the other shooting positions (prone, kneeling).

5 References

1. ČIHÁK, Radomír, GRIM, Miloš a Oldřich FEJFAR (eds.). *Anatomie*. 3., upr. a dopl. vyd. Praha: Grada, 2011. ISBN 978-80-247-3817-8.
2. KADAŇKA, Zdeněk, Josef BEDNÁŘÍK a Stanislav VOHÁŇKA. *Praktická elektromyografie*. Brno: Institut pro další vzdělávání pracovníků ve zdravotnictví, 1994. ISBN 80-7013-181-0.
3. KITTNAR, Otomar. *Lékařská fyziologie*. Praha: Grada Publishing, 2011. ISBN 978-80-247-3068-4.
4. Horneber, R.: *Wettkampfsport Gewehrschießen. Technik, Taktik, Training*, 139 stran. ASIN B001UKT85M

Environmental Analysis of Emergency Department and Development of Databases Based on IoT

Tomas Urbanczyk

Department of Electrical Power Engineering, FEECS,
VŠB – Technical University of Ostrava, 17. listopadu 15,
708 33 Ostrava – Poruba, Czech Republic
tomas.urbanczyk@vsb.cz

Abstract. This paper is about environmental analysis of hospital and design of database which is based on the concept of the Internet of Things. First part of analysis focus on environment of emergency department with possibility of using suitable low-cost identifiers. Identifiers enable new possibilities of evidence in medical documentation.

Next part of paper focus on analysis of monitoring patient on emergency department. Outputs of analysis are reserved characteristic groups that work with the patient and create a record of intensive care. In paper are describe hazards of paper medical documentation and is design electrical documentation with design and implementation of database.

Final part is about testing the database and was made a conclusions for improvement of medical documentation.

For the database MySQL database server with client MySQL Workbench 5. 2. 42. CE application was used

Keywords: Database, Internet of Thing, Analysis, Near Field Communication, emergency department,

1 Introduction

Nowadays, thanks to the concept of Internet Of Things (IoT) is possible to make the structuring of the world around us. It means to work with information and data more effective and unique form for better possibility of analysing and processing. This kind of process would be advantageous for streamlining the work of employers and if it will be focused on medical area also for comfort for the patient. It will be possible to monitor individual workplace in hospital and to have a view of marked patient, employer or item from whichever computer, tablet or smartphone. [1] There are existing technology which is possible to use for this kind of purpose. It is necessary to marked person or

item with low-cost identifier which is called Near Field Communication (NFC) and it is based on Radio Frequency Identification (RFID) technology. [2] This work was based on cooperation with the urgent department of the Faculty Hospital in Ostrava. This department is admitted almost for all of medical cases. There is a big effort to improve medical case but this is connected with storing of more quantity of data. [3] Most of the time, because of bureaucracy, there is necessary to find equilibrium between the writing of medical record and treatment of patients. It would be interesting to make easier the work with medical records for medical doctors or nurses and so increase their attention on patient. [4]

2 Problem definition

Paper documentation is not so convenient for making of statistical analysis or long time monitoring of actions in the hospital and also processing of it is time consuming. With the using of it technology is possible to work with electronic registration and electronic medical records thanks to RFID. Electronic record of medical care allows to quickly store and to structure data registered in the timeline. This creates the possibility of further work with the data and conduct studies to support emergency medicine. [5]

Patient's records is done for the purpose of record keeping and report for health insurance. Records of the patient is done by nurse who is working with database as administrator and she enters the information about patient into the database and keeps its data actual. This is made thanks to assign number code to the patient. Record of intensive care is an internal affair of the hospital. [6] Form A3 structured and arranged. To form symbols are written in the agreed timeline, eg. Medication, vital functions ie. Blood pressure, pulse but also the performances, lab specimens, blood bank, Consilium, height, weight, pain and many other parameters. This record shall be attached to the card the patient and travels with him to another department. This work is focused on developing of a hospital information system. It looks at the hospital medical records of the patient, such as a profile with timeline and marked tasks.

3 Implementation of new solution

For developing of such information hospital system is necessary to:

- analyse urgent department of hospital
- define suitable identifier for hospital environment
- define technology of scanning of identifiers
- analyse work sequence of urgent department

The condition of developing our system is the WiFi network and card identifier. The urgent department is covered by WiFi network and as a card identifier can be used commercial mobile phones containing NFC and an optical sensor.

3.1 Analysis of urgent department of hospital

This analyses was focused mainly on analyses of entities registered with paper medical records. It was necessary to clearly identify the elements that can be electronically recorded by the mobile reader. Elements that must be marked the tags and elements that do not indicate at all (eg. physiological patient value). The next phase of the analysis was to describe the process and the work of staff to the patient during the patient's stay in the urgent department.

3.2 Definition of suitable identifier for hospital environment

It was necessary to define appropriate identifiers for the hospital environment. For hospital environment is most suitable to use European Article Number (EAN), Quick Response (QR) or RFID technology because of their advantages and also because this kind of technologies is already used. At the department are already used bar codes and QR codes. It is used for marking of drugs, devices, blood bags, etc. It is highly recommended to replace these identifiers by the RFID technology specifically Near Field Communication (NFC) passive tags. Passive NFC tags operate at a frequency of 15.56 MHz and can emit an identification code, without having to have a user tag in visual contact (no camera shooting). This code reading becomes less onerous for hospital staff. Into NFC tag (fig.1) is recorded an unique ID and tag is locked. In the database are write detail information about concrete entity thanks its ID. When it is read by the reader it is displayed a list o the entities from the database.

3.3 Definition of technology scanning of identifiers

Mobile ID Reader was selected commercially available mobile phone Samsung S4 1.9 MHz processor, RAM memory and 2048 MB and 16 GB internal memory. This mobile phone has an NFC antenna with a communication protocol ISO / IEC 4443 Type A. [1] It is possible to write and read from the tag. It was necessary to develop a mobile application for Android 4.4 which was developed in Android 1.1.0 studio with the Java programming language. To register optic identifier was used ZXing library which allows to read 1D and 2D codes. The appropriate form of communication via NFC mobile phone was used NFC Data Exchange Format (NDEF) reports. This format defines the communication between two active, one active and one passive NFC tag. It can wrap many records into one report.

4 Analysis of the urgent department environment

It was necessary to make an analysis of work sequences of urgent department. It is possible to see the four actors who have their own distinctive work.

- The patient

- The nurse who is working with the database as administrator. Its task is to record the patient's medical records and write a record of intensive care.
- The medical team is an organized group of people working directly with the patient. It includes doctors, nurses and assistants from other departments.
- The time which is the most important parameter. The patient in the urgent department may, according to law, spend 45 min. After that it has to be transport to the outrageous workplace.

After the takeover of the ambulance service, the patient is laid on the medical bed and checked. A major role in these processes plays a patient's consciousness. Consciousness is the basic element of the differential with the work with the patient. If the patient communicates and cooperates, the treatment is easier. After changing clothes and cleaning the patient, it is transported to specific department. The child is transported in a special box for paediatric patients.

5 Implementation of database

It was made an analysis of appropriate database systems. Compared with database systems such as MySQL, PostgreSQL, Microsoft SQL Server and Firebird. Because of work with internal Linux server was used MySQL with upgrade MySQL Workbench CE 5.2.42. [7] For design of database was started from the waterfall model.

In the process of requirements specification and concept developing it was necessary to define the baseline system and create a primary proposal and entity types in cooperation with the client. According to the model of work diagram was formed entity types. It was set attributes associated with particular characteristic, for example medical devices, procedures, tests, medications, patients, etc. For developing database was necessary to make the data dictionary. It says what types of data are added to the database and how many characters it takes. It had to be determine the reciprocal relationships between each tables in developed database. It can be below thanks to ER diagram

It is necessary to create data flow diagram to clarify the basic processes and data flow. In complex database models are formed in the sublayers. The base layer is defined by an external groups who work with databases. At the urgent department was identified four basic groups which affected the database.

- **The patient** is the main element that provides personal information.
- **The nurse** edits and creates electronic records, is able to search data from the database.
- **The mobile device** sends the scanned ID of a specific identifier to the database. It is added to the patient profile and creates.
- **The medical team** complements the information system of the entities that cannot be marked by identifying element.

Evidence of the patient is always performed when patient comes to the department. The nurse has a database of patients. If the patient has ever been in the hospital for an examination it is possible to download their personal information. This makes registration

faster. Procedures and examinations are performed by medical staff. Any action on the patient must be recorded and stored in an electronic record.

To the database can be data stored by a mobile device through identification elements or just thanks to addition by medical staff.

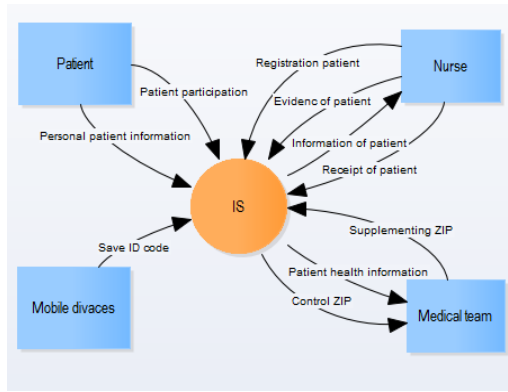


Fig. 1. It can be seen the top layer of data flow diagram. It describes the basic groups that work with the information system. It shows a single characteristic data flow for the group.

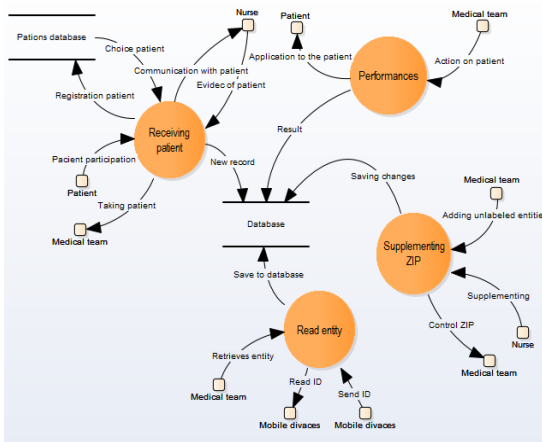


Fig. 2. It can be seen the second layer of data flow diagram. It describes the data flow and processes for the modification of the database.

6 Testing of database

It was made two SQL questions which were 99 times repeated:

- SELECT * FROM Patient

- `SELECT * FROM Patient WHERE kod_pojistovny = 205 AND datum_narozeni < '1993-04-11'`

The results from the testing showed that the database works very fast with average time of looking up to 0.3 s even at high volumes. This is due to the good indexing and database design. For specific inquiries the time of looking is slightly lower.

It was also made a testing speed of reading of identification elements. It was detected time of loading of identifier to 0.5 s.

7 Conclusion

Electronic record of intensive care has a big potential to create new and effective medical documentation. It allows further analysis and processing of the results thanks to the concept of the Internet of things when data are structured. Commonly used paper form of registration can be affected by some risks, damage it by the fluid, illegible handwriting or human error. These risks can bring problems with processing of stored data. All these risks are reduced or eliminated thanks to electronic record.

At the urgent department was created electronic documentation that fully replaces paper documentation. Data into this documentation are inserted by a mobile device, some kind of smartphone or tablet, which allows to read a few types of identifier.

It was necessary to make analysis of environment of urgent department and thanks this analysis performed marking of each entity which is stored in the database.

The developed database was tested in real conditions during standard daily hospital period. Results are promising. The database is able to store a lot of important data and it is intuitive controllable. It can be extended to monitor contraindication drugs, supplies of medication or control inspection period of medical devices

8 References

1. Vogell, L. (2013). Android sqlite database and contentprovider.
2. Sommerov' a, M. (2011). Základy rfid technologií. Mezinárodní
3. Tomala, K., Plucar, J., Dubec, P., Rapant, L., and Voznak, M. (2013). The data extraction using distributed crawler inside multi-agent system. *Advances in Electrical and Electronic Engineering*, 11(6), 455.
4. Bubenikova, E., Holecko, P., and Pirnik, R. (2013). Optimisation of video-data transmission in telematic system. *Advances in Electrical and Electronic Engineering*, 11(2), 123.
5. Sujansky, W. (2001). Heterogeneous database integration in biomedicine. *Journal of biomedical informatics*, 34(4), 285–298.
6. Silberschatz, A., Korth, H.F., Sudarshan, S., et al. (1997). *Database system concepts*, volume 4. McGraw-Hill New York.
7. Welling, L. and Thomson, L. (2003). *PHP and MySQL Web development*. Sams Publishing.

Standalone Data Acquisition Device with NFC Interface

Marketa Venclikova

Department of Cybernetics and Biomedical Engineering, FEECS,
VŠB – Technical University of Ostrava, 17. listopadu 15,
708 33 Ostrava – Poruba, Czech Republic
marketa.michalikova@vsb.cz

Abstract. This article describes a possibility of NFC interface deployment in embedded monitoring system together with a proposal of communication protocol concept utilizing a non-volatile EEPROM and benefiting from a low energy efficient transmission on the side of the embedded device. The measurement system is based on Kinetis FRDM-KL25Z Freedom development platform. The testing has proved that the NFC communication interface is not eligible only for configuration data recording and the wireless diagnostics. The merge between the NFC interface and EEPROM technology is suitable also for a limited measured data transfer.

Keywords: NFC, standalone data acquisition, embedded system, energy efficiency

1 Introduction

Within the range of embedded systems utilized to gather various type of data either from natural sources [1] or as a product of technological process [2] there often arises conflicts of goals. Such conflicts are tied up mainly with requirements onto system functionality which are in a direct conflict with a deliverable power supply options [3]. While the system functionality requirements are extensive in terms of various sensor measurement options, data storage and data transfer, the power supply sources for those systems are habitually limited by battery dimensions or the variability of the alternative source of energy [4]. Control of the above mentioned systems is mainly based on fuzzy control algorithm [5], prediction of obtainable energy gained from alternative sources [6] and utilization of the optimization algorithms designated for various specifics of operation [7].

A broad range of wireless communication interfaces opens up today to be utilized by such a systems benefiting from a low energy efficient transmission on the side of embedded monitoring systems whilst the main energy load is on the side of the data acquisition device [8]. Near Field Connection (NFC) appears to be a suitable communication interface for embedded monitoring devices not having any energy budget available.

2 NFC - Near Field Communication

The NFC is a standard described by the ISO/IEC 14443, ISO/IEC 18092 and other standards published by NFC Forum. The NFC Forum is an association founded by NXP Semiconductors, Sony and Nokia to unify companies participating the NFC technology development, today covering up to 200 of companies. The NFC expands the Radio Frequency Identification (RFID) system, whereas the NFC focus bandwidth is rather narrow. It utilizes loop antennas operating on frequency of 13.56 MHz for communication intentionally limited by the reach up to 10 cm in maximum, while the real reach is halved of the maximum declared reach or less.

The NFC Forum defines a data exchange format among the NFC entities called NDEF (NFC Data Exchange Format). A fundamental unit is called NDEF record comprising information about data type, data length and the transferred data itself. The data can be some of the NFC Forum defined types, URI, MIME or even unknown. Records of the same type are being merged into NDEF message. The entire problematics of the NDEF mechanism is complex, targeting to optimize the communication. The NFC is systematically divided into several groups according to purpose of the NFC utilization corresponding to NFC modes of operation:

- Reader/Writer mode means that the reader can access tag data. The communication is regulated according to ISO/IEC 14443 standard, or FeliCa. The reader provides the source of energy to the tag which determines this mode to be the least energy efficient.
- Peer-to-peer mode means that two readers communicate mutually and exchange data between each other. The communication is regulated by NFCIP-1 standard, which introduces basic mechanisms in the link layer. A LLCP protocol extends the NFCIP-1 standard on advanced mechanisms in the way of the link layer behavior.
- Card emulation mode is an NFC speciality since the reader acts as a tag and the communication is going in the same way as in reader/writer mode.

3 Standalone data acquisition device concept

The device (block diagram on figure 1) is composed of essential blocks comprising a microcontroller forming the basis of the system, digital and analog interfaces to connect sensors, NFC interface and a smartphone. The device is supplied from the inner power supply source.

3.1 Microcontroller - MCU

The Freescale Kinetis L microcontroller (MCU) creates a core of the embedded measurement system. This Kinetis L MCU series, based on the ARM Cortex-M0+ 32-bit core is targeted to ultralow power applications benefiting from low

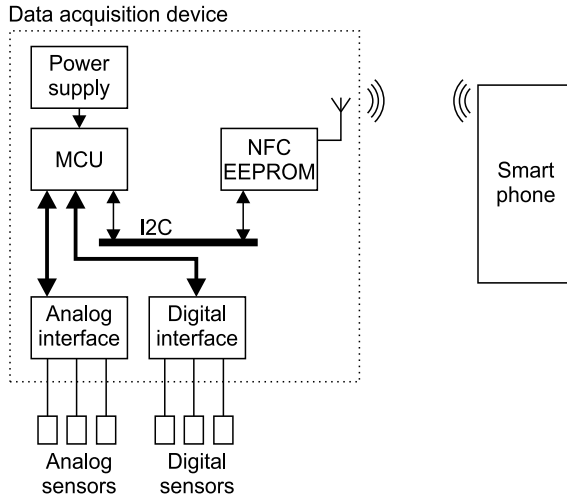


Fig. 1. Block diagram of embedded measurement concept with NFC interface

consumption and sufficient performance at the same time. This makes the Kinetis L MCU series ideal for such a system where an accumulator serves as a power supply source alongside with the demand onto computational power.

3.2 Power Supply

The device is supplied from an independent source, a coin cell CR2032 specifically. This source enables operation of the device independent on the additional sources, however there is no longer possible to keep wireless subblock of the device energy-efficient. The coin cell source is connected to the device without utilizing any DC/DC converters, which causes the efficiency to be approaching 100. For the future design there is a possibility to use another source of energy (e.g. Li-ion cell) or utilize a supercapacitor to supply the system. There is also an option to use renewable energy sources available from the environment gained with solar panels and other converters (mechanical, thermoelectric etc.).

3.3 NFC Interface

The ST Microelectronics integrated chip M24SR was used to implement a physical layer of the NFC standard. This chip consists of several components: an EEPROM of 8 kilobyte capacity constitutes a basis of the chip that interconnects other two communication components. The first one is I2C communication interface, where the chip acts as a slave, the second one is NFC interface connected to antenna. Within the NFC the chip is responsible for planning specification of ISO/IEC 14443 type A and NFC Forum type 4, and receives messages on 13.56 MHz frequency over a short distances. There is no need to plug in an additional power supply to perform NFC communication since the antenna

serves also as a source of energy during ongoing communication. In addition the chip features one input and one output pin. The input pin marked RF disable disables the antenna when reading log. one so it cannot be even recognized by the active devices. The output pin function (marked as GPO) is to notify the external MCU about the NFC activity. The chip provides several modes of operation including manual control or it is capable of automatic reflection of the smartphone to antenna etc. The purpose of the communication is to perform reading/writing to/from the memory. A certain arbitration is implemented in the chip preventing the coincident access to the memory. Both sides does not have an equal level of rights. Certain operations cannot be performed via NFC, for instance the GPO mode cannot be configured this way. On the other hand I2C is has the option to disable the NFC functionality and even to terminate ongoing NFC communication.

3.4 Analogue and digital sensors

The concept of the device enables to connect either analogue or digital sensors. A certain demands are placed onto sensors to be connected, particularly in terms of low power consumption not to load down the available source of energy significantly. A group of recommended sensors comprises all the active analogue sensors acting as a current source in their run mode, followed by energy efficient digital sensors usually connected via UART, SPI, I2C or 1-wire communication interfaces.

4 Application and testing

The application has been developed using JAVA language and put into the test utilizing two methods - a White and a Black box. The testing was performed with a help of Huawei P8 Lite smartphone having the Android Lollipop 5.0.1 operational system. During the Black box testing the application was being used in the common way, it means that measurements were repeatedly performed, interrupted, data were read and deleted, the configuration was changed, all together to simulate a common application user. The application was assessed as a flawless based on the results of the Black box testing. Afterwards the White box testing method was performed, where all the possible combinations of options were intentionally configured, incorrect data and non-ideal inputs were fed into the application. The entire system was also tested on the experimental measurement the charging characteristic of the capacitor. An RC circuit was connected to the device analogue inputs to perform a simulation of the charging and discharging. Also a period of measurement and a number of samples could be modified using the developed application on the smartphone. After a successful measurement sequence initiation, the device has started to measure. When the sequence has been finished, the data could be read using the smartphone and the awaited charging and discharging characteristics of the capacitor could be checked.

The algorithm 1 describes the way of data acquisition which is under the control of the MCU. The measurement is performed on demand (an interrupt clocked by the real time clock is generated). This approach enables scheduling of the individual measurement sequences and alongside the MCU can be in a powersafe mode during the period of time when no measurements are required. The data are stored in externally approachable EEPROM which makes the data writing operation being independent both on the level of the energy available in the power supply and the current MCU mode.

Algorithm 1 Measurement algorithm

```

1: if Measurement running then
2:   if RTC alarm then
3:     Validate date
4:     if Datum correct then
5:       Measure and write sample
6:       if Maximum reached then
7:         Terminate measurement
8:         return
9:       else
10:        Calc next alarm
11:        Set alarm
12:        return
13:      end if
14:    end if
15:  end if
16: end if
17: if Phone appears then
18:   Measure battery
19:   if Is phone away then
20:     Assesment
21:   end if
22: end if

```

5 Conclusion and future work

This article presents a solution enabling to connect an energy passive communication interface in form of NFC. This solution is suitable for applications having energy constraints from the power supply side and the power supply of the wireless communication interface itself is inconvenient or technically demanding. The testing has proved that the NFC communication interface is not eligible only for configuration data recording and the wireless diagnostics. The merge between the NFC interface and EEPROM technology is suitable also for a limited measured data transfer. The solution is then appropriate for measurement systems having a long measurement period. NFC also fulfills such a power supply concept

demands utilizing a coin cell battery. In the future work this concept will be put through the long term testing along with the analysis of the operation time of such monitoring devices and a possibility of the data reading automation will be inspected. An option of interconnection NFC monitoring systems with the devices utilizing automated localization (as described in Konecny et al. (2016)) will be the next subject of the study.

References

1. M. Prauzek, P. Musilek, A. Watts, and M. Michalikova, "Powering environmental monitoring systems in arctic regions: A simulation study," *Elektronika ir Elektrotechnika*, vol. 20, no. 7, pp. 34–37, 2014.
2. M. Pies, R. Hajovsky, M. Latocha, and S. Ozana, "Radio telemetry unit for online monitoring system at mining dumps," *Applied Mechanics and Materials*, vol. 548–549, pp. 736–743, 2014.
3. M. Prauzek, A. G. Watts, P. Musilek, L. Wyard-Scott, and J. Koziorek, "Simulation of adaptive duty cycling in solar powered environmental monitoring systems," in *Electrical and Computer Engineering (CCECE), 2014 IEEE 27th Canadian Conference on*, May 2014, pp. 1–6.
4. R. Hajovsky, M. Pies, and L. Richtar, "Analysis of the appropriateness of the use of peltier cells as energy sources," *Sensors (Switzerland)*, vol. 16, 2016, in print.
5. A. G. Watts, M. Prauzek, P. Musilek, E. Pelikan, and A. Sanchez-Azofeifa, "Fuzzy power management for environmental monitoring systems in tropical regions," in *Neural Networks (IJCNN), 2014 International Joint Conference on*, July 2014, pp. 1719–1726.
6. M. Prauzek, P. Musilek, P. Kromer, J. Rodway, M. Stankus, and J. Hlavica, "Energy availability forecasting for harvesting-aware wireless sensor networks: Analysis of energy demand of a predictor based on evolutionary fuzzy rules," *Proceedings - 2015 International Conference on Intelligent Networking and Collaborative Systems, IEEE INCoS 2015*, pp. 200–203, 2015.
7. P. Krömer, M. Prauzek, and P. Musilek, "Harvesting-aware control of wireless sensor nodes using fuzzy logic and differential evolution," in *Workshop on Energy Harvesting Communications, IEEE International Conference on Sensing, Communication, and Networking (SECON 2014)*, June 2014.
8. K.-Y. Lian, S.-J. Hsiao, and W.-T. Sung, "Mobile monitoring and embedded control system for factory environment," *Sensors (Switzerland)*, vol. 13, no. 12, pp. 17 379–17 413, 2013.

Simple Action Recognition Based on Skeleton Detection from Depth Images

Martin Barteček

Department of Computer Science, FEECS,
VŠB – Technical University of Ostrava, 17. listopadu 15,
708 33 Ostrava – Poruba, Czech Republic
`martin.bartecek@vsb.cz`

Abstract. A human action recognition is a very important and discussed topic of computer vision. A method which directly describes the trajectory is proposed. The method works with skeleton joint positions in 3D space obtained from a depth camera. The input data are processed directly in 3D space. The trajectory of skeleton joints is described by set of line directions. these directions are used as descriptors and form feature vectors for SVM classifier. The descriptors are able to describe the trajectory and the action successfully so the SVM classifier is able to distinguish tested actions.

1 Introduction

Computer vision is subject of research all over the world and has a great potential in many applications such as medical applications, public surveillance or even entertainment. One of the important parts of computer vision studied by many researchers is computer based human action recognition. There are several methods how to approach this task using different types of input data, different capture devices and large variety of algorithms to analyse and process the information.

This paper contains a brief description of approaches used in the area of human action recognition and their basic division. The other part of this paper describes my research with experimental methods of action trajectory description.

2 Previous Work

There are two basic divisions of approaches to the human action recognition from images. One concerns input data gathering. There are three basic methods how to capture data for future use of action recognition algorithms. Data can be obtained by single camera, multiple cameras or depth maps provided by special depth cameras.

The second way how to divide approaches in this area is by movement detection algorithms. There are four main methods how to detect and analyse

movement among images in video sequence. First is a method based on optical flow [8, 7] which uses basic color images as two-dimensional input data. This method measures motion of pixels between two frames. The method is rather good for static scenes and is prone to noise in the images or camera movement. Second method also uses standard RGB images as input data, but the movement detection is done by use of STIP(Spatio-Temporal Interest Point). The method is based on detection of variation of image intensity in three dimensions, two dimensions of the picture and the time [1, 4, 5]. Another method of movement detection uses Spatio-Temporal Shape. This method adds time domain to video sequences and thus forms a space-time shape as presented in [2]. Similar technique to Spatio-Temporal Shape is to generate a Motion History Volumes [9]. This method was originally developed for two-dimensional input data but it was later extended for three-dimensional samples to develop view-independent methods of action recognition. Last method in this description uses motion tracking algorithms to detect movement in images. The one of the interesting approach based on motion tracking is to detect the action and to describe it using a SSM (Self-Similarity Matrix) on two-dimensional projection of trajectory of particular part of human body as described in [6]. This method was used as a base for my research described in the next section of this paper.

3 Action Recognition

The research described in this paper was focused on recognition simple actions of particular parts of the human body. In this research the different types of arm movement were analysed. The goal is to develop a method how to describe the action with the most simplicity in order to achieve better and faster recognition.

For this research the tracked human skeleton is used as input data. This skeleton is tracked in the scene by use of depth camera. The skeleton consist of sixteen joints but for my purpose only three joints of arm are used in the research.

The research is divided in two parts. Both parts analyse movement of an arm of the human skeleton. Two actions are considered for basic determination of abilities of the methods used in each part of the research. The first action represents waving the arm as shown in Fig. 1. The second action represents the stretching of the arm as shown in Fig. 2. Number of frames captured for every sample of each action ranges from about 20 to 70 frames per sample. This number of frames depends on the length of the action and frame rate of the device which in this case was 30 fps.

3.1 Self Similarities

The first part of the research focuses on description using SSM computed from joint trajectories of an action. But unlike the method presented in [6] the SSM is computed directly in three-dimensional space using Euclidean distance. The following equation shows the computation of one element in the SSM where d_{ij}



Fig. 1. Samples of the action of waving the arm.



Fig. 2. Samples of the action of stretching the arm.

is one element of the matrix, M is the number of joints in the skeleton used for describing the trajectory of the action and \mathbf{x} is three-dimensional position of a point on the trajectory at time instances i and j .

$$d_{ij} = \frac{1}{M} \sum_{m=1}^M \|\mathbf{x}_i^m - \mathbf{x}_j^m\|_2 \quad (1)$$

Despite the joint trajectories being different as described in the second part of my research the SSM calculated on such trajectories are not. The same action performed by different people produces almost the same SSM but there is only a small difference between matrices of each tested action as shown on Fig. 3. For successful recognition it is essential that each action produces a different matrix that can be later used for analysis.

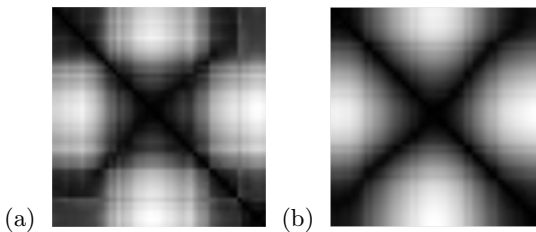


Fig. 3. Self-Similarity matrices of the three-dimensional trajectories of both actions tested in first part of the research. The stretch action (a) and the wave action (b).

3.2 Trajectory Directions

The second part of this research focuses on the trajectories themselves and the way how to describe them directly. During experiments in this part of the research the goal was to extract descriptors from the trajectories and recognize each action using a binary SVM (Support Vector Machine) classifier [3]. Furthermore the descriptors should be extracted directly from three-dimensional space instead of some kind of projection.

The action trajectory in this research consists of separate position of the arm joints for every frame of the action. The trajectory is therefore analysed as set of 3D points. This set of points is divided into several groups. Each group of points is used to form a line using an OpenCV *fitLine()* function. The directions of all lines on the trajectory are used as descriptors of the trajectory for future recognition. The feature vector for joint trajectory is created by combining the directions of the lines of all point groups of the trajectory. The final feature vector consists of feature vectors of all joints of the arm. In this case the joints represent the shoulder, elbow and wrist on the arm. The biggest difference in trajectory of tested actions is observed in the wrist joint trajectory. For illustration, the Fig. 4 and the Fig. 5 show three views of the trajectory of the wrist joint in one sample for each considered action.

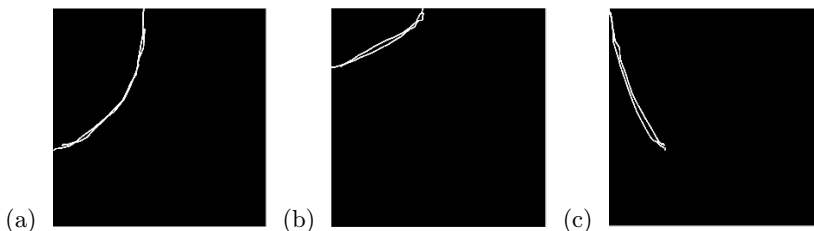


Fig. 4. Trajectory of the wrist joint while performing the action of waving the arm. This figure shows three views of the trajectory. From the front (a), from the top (b) and from the left (c).

4 Experiments

The experiments was focused on the second described part of my research because there is a more promising difference between the trajectories of the tested actions. The actions for these experiments were performed by five people. Each person performed both actions several times. The action samples of four people were used for training the binary SVM classifier while the samples of the fifth person were used as test samples for the recognition later. The goal of these tests was to determine which of those two actions is performed, not to recognize the actions in real-time in video sequence. That kind of experiment is subject of

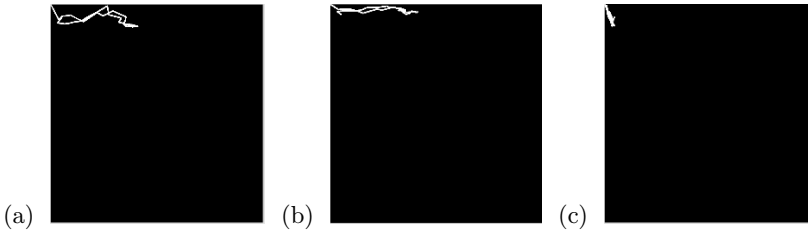


Fig. 5. Trajectory of the wrist joint while performing the action of stretching the arm. The trajectory is shown from the front (a), from the top (b) and from the left (c).

future research of the approach described here. There were total of 34 samples of the arm stretch action and 37 samples of the arm wave action used for training the SVM. The set of test samples contained 10 samples for the arm stretch action and 8 samples for the arm wave action. Since the trajectories in my research was divided to 10 groups of position points, the final dimension of the feature vector was 90. The test result of the recognition of those two actions are shown in the Tab. 1.

These experiments successfully recognized tested actions among each other and shown that this kind of descriptors can be useful in future more detailed research of this method of action recognition. However these test contained very limited set of data for both training and testing purposes. It is expected that with large amount of data, the method described here will be less successful and will require modifications and much more testing. The upcoming challenges are recognition of more then two actions in the background, actions of other parts of the human body or entire skeleton and real-time action recognition.

Table 1. The result of the experiments described in this section of the paper

	Wave	Stretch
Arm wave action test vectors	8	0
Arm stretch action test vectors	0	10

5 Conclusion

Two methods how to recognize human action from images from skeleton joint trajectories were approached. The simple way how to describe the trajectories in 3D space was described. The experiments have shown that the method described in this paper, using the line direction descriptors, has a potential for future, more robust, research and development.

References

1. Ballan, L., Bertini, M., Bimbo, A.D., Seidenari, L., Serra, G.: Effective codebooks for human action representation and classification in unconstrained videos. *IEEE Transactions on Multimedia* 14(4), 1234–1245 (Aug 2012)
2. Blank, M., Gorelick, L., Shechtman, E., Irani, M., Basri, R.: Actions as space-time shapes. In: Tenth IEEE International Conference on Computer Vision (ICCV'05) Volume 1. vol. 2, pp. 1395–1402 Vol. 2 (Oct 2005)
3. Cortes, C., Vapnik, V.: Support-vector networks. *Machine Learning* 20(3), 273–297 (1995), <http://dx.doi.org/10.1007/BF00994018>
4. u. Haq, A., Gondal, I., Murshed, M.: On temporal order invariance for view-invariant action recognition. *IEEE Transactions on Circuits and Systems for Video Technology* 23(2), 203–211 (Feb 2013)
5. Holte, M.B., Chakraborty, B., Gonzalez, J., Moeslund, T.B.: A local 3-d motion descriptor for multi-view human action recognition from 4-d spatio-temporal interest points. *IEEE Journal of Selected Topics in Signal Processing* 6(5), 553–565 (Sept 2012)
6. Junejo, I.N., Dexter, E., Laptev, I., Perez, P.: View-independent action recognition from temporal self-similarities. *IEEE Transactions on Pattern Analysis and Machine Intelligence* 33(1), 172–185 (Jan 2011)
7. Mahbub, U., Imtiaz, H., Ahad, M.A.R.: An optical flow based approach for action recognition. In: Computer and Information Technology (ICCIT), 2011 14th International Conference on. pp. 646–651 (Dec 2011)
8. Wang, H., Klser, A., Schmid, C., Liu, C.L.: Action recognition by dense trajectories. In: Computer Vision and Pattern Recognition (CVPR), 2011 IEEE Conference on. pp. 3169–3176 (June 2011)
9. Weinland, D., Ronfard, R., Boyer, E.: Free viewpoint action recognition using motion history volumes. *Computer Vision and Image Understanding* 104(23), 249 – 257 (2006), <http://www.sciencedirect.com/science/article/pii/S1077314206001081>, special Issue on Modeling People: Vision-based understanding of a persons shape, appearance, movement and behaviour

Evolutionary Algorithms as a Classification Method

Petr Buček

Department of Computer Science, FEECS,
VŠB – Technical University of Ostrava, 17. listopadu 15,
708 33 Ostrava – Poruba, Czech Republic
`petr.bucek.2@vsb.cz`

Abstract. Data processing is a research field which consists of many approaches and methods. It can be divided into many broad categories such as data mining, classification or machine learning. In this article, we focus on data classification based on evolutionary algorithms. Classification methods are used to assign objects from the input data set into a particular category. Output of this type of methods is a set of object partitioned into several groups by a given special property.

Keywords: classification, data processing, evolutionary algorithms

1 Introduction

Data classification can be used in many science disciplines. Object represented as a vector of values can be based on various sources such as image data, text data, etc. Input of a particular classification method is often represented by a set of uncategorized objects. When the process of classification ends, each object is assigned into a particular category [1, 3, 7].

This problem can be addressed by many algorithms often coming from the machine learning category. First we need to create a model which is used by classifiers to predict the category for each uncategorized object. The model is obtained from a training dataset, but this process is very time-consuming and depends on its size. One option is to use an evolutionary based algorithm for this calculation, which was introduced in [10] with first algorithm called Particle Swarm Optimization.

As mentioned, each object is represented by a vector of values. We need to define the similarity between each pair of objects in dataset. There are a lots of similarity measured such as Euclidean, Mahalanobis or Manhattan similarity, etc. [8] In this article, cosine similarity is used, as is described in [10].

Cosine similarity between vectors u and v is defined as:

$$\text{sim}(u, v) = \frac{u \cdot v}{\|u\| \|v\|} \quad (1)$$

Each used evolutionary based algorithm is presented in the following sections of this article. List of all used algorithms is shown in 1.

	Algorithm	Year	Source
BA	Bat Algorithm	2010	[12]
BEA	Bees Algorithm	2005	[6]
CSA	Cuckoo Search Algorithm	2009	[15]
FA	Firefly Algorithm	2010	[11]
FPA	Flower Pollination Algorithm	2012	[13]
PSO	Particle Swarm Optimization	1995	[4]
SOMA	Self-Organizing Migrating Algorithm	1999	[16]

Table 1. Investigated Evolutionary Algorithms

2 Evolutionary Based Algorithms

This group of algorithms is inspired by processes which are commonly found in nature. There are a few terms associated with the evolutionary based algorithms, such as:

similarity The degree of similarity between the two objects (similarity metric).

particle Part of evolutionary based algorithms; each particle is one object from the input dataset.

cost function Calculates the result for each particle.

2.1 Bat Algorithm

This meta-heuristic algorithm is inspired by behavior of bats which use ultra sound echolocation for navigation. This algorithm was first published in [12]. Bats are represented as particles in similar way as in the Particle Swarm Optimization (PSO) algorithm. Compared to the standard PSO, the particles in this case have two additional properties – frequency and velocity. The exact description of the movement rules is in the original article [12].

2.2 Bees Algorithm

This algorithm is inspired by the honey bees and it was first published in 2005 in [6]. Scout bees are randomly placed across the input space. Each bee then tries to find the best solution from its initial position and the best one is selected as the result. Rules of the algorithm are described in [6].

2.3 Cuckoo Search

This algorithm is inspired by the parasitic behavior of the cuckoo bird which lays its eggs into the nests of other birds. One of the methods used in this algorithm is Lévy flights. Particles are moving in the following patterns:

- There is a limit of one egg for each cuckoo (placed to random nest).

- Eggs with the best score are passed to next generation.
- Host bird can discover cuckoo egg with calculated probability.

When host bird discovers the cuckoo egg, it has three options.

- New nest can be created.
- Current nest can be abandoned.
- Cuckoo egg can be removed [5].

2.4 Firefly Algorithm

This algorithm was first published in [11] (2008) and is inspired, as the name suggests, by the fireflies and their behavior. The basis of the firefly algorithm is the specific flashing characteristic of each firefly (particle) which represents how much are other fireflies attracted to it. Light intensity also depends on the distance between a pair of fireflies [14].

The following basic rules for the firefly algorithm are used more or less in each variant of the algorithm [9]:

- Fireflies are attracted to each other.
- Firefly is moving towards the brightest one.
- Brightness of the firefly is defined by a cost function [11].

2.5 Flower Pollination Algorithm

This algorithm is based on a process of the pollen transport between flowers. It was first published in 2012 in [13]. Each particle is represented by a flower and its reproduction depends on the similarity of the flowers and Lévy flights. Steps of the algorithm are as follows:

$$x_i^{t+1} = x_i^t + Levy(x_i^t - gBest)$$

where $gBest$ is the best known flower solution [13].

2.6 Particle Swarm Optimization

This algorithm was first published in 1995 in [2, 4]. Each particle (vector of values) represents one set of values of the cost function parameters. The aim is to find such parameters values (solution) which minimize the cost function. Behavior of the particles in each generation is derived from the bird swarm. The parameters of a particle (position and velocity) are recomputed in each iteration of the algorithm.

There is a way to calculate the velocity (v_i^{t+1}) of a particle in the generation $t + 1$ (r_1, r_2 are random numbers, c_1, c_2 are learning factors, $lBest$ and $gBest$ are the best solutions) [2, 4]:

$$v_i^{t+1} = wv_i^t + c_1r_1 \times lBest - x_i^t + c_2r_2 \times gBest - x_i^t$$

2.7 Self-Organizing Migrating Algorithm

This algorithm was published in 1999. In this algorithm, a leader is chosen (particle with the best solution) which is followed by the rest of the particles. The size of the step is one of the input parameters of the algorithm, much like the path length, population size, etc. There are also a few strategies in SOMA [16]:

AllToOne Basic variant of algorithm.

AllToAll Variant with no leader, particles migrates to others.

AllToAllAdaptive Modified variant of AllToAll.

AllToOneRand Same as AllToOne but leader is chosen randomly in each generation.

3 Conclusion

Strategies for implementation of the selected algorithms for the CPU and GPU platforms were evaluated. The most feasible implementations were created and tested. Standard data sets were used to verify the correctness of the implementations. Most of the algorithms showed comparable execution times. The Firefly algorithm had the best execution time which increased very slowly with the size of the input dataset.

References

1. I. Androutsopoulos, J. Koutsias, K. V. Chandrinou, G. Paliouras, and C. D. Spyropoulos. An evaluation of naive bayesian anti-spam filtering. *arXiv preprint cs/0006013*, 2000.
2. R. Eberhart and J. Kennedy. A new optimizer using particle swarm theory. In *Micro Machine and Human Science, 1995. MHS '95., Proceedings of the Sixth International Symposium on*, pages 39–43, oct 1995.
3. R. Jain, R. Kasturi, and B. G. Schunck. *Machine vision*, volume 5. McGraw-Hill New York, 1995.
4. J. Kennedy and R. Eberhart. Particle swarm optimization. In *Neural Networks, 1995. Proceedings., IEEE International Conference on*, volume 4, pages 1942–1948 vol.4, nov/dec 1995.
5. P. Manikandan and S. Selvarajan. *Data Clustering Using Cuckoo Search Algorithm (CSA)*, pages 1275–1283. 2012.
6. D. T. Pham, A. Ghanbarzadeh, E. Ko, S. Otri, S. Rahim, and M. Zaidi. The bees algorithm a novel tool for complex optimisation problems. 2005.
7. F. Sebastiani. Machine learning in automated text categorization. *ACM Comput. Surv.*, 34(1):1–47, Mar. 2002.
8. V. Snášel, H. Řezanková, and D. Húsek. *Shluková analýza dat*. Professional publishing, 2007.
9. P. R. Srivatsava, B. Mallikarjun, and X.-S. Yang. Optimal test sequence generation using firefly algorithm. *Swarm and Evolutionary Computation* 8 (2013) 4453, 2012.

10. Z. Wang, Q. Zhang, and D. Zhang. A pso-based web document classification algorithm. In *Proceedings of the Eighth ACIS International Conference on Software Engineering, Artificial Intelligence, Networking, and Parallel/Distributed Computing - Volume 03*, SNPD '07, pages 659–664, Washington, DC, USA, 2007. IEEE Computer Society.
11. X.-S. Yang. *Nature-Inspired Metaheuristic Algorithms Second Edition*, pages 81–89. Luniver Press, 2010.
12. X.-S. Yang. A new metaheuristic bat-inspired algorithm. *Nature Inspired Cooperative Strategies for Optimization*, 2010.
13. X.-S. Yang. Flower pollination algorithm for global optimization. *Unconventional Computation and Natural Computation 2012*, 2012.
14. X.-S. Yang. *Nature-Inspired Optimization Algorithms*. School of Science and Technology Middlesex University London, London AMSTERDAM, 2014.
15. X.-S. Yang and S. Deb. Cuckoo search via lvy flights. *Proc. of World Congress on Nature & Biologically Inspired Computing*, 2009.
16. I. Zelinka. *Uml inteligence v problmech globln optimalizace*. BEN-Technick literatura, BEN-Technick literatura.

Solar Irradiance Forecasting in the Active Demand Side Management

Tomas Burianek

Department of Computer Science, FEECS,
VŠB – Technical University of Ostrava, 17. listopadu 15,
708 33 Ostrava – Poruba, Czech Republic
tomas.burianek@vsb.cz

Abstract. The Off-Grid systems are energy units independent of the external grid that are controlled by the Active Demand Side Management (ADSM). The renewables (RES) are one of the most important parts of the Off-Grid systems and sometimes it is the only source of energy. In case of photovoltaic power plant (PVP) as a main RES the need of forecasting of available energy supply is required in the ADSM that ensures safety and reliability of the system. The need of forecasting is mainly caused by dependence on solar irradiance that has stochastic character influenced by weather conditions. This paper introduces solar irradiance forecasting model implemented as a part of the Active Demand Side Management.

Keywords: Time-series forecasting, Extreme Learning Machine, Support Vector Regression

1 Introduction

Photovoltaic power plants (PVP) are very popular Renewable energy sources (RES) that are utilized in the Off-Grid Systems. The Off-Grid Systems are energy systems independent of the energy supply from an external grid and in general case the RES are sole source of energy. One of the most important parts of the Off-Grid System is the Active Demand Side Management (ADSM) that is an active system that controls flows of energy in the Off-Grid system. This includes controlling of the system consumption by managing plan of connected appliances. Because of a stochastic character of the RES an appliances plan optimization requires forecast of available energy. This ensures balanced state when the Off-Grid system works safe and reliable. This forecast must be at least 24 hours to the future and should approach at least approximate production for a day. Unexpected rapid changes of the real production are covered by a storage device that is used for accumulation of the surplus of energy. PVP production is a function of solar irradiance at the location of the PVP. Intensity of solar irradiance is mainly dependent on position of the sun and actual weather conditions. It is supposed that solar irradiance is mainly reduced by cloudiness. Forecasting of cloudiness with other parameters is obtained from the available meteorological forecasting model. The task is to obtain ideal solar irradiance unaffected by

cloudiness. This must be done for every day of the year, because the position of the sun is variable through the day from sunrise to sunset and each day of the year has different development from summer to winter solstice. It is done by analyzing collected historical data of solar irradiance for the reference PVP. Produced dataset is used in regression method to find relation between presented inputs and output. This paper focuses on utilization and comparison of two regression methods: Support Vector Regression (SVR) [4] with different kernel functions and Extreme Learning Machine [2] with different activation functions.

2 Data Analysis

2.1 Meteorological Forecasting Data

Production from the reference PVP is mainly dependent on actual solar irradiance. Meteorological forecasting data for specific location of the PVP are obtained from available meteorological model contains four classes of cloudiness, humidity, atmospheric pressure, temperature and other parameters. The data are with an hour resolution and forecasting is done for 55 consecutive hours to the future. The idea is that forecasting of real solar irradiance could be expressed as relation of ideal solar irradiance derived from position of the sun and forecasting of cloudiness at the same time. The dataset is then constructed for further machine learning algorithm.

2.2 Unaffected ideal solar irradiance estimation

The irradiance not influenced by cloudiness is reconstructed from the historical data and from the knowledge of the sun movement. In this paper it is assumed that estimated ideal irradiance together with forecast of cloudiness create relation and its result is the real solar irradiance. The ideal solar irradiance must be obtained for a whole day, because its development is changing from sunset to sunrise with maximum at a midday. Also this daily solar irradiance must be obtained for each day of the year, because sunrise and sunset is different for each day and also an intensity of the solar irradiance is changing through the year with overall maximum at the summer solstice and minimum at the winter solstice. The historical data of solar irradiance were collected from the reference PVP with 1 minute resolution for a whole year. The unaffected ideal solar irradiance estimation procedure is accomplished by partial steps, followed:

- sunny days selection,
- key points calculation in each sunny day,
- interpolation of key points through the year,
- interpolation of each day of the year.

This procedure is described in previous conference paper [1] in more details. The resulting unaffected irradiance is showed in Figure 1 as a 3D plot to visualize progress of irradiance for each day through the year. This daily data are finally transformed to the consecutive single variable time-series necessary for dataset construction.

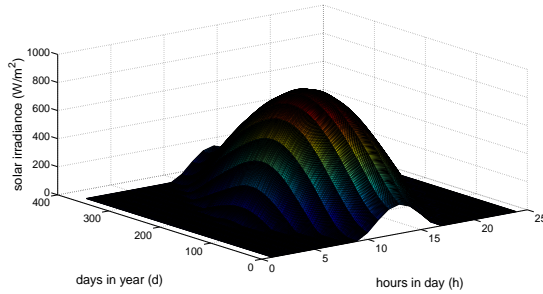


Fig. 1. Ideal solar irradiance 3D plot

2.3 Solar irradiance to PVP production conversion function

Solar irradiance (W/m^2) forecast must be converted to produced power (W) forecast and this is done by finding function $P = f(R)$ between real solar irradiance R and real produced power P stored as historical data. The data must be at first preprocessed to filter out undesired data points. These undesired data points are caused by situation when the battery is fully charged and the power from the PVP is limited, that doesn't reflect actual relation between solar irradiation and produced power. This could be detected by voltage level of the battery stored as parameter U_{BAT} . For filtering of the data a simple function is presented:

$$f(U_{\text{BAT}}, thr) = \begin{cases} 0 & \text{if } (U_{\text{BAT}} > thr) \\ 1 & \text{otherwise} \end{cases} \quad (1)$$

where thr is a threshold value and values 0 and 1 means discarded and retained data points respectively. Based on previous experiments the threshold is set to 57.3V . Remaining data points are then approximated by polynomial curve fitting with degree set to 2. Resulted fit is depicted in Figure 2 as a black curve that approximates red retained data points and ignores blue discarded data points. The coefficient of determination of this curve fitting is $R^2 = 0.99371$ that is satisfactory for utilization of this fitting as conversion between solar irradiance and actual production from reference PVP.

2.4 Dataset construction

For supervised learning procedure the dataset S is constructed. This dataset contains N pairs of samples $(\mathbf{x}_i, \mathbf{y}_i)$ where input vector for sample i is $\mathbf{x}_i = [C_{i1}, \dots, C_{i4}, I_i] \in \mathbb{R}^5$. Values C_{ik} where $k = 1, \dots, 4$, represents high, low, medium and total cloudiness data and I_i represents ideal irradiance. Ideal irradiance must be normalized to $(0, 1)$ range, same as cloudiness data for needs of regression method. Output vector for sample i is $\mathbf{y}_i = [R_i]$ that contains single value of the expected real irradiance R_i . All data are sampled with an hour resolution.

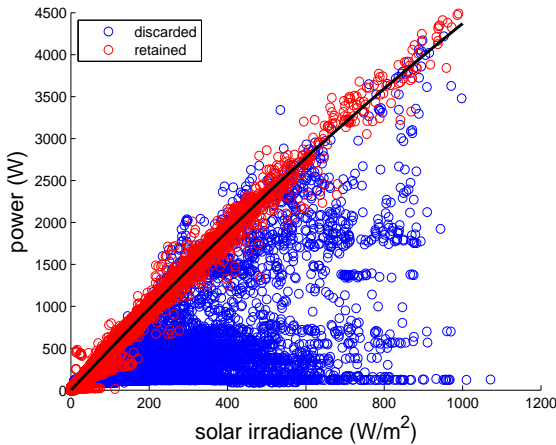


Fig. 2. Solar to power regression plot

3 Experiments and Results

For the comparative experiments in problem of regression were selected two machine learning algorithms: Support Vector Regression(SVR) and Extreme Learning Machine (ELM), both for its fast learning ability and generalization performance.

SVR [4] is a specific version of Support Vector Machine algorithm, that is suitable for regression type problems. SVR utilizes so-called kernel trick that brings non-linearity to this model. Three particular kernels are used in experiments, namely linear, polynomial and radial basis function kernel.

ELM [2] is a kind of feed-forward neural network with two layers of neurons. ELM is specific by random initialization of weights in the hidden layer that is fixed for the whole process of training and testing. The output layer weights could be then computed by simple linear regression. This brings very much faster training of the model in comparison with conventional Back-propagation algorithm used for feed-forward neural networks. Two activation functions are utilized in ELM algorithm, namely sigmoid and sinus function.

Experiments were done on constructed dataset S that consists of 7460 data samples collected in an hour interval. This interprets almost 311 days of the data. Testing of the whole model performance was done by k -fold Cross-Validation (CV) procedure [3] that divides dataset to k subsets. Then the optimization is done k times when each k th subset is used for testing and rest of the dataset is used for training the model. To measure model's accuracy during training and testing phase the Mean Absolute Percentage Error (MAPE) is employed:

$$\text{MAPE} = \frac{1}{N} \sum_{i=1}^N \frac{|o_i - y_i|}{|y_i|}, \quad (2)$$

representing deviations in scale independent manner and usually could be expressed as percentage error.

While training and testing by CV procedure, k -forecasts are produced for each testing and training step. Accuracy of each forecast is measured by MAPE and final results are shown in Table 1. There are 5 results for each training and testing phase for all SVR and ELM versions. Error values are taken as mean of k results including standard deviation of the results. It is evident that results by

phase	algorithm	MAPE
training	SVR linear	0.509 ± 0.019
	SVR poly	0.457 ± 0.013
	SVR RBF	0.266 ± 0.008
	ELM sinus	0.265 ± 0.006
	ELM sigmoid	0.264 ± 0.007
testing	SVR linear	0.601 ± 0.183
	SVR poly	0.535 ± 0.155
	SVR RBF	0.298 ± 0.058
	ELM sinus	0.284 ± 0.034
	ELM sigmoid	0.287 ± 0.041

Table 1. Table of errors

SVR RBF, ELM sinus and ELM sigmoid are very close with error under 30%. Rest of the models were much more inaccurate. This reveals fact, that relation between input and output dataset is highly non-linear and it is necessary to utilize some non-linear mapping by RBF kernel function in SVR or by sinus or sigmoid activation function in ELM. The particular forecast comparison by best model ELM with sinus activation function is depicted in Figure 3 for both sunny and cloudy days. In the first case of sunny days, the forecast is very accurate. This is mainly caused by accurate forecast of cloudiness for stable sunny days weather conditions. The second case of cloudy days has lower accuracy mainly caused by unpredictable sudden changes of cloudiness. Still these forecast preserve general character of the day solar irradiance development.

4 Conclusion

In this paper the solar irradiance forecasting model was presented. At first, the data were analyzed and prepared for further processes. The ideal unaffected irradiance for the whole year was computed from historical data by introduced sophisticated algorithm. This data together with cloudiness forecasting data and real cloudiness form dataset suitable for regression methods. The comparative experiments for regression were then performed by supervised learning algorithms: Support Vector Regression and Extreme Learning Machine, with three different kernel functions for SVR and two activation functions for ELM. Five different

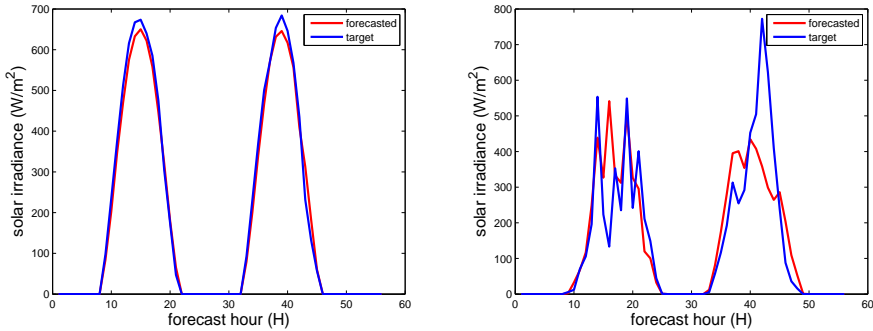


Fig. 3. ELM sinus forecast comparison, left for sunny days and right for cloudy days

results were obtained for both training and testing phase and compared by error measurement. The results reveals non-linear character of the data, where most accurate were models with the non-linear mapping. These models, with almost same accuracy, were ELM with both activation functions and SVR with RBF kernel function. The performances of ELM and SVR are very promising and by meeting given requirements both models are suitable for the system. This whole concept is now utilized in the Active Demand Side Management where the part of the regression could be easily performed by both presented algorithms.

References

1. Burianek, T., Misak, S.: Solar irradiance forecasting model based on extreme learning machine. In: 2016 IEEE 16th International Conference on Environment and Electrical Engineering, EEEIC 2015 - Conference Proceedings (2016)
2. Huang, G.B., Zhu, Q.Y., Siew, C.K.: Extreme learning machine: a new learning scheme of feedforward neural networks. In: Neural Networks, 2004. Proceedings. 2004 IEEE International Joint Conference on. vol. 2, pp. 985–990 vol.2 (July 2004)
3. Kohavi, R.: A study of cross-validation and bootstrap for accuracy estimation and model selection. In: Proceedings of the 14th International Joint Conference on Artificial Intelligence - Volume 2. pp. 1137–1143. IJ-CAI'95, Morgan Kaufmann Publishers Inc., San Francisco, CA, USA (1995), <http://dl.acm.org/citation.cfm?id=1643031.1643047>
4. Vapnik, V.N.: The Nature of Statistical Learning Theory. Springer-Verlag New York, Inc., New York, NY, USA (1995)

Flexible Neural Tree and Betweenness Centrality Algorithms

Jiří Hanzelka

Department of Computer Science, FEECS,
VŠB – Technical University of Ostrava, 17. listopadu 15,
708 33 Ostrava – Poruba, Czech Republic
IT4Innovation, VŠB – Technical University of Ostrava, 17. listopadu 15,
708 33 Ostrava – Poruba, Czech Republic
jiri.hanzelka@vsb.cz

Abstract. The purpose of this paper is to show developed parallel approach of Flexible Neural Tree and Betweenness centrality algorithms based on Message Passing Interface at High Performance Computing environment. Experiments prove good performance results.

Keywords: flexible neural tree, betweenness centrality, MPI, HPC

1 Introduction

1.1 Artificial neural networks

Artificial neural networks (ANN) have been successfully applied to a number of scientific and engineering areas in recent years. These areas include for example function approximation, time-series prediction, system control, image processing and so on. A performance of a neural network is highly dependent on its structure. There were a number of attempts to design artificial neural network architecture automatically. In 1997 Zhang et al. proposed concept of evolutionary induction of sparse neural tree [2]. Chen et al. simplified concept of sparse neural tree to *Flexible Neural Tree* (FNT) and described in book [11]. Section 2 gives the brief description of the FNT, our parallel approach for evolving FNT and measured scalability. Some concluding remarks are presented in Sect. 4.

1.2 Graph algorithms

The important area of computations are big graph problems which are mostly used in order to model large real life networks, i.e. traffic networks, social networks but also in areas like the modeling of connections in the human brain [7]. For example, one of the used algorithms in area of traffic networks is betweenness centrality described in this paper. The general assumption of betweenness centrality in traffic routing is that the most frequently used roads can be considered as bottlenecks [6]. The main goal of betweenness centrality is to identify such bottlenecks in a traffic network represented by oriented weighted graph.

This way, betweenness centrality can help to optimize routing since it allows us to monitor how bottlenecks change during the day. Since betweenness centrality is based on the shortest path search, it can also be used to monitor and examine bottlenecks behavior based on wide number of factors. Besides the distance, graph weights could reflect actual weather conditions, speed, time of the day, etc. Betweenness centrality algorithm is described in Section 3.

2 Flexible Neural Tree

The Flexible Neural Tree is a special type of feed-forward artificial neural network. The neural network has an irregular tree structure with one output only. Formally speaking FNT is union of set of terminal symbols T and set of functional symbols F . The terminal symbols x_1, \dots, x_K are leaf nodes in the tree structure of the network and taking no arguments each. While functions symbols $+_1, \dots, +_M$ are inner, non-leaf, nodes, taking i input arguments. The functional symbol $+_i$ is also called a *flexible neuron operator* with i inputs. Typical structure of the FNT is shown in Fig. 1.

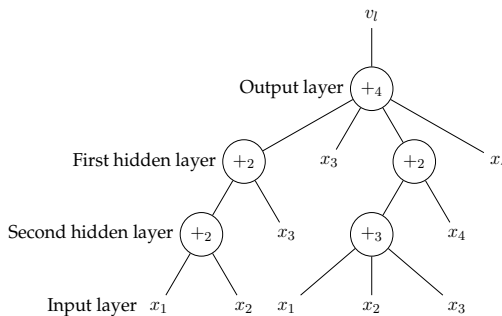


Fig. 1: A typical representation of neural tree with functional symbols $F = \{+_2, +_3, +_4\}$, and terminal symbols $T = \{x_1, x_2, x_3, x_4\}$

2.1 Structure and Parameter Learning

The hierarchical structure of the FNT could be evolved by using tree-structure based evolutionary algorithms. The fine tuning of the weights and activation function's parameters could be accomplished by using parameter optimization algorithms. The flexible neural tree method uses both optimizations in cyclic manner. Starting with population of random tree structures and random parameters, it first tries improve the structure of the given tree and then it fine tunes its parameters. Then goes back to improve tree structure to find better structure, it fine tunes parameters again. This loop continues till acceptable flexible neural tree is found.

2.2 Parallel Approach

The tree structure is evolved using standard *Genetic Algorithm* (GA), while tree parameters are optimized using *Differential Evolution* (DE) [1]. Parallel FNT learning algorithm is developed for HPC cluster, so Message Passing Interface (MPI) [8] is straightforwardly used to implement GA and DE algorithms. GA was implemented using the asynchronous model where as the DE is implemented using the synchronous one. Asynchronous computation model for GA was selected due to very different sizes of FNT in the population and whence execution times for each tree in the population can be different.

2.3 Experiments

The implemented FNT is tested on well-known time-series prediction benchmark problem: The gas furnace data (serie J) of Box-Jenkins time series [3]. First part of data is used for training (200 patterns) and the rest of the data is used for testing. The actual time-series, the FNT output and the prediction error is given in Fig. 2. The experimental results are comparable to results obtained by Chen and Abraham [11], their RMSE was 0.026, our average RMSE was 0.038 for same inputs.

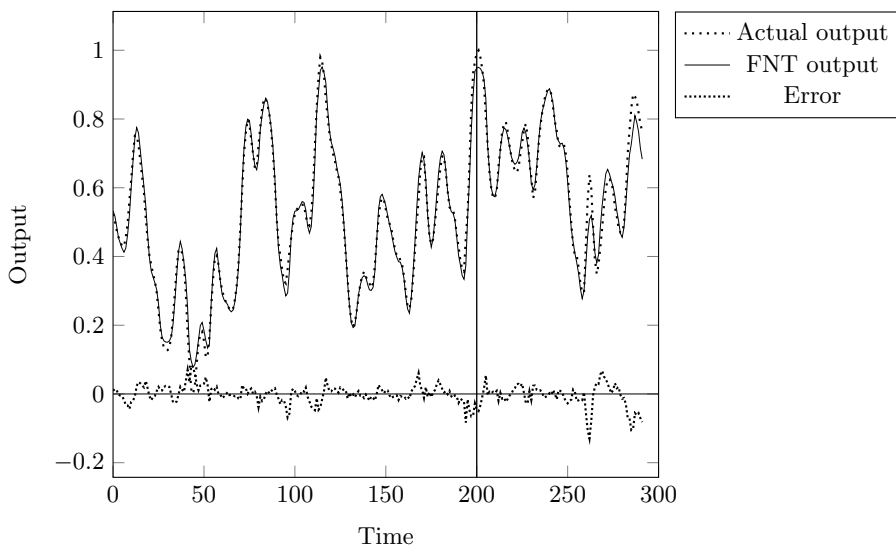


Fig. 2: Comparison of desired output with actual output of founded neural tree for Box-Jenkins series

2.4 Scalability

This test was carried out to check the scalability of proposed FNT parallel learning algorithm. The most time consuming part were evolution of FNT structure together with optimization of FNT parameters. The first evolution was done using genetic algorithm (GA) and the second one is done using differential evolution (DE). Test was performed for 1000 and 5000 patterns in training set. Both optimization algorithms used same population size with 128 individuals. The performance of algorithm was tested on ANSELM cluster operated by IT4Innovations National Supercomputing Centre in the Czech Republic. Speedup values are shown in Fig. 3.

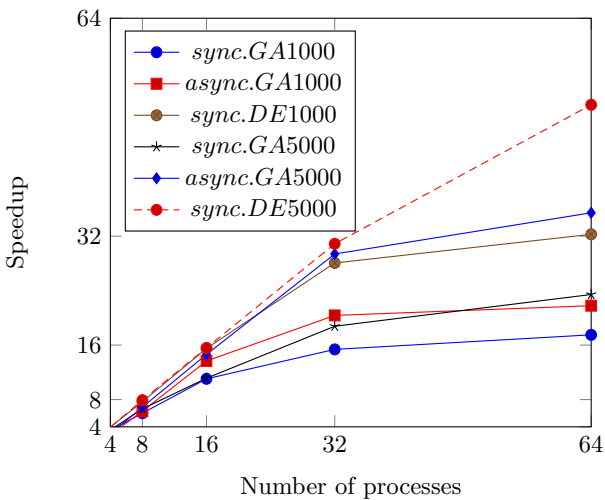


Fig. 3: Speedup of optimization algorithms

3 Betweenness Centrality Algorithm

Betweenness is widely used graph metric used mainly in order to find the most significant vertices within the graph. Betweenness centrality quantifies the number of times a node is a bridge along the shortest path between two other vertices.

For the purpose of the benchmark, the input graph for betweenness centrality is generated from the Czech Republic traffic network map that was obtained from OpenStreetMap project [9]. The traffic network graph is stored in a simple csv file with one edge in each row. Betweenness centrality was tested using our C++ implementation of Brande’s algorithm [10] that was parallelized by OpenMP and MPI. The performance was tested on SALOMON cluster operated by IT4Innovations National Supercomputing Centre using the Xeon processors and Xeon-Phi coprocessors.

Table 1: Experiments for the betweenness centrality algorithm on 1 node (2×12 cores) for different number of used threads and MPI processes

Nodes	MPI processes	Threads	Avg. Time [s]	Expected Time [s]	Efficiency	Speedup
1	1	1	4804.0	4804.00	1.00	1.00
1	8	1	955.0	600.50	0.62	5.03
1	16	1	513.0	300.25	0.59	9.37
1	24	1	362.0	200.17	0.55	13.27
2	48	1	190.6	100.09	0.53	25.20
4	96	1	95.1	50.04	0.53	50.52
8	192	1	47.6	25.02	0.52	100.86
16	384	1	24.0	12.51	0.52	200.17
32	768	1	12.7	6.26	0.49	379.46
32	384	2	12.4	6.26	0.50	386.48

Table 2: Experiments for the betweenness centrality algorithm on MIC (61 cores – 244 HW Threads) for different number of used threads and MPI processes

Used MICs	MPI processes	Threads	Avg. Time [s]	Expected Time [s]	Efficiency	Speedup
1	1	4	25542	25542.00	1.00	4.00
1	244	1	946	418.72	0.44	108.00
1	61	4	712	418.72	0.59	143.49
2	122	4	363	209.36	0.58	281.45
4	244	4	192	104.68	0.55	532.13
8	488	4	106	52.34	0.50	973.03

3.1 Experiments

This experiment was focused on measuring the speed of the betweenness centrality algorithm parallelized using MPI and OpenMP in a hybrid way on a graph generated from the actual Czech Republic traffic network described earlier as an input. Table 1 shows the results of experiments, in which also the MPI processes were used. In Table 2 are shown hybrid runs with combination of different number of used MPI processes and threads on Xeon Phi (MIC) in native mode to see difference of speed compared to CPU. We used 1 process with 4 threads as minimum for MIC tests because of time limit.

Table 2 contains time, efficiency and speedup of the betweenness centrality algorithm for MIC. It can be observed from the tests that the best efficiency of the betweenness centrality algorithm is when 61 processes and 4 threads per the process is used per MIC. If we use 2 MICs with the same setup then the efficiency is almost the same and adding more MIC increase the speed of the

algorithm almost linearly as in the case of adding nodes for the CPU test. For our algorithm, two MICs had a bit slower speed (363 seconds) in comparison with two CPUs (362 seconds).

4 Conclusion

The parallel learning algorithm for Flexible Neural Tree on HPC platform was presented in the paper. The learning algorithm is built on two bio-inspired evolutionary algorithms. The structure of the FNT is evolved using Genetic Algorithm and fine tuning of the parameters of FNT is done using Differential Evolution. The FNT is implemented with Message Passing Interface, where synchronous computation model is used for DE whilst GA is running using asynchronous model. Implementation correctness and scalability are tested in presented experiments.

In this paper, we also tested the performance of Xeon processor and Xeon-Phi coprocessor on graph problems. We used Betweenness centrality algorithm. It was tested on real data set using the graph generated from the Czech Republic traffic network. It is obvious from results in Section 3.1 that the performance of one MIC is comparable with performance of one Xeon processor for our implementation of Brande's algorithm [10]. More results about these algorithms can be found in publications [4, 5].

References

1. Abdual-Salam, Abdul-Kader, Abdel-Wahed, Comparative study between Differential Evolution and Particle Swarm Optimization algorithms in training of feed-forward neural network for stock price prediction, IEEE, 2010
2. Byoung-Tak Zhang, Peter Ohm, Heinz Mühlenbein, Evolutionary Induction of Sparse Neural Trees, MIT Press, 1997
3. George Box, Gwilym Jenkins, Time Series Analysis: Forecasting and Control, San Francisco: Holden-Day, 1970
4. J. Hanzelka, J. Dvorský, Flexible Neural Trees – Parallel Learning on HPC, ACSS, 2016 (accepted and revised)
5. J. Hanzelka, R. Skopal, K. Slaninová, J. Martinovič, J. Dvorský, Graph problems performance comparison using Intel Xeon and Intel Xeon-Phi, ACSS, 2016 (accepted and revised)
6. K. Fujisawa, H.P. Matsuo, Graph analysis & HPC Techniques for Realizing Urban OS, ISC15, 2015
7. L. Lovász, Large Networks And Graph Limits, Colloquium Publications Volume 60, 2012
8. Message Passing Interface Forum, MPI: A Message-Passing Interface Standard : Version 2.2, <http://www.mpi-forum.org/docs/mpi-2.2/mpi22-report.pdf>, cited Feb 28th 2015
9. OpenStreetMap [online], <http://www.openstreetmap.org>, cited Jun 1st 2016
10. U. Brandes, A Faster Algorithm For Betweenness Centrality, Journal of Mathematical Sociology, 2001
11. Yuehui Chen, Ajith Abraham, Tree-Structure based Hybrid Computational Intelligence: Theoretical Foundations and Applications, Springer, 2010

Neural Stegoclassifier

Jakub Hendrych

Department of Computer Science, FEECS,
VŠB – Technical University of Ostrava, 17. listopadu 15,
708 33 Ostrava – Poruba, Czech Republic
jakub.hendrych@vsb.cz

Abstract. This article deals with the application of neural networks on the issues of steganalysis. The aim is to improve the detection capability of conventional steganalytical tools with using of ANN. We analyze the ability of the tool, which utilizes calibration and blockiness to detect the presence of steganography message in suspected image. We verify if deployment of neural network improves this detection by finding some hidden pattern.

Keywords: steganography, steganalysis, cover, stegogramme, ANN, calibration, blockiness, JPEG

1 Introduction

The development of information technologies has brought new opportunities to apply the steganography methods. It is the art of hiding information into a cover – in computer science the covers are especially images or videos. The observer is unaware that the picture or video (stegogramme) contains some secret message. Steganography attack [1] can be very dangerous especially for the corporate sector and can lead to leak of company secrets. Consider a situation where an offender A sent a harmless email with JPEG image to a company email server. Accomplice B embeds some company secret to this JPEG image by using steganography system and sends it back to A. Then is easy for A use a decoder and obtain the company secrets. There are many others similar scenarios – consider using of social networks, internet forums, etc. For the observer (company security layer) it is just harmless and unsuspecting image, because one of the most commonly used image format – JPEG – was used as cover in this case.

The opposite of steganography is steganalysis, which serve to detecting a stegogrammes. We can basically consider two different types of steganalysis, depending on the fact, if the cover is known or not during the analysis. If so, we can speak about “Targeted steganalysis”. Otherwise it is called “blind steganalysis”. Most important is especially the blind steganalysis that can be applied to image and video files because it is the same situation as in previous scenarios.

2 Materials and Methods

If we want to detect steganogrammes, first we must determine what steganography system (algorithm) was used to information hiding. There are several types of methodologies [1], how to enter information into the cover. The simplest method is a modification of the least significant bit (LSB) of image pixel. Modification of the bit may be performed sequentially or randomly. However, these methods of inserting information directly into spatial regions of the image are easily detectable. Therefore, new methods were developed. The data was embedded into the transform domain. The JPEG technology uses the compression that converts image into DCT domain. This DCT domain presents the data as the high and low frequencies. High frequencies are related to the areas of an image with high details, and low frequencies are associated with low details. To reduce the size of JPEG image, some of high details are omitted – the human eye is unable to distinguish these areas. So there is no obstacle to modifying these values (DCT coefficients) to hide the secret information. Exactly this methodology is used by the steganography tool OutGuess 2.0 on which we are focusing in this paper. It is an open source algorithm. OutGuess 2.0 is also implemented with own GUI, which does not need great knowledge of steganography for the end user and increasing the likelihood of use in the corporate sector.

2.1 Calibration

The authors of [2] present a new method of blind steganalysis for grayscale images. Thus, there is not a cover image, that we can compare with the suspected image and detect differences. This disadvantage authors remove by using a method called calibration. The input of this method is a suspected image and the output is a calibrated image. Calibrated image is not 100% copy of the cover image, but it is very similar (Fig. 1.).

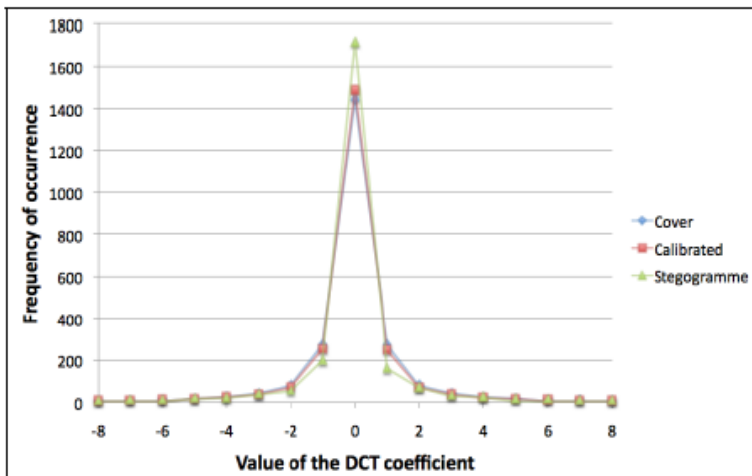


Fig. 1. Histogram comparison of the calibrated and the cover image [1]

In our implementation we used a simpler version of algorithm, where we do not need to calculate the length of hidden message, but with improvement for colorful images. However, there are cases when huge error appears during the calibration process. This error can be caused by multiple compressed JPEG file that was used as a cover file. The OutGuess use for recompression its own quality factor Q_S . If the Q_S is different from the Q_C (quality factor of cover image), the stegogramme passed double compression. Therefore, it is necessary compress the suspected image by factor Q_C and consequently by factor Q_S . This process will simulate the situation of embedding message by using the OutGuess system. The algorithm for creating the calibrated image follows these steps:

- (a) cropping the image by 4px from every side
- (b) compress the image using Q_C
- (c) compress the image using Q_S

To obtain a quality factor Q_S we use the ImageMagick library for Java in our implementation. The question is how to get quality factor Q_C when the cover is unknown. The advantage is that the OutGuess preserves the histogram. For this purpose the authors [2] developed Eq. (1).

$$Q_C = \arg \min_Q \sum_{(i,j)} \sum_d |h_d(i,j) - h_d(i,j,Q)|^2, \quad (1)$$

where $h_d(i,j)$ is histogram of values (i,j) -th DCT mode of the suspected image, $h_d(i,j,Q)$ is the same histogram of the cropped image with using of quality factor Q , that is subsequently compressed by quality factor Q_S .

2.2 Blockiness

We also need to find a metric that would detect the presence of hidden message in the image. This metric must respond to the variable lengths of the messages. The authors in [3] present Blockiness values. It is a statistical property that is different for the calibrated and the suspected image, so we can determine whether the image is stegogramme. The Blockiness value is defined as the sum of spatial discontinuities along the boundary of all 8x8 blocks of JPEG image. Stegogrammes contain different coefficients along the borders of 8x8 blocks than the clear image. Again, the input is an image and the output is the Blockiness Eq. (2) value itself.

$$B = \sum_{i=1}^{\lfloor \frac{M-1}{8} \rfloor} \sum_{j=1}^N |p_{8i,j} - p_{8i+1,j}| + \sum_{j=1}^{\lfloor \frac{N-1}{8} \rfloor} \sum_{i=1}^M |p_{i,8j} - p_{i,8j+1}|, \quad (2)$$

where $p_{i,j}$ denotes coordinates of pixel values on the $M \times N$ image.

As we can see from Eq. (2), the calculation operates with individual columns and rows. First, the sum of all differences between the values of the eighth and ninth row (generally the row below) is calculated. The sum is continuously accumulated for the others pair of the rows (generally the rows $8i$ and $8i+1$). Second sum that accumulates the pair of columns (generally the columns $8j$ and $8j+1$) is counted as same as previous. Finally, the two sums are added together and we get the Blockiness value.

Now we can combine methodologies, calibration and Blockiness, for detecting stegogrammes. The input image will be suspected image S_S . From the S_S we will create the calibration image S_C . Then Blockiness calculation is applied on both images. At the end we can easily compare both Blockiness values B_S and B_C to determine whether the suspect image is a stegogramme or not. If the value $B_S > B_C$ it is a stegogramme. Conversely, if the value $B_S < B_C$ it is a clear image without the embedded message.

2.3 Artificial Neural Network

Stegoclassifier is now completed. Consequently we will apply the neural network. Neural networks are inspired by biological neural networks [4]. Due to this fact, we are able to simulate a simple function of the human mind. Similar to the case of the human model, the artificial neural network (ANN) needs to gain experiences by learning. According to this experiences it will then decide – it is a set of data (inputs), for which we know the correct result (output).

In our neural network the Perceptron was used. It is one of the most used models, whose potential is defined as the weighted sum of the incoming signals (inputs). If the threshold is exceeded, it leads to excitation of the neuron (to 1), otherwise it leads to inhibition (to 0) [4]. In order to properly recognize the input values of the ANN, every neuron's weight must be correctly set. This is done by learning from training set. Our ANN is consisted from three neurons – two inputs and one output neuron as in Fig. 2. To the inputs we gave Blockiness values of the suspected and calibrated images. The output then generates a value of 1 or 0. Value 1 indicates stegogramme and value 0 indicates a clear image without any secret message.

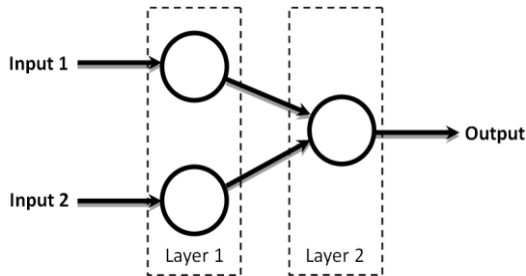


Fig. 2. Diagram of the Artificial Neural Network

3 Results and Discussion

For development and testing purposes, we create a database of color images taken with the Huawei P7 camera. The database is consisted from two parts – the testing and the training set. The testing set was designated for testing of the stegoclassifier without and with using of the ANN. The train section was prepared for the learning of the ANN. Each section contains clear images and stegogrammes created by OutGuess 2.0.

Individual's images were available in six different resolutions – 800 x 449, 1024 x 575, 1280 x 719, 1440 x 809, 2560 x 1438 and 4160 x 2336. For every resolution we prepared 100 images with message length of 200B, 100 images with message length of 600B and 100 images with message length of 1000B. For testing or training se there were 2400 images.

For comparing the detection success of the stegoclassifier without and with the use of ANN, we prepared six testing sets (one for each resolution). These sets contained 400 randomly mixed vectors – with message length of 200B (100x), with message length of 600B (100x), with message length of 100B (100x) and clear image (100x). These vectors were consisted from three values:

(Blockiness value of the suspected image, Blockiness value of the calibrated image, 0 or 1)

The third vector – value 0 indicates clear image, value 1 indicates stegogramme.

For the purpose of learning of the ANN we prepared set of 2400 randomly sorted vectors. As the stegogrammes were used images with message length of 200B, 600B and 100B for each of the six resolutions. To this set were randomly inserted vectors of clear images.

The ANN was designed in Neuroph (Java Neural Network Framework). Learning was performed with a maximum error rate ~0.06, so 6%.

Table 1 shows the success and error rates of the stegoclassifier without (column A) and with using of the ANN (column B). From the result it is clear that applying of the ANN improves success rate. Also, we can confidently say that the stegoclassifier responds better to images that have a higher resolution (approximately more than 3 MPx). During the subsequent testing, we also discovered that the success rate of detection is also dependent on the actual length of embedded message, especially in smaller resolution. For this purpose we prepared specific testing sets. Our results were statistically evaluated and proved that ANN improved the detection significantly. All statistical calculations were done in Statgraphic Centurion.

Table 1. Comparison of the stegoclassifier without (A) and with the ANN (B)

	800 x 449		1024 x 575		1280 x 719		1440 x 809		2560 x 1438		4160 x 2336	
	A	B	A	B	A	B	A	B	A	B	A	B
<i>Samples total</i>	400		400		400		400		400		400	
<i>Correct classification</i>	352	362	355	370	343	352	343	361	384	384	391	397
<i>Miss classification</i>	48	38	45	30	57	48	57	39	16	16	9	3
<i>Success rate [%]</i>	88.0	90.5	88.8	92.5	85.8	88.0	85.8	90.3	96.0	96.0	97.8	99.3
<i>Error rate [%]</i>	12.0	9.5	11.2	7.5	14.2	12.0	14.2	9.7	4.0	4.0	2.2	0.7

4 Conclusion

In this paper, we verified that the applying of the artificial neural network to existing methods of steganalysis really improved the detection capability by finding some hidden pattern in data training set. It is mainly done by the generalization of ANN, which brings it to this issue. Paradoxically, we assumed that embedded messages will be better detectable on the smaller images than the larger ones, since the modification should be easier to detect – the opposite was true. Next contribution of this implementation is the application on grayscale and colorful images too.

In the future work, we want to improve the detection capability of stegoclassifier itself (especially for smaller images) with the capability of detecting stegogrammes of the others steganography systems as F5 algorithm. We also want to include the calculation of approximate length of the message, which can be very useful for additional analysis that may lead to the discovering of the message content itself. Another extension may be an extra layer for the ANN that will distinguish which steganography algorithm that was used to embedding the message.

Acknowledgment

The following grants are acknowledged for the financial support provided for this research: Grant Agency of the Czech Republic -- GACR P103/15/06700S and partially supported by Grant of SGS No. SGS 2016/175, VSB-Technical University of Ostrava and by The Ministry of Education, Youth and Sports from the National Programme of Sustainability (NPU II) project "IT4Innovations excellence in science - LQ1602".

References

1. P. Bateman, H. G. Schaathun, Image steganography and steganalysis. Department Of Computing, Faculty of Engineering and Physical Sciences, University of Surrey, Guildford, Surrey, United Kingdom, 4th August, 2008.
2. J. Fridrich, M. Goljan, D. Hoge, Attacking the outguess. In: Proceedings of the ACM Workshop on Multimedia and Security. Juan-les-Pins, France, 2002.
3. D. Fu, Y. Q. Shi, D. Zou, G. Xuan, JPEG Steganalysis Using Empirical Transition Matrix in Block DCT Domain. In: MMSP (pp. 310-313), 2006.
4. I. Vondrák, Artificial Intelligence and Neural Networks - Umělá inteligence a neuronové sítě. 3. ed. Ostrava: VŠB – Technická univerzita Ostrava, 2009. ISBN 978-80-248-1981-5.

Polar Lines Registration via Functions of Angles in 2D LIDAR Scans

Branislav Holý

Department of Computer Science, FEECS,
VŠB – Technical University of Ostrava, 17. listopadu 15,
708 33 Ostrava – Poruba, Czech Republic
branislav.holy@vsb.cz

Abstract. Registration of LIDAR scans is an important problem in many applications that need to align two LIDAR scans optimally. A novel algorithm for registration of 2D LIDAR scans that combines two already known but different concepts has been proposed. The algorithm combines the registration of lines and the registration in polar coordinates. The main idea is a new representation of the surrounding area that makes the combination possible. The algorithm works with line segments that are expressed as functions of angles. This representation significantly decreases the computation time and enhances the resulting alignment. The algorithm has been tested with many indoor LIDAR scans and is able to align them with high accuracy and in real-time.

Keywords: registration, scan-matching, lines, lidar, transformation

1 Introduction

Over the last years, the popularity of LIDAR (Light Detection and Ranging) data is still increasing and the LIDAR technology is used in a wide range of applications. Very often, LIDAR data provide information about the surrounding area for the tasks like robot navigation, autonomous car driving, or even mapping of an unknown environment.

The main goal of LIDAR scan registration is to find the best orthonormal transformation between two LIDAR scans. The transformation has to align the scans with the best fitness. However, the LIDAR scans are only partially overlapped because they are scanned from different locations and also the correspondences between the points are unknown. These two properties make the registration problem difficult. The state-of-the-art algorithms solve this problem in different ways. Mostly, the correspondence problem is solved by searching for the closest point in the second set. The presented algorithm eliminates this problem by making use a continuous function that is defined in polar coordinates.

This paper is organized as follows. The next section contains a brief description of the previous methods. Section 3 describes every step of the new algorithm, and Section 4 shows the results of experiments. The conclusion is presented in the final section.

2 Previous Work

The most commonly used algorithm for registration of two sets of points is Iterative Closest Points (ICP) [2, 13]. There are a lot of variants of ICP [4, 7, 12]. As mentioned in [11], over 400 papers have been published about ICP and its variants. All of these ICP variants need to find the correspondences between the points by searching for the closest points in the second set. Even the use of k -D trees has the asymptotic complexity of $\mathcal{O}(n \log(n))$ to find the correspondences for all points.

The method of Cox [5] and Iterative Closest Line (ICL) [1] use linear features as well as the presented method but in a different way. The method of Cox uses lines only for the first scan but our method uses them for both scans, which improves the computation time. Searching for the corresponding lines in ICL needs n^2 iterations and in the method of Cox and mn iterations. In contrast, our new algorithm needs only n iterations because it uses polar coordinates.

Polar coordinates were used in some previous papers as well [6, 9]. The purpose is fast correspondence search ($\mathcal{O}(n)$) preserving the inclusion of all points. However, the description of the surrounding space differs from the presented one. Both earlier papers use the sets of points in polar coordinates, but the presented algorithm uses a function as a more general and continuous description of the surrounding area. This generalization allows the use of line segments as functions of angles as described below. Line segments were used in [9] as well but only for better detection of feature points, not for registration.

3 New Algorithm

The mentioned algorithms use the sets of points for the description of surrounding area. However, a set of points is too general and can contain more points that seem to be scanned in one angle. Since the LIDAR technology is able to scan only one distance in every angle, it is not necessary to use the sets of points. We can take advantage of this special property of the LIDAR scans and represent the surrounding area with a function called the LIDAR function defined as

$$\text{surrounding area} = \int_0^{2\pi} F(\varphi) d\varphi, \quad (1)$$

where the LIDAR function $F(\varphi)$ returns a distance to the closest obstacle in angle φ . The error of alignment between two LIDAR scans (F and F') can be expressed with an error function E as

$$E(\mathcal{T}) = \int_0^{2\pi} \left(F(\varphi) - \hat{F}'(\varphi) \right)^2 d\varphi, \quad (2)$$

where \hat{F}' is the transformed LIDAR function F' according to the orthonormal transformation denoted by \mathcal{T} defined as follows

$$M = \left\{ \left(\hat{\varphi}, \tilde{F}(\hat{\varphi}) \right) \right\} = \left\{ \mathcal{T} \left\{ (\varphi, F(\varphi)) \right\} \right\}, \tag{3}$$

$$N(\gamma) = \left\{ \tilde{F}(\gamma) \mid (\gamma, \tilde{F}(\gamma)) \in M \right\}, \tag{4}$$

which saves every transformed point of the LIDAR function into the set M . Since some transformed points would share the angle $\hat{\varphi}$, we need to choose only one of them that has the smallest value $\tilde{F}(\hat{\varphi})$. For this purpose, we introduce the function $N(\gamma)$ that returns the set of all distances $\tilde{F}(\gamma)$ that correspond to the chosen value of γ . The final transformed function \hat{F} is shown in (5) where we choose the min from the set returned by the function N

$$P = \left\{ \left(\hat{\varphi}, \hat{F}(\hat{\varphi}) \right) \mid \left(\hat{\varphi}, \hat{F}(\hat{\varphi}) \right) = \left(\hat{\varphi}, \min N(\hat{\varphi}) \right); \left(\hat{\varphi}, \hat{F}(\hat{\varphi}) \right) \in M \right\}. \tag{5}$$

The following conditions must be met (for small ε) to keep the order of transformed points. It also removes invisible points that seem to be scanned from the opposite side

$$\left(\hat{\varphi} + \hat{\varepsilon}, \hat{F}(\hat{\varphi} + \hat{\varepsilon}) \right) = \mathcal{T} \left\{ (\varphi + \varepsilon, F(\varphi + \varepsilon)) \right\}, \tag{6}$$

$$\varphi < \varphi + \varepsilon \iff \hat{\varphi} < \hat{\varphi} + \hat{\varepsilon}. \tag{7}$$

Unlike other environments, the indoor environments (consisting of doors, furniture, etc.) are ideal for the description of area via line segments. The presented method uses the line segments in the polar coordinate system for the fast correspondence search.

3.1 Line Segment Detection

A line detection algorithm can be used to extract the lines from the scans. Split-and-Merge algorithm [10] is suitable for this purpose. Since every line is constructed from a set of points, the first and last point define the end points of the line segment. A line in polar coordinates can be expressed as a function

$$L(\varphi) = \frac{l}{\cos(\varphi - \alpha)}, \tag{8}$$

where l is the distance from the origin and α is the angle between the normal vector of the line and the x axis. The function L returns the distance from the origin in angle φ . Since we work with the line segments, the domain is bounded by the end points A and B . After that, the LIDAR function F can be constructed of the detected line segments as a piecewise function.

3.2 Transformation

The function L is defined by two components α and l . Equation (5) transforms the components into $\hat{\alpha}$ and \hat{l} as

$$\hat{\alpha} = \alpha + \theta, \quad (9)$$

$$\hat{l} = l + t_x \cos(\alpha + \theta) + t_y \sin(\alpha + \theta), \quad (10)$$

where t_x , t_y , and φ defines the transformation \mathcal{T} in (3). The domain of the function L needs to be transformed as well via its endpoints.

3.3 Line Segment Visibility

Some transformations can make the LIDAR function invalid because the domains of partial line functions become not disjoint, or some line segments seem to be scanned from the opposite side.

In the case of not disjoint domains, an ordered set can be created from the bounds of the domains $D(L_i)$. Then it is needed to check which line segment function has the smallest value in the middle of the examined interval of two consecutive bounds. After this step, all domains $D(L_i)$ are disjoint again, which solves the problem in (4) and (5).

In the second case, line segments that seem to be scanned from the opposite side need to be rejected. These line segments can be easily found if their domain $D(\hat{L}) \in \langle a; b \rangle$ meets the condition $a > b$ as described in (6) and (7).

3.4 Error of Alignment

The partial error $e_i(\mathcal{T})$ of two corresponding line segments L_i and \hat{L}'_i can be computed within the $\langle \bar{a}_i; \bar{b}_i \rangle$ interval where both functions are defined where $\bar{a}_i = \max(a_i, \hat{a}'_i)$ and $\bar{b}_i = \min(b_i, \hat{b}'_i)$. The final error (2) is then defined as

$$e_i(\mathcal{T}) = \int_{\bar{a}_i}^{\bar{b}_i} \left(L_i(\varphi) - \hat{L}'_i(\varphi) \right)^2 d\varphi, \quad (11)$$

$$E(\mathcal{T}) = \sum_{i=0}^n e_i(\mathcal{T}). \quad (12)$$

3.5 Minimization

To minimize (11), the method of gradient descent can be used. The values of gradient can be computed analytically as partial derivatives of the expression in (11). It is necessary to transform the LIDAR function in every iteration of gradient descent and compute the most accurate gradient value at $(0, 0, 0)$.

4 Results

The algorithm has been tested with many indoor datasets. Every test has compared the proposed method against PSM [6] and two variants of ICP (TrICP [11] and Sparse-ICP [3]). The results of Intel Reserach Lab dataset [8] are presented.

Figure 1 shows one of the results of registration of all compared scan matching algorithms. We used the first 1,700 scans to create the loop around the center of Intel Research Lab.

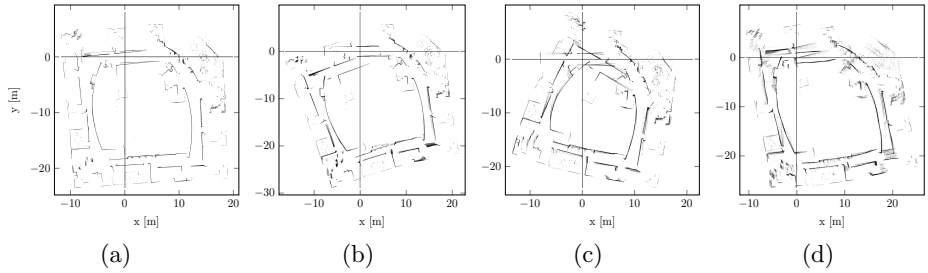


Fig. 1. The result of the first 1,700 scans aligned by the presented algorithm (a), Sparse-ICP (b), TrICP (c), and PSM (d).

The cumulated location and orientation errors are shown in Fig. 2. The algorithms were compared with MSE and the computation time as well. Our algorithm achieved the smallest MSE (0.732), Sparse-ICP (1.044), TrICP (2.06), and PSM (2.93). PSM has the lowest computation time (1.95 ms), our algorithm (2.11 ms), TrICP (10.43 ms), and Sparse-ICP (81.75 ms).

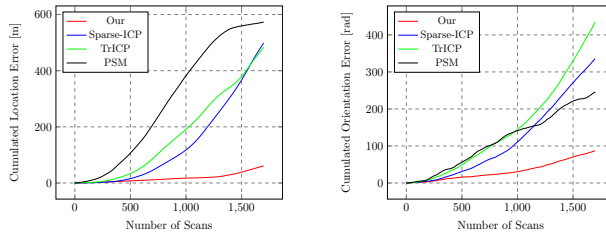


Fig. 2. The comparison of cumulated errors between the estimated and correct locations and orientations for all tested algorithms.

5 Conclusion

A novel algorithm for registration of LIDAR scans has been presented. The algorithm is based on line segments described as functions in polar coordinates.

This new representation brings a better final alignment and lower computation time. As experiments proved, the presented algorithm is accurate and fast. Future works will focus on a 3D variant of the algorithm that could bring even better improvements in the computation time and alignment.

Acknowledgements

This work was partially supported by the Grant of SGS No. SP2016/58, VŠB - Technical University of Ostrava, Czech Republic.

Author's Publications

More details are available in the original paper: Holý B.: Registration of Lines in 2D LIDAR Scans via Functions of Angles. In 4th IFAC Conference on Intelligent Control and Automation Sciences, ICONS 2016, Reims, France, 1-3 June 2016.

References

1. Alshawa, M.: Icl: Iterative closest line. *Ekscentar* (10) (2007)
2. Besl, P.J., McKay, N.D.: A method for registration of 3-d shapes. *IEEE Transactions on Pattern Analysis and Machine Intelligence* 14(2), 239–256 (1992)
3. Bouaziz, S., Tagliasacchi, A., Pauly, M.: Sparse iterative closest point. In: *Computer graphics forum*. vol. 32, pp. 113–123. Wiley Online Library (2013)
4. Chetverikov, D., Svirko, D., Stepanov, D., Krsek, P.: The trimmed iterative closest point algorithm. In: *Pattern Recognition, 2002. Proceedings. 16th International Conference on*. vol. 3, pp. 545–548. IEEE (2002)
5. Cox, I.J.: Blanche-an experiment in guidance and navigation of an autonomous robot vehicle. *Robotics and Automation, IEEE Transactions on* 7(2), 193–204 (1991)
6. Diosi, A., Kleeman, L.: Laser scan matching in polar coordinates with application to slam. In: *Intelligent Robots and Systems, 2005.(IROS 2005). 2005 IEEE/RSJ International Conference on*. pp. 3317–3322. IEEE (2005)
7. Fitzgibbon, A.W.: Robust registration of 2d and 3d point sets. *Image and Vision Computing* 21(13), 1145–1153 (2003)
8. Haehnel, D.: Intel reserach lab dataset (2000), <http://www2.informatik.uni-freiburg.de/~stachnis/datasets.html>
9. Lingemann, K., Nüchter, A., Hertzberg, J., Surmann, H.: High-speed laser localization for mobile robots. *Robotics and autonomous systems* 51(4), 275–296 (2005)
10. Pavlidis, T., Horowitz, S.L.: Segmentation of plane curves. *IEEE transactions on Computers* (8), 860–870 (1974)
11. Pomerleau, F., Colas, F., Siegwart, R., Magnenat, S.: Comparing ICP Variants on Real-World Data Sets. *Autonomous Robots* 34(3), 133–148 (Feb 2013)
12. Segal, A., Haehnel, D., Thrun, S.: Generalized-icp. In: *Robotics: Science and Systems*. vol. 2 (2009)
13. Zhang, Z.: On local matching of free-form curves. In: *BMVC92*, pp. 347–356. Springer (1992)

Practical NFC Reader Design and the Electromagnetic Interference Measurement

Josef Hrabal

Department of Computer Science, FEECS,
VŠB – Technical University of Ostrava, 17. listopadu 15,
708 33 Ostrava – Poruba, Czech Republic
`josef.hrabal@vsb.cz`

Abstract. This paper is focused on electromagnetic interferences of an experimental NFC reader. The design, implementation and verification is presented in the first part. Proper implementation of a NFC reader usually requires expensive equipment like vector network analyzer (VNA). This paper describes an alternative way of the reader design using only an oscilloscope and presents an evaluation of its parameters, including measurement of possible electromagnetic interferences.

Keywords: NFC, Near-field communication, EMC, electromagnetic compatibility, EMI, electromagnetic interference, antenna matching, Q-factor

1 Introduction

Near-field communication (NFC) is the most common *Radio-frequency identification* (RFID) technology of these days. The NFC can be found almost everywhere: access control, tracking and identification, payment and stored-value systems, anti-counterfeiting, etc. It is also used for secure data exchange. We have introduced a novel NFC reader design which is described in this article.

2 Near Field Communication

The NFC is one of many new RFID technologies, which are starting to replace the older *Low Frequency RFID* specification, also known as 125 kHz RFID or just RFID. The NFC, unlike the RFID, offers many additional features, such as bidirectional communication or data and transfer encryption, which greatly extends possible areas of its application.

The NFC operates at 13.56 MHz and uses an inductive coupling to communicate. This type of communication require induction coils of a defined size implemented as a part of the antenna. An information is then transferred through changes in the magnetic field between pair of the antennas.

There are two modes of communication: active and passive. In active mode both devices use their own self-generated RF field to enable the communication, this is the standard peer-to-peer communication. For the passive communication mode the initiator generates the RF field and the target answers in a load

modulation scheme. In this case, the target is powered from the magnetic field supplied by the initiator and does not require its own power source. The passive mode is used in smart cards and tags, where is space for conventional energy source is limited or is this type of energy source is not desired. The need to supply the target with power makes well-designed NFC antenna crucial for optimal performance of the data transfers.[3]

3 NFC reader topology and design

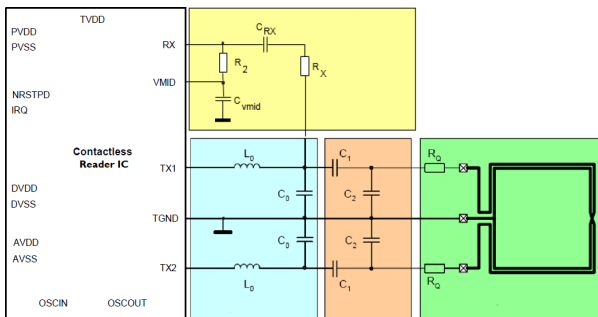


Fig. 1. NFC reader topology [4]

The parts of the NFC reader are depicted in Figure 1. Its main component is the contactless reader *integrated circuit* (IC). We have chosen a modern NFC controller PN532 from NXP Semiconductors.[5] The signal from the controller is then fed into the *electromagnetic compatibility* (EMC) filter (cyan color) which has two functions: signal shaper and harmonic frequency filter. After the signal is shaped, it must be matched to the antenna impedance by the matching circuit (red color). The impedance of the controller is selected from 35Ω to 80Ω and antenna (green color) must be tuned to the same impedance. The last one is the receiver circuit (yellow color) which brings the received signal to the controller. Design of these components will be described in the following chapters.

3.1 Antenna design

An antenna coil can be designed in many shapes. In the most cases it has circular or rectangular shape, but combination of shapes is possible; it mostly depends on a particular application [1]. In our case we had to fit the NFC reader circuits together with antenna coil on single *printed circuit board* (PCB). Dimensions of the PCB corresponds to a standard electrical installation box with many drills and holes. Diameter of this box is only 73 mm, thus some compromises had to be made.

The size of the antenna coil depends on the desired communication distance which generally rises with larger dimensions of the antenna [4]. In the first design

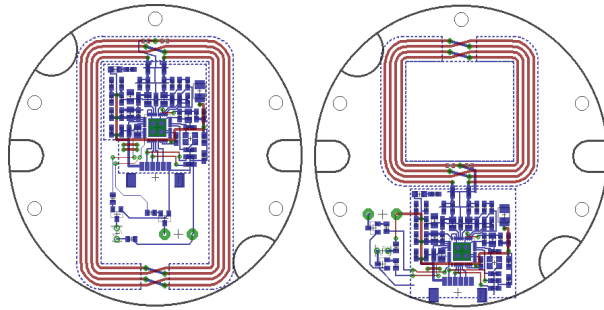


Fig. 2. Possible NFC PCB design

(Figure 2 left) we made the antenna coil as large as possible and the reader circuit was placed in the middle of the coil. However this design isn't generally the best one. If the reader circuit is placed very near to the antenna, the alternating magnetic field generates eddy currents. These eddy currents absorb power and lead to detuning of the antenna and to decrease of the communication distance [2]. Moreover, it can interfere with the reader circuit and cause disturbances in its functionality.

Because of these possible negative effects of the first design, we decided to make another one and minimize the negative influence of the antenna coil towards the reader circuit and vice versa. Due to the limitation of the PCB dimensions the size of the antenna had to be reduced, otherwise it would not be possible to separate the antenna coil and the reader circuit. The result of the second design is depicted in Figure 2 right.

3.2 EMC filter

The main purpose of the EMC filter is to suppress an unwanted harmonic frequencies. It is therefore a lowpass filter with a cutoff frequency near to the upper sideband frequency determined by the highest data rate in the system. The carrier frequency is 13.56 MHz and the subcarrier frequency is 848 kHz which gives the filter cutoff frequency 14.408 MHz. According to [2] the inductor L_0 is chosen from values between 390 nH and 1000 nH. Then the capacitor C_0 can be determined by equation 1:

$$C_0 = \frac{1}{(2 \cdot \pi \cdot f_{r0})^2 \cdot L_0} \quad (1)$$

where:

C_0	Capacitance in F
f_{r0}	Cutoff frequency in Hz
L_0	Inductance of chosen inductor in H

For example: with inductor $L_0 = 560 \text{ nH}$ we calculate $C_0 = 218 \text{ pF}$. A nearest capacitor in the series is 220 pF.

3.3 Matching circuit

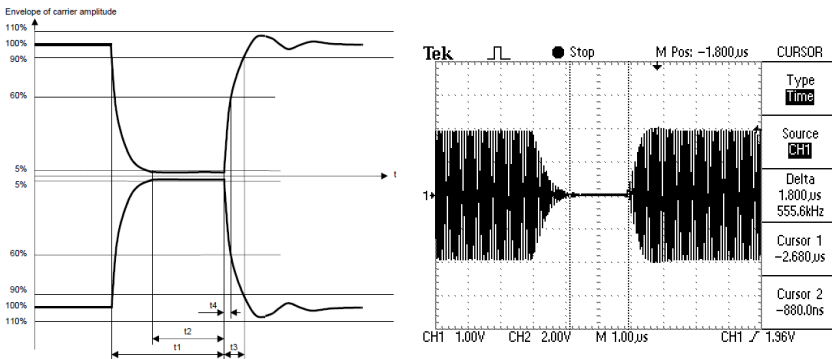
For a proper antenna matching circuit calculations it is necessary to determine the parameters of the antenna. The main parameters of the antenna is inductance, capacitance and resistance. The best way to do this is to use a *vector network analyzer* (VNA). The VNA can measure the antenna parameters with ease, but it isn't a common lab equipment due to its price.

In our project we decided to do the impedance matching without the VNA, only with the help of an oscilloscope. The inductance of the antenna coil must be calculated as the first. These calculations are described in [6]. Our antennas are composed of 4 turns of the wire, where each turn has 4 segments. Because of the rectangular shape of the antenna, each pair of two opposite segments is the same; 8 calculations are needed in total.

The calculated inductance of our antennas is 1655 nH for the first antenna and 1097 nH for the second antenna designed. The capacitors C_1 and C_2 can be now calculated using a spreadsheet described in [8]. The capacitor C_1 relies only on EMC filter components, which are known, and on antenna inductance calculated before. In our case it is 26 pF and 33 pF . The second capacitor C_2 depends also on capacitance of the antenna coil, which is unknown. The typical capacitance value is between 3 pF and 30 pF [2]. We recommend the use of capacity 30 pF which result in lower computed C_2 . [7]

All components are now known and the antenna matching can be carried out. For the matching purposes capacitance trimmer is connected parallel to C_2 . The PN532 circuit is put into operation so that its output produces a continuous signal. The oscilloscope probe is connected to the antenna and the peak-to-peak voltage is measured. The capacitance trimmer is then slowly rotated until the maximum voltage using the oscilloscope. Now the antenna is matched.

3.4 Quality factor



a) Measurement points [2]

b) Measurement example

Fig. 3. Q-factor measurement

Because resistance of the antenna wasn't measured, the *quality factor* (Q-factor) verification is needed and a damping resistor R_Q must be added eventually. The Q-factor can be checked by using the fact that the Q-factor has a direct influence on the edges of the modulation shape. The PN532 controller is switched into a *RF Regulation Test* mode.[5] The loop with the ground is used on the oscilloscope probe to enable inductive signal coupling and the probe is hold close to the antenna coil. The measurement points are depicted in Figure 3a and the example of the oscilloscope data is shown in Figure 3b.

	$t_1 [\mu s]$	$t_2 [\mu s]$	$t_3 [\mu s]$	$t_4 [\mu s]$
Limit values	2 – 3	0.5 – t_1	0 – 1.5	0 – 0.4
Antenna 1	2.96	1.84	0.86	0.28
Antenna 2	2.94	0.62	0.2	0.1

Table 1. Q-factor measurement

The measured data are in Table 1. It is evident that neither one antenna exceeded the limits and therefore no additional damping resistor is required. [2]

3.5 Receiver circuit

The receiver circuit consist of a resistor divider which adjust voltage from the antenna to input of the PN532 controller. According to [5] the input voltage level is specified as $1 V_{p-p}$ in idle state of the reader. The predefined parts are: $C_{RX} = 1 nF$, $C_{vmid} = 100 nF$, $R_2 = 1 k\Omega$ and R_X must be calculated by Equation 2:

$$R_X = R_2 \cdot \left(\frac{U_{C0}}{U_{RX}} - 1 \right) \quad (2)$$

where:

R_X	Calculated resistor in Ω
R_2	Predefined resistor in Ω
U_{C0}	Voltage in junction of L_0 , C_0 and C_1 in V
U_{RX}	Target voltage in V

4 Electromagnetic interference measurements

The EMC is a property of the electrical equipment based on the fact, that it doesn't affect the other object including itself and that it is resistant to the other devices. The EMC is divided into two subcategories: *electromagnetic interference* (EMI) and *electromagnetic susceptibility* (EMS). The EMI was measured in EMC laboratory equipped with the GtemCell-400 and the AFJ Instruments FFT 3000. The equipment lacks proper calibration and the results have only informative character.

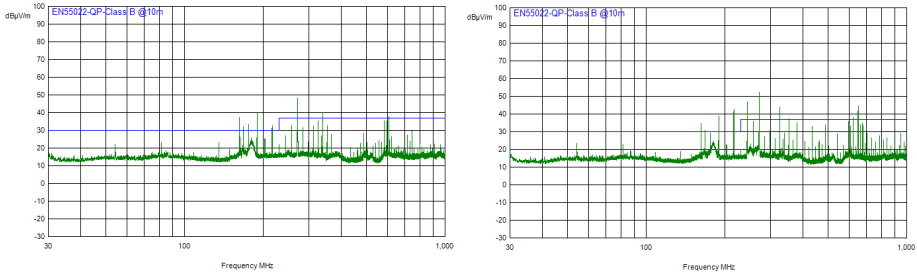


Fig. 4. EMI measurements

Figure 4 shows results of EMI measurement. As can be seen, both designs exceeds limits showed as a blue line. Although the first design have the worst component placement with more room for possible interferences, the EMI measurement proved that these hypotheses were false

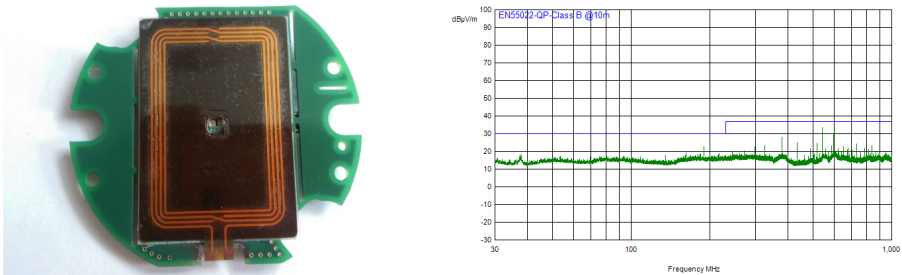


Fig. 5. Modified design and EMI measurement

Because neither antenna design meets the EMI limits, we decided to make another design with added shielding between the PCB layers and to isolate the antenna coil with a ferrite polymer. This NFC reader design is depicted in left side of Figure 5. After the proper circuits matching the EMI was measured (Figure 5 right). This modified design passes the EMI measurements without exceeding the blue limit line.

5 Conclusion

In this paper we have shown that it is possible to create a correct NFC reader design even with the basic lab equipment. We have designed in total three NFC reader circuits. All these designs were implemented and their communication ability was tested. The first and the last design have almost the same reading distance of 4 cm for a standard NFC smart card. The design with the smallest antenna coil has reading distance of just about 2.5 cm. The size of the antenna

coil is therefore very important. Even though the performance of the first and the third design is satisfactory, without proper shielding and antenna coil isolation the EMI requirements cannot be met.

References

1. Lee, B., Kim, B., Harackiewicz, F.J., Mun, B., Lee, H. 2014, "NFC antenna design for low-permeability ferromagnetic material", IEEE Antennas and Wireless Propagation Letters, vol. 13, pp. 59-62.
2. NXP Semiconductors. "Antenna design guide for MFRC52x, PN51x and PN53x" AN1445, Rev 1.2, 2010
3. ST Microelectronics. "NFC guide" TN1216, Rev 1, June 2015
4. NXP Semiconductors. "NFC Reader Design: Antenna design considerations" MobileKnowledge, February 2015
5. NXP Semiconductors. "NFC controller PN532/C1" Datasheet, Rev 1.2, 2011
6. Microchip Technology Inc. "Antenna Circuit Design for RFID Applications" AN710, 2003
7. Gebhart, M. "RF Basics and Components - Loop Antennas" 2013 [Online]. Available: <http://rfid-systems.at/> [Accessed Aug. 3, 2016]
8. NXP Semiconductors. "Directly matched antenna design" Excel sheet AN11246, Ver. 1.0

Clustering using Ensemble of GMM

Jan Janoušek

Department of Computer Science, FEECS,
VŠB – Technical University of Ostrava, 17. listopadu 15,
708 33 Ostrava – Poruba, Czech Republic
jan.janousek@vsb.cz

Abstract. Ensemble methods are widely used in the area of classification and regression, but not that often in the area of clustering. This article describes a new ensemble clustering algorithm based on Cluster Forest (CF) [1] that internally uses a probabilistic model called Gaussian Mixture Model (GMM). The proposed ensemble clustering algorithm was compared with several different approaches and tested on eight datasets. The final results show that proposed variant of the algorithm can provide noticeably better results than the original algorithm and other ensemble clustering methods.

Keywords: ensemble clustering, Cluster Forest, clustering, Gaussian Mixture

1 Introduction

Clustering belongs to unsupervised learning techniques, hence there is not information on classes. Several clustering algorithms were developed in the past years, and one of the best known is called k -means [2] which is very popular due to its small computation time and usually sufficient results. K -means can be seen as a special case of the more robust clustering method called *Gaussian Mixture Model clustering* [3].

This article is primarily focused on *ensemble* methods, more precisely on its representative called Cluster Forest, that is inspired by Random Forests (RF) [4], that is commonly used for classification and regression.

A new modification of CF is introduced in this paper. It utilizes Gaussian Mixture Model that replaces k -means clustering algorithm used within standard CF.

2 Cluster Forest algorithm

As it was already mentioned, Cluster Forest was inspired by Random Forests algorithm. Both algorithms can be divided into two main phases. The first phase covers an application of multiple weak learners (base clustering/classification algorithms). Particular application results in assignment of input points to clusters. Then, all the assignments are aggregated in the second phase of the algorithm.

The original CF uses k -means in the second phase. There exists a hidden constraint that weak learners must not produce the same assignments. Otherwise, the aggregation does not bring any additional information. This is the main disadvantage of k -means algorithm whose frequent application produces almost the same results. In RF, the mentioned problem is solved using bagging and random selection of features. CF solves this problem using the *clustering vector growing method* (CVG) shown in Algorithm 1. Here, the Cluster vector is a subset of features used for clustering, hence it will be called the *feature vector*. In the first step of CVG, the feature vector is initialized with n randomly selected features. Then, k -means algorithm is applied and quality ρ of obtained clustering is evaluated using Formula 1, where c is result of the k -means clustering (positions of cluster centers), SS_w [5] is the within cluster sum of squares and SS_b [5] is the between cluster sum of squares.

$$\rho(c) = \frac{SS_w(c)}{SS_b(c)} \quad (1)$$

After this, other n features are selected randomly and merged with the previous feature vector. k -means algorithm is applied to this temporary created vector and if the quality of obtained clustering is higher, then the previous feature vector is replaced by the new one.

All features are selected randomly in each step. This can lead to poor selection if the data contains only a small number of significant features. To solve this problem, feature competition is used for feature vector initialization. In this procedure, the base clustering algorithm is applied to multiple randomly selected feature subsets. And subset with the highest quality is selected as initial vector.

The output of the CVG described above is represented by the final feature vector and related clustering. This clustering is equivalent to a single tree in the RF algorithm. The algorithm must be executed multiple times to build the set of clusterings.

In the second phase, all results of the weak learners are aggregated. Spectral clustering [6] was selected as an optimal aggregation method, that is based on the spectral graph theory. Clustering can be viewed as partitioning a similarity graph (fully connected weighted graph where nodes represents input data and edge weights are equal to data similarity). Spectral clustering tries to split graph nodes into two groups using the algorithm called *Normalized cut* [6].

Normalized cut algorithm is applied on the matrix D which elements are obtained using formula 2. This formula describes clustering aggregation, where c_t returns a cluster index to which a point j was assigned to in the iteration t .

$$D_{ij} = \exp\left(\frac{1}{T} \sum_{t=1}^T \begin{cases} 1 & \text{if } c_t(i) = c_t(j) \\ 0 & \text{otherwise} \end{cases}\right) \quad (2)$$

where $i, j \in \{1, \dots, n\}$, and T is the total number of iterations.

Obtained matrix is regularized using thresholding, when element D_{ij} is set to zero, if it is less than configuration parameter β with value in interval $(0, 1]$.

Algorithm 1 Cluster vector growing method

Require:

f : list of all features
sampleFeatures: randomly sample n features
KMeans: k -means clustering

```

1:  $iter = 0$ 
2:  $v = \text{featureCompetition}(f)$ 
3:  $clustering_{old} = \text{KMeans}(v)$ 
4: while  $iter < iter_{max}$  do
5:    $iter = iter + 1$ 
6:    $v_{tmp} = \text{sampleFeatures}(f)$ 
7:    $clustering_{new} = \text{KMeans}(v_{tmp})$ 
8:   if  $\rho(clustering_{old}) > \rho(clustering_{new})$  then
9:      $v = v_{tmp}$ 
10:     $clustering_{old} = clustering_{new}$ 
11:     $iter = 0$ 
12:   end if
13: end while

```

After this, all elements of matrix D are scaled using $D_{ij} = \exp(\gamma D_{ij})$, where γ is a configuration parameter with the value in interval $[0, 1]$. β was set to 0.1, and γ to 0.4 in this article just to compare the reference results of experiments.

When eigendecomposition of the matrix D is solved, the eigenvector v_2 with the second smallest eigenvalue is used to split the point set into two subsets using Formula 3.

$$S_1 = \{i : v_{2i} > 0\}, S_2 = \{i : v_{2i} \leq 0\} \quad (3)$$

where v_{2i} is the i -th element of vector v_2 , and $i \in \{1, \dots, n\}$. This algorithm is applied recursively until the number of parts is not equal to the required number of clusters.

In the modified version of the proposed algorithm, k -means was substituted by clustering with Gaussian Mixture Model initialized with k -means algorithm. The metric describing quality of clustering in Formula 1 was replaced with maximum log-likelihood.

3 Gaussian Mixture Model Clustering

Gaussian Mixture Model (GMM)[7] is a probabilistic model based on *Gaussian distribution*. Mixture models describes the probability distribution of observations in the overall population. In case of GMM, this distribution is a multivariate Gaussian. GMM is formally defined as:

$$p(x|\alpha, M, S) = \sum_{i=1}^n \alpha_i * p(x|\mu_i, \Sigma_i) \quad (4)$$

where x is a vector of particular observation, n is the number of sub-populations, α is a vector of mixture proportions (i.e. the probability, that a randomly selected observation was generated from the i -th sub-population), M is a set of mean vectors, S is a set of covariance matrices, i -th mean vector $\mu_i \in M$, i -th covariance matrix $\Sigma_i \in S$, and $p(x|\mu_i, \Sigma_i)$ is a *Probability density function* (PDF) of Gaussian distribution, defined as:

$$p(x|\mu, \Sigma) = \frac{1}{(2\pi)^{\frac{d}{2}} \det(\Sigma)^{\frac{1}{2}}} \exp\left(-\frac{1}{2}(x - \mu)^T \Sigma^{-1}(x - \mu)\right) \quad (5)$$

where x , Σ and μ have the same meaning like in Formula 4 and d is the dimension of the observation vector x .

GMM is often used for clustering. For this purpose, every cluster represents one sub-population. This sub-population is described using mean vector μ and covariance matrix Σ . The goal of the clustering process is to estimate corresponding parameters for each cluster. Particular observation is assigned to the cluster based on the probability that it has been generated from distribution is represented by the cluster. This probability is computed for each cluster using Formula 6.

$$p(x|\alpha, \mu, \Sigma) = \alpha * p(x|\mu, \Sigma) \quad (6)$$

The clustering will be equivalent to k -means, if Σ is set as identity matrix and mixture proportions will be the same for all clusters.

In our experiment we used standard Expectation-maximization (EM)[8] algorithm to estimate parameters of GMM.

4 Experiments

Eight freely available dataset from UC Irvine Machine Learning Repository [9] were used in our experiments (see Table 1). Moreover, these datasets were chosen for purposes of further comparison with the original version of the algorithm that was already published [1].

Table 1. Data collections

Dataset	Abbr.	Instances	Features	Classes
Statlog (Heart)	Heart	270	13	2
Image Segmentation	ImgSeg	2100	19	7
Madelon	Madelon	2000	500	2
Robot Execution Failures	Robot	164	90	5
Soybean	Soybean	47	35	4
SPECT Heart	SPECT	267	22	2
Wine	Wine	178	13	3
Breast Cancer Wisconsin	Breast	569	30	2

Two main experiments were performed. The results achieved by the Gaussian Mixture Model Cluster Forest (GMM-CF) method were compared with the

results made by the original CF and others clustering methods during the first experiment. The second experiment revealed an impact of different number of clusterings on the quality of the final clustering.

There exists a lot of metrics that can be used for clustering quality comparison. Two metrics based on classification performance were used. The first metric is ρ_r :

$$\rho_r = \frac{\sum_{i=1}^N \sum_{j=1}^N \sigma(O_i, O_j) \sigma(A_i, A_j)}{N(N-1)} \quad i \neq j \tag{7}$$

where σ is the function that returns 1 if the values of both attributes are the same, 0 otherwise. O is the vector of the original (expected) classes and A is the vector of assigned classes. N is the number of classified vectors. This metric is based on an assumption that all possible pairs of vectors that have the same class in the original class vector, should have the same class in the assigned class vector. The second metric is ρ_c :

$$\rho_c = \max_{\tau \subset T} \left\{ \frac{1}{N} \sum_{i=0}^N \sigma(\tau(O_i), A_i) \right\} \tag{8}$$

where T is the set of all class permutations. σ , O_i and A_i have the same meaning like in Formula 7. This metric is equivalent to the standard classification accuracy. For both metrics, the higher value the better result.

There are results of comparisons between cluster forest based on GMM with the original cluster forest and standard clustering methods like k -means and three others ensemble methods called *bagged clustering* (bC2) [10], *evidence accumulation* (EA) [11] and *random projection* (RP) [12] in Tables 2 and 3. All results for bC2, EA and RP are taken from the paper [1].

From Table 2 can be seen that GMM-CF outperforms the other clustering methods including the original version of CF in all but one cases for metric ρ_r . In Table 3, there are results for metric ρ_c , where GMM-CF outperforms other algorithms in 7 of 8 cases.

Table 2. Comparison of results for metric ρ_r

	GMM-CF	CF	GMM	k -means	bC2	EA	RP
Heart	68.45	56.8	50.03	47.3	51.50	53.20	52.41
ImgSeg	81.05	79.71	58.18	23.61	82.19	85.75	85.88
Madelon	50.92	50.76	49.97	49.98	49.98	49.98	50.82
Robot	71.87	63.42	51.86	53.26	39.76	58.31	41.52
Soybean	96.96	92.36	82.05	85.14	83.16	86.48	87.04
SPECT	58.92	56.78	52.79	49.22	50.61	51.04	49.89
Wine	94.19	79.7	82.52	32.05	71.97	71.86	71.94
Breast	86.47	79.66	82.51	82.14	74.87	75.04	74.89

Table 3. Comparison of results for metric ρ_c

	GMM-CF	CF	GMM	k -means	bC2	EA	RP
Heart	80.43	68.26	53.33	57.3	59.10	59.26	60.54
ImgSeg	48.60	48.24	28.71	43.42	49.91	51.30	47.71
Madelon	55.75	55.12	50.01	51.73	50.20	50.30	55.19
Robot	47.62	41.2	51.86	42.05	35.37	37.19	35.50
Soybean	96.38	84.43	70.21	82.142	72.34	76.59	71.83
SPECT	70.60	68.02	62.17	55.9	56.28	56.55	61.11
Wine	95.70	79.19	84.83	46.53	70.22	70.22	70.79
Breast	92.71	88.7	90.33	82.142	85.38	85.41	70.79

5 Conclusion

The improved variant of CF algorithm that utilizing GMM model was described in this article. The presented algorithm *GMM-CF* brought the best results in seven from eight examples. In case of *ImgSeg* dataset, Random Projection (RP) brought better results in ρ_r , while Evidence Accumulation (EA) has the highest value of ρ_c on the same dataset.

References

1. D. Yan, A. Chen, and M. I. Jordan, "Cluster Forests," *ArXiv e-prints*, Apr. 2011.
2. J. A. Hartigan and M. A. Wong, "Algorithm AS 136: A k-means clustering algorithm," *Applied Statistics*, vol. 28, no. 1, pp. 100–108, 1979.
3. M.-S. Yang, C.-Y. Lai, and C.-Y. Lin, "A robust {EM} clustering algorithm for Gaussian mixture models," *Pattern Recognition*, vol. 45, no. 11, pp. 3950 – 3961, 2012.
4. L. Breiman, "Random forests," *Machine Learning*, vol. 45, no. 1, pp. 5–32, 2001. [Online]. Available: <http://dx.doi.org/10.1023/A:1010933404324>
5. M. Halkidi, Y. Batistakis, and M. Vazirgiannis, "Clustering validity checking methods: part ii," *ACM Sigmod Record*, vol. 31, no. 3, pp. 19–27, 2002.
6. J. Shi and J. Malik, "Normalized cuts and image segmentation," in *Computer Vision and Pattern Recognition, 1997. Proceedings., 1997 IEEE Computer Society Conference on*, Jun 1997, pp. 731–737.
7. J.-M. Marin, K. Mengersen, and C. P. Robert, "Bayesian modelling and inference on mixtures of distributions," *Handbook of statistics*, vol. 25, no. 16, pp. 459–507, 2005.
8. M.-S. Yang, C.-Y. Lai, and C.-Y. Lin, "A robust {EM} clustering algorithm for Gaussian mixture models," *Pattern Recognition*, vol. 45, no. 11, pp. 3950 – 3961, 2012.
9. M. Lichman, "UCI machine learning repository," 2015. [Online]. Available: <http://archive.ics.uci.edu/ml>
10. S. Dudoit and J. Fridlyand, "Bagging to improve the accuracy of a clustering procedure," *Bioinformatics*, vol. 19, no. 9, pp. 1090–1099, 2003.
11. A. L. N. Fred and A. K. Jain, "Data clustering using evidence accumulation," 2002, pp. 276–280.
12. X. Z. Fern and C. E. Brodley, "Random projection for high dimensional data clustering: A cluster ensemble approach," 2003, pp. 186–193.

Classification of Astroinformatic Big Data by Means of Analytic Programming

Lumír Kojecký

Department of Computer Science, FEECS,
VŠB – Technical University of Ostrava, 17. listopadu 15,
708 33 Ostrava – Poruba, Czech Republic
lumir.kojecky@vsb.cz

Abstract. This article describes our initial experiments of automatic classification of Be stars in large astrophysical archives. With enormous amount of stellar data it is no longer feasible to analyze it using classical approaches and therefore we introduce an alternative classification approach based on evolutionary synthesis of the stellar spectra by means of Analytic Programming. This approach is able to synthesize a mathematical formula that approximates class-representative spectra samples. As a result is then chosen a class whose representative approximated formula is the most similar to the particular spectrum.

Keywords: Be stars, stellar spectra, Analytic Programming, SOMA, Open MPI

1 Introduction

The goal of a data classification is to find patterns in the data and translate them into useful information. One of many classification problems in astrophysics is classification of Be stars [2, 1]. Be stars are hot and rapidly rotating B-type stars with equatorial gaseous disk producing prominent emission lines of different shapes (Fig. 1) in their spectrum. Classification of Be stars is based on the shape recognition of these emission lines.

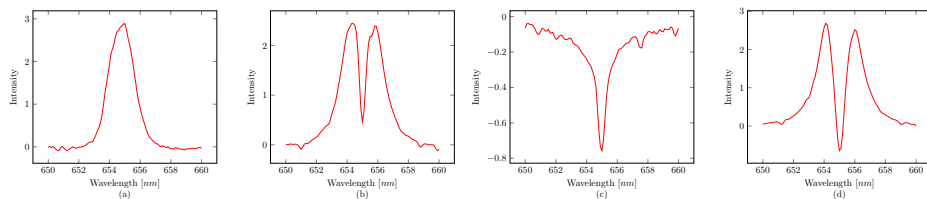


Fig. 1. Example of selected data samples typical for each class. In class 1 (a) there is a pure emission. Class 2 (b) contains a small absorption part. In class 3 (c) there is a pure absorption part. Class 4 (d) consists of a larger absorption part.

Since technological progress is causing data avalanche in almost all sciences, including astrophysics, it is no longer feasible to classify the data using classical approaches. This article focuses on evolutionary synthesis of Be stars based on typical shapes of their emission lines by means of Analytic Programming. The results show us that this approach is able to identify different shapes of the spectra and classify them.

2 Used Methods

2.1 Analytic Programming

Analytic Programming [8], as well as Genetic Programming [4] or Grammatical Evolution [6], is one of methods of symbolic regression, process of composition of simple elements into more complex units – programs. The elements, placed in General Functional Set (GFS), can be represented by mathematical operators, functions, variables or constants and can be composed into mathematical expressions. Purpose of AP is to find the most suitable mathematical expression to best approximate an input data.

Process of AP is visualized in Fig. 2. At the input there is a set of numbers-indexes to the GFS. The output consists of an expression that is composed of elements indexed at the input. Arguments of each element are substituted in FIFO order in form of next indexed elements. Finally, the output expression quality is evaluated by its comparison with the input data (1). It is obvious that to find the most suitable expression we need to find the best input number set.

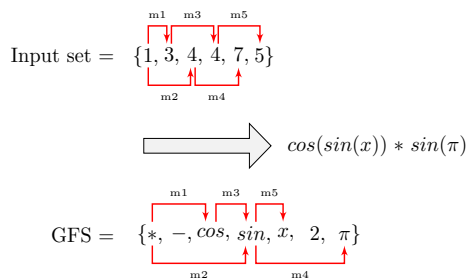


Fig. 2. Main Principle of AP

$$\sum_1^n |data_i - synthesized_data_i| \tag{1}$$

2.2 SOMA

To find the best input set it is not feasible to simply generate and evaluate all input combinations, thus we need to use an optimization algorithm. For AP

purposes it is possible to use an arbitrary evolutionary algorithm like Differential Evolution [7], Particle Swarm Optimization [3] or Self Organizing Migrating Algorithm [5]. SOMA is a stochastic optimization algorithm based on vector operations, imitating the social behavior of cooperating individuals looking for the best food source. Quality of the food source is determined by so-called cost function f_{cost} .

SOMA starts with randomly initialized population of individuals (points in n -dimensional space) evaluated by f_{cost} . In each migration loop is chosen the leader – an individual with the best cost value. All other individuals move through the space towards the leader, seeking their best position with the best cost value. The movement towards the leader in allowed dimensions is also controlled by creation of binary perturbation vector – individuals don't move towards the leader directly and thus probability of finding the global minimum increases.

2.3 Parallel Version of SOMA

There are two ways how to handle constants in AP. The first approach is to add many randomly generated constants into GFS and handle them as terminals. This approach increases cardinality of GFS and the number of all possible generated expressions. The second approach adds only one general constant (called K) into GFS. At the time of an expression composition, the constant is indexed as the K_1, K_2, \dots, K_n and values of used constants are estimated by means of secondary evolutionary algorithm.

With the constant estimation, the whole process becomes unfortunately too slow on a single computer (> 30 hours) and therefore this algorithm was implemented in Open MPI, one of the most widespread programming architecture, to reduce the computational time. Since the evaluation time of each individual is generally different (each expression can consist of different number of constants), we implemented a master-slave load balancing algorithm where the master rank distributes the work to slave ranks to evaluate each individual.

3 Stellar Data Classification

The stellar data is downloaded from the archive of the Astronomical Institute of the Academy of Sciences of the Czech Republic in Ondřejov. The downloaded data consists 1564 sample spectra, manually divided into four classes (Fig. 1), containing 177, 172, 1159 and 56 samples. The data represents dependency of the light intensity on light wavelength.

3.1 Data Preprocessing

Although each spectrum is given by 1863 equidistant points, the characteristic part lies in 100-point area and the remaining part can be considered as noise and omitted to save the computational time. Considering our previous results, AP provided the best performance on interval $[-1; 1]$ and therefore all spectra

were normalized to this interval. All spectra intensities were also shifted to have its non-characteristic part around zero. Visual observation of the spectra showed us that each spectrum has its peak on different wavelength and thus the peak was shifted to the same wavelength.

For each class was created 20 class-representative spectra by taking 5 % of the particular class spectra as the input. For each wavelength was calculated average of all intensities and placed as the output value. This process (visualized in Fig. 5) reduces noise and also computational time.

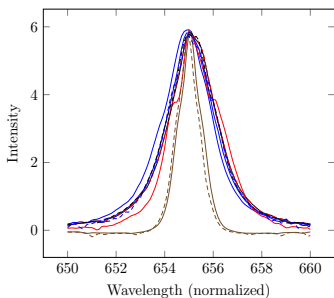


Fig. 3. 5 % of the class 1 spectra

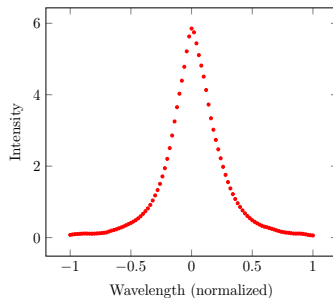


Fig. 4. Normalized output

Fig. 5. Process of the spectra normalization

3.2 Classification Method

For each of 80 normalized spectra was found the most suitable mathematical function by Analytic Programming. All 80 output functions were imported into the classifier – C# based application, which compares the functions with the original spectra according to Eq. 1. The class, whose class-representative mathematical function has the lowest difference compared to the particular spectrum, is selected as a result. Example of the comparison is visualized in Fig 8.

4 Simulations and Results

All simulations of AP estimation were performed on Anselm, x86-64 based cluster hosted at national supercomputing center IT4Innovations. Data preprocessing and following classification of the spectra using synthesized AP functions was done on classic desktop PC with Intel Core i5 processor at 3.3 GHz.

Operating parameters of SOMA algorithm are summarized in Table 1. In AP, GFS consists of basic functions and terminals $\{+, -, *, /, x, K\}$.

All results from the simulations are summarized in Table 2, where are the numbers of correctly and incorrectly identified spectra for each class and total percentage of successfully classified spectra. In the result there are also spectra that are classified incorrectly. This is caused by fact that, for example, some spectra from class 2 have almost none of its characteristic absorption part and thus comparison with AP formula from class 1 can result in lower cost value.

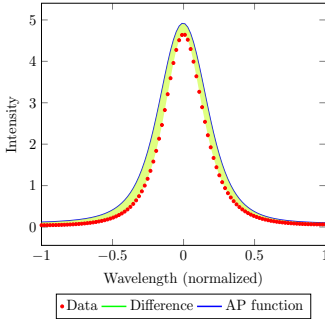


Fig. 6. Comparison of spectrum from class 1 with AP function from class 1

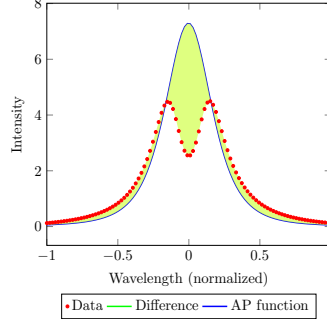


Fig. 7. Comparison of spectrum from class 2 with another AP function from class 1

Fig. 8. Comparison of the original spectra with AP function. Difference in Fig. 6 is much lower than difference in Fig. 7 – spectrum is classified as class 1

Table 1. Algorithm settings of SOMA. The dimension of the inner EA equals to the number of estimated constants.

Parameter	Outer EA	Inner EA
Dimension	100	-
PopSize	100	50
Migrations	15	15
PRT	0.1	0.1
PathLength	5	3
Step	0.11	0.11

Table 2. The simulation results

		Predicted				Success rate [%]
		1	2	3	4	
Actual	1	172	5	0	0	97.2
	2	13	159	0	0	92.4
	3	0	0	1157	2	99.8
	4	0	0	2	55	96.5

5 Conclusion

This paper describes the initial experiments of classification of astrophysical big data by means of Analytic Programming. The results show us that AP is able to identify different shapes of stellar spectra and to classify them. Success rate of the described classification is 92.4 %. However, some spectra from dif-

ferent classes have very similar shape (e.g. spectra from class 1 and 2) and thus classification by AP can result in wrong output class. For this part, research improvements are needed.

In the future work we will focus on another methods of stellar data classification to provide even better results. At this time, classifier is written as a single-threaded application and although the classification of the sample data is very fast, there are billions of stellar spectra in the virtual observatory database. Therefore it will also be necessary to parallelize the classifier to make the process feasible in real-time.

The full version of this paper was published in the International Journal of Parallel, Emergent and Distributed Systems and also as extended abstract in the conference ICNAAM 2015.

Acknowledgment

The following grants are acknowledged for the financial support provided for this research: Grant Agency of the Czech Republic – GACR GACR P103/13/08195S and partially supported by Grant of SGS No. SGS 2016/175, VSB-Technical University of Ostrava and by The Ministry of Education, Youth and Sports from the National Programme of Sustainability (NPU II) project "IT4Innovations excellence in science - LQ1602". Special thanks belongs also to the Astronomical Institute of the Academy of Sciences of the Czech Republic for datasets based on spectra obtained by Perek 2m Telescope of Ondřejov observatory.

References

1. Bromová, P., Barina, D., Škoda, P., Vážný, J., Zendulka, J.: Classification of spectra of emission-line stars using feature extraction based on wavelet transform. In: Proceedings of 23rd Annual Astronomical Data Analysis Software and Systems (ADASS) Conference. pp. 1–9999 (2013)
2. Bromová, P., Škoda, P., Vážný, J.: Classification of spectra of emission line stars using machine learning techniques. *International Journal of Automation and Computing* 11(3), 265–273 (2014)
3. Kennedy, J., Kennedy, J.F., Eberhart, R.C.: *Swarm intelligence*. Morgan Kaufmann (2001)
4. Koza, J.R.: *Genetic programming III: Darwinian invention and problem solving*, vol. 3. Morgan Kaufmann (1999)
5. Onwubolu, G.C., Babu, B.: *New optimization techniques in engineering*, vol. 141. Springer Science & Business Media (2004)
6. Ryan, C., Collins, J., Neill, M.O.: Grammatical evolution: Evolving programs for an arbitrary language. In: *Genetic Programming*, pp. 83–96. Springer (1998)
7. Storn, R., Price, K.: Differential evolution—a simple and efficient heuristic for global optimization over continuous spaces. *Journal of global optimization* 11(4), 341–359 (1997)
8. Zelinka, I.: Analytic programming by means of soma algorithm. In: *Proceedings of the 8th International Conference on Soft Computing, Mendel*. vol. 2, pp. 93–101 (2002)

Basic Cellular Automaton Rule Extractor

Lukáš KroczeK

Department of Computer Science, FEECS,
VŠB – Technical University of Ostrava, 17. listopadu 15,
708 33 Ostrava – Poruba, Czech Republic
lukas.kroczeK@vsb.cz

Abstract. This article describes using a Differential evolution to finding an original rule of generated 1D cellular automaton. In this article will be verified possibility and precision of searching rule from generated 1D cellular automaton using different rule definition. This extractor can be used for finding cellular automaton rule generating animals patterns like pigment patterns on the shells of mollusks.

Keywords: Cellular automaton, Evolutionary algorithms, Differential evolution

1 Introduction

A cellular automaton is a model of a world with very simple physics. Cellular means that the space is divided into discrete chunks, called cells. An automaton is a machine that performs computations it could be a real machine, but more often the machine is a mathematical abstraction or a computer simulation.

Automata are governed by rules that determine how the system evolves in time. Time is divided into discrete steps, and the rules specify how to compute the state of the world during the next time step based on the current state. [1]

A self-reproduction automaton was first presented by Von Neumann. He considers such a model, and incorporated a cellular model into his "universal constructor". A CA consists of regular square cells with discrete variables. The actual value of each cell is updated simultaneously based on the value of current and neighbors cells at the preceding step and according to a definite set of a local rules. Since the local rule is defined so as to govern only local relationships among the neighbors cells, the governing equation for the whole domain is not necessary.

Stephen Wolfram did extensive research in the properties of the simplest of cellular automaton; Elementary Cellular Automaton [2][3]. Every cell has two neighbors and two states. By a combinatorial approach of rules, there are 256 of such elementary cellular automaton. This Elementary Cellular Automaton we will use in this paper.

Differential evolution (DE) is a method that optimizes a problem by iteratively trying to improve a candidate solution with regard to a given measure of quality. Such methods are commonly known as metaheuristics as they make few



Fig. 1: Example of the pigment patterns on the shells of mollusks.

or no assumptions about the problem being optimized and can search very large spaces of candidate solutions.[4]

Some elementary cellular automaton rules can create structure similar to structure on the shell.

Using cellular automaton extractor introduced in this paper can be used to finding cellular automaton rule which generates pattern on the shells of mollusks or on the another animals.

2 Experiment Design

The main idea of experiment and its results reported here is to verify possibility to find origin rule which generates 1D cellular automaton. Generated 1D cellular automaton will be clear (without a noise) to verify if idea is correct. In the experiment in this paper will use Differential evolution and 3 types how we can specify rule and individual of used evolutionary algorithm. Experiments will use same and known configuration of cells in step 0.

The extractor is running selected evolutionary algorithm (Differential evolution) which an individual define the settings of the cellular automaton and the extractor is searching for the origin rule of the the generated cellular automaton. The setting of the cellular automaton (for this paper) mean a rule which will be used for generating.

Differential evolution starts with population of individuals, that are evaluated by cost function. In the cost function of the evolutionary algorithm is generated a cellular automaton with a setting which is defined by individuals and count cost value of individuals as a sum of a differences between a values on the same position in the generated and the original cellular automaton. On the end of each iteration is choosed best individual (by minimal cost value) and when the evolutionary algorithm find the searched rule then searching is finished.

The experiment results reported in this paper use simplest two state cellular automaton. A world is generated for 10 thousands steps. Experiment run on virtual server with 6 virtual CPUs (Intel Xeon E5-2650 @ 2.6 GHz) and 4GB RAM. Experiment application is written in C#.

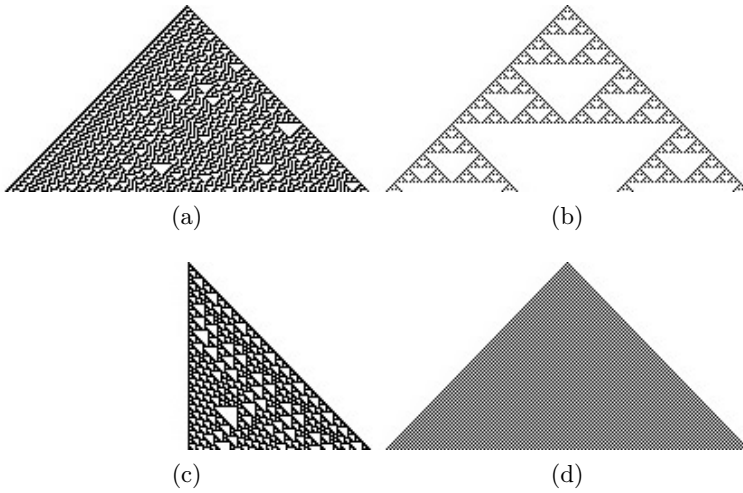


Fig. 2: Example of a generated cellular automaton. First 100 steps of rule 30 (a), rule 90 (b), rule 124 (c) and rule 250 (d).

$$cost = \sum_{s=0}^{steps} \sum_{x=0}^{width} |v1_{s,x} - v2_{s,x}| \tag{1}$$

Success in this paper mean the extractor algorithm find rule which is the origin rule of generated cellular automaton or a rule which can generates completely same cellular automaton for same settings. Time measures in tables define how long in maximum, minimum and average takes to the extractor finish searching of the origin rule.

A Rule/Individual definition defines how will be rule of cellular automaton defined. Same definition will be used in individual. That mean how many dimensions and which values will individual contains.

In this paper we will have this possible types of Rule/Individual definition:

1. Decimal - for decimal number we have an individual with only 1 dimension having possible values in range from 0 to $K^{K^{(2r+1)}}$. For elementary cellular automaton used in this paper values will be from 0 to 255.
2. Binary - for Binary number we have in this paper 8 dimensions with possible values from 0 to 1.
3. Gray code - it is Binary number specified in Gray code. An individual for gray code is same as for Binary number. Gray code is a binary numeral system where two successive values differ in only one bit (binary digit). [5]

3 Results

In table 1 are presented results of experiment. The best is Binary definition with 100% success rate. The worst is for Decimal definition with 99.8% success rate but decimal was fastest in average. The slowest in average time is Gray code definition with 99.87% success rate. There was processed 1536 experiments for each Rule/Individual definition.

Table 1: This table shows results for each Rule/Individual definition ordered by Success rate

Rule/Ind. def.	Min [ms]	Max [ms]	Avg [ms]	Success [%]
Binary	5194	209073	18581.77	100
Gray code	5272	180306	19202.92	99.87
Decimal	5288	453262	18059.17	99.8

4 Conclusion and Future Work

Basic implementation of Cellular Automaton Extractor is presented. We verify there is possibility to use Cellular Automaton Extractor for extracting rule which generate Cellular automaton. Future work will focus on implementation of Cellular automaton Extractor for more evolutionary algorithms and random number generators.

References

1. Downey, A.B.: Think complexity: Complexity science and computational modeling (2012)
2. S. Wolfram. Universality and complexity in cellular automata. *Physica*, 10D: 135, 1984.
3. S. Wolfram - Stephen Wolfram: A New Kind of Science - Wolfram Media - 2002.
4. R. Storn and K. Price, Differential evolution - a simple and efficient heuristic for global optimization over continuous spaces, *Journal of global optimization* 11 (1997), pp. 341-359.
5. F. Gray, (March 1953). Pulse code communication. US Patent 2,632,058.

Statistical Analysis of Steganalytical Method for Steghide Detection

Radim Kuncicky

Department of Computer Science, FEECS,
VŠB – Technical University of Ostrava, 17. listopadu 15,
708 33 Ostrava – Poruba, Czech Republic
radim.kuncicky@vsb.cz

Abstract. Steganography can serve as an effective tool hidden data transfers or watermarking. But it can be misused for salvaging data or information transfer in illegal activities. Revealing this data is very difficult and nontrivial, many used methods are complicated and hard to analyze. This article gives an idea about behavior of one of the modern methods and its hidden dependencies.

Keywords: cybersecurity, steganography, artificial neural network, Steghide

1 Introduction

The rise of computers opened new possibilities for criminals and created new security discipline - cybercrime. The new computer world created new possibilities for usage of cryptography. Nowadays almost all data transfers are protected with cryptographic methods. But we can still detect that the data are transferred and cryptanalysts can attempt to break used cipher. Along with cryptography exists very close, but not so known discipline - steganography. Main aim of steganography is to hide a data in some kind of cover.

Today we can consider images and videos data as most interesting covers. If you see a photo that your company colleague sends after his vacations to somebody you cannot recognize that uploaded unsuspecting photos contains hidden stolen company data. A lot of injection methods were introduced [1–3] and steganography softwares like OutGuess or Steghide are very userfriendly and can be used without advanced knowledge. On the other hand is necessary to have method that can be used to detect injected data. Such detection is not trivial but in recent years there were introduced methods with success rate higher than 99 percent.

This article describes extended statistical analysis of stegodetection method that was introduced in [4], where all dependencies were not described. During testing of this method we found that extended analysis of method behavior will be required. Original work did not mention relation between resolution of images, message length or neural network structure and success rate.

2 Steghide

Steghide is a steganography program that is able to hide data in various kinds of image and audio files. The color - respectively sample - frequencies are not changed thus making the embedding resistant against first-order statistical tests. Steghide is available for Windows as a command prompt utility and Linux. More can be found in [5].

3 Detection method

The surveyed method is based on structural properties of JPEG format. JPEG uses discrete cosine transform (DCT) to convert data from spatial domain to frequency domain. At first an image divided in regions of 8x8 pixels and then DCT is applied. Results of DCT are coded by Huffman coding to changeable length code and stored to transfer medium. Where shortest code represents sequence with most often appearance. These codes can be imagined like bricks with different sizes. Authors found that if we take clear and stego image the stego image Huffmans code looks different the resulting wall is same but the structure is different. These differences can be easily shown on histograms based on Huffmans coding as in Fig. 1.

For detection based upon these observations authors in [4] supposed usage of artificial neural network (ANN), where input is vector created from histogram mentioned above.

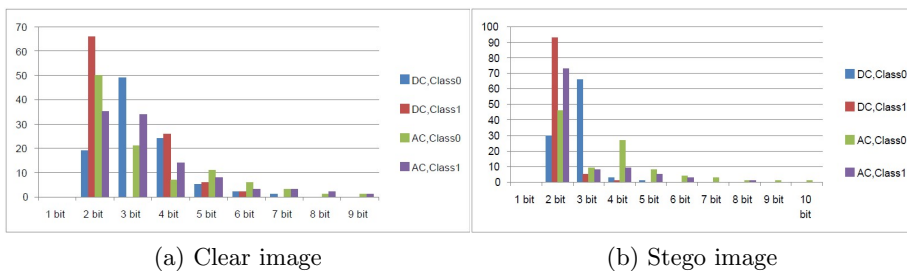


Fig. 1: Histogram of Huffmans coding (maximal code length is 16 bit but lengths without occurrence were omitted)

4 Experiments

Our software was written in python scripting language. For reading the Huffmans coding we prepared custom JPEG reader. ANN simulations were performed using Neurolab library.

We used feed forward perceptron in four layers configuration with two hidden layers. All networks were trained by gradient descent with momentum and adaptive learning rate backpropagation.

Every experiment was repeated at least 200 times, but due to low learning success rate our smaller sample size was 66. Average sample size was 150.

4.1 Database

For testing purposes we had to create testing database. Our database consists from more than 8000 images from two cameras. Images are available in four resolutions with widths of 800, 1024, 1440 and 2560 pixels and variable four lengths of hidden messages 200, 600, 800 and 1000 bytes.

This database was divided into two parts, training set and testing set.

4.2 Hidden message length vs. detection rate and resolution vs. detection rate

For these experiments the training and the testing sets were limited to considered resolution or message length. After successful learning, the ability to generalize was tested on testing set. For these test we used large of considered ANN topologies 64 input neurons, 64x64 neurons in hidden layer and one output neuron.

4.3 ANN structure vs. success rate

Original work supposed feed forward perceptron with 16 and 4 layers. At our test we found that number of successfully learned networks is dependent on chosen structure. Likewise, we saw some differences in detection rate.

We expected this behavior, because the memory size of ANN is closely proportional to number of weights in ANN. We decided to test different inner topologies in hidden layer as in Fig. 3. We chose different topologies a tested their ability to learn and detection rate. Tested ANN was learned with whole learning database.

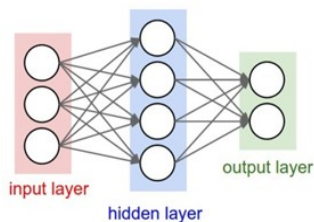


Fig. 2: ANN Topology

5 Results

Initial exploration analysis solved one of examined dependencies. We found that message length has no influence to detection rate which reached 0,89% in this case. The lengths of injected messages were chosen same as in original work (200-1000B). It is appropriate to ask, whether the lengths were chosen correctly and the result of very short (1-100B) or very long messages would show different results.

For different resolution the exploration analysis showed that detection rate median differs in groups as can be seen on Fig. 3 and Tab. 1. This assumption was verified by Kruskal-Wallis statistical test with null hypothesis that medians in groups are the same. With p value equal to zero we rejected the null hypothesis, so there are statistical significant differences between groups.

Post-hoc analysis was performed with Dunnett's method which showed that for higher resolution we achieved higher detection rate except the resolution with width of 2560 pixels. We expected reverse dependency, but our results indicates that method is more successful for higher resolution but with detection rate decreased for 2560 pixel width. This can be caused by undetected properties of training set or inner ANN structure. This result have to be verified and further investigated in future.

Table 2 shows basic summary statistics for detection success rate and hidden ANN layer topology. In same table you can find informations about total number of ANN weights and learning success rate. As we expected larger ANN topologies has higher ability to detect embeded messages. This feature was statistically verified by Kruskal-Wallis test where we rejected hypothesis of same medians. Subsequent post-hoc analysis by Dunnproved that detection ability grows with size of ANN i.e. with number of weights.

Most interesting result we found dependence between number of successfully learned ANNs and number of weights as can be seen in Fig 4. Values can be easily interleaved with exponential curve, but three points significantly deviate from series. On graph we can demonstrate that number of successfully learned network is almost the same for 16_16 and 32_4 topology but with quarter number of weights which, increase speed of computationally expensive learning.

6 Conclusion

This article gives an idea of the behavior and characteristics of steganalytical method. Our results can greatly facilitate further testing that is required for further expansion of this method. The real deployment of this method is conditioned by good functionality at multiple resolutions and lengths. The next step should be to find solutions to the problem of multiple compression that can occur with JPEG file.

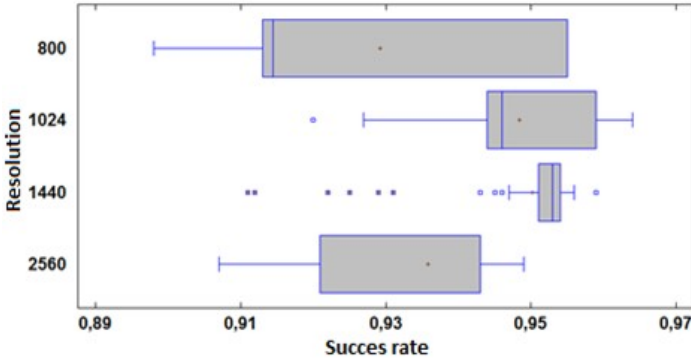


Fig. 3: Box and whisker plot for resolution vs. detection success rate

Resolution	Count	Average	Median	Std. dev.	Coeff. of variation	Minimum	Maximum
800	88	0,929	0,914	0,01947	0,02096	0,898	0,955
1024	75	0,948	0,946	0,00961	0,01013	0,920	0,964
1440	66	0,950	0,953	0,00977	0,01028	0,911	0,959
2560	149	0,935	0,943	0,01106	0,01182	0,907	0,949
Total	378	0,939	0,943	0,01535	0,01635	0,898	0,964

Table 1: Summary statistics for resolution vs detection success rate

Topologie	ANN Weights	Learning rate (in %)	Count	Median	Standard deviation	Coeff. of variation
16_2	1058	76,3	135	0,920	0,064	0,073
4_4	276	75,0	150	0,920	0,063	0,072
8_2	530	70,4	139	0,920	0,055	0,062
8_8	584	85,0	170	0,921	0,047	0,052
16_16	1296	86,5	172	0,922	0,035	0,038
16_8	1160	82,9	120	0,922	0,036	0,040
32_4	2180	82,4	205	0,922	0,029	0,031
32_8	2312	82,6	166	0,926	0,034	0,036
32_32	3104	86,0	172	0,934	0,024	0,026
64_4	4416	88,5	162	0,934	0,015	0,016
64_64	8256	90,3	501	0,937	0,028	0,030
64_16	5136	89,0	178	0,942	0,018	0,019
64_32	6176	89,6	267	0,944	0,023	0,025
Total	-	-	2537	0,922	0,041	0,044

Table 2: Summary statistics for ANN topology vs detection succes rate. There are learning rate and number of weights too.

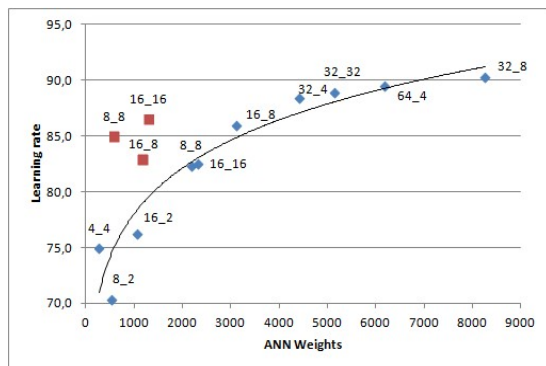


Fig. 4: Learning rate against number of ANN weights

Acknowledgment

The following grant are acknowledged for the financial support provided for this research: Technology Agency of the Czech Republic - TACR - TF01000091.

References

1. SUN, Shuliang. A novel edge based image steganography with 2k correction and Huffman encoding. *Information Processing Letters* [online]. 2016, 116(2), 93-99 [cit. 2016-08-01]. DOI: 10.1016/j.ipl.2015.09.016. ISSN 00200190
2. OU, Duanhao a Wei SUN. High payload image steganography with minimum distortion based on absolute moment block truncation coding. *Multimedia Tools and Applications* [online]. 2015, 74(21), 9117-9139 [cit. 2016-08-01]. DOI: 10.1007/s11042-014-2059-2. ISSN 1380-7501.
3. KOIKARA, Rosemary, Dip Jyoti DEKA, Mitali GOGOI a Rig DAS. A Novel Distributed Image Steganography Method Based on Block-DCT [online]. s. 423 [cit. 2016-08-01]. DOI: 10.1007/978-3-319-07674-4_42.
4. OPLATKOV, Zuzana, Jiri HOLOSKA, Ivan ZELINKA a Roman SENKERIK. Detection of Steganography Inserted by OutGuess and Steghide by Means of Neural Networks. In: 2009 Third Asia International Conference on Modelling & Simulation [online]. IEEE, 2009, s. 7-12 [cit. 2016-08-01]. DOI: 10.1109/AMS.2009.28. ISBN 978-1-4244-4154-9.
5. HETZL, S.: Steghide (1) - Linux man page, [cit. 2016-08-01], <http://steghide.sourceforge.net/documentation/manpage.php>

Effort Estimation Supported by Artificial Intelligence and Machine-learning

Radoslav Štrba

Department of Computer Science, FEECS,
VŠB – Technical University of Ostrava, 17. listopadu 15,
708 33 Ostrava – Poruba, Czech Republic
`radoslav.strba.st@vsb.cz`

Abstract. This paper introduces new advanced method for software process support in early phase of software development. This method helps to improve software process development, using results of requirements classification. Requirements are classified using machine-learning methods like feed-forward neural network or Naïve Bayes classifier. The results of classification help to support estimations in the software project.

Keywords: Software Process, Naïve-Bayes, Neural Network, Classification, Effort Estimation, Use Case

1 Introduction

Main idea of this research is to support the estimation using machine-learning methods that are not so common in this area and can bring a new point of view. Our methods can help to project manager to estimate the project complexity and the risk of additional work for existing projects based on the analysis of requirements. The method uses knowledge base of historical data and provides a decision support in the form of a probability given by estimation of work in the project. In nutshell, the guidance for support of effort estimation based on classification of use case scenarios is currently provided. In our method, we used the Feed-forward Neural Network architecture with the Back-propagation training algorithm. Next technique used in for use case classification purpose is called Naïve Bayes Classifier. [1]

Use case scenarios are used in software requirements analysis for capturing and describing the functional requirements of a software system. Methods that can help to project managers automatically classify use case scenarios are presented. Use case scenarios are made during the first phase of software development, which is called elaboration phase.

Decision of project manager is supported by classification. In our method, we used the Feed-forward Neural Network with the Backpropagation training algorithm and also Naïve Bayes Classifier.

2 Effort Estimation Supported by Classification

This paper speaks about importance of estimation of the projects. Proper software effort estimation is the foremost activity adopted in every software development life cycle. Several features offered by object-oriented programming concept such as Encapsulation, Inheritance, Polymorphism, Abstraction and Coupling play an important role to manage the development process [2]. Currently used software development effort estimation models can be divided into three categories. The first is called algorithmic models. Second is expert judgment and estimation by analogy. Third category is soft computing models. [3]

Classification methods can be used as supportive tool for effort estimation. Machine-learning methods help us to classify use case scenarios and predict risk factor of inappropriate estimation of working time. We call working time like “extended work” parameter. Use case scenarios are used in the requirements, analysis and design stages in the software life cycle.

The use case model of the evaluated project includes a set of parameters of each use case. Basically we use three types of parameters: descriptive, structural and really evaluated parameters. These parameters are based on the use case point (UCP) algorithmic model. [4] a.) Descriptive parameters are evaluated from the description of the use case scenario, there were explained in detail in papers [5] [6]. We use following descriptive parameters: Overall difficulty – difficulty of words, rows and paragraphs. RFC – project ID b.) Structural parameters are evaluated by the structural or relational property of the use case on given project. Set of structural parameters was defined as a result from the interview with several senior project managers. We use following structural parameters and values: NSC (New = 3 / Standard = 1 / Change = 2) functionality of the system. Concerned activities (1 / 2 / 3) means how many business processes are touched by the implementation of this use case. Use-Case type (1 – summary use case / 0 – user or sub function). Remote work (1 – work can be done remote, 0 – work must be done onsite). Implementation remote (Yes = 1 / No = 0). Testing level (Easy = 0 / Normal = 1 / Complex = 2) – means, how difficult will be the testing of implemented functionality. c.) Evaluated parameters are evaluated backward after project end. We use following evaluated parameter in our experiment: Extra work (1 - additional work turned up, 0 – without additional work) – if there was some additional work then was expected for the use case scenario. [1]

3 Experiments and Results

3.1 Neural Network Classification - Results

We tried to test neural network using all vectors from current and all vectors from next dataset. For example, the neural network is trained using use cases from year 2008 and is tested using use cases from year 2009. Table I. shows results of testing neural network after online training process. [9]

TABLE I
RESULTS OF ONLINE TRAINING USING TESTING SET FROM NEXT YEAR [9]

Training vectors from years	Training iterations	Hidden neurons	Testing accuracy (all vectors / 10 vectors) from year:
2008	5832	3	2009 (102 vectors) 81,52% / 100%
2008-2009	2744	5	2010 (110 vectors) 68,00% / 70%
2008-2010	5832	3	2011 (110 vectors) 73,00% / 90%
2008-2011	2744	5	2012 (110 vectors) 59,00% / 30%
2008-2012	1728	6	2013 (109 vectors) 83,84% / 90%

Table IV. shows the best measured results of testing neural network after batch training process. [9]

TABLE II
RESULTS OF BATCH TRAINING USING TESTING SET FROM NEXT YEAR [9]

Training vectors from years	Training iterations	Hidden neurons	Training accuracy (all vectors / 10 vectors) from year:
2008	2744	5	2009 (102 vectors) 76,09% / 80%
2008-2009	8000	2	2010 (110 vectors) 71,00% / 70%
2008-2010	4096	4	2011 (110 vectors) 72,00% / 90%
2008-2011	8000	2	2012 (110 vectors) 66,00% / 30%
2008-2012	4096	4	2013 (109 vectors) 86,86% / 90%

3.2 Naïve Bayes Classification - Results

Use cases were divided into two categories. In the first category extra work on use case was needed. In this case $xWork$ parameter obtain value 0. If extra-work was not needed than parameter obtain value 1. [8]

TABLE III
RESULTS OF TRAINING USING TESTING SET OF 10 USE CASES [8]

Use Case sets from years	Training accuracy / testing accuracy	Testing accuracy (all vectors / 10 vectors) from year:
2008	63,28% / 40%	2009 (102 vectors) 63,76% / 70%
2008-2009	66,41% / 60%	2010 (110 vectors) 66,71% / 80%
2008-2010	65,78% / 70%	2011 (110 vectors) 66,43% / 90%
2008-2011	66,20% / 90%	2012 (110 vectors) 66,60% / 70%
2008-2012	66,91% / 70%	2013 (109 vectors) 66,94% / 70%
2008-2013	68,01% / 60%	

The difference between accuracy of testing after trained feed-forward neural network and naive Bayes Classifier is shown in Tables IV, V. Results of testing using last ten use cases from the current dataset in Table IV. Results of testing using all use cases from the next dataset in Table V. For both approaches (feed-forward Neural Network and Naive Bayes), the classifier is trained using five datasets (2008 – 2012) and tested using also five datasets (2009-2013). It means that we used five datasets from six available datasets of Use Cases for training and testing. Results are copied from tables from Table I and II for feed-forward neural network and from Table III, IV for Naive Bayes Classifier. [8]

TABLE IV
RESULTS OF TESTING USING SET OF 10 TESTING USE CASES FROM THE CURRENT DATASET [8]

Training vectors from years	Feed-Forward Neural Net- work – Online Training (training / testing accuracy)	Feed-Forward Neural Network – Batch (Offline) Training (training / testing accuracy)	Naive Bayes Classifier (training / testing accuracy)
2008	71,03% / 20%	70,85% / 20%	63,28% / 40%
2008-2009	72,16% / 80%	71,85% / 100%	66,41% / 60%
2008-2010	73,36% / 90%	73,37% / 90%	65,78% / 70%
2008-2011	73,98% / 100%	73,75% / 100%	66,20% / 90%
2008-2012	74,33% / 70%	74,33% / 70%	66,91% / 70%
2008-2013	75,51% / 90%	75,60% / 90%	68,01% / 60%

TABLE V
RESULTS OF TESTING USING SET OF ALL USE CASES FROM THE NEXT DATASET

Training vectors from years	Feed-Forward Neural Network – Online Training (training / testing accuracy)	Feed-Forward Neural Network – Batch (Offline) Training (training / testing accuracy)	Naive Bayes Classifier (training / testing accuracy)
2008	81,52% / 100%	76,09% / 80%	63,76% / 70%
2008-2009	68,00% / 70%	71,00% / 70%	66,71% / 80%
2008-2010	73,00% / 90%	72,00% / 90%	66,43% / 90%
2008-2011	59,00% / 30%	66,00% / 30%	66,60% / 70%
2008-2012	83,84% / 90%	86,86% / 90%	66,94% / 70%

4 Conclusion

The results show that the method can estimate an extra work parameter with the accuracy for testing usecases (selected by project manager) in most cases is between 70-100% success (years 2008-2009, 2008-2010, 2008-2011 in tables I. and II). The accuracy is higher when there are more data available for the training. The first dataset is trained with more than 70% accuracy but the testing set showed 20% accuracy using feed-forward neural network. The problem is that project manager has selected training datasets. It means that he selected problematic use cases that he would like to have predicted. [8], [9]

Acknowledgment

Work is partially supported by Grant of SP2016/100 - Knowledge modeling and its applications in software engineering II, VŠB - Technical University of Ostrava, Czech Republic.

Related publications

- Štrba, R., Svatopluk, Š., Štolfa, J.: Finding an optimal Configuration of Feed-forward Neural Network; In Proceedings of the 25rd European-Japanese Conference on Information Modeling and Knowledge Bases; Editors: Yasushi Kiyoki, Takehiro Tokuda; 2015, Maribor, Slovenia
- Štrba, R., Briš, R., Vondrák, I., Štolfa, S.: Application of Naïve Bayes in Classification of Use Cases; Proceedings of the Second International Afro-European Conference for Industrial Advancement AECIA 2015
- Štrba, R., Svatopluk, Š., Štolfa, J., Vondrák, I., Snášel, V.: An Application of Neural Networkin Method for Use Case basedEffort Estimation; In Proceedings of the 26rd European-Japanese Conference on Information Modeling and Knowledge Bases; 2016, Tampere, Finland

Other references.

1. Štolfa J, Koběřský O, Kopka M, Krömer P, Štolfa S, Kožuszník J, et al. Value estimation of the use case parameters using SOM and fuzzy rules. Proc. Int. Conf. Manag. Emergent Digit. Ecosyst. - MEDES '12 [Internet]. 2012;166. Available from: <http://dl.acm.org/citation.cfm?doid=2457276.2457305>
2. Gill NS, Sikka S. New complexity model for classes in object oriented system. ACM SIGSOFT Softw. Eng. Notes. 2010;35:1.
3. Nassif AB. Software Size and Effort Estimation from Use Case Diagrams Using Regression and Soft Computing Models. 2012.
4. Albrecht A. Measuring application development productivity. IBO Conf. Appl. Dev. [Internet]. 1979;83–92. Available from: <http://scholar.google.com/scholar?hl=en&btnG=Search&q=intitle:Measuring+Application+Development+Productivity#0>
5. Štolfa J, Štolfa S, Koběřský O, Kopka M, Kožuszník J, Snášel V. Methodology for estimating working time effort of the software project. CEUR Workshop Proc. 2012. p. 25–37.
6. Štolfa S, Štolfa J, Krömer P, Koběřský O, Kopka M, Snášel V. Fuzzy Rules and SVM Approach to the Estimation of Use Case Parameters. 2014. p. 37–47. Available from: http://link.springer.com/10.1007/978-3-319-01781-5_4

Extraction of Abstract Models of Communication from Message-passing Applications

Martin Šurkovský

Department of Computer Science, FEECS,
VŠB – Technical University of Ostrava, 17. listopadu 15,
708 33 Ostrava – Poruba, Czech Republic
`martin.surkovsky@vsb.cz`

Abstract. The message-passing paradigm represents a well-known manner of exchanging information among processes in distributed systems by passing messages. In comparison to standard programming where a process or function is directly invoked by its name, using a message-passing system means that processes select “the right code” to run according to received messages. The *de facto* standard in this area is MESSAGE-PASSING INTERFACE (MPI). By definition, MPI represents quite a low-level interface, that on the one hand gives it a great flexibility but on the other makes it harder to use. What is more, after a while even the authors of such programs can have a serious problem understanding them. This and other reasons have led to the idea of extracting an abstract model of communication from these programs, presented in this article. Such a model may be very useful to programmers and help them to understand their or other people’s programs, realize the real structure of communication, and identify potential problems.

Keywords: Parallel programs, communication, abstract model, C++, MPI

1 Introduction

This article presents the author’s current work that has not been published yet.

The usage of parallel computers is becoming more and more common. Every year we can see a growing number of newer and more powerful clusters of computers¹. However, such a growth raises the demand for people who can create programs that are able to utilize this computational power. When we take into account the fact that developing programs for parallel computers is generally considered harder in orders of magnitude in comparison to sequential ones, it is not surprising that there are many attempts to make it easier for as much developers as possible.

The *de facto* standard in the area of distributed-memory system is Message-Passing Interface² (MPI). As the name suggests, it is an interface defining the

¹ <http://top500.org/>

² <https://www.mpi-forum.org/>

functions for handling interaction between processes. This interface may then be implemented by vendors of computer clusters that usually provide the implementation tuned to the used hardware set. On the other hand, there are also freely available implementation such as MPICH³.

In the past, a lot of effort has been put into making the programming of parallel applications more comfortable. As a result, supportive tools (e.g. SCALASCA⁴ or VAMPIRE⁵), new paradigms (e.g. *MapReduce*[3]), or specific techniques (e.g. *verification*) have been created that may be very helpful during the development of such programs. KAIRA⁶, a tool developed by a research group of which the author of this text is a member, is another example of similar effort.

KAIRA is an open-source development environment for creating distributed applications using MPI. It uses a combination of visual language for describing parallel aspects and communication on the one side, and a standard code in textual form used for sequential parts on the other. The visual language is strongly inspired by Coloured Petri nets[4] and for the sequential parts the C/C++ language is used. As a result it produces a standalone MPI C/C++ application. Apart from creating programs, KAIRA provides other supportive activities that programmers may need during development, such as: *debugging*, *performance analysis*, *performance prediction*, and/or *verification*.

In comparison with a pure MPI that is considered to be a low-level interface and programs using it written in a standard textual way, KAIRA utilizes the inherent two-dimensional nature of parallel programs and separates the computational and communication layers, thus making them more comprehensible. As said above, the program's communication layer is described visually while the computational parts are still written textually. The problem of the standard textual form used for describing both layers is in their interweaving, since parallel programs are spread alongside both time and space[2], therefore regarded to be two-dimensional.

In spite of all KAIRA's advantages, it has never been widely used. Most likely there are more reasons for that. Nevertheless, one of the most visible can be that it takes considerable time to get familiar with, although the time needed to learn KAIRA is significantly shorter than the one needed to learn MPI. Moreover, even experienced programmers of sequential applications who encounter parallel programming for the first time usually have a problem with understanding its concept, let alone the concept of KAIRA. On the other hand, people who already know parallel programming and could appreciate KAIRA's possibilities don not see a reason to invest their time in learning a new tool. Especially in the case when they would have to rewrite their already existing program if they wanted to use KAIRA in the following process of development.

Regardless the above mentioned issues, the author believes that the idea of separating the communication a computational parts of a program is right and

³ <https://www.mpich.org/>

⁴ <http://scalasca.org/>

⁵ <https://www.vampir.eu/>

⁶ <http://verif.cs.vsb.cz/kaira/>

that having access to an abstract model of its communication may be very useful for experienced parallel programmers too. Nevertheless, such a model has to be extracted from their already existing MPI applications and the usage of such a tool has to be as easy as possible.

The structure of this text is as follows. Firstly the basic principles of KAIRA’s visual language are introduced. Then is presented a proposed model of a program’s communication that is based on KAIRA’s visual language. It introduces new elements that help to depict MPI communication precisely. Based on the defined model a simple example is presented showing the main concept.

2 Kaira’s Visual Language

In this chapter KAIRA’s visual language (KVL) is briefly described. For this purpose the following example (Fig. 1) is used. It depicts most of the common constructs needed to understand the concept of KAIRA. For more details about KAIRA’s visual language, the reader is referred to the text[1].

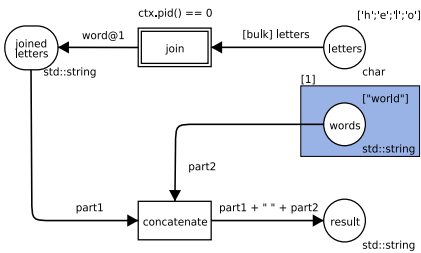


Fig. 1. Example of a KAIRA program.

```

struct Vars {
    ca::TokenList<char > &letters;
    std::string &word;
};

void transition_fn(ca::Context &ctx, Vars &var)
{
    std::stringstream ss;
    ca::Token<char > *t;
    for (t = var.letters.begin();
         t != NULL; t = var.letters.next(t)) {
        ss << t->value;
    }
    var.word = ss.str();
}
    
```

Fig. 2. Code inside *join* transition.

Firstly, the structure and used elements are described. A user can see a diagram very similar to a coloured Petri net. As in the Petri nets terminology, the rectangular boxes are called *transitions* and represent actions in the program, while the rounded boxes are called *places* and represent memory space. Each place is of a specific data type (written bottom-right of the place). Double bordered elements contain a block of C/C++ code inside. For instance, the code inside *join* transition may look like in Fig. 2. The difference between the code inside a transition and a place is in the time of its execution. While the code inside a transition is performed whenever the transition occurs, the code inside places is performed once – at the beginning of the program’s run – and it initializes their content. Unless otherwise stated, the data is initialized only on process 0. To initialize data on other processes, the involved places have to be enclosed inside a *blue area* (see *words* place). Transitions and places may be connected by arcs. These arcs may lead either from a place to a transition (*input arc*) or from a transition to a place (*output arc*). Arcs between the same type of elements are prohibited. Each arc is labeled by an *arc expression*. Its syntax

is as follows: `[configuration] main-expression@target`, where *configuration* consists of a list of *configuration items*, *main-expression* is a C++ expression that defines values of tokens taken from/put into the arc's place, and *target* specifies the processes where the produced tokens are sent. Note, the expression after the '@' sign can be used only on output arcs.

Since KAIRA's visual language is a Petri-net-like structure, it uses the same mechanism to describe its behavior, i.e. how the resulting program is performed. Similarly, *enabling* and *occurrence* rules for transitions are defined. Roughly speaking, a transition is enabled if its input places contain enough "right" tokens and the *guard* expressions (written above the transition) hold. The fundamental difference in comparison with standard Petri nets is that places in KAIRA store tokens in the form of queues and not multi-sets. The values of the desired tokens for a specific transition emerge out of the evaluation of the expressions on its input arcs. Every enabled transition can occur. After the execution new tokens are produced according to the transition output arc expressions and put into corresponding places. If there are more enabled transitions they can occur concurrently. It is important to emphasize that each parallel process contains its own copy of the net, as in the run of an MPI application. These nets communicate with one another according to the *target* specification on the output arc expressions.

3 Proposed Abstract Model of Communication

The model used to describe the communication inside an MPI application is strongly inspired by KVL, however, necessarily richer. The issue is that KVL represents too high-level abstraction above the MPI. For the purpose of presenting the communication model of an existing MPI application, it is important to move on a lower-level of abstraction to be as precise as possible. Nevertheless, the drop has to be slight in order to keep the model still comprehensive.

The main difference between an application written in textual form and one created in KAIRA is in the number of causal dependencies. Standard code naturally contains many implicit causal dependencies because the commands are processed one after another in the order as they are written in the source code. To overcome this issue MPI defines specific constructs, e.g. non-blocking operations that start the communication but do not wait until they finish. Therefore, when programmers need get rid of some of these dependencies in their program, they have to do it explicitly. On the other hand, KAIRA does not contain such implicit causal dependencies given by the order of commands. Actually, if one needs to add such a dependency they has to express it explicitly. Moreover, KAIRA has an implicit receive, which means that a programmer can only specify the send of a message. Its receive, however, is done by KAIRA's environment. Therefore, the following elements are designed to express these dependencies. Note the fewer causal dependencies a program contains, the more parallel it is; each unnecessary dependency shifts the program to being more sequential.

The new elements that enrich the KVL are the following. Firstly it's important to explicitly express the receive of a sent message. For this purpose special types of places and transitions are reserved (gray elements in Fig. 3) – *communication elements*. Their behavior is the same as of the standard elements. There are two reasons why they are set aside. Firstly, to stress that they are related to the communication and secondly that they will be used later in a refinement procedure. This procedure tries to hide as many gray elements as possible. Roughly speaking, the fewer such elements are present, the better an extracted model is considered to be. Nevertheless, this paper presents only the first coarse-grained extracted model. The next newly introduced element is a *white area*. Unlike the blue one that specifies processes where the data are initialized, this one selects the elements on particular processes and only those are influenced. It is used as a finer view on send arcs (arcs with an expression containing '@'-sign). Moreover, the white area is split according to the sources that represent processes which sent the data to places in particular white area. Therefore, the gray places in a white area can be viewed as queues of sent but not yet received messages, and the gray transitions taking data from them as the action of their receive. The last *case* element represents a decision statement that picks only those paths that satisfy the condition.

4 Example

This part presents an abstract model of communication gained from a simple MPI program. The program is designed so that it contains the above mentioned causal dependencies and demonstrates how they are expressed by the model. As for the program itself, it only does that zero process receives in a loop one number from all of the other processes. The important thing is that the messages are received in one specific order, given by process rank. The abstract model of communication that expresses this situation can be seen in Fig. 3.

At the beginning, all of the processes except the zero one initialize the number they will sent (standard place enclosed within the blue area). Alongside this place is also created a communication (gray) place serving for acknowledgment of the receive, because of the used blocking version of `MPI_Send`. This place has a labeled “CP 1” that marks so called compound places. All places sharing the same label behave like they were only a one place. Each process than can send its number to process zero (arcs going to places enclosed within the white area). The right place is chosen by the case element according to the *source* value. As can be seen, receive transitions occur in the same order as in the code because of restrictive places attached to them. Therefore all of the values appear in the right-most place in the right order.

5 Conclusion

This article has presented the idea of extracting an abstract model of communication from an exiting MPI application. The model is strongly inspired by

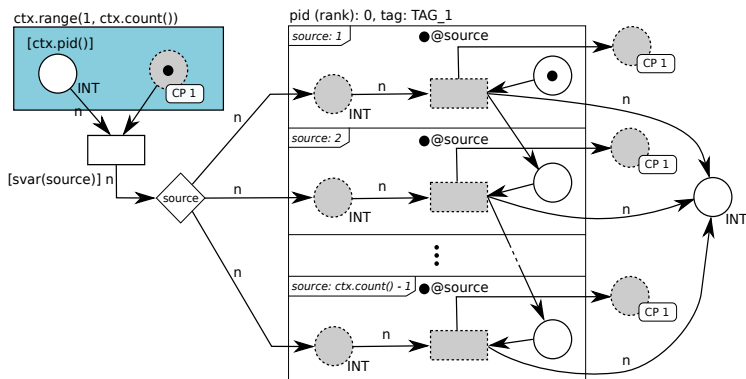


Fig. 3. Example of an extracted abstract model of communication.

KAIRA's visual language and utilizes its power to visualize a program's communication by relatively small pictures. However, unlike the KAIRA this work focuses on experienced parallel programmers and the main aim is to provide them an abstraction above the MPI that can help them to understand programs behavior better and identify potential issues. Even though the used example is very simple, it demonstrate the main idea how to express a program's communication and what needs to be depicted in it. The same model has already been used to present an issue in a mistaken implementation of Cannon's algorithm. The issue was caused by overtaking messages which were nicely visible in the extracted model. Nevertheless, its presentation is not possible within the limited scope of this article. In the near future the next work will focus on programs with non-deterministic matching between sends and receives and the problems related to it.

Acknowledgment The work was supported by the student project SP2016/118.

References

1. Böhm, S.: Unifying Framework For Development of Message-Passing Applications. Ph.D. thesis, FEI VŠB-TUO Ostrava, 17. listopadu 15, Ostrava (11 2013), <http://verif.cs.vsb.cz/sb/thesis.pdf>
2. Cai, W., Milne, W., Turner, S.: Graphical views of the behavior of parallel programs. *Journal of Parallel and Distributed Computing* 18(2), 223 – 230 (1993), <http://www.sciencedirect.com/science/article/pii/S0743731583710580>
3. Dean, J., Ghemawat, S.: Mapreduce: Simplified data processing on large clusters. In: *Proceedings of the 6th Conference on Symposium on Operating Systems Design & Implementation - Volume 6*. pp. 10–10. OSDI'04, USENIX Association, Berkeley, CA, USA (2004), <http://dl.acm.org/citation.cfm?id=1251254.1251264>
4. Jensen, K., Kristensen, L.M.: *Coloured Petri Nets - Modelling and Validation of Concurrent Systems*. Springer (2009)

Complex Network Models of Self Organizing Migrating Algorithms

Lukas Tomaszek

Department of Computer Science, FEECS,
VŠB – Technical University of Ostrava, 17. listopadu 15,
708 33 Ostrava – Poruba, Czech Republic
lukas.tomaszek@vsb.cz

Abstract. In this article we summarize results of our research of two different areas: complex network and evolutionary computation. In this article we describe three propose conversion of SOMA algorithm to a complex network and we show, how we improve classical SOMA algorithm by Remove strategy. At the and of article we compare classical SOMA algorithm with new SOMA Remove algorithm.

Keywords: swarm algorithms, evolutionary algorithms, complex networks, algorithm performance, SOMA algorithm, strategy

1 Introduction

In this article, we summarise our research results of two different areas: evolutionary computations and complex networks(CN). Evolutionary computation is a sub-discipline of computer science belonging to the “bio-inspired” computing area. The main ideas of evolutionary computation has been published [1] and widely introduced to the scientific community [5], [7]. The most well known evolutionary techniques are Genetic Algorithms (GA) introduced by J. Holland [5], [7] based on ideas of A.M Turing [6] and based on first computer experiments by Barricelli in [2], Evolutionary Strategies (ES) by Schwefel [10] and Rechenberg [9] and Evolutionary Programming (EP) by Fogel [4] for example.

It this article we work with the Self Organizing Migrating Algorithms (SOMA) swarm algorithm [14], [3]. For similar experiment with Differential Evolution please look at [11], [12].

2 Motivation

In our research, we are trying to capture the dynamics of evolutionary algorithm into complex network. Such network then can be analysed and give us feedback. According to this feedback, we can improve the original algorithm.

3 Cost functions and parameters

For this article we used CEC benchmark functions [8]. Each function has searching range $[-100, 100]^D$. For more details, please look at [8].

In this article we set parameters like this: PathLength = 3, Step = 0.11, PopSize = 40 + D, PRT = 0.2, numberOfEvaluations = $D * 10^4$, ReduceIn = 10.

4 Models

We proposed three different CN models. Three different altitudes, how to capture dynamic of SOMA algorithm into CN.

4.1 Add model

This model is very simple. We add oriented edge into network from node i to node j if individual jumping individual j find better position, than is the position of leader i . In another words we add edge between leader and jumping individual, if we were able to improve individual and this individual is now better than leader. For more informations about this altitude please look at [13], [15].

4.2 Probabilistic model

Second model is based on probability. The edge between two individuals represents the probability, that there were positive improvement between those two individuals. The weight between vertex i and vertex j in migration loop m is given by equation (1). $NM_{i,j}$ represents number of moves between individual i and individual j , so it counts situations when jumping individual find better solution, so the individual will not return to starting position.

$$w_{i,j}^m = \frac{NM_{i,j}}{m} \quad (1)$$

4.3 Ant model

Last model is inspired by ants. When ants travel, they release pheromones. Number of released pheromones is equals to distance they reached. During the time pheromones vaporise. In our case, distance is given as improvement of individual. So we can write that distance d is given by equation (2), where f_I^S is cost value of starting position of jumping individual, f_I^E is cost value of ending position of jumping individual and f_L is cost value of leader.

$$d = \frac{f_I^S - f_I^E}{f_I^S - f_L} \quad (2)$$

As we wrote, number of released pheromones is equals to distance. Number of released pheromones PR could be linear ($PR = d$), logarithmic ($PR = \ln(d +$

1)), exponential ($PR = e^d - 1$) or another, so if jumping individual i reached distance d during jumping to leader l , we add the number of released pheromones PR to weight of edge $w_{i,l}$ between vertices i and l .

After each migration loop we make vaporisation. So we just remove n percent of pheromones, so we just subtract n percent from all edges weights. For more informations about this altitude please look at [16]

5 Improvement of SOMA algorithm

We proposed three models, those models could be analysed and give us feedback. As it shown, CN given by first model creates networks with size of component significantly lower, than is the population size. As you can see on Figure 1 only for function creates network with size of component equals to maximum possible size. Another functions creates graph with limited size of connected component. This led as to SOMA algorithm with Remove strategy.

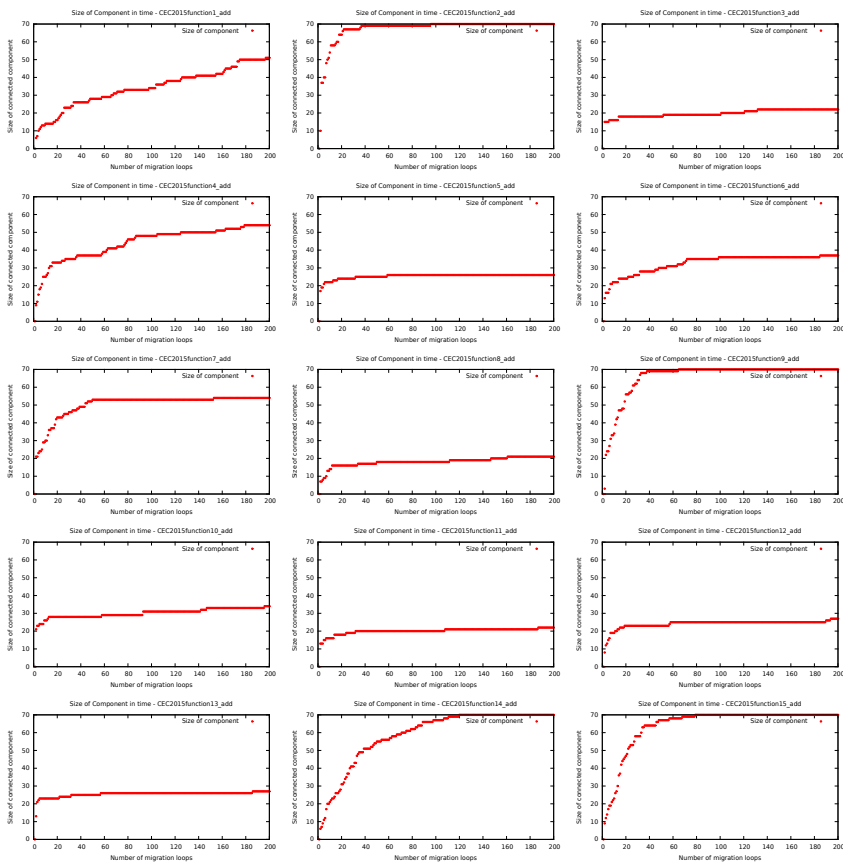


Fig. 1. Size of connected component for all CEC functions - CN created by adding

In Remove strategy we run classical SOMA algorithm for N migration loops. During these migration loops we are creating CN. Then we just remove vertices (individuals) with degree equals to 0 and continue with limited number of population. As you can see in result, this modification led to improvement of algorithm.

6 Results

In Table 1 you can see results for SOMA Remove algorithm and SOMA AllToOne algorithm. Also you can see here comparison of those two algorithms by two-sample Wilcoxon test. The + symbol represents that SOMA Remove is significantly better than SOMA AllToOne. - symbol opposite. The count of the sign symbols corresponds to the achieved significance level of the rejection of null hypothesis (0.05, 0.01, 0.001). More results you can find in [13].

7 Conclusion

In this article we presented three different models of CN and show how to improve SOMA algorithm by Remove strategy. As you can see SOMA with Remove strategy were significantly better on 8 functions on dimension 30 and on 10 functions on dimension 50 and were worse only on 2 function on each dimension.

Acknowledgment

The following grants are acknowledged for the financial support provided for this research: Grant Agency of the Czech Republic - GACR P103/15/06700S, VSB-TU internal grant SGS 2016/175 and by The Ministry of Education, Youth and Sports from the National Programme of Sustainability (NPU II) project "IT4Innovations excellence in science - LQ1602".

Parameters: D = 30, PathLength = 3, Step = 0.11, PopSize = 70, PRF = 0.2, Eval = 300000, Reduceln = 10														
Function number	SOMA Remove					SOMA AllToOne					Comparison	Std	Mean	Std
	Best	Worst	Median	Mean	Std	Best	Worst	Median	Mean	Std				
1	4.93E4	6.43E5	2.16E5	2.43E5	2.43E10	1.84E5	2.63E6	1.25E6	1.26E6	1.80E13	+++			
2	0.00E0	0.00E0	0.00E0	0.00E0	0.00E0	3.70E-7	5.72E-5	6.21E-6	1.12E-5	8.27E-9	+++			
3	2.04E1	2.06E1	2.05E1	2.05E1	4.28E-3	2.05E1	2.07E1	2.06E1	2.06E1	7.50E-2	+++			
4	3.69E1	9.05E1	6.65E1	6.31E1	1.52E2	3.45E1	1.01E2	7.35E1	7.13E1	1.16E4	+++			
5	2.56E3	4.72E3	3.71E3	3.62E3	2.02E5	3.87E3	4.82E3	4.37E3	4.36E3	2.95E6	+++			
6	6.41E4	1.80E6	5.59E5	7.28E5	2.40E11	1.34E5	1.87E6	6.75E5	7.45E5	8.74E12	=			
7	3.03E0	9.38E0	5.99E0	6.15E0	3.52E0	3.10E0	8.39E0	5.70E0	5.58E0	1.05E2	--			
8	3.55E3	4.12E5	5.65E4	8.63E4	6.69E9	9.19E3	3.00E5	5.02E4	7.09E4	1.96E11	=			
9	2.01E2	2.01E2	2.01E2	2.01E2	1.13E-2	2.01E2	2.01E2	2.01E2	2.01E2	3.05E-1	+++			
10	1.20E4	2.12E5	6.63E4	7.87E4	3.04E9	1.07E4	2.31E5	6.09E4	7.46E4	1.10E11	=			
11	2.02E2	2.06E2	2.03E2	2.04E2	1.27E0	2.03E2	2.08E2	2.05E2	2.05E2	6.59E1	+++			
12	1.10E2	1.13E2	1.11E2	1.11E2	4.24E-1	1.09E2	1.13E2	1.11E2	1.11E2	2.08E1	=			
13	8.75E1	1.11E2	1.01E2	1.02E2	2.42E1	9.41E1	1.13E2	1.06E2	1.05E2	8.78E2	+++			
14	2.73E4	3.23E4	2.74E4	2.88E4	4.00E6	2.73E4	3.24E4	2.74E4	2.87E4	1.98E8	=			
15	2.74E2	2.76E2	2.74E2	2.74E2	2.56E-1	2.74E2	2.76E2	2.74E2	2.74E2	4.64E0	--			

Parameters: D = 50, PathLength = 3, Step = 0.11, PopSize = 90, PRF = 0.2, Eval = 500000, Reduceln = 10														
Function number	SOMA Remove					SOMA AllToOne					Comparison	Std	Mean	Std
	Best	Worst	Median	Mean	Std	Best	Worst	Median	Mean	Std				
1	6.45E5	1.25E7	4.04E6	4.24E6	6.13E12	2.13E6	1.44E7	5.42E6	5.57E6	2.40E14	+++			
2	1.67E-4	2.84E0	3.82E-2	1.96E-1	2.12E-1	1.28E-1	6.19E3	1.10E2	6.24E2	6.55E7	+++			
3	2.07E1	2.09E1	2.09E1	2.09E1	1.73E-3	2.08E1	2.10E1	2.09E1	2.09E1	5.17E-2	+++			
4	5.71E1	2.39E2	1.46E2	1.39E2	2.18E3	7.13E1	2.34E2	1.76E2	1.71E2	8.58E4	+++			
5	6.54E3	1.05E4	9.57E3	9.45E3	5.43E5	8.98E3	1.10E4	1.04E4	1.03E4	7.41E6	+++			
6	1.09E5	2.01E6	7.08E5	7.99E5	1.73E11	3.22E5	1.70E6	7.62E5	8.08E5	4.37E12	=			
7	7.25E0	8.47E1	4.63E1	5.66E1	3.35E2	8.27E0	8.44E1	4.49E1	5.39E1	1.71E4	-			
8	1.58E5	2.85E6	1.09E6	1.26E6	4.41E11	3.89E5	2.28E6	1.15E6	1.11E6	1.00E13	=			
9	2.02E2	2.03E2	2.02E2	2.02E2	1.77E-2	2.02E2	2.03E2	2.02E2	2.02E2	1.03E0	+++			
10	5.58E3	5.24E5	9.42E4	1.16E5	1.11E10	4.92E4	1.10E6	3.34E5	3.60E5	2.36E12	+++			
11	2.08E2	1.62E3	7.32E2	7.09E2	1.28E5	2.12E2	1.46E3	5.55E2	5.00E2	2.81E6	---			
12	1.10E2	1.13E2	1.11E2	1.11E2	5.13E-1	1.10E2	1.13E2	1.11E2	1.11E2	2.89E1	=			
13	1.84E2	2.03E2	1.95E2	1.94E2	2.38E1	1.81E2	2.09E2	2.00E2	1.99E2	1.45E3	+++			
14	2.98E4	2.98E4	2.98E4	2.98E4	1.99E-9	2.98E4	2.98E4	2.98E4	2.98E4	1.10E-2	+++			
15	2.84E2	2.87E2	2.85E2	2.85E2	2.13E1	2.84E2	2.88E2	2.86E2	2.86E2	5.17E-1	+++			

Table 1. Result for SOMA Remove and SOMA AllToOne for all CEC functions

References

1. T. Back, B. Fogel, and Michalewicz Z. Handbook of evolutionary computation, institute of physics. *Institute of Physics, London*, 1997.
2. N. Barricelli. Esempi numerici di processi di evoluzione. *Methodos*, pages 45–68, 1954.
3. D.D. Davendra and I. Zelinka. Self-organizing migrating algorithm methodology and implementation. *Springer, in print*, 2016.
4. G. Fogel and D. Corne. *Evolutionary Computation in Bioinformatics*. Bioinformatics artificial intelligence. Morgan Kaufmann, 2003.
5. J.H. Holland. Adaptation in natural and artificial systems. *The University of Michigan Press, Ann Arbor*, 1975.
6. J.H. Holland. Intelligent machinery, unpublished report for national physical laboratory. 1975.
7. J.H. Holland. *Adaptation in Natural and Artificial Systems: An Introductory Analysis with Applications to Biology, Control and Artificial Intelligence*. MIT Press, Cambridge, MA, USA, 1992.
8. JJ Liang, BY Qu, PN Suganthan, and Q Chen. Problem definitions and evaluation criteria for the cec 2015 competition on learning-based real-parameter single objective optimization. *Technical Report201411A, Computational Intelligence Laboratory, Zhengzhou University, Zhengzhou China and Technical Report, Nanyang Technological University, Singapore*, 2014.
9. I. Rechenberg. *Evolutionsstrategie: optimierung technischer systeme nach prinzipien der biologischen evolution*. Frommann-Holzboog, 1973.
10. H.P. Schwefel. *Numerische Optimierung von Computer-Modellen mittels der Evolutionsstrategie*, volume 26 of *ISR*. Birkhaeuser, Basel/Stuttgart, 1977.
11. L. Skanderova, T. Fabian, and I. Zelinka. Differential evolution enhanced by the closeness centrality: Initial study. In *2015 International Conference on Intelligent Networking and Collaborative Systems, INCoS 2015, Taipei, Taiwan, September 2-4, 2015*, pages 346–353, 2015.
12. L. Skanderova and Tomas T. Differential evolution dynamics analysis by complex networks. *Soft Computing*, pages 1–15, 2015.
13. L Tomaszek and I Zelinka. On performance improvement of the soma swarm based algorithm and its complex network duality. In *CEC. IEEE*, 2016.
14. I. Zelinka. Soma - self organizing migrating algorithm. In: *Onwubolu , Babu B (eds), New Optimization Techniques in Engineering, (Springer-Verlag, New York), ISBN 3-540-20167X, 167-218*, 2004.
15. I Zelinka and L Tomaszek. Competition on learning-based real-parameter single objective optimization by soma swarm based algorithm with somaremove strategy. In *CEC. IEEE*, 2016.
16. I Zelinka, L Tomaszek, and L Kojecky. On evolutionary dynamics modeled by ant algorithm. In *INCOS. IEEE*, 2016.

Nearest Neighbors Search Using the Regular Grids and Space Filling Curves

Vojtěch Uher

Department of Computer Science, FEECS,
VŠB – Technical University of Ostrava, 17. listopadu 15,
708 33 Ostrava – Poruba, Czech Republic
vojtech.uher@vsb.cz

Abstract. There are many methods solving the nearest neighbor (NN) problem. Some of them search the exact result, other just an estimate. The current research aims at fast parallel algorithms searching the NN. Most of the widely utilized methods use some hierarchical spatial structures to quickly browse the areas, which can contain the neighbors. On the other hand, the uniform grids dividing the space into the cells of the same size and shape can be utilized. This paper summarizes several methods using the uniform grids for nearest neighbors search.

Keywords: NN, space filling curves, nearest neighbors, CUDA, GPU

1 Introduction

There are several types of the algorithms searching the nearby vertices:

- Nearest neighbor (NN) - searches the closest vertex to a query vertex \mathbf{p}
- Fixed-radius nearest neighbors (FRNN) - searches all the neighbors within the fixed radius, which is known in advance
- k -nearest neighbors (k-NN) - searches exactly the k closest vertices to a query vertex \mathbf{p}
- Fixed-radius k -nearest neighbors (FR-k-NN) - k-NN limited to area defined by the radius

Franklin [1] described the basic idea using the uniform orthogonal grid for the nearest neighbor search. His experiments showed that it is possible to find the result with constant complexity, but the query time of the hierarchical methods is at least $\log|V|$, where $|V|$ is the number of vertices. The construction times of hierarchies are even greater. The following sections briefly describe several of our published methods using the orthogonal and hexagonal regular grids for the nearest neighbors search and vertex clustering.

2 Application of hexagonal coordinate systems for searching the k-NN in 2D space

This method uses the regular hexagonal grid to address the neighboring cells, which may contain the searched neighbors. It is based on the hexagonal metrics

and coordinate systems described in [4]. The hexagons are closer to the circular shape than squares. The method can represent all the algorithm types summarized in Section 1. All the $|V|$ vertices are localized in the hexagonal grid and the coordinates of the corresponding hexagons are hashed according to the C-curve. Thus, all the vertices are sorted and linearly stored in the memory, as it is displayed in Figure 1B. The searching of neighbors is based on the sequential browsing of the surrounding circles of hexagonal cells. Each cell is searched binary in the linear list of the hexagons. This approach can find the exact neighbors and the linear representation of the grid cells is convenient even for a sparse space clustering. The experiments presented in our paper [5] showed that the

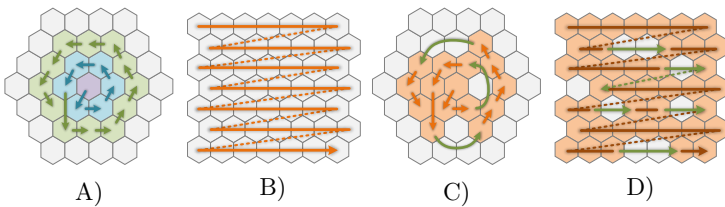


Fig. 1. A: Indexation of hexagonal neighborhood **B:** Cell memory alignment **C:** Sparse neighborhood **D:** Sparse cell memory alignment

method is relatively fast. The number of computed distances required to find the k neighbors is just slightly greater than k (see Figure 2), which is comparable with Quad-tree based methods. The algorithm is well scalable depending on the radius and cell sizes and it represents potentially interesting approach for parallel processing and building of hexagonal hierarchies.

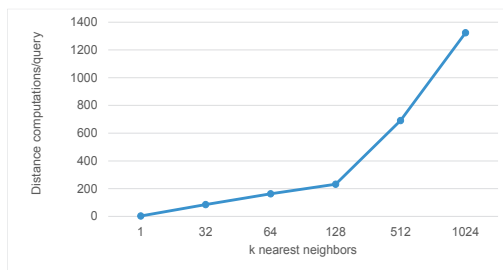


Fig. 2. Numbers of distances computed by the hexagonal k-NN algorithm for different k on $2 \cdot 10^2$ uniformly distributed vertices

3 The Visualization of Large Graphs Accelerated by the Parallel Nearest Neighbors Algorithm

The Fruchterman-Reingold (FR) algorithm is a force-directed graph layout algorithm, which visualizes the relationships between objects [6]. The most time consuming part is the computation of the repulsive forces. Our method represents a parallel CUDA based FR algorithm accelerated by a novel parallel FR-k-NN algorithm. It improves the idea presented in [6]. The principle is similar to the one utilized in Section 2. The surrounding rectangular cells are browsed to find the required neighbors hit by the radius. The vertices are localized in the orthogonal grid and hashed according to Z-order space filling curve (SFC), which is based on the Octree hierarchical clustering [6]. The cells are sorted and linearly stored in the memory. Our paper presents a novel way of parallelization of the nearest neighbors algorithm. First, the general set of neighbors which is the same for all the vertices contained in one cell is found. Next, the final neighbors important for a particular graph vertex p are selected for the repulsive forces computation. The parallel FR-k-NN algorithm works in two states. In the first

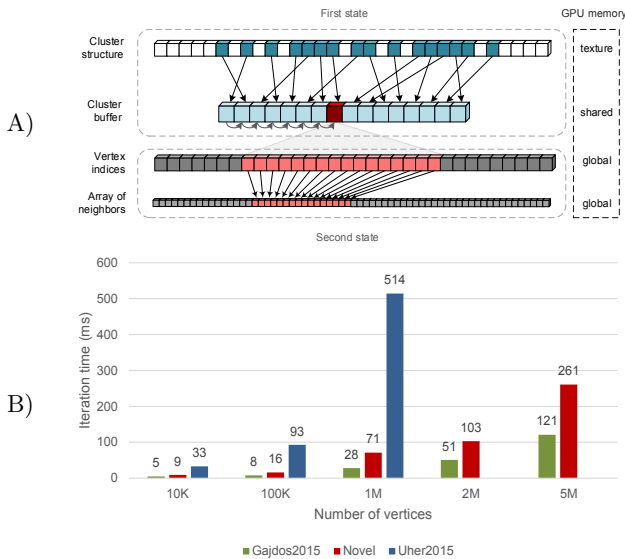


Fig. 3. A) The principle of parallel K-NN computation. The both states of the process and the GPU memory types are highlighted here. **B)** The computation times of one iteration of the Fruchterman-Reingold algorithm for different number of vertices. The three discussed methods are compared.

state of computation, every thread searches a neighborhood of one cell stored in the list of cells (Figure 3A). A thread holds its current cell coordinates and iteratively shifts them to the other cells of the neighborhood. The checked cell

hit by a radius is binary searched in the list of cells (cluster structure) according to its hash code (Z-order). The found cell pointers are added to the queue in the shared memory including the corresponding thread id, which represents the thread which added a cell and also the memory block of the neighborhood. The threads are synchronized and the algorithm is switched to the second state. All the threads of a block sequentially browse the shared queue and read the cell pointers. The vertices of each cell are checked in parallel. The suitable vertices are stored to the global memory of neighborhoods.

This parallel FR-k-NN was successfully applied to speed up the Fruchterman-Reingold algorithm. It was compared with our previous algorithms [6] [2]. The chart in Figure 3B shows that our novel approach is faster than the Uher2015 algorithm [6]. The Gajdos2015 approach [2] is still faster, but it returns only quick estimates of the neighbors. The novel algorithm computes precise results in short time and is applicable for millions of vertices. The occupancy of the GPU with the novel algorithm is about 90% and it is well scalable for different datasets and number of vertices.

4 A Proposal of Hierarchical Vertex Clustering Based on the Gosper Curve

The hexagonal tiling is an alternative to the rectangular tiling methods. In comparison with the rectangle, the hexagonal shape is closer to the circle, and thus more appropriate for a circular neighborhood search [5] [3]. Most of the space filling curves (SFCs) are based on the orthogonal grids (Figure 4), but there is a fractal called the Gosper curve (Figure 4D), which joins the regular hexagons to a composite called the Gosper island (Figure 5). The Gosper curve has been

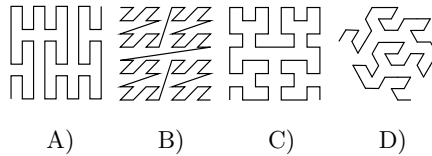


Fig. 4. Examples of space filling curves: **A)** Peano, **B)** Z-order, **C)** Hilbert, **D)** Gosper

designed as a fractal [7]. Our paper presents a way how to use the Gosper curve for a hierarchical vertex clustering. The contribution of our research is a Gosper-like space filling curve, which assigns a hash to each vertex defining the Gosper order of vertices. Our method is based on the Node-Gosper representation (Figure 5B). The basic principle is that a vertex p is localized in the iteratively transformed hexagonal grid. The grid transformation is explained in [7]. Figure 6 shows the vector transformation between two hierarchical levels representing the computation of the hexagon center, which is the nearest one to the vertex p .

Practically, the vertex is localized in the pattern of the seven hexagons on each level. The chosen hexagon is then replaced by the properly transformed pattern and the whole process is repeated for the next level. Our paper addresses all the difficulties related to the computation of angles, recursive grid transformation and hexagon order determination. The hexagon is not a reptile, which means that one hexagon cannot be simply divided to more hexagons of the same size. This can be seen in Figure 5C in comparison with Figure 5D. However, this defect is appropriate for hierarchical hexagonal structure building and a vertex localization. Our curve was compared with Octree based curves. It seems that it has better distance characteristics than the Z-order curve and is comparable with the Hilbert curve.

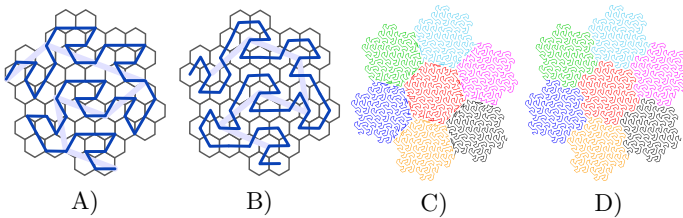


Fig. 5. The second iteration of: **A)** classical Gosper and **B)** Node-Gosper curve. The fourth iteration of **C)** our Gosper-like curve and **D)** complete Node-Gosper curve.

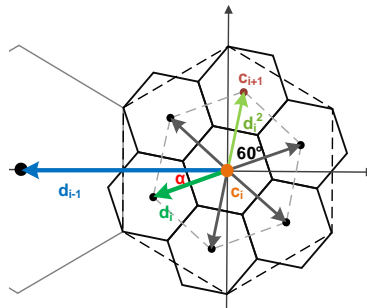


Fig. 6. Transformation of directional and position vectors of the Gosper curve.

5 Publications

Published:

Uher, V., Gajdoš P., Jeżowicz T., and Snášel V. *Application of Hexagonal Coordinate Systems for Searching the K-NN in 2D Space*. IBICA 2015.

Accepted:

Uher, V., Gajdoš P., and Snášel V. *The Visualization of Large Graphs Accelerated by the Parallel Nearest Neighbors Algorithm*. IEEE BigMM 2016.

Uher, V., Gajdoš P., Radecký M., and Snášel V. *A Proposal of Hierarchical Vertex Clustering Based on the Gosper Curve*. IEEE SMC 2016.

Uher, V., Gajdoš P., Radecký M., and Snášel V. *A Novel Approach of Applying the Differential Evolution to Spatial Discrete Data*. ECAI 2016.

Under review:

Uher, V., Gajdoš P., Radecký M., and Snášel V. *The Construction of the Gosper Space Filling Curve of Unordered Point Clouds*.

Uher, V., Gajdoš P., Radecký M., and Snášel V. *Utilization of the Discrete Differential Evolution for Optimization in Multidimensional Point Clouds*.

Uher, V., Gajdoš P., and Snášel V. *Searching of Circular Neighborhoods in the Square and Hexagonal Regular Grids*.

6 Conclusion

We finished several papers about vertex clustering, nearest neighbors search and spatial data structures. Most of our ideas are based on the principle of the space filling curves (SFCs) and uniform grids. We successfully utilized the hexagonal grid for 2D vertex querying and found two variants of the Gosper space filling curve (Figure 5C and 5D). The simpler variant has been accepted for the IEEE SMC conference, the algorithm generating the complete Gosper curve is under review now. We also successfully addressed the problems of the nearest neighbors parallelization and utilization of SFCs for bio-inspired optimizations in spatial data.

References

1. W. Randolph Franklin. Nearest point query on 184,088,599 points in e^3 with a uniform grid, 2006.
2. Petr Gajdoš, Tomáš Jeřowicz, Vojtěch Uher, and Pavel Dohnálek. A parallel fruchterman-reingold algorithm optimized for fast visualization of large graphs and swarms of data. *Swarm and Evolutionary Computation*, pages –, 2015.
3. Herman J. Haverkort. Recursive tilings and space-filling curves with little fragmentation. *CoRR*, abs/1002.1843, 2010.
4. Amit J. Patel. Red blob games - hexagonal grids, September 2015.
5. Vojtěch Uher, Petr Gajdoš, Tomáš Jeřowicz, and Václav Snášel. Application of hexagonal coordinate systems for searching the k-nn in 2d space. In *Innovations in Bio-Inspired Computing and Applications*, volume 424 of *Advances in Intelligent Systems and Computing*, pages 209–220. Springer International Publishing, 2016.
6. Uher V., Gajdoš P., and Jeřowicz T. Solving nearest neighbors problem on gpu to speed up the fruchterman-reingold graph layout algorithm. In *Cybernetics (CYB-CONF), 2015 2nd IEEE International Conference on*, June 2015.
7. Jeffrey Ventrella. Brainfilling curves - the root 7 family, January 2016.

Complex Network Based Feature Extraction for Fault Detection on Covered Conductors Medium Voltage Overhead Lines

Tomas Vantuch

Department of Computer Science, FEECS,
VŠB – Technical University of Ostrava, 17. listopadu 15,
708 33 Ostrava – Poruba, Czech Republic
`tomas.vantuch@vsb.cz`

Abstract. The representation of analyzed data by complex network brings different views on the problem which could lead into the increase of the number of valuable features. The study described in this paper aims on the representation of the similarities of pulses of the classified signal into the complex network. The analysis of signals' pulses is purposed by correct classification of the signals measured on medium voltage (MV) overhead lines with application of covered conductors (CC). The extracted features serve as input values for such classification performed by Random Forest algorithm, which is lately compared to our previous approaches.

Keywords: Partial Discharges, Complex Networks, Random Forest, Feature Extraction, Covered Conductors

1 INTRODUCTION

The medium voltage (MV) overhead lines based on application of covered conductors (CC) are conductors with additional insulation. These CC are typical for their higher operational reliability and safety compare to the Aluminium-Conductor Steel-Reinforced (ARCS) which is given by additional insulation system (SAX-W CC) [8] and by additional insulation system combined with semi-conducting layer (BLT CC) [8].

In case of CC rupture with subsequent CC downfall, this CC fault is not possible to detect by standard digital relays because the standard earth fault does not arise [3]. The low-energy current passes through the fault point and therefore standard digital relays working on current principle cannot detect this fault. Nevertheless, in fault point there is possible to detect partial discharges (hereinafter PD) activity which is generating inhomogeneous electric field in round of degradation of insulation system by fault. The evaluation of PD activity is the basic principle of some methods for CC fault detection. Our research is aimed on methods evaluating PD activity as a voltage signal measured in CC vicinity [5] which simply means that the electric field is evaluated in vicinity of CC measured as the voltage signal. The high-frequency component (hereinafter impulse

component) within the limits (1-10) MHz of voltage signal is obtained from this voltage signal as a so called PD-Pattern. For no-fault state of CC, the impulse component approximates to zero value and PD-Pattern has created by high-frequency disturbances of external radio transmitters. For fault state, impulse component is generated by PD activity and shape of PD-pattern corresponds to this impulse component change.

The main goal of this paper is to design and evaluate the machine learning based detection model of CC's faults from the voltage signal using the features derived from the complex networks (CN). According to our knowledge from the state-of-the art, the analysis of PD-pulses of the PD-Pattern based on complex network features is applied for the first time. This paper covers the entire work flow of the experiment, testing and comparison to our previous models based on denoising and feature extraction.

The application of CN based features is reasonable in more ways. The natural environment where all of the signals are obtained contains high presence of noise disturbance, which creates a lot of false-hit pulses (pulses similar to PD activity but created by noise interference) inside of the signals. Such pulses are not implying any kind of damage on CC, but they could be sometimes very similar to the PD-pulses (according to application of our measuring device- section ??). The differences are only in small number of features and in distribution of the pulses inside of the signal. These assumption leads us to apply the modeling of similarity relations between the pulses as a complex network.

2 Experiment design

The work-flow of complex network modeling and data-mining is as follows:

1. The denoising of the raw signal is performed by univariate wavelet based denoising. We also remove the sinusoidal shape of the signal and the suppression of the major amount of noise leads to more precise pulse extraction in the next step.
2. Each pulse is defined by its measurable features (feature vector), which are relevant for the classification. We chose such features according to our previous research and according to the extensive research, that was already published. Such features are the pulses' width, height, position on sinusoidal form, closeness of the opposite pulse and heights ratio with closest opposite pulse. Each signal contains more than 150 of pulses, so the feature matrix (pulse times features) is extracted from all of them.
3. The feature matrix from previous step is turned into complex network, where each row (pulse) represents the node of the network and edge of the network represents the amount of similarity between those two pulses. All off the nodes' combinations reach some level of similarity, but the edge is drawn only if the similarity reaches the given threshold. In case of our experiments the Euclidean distance was considered as the similarity function.
4. There are several features that are able to be computed from relationships inside of the complex network. The assumption about this experiment is to

reflect the pulse appearance by clusters formed by complex network. PD-pulses are often formed in specific positions of the sinusoidal shape and their size does not vary so much in one signal but it varies according to the time and place of the disturbance or the changes of the weather conditions.

5. The obtained feature vectors of each CNs are extended by class label of the signal (0 for failure-free signal and 1 for the presence of partial discharges) and this dataset is applied for machine learning algorithm to create prediction based on CNs features.

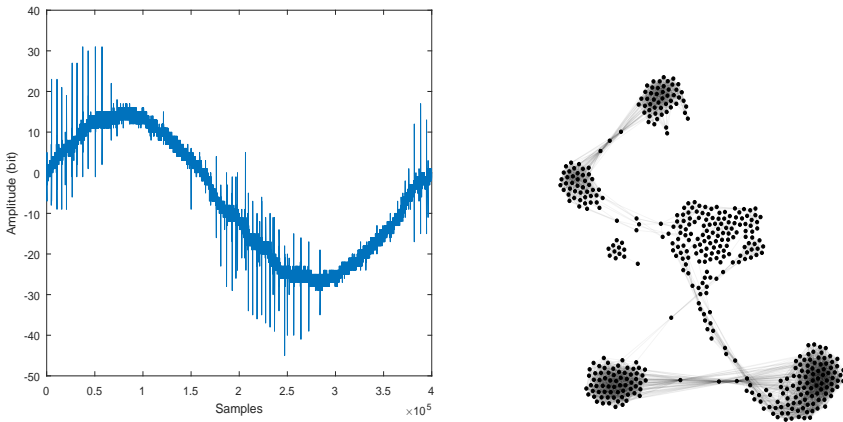


Fig. 1. Figure 2 failure-free signal containing false-hit pulses (left) turned into complex network (right)

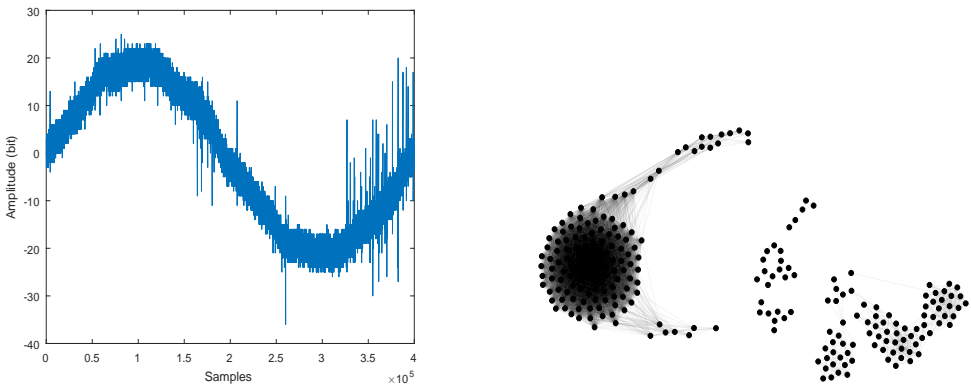


Fig. 2. Figure 1 signal containing the PD-pulses (left) turned into complex network (right)

The features derived from CNs are the density of the network, the global clustering coefficient [6], the local clustering coefficient which was introduced much sooner [9] and it determines whether a graph is a small-world network. This coefficient is computed for each node and the averaged value of all nodes is taken as one feature for classification in this experiment.

The other very important features comes from the distribution of degree, node betweenness, and edge betweenness which were evaluated by feature vector of Interval Degree Probabilities (IDP) proposed by Aliakbary [1].

The last bulk of features were synthesized by injecting two additional nodes into the evaluated complex network. Those nodes were chosen statistically as a most typical PD pulses and their position in the complex network described by degree and betweenness of the node brought more clue about the entire network.

2.1 Random forest classification

Random Decision Forest is a general title for ensemble based machine learning model which was proposed by Breiman in 2001 [2]. This model was successfully applied in many machine learning studies. The core idea of the algorithm is focused on combined application of an ensemble of CART-like tree classifiers (boosting) and their learning performed on the boosted-aggregated observations (bagging).

Learning of the ensemble of trees means to train the set of trees where each of them obtain different random subset of observation and different random subset of variables. This process minimizes the correlation between the trees, which increase the robustness of the model and decrease the possible amount of over-fitting. The final classification is derived from voting mechanism where votes from all of the trees are taken into account and final class is assigned to the observation by votes of the majority of the ensemble.

The bootstrapping mechanism comes from statistic and it is also know as random sampling with replacement. This mechanism in context of RF algorithm produces balanced subset of observations for each of the tree. They are trained on resampled observations, which can handle the imbalanced problem or the problem of inability to learn some specific observations.

2.2 Settings and results

The following section summarizes the setting and results of the entire experiment. The settings of the RF classifier were adjusted experimentally with respect to the previous research and those settings were kept during entire experiment (100 trees in ensemble, random subset of variables and random subset of observations for each tree to prevent over-fitting) - for all levels of threshold value.

The value of the threshold T varied. We had to examine different levels of this value to compare if the obtained CN contains enough information for best classification performance. On the other hand, in case when the value T was too high, new edges of the CN brought only noise or uncertainty.

The cross-validation method [4] was applied for testing of classification performance and the results covers calculated values of accuracy, precision, recall, specificity, and basic F-score. The best results in our experiment were obtained on 30% value of the threshold (see Fig. 2.2 and Table 1).

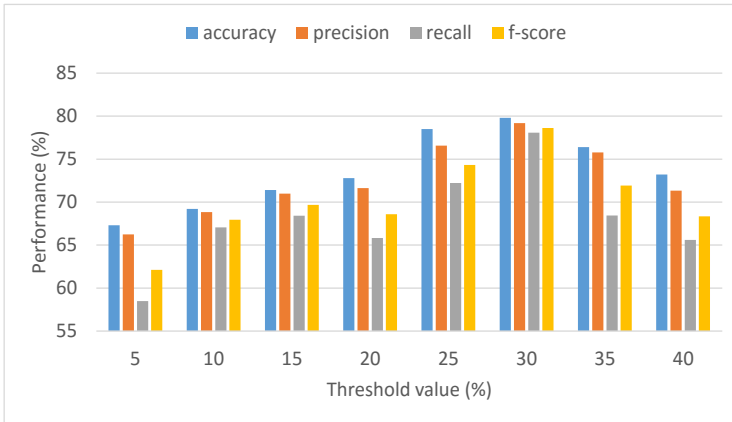


Fig. 3. Graphical comparison of classification performance based on application of different threshold levels.

The performance has increased for all measured metrics compared to the previous experiment [7] (see in Table 1), which confirms the relevancy of application of complex network based features.

3 Conclusions

This paper covers the very first application of complex network based features for detection of CC fault behavior on covered conductors. The complex network created from extracted signal's pulses reflects valuable features for PD-pulses classification. This hypothesis was confirmed by increase of performance of the classification model compared to our previous research [7].

Model based on CN's features can be used as a supportive tool classification for signals with higher noise interference, because signals without any pulses (PD or false-hits) are automatically considered as failure-free signals and they were not studied in this paper.

The future work will cover the increased aim of data-mining on the CN's features and application of different approaches of constructing the CN. On the other hand there is still an option to study the parts of the signal separately and examine the network's dynamic for another set of relevant features for classification.

Table 1. Comparison of classification performance to our previous models based on different types of de-noising, basic feature extraction and machine learning [7].

Model	Accuracy (%)	Precision (%)	Recall (%)	F-score (%)
DWT + ANN	55.65	61.36	76.47	63.58
WPD + ANN	54.36	61.36	74.14	62.59
PSOSVD + ANN	61.85	67.73	61.21	61.85
CN's features + Random Forest	79.82	79.24	78.13	78.61

Acknowledgment This research was conducted within the framework of the project TUCENET Sustainable Development of Centre ENET LO1404 and Students Grant Competition project reg. no. SP2016/175, SP2016/177, SP2016/128.

References

1. Aliakbary, S., Habibi, J., Movaghar, A.: Feature extraction from degree distribution for comparison and analysis of complex networks. *The Computer Journal* p. bxv007 (2015)
2. Breiman, L.: Random forests. *Machine learning* 45(1), 5–32 (2001)
3. Hashmi, G., Lehtonen, M., Nordman, M.: Calibration of on-line partial discharge measuring system using rogowski coil in covered-conductor overhead distribution networks. *IET Science, Measurement & Technology* 5(1), 5–13 (2011)
4. Kohavi, R., et al.: A study of cross-validation and bootstrap for accuracy estimation and model selection. In: *Ijcai*. vol. 14, pp. 1137–1145 (1995)
5. Mišák, S., Pokorný, V.: Testing of a covered conductors fault detectors. *IEEE Transactions on Power Delivery* 30(3), 1096–1103 (2015)
6. Newman, M.E.: The structure and function of complex networks. *SIAM review* 45(2), 167–256 (2003)
7. Vantuch, T., Misak, S., Burianek, T., Jezowicz, T., Fulneczek, J.: Swarm intelligence based denoising for detection of partial discharges on covered conductors in natural environment. *Advances in Electrical and Electronic Engineering* 2016 (in press)
8. Wareing, J.: Covered conductor systems for distribution. Tech. Rep. 70580. EA Technology Ltd, Capenhurst Technology Park, Capenhurst, Chester (2005)
9. Watts, D.J., Strogatz, S.H.: Collective dynamics of small-world networks. *nature* 393(6684), 440–442 (1998)

Data Compression using Delimiters

Michal Vašinek and Jan Platoš

Department of Computer Science, FEECS,
VŠB – Technical University of Ostrava, 17. listopadu 15,
708 33 Ostrava – Poruba, Czech Republic
{michal.vasinek, jan.platos}@vsb.cz

Abstract. Even though the least size grammar representation of input messages is NP-hard problem, many heuristical and greedy approaches were proposed to overcome related computational complexity issues. The most successful representant of the class of grammar based compression algorithms is Re-Pair algorithm. The algorithm repeatedly selects the most frequent digram and replaces it by some unused symbol. Recently the approach called Delimiter-Based Compression (DBC) inspired by Re-Pair has been proposed. The key idea of the approach is the establishing of the special parsing induced by delimiting symbol, such that the whole phrase residing between two delimiting symbols is transformed into alphabet of unused symbols. This transformation remarkably simplifies the storage of the dictionary of phrases. DBC is fast in encoding as well as decoding phase and it is still able to maintain high level of compression comparable to the popular data compression algorithms ZIP and Deflate.

Keywords: data compression, Re-Pair, grammar compression, delimiter, DBC

1 Introduction

This paper summarizes evolution of context dependant transformations of messages intended for data compression, presented in [1]. The generalized context transformation[2] was adjusted to process translation of patterns in input message m to the symbols in compressed message over new alphabet Θ . Symbols from the new alphabet Θ are used to encode phrases found in m . The proposed algorithm is based on using delimiting symbols for separation of phrases. The process of replacement for the unused symbol was inspired by the Re-Pair algorithm developed by Larsson and Moffat[3]. The main idea of the Re-Pair algorithm is the replacement of the most frequent digram for some unused symbol. We shall demonstrate that the proposed delimiter based compression algorithm is fast and yet efficient in the sense of compression ratio.

The rest of the paper is organized as follows. Section 2 provides basic notation conventions and terminology used across the paper. Section 3 provides description of the proposed compression and decompression schemes. Section 4 contains achieved results compared to the popular data compression algorithms. Last Section 5 concludes the paper, discusses achieved results and future work.

2 Notation and Terminology

Let the input message m is a sequence of symbols of the length $|m|$ over alphabet Σ . The parsing of the message is a set of strings $s_i \in \Sigma^*$, where Σ^* is a set of all strings over symbols of Σ , such that the concatenation of s_i yields message m , i.e. $s_1 s_2 \dots s_n = m$.

There are several well known parsings for data compression, for instance one established by Lempel and Ziv[4] in their LZ78 algorithm or BISECTION used by Kiefer and Yang[5]. The parsing established in this paper is based on delimiting symbol d . Let the phrase p is a string over symbols from Σ , particular position in a phrase p is denoted using square brackets with index i : $p[i]$. The phrase separated by delimiter begins with a delimiting symbol, i.e. $p[0] = d$, and for all other symbols in p , $p[j] \neq d$, given that $j \neq 0$. In the special case when message m doesn't begin with d , we identify the phrase to be a substring $m[0, k]$, where $m[i, j]$ denotes a substring of m that begins in the position i and ends in the position j , such that the symbol in position $k + 1$ is d , i.e. $m[k + 1] = d$ and $m[i] \neq d$, $i < 0; k >$.

The delimiter based parsing of message m forms a set of phrases p_i , whose concatenation recovers former message m . The intuitive way how one can imagine how delimiters works is to think about text messages. Suppose that the delimiting symbol is a space character in ordinary text, then phrases represent words of the natural language.

3 Compression and Decompression

As was outlined in the previous section the compression algorithm is based on parsing by delimiting symbol. The compression algorithm is divided into three stages:

1. Collection of involved statistical quantities and selection of the delimiter.
2. Transformation of phrases into symbols from the new alphabet.
3. Application of Huffman coding[6] and storage of compressed message and dictionary.

In the first phase, the algorithm have to pass twice through the input message. In the first pass it collects frequencies of all symbols¹ and the most frequent symbol is selected as a delimiter. The algorithm then passes through the input message again and collects all positions where delimiter resides. Suppose the input message size is n , then the time complexity of the first stage is $O(n)$. In the worst case when the input message consists only of one symbol, then the space needed to store locations of delimiter in the message is at most $4n$ bytes² and generally it needs $4f(d)$ bytes, where $f(d)$ is a frequency of the delimiter.

¹ In our implementation we interpret individual byte values as symbols.

² The message size is multiplied by 4, since each pointer is being stored using 4-byte unsigned integer value.

The frequency of delimiter $f(d)$ is equal to the final number of phrases: $|p| = f(d)$, or $|p| = f(d) + 1$ in case when $m[0] \neq d$ and consequently also the resulted size of the transformed message, since each phrase is represented by exactly one symbol of the new alphabet Θ . To make a time complexity of the second stage of the algorithm linear, we need to possess with the knowledge of the rank of the symbols given by their assortment by frequency. Given that we know frequencies, we can sort these symbols on average using QuickSort in $O(|\Sigma| \log |\Sigma|)$. The sorting yields alphabet in the new order denoted by Σ_S .

The second stage of the algorithm is responsible for translation of phrases into the new alphabet. The algorithm begins with a collection of positions following delimiter in m : $pos = \{i + 1 | m[i] = d, i \in < 0; |m|\}$. Before we formulate translation algorithm, we shall discuss grouping of the same symbols in a random string according Σ_S . Suppose we have the following string: $s = baabac$, clearly $f(a) > f(b) > f(c)$, so $\Sigma_S = [a, b, c]$, we need to group same symbols such that: $\Sigma_S[s[i]] \leq \Sigma_S[s[i + 1]]$, i.e. $s_1 = aaabbc$. This can be made in $O(|s|)$ if we first compute frequencies of symbols in s and offset O of each distinct symbol in the grouped order. For instance: $O[a] = 0, O[b] = f(a) = 3, O[c] = f(a) + f(b) = 5$. The problem simplifies because we don't have to sort symbols of the same value. It is sufficient to loop once through all symbols in s . The position of the symbol $s[i]$ in the grouped string s_1 is given by: $s[i] = s_1[O[s[i]]_j]$, the index j denotes iteration of the loop. Each time algorithm assigns a symbol c into proper order in s_1 , it increments pointer $O[c]$.

By careful look we see, that the grouped string filtered delimiter symbols into the beginning of the string. Using this technique we identify which phrases terminate, because each phrase beginning with the delimiter ends either by the end of message or by the symbol preceding the next delimiter. Each time algorithm arrives at phrases that terminate, it assigns them a unique code number. Equal phrases have equal code numbers. The initial code number c for the first phrase is set to $c = 0$. For instance if the input message contains adjacent delimiters, then the phrase consisting only of one delimiter is transformed into 0. The listing of the transformation is provided in Algorithm 1. The first call of the function *Transform* is called with parameter *symbol* set to delimiter and *code* = 0.

The entry of the position set *posRanks* is actually a pair of numbers, the rank of the particular delimiter in m and the rank of the delimiter in the ordered set of their positions *delimRanks*. For instance: in the string $s = aba$, with delimiter in positions 0 and 2, for the first delimiter a the pair is (0, 0) and for the second (2, 1). So when we sort symbols, using procedure described above, in positions *posRanks*, we also sort their corresponding ranks in the set *delimRanks*. This additional structure is useful for immediate writings of the transformation into the output buffer *outbuf*.

During the translation process, algorithm simultaneously writes newly discovered phrases into dictionary using function *WriteToDict*, the function has two arguments, the first is the symbol whose following symbols are being transformed and the number of unique non-zero frequency symbols, except delimiter, in the set *freqs*. For instance, string $abac$. The symbol a is followed in m by

Algorithm 1 Transformation

```

function TRANSFORM(delim, symbol, posRanks, delimRanks, code)
  freqs, uniquesNumber  $\leftarrow$  FREQUENCIES(posRanks)
  posRanks, delimRanks  $\leftarrow$  SORT(posRanks, delimRanks, freqs)
  start  $\leftarrow$  0
  end  $\leftarrow$  freqs[0]
  WRITETODICT(symbol, uniquesNumber-1)
  for i in  $\langle$  start, end  $\rangle$  do
    outbuf[delimRanks[i]]  $\leftarrow$  code
  end for
  code  $\leftarrow$  code + 1
  for c in  $\langle$  1,  $|\Sigma|$   $\rangle$  do
    start  $\leftarrow$  end
    end  $\leftarrow$  start + freqs[c]
    TRANSFORM(delim, symbol, posRanks[start, end], delimRanks[start, end], code)
  end for
end function

```

b and c , algorithm writes to the dictionary pair $(a, 2)$, if then b is not followed by any symbol other than a , algorithm writes the pair $(b, 0)$ and similarly for symbol c , the pair $(c, 0)$, so the dictionary D is: $D = a2b0c0$. The output buffer *outbuf* and the dictionary string D are the output of the second stage.

In the third stage, the output buffer and the dictionary are encoded separately using Huffman coding and then merged together yielding the final compressed output message.

3.1 Decompression

Decompression begins with reversing the Huffman coding applied in the third stage of the compression algorithm, yielding the former *outbuf* and dictionary string D . The dictionary string D is crucial for proper recovery of message m from *outbuf*. Actually the dictionary D can be equally represented by special form of the prefix tree called delimiter based phrase tree (DBPT). DBPT of a message m over Σ with delimiter d_m is a tree with each node having at most $(|\Sigma| - 1)$ children, each representing one symbol distinct from d_m , the root node denotes the delimiting symbol d_m and the path from the root to the leaf represents the particular phrase. The order of the children symbols corresponds to the order of symbols in Σ_S .

The code numbers and their corresponding phrases can be simply derived using DBPT, by reading the tree from the root, followed by the most left path, each time algorithm visits some node it assigns a code number to the phrase that has been so far represented by the path from the root. Having the codetable *codes* with phrases, we can immediately translate *outbuf* into m as is demonstrated in the listing of Algorithm 2.

Algorithm 2 Inverse transformation.

```

function INVERSE(outbuf, codes)
  for i in < 0, |outbuf| do
    WRITE(codes[outbuf[i]])
  end for
end function

```

4 Results and Discussion

The compression efficiency of delimiter based compression algorithm(DBC) is compared with several popular algorithms, including PPMd, ZIP, bzip2 and DEFLATE. The final bits per byte ratio achieved by different algorithms is presented in Table 1.

Table 1. Bits per byte ratio over selected files from Calgary corpus[7].

File	PPMd	ZIP	bzip2	deflate	DBC
book1	2.18	3.32	2.42	3.12	2.52
book2	1.85	2.75	2.06	2.59	2.47
obj1	3.57	3.87	4.02	3.81	4.73
paper1	2.21	2.82	2.49	2.71	2.85
progc	2.25	2.71	2.53	2.62	3.31

It was expected and verified that the DBC algorithm can handle well text files and actually DBC overcomes ZIP and DEFLATE methods over them, but the algorithm's compression efficiency over other files was mostly worse than ordinary methods.

When compared to the Re-Pair algorithm, DBC transforms phrases rather than digrams. Additionally DBC translates former message m directly into the new message over the new alphabet, meanwhile Re-Pair produces the final message as a mixture of symbols from Σ and Θ . This allows us to store dictionary in a very compact, easy to write and to restore, form. Also since we have removed the necessity for the search of some extremal statistical quantity, as the most frequent digram in the Re-Pair case, DBC is much faster than the Re-Pair.

5 Conclusion and future works

We proposed and demonstrated, fast compression and almost instant decompression, algorithms using delimiting symbols. The concept of delimiters for data compression, especially of text files, has proved itself and will be further explored. We will focus particularly at a formulation of theoretical bounds for several types of information sources using DBC.

The specific formulation of phrase tree offers us further opportunity for use of DBC in compressed pattern matching. It is possible to compute exact position of any phrase in m without decompression of the output message, and one can random access and decompress whatever part of the message at will.

Publications

The algorithm has been presented sofar at the ISCAMI(International Student Conference on Applied Mathematics and Informatics) and the full size paper about delimiter based compression will be published soon in the journal Acta Polytechnica Hungarica.

Acknowledgement

This work is supported by Grant of SGS No. SP2016/97, VŠB - Technical University of Ostrava, Czech Republic

References

1. Vašínek, Michal and Platoš, Jan, *Entropy reduction using context transformations* Data Compression Conference(DCC), pp. 431-431, 2014
2. Vašínek, Michal and Platoš, Jan, *Generalized Context Transformations - Enhanced Entropy Reduction* Data Compression Conference(DCC), pp. 474-474, 2015
3. Larsson, N. J. and Moffat, A., *Off-line dictionary-based compression*, Data Compression Conference(DCC), pp. 1722-1732, 2000
4. Ziv, J. and Lempel, A., *Compression of individual sequences via variable-rate coding*, IEEE Transactions on Information Theory, vol. 24, pp. 530-536, 1978
5. Kieffer, John C. and Yang, En-hui, *Grammar Based Codes: A new class of Universal Lossless Source Codes*, IEEE Transactions on Information Theory, vol. 46, pp. 737-754, 2000
6. Huffman, David A., *A Method for the Construction of Minimum-Redundancy Codes*, Proceesings of the I.R.E., pp. 1098-1102, 1952
7. *Calgary Corpus*, <http://www.data-compression.info/Corpora/CalgaryCorpus>

The Malware Analysis based on Static Methods

Filip Zatloukal

Department of Computer Science, FEECS,
VŠB – Technical University of Ostrava, 17. listopadu 15,
708 33 Ostrava – Poruba, Czech Republic
filip.zatloukal@vsb.cz

Abstract. The analyzing of a malware program is very important for computer security, especially for the new kinds of threads. There are lots of ways how to analyze the malware program and how to get useful information. We can divide the methods into static analysis and dynamic analysis. However, this paper is focused on some of the static methods. More advanced methods and also dynamic methods will be described in a future work.

The analysis of real malware samples was made by described methods and also some interesting results are discussed.

Keywords: malware, malware analysis, static analysis, PE header

1 Malware analysis

When we are able to analyze malware, we can get plenty of useful information about a malware structure and behavior. Then we can use it for future detection, protection against it and also for removing malware from infected systems and for damage reparation, if it is possible. In many cases, it is also possible to identify the whole malware family with the similar structure.

1.1 Static and dynamic methods

The main difference between the static and dynamic analysis is way of gathering information about malware. With static methods we collect data by analyzing of the malware executables and libraries without running it. In terms of dynamic methods, we analyze malware while it is running and we collect information about behavior and malware itself. [5] Dynamic methods can also test responses to unexpected inputs. Both methods are useful for the analysis and it is suitable to use both of them for the complete analysis process.

1.2 Methods used in static analysis

The paper and experiment is focused on analyzing malware binary executables and libraries on Windows AMD64(x86 including) platform. In Windows systems, there is the most used format for the native executable called “Portable Executable” with

“.exe” extension. This format encapsulates meta-information about the code and some parts are also necessary to manage the executable by OS. The final PE file contains of headers, flags, tables describing included code and code itself. [2][4]

Executables are compiled from source codes to machine codes (binary files) of the specified platform. [3] The machine code is difficult to analyze by a person. For a deeper analysis it is appropriate to use a next method also – to analyze a disassembled code.

1.3 Import/Export functions

In PE headers there are besides two tables that are useful for the static analysis. Import functions and export functions. [2] Executables and libraries can use functions from other libraries and executables that are offered. Libraries offer their functions to be used in such programs. This kind of functions is called exported functions.

On the other hand, the imported functions are those functions that are included in software from exported functions. Imported functions are very common in executables (also in libraries), exported functions are common for libraries and rare for executables. However, it is possible to make exported functions in executables too. [1]

It is important for the malware analysis that operating systems offer own libraries with exported functions to manipulate the system and make basic and advanced operations. Windows offers these functions in Windows API specification. [6]

Since we have information about imported/exported functions in PE headers, we are able to extract them, including libraries, where the functions are presented. The finished analysis shows that it is common practice to include system libraries to malware and to use their functions.

1.4 Library linking

There are three common ways how a library can be linked to the executable - static linking, dynamic linking or at runtime. Every approach has some advantages and disadvantages. [2][3]

When using the static linking, code from included library is copied to the application in compile time. When analyzing malware, it is difficult to find the original library. Information about library and used functions are not included in the PE header and also the original names of the libraries and functions are lost.

The dynamic linking has a different approach: the library code is not copied in compile time to code of final application. Instead of that, only the meta-information about libraries is inserted to file. In terms of this information, the system is able to offer the libraries (if presented on the infected system) to be used. When using this approach, the necessarily information about external libraries is stored in PE headers with used functions. The experiment was based on this kind of functions and it is evident from results, that this approach is commonly used - at least for certain kinds of system tasks.

The last mentioned approach is focused on loading libraries at runtime. This method is not so common in “friendly” applications, but it is interesting for malware programming. [1] This approach combines both previous methods – the exact library is loaded from the infected system when running malware asks for it. The problem for the analysis is that the exact libraries loaded by runtime approach are not included in the PE header. Nevertheless, this method is significant by system functions, which allows library runtime loading. In the Windows system, while being at runtime, the external libraries can be loaded by some of these functions: LoadLibrary, LdrLoadDll, GetProcAddress or LdrGetProcAddress. This approach is commonly used when a malware body uses packager to hide the code.

1.5 Malware protection

It’s common practice to protect malware against detection and analyzing. When malware is packed, it’s more difficult to use static analysis. Sample must be unpacked before. Packers takes origin malware, makes wrapper and creates a new binary file. The whole binary or only part of the file can be packed. Import section of the PE header must be reconstructed for PE header static analysis. [1]

2 Experiment

The described experiment is based on the analyzing of data from PE headers and imported functions. This approach is suitable for the analyzing of a large number of malware samples to obtain information that can allow the quick classifying of whole package of malware. The method has also some disadvantages that can lead to the incorrect classification of some samples. On the other hands, small abnormalities are acceptable in large packages to provide good performance.

The virtual environment has been created for safer work. Both of them were used for gathering information - existing tools and also new tools were programmed. These new tools were also created to make the necessary analysis and to allow the automation of the whole process and to allow analyzing of the large number of samples. Also existing unpackers were included.

Before each of the samples is analyzed, unpacking tools tests, if the executable is packed and if it’s possible to unpack it with some of the known methods. [7] If unpacking fails, the sample is excluded. The tools collect information from every sample (if possible), allow classification, but also collect global statistics of whole package to offer a final summary.

2.1 Results

The most common functions from the analyzed package (and also interesting functions [1] for malware) were classified manually. According to this classification, new samples are evaluated. WinAPI functions are well documented and it was possible to assign classification for selected functions. [8]

The described experiment was made with the package of malware collected from “virusshare.com” database¹, with total number of 997 samples. The 846 samples were evaluated 151 were skipped because the method of unpacking was unknown.

The most used libraries were:

Table 1. No. of samples using the WinAPI libraries.

Library name	Absolute value	Relative value
Kernel32.dll	718	84,87 %
Advapi32.dll	639	75,53 %
User32.dll	589	69,62 %
Gdi32.dll	407	48,11 %
Version.dll	360	42,55 %
Msvcrt.dll	301	35,58 %
Shell32.dll	273	32,27 %

Libraries are described with functions together below. For deeper description about libraries is practical to use Microsoft WinAPI documentation.

The most used functions from libraries above:

Table 2. No. of samples using the functions from Kernel32.dll library.

KERNEL32.DLL	Absolute value	Relative value
GetLastError	691	81,68 %
LoadLibrary	690	81,56 %
Sleep	666	78,72 %
GetProcAddress	664	78,49 %
GetModuleFileName	663	78,37 %

Table 3. No. of samples using the functions from Advapi32.dll library.

ADVAPI32.DLL	Absolute value	Relative value
RegCloseKey	550	65,01 %
RegOpenKey	537	63,48 %
RegQueryValue	527	62,29 %
RegSetValue	479	56,62 %
RegCreateKey	468	55,32 %

¹ <https://virusshare.com/>

Table 4. No. of samples using the functions from User32.dll library.

USER32.DLL	Absolute value	Relative value
DispatchMessage	463	54,73 %
MessageBox	459	54,26 %
SendMessage	428	50,59 %
ShowWindow	413	48,82 %
LoadString	403	47,64 %

Table 5. No. of samples using the functions from Gdi32.dll library.

GDI32.DLL	Absolute value	Relative value
GetDeviceCaps	370	43,74 %
DeleteObject	175	20,69 %
SelectObject	164	19,39 %
SetTextColor	154	18,20 %
DeleteDC	152	17,97 %

Table 6. No. of samples using the functions from Version.dll library.

VERSION.DLL	Absolute value	Relative value
VerQueryValue	360	42,55 %
GetFileVersionInfoSize	356	42,08 %
GetFileVersionInfo	353	41,73 %

Note: There can be more version of the same function in Windows API. These functions have suffix as "Ex" (old/incompatible function), "A" (ASCII version of function) or "W" (wide characters version of function). In statistics, these functions were unified, because the meaning of the function is the same.

2.2 Discussion

Library "Kernel32.dll" is very common in malware, because it provides core functionality. The important function "LoadLibrary" and "GetProcAddress" shows, that at least 81,56% of samples can load libraries in runtime.

The most used functions from "Advapi32.dll" library are those to manipulate with Windows registry. We can expect that about 56,62 % of the samples can register themselves as "startup" programs.

From "User32.dll" is evident, that about 55% samples of the package can use GUI elements, but not only for showing GUI components, but for spying also. There are methods that can be used by keyloggers. The "Gdi32.dll" allows manipulating with graphics. The "Version.dll" library allows getting system information. [8]

Not only the most used functions are interesting:

- “WriteFile” (72,10 %), “ReadFile” (55,79 %): file access is common also
- “CreateProcess”: at least 53,78 % of samples can run a new process
- “IsDebuggerPresent” (36,88 %): interesting function that tells, if the process is being debugged. The malware can perform different behavior for usual run and debugging.
- Network functions are not so often in this set of malware: WSock32.dll (11,11 %) and Wininet.dll (8,63 %)

3 Conclusion

The experiment shows that it is possible to classify malware by static methods in an effective way. However, there is also a certain difficulty to distinguish malware from the “friendly” application with this approach. The next research will connect the analysis with artificial intelligence and it will attempt to solve this problem.

The malware analysis is a large topic and lots of work is ahead. The next work will connect the artificial intelligence to the analyzing process. In the first step, the analyzing application will collect all interesting data from unknown application and neural networks will try to identify and classify application in detail.

The application will be also extended by other analyzing methods, including dynamic methods. In any case, required goals will be to automate all the methods and will try to improve existing methods by artificial intelligence.

4 Acknowledgement

The following grants are acknowledged for the financial support provided for this research: Grant of SGS No. SP2016/175, VSB – Technical University of Ostrava.

This work was supported by The Technology Agency of the Czech Republic TACR TF01000091.

References

1. SIKORSKI, Michael and Andrew HONIG. *Practical malware analysis: the hands-on guide to dissecting malicious software*. San Francisco: No Starch Press, 2012. ISBN 978-1-59327-290-6.
2. EILAM, Eldad. *Reversing: Secrets of reverse engineering*. Indianapolis: Wiley, 2005. ISBN 0-7645-7481-7.
3. AQUILINA, James M., Eoghan CASEY and Cameron H. MALIN. *Malware forensics: investigating and analyzing malicious code*. Burlington, MA: Syngress Pub., 2008. ISBN 978-1-59749-268-3.
4. XU, J.-Y., A.H. SUNG, P. CHAVEZ and S. MUKKAMALA. Polymorphic Malicious Executable Scanner by API Sequence Analysis. *Fourth International Conference on Hybrid Intelligent Systems (HIS'04)*. IEEE, 2004, 378-383. DOI: 10.1109/ICHIS.2004.75. ISBN 0-

- 7695-2291-2. Available from:
<http://ieeexplore.ieee.org/lpdocs/epic03/wrapper.htm?arnumber=1410033>
5. EGELE, Manuel, Theodoor SCHOLTE, Engin KIRDA and Christopher KRUEGEL. A survey on automated dynamic malware-analysis techniques and tools. *ACM Computing Surveys*. 2012, 44(2), 1-42. DOI: 10.1145/2089125.2089126. ISSN 03600300. Available from: <http://dl.acm.org/citation.cfm?doid=2089125.2089126>
 6. YE, Yanfang, Dingding WANG, Tao LI, Dongyi YE and Qingshan JIANG. An intelligent PE-malware detection system based on association mining. *Journal in Computer Virology*. 2008, 4(4), 323-334. DOI: 10.1007/s11416-008-0082-4. ISSN 1772-9890. Available from: <http://link.springer.com/10.1007/s11416-008-0082-4>
 7. ALAZAB, Mamoun, Sitalakshmi VENKATARAMAN and Paul WATTERS. Towards Understanding Malware Behaviour by the Extraction of API Calls. In: 2010 *Second Cybercrime and Trustworthy Computing Workshop* [online]. IEEE, 2010, 52-59 [cit. 2016-07-20]. DOI: 10.1109/CTC.2010.8. ISBN 978-1-4244-8054-8. Available from: <http://ieeexplore.ieee.org/lpdocs/epic03/wrapper.htm?arnumber=5615097>
 8. Windows API Index. *Microsoft MSDN* [online]. 2016 [cit. 2016-07-20]. Available from: <https://msdn.microsoft.com/en-us/library/windows/desktop/ff818516%28v=vs.85%29.aspx>

Multiple Range Query Processing

Martin Zwierzyna and Michal Krátký

Department of Computer Science, FEECS,
VŠB – Technical University of Ostrava, 17. listopadu 15,
708 33 Ostrava – Poruba, Czech Republic
{martin.zwierzyna, michal.kratky}@vsb.cz

Abstract. In this paper we present multiple range query processing for various data structures. We review a multiple range query algorithm developed for multidimensional data structures and we discuss its adaptation for the B-tree. We also show that the multiple range query processing outperforms the range query algorithm where a set of queries is processed query by query. The main idea of these algorithms is to minimize the IO and CPU cost.

Keywords: Multiple Range Query Processing, B-tree, multidimensional data, R-tree

1 Introduction

With multidimensional data we encounter every day, they can represent an eshop catalog structure or the geometrical shape of objects. Query processing of multidimensional data is discussed for many years and also many algorithms have been developed. Multidimensional data query processing has some performance issues which is more evident when the space dimensionality increases. In [1] authors introduced a multiple range query algorithm for the R-tree and we decided to apply a similar solution for the B-tree.

2 Adaptation of Algorithm for B-tree

As we mentioned in introduction, our multiple range query algorithm for the B-tree is based on the algorithm introduced for the R-tree. The R-tree (see Figure 1) is a multidimensional data structure which was introduced by Antonin Guttman in 1984 [2]. Each space object is represented as an *MBR* (*minimum bounding rectangle*) to overlap each other. The maximum number of items in every node is called the branched factor (M). The minimal number of items in a node is represented by the variable m , the following rule must be met [2]:

$$m \leq \frac{M}{2}$$

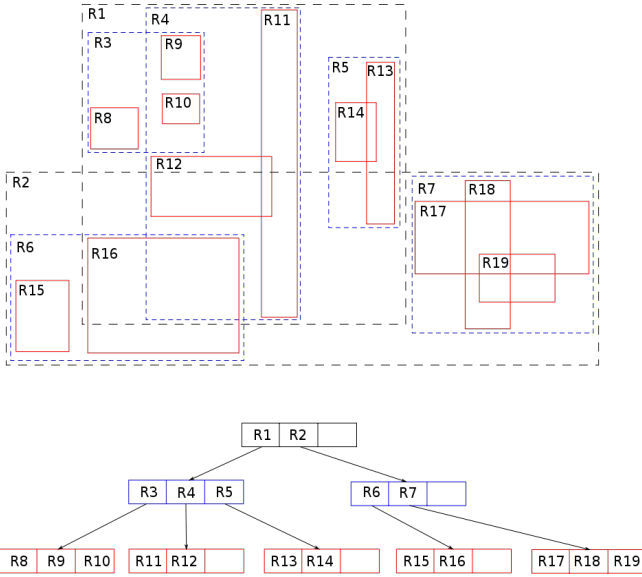


Fig. 1. An instance of the R-tree

The height of the R-tree containing N tuples is at most $\lceil \log_m N \rceil - 1$ because the branching factor of each node is at least m .

The B-tree (see Figure 2) is represented as an ordered data structure distinguishing inner and leaf nodes, where inner nodes include the low and high boundaries of child nodes and divide items to smaller ordered sets. In general [3], each node in the B-tree of the order d contains at most $2d$ keys and $2d + 1$ pointers. When we want to find an item, it is necessary to start in the root node and node boundaries set which child node has to be accessed. It continues until a leaf node is reached; it contains a set of items found.

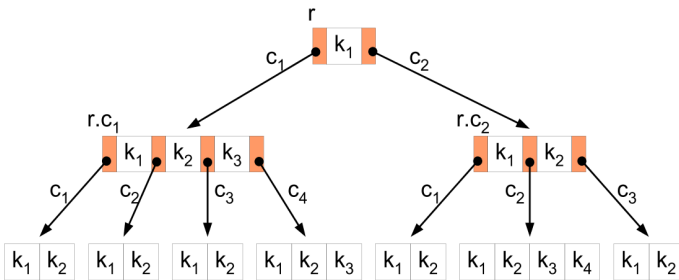


Fig. 2. An instance of the B-tree

It is evident that the R-tree and the B-tree range query algorithms are different. In the R-tree we use *IsIntersected* and *IsInRectangle* functions for testing of queries in nodes, whereas in the case of the B-tree we use the *Compare* function for inner as well as leaf nodes. We distinguish two types of range queries:

1. Range query
2. Multiple range query

Range query represents a method applying every query one-by-one which is not the most efficient solution in each situation. However *multiple range query* allows us to apply all queries in one B-tree search. However there is a performance issue which it is necessary to solve; when we take all queries and apply them on every node of a tree we find out that it is not efficient. There could arise cases, where the node contains relevant items only for some queries, i.e. some queries all tested redundantly. Therefore it is not necessary to apply them on all nodes, but choose only a set of relevant queries. And it is also useless, if we know, that we found all relevant items for a query to use it later, because it is impossible to find for it any relevant item in the next part of the B-tree. Therefore we invented an algorithm checking the relevance of the queries for each upcoming node and also throws already used queries. In Figure 3 you can see a partial example of filtering the individual queries in a query batch.

In the first step, the algorithm contains all possible queries for the level 0. In the second step, it knows that it has to move to the node *1-2* and it is certainly, that *Q1* and *Q2* are relevant for the upcoming subtree. So, we push them to the query array for the level 1 and also, because they can not match any item on the next node *3-4*, we remove them from the query array for the level 0. In Step 3 it moves to the next node, finds *Q1* as relevant for the upcoming subtree, pushes it to the query array of level 2 and removes from the query array for level 1. *Q2* is not matched for the node 1 of level 2 and it will be used in scanning of next leaf node 2.

2.1 Search Methods

In this subsection we describe two main types of search algorithms:

1. Sequence search
2. Binary search

But, in relation to the B-tree, we must split this two basic types to the next two others:

1. Search on the inner node
2. Search on the leaf node

In practice it works that inner node search is used for pass through the B-tree and to generate relevant queries for each level. Leaf node search is used to create the final result set, which represents items matched by the queries.

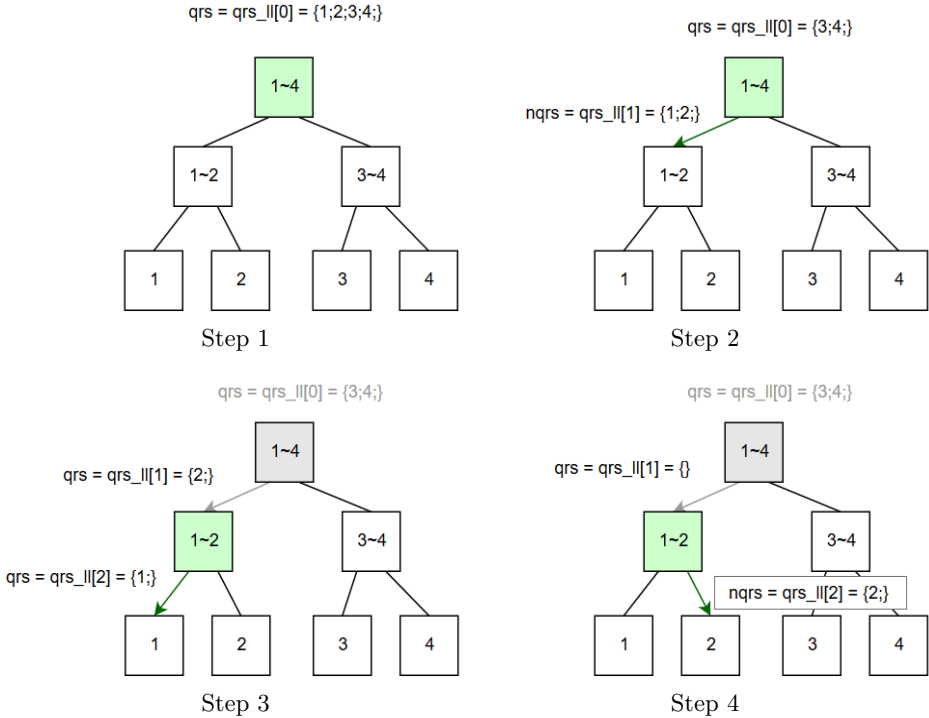


Fig. 3. Filtering of Individual Queries in a Batch

After performing some experiments with sequence and binary search we observed that it is a good idea to make some more search methods combining this two search types. We implemented next two search methods:

1. **LOSEQ** - search using sequence scan on the root node (binary search on other nodes)
2. **LLBIN** - search using binary scan on the leaf level (sequence on other nodes)

3 Preliminary Results

In our test we focus on the dimension length, selectivity of individual queries, number of queries and also number of items in the B-tree. It is clear that batch range query has better results in both cases (comparisons count and execution time) than standard range query. For queries with high selectivity binary search has better comparison results by 15% than sequence search and LLBIN even by 22%. For low selectivity binary and sequence search achieve similar results (difference about 0.1%) and LLBIN only by 2% better results than sequence and binary search methods.

References

1. P. Chovanec and M. Krátký, “On the Efficiency of Multiple Range Query Processing in Multidimensional Data Structures,” in *IDEAS*, IDEAS, 2013.
2. A. Guttman, “R-Trees: A Dynamic Index Structure for Spatial Searching,” in *Proceedings of ACM International Conference on Management of Data (SIGMOD 1984)*, pp. 47–57, ACM Press, June 1984.
3. D. Comer, “The Ubiquitous B-Tree,” *Computing Surveys*, vol. 11, no. 2, p. 123137, 1979.

Global Optimization Using Space Filling Curves

Michaela Bailová

Department of Applied Mathematics, FEECS,
VŠB – Technical University of Ostrava, 17. listopadu 15,
708 33 Ostrava – Poruba, Czech Republic
michaela.bailova@vsb.cz

Abstract. Many engineering problems lead to a multivariate global optimization. Such issue can be difficult to solve. An approach presented in this paper is to simplify the problem reducing its dimension. A way how to provide such simplification is to use a space filling curve. The article introduces the concept of space filling curves, some of their properties, and an analytic way how to compute its coordinates. Subsequently, an advantage of the space filling curve is revealed by comparing it with another type of a curve.

Keywords: Global optimization, dimension reduction, space filling curves, Lipschitz continuity, Hölder continuity

1 Introduction

This paper will deal with the following problem of searching a global minimum

$$F^* = F(y^*) = \min\{F(y), y \in D\}, \quad (1)$$

where D is a domain of the search

$$D = \{y \in \mathbb{R}^N, -2^{-1} \leq y_j \leq 2^{-1}, 1 \leq j \leq N\}. \quad (2)$$

The objective function $F(y)$ also satisfies the Lipschitz condition with a constant L , $0 < L < \infty$. The main idea of the paper is to turn the multivariate optimization problem into its one-dimensional equivalent, which can be solved using some techniques developed for univariate optimization. One way how to do so is to develop a continuous correspondence y mapping an one-dimensional interval onto the hypercube. The problem (1) will turn into the following one

$$F^* = F(y^*) = F(y(x^*)) = \min\{F(y(x)) : x \in [0, 1]\}. \quad (3)$$

2 Space filling curves

Main ideas in this chapter are gained from [1] and [2]. At the beginning it is important to write a definition of an object of our interest.

Definition 1. A single-valued continuous correspondence $y(x)$ mapping the unit interval $[0, 1]$ on the x -axis onto the hypercube D from (2) is said to be a space filling curve.

Hereinafter, the most common type of the space filling curve will be described as a limit object generated by the following scheme. For the purpose of this paper, the construction will be illustrated only for a two-dimensional case. At first, divide the domain into 2^N equal hypercubes. Number all of the subcubes using the index z_1 , $0 \leq z_1 \leq 2^N - 1$. Each subcube of the first partitioning is designated $D(z_1)$. Consequently, divide (using the same approach) each of the subcubes from the previous partitioning into 2^N second-partition subcubes and number them with the index z_2 , $0 \leq z_2 \leq 2^N - 1$. Each subcube of the second partitioning is now designated $D(z_1, z_2)$. Continuing the same process yields hypercubes $D(z_1, z_2, \dots, z_M)$ and the edge length will be 2^{-M} . Total amount of the subcubes in M -th partition will be equal to 2^{MN} and

$$D \supset D(z_1) \supset D(z_1, z_2) \supset \dots \supset D(z_1, z_2, \dots, z_M).$$

The process is illustrated by Fig.1.

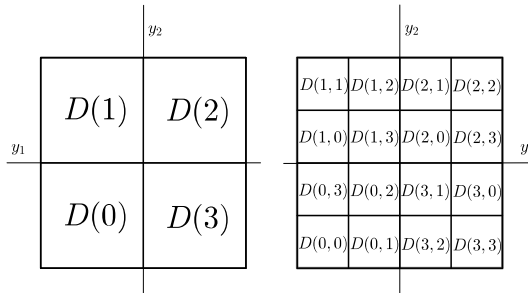


Fig. 1. The first and the second partition of the cube D .

Now, cut the interval $[0, 1]$ in 2^N equal subintervals. Every single part is designated $d(z_1)$, $0 \leq z_1 \leq 2^N - 1$. In the same manner, cut all the subintervals once again, etc. Continuing the same process leads to 2^{MN} subintervals with length equal to 2^{-MN} , which are designated $d(z_1, z_2, \dots, z_M)$. It is also true, that

$$[0, 1] \supset d(z_1) \supset d(z_1, z_2) \supset \dots \supset d(z_1, z_2, \dots, z_M).$$

The process is illustrated by Fig.2. To ensure some significant properties, the introduced correspondence must fulfil the following conditions.

Condition 1. $D(M + 1, v') \subset D(M, v'')$ if and only if $d(M + 1, v') \subset d(M, v'')$.

Condition 2. Two subintervals $d(M, v')$, $d(M, v'')$ have a common end-point if and only if the corresponding subcubes $D(M, v')$, $D(M, v'')$ have a common face.

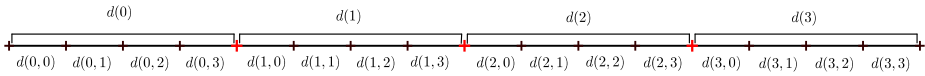


Fig. 2. The first and the second partition of the unit interval.

Simply put, the subintervals and the corresponding subfaces have to be in the same relationship.

The question is how to construct a correspondence which satisfies both of the above mentioned conditions. The approach in this paper is based on usage of a single valued Hilbert curve according to [1], and will be introduced in the subsequent chapter.

3 Hilbert Curve and its Complex Representation

For the purpose of the article, a modified version of the Hilbert space filling curve will be used. The first iterations can be seen in the following figures. Looking at

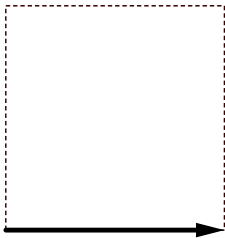


Fig. 3.

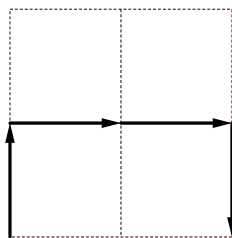


Fig. 4.

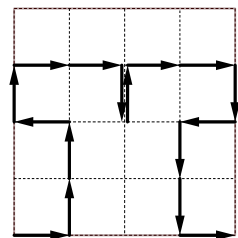


Fig. 5.

the pictures above, it is obvious that the Hilbert curve originates in the lower-left corner and terminates in the lower right corner. The subsquares have to be oriented in such a way that the exit point of each subsquare coincides with the entry point of the next one. The correct orientation of the subsquares is illustrated by the bold arrows. Configurations in the figures 4, 5 can be gained from the previous ones using the following transformations:

1. Shrink Q in the ratio 2:1, rotate the resulting square through $\frac{\pi}{2}$ and reflect it on the imaginary axis. Combining these three transformations leads to:

$$h_0z = \frac{1}{2}\bar{z}i.$$

2. Shrink Q in the ratio 2:1 and shift it $\frac{1}{2}$ unit upwards: $h_1z = \frac{1}{2}z + \frac{i}{2}$.
3. Shrink Q in the ratio 2:1 and shift it $\frac{1}{2}$ unit upwards and $\frac{1}{2}$ unit to the right: $h_2z = \frac{1}{2}z + \frac{1}{2} + \frac{i}{2}$.
4. Shrink Q in the ratio 2:1, rotate it through $-\frac{\pi}{2}$, reflect it on the imaginary axis, shift it one unit to the right and $\frac{1}{2}$ unit upwards: $h_3z = -\frac{1}{2}\bar{z}i + 1 + \frac{i}{2}$.

Application of these transformations to Fig.3 leads to Fig.4. Application of these transformations to Fig.4 yields Fig.5, etc.

Furthermore, assume that $x \in I$ is represented in a quaternary form:

$$x = 0_4q_1q_2q_3 \dots, \quad \text{where } q_i \in \{0, 1, 2, 3\}.$$

The variable x belongs to the $(q_1 + 1)$ -th subinterval of the first partition of I into four subintervals. Hence, its image lies in the $(q_1 + 1)$ -th subsquare of the first partition of Q into four subsquares: $y(x) \in h_{q_1}Q$. It also lies in the $(q_2 + 1)$ -th subinterval of the second partition of $(q_1 + 1)$ -th subsquare $h_{q_1}Q$. It means that $y(x) \in h_{q_1}h_{q_2}Q$. Continuing the process ad infinitum leads to

$$y(x) = \begin{pmatrix} Re \\ Im \end{pmatrix} \lim_{M \rightarrow \infty} h_{q_1}h_{q_2} \dots h_{q_M}Q. \tag{4}$$

The formula can be facilitated by using knowledge of complex analysis and substitutions. Reader can find the whole process of simplification in [1] (page 13). For the sake of the paper, the function F was evaluated only in the discrete points using (4). Continuous version of the curve can be also found in [1].

3.1 Properties of the Hilbert Curve

Theorem 3. *Let $y : [0, 1] \rightarrow D$ be the Hilbert curve. If the function $F(y)$, $y \in D$, is Lipschitzian with the constant L , then the one-dimensional function $F(y(x))$, $x \in [0, 1]$, fulfills the uniform Hölder condition with the constant $2L\sqrt{N + 3}$, i.e.*

$$|F(y(x')) - F(y(x''))| \leq 2L\sqrt{N + 3}(|x' - x''|)^{\frac{1}{N}}, \text{ where } x', x'' \in [0, 1]. \tag{5}$$

Proof. The proof is based on some geometrical properties of the space filling curve and can be found in [2].

Theorem 4. *Assume that:*

- $y_\varepsilon : [0, 1] \rightarrow D$,
- $F(y)$, $y \in D$, is Lipschitzian with the constant L ,
- $\exists! y^* : F(y^*) = \min_{y \in D} F(y)$,
- $\varepsilon > 0$,
- $\forall y \in D : \text{dist}(y, y_\varepsilon([0, 1])) < \varepsilon$,
- $x_\varepsilon^* \in [0, 1] : F(y_\varepsilon(x_\varepsilon^*)) = \min_{x \in [0, 1]} F(y_\varepsilon(x))$.

Then

$$\begin{aligned} |F(y^*) - F(y_\varepsilon(x_\varepsilon^*))| &\leq \varepsilon L, \\ \|y^* - y_\varepsilon(x_\varepsilon^*)\| &\rightarrow 0 \text{ for } \varepsilon \rightarrow 0^+. \end{aligned}$$

Proof. The proof can be found in the extended version of this paper, which is currently in the progress.

The question may be why does the paper deal with the complicated Hilbert curves. There are obviously many types of curves that fulfil the desired conditions of the Theorem 4 and are much easier to construct. One of them is illustrated by the Fig.6.

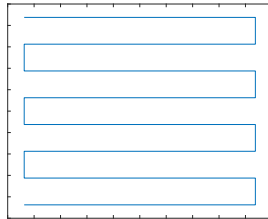


Fig. 6. Piecewise linear curve.

The problem is that the described curve contains some linear segments, which cover a large number of nodes. In [2] is shown that in this case there is no way how to provide the validity of a relation similar to (5). In other words, two distant points in the interval $[0, 1]$ can be very close in D . The issue is illustrated in the Fig.7, 8. for a function of the type $F(x, y) = x^2 + y^2$.

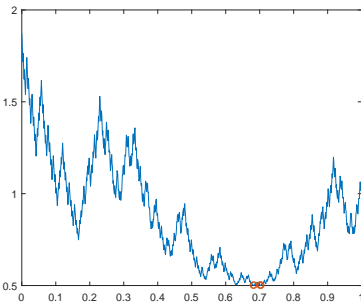


Fig. 7. Plot of $F(y(x))$, y is a SFC.

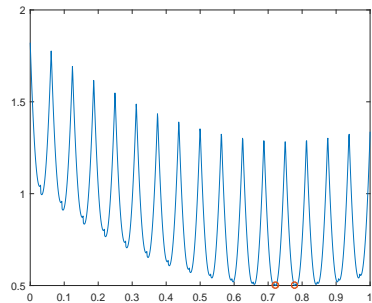
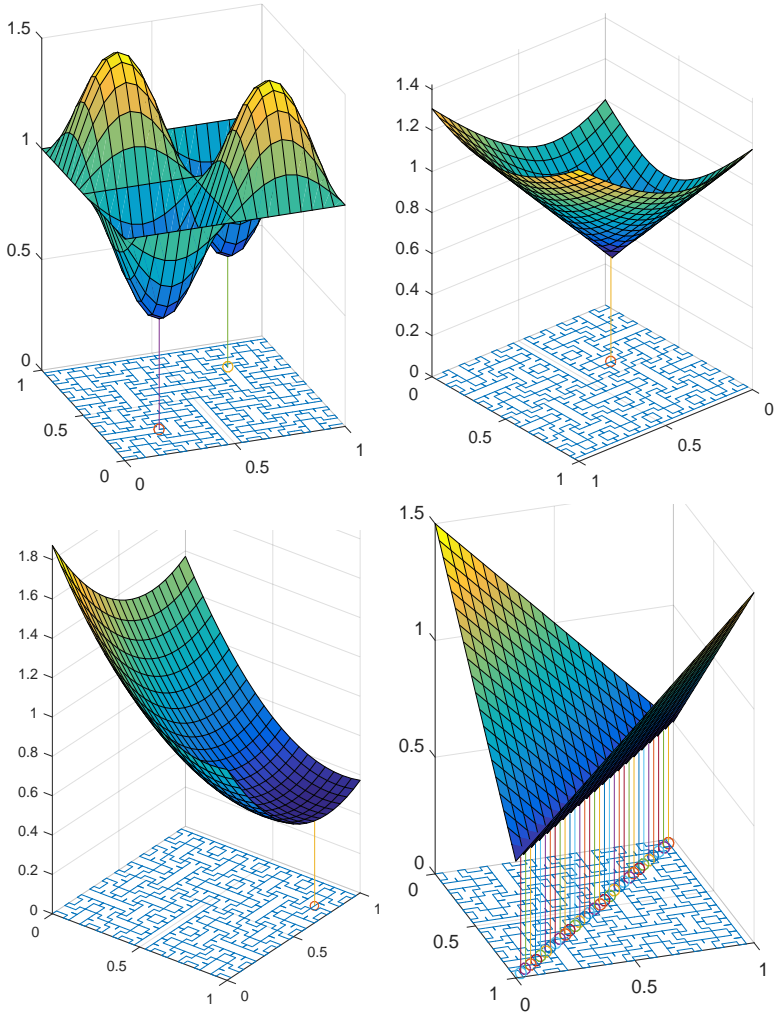


Fig. 8. Plot of $F(l(x))$, l from (6)

4 Results

For illustration, 5-th iteration of the curve and four types of functions were chosen: $F_1(x, y) = -\sin(\pi x)\sin(\pi y)$, $F_2(x, y) = \sqrt{x^2 + y^2}$, $F_3(x, y) = x^2 +$

y^2 , $F_4(x, y) = |x + y|$. My algorithm based on the knowledge summarized in this paper also worked for some multiextremal functions and for a nonsmooth function. The results are illustrated in the following figures.



References

1. Sagan, Y. D., : Introduction to Global Optimization Exploiting Space-Filling Curves. Springer, 2013
2. Sergeyev, H., Strongin, R. G., Lera, D.: Space Filling Curves. Springer New York, 1994

Application of Three-way Contingency Tables

Michal Běloch

Department of Applied Mathematics, FEECS,
VŠB – Technical University of Ostrava, 17. listopadu 15,
708 33 Ostrava – Poruba, Czech Republic
michal.beloch@vsb.cz

Abstract. Medical data usually contains a variety of the categorical variables. The experiment itself is also typically designed with at least two groups of patients in mind. The standard tool to decide the dependence between two categorical variables is the contingency tables. Sometimes the third categorical variable is considered as well as its influence on the mutual dependence, requiring another dimension in conventional contingency table. First, the general theory and the types of dependencies in three-way tables are described. Then it is applied on simulated data based on ongoing research of diabetes in Faculty hospital of Ostrava, showing the possible processing of the data and the interpretation of the result.

Keywords: three-way contingency tables, categorical data

1. Three-way contingency tables

A three-way contingency table [1, 2, 3] is an array of observed values o_{ijk} , where $i = 1, \dots, I$, $j = 1, \dots, J$, $k = 1, \dots, K$. It represents the relationship between three categorical variables X, Y, Z . The variable X forming rows has I categories and is called an explanatory variable. The variable Y forming columns has J categories and is called a response variable. Finally the variable Z forming layers has K categories and is called a control variable. Standard depiction of three-way table is as K two-way tables, although it is possible to partition the original table across the other variables as well. This way we obtain XY , XZ or YZ partial tables (omitted variable is the one kept at fixed

level). Summing all possible layers of a set of partial tables leads to the corresponding marginal table. Therefore partial table controls over the third variable while marginal table ignores it.

1.1 Types of independence

In three-way tables there are numerous ways of describing the different models of independence. The various types of independence are computed and interpreted with the help of odds ratio. The odds ratio can be think of in the same way as in the two-way tables. In the case of three-way tables we can extend the odds ratio to the marginal tables and the partial tables. The considered types of independence are:

- **Complete independence** – All variables are independent of one another. It means that

$$P(X = i, Y = j, Z = k) = P(X = i) \cdot P(Y = j) \cdot P(Z = k).$$
 Short way to express this model is (X, Y, Z) . Complete independence implies joint independence.
- **Joint independence** – Two variables are jointly independent of the third. This type says nothing about the relationship of the joint variables. They might be related or not. This fact makes the complete independence special case of the joint independence. This model can be expressed as (XY, Z) . In total three models can be constructed (other possibilities are (XZ, Y) and (YZ, X)). Joint independence implies marginal independence.
- **Marginal independence** – Two variables are marginally independent if they are independent within their marginal table. Short expression is (X, Y) meaning we consider independence model for variables X and Y while ignoring the effect of variable Z . There are three marginal independence models within the three-way table (other models are (X, Z) and (Y, Z)). Marginal independence does not imply joint independence.
- **Conditional independence** – Two variables are conditionally independent with respect to the third variable. In probability notation

$$P(X = i, Y = j | Z = k) = P(X = i | Z = k) \cdot P(Y = j | Z = k).$$

This type is tied with partial tables. We test whether the odds ratio is significantly different from 1 for each level of the partitioning variable. Short expression of this model is (XZ, YZ) . In general there are three types of conditional independence models (other models are (XY, XZ) and (XY, YZ)). Conditional independence does not imply marginal independence and vice versa. In fact conditional and marginal independence can even go in the opposite direction. This fact is known as Simpson's paradox.

2. Application on diabetes data

2.1 Medical overview

One of the complications tied with the diabetes mellitus is the peripheral arterial disease [4]. It occurs when blood vessels in the legs are narrowed or blocked and the blood flow to legs and feet is decreased. Intervention may include conservative therapy, revascularization or amputation. Compared with amputation, revascularization is more cost effective.

2.2 Data description

The data set contains patients with diagnosed diabetes mellitus with peripheral arterial disease. Each patient is described by numerous parameters so for the purpose of this article, three parameters were chosen. The first is the sex of the patient, either male or female. The second is the treatment group. The patients are divided into four groups (A, B, C, D). The patients in the first three groups were treated with the different approach, while the last group D is the referential group. The last parameter is the amputation, whether the leg of the patient had to be amputated or not.

In accordance with the theory in section 1, the explanatory variable X is the treatment *group* with values {A, B, C, D}, the response variable Y is the *amputation* with values {No, Yes} and the control variable Z is the *sex* with values {Female, Male}. The original number of the patients was 58, which was too low, therefore other values were sampled up to 200 in total (table 1 and table 2).

		Amputation		
Sex	Group	No	Yes	Total
Female	A	15	2	17
	B	8	7	15
	C	7	3	10
	D	9	6	15
	Total	39	18	57
Male	A	28	12	40
	B	17	6	23
	C	30	16	46
	D	19	15	34
	Total	94	49	143

Table 1. Structure of the data set – XY partial table

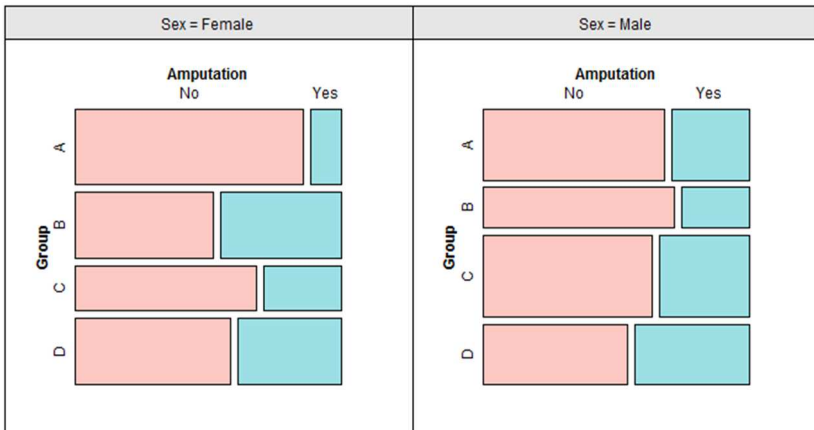


Fig. 1. Mosaic plot for table 1

Group	Amputation		Total
	No	Yes	
A	43	14	57
B	25	13	38
C	37	19	56
D	28	21	49
Total	133	67	200

Table 2. Structure of the data set – XY marginal table

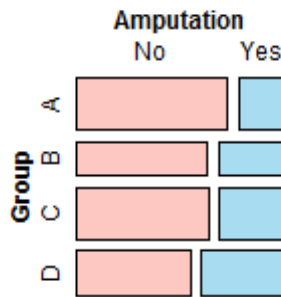


Fig. 2. Mosaic plot for table 2

2.3 Results

We first perform the test for complete independence. The hypotheses to test are:

H_0 : The model of complete independence is true

H_A : The model of complete independence is not true

For purpose of testing we use the χ^2 -test of independence. The prerequisite is that all of the expected values are sufficiently large. We assume this condition holds. After running the test, we can conclude that we do not reject null hypothesis (χ^2 -test of independence, p-value = 0.1776), the model of complete independence is true. Since the complete independence implies the joint independence, we do not need to perform the separate test.

We continue with marginal independence:

H_0 : The amputation is independent of the group

H_A : $\neg H_0$

In this case we cannot reject the null hypothesis (χ^2 - test of independence, p-value = 0.2633), the occurrence of amputation does not depend on treatment group while ignoring the effect of the sex. In other words, the type of the chosen treatment does not increase the chance to avoid the leg amputation.

Lastly we check whether the sex influence the relationship between group and amputation.

H_0 : The amputation is independent of the group with respect to sex

H_A : $\neg H_0$

We do not reject the null hypothesis (Cochran-Mantel-Haenszel test, p-value = 0.2658), so the independence between the treatment group and the need for amputation holds even when the sex of the patients is taken into account.

Acknowledgement:

This work was supported by The Ministry of Education, Youth and Sports from the National Programme of Sustainability (NPU II) project “IT4Innovations excellence in science - LQ1602”.

References

1. Andersen, E.B. Introduction to the statistical analysis of categorical data. Springer Science & Business Media, 1997.
2. Azen, R., Walker, C.M. Categorical data analysis for the behavioural and social sciences, 2011.
3. Kateri, M., Contingency table analysis: Methods and implementation using R, Springer, 2014.
4. Santilli, J.D., Santilli, S.M., Chronic critical limb ischemia: Diagnosis, treatment and prognosis, Minneapolis, Minnesota, Am Fam Physician. 1999 Apr 1;59(7):1899-1908.

Stochastic Galerkin Method for Random Material Problem

Michal Béréš

Department of Applied Mathematics, FEECS,
VŠB – Technical University of Ostrava, 17. listopadu 15,
708 33 Ostrava – Poruba, Czech Republic
michal.beres@vsb.cz

Abstract. This article presents a short study of the stochastic Galerkin method (SGM) applied on the Darcy flow problem with a random material field. We consider random material as log-normal random field with zero mean and a given auto-covariance function. The solution of this kind of problems can be generally divided into two parts, first we need to decompose the random field into product of random vector and function of spacial coordinates. This can be achieved using the Karhunen-Loève decomposition. The second part is the solution of randomly discretized problem via the SGM. The SGM is a simple extension of the Galerkin method, where random variables present additional problem dimensions. For discretization of the problem we use a standard finite element basis for spatial variables and a polynomial chaos discretization for random variables. The results of the SGM can be used for the analysis of the problem like examination of the average flow or as a tool for Bayesian inversion problems.

Keywords: Darcy flow, Gaussian random field, Karhunen-Loève decomposition, polynomial chaos, Stochastic Galerkin method

1 Introduction and problem setting

In a standard mathematical modelling approach to solving physical phenomena we usually use deterministic parameters of solved problems such as boundary conditions, material constants etc. This simplifications neglect natural uncertainty in these parameters, which can lead to unreliable solutions. Fast development of computational resources such as supercomputers allows us to compute very extensive problems e.g. solving partial differential equations with uncertainty in parameters. Popular methods for computation of this kind are for example the Multilevel Monte Carlo method or stochastic Galerkin method, which will be presented in this article. A survey of the Multilevel Monte Carlo method applied to the same problem can be found in [1].

Consider 2D Darcy flow problem on unit square with pressure drop from 1 on the left side to 0 on the right side and no flow condition on bottom and upper

side:

$$\begin{cases} -\operatorname{div}(k(x; \omega) \cdot \nabla u(x; \omega)) = 0, & \forall x \in \mathcal{D} = \langle 0, 1 \rangle \times \langle 0, 1 \rangle, \forall \omega \in \Omega \\ u(x; \omega) = 1, & \forall x \in 0 \times \langle 0, 1 \rangle, \forall \omega \in \Omega \\ u(x; \omega) = 0, & \forall x \in 1 \times \langle 0, 1 \rangle, \forall \omega \in \Omega \\ \frac{\partial u(x; \omega)}{\partial n(x)} = 0, & \forall x \in \langle 0, 1 \rangle \times \{0, 1\}, \forall \omega \in \Omega \end{cases}, \quad (1)$$

where ω represents an event from the sample space Ω . In general functions $k(x; \omega), u(x; \omega) : \mathcal{D} \times \Omega \rightarrow \mathbb{R}$ are understood as random fields, which mean that for every point $x_0 \in \mathcal{D}$ is $K_0 = k(x_0; \omega) : \Omega \rightarrow \mathbb{R}$ a random variable and for every $\omega_0 \in \Omega$ is $k_0(x) = k(x; \omega_0) : \mathcal{D} \rightarrow \mathbb{R}$ a function of spacial domain.

Such a problem is very complex, because the random field k represents infinite number of random variables (value in each point of domain). For solving this kind of problem we have to reduce the number of random variables to some finite, ideally small, number. This can be done by the Karhunen-Loève (KL) decomposition.

For more detailed insight into SGM and KL decomposition see [3].

2 Karhunen-Loève decomposition

Let $k(x; \omega)$ be a Gaussian random field with zero mean $\mu_k(x) = 0$ and auto-covariance function $c(x, y) = \operatorname{cov}(k(x; \omega), k(y; \omega))$. As auto-covariance function we take $c(x, y) = \sigma^2 \cdot \exp(\|x - y\| / \lambda)$, where σ represents standard deviation of random variables in single points and λ states for correlation length.

To define KL decomposition we first introduce operator $[Cu](x) = \int_{\mathcal{D}} c(x, y) \cdot u(y) dy$, which is compact, positive and self-adjoint.

KL decomposition of random field is than defined as

$$k(x; \omega) = \mu_k(x) + \sum_{i=1}^{\infty} \sqrt{\lambda_i} \cdot \psi_i(x) \cdot Z_i(\omega),$$

where λ_i, ψ_i are eigenpairs of operator C and $Z_i(\omega)$ are mutually uncorrelated random variables satisfying $\mathbb{E}(Z_i) = 0, \mathbb{E}(Z_i Z_j) = \delta_{ij}$. In the case of Gaussian random field random variables Z_i will be also Gaussian. Note that random variables Z_i are only uncorrelated, but in case of Gaussian random variables it implies independency.

The difficult part of the KL decomposition is spectral decomposition of operator C . The spectral decomposition can be obtained by solving the following eigenvalue problem

$$\int_{\mathcal{D}} c(x, y) \cdot \psi_i(y) dy = \lambda_i \cdot \psi_i(x), \forall i \in \mathbb{N},$$

which is a case of Fredholm integral equation and it can be solved by the Galerkin method. First we construct weak formulation

$$\begin{cases} \text{Find } \psi_i, \lambda_i : \\ \int_{\mathcal{D}} v(x) \cdot \int_{\mathcal{D}} c(x, y) \cdot \psi_i(y) dy dx = \lambda_i \cdot \int_{\mathcal{D}} v(x) \cdot \psi_i(x) dx, \quad \forall v \in V, \end{cases} \quad (2)$$

where space V can be understood for example as $L_2(\mathcal{D})$. To complete the solution we need to choose some discretized basis $\langle \phi_1(x), \dots, \phi_n(x) \rangle = V_n \subset V$ and assemble Galerkin system of equations

$$\mathbb{A} \overline{\psi_i^n} = \lambda_i^n \cdot \mathbb{W} \cdot \overline{\psi_i^n}, \tag{3}$$

where $\mathbb{A}_{ij} = \int_{\mathcal{D}} \int_{\mathcal{D}} c(x, y) \cdot \phi_i(y) \cdot \phi_j(x) dy dx$ and $\mathbb{W}_{ij} = \int_{\mathcal{D}} \phi_i(x) \cdot \phi_j(x) dx$. System (3) is generalized eigenvalue problem.

2.1 Numerical results

In this part we compute the approximation of the KL decomposition. As discretized basis $\langle \phi_i(x), \dots, \phi_n(x) \rangle$ we use goniometric basis of tensor product of 1D analytical solution, which can be found in [2]. Because this basis is orthogonal, matrix \mathbb{W} is diagonal. The difficult part is calculation of 4D integrals for every \mathbb{A}_{ij} .

A sample solution with basis containing 20×20 function and integration with Gauss-Legendre quadrature of 50 points per dimension can be seen in the following figure.

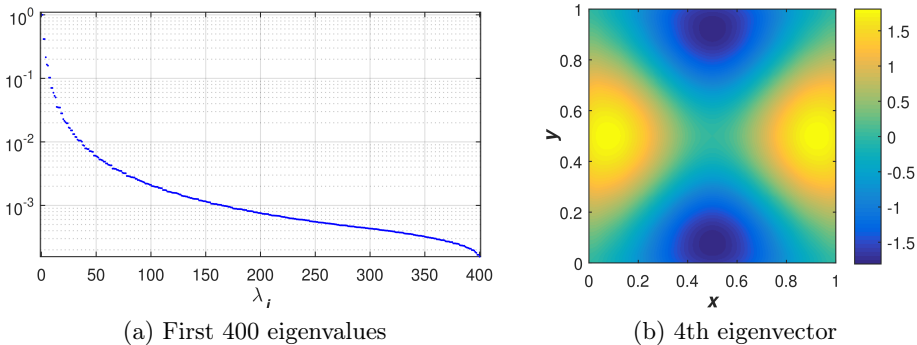


Fig. 1. Approximation of spectral decomposition

3 Stochastic Galerkin Method

The random field in (1) will be considered as log-normal random field, which can be expressed as exponential of Gaussian random field. Using truncated KL decomposition (note very fast decay of eigenvalues in figure 1a), $\mu_k(x) = 0$ and notation $k_i(x) = \sqrt{\lambda_i} \cdot \psi_i(x)$ we get following random field representation

$$k(x; \mathbf{Z}) = \exp \left(\sum_{i=1}^N k_i(x) \cdot Z_i \right),$$

where $\mathbf{Z} = (Z_1, \dots, Z_N)$ denotes random vector.

Now we can approximate the solution $u(x; \omega)$ as a function of the spacial variable and the random vector \mathbf{Z} . So we want to find $u(x; \mathbf{Z}) : \mathcal{D} \times \mathbb{R}^N \rightarrow \mathbb{R}$.

In the weak formulation we assume $u(x; \mathbf{Z})$ to be from tensor product of $H^1(\mathcal{D})$ and $L^2_{dF\mathbf{Z}}(\mathbb{R}^N) := \left\{ f : \mathbb{R}^N \rightarrow \mathbb{R} : \int_{\mathbb{R}^N} f(z)^2 dF\mathbf{Z} < \infty \right\}$, where $dF\mathbf{Z}$ denotes measure given by the distribution of the random vector \mathbf{Z} (in case of Gaussian random variables it's probability density of \mathbf{Z}). It can be shown, that the space $V := H^1(\mathcal{D}) \otimes L^2_{dF\mathbf{Z}}(\mathbb{R}^N)$ is a Hilbert space.

We will assume, that the solution $u(x; \mathbf{Z}) = u_H(x; \mathbf{Z}) + u_0(x; \mathbf{Z})$, where $u_0 \in V$ and satisfies Dirichlet boundary condition and $u_H \in V_0 := H^1_0(\mathcal{D}) \otimes L^2_{dF\mathbf{Z}}(\mathbb{R}^N)$. Now we construct the weak formulation

$$\left\{ \begin{array}{l} \text{Find } u(x; \mathbf{Z}) = u_H(x; \mathbf{Z}) + u_0(x; \mathbf{Z}), u_H \in V_0 : \\ \int_{\mathbb{R}^N} \int_{\mathcal{D}} k \cdot \nabla u_H \cdot \nabla v \, dx \, dF\mathbf{Z} = - \int_{\mathbb{R}^N} \int_{\mathcal{D}} k \cdot \nabla u_0 \cdot \nabla v \, dx \, dF\mathbf{Z}, \quad \forall v(x; \mathbf{Z}) \in V_0. \end{array} \right.$$

Because V_0 is a tensor product of spaces, we can replace $\forall v(x; \mathbf{Z}) \in V_0$ with $\forall v_P(\mathbf{Z}) \in L^2_{dF\mathbf{Z}}(\mathbb{R}^N), \forall v_D(x) \in H^1_0(\mathcal{D})$, so $v(x; \mathbf{Z}) = v_D(x) \cdot v_P(\mathbf{Z})$. This allows us to use separate basis functions for spacial variable x and stochastic variable \mathbf{Z} . As basis functions for spacial variable we choose finite elements basis and for stochastic variable we choose the polynomial chaos basis.

3.1 Polynomial chaos expansion

Let Z be a random variable such $\mathbb{E}(Z^{2-n}) < \infty, \forall n$. Polynomial chaos denotes a set of polynomials $\psi_i(Z)$ (i denotes the order of polynomial) satisfying $\mathbb{E}(\psi_i(Z) \psi_j(Z)) = \gamma_i \delta_{ij}$, where $\gamma_i = \mathbb{E}(\psi_i(Z)^2)$. With polynomial chaos we can approximate a function of random variable $f(X) \in L^2_{dFX}$ by polynomial chaos of random variable X

$$f_N(X) = \sum_{i=0}^N \psi_i(X) \cdot \frac{\mathbb{E}(\psi_i(X) \cdot f(X))}{\gamma_i}, \quad \|f_N(X) - f(X)\|_{L^2_{dFX}} \xrightarrow{N \rightarrow \infty} 0.$$

f_N is than projection of f into space of polynomials up to order N .

In case of random vector \mathbf{Z} of i.i.d. standard normal variables we will have polynomial chaos

$$\Psi_i(\mathbf{Z}) = \prod_{k=1}^N \psi_{i_k}(Z_k),$$

where N denotes length of \mathbf{Z} , i denotes multi-index of size N , and $\psi_{i_k}(Z_k)$ are Hermite polynomials of order i_k .

3.2 Assembling stiffness matrix

As mentioned before we use finite elements basis $\varphi_i(x)$ for spacial domain and Hermite polynomials basis $\psi_j(\mathbf{Z})$ (we now simplify aforementioned multi-index

into simple index) for random vector \mathbf{Z} . Discretized solution will take form of

$$u_H^h(x; \mathbf{Z}) = \sum_{i=1}^{N_P} \sum_{j=1}^{N_D} (\overline{u_H})_{ij} \cdot \varphi_j(x) \cdot \psi_i(\mathbf{Z}).$$

Using this discretization we obtain a system of linear equations $\mathbb{A} \cdot \overline{u_H} = \overline{b}$,

$$(\mathbb{A})_{ij,kl} = \int_{\mathbb{R}^N} \int_{\mathcal{D}} \exp\left(\sum_{m=1}^N k_m(x) Z_m\right) \nabla \varphi_j(x) \nabla \varphi_l(x) \psi_i(\mathbf{Z}) \psi_k(\mathbf{Z}) dx dF\mathbf{Z},$$

$$(\overline{b})_{ij} = \int_{\mathbb{R}^N} \int_{\mathcal{D}} \exp\left(\sum_{m=1}^N k_m(x) Z_m\right) \nabla \varphi_j(x) \psi_i(\mathbf{Z}) \nabla u_0(x) dx dF\mathbf{Z},$$

where integration over stochastic domain can be analytically expressed as some function of $k_m(x)$. This allows us to use the existing code for assembling matrix \mathbb{A} and vector \overline{b} , because

$$(\mathbb{A})_{ij,kl} = \int_{\mathcal{D}} d_{i,k}(x) \nabla \varphi_j(x) \nabla \varphi_l(x) dx, \quad (\overline{b})_{ij} = \int_{\mathcal{D}} d_{i,1}(x) \nabla \varphi_j(x) \nabla u_0(x) dx.$$

3.3 Numerical results

For numerical testing we chose a regular 50×50 grid for physical domain and truncated KL decomposition with 6 random variables with polynomial chaos up to order 5. Resulting matrix \mathbb{A} consist of 462×462 non-zero blocks (size of the polynomial chaos), each of size 2499×2499 (51×51 FEM basis function minus basis functions on Dirichlet boundary). In the following figure we can see mean and standard deviation of resulting pressure random field.

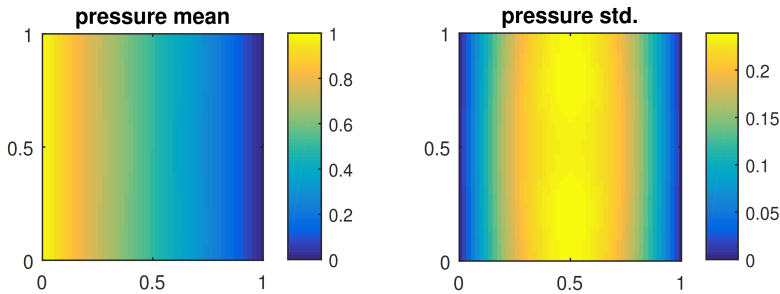


Fig. 2. Mean value and standard deviation of pressure solution random field

As a very simple error verification (only for discretization over random dimension) we can compare SGM solution with FEM solution with random material formed with same replication of random vector \mathbf{Z} .

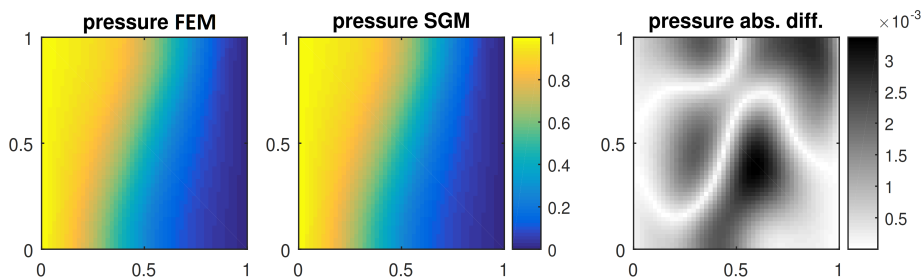


Fig. 3. Comparison of SGM solution and FEM solution at random point of Ω

4 Conclusions and future work

This article was meant as a short introduction to SGM, we outlined a path from differential equation with random field as input material parameter to discretized approximation of solution random field. We dealt with the spectral decomposition of operator given by the auto-covariance function and used the out-coming decomposition for assembling the SGM system of equations. The solved system had 1 154 538 unknowns and was solved by conjugated gradient method with block diagonal preconditioner. Resulting approximation can be for example used to calculate basic properties of pressure random field as mean and standard deviation see figure 2.

As continuation of this work the SGM solution can be used in Bayesian inverse problems as replacement of exhausting repeating solution of inspected PDE. Other future plan is solution of such problems with mixed formulation over spatial domain, using existing code in [4], which will give us also information about velocity field.

Acknowledgement

This work was supported by The Ministry of Education, Youth and Sports from the National Programme of Sustainability (NPU II) project “IT4Innovations excellence in science - LQ1602”.

References

- [1] Blaheta, R.; Běreš M.; Domesová, S. *A study of stochastic FEM method for porous media flow problem*. Proceedings of the 1st ICAMER. CRC Press, 2016.
- [2] Zhang, D.; Lu, Z.; *An efficient, high-order perturbation approach for flow in random porous media via Karhunen–Loeve and polynomial expansions*. Journal of Computational Physics, 2004.
- [3] Xiu, D.; *Numerical methods for stochastic computations: a spectral method approach*. Princeton University Press, 2010.
- [4] Blaheta, R.; Hasal, M.; Domesová, S.; Běreš M. RT1-code: A mixed RT0-P0 Raviart-Thomas finite element implementation, 2014. URL: <http://www.ugn.cas.cz>.

Parallel Tempering Algorithm in Path Integral Monte Carlo Simulations

Rajko Čosić

Department of Applied Mathematics, FEECS,
VŠB – Technical University of Ostrava, 17. listopadu 15,
708 33 Ostrava – Poruba, Czech Republic
rajko.cosic@vsb.cz

Abstract. The main aim of the present paper is to deal with one of the bottlenecks of the path integral Monte Carlo simulations, which is the ergodicity of the random walk. The parallel tempering algorithm, well-known from classical Monte Carlo simulations, is used to enhance the ergodicity and speed up the convergence of the simulation. In the present paper the algorithm is described and the implementation is discussed as well as possible connection with the advanced sampling methods.

Keywords: quantum systems, path-integral Monte Carlo, parallel tempering algorithm

1 Motivation

Sampling in path integral Monte Carlo (PIMC) simulations is based on Metropolis algorithm [1]. Although the Metropolis walk, along which the system is sampled, is ergodic¹ in the limit of infinite steps, the number of steps needed to explore different minima can be incredibly large. This often happens in simulations with complicated potentials with lots of minima and high barriers between them, especially if the systems are sampled at low temperatures. One of the methods used in Classical Monte Carlo simulations is the *parallel tempering algorithm* [2], which ensures the ergodic walk in much smaller numbers of steps.

2 Methodology

The idea of the parallel tempering algorithm is to simultaneously run simulations of the same system at different temperatures (and/or pressures) and periodically attempt to swap configurations between these temperature (and/or pressure) levels (see Figure 1). The sampling processes at low temperature levels

¹ The ergodicity of the random walk is needed to ensure sampling from the correct probability distribution. It is equivalent to the possibility to access and revisit (non-periodically) all the points at which the sampled distribution is nonzero, i.e. the walk must sample all the minima which contribute to the calculation.

will tend to stay in the basin of attraction of the closest local minimum. This happens due to low mean energies corresponding to low temperatures, which make the sampling procedure less likely to cross the barrier between minima. On the other hand, systems at higher temperature levels may have enough energy to cross the barriers and sample all relevant basins of attraction. If we periodically attempt to swap between low and high temperature levels, it will eventually happen that the cluster at higher temperature level samples a different basin of attraction than the one simulated at a lower temperature level, and hence the swap will make the system at the lower temperature level sample another basin of attraction without virtually crossing the barrier between them (see Figure 2).

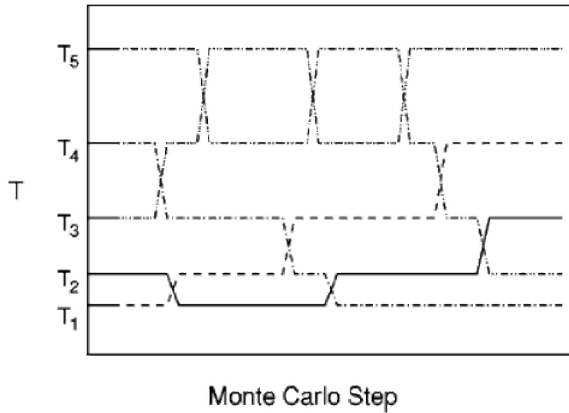


Fig. 1. Scheme of the parallel tempering simulation (picture taken from [2]).

The attempt to swap the configurations between temperature levels at T_i and T_j are accepted with probability [2]

$$P(T_i \leftrightarrow T_j) = \min \left\{ 1, \frac{\pi_i(\mathcal{R}_j) \pi_j(\mathcal{R}_i)}{\pi_i(\mathcal{R}_i) \pi_j(\mathcal{R}_j)} \right\}, \quad (1)$$

where $\pi_k(\mathcal{R}_l) = e^{-E_p(\mathcal{R}_l)/k_B T_k}$, $E_p(\mathcal{R}_l)$ is the potential energy of the configuration \mathcal{R}_l , T_k is the temperature of the k -th temperature level and k_B is the Boltzmann constant. This definition satisfies the detailed balance which is crucial for the Metropolis sampling.

Since it is not very likely to accept the swapping of configurations if the temperature difference is too large it can be useful to run simulations for multiple temperatures and attempt to swap only the neighbouring ones. Then the swap between the lowest and the highest temperature levels is not made directly but by a cascade of swaps. In our library the cascade is constructed so that the

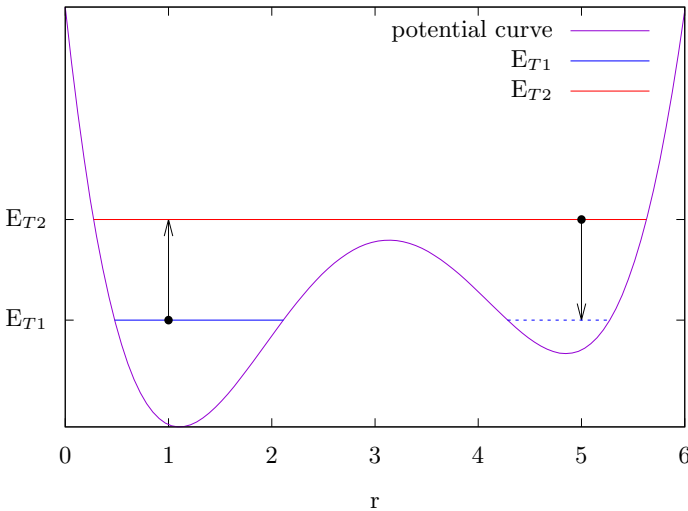


Fig. 2. Crossing the barrier via parallel tempering algorithm in double-well type potential.

average probability of acceptance is kept between 0.2 and 0.7. This requirement is fulfilled by using a set of temperatures which is very close to the geometric one given by

$$T_k = T_0 + (T_1 - T_0) \cdot \frac{q^k - 1}{q - 1}, \quad (2)$$

where k is the temperature level, T_0 is the lowest temperature and q is an adjustable coefficient. Alternatively, the user may provide the desired length of the gap between T_1 and T_0 .

3 Implementation

The parallelization of standard PIMC routines (on top of which the parallel tempering algorithm is implemented) is discussed in [3] [4]. Since the computations at different temperature levels can run independently for most of the time, the parallel tempering algorithm is very well parallelizable. Hence we get the double layer parallelism where the parallel tempering algorithm splits the processes into groups which independently simulate the system at given temperature levels (either generated by the program or given in initialization file). The communication between master processes of the groups occurs only when the system attempts to swap the configurations between two temperature levels and hence the communication overhead is acceptable.

Since the PIMCSimul library is implemented in Fortran 90 using the MPI standard, the parallel tempering algorithm is implemented also in Fortran 90

using the MPI standard. Currently, the user can choose if the temperature levels will be loaded from a file or if they will be generated using Equation (2).

4 Calculations

The very first test was done on the small system (4 particles and 16 path variables) with the Lennard-Jones interaction potential [5]. The test was performed on the Anselm cluster on the total amount of 64 processors which were split into 4 temperature levels per 16 processors.

Once the swapping was successful the parallel tempering algorithm was connected to the PIMCSimul library and the first tests with the aim to find the optimal cascade of temperatures for a selected test system (He_4^+ with 64 path variables, temperatures between $T_{min} = 50$ K and $T_{max} = 200$ K) were done (see Figure 2).

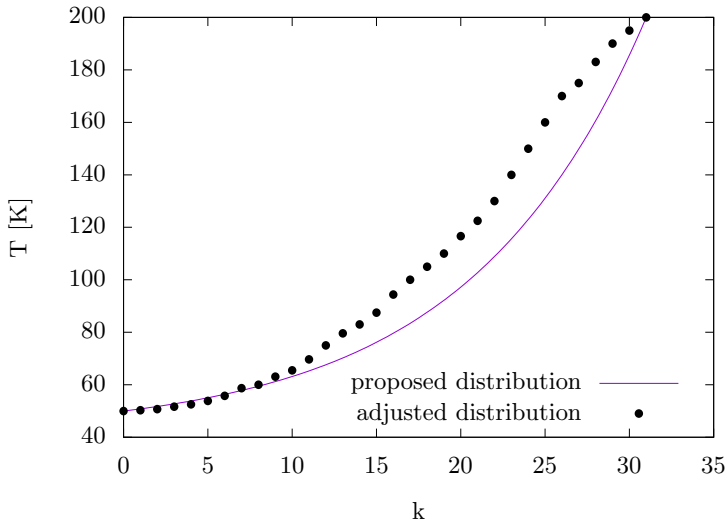


Fig. 3. Temperature levels proposed by Equation (2) with $q = 1.1$ (blue line) and the adjusted distribution with the acceptance probability between 20 % and 70 % (black dots).

The parallel tempering PIMC simulations are currently under testing in terms of convergence and ergodicity. The first tests are being performed on He_4^+ , for which the classical minima of the electronic ground-state surface and zero point energies are known, and which is neither computationally too much demanding.

5 Outlooks

There are two main branches which may affect the efficiency of parallel tempering PIMC simulations. The first one is the hybrid OpenMP/MPI implementation to complement already implemented double-layer MPI/MPI implementation and to fully exploit the architecture of the Salomon cluster. Since the implementation of DIM based interaction potentials [6], which is currently used for simulations of charged helium clusters, does not allow us to use OpenMP parallelization, the hybrid implementation will be tested and used during future simulations of different clusters.

The second one is the interconnection of the parallel tempering algorithm with one of the advanced single-temperature sampling methods (e.g. Fourier path representation [7], multigrid methods [8]). These methods allow us to efficiently sample path variables at particular temperatures while the interconnection with the parallel tempering algorithm will enable us to exploit the fact that the higher the temperature is, the less path variables are needed. Hence the computational resources can be saved at higher temperature levels or redistributed to lower ones.

References

1. Metropolis N. et al.: Equation of state calculations by fast computing machines J. Chem. Phys. 21, (1953).
2. Falcioni, M., Deem, M. W.: A biased Monte Carlo scheme for zeolite structure solution. J. Chem. Phys. 110, (1999).
3. Ćosić, R.: Path Integral Monte Carlo Methods. WOFEX 2015, p. 436, ISBN 978-80-248-3787-1, (2015).
4. Ćosić, R.: Modelling of Thermodynamics of Quantum Systems via Path-Integral Monte Carlo Methods. Dissertation thesis abstract, (2016).
5. Jones J. E.: On the Determination of Molecular Fields. II. From the Equation of State of a Gas Proceedings of the Royal Society of London A: Mathematical, Physical and Engineering Sciences 106, (1924).
6. Oleksy, K., Karlický, F., Kalus, R.: Structures and energetics of helium cluster cations: Equilibrium geometries revisited through the genetic algorithm approach. J. Chem. Phys. 133, (2010).
7. Coalson, R. D.: On the connection between Fourier coefficient and Discretized Cartesian path integration. J. Chem. Phys. 85, (1986).
8. Goodman, J., Sokal, A. D.: Multigrid Monte Carlo method. Conceptual foundations. Phys. Rev. D 40, (1989).

A Bayesian Inverse Approach to Material Parameters Estimation in Darcy Flow Problem

Simona Domesová

Department of Applied Mathematics, FEECS,
VŠB – Technical University of Ostrava, 17. listopadu 15,
708 33 Ostrava – Poruba, Czech Republic
simona.domesova@vsb.cz

Abstract. Standard numerical methods for solving inverse problems in differential equations do not reflect the possible inaccuracy in the observed data. However in real engineering applications we cannot avoid uncertainties caused by measurement errors. In the Bayesian approach every inaccurate or unknown value is treated as a random variable. This paper presents an application of the Bayesian inverse approach to a reconstruction of a porosity field as a parameter of the Darcy flow problem, however this framework can be applied to a wide range of problems that involve some amount of uncertainty. The resulting posterior distribution of the unknown parameters is studied using the Cross-Entropy method and the Metropolis-Hastings algorithm.

Keywords: Bayesian statistics, Gaussian random field, inverse problem, uncertainty quantification

1 Introduction to the Bayesian Inversion

Consider a problem of finding a vector $u \in \mathbb{R}^n$ that satisfies the equation $y = G(u)$, where $y \in \mathbb{R}^m$ is a known vector of observed data and $G: \mathbb{R}^n \rightarrow \mathbb{R}^m$ is a generally nonlinear function, usually called observation operator. In practical applications the observed data is corrupted by noise, therefore we consider a modified equation

$$y = G(u) + \eta, \quad (1)$$

where $\eta \in \mathbb{R}^m$ is the observational noise. The resulting inverse problem usually has no exact solution or multiple solutions, however the Bayesian approach naturally overcomes this difficulties.

In the Bayesian statistics the unknown vector u is understood as a random vector. Consequently the objective is to find the probability density function (pdf) of this random vector while y is given, i.e. to find the conditional probability density function $\pi(u|y)$, which specifies the so called posterior distribution. According to the Bayes theorem, the posterior distribution is defined by

$$\pi(u|y) = \frac{f(y|u) \pi_0(u)}{\int f(y|u) \pi_0(u) du},$$

where $f(y|u)$ indicates the data likelihood, i.e. the pdf of y when u is given, and $\pi_0(u)$ indicates the prior distribution. In fact π_0 expresses our prior belief about the random vector u , which is then refined according to the observed data y .

In order to use the Bayesian approach to solve the inverse problem (1), we notice, that $f(y|u)$ equals exactly the pdf of the noise $\eta = y - G(u)$, i.e. $f(y|u) = f(y - G(u))$, for the explanation see [1]. Further notice that the relation

$$\pi(u|y) \propto f(y|u) \pi_0(u) = f(y - G(u)) \pi_0(u)$$

fully specifies the posterior distribution, therefore the aim of the following text is to find the posterior pdf only up to a normalizing constant.

2 The Gaussian model

The random vector η can be understood as a measurement error, which often follows the normal distribution with zero mean, i.e. $\eta \sim \mathcal{N}(0, \Sigma)$, where $\Sigma \in \mathbb{R}^{m \times m}$ is the covariance matrix. For convenience we further assume, that $\Sigma = \gamma^2 I_m$, where $\gamma^2 \in \mathbb{R}$ and $I_m \in \mathbb{R}^{m \times m}$ is a matrix of identity, i.e. the elements of the vector η are independent. The data likelihood then satisfies

$$f(y|u) = f(y - G(u)) = \frac{1}{\sqrt{(2\pi\gamma^2)^m}} \exp\left(-\frac{(y - G(u))^T (y - G(u))}{2\gamma^2}\right).$$

When G is linear, this pdf is Gaussian, but in general case it is not, as explained in [2].

It is further assumed, that the prior distribution of the random vector u is also Gaussian, for simplicity $u \sim \mathcal{N}(0, \sigma^2 I_m)$, where $\sigma^2 \in \mathbb{R}$. With this assumption

$$\pi_0(u) = \frac{1}{\sqrt{(2\pi\sigma^2)^n}} \exp\left(-\frac{u^T u}{2\sigma^2}\right).$$

Consequently the posterior pdf is given by

$$\pi(u|y) \propto \exp\left(-\frac{(y - G(u))^T (y - G(u))}{2\gamma^2} - \frac{u^T u}{2\sigma^2}\right). \quad (2)$$

If the data likelihood and prior information are both Gaussian, the posterior distribution (as their product) is also Gaussian and it is fully specified by its mean and covariance operator. However in this case a general non-linear observation operator G is considered, therefore the posterior distribution is not Gaussian and its properties must be studied differently.

3 Properties of the posterior distribution

A possible way to study the posterior distribution is through finding $\hat{u} \in \mathbb{R}^n$, that maximizes the posterior pdf. Denoting

$$S(u) = \frac{(y - G(u))^T (y - G(u))}{2\gamma^2} + \frac{u^T u}{2\sigma^2}$$

we can write

$$\hat{u} = \arg \max_{u \in \mathbb{R}^n} \pi(u|y) = \arg \min_{u \in \mathbb{R}^n} S(u).$$

In case of a Gaussian pdf, the value of \hat{u} equals to the mean, here \hat{u} is the mode, i.e. the “most probable” value of u .

Another method of studying the posterior distribution is based on approximate sampling from the posterior pdf using Markov chain Monte Carlo (MCMC) methods. This is particularly useful in case of high dimensions of u , see [1].

3.1 Pdf maximization using the Cross-Entropy method

The Cross-Entropy (CE) method, more specifically its variant for continuous optimization, is applied to the problem

$$\min_{u \in \mathbb{R}^n} S(u).$$

In this case we are not interested in the minimal value, but in the argument of the minimum. As an arbitrary distribution the Gaussian distribution $\mathcal{N}(\mu_0, \sigma_0^2 I)$ is chosen. This distribution is refined gradually by the smoothed iterative updating of parameters μ_0 and σ_0^2 and it converges to a degenerated distribution with mean equal to \hat{u}_{CE} and zero variance. The value of \hat{u}_{CE} is a CE approximation of the mode (or one of the modes) \hat{u} . The CE method is thoroughly explained in [3].

3.2 Sampling from $\pi(u|y)$ using the Metropolis-Hastings algorithm

The Metropolis-Hastings (MH) algorithm belongs to the Markov chain Monte Carlo methods, the principle of these methods is explained e.g. in [4]. The MH algorithm is used for sampling from a given pdf known up to a normalizing constant, which is exactly this case. As the instrumental pdf we take

$$q(u, x) = \frac{1}{\sqrt{(2\pi\sigma_{MH}^2)^n}} \exp\left(-\frac{(u-x)^T(u-x)}{2\sigma_{MH}^2}\right)$$

and as the initial state we can choose e.g. $u_0 = \hat{u}_{CE}$, see [2]. The MH algorithm for sampling from the posterior pdf $\pi(u|y)$ is as follows:

- for $t = 0, 1, \dots, T$
 - generate x from $q(u_t, x)$ and compute the acceptance probability

$$\alpha(u_t, x) = \min \left\{ 1, \frac{\pi(x|y)q(x, u_t)}{\pi(u_t|y)q(u_t, x)} \right\}, \tag{3}$$

- set $u_{t+1} = x$ with probability $\alpha(u_t|x)$, otherwise set $u_{t+1} = u_t$.

The samples u_1, \dots, u_T are not independent, but u_T is approximately distributed according to $\pi(u|y)$ for large T .

We can further substitute (2) for $\pi(\cdot|y)$ in (3) and notice that $q(u, x)$ is symmetric, we thus obtain a simplified formula for acceptance probability calculation

$$\alpha(u_t, x) = \min \left\{ 1, \exp \left(\frac{\|y - G(u_t)\|^2 - \|y - G(x)\|^2}{2\gamma^2} + \frac{\|u_t\|^2 - \|x\|^2}{2\sigma^2} \right) \right\}.$$

4 Application to a Gaussian random field reconstruction

Consider a two field form of the groundwater flow boundary value problem on a unit square with a prescribed pressure on the left and the right side and no flow on the upper and the lower side

$$\left. \begin{aligned} v + k\nabla p &= \mathbf{0} \\ \operatorname{div}(v) &= 0 \end{aligned} \right\} \text{ in } D = \langle 0, 1 \rangle \times \langle 0, 1 \rangle$$

$$\begin{aligned} p &= 1 && \text{on } 0 \times \langle 0, 1 \rangle \\ p &= 0 && \text{on } 1 \times \langle 0, 1 \rangle \\ v \cdot n_0 &= 0 && \text{on } \langle 0, 1 \rangle \times \{0, 1\}, \end{aligned}$$

where $p : D \rightarrow \mathbb{R}$ is the pore pressure, $v : D \rightarrow \mathbb{R}^2$ is the Darcy's velocity, n_0 is the unit outer normal to the boundary and k is the permeability of the material. We consider a non-homogeneous isotropic material. The permeability is computed as $k = \exp(\phi)$, where ϕ is the porosity, which is modeled as a Gaussian random field specified by zero mean and the autocovariance function

$$c(x, y) = \rho^2 \exp\left(-\frac{\|x - y\|}{\lambda}\right),$$

for details see [5].

4.1 The forward problem

This model problem is solved by the mixed finite element method using lowest order Raviart-Thomas discretization, as described in [6]. The input of the forward problem is a sample of the random vector $\tilde{\phi}$ (defined as a discretization of the Gaussian random field ϕ on a regular $N \times N$ grid). Outputs are the discretization \tilde{p} of the pore pressure field and the discretization \tilde{v} of the Darcy's velocity vector field. The covariance matrix $C \in \mathbb{R}^{N^2 \times N^2}$ of the random vector $\tilde{\phi}$ is given by $C_{ij} = c(g_i, g_j)$, where g_i and g_j are grid points. In [5] we use the Choleski decomposition to generate the field, however for this purpose it is preferable to use the eigenvalue decomposition of C ,

$$C = QAQ^{-1},$$

where A is a diagonal matrix with eigenvalues on the diagonal, sorted from the largest to the smallest, and Q is a matrix with eigenvectors in rows. Assume $u \sim \mathcal{N}(0, I_{N^2})$, then

$$\tilde{\phi} = Q\sqrt{\Lambda}u$$

is a Gaussian random field correlated according to C . The random vector u can be understood as the input of the forward problem instead of $\tilde{\phi}$. At this point we can define the Bayesian inverse problem.

4.2 The inverse problem

We assume, that \tilde{v} and \tilde{p} are known, presumably only in several discretization points. Denote V and P the sets of points, where the pressure and the velocity (in certain directions) is known, respectively. Again the observed data is corrupted by noise η . With this notation the inverse problem is defined as finding $u \in \mathbb{R}^n$ that satisfies the equation

$$y = (\tilde{v}|_V, \tilde{p}|_P) + \eta = G(u) + \eta. \tag{4}$$

The posterior distribution is defined by (2), where $\sigma = 1$, vector y and function G is given by (4). This pdf can be maximized using the CE method, but the optimized vector has N^2 elements and such a high-dimensional optimization is computationally intensive and requires a large number of iterations to obtain a good result. The dimension can be decreased by neglecting small eigenvalues. Denote $\Lambda_t \in \mathbb{R}^{t \times t}$ a diagonal matrix containing t largest eigenvalues and $Q_t \in \mathbb{R}^{N^2 \times t}$ a rectangular matrix containing the corresponding eigenvectors. The approximation $\tilde{\phi}_t$ of the Gaussian random field using t eigenvectors is now given by

$$\tilde{\phi}_t = Q_t \sqrt{\Lambda_t} u_t,$$

where $u_t \sim \mathcal{N}(0, I_t)$. The dimension of the CE optimization is thus decreased to t , the resulting vector will be denoted by $\hat{u}_{CE,t}$.

For the numerical experiments the following settings were chosen: $N = 50$, $\rho = 1$, $\lambda = 0.4$, P is a set of discretization points at the Neumann boundary of the domain and V is a set of 100 points regularly distributed over the domain. With this settings the original porosity field was simulated as a sample of the Gaussian random field and vectors $\tilde{v}|_V$ and $\tilde{p}|_P$ were calculated, see Fig. 1a, 1b (the first coordinate of the velocity) and 1c. To obtain the simulated observed data y , the output $(\tilde{v}|_V, \tilde{p}|_P)$ was corrupted by noise with parameter $\gamma = 0.05$. The values of vector y are understood as noisy measurements and they are used for the reconstruction of the porosity field.

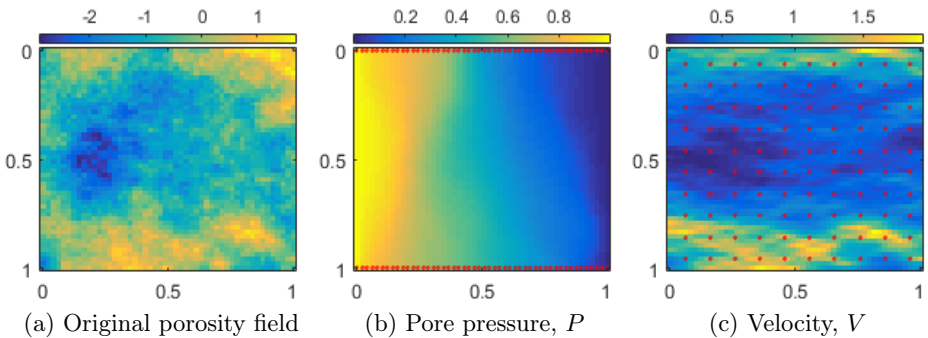


Fig. 1. Original material field $Q\sqrt{\Lambda}u$ and the illustration of the measurements $\tilde{v}|_V$ and $\tilde{p}|_P$ before the application of the noise

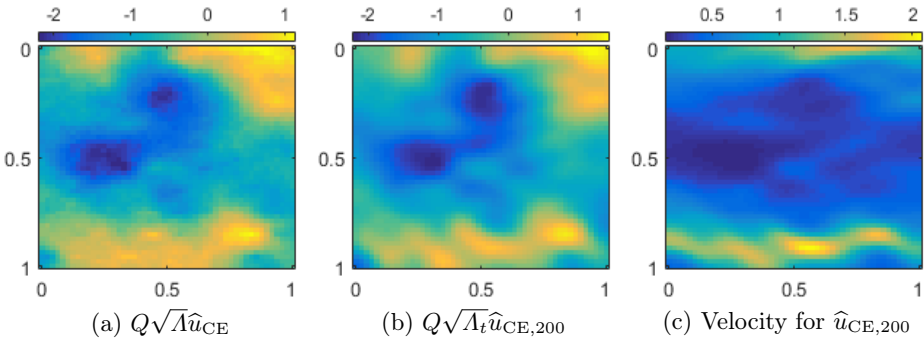


Fig. 2. Reconstruction of the material field from noisy measurements

The original porosity field was first estimated by the CE method using all eigenvectors, 120 samples were generated in each of $2 \cdot 10^3$ iterations, Fig. 2a shows the resulting approximation of the original material given by \hat{u}_{CE} . The approximation in Fig. 2b uses $t = 200$ eigenvectors, the vector $\hat{u}_{CE,200}$ was calculated in 10^4 iterations of the CE method, 120 samples per iteration. The field in Fig. 2c illustrates the first coordinate of the velocity calculated for $\hat{u}_{CE,200}$, it can be compared with the original velocity field in Fig. 1c.

Each sample of the CE method involves a solution of the forward problem. In this case it means 120 solutions of the Darcy flow problem per iteration using the mixed finite element method [6]. Therefore the future work may include alternative ways of solving the Darcy flow problem (or other differential equations) with random material, for example using the stochastic Galerkin method.

Acknowledgement

This work was supported by The Ministry of Education, Youth and Sports from the National Programme of Sustainability (NPU II) project “IT4Innovations excellence in science - LQ1602”.

References

- [1] Stuart, A. M. *Inverse problems: a Bayesian perspective*. Acta Numerica, 2010.
- [2] Bui-Thanh, Tan. *A gentle tutorial on statistical inversion using the Bayesian paradigm*. The University of Texas at Austin, 2012.
- [3] Rubinstein, R. Y.; Kroese, D. P. *The Cross-Entropy method: a unified approach to combinatorial optimization, Monte-Carlo simulation and machine learning*. Springer Science & Business Media, 2013.
- [4] Kroese, D. P.; Taimre, T.; Botev, Z. I. *Handbook of Monte Carlo methods*. John Wiley & Sons, 2013.
- [5] Blaheta, R.; Béréš M.; Domesová, S. *A study of stochastic FEM method for porous media flow problem*. Proceedings of the 1st ICAMER. CRC Press, 2016.
- [6] Blaheta, R.; Hasal, M.; Domesová, S.; Béréš M. *RT1-code: A mixed RT0-P0 Raviart-Thomas finite element implementation*, 2014. URL: <http://www.ugn.cas.cz>.

Parallel Space-time Discretization Methods

Ladislav Foltyn

Department of Applied Mathematics, FEECS,
VŠB – Technical University of Ostrava, 17. listopadu 15,
708 33 Ostrava – Poruba, Czech Republic
ladislav.foltyn@vsb.cz

Abstract. In this paper we are trying to work with space-time domains in that way, that we treat a time variable as an additional dimension to Galerkin discretization. This approach has some advantages like a decrease of computational error more than if we use an iterative solver of space-time problems. Another advantage is ability to operate with complete space-time domain, i.e. we do not resolve problem in iterative way by individual time steps but we are able to discretize problem in whole space-time domain and we can use a finite element method for solving this problem. In the first section of paper we will talk about advantages of this approach, in other sections a variational formulation and discretization of space-time domain will be shown. At the end of paper we will discuss future outlooks.

Keywords: variational formulation, space-time discretization, space-time methods

1 Motivation

We will assume that we have to solve some space-time problem. One way how to solve the problem is a solution through successive iterations. In that way we only have to discretize a spatial domain. We divide time domain into a specific number of steps. To solve the problem we first discretize the spatial domain and do the subsequent calculation in the initial time. After that, we make a time step in the time direction by a predetermined fixed time step and discretization of a new spatial domain and the subsequent calculation in this new time will be done. The procedure will be repeated until the calculation in a final iteration will be done. The main disadvantage of this method is that in each time step the computational error is accumulated more and more. With each time step another local error is added to a current computational error. This may have fatal consequences for some problems. Let us consider another approach how to solve the space-time problem. Let us avoid the iterative solution in time and assume the time variable as an additional space variable, i.e. a 1D problem in time yields a 2D problem, a 2D problem in time yields a 3D problem and so on. Advantage of this approach is that we are able to operate with complete

space-time domain. We will obtain a discretization scheme in which the space-time domain is decomposed by a tensor product of space-time elements. Other advantage is, that the computational error is not accumulated in each time step. The computational error is same for entire problem independently of the time step. In our current work we would like to understand to this approach in details and explore its possibilities in the field of parallel computing. The variational formulation of space-time problem and the subsequent discretization will be shown in next sections.

2 Variational formulation

Consider the Dirichlet boundary value problem for the heat equation

$$\begin{aligned}
 c_H \frac{\partial u}{\partial t}(x, t) - \operatorname{div}_x [K(x, t)\nabla_x u(x, t)] &= f(x, t) \quad \forall (x, t) \in \Omega \times (0, T) \\
 u(x, t) &= 0 \quad \forall (x, t) \in \Gamma \times (0, T) \\
 u(x, 0) &= u_0(x) \quad \forall x \in \Omega,
 \end{aligned} \tag{1}$$

where $\Omega \subset \mathbb{R}^n$, $n = 1, 2, 3$ is a bounded domain with Lipschitz boundary (for $n = 2, 3$) and $\partial\Omega = \Gamma$. $K(x, t) \in \mathbb{R}^{n \times n}$ represents the coefficient matrix which is assumed to be symmetric and positive definite uniform in $(x, t) \in \Omega \times (0, T)$. c_H is a given heat capacity constant which is positive ($c_H > 0$). $f \in L_2(0, T; H^{-1}(\Omega))$ is a given source term. We finally assume that $u_0(x) \in H_0^1(\Omega)$.

We multiply first equation of (1) by test function $v(x, t)$ from appropriate space of test functions, denoted \mathcal{V} , and we integrate it over spatial domain at first, then over time interval. We obtain

$$\begin{aligned}
 c_H \cdot \int_0^T \int_{\Omega} \frac{\partial u}{\partial t}(x, t)v(x, t)dxdt - \int_0^T \int_{\Omega} \operatorname{div}_x [K(x, t)\nabla_x u(x, t)] v(x, t)dxdt = \\
 = \int_0^T \int_{\Omega} f(x, t)v(x, t)dxdt.
 \end{aligned} \tag{2}$$

Using the Green theorem in spatial domain and a straightforward computation rewrite (2) to

$$\begin{aligned}
 & - \int_0^T \int_{\Omega} \operatorname{div}_x [K(x, t)\nabla_x u(x, t)] v(x, t)dxdt = \\
 & = \int_0^T \int_{\Omega} [K(x, t)\nabla_x u(x, t)] \nabla_x v(x, t)dxdt - \\
 & \quad - \int_0^T \int_{\partial\Omega} K(x, t) \frac{\partial u}{\partial n}(x, t)v(x, t)ds(x)dt.
 \end{aligned} \tag{3}$$

We know that $v(x, t) = 0$ for $x \in \Gamma$, so we obtain

$$\begin{aligned}
 c_H \cdot \int_0^T \int_{\Omega} \frac{\partial u}{\partial t}(x, t)v(x, t)dxdt + \int_0^T \int_{\Omega} [K(x, t)\nabla_x u(x, t)] \nabla_x v(x, t)dxdt = \\
 = \int_0^T \int_{\Omega} f(x, t)v(x, t)dxdt .
 \end{aligned}
 \tag{4}$$

Thus the variational formulation of (1) is

$$\begin{cases} \text{Find } u(x, t) \in \mathcal{U} , \text{ such that} \\ a(u, v) = b(v) \quad \forall v \in \mathcal{V} , \end{cases}
 \tag{5}$$

where

$$\mathcal{U} = \{w \in L_2(0, T; H_0^1(\Omega)) \cap H^1(0, T; H^{-1}(\Omega)) : w(x, 0) = u_0(x) \text{ for } x \in \Omega\} ,
 \tag{6}$$

$$\mathcal{V} = \{w \in L_2(0, T; H_0^1(\Omega)) : w(x, 0) = 0 \text{ for } x \in \Omega\} ,
 \tag{7}$$

$$\begin{aligned}
 a(u, v) = c_H \cdot \int_0^T \int_{\Omega} \frac{\partial u}{\partial t}(x, t)v(x, t)dxdt + \\
 + \int_0^T \int_{\Omega} [K(x, t)\nabla_x u(x, t)] \nabla_x v(x, t)dxdt
 \end{aligned}
 \tag{8}$$

is a bilinear form and

$$b(v) = \int_0^T \int_{\Omega} f(x, t)v(x, t)dxdt
 \tag{9}$$

is a linear functional. Whereas the solution $u(x, t)$ can be splitted into $u(x, t) = u_H(x, t) + u_0(x, t)$ for $(x, t) \in \Omega \times (0, T)$, where

$$u_0(x, t) \in L_2(0, T; H_0^1(\Omega)) \cap H^1(0, T; H^{-1}(\Omega))
 \tag{10}$$

is some extension of the given initial datum $u_0(x) \in H_0^1(\Omega)$, after homogenization we get

$$\begin{cases} \text{Find } u_H \in \mathcal{U}_H , \text{ such that} \\ a(u_H, v) = b(v) - a(u_0, v) \quad \forall v \in \mathcal{V} , \end{cases}
 \tag{11}$$

where

$$\mathcal{U}_H = \{w \in L_2(0, T; H_0^1(\Omega)) \cap H^1(0, T; H^{-1}(\Omega)) : w(x, 0) = 0 \text{ for } x \in \Omega\} .
 \tag{12}$$

3 Space-time discretization

To satisfy a range of this contribution, we will state only a rough principle of discretization in space-time domain. At first we discretize space-time domain, i.e. we consider finite dimensional spaces which satisfy $\mathcal{U}_H^h \subset \mathcal{U}_H$ and $\mathcal{V}^h \subset \mathcal{V}$. \mathcal{U}_H^h and \mathcal{V}^h represents a finite dimensional subspaces. So the variational formulation after homogenization (11) is rewritten to

$$\begin{cases} \text{Find } u_H^h \in \mathcal{U}_H^h, \text{ such that} \\ a(u_H^h, v^h) = b(v^h) - a(u_0^h, v^h) \quad \forall v^h \in \mathcal{V}^h. \end{cases} \quad (13)$$

We are able to rewrite (13) to an algebraic form after selecting appropriate basis functions (for example piecewise linear functions). We obtain a system of linear equations

$$A \cdot \bar{u} = \bar{b} - \hat{A} \cdot \bar{u}_0, \quad (14)$$

where $A \cdot \bar{u}$ correspond to $a(u_H^h, v^h)$, \bar{b} to $b(v^h)$ and $\hat{A} \cdot \bar{u}_0$ to $a(u_0^h, v^h)$. This system can be solved using typical solvers. It is necessary to emphasize that we have done the discretization of whole space-time domain, i.e. we have used a finite element discretization to the spatial domain and time interval because we assume time variable as added spatial coordinate. This method is called Petrov-Galerkin (due to a fact that $\mathcal{U} \neq \mathcal{V}$).

4 Outlooks

In the future, we would like to analyze this approach more in details in the terms of rate of the convergence and computational error, see, e.g., [1–3]. Main aim of thesis is preconditioning and parallelization possibilities of space-time methods.

References

1. Neumüller, M.: *Space-time methods: Fast solvers and applications*. Graz: Verlag der Technischen Universität, 2013. 978-3-85125-291-0 (e-ISBN)
2. Steinbach, O.: *Space-time finite element methods for parabolic problems*. Institut für Numerische Mathematik, TU Graz, 2015.
3. Peterek, I.: *Paralelní řešení časoprostorových úloh*. VŠB - Technická univerzita Ostrava, 2016. Bakalářská práce. Vedoucí práce: doc. Ing. Dalibor Lukáš, Ph.D.

Kernel Detection of the Stiffness Matrix in the FETI Methods

Pavla Jirůtková and Alexandros Markopoulos

Department of Applied Mathematics, FEECS,
VŠB – Technical University of Ostrava, 17. listopadu 15,
708 33 Ostrava – Poruba, Czech Republic
{pavla.jirutkova, alexandros.markopoulos}@vsb.cz

Abstract. We describe the Total FETI domain decomposition method. A special attention is paid to the kernel detection and to the description of our new heuristic approach. The experiments and results are presented here.

1 Introduction

The FETI domain decomposition method was introduced by Farhat and Roux [1] in 1992 as an efficient algorithm for a massively parallel solution of many engineering problems. The main idea is decomposition of a large body into non-overlapping subdomains, so the original problem is reduced to a small problem defined for each subdomain, and intersubdomain field continuity is enforced via Lagrange multipliers. Thanks to that the original problem can be solved efficiently in parallel. In the Total FETI method, the Dirichlet boundary conditions are also enforced by Lagrange multipliers, hence all subdomain stiffness matrices are singular.

The matrix, the columns of which are basis vectors of the stiffness matrix kernels can be assembled directly from the coordinates. However this is possible only for specific problems, for problems with 'nice' partitioning, for linear problems without jumps in material coefficients, but not for general utilization. In other cases the detection of the kernel can be a very difficult procedure. In this paper, our new heuristic approach to the kernel detection is described, and new results are presented.

2 Total FETI method

The Total FETI (Total Finite Element Tearing and Interconnecting) method was described by Dostál, Horák and Kučera in [2] as a variant of the FETI method. Unlike the FETI method, in this method gluing conditions are introduced also on the Dirichlet boundaries to enforce the Dirichlet conditions.

Let us consider an elliptic boundary value problem for linear elasticity. By applying the Finite Element Method (FEM), we obtain the globally assembled discretized problem

$$\mathbf{K}_g \mathbf{u}_g = \mathbf{f}_g,$$

where \mathbf{K}_g is a global stiffness matrix, \mathbf{f}_g is a global load vector and \mathbf{u}_g is a solution vector of displacement.

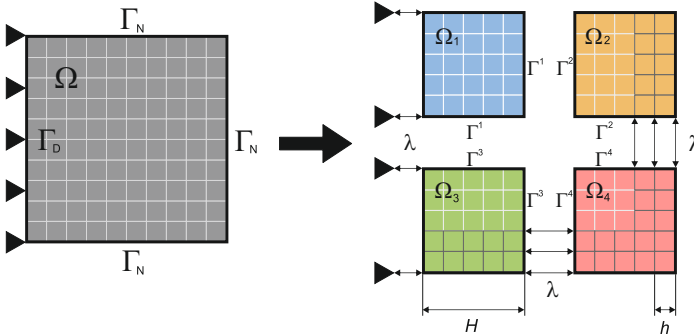


Fig. 1. Domain decomposition by Total FETI.

Now we partition the domain Ω into N non-overlapping subdomains $\Omega_i \subset \Omega, i = 1, \dots, N$, see Figure 1. The Dirichlet boundary is denoted by Γ_D , the Neumann boundary by Γ_N , and the interfaces between the subdomains by Γ^i . For all subdomains Ω_i local stiffness matrices \mathbf{K}_i and local load vectors \mathbf{f}_i are assembled. Now we obtain the minimization problem with constraints, so called energy formulation:

$$\min_{\mathbf{u}} \frac{1}{2} \mathbf{u}^\top \mathbf{K} \mathbf{u} - \mathbf{f}^\top \mathbf{u} \text{ subject to } \mathbf{B} \mathbf{u} = \mathbf{c} \tag{1}$$

with symmetric positive semidefinite block-diagonal singular stiffness matrix $\mathbf{K} = \text{diag}(\mathbf{K}_1, \dots, \mathbf{K}_N)$, load vector $\mathbf{f} = (\mathbf{f}_1, \dots, \mathbf{f}_N)^\top$, displacement vector $\mathbf{u} = (\mathbf{u}_1, \dots, \mathbf{u}_N)^\top$ and signed matrix called the jump operator $\mathbf{B} = (\mathbf{B}_1, \dots, \mathbf{B}_N)$ with entries $-1, 0, 1$ describing the subdomain interconnectivity.

The formulation of the problem (1) is not suitable for a numerical solution, because the \mathbf{K} is ill-conditioned and very large matrix. Thus, we introduce the Lagrangian associated with problem (1) by

$$L(\mathbf{u}, \boldsymbol{\lambda}) = \frac{1}{2} \mathbf{u}^\top \mathbf{K} \mathbf{u} - \mathbf{f}^\top \mathbf{u} + \boldsymbol{\lambda}^\top (\mathbf{B} \mathbf{u} - \mathbf{c}) \tag{2}$$

From (2) we can derive the Karush-Kuhn-Tucker (KKT) conditions, so we obtain system

$$\begin{pmatrix} \mathbf{K} & \mathbf{B}^\top \\ \mathbf{B} & \mathbf{O} \end{pmatrix} \begin{pmatrix} \mathbf{u} \\ \boldsymbol{\lambda} \end{pmatrix} = \begin{pmatrix} \mathbf{f} \\ \mathbf{c} \end{pmatrix}. \tag{3}$$

Because \mathbf{K} is badly conditioned and the vector of solution has a big dimension, the problem (3) is transformed to its dual formulation

$$\begin{pmatrix} \mathbf{F} & \mathbf{G}^\top \\ \mathbf{G} & \mathbf{O} \end{pmatrix} \begin{pmatrix} \boldsymbol{\lambda} \\ \boldsymbol{\alpha} \end{pmatrix} = \begin{pmatrix} \mathbf{d} \\ \mathbf{e} \end{pmatrix}, \tag{4}$$

where $\mathbf{F} := \mathbf{BK}^+\mathbf{B}^\top$, $\mathbf{G} := -\mathbf{R}^\top\mathbf{B}^\top$, $\mathbf{d} := \mathbf{BK}^+\mathbf{f} - \mathbf{c}$ and $\mathbf{e} := -\mathbf{R}^\top\mathbf{f}$. Matrix \mathbf{F} is much better conditioned than \mathbf{K} and the dimension of solution vector $(\boldsymbol{\lambda}, \boldsymbol{\alpha})$ is much smaller than $(\mathbf{u}, \boldsymbol{\lambda})$. Matrix \mathbf{K}^+ is a generalized inverse of \mathbf{K} satisfying $\mathbf{KK}^+\mathbf{K} = \mathbf{K}$. Matrix \mathbf{R} is a block-diagonal matrix, the columns of which span the null space of \mathbf{K} .

For elimination of variable $\boldsymbol{\alpha}$ in (4) an orthogonal projector on $\text{Im } \mathbf{G}^\top$ and on $\text{Ker } \mathbf{G}$ are introduced as

$$\mathbf{Q} = \mathbf{G}^\top(\mathbf{GG}^\top)^{-1}\mathbf{G} \quad \text{and} \quad \mathbf{P} = \mathbf{P}^\top = \mathbf{I} - \mathbf{Q},$$

respectively. The problem (4) is then equivalent to minimalization problem

$$\min_{\boldsymbol{\lambda}} \frac{1}{2} \boldsymbol{\lambda}^\top \mathbf{PFP} \boldsymbol{\lambda} - \boldsymbol{\lambda}^\top \mathbf{Pd} \quad \text{subject to} \quad \mathbf{G}\boldsymbol{\lambda} = \mathbf{o},$$

which can be solved effectively by the conjugate gradient method. We obtain the variable $\boldsymbol{\alpha}$ easily as $\boldsymbol{\alpha} = (\mathbf{GG}^\top)^{-1}\mathbf{G}(\mathbf{d} - \mathbf{F}\boldsymbol{\lambda})$ and finally the solution is given by

$$\mathbf{u} = \mathbf{K}^+(\mathbf{f} - \mathbf{B}^\top\boldsymbol{\lambda}) + \mathbf{R}\boldsymbol{\alpha}. \tag{5}$$

3 Factorization and kernel detection of the \mathbf{K}

In the Total FETI method the stiffness matrix \mathbf{K} is a symmetric positive semidefinite singular matrix. It stems from the fact that the body, which is represented by matrix \mathbf{K} , is not fixed yet in the space (the Dirichlet boundary condition is not applied in matrix \mathbf{K} and all subdomains are separated). It means the body can move without elastic deformations, just like rigid body. For example, for 3D elasticity each subdomain has 6 rigid-body movements (3 rotations and 3 translations) and so defect of all matrices \mathbf{K}_i , $i = 1, \dots, N$, is equal to six.

By using generalized inverse \mathbf{K}^+ in (5), several zero pivots will appear during the factorization (LU, LDL, Cholesky) [3]. The total number of those zero pivots corresponds to the defect of matrix \mathbf{K}_i . The detection of these zero pivots, and so assembly of matrix \mathbf{R}_i , can be very difficult procedure highly depending on the solved problem (big jumps in material coefficients, irregular shape of borders between subdomains, ...). Together with rounding errors it can be very ambitious or even impossible. This work continues with the results of [4] and [5].

For the problems mentioned above the kernel detection with no need to know nodal coordinates is the appropriate approach. Our heuristic approach meets this requirement. We try to find appropriate index sets s and r to permute original stiffness matrix \mathbf{K}_i for each subdomain by permutation matrix \mathbf{Q}_i and get decomposition

$$\mathbf{Q}_i\mathbf{K}_i\mathbf{Q}_i^T = \begin{pmatrix} \mathbf{K}_i^{r,r} & \mathbf{K}_i^{r,s} \\ \mathbf{K}_i^{s,r} & \mathbf{K}_i^{s,s} \end{pmatrix},$$

where s denotes singular and r denotes nonsingular. According to this notation matrix $\mathbf{K}_i^{r,r}$ will be non-singular and invertible matrix. The Schur complement is defined in the form

$$\mathbf{S}_i = \mathbf{K}_i^{s,s} - \mathbf{K}_i^{s,r}(\mathbf{K}_i^{r,r})^{-1}\mathbf{K}_i^{r,s}. \tag{6}$$

We make a random choice of the fixing nodes (FNs) (every node with 3 degrees of freedom (DOFs)), which represent set s and look at the number of bad choices (nodes lying on the same line) depending on the number of body partitions and on the number of the fixing nodes, see examples in Figure 2. The least number of chosen FNs is 3, it means 9 DOFs and so the size of set s will be 9. Naturally we can choose more FNs, thereby the kernel detection will be more reliable, but we also need to get a relatively small set s because the Schur complement (6) will be analyzed by the algorithm for dense matrices. We suppose the probability of bad choice of the FNs is minimal. In the next section, it will be shown that our assumption is right.

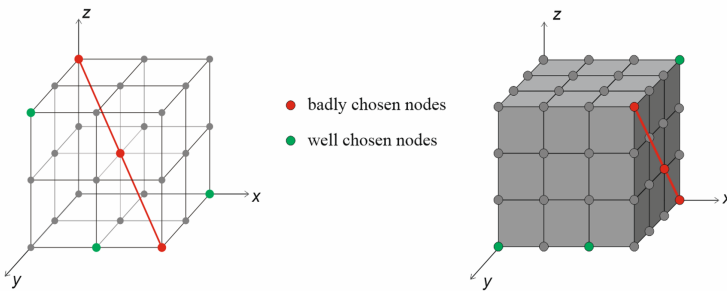


Fig. 2. The examples of bad and good choices of the fixing nodes.

Assume, set s is already well-chosen and set r is assembled as complement of set s . The kernel of \mathbf{K}_i can be derived from homogeneous system

$$\begin{aligned} \mathbf{K}_i^{r,r} \mathbf{R}_i^r + \mathbf{K}_i^{r,s} \mathbf{R}_i^s &= \mathbf{O}^r, \\ \mathbf{K}_i^{s,r} \mathbf{R}_i^r + \mathbf{K}_i^{s,s} \mathbf{R}_i^s &= \mathbf{O}^s. \end{aligned} \tag{7}$$

From the first equation in (7), we derive

$$\mathbf{R}_i^r = -(\mathbf{K}_i^{r,r})^{-1} \mathbf{K}_i^{r,s} \mathbf{R}_i^s. \tag{8}$$

By substituting (8) to the second equation of (7) and after some modifications we obtain

$$(\mathbf{K}_i^{s,s} - \mathbf{K}_i^{s,r} (\mathbf{K}_i^{r,r})^{-1} \mathbf{K}_i^{r,s}) \mathbf{R}_i^s = \mathbf{O}^s,$$

which can be rewritten into $\mathbf{S}_i \mathbf{R}_i^s = \mathbf{O}^s$.

The initial problem, the kernel detection of symmetric stiffness matrix \mathbf{K}_i , was reduced to the kernel detection of symmetric Schur complement \mathbf{S}_i . Now we can apply a singular value decomposition (SVD) for the symmetric matrix on matrix \mathbf{S}_i and obtain

$$\mathbf{S}_i = \mathbf{U}_i \boldsymbol{\Sigma}_i \mathbf{U}_i^T = (\tilde{\mathbf{U}}_i \mathbf{R}_i^s) \begin{pmatrix} \tilde{\boldsymbol{\Sigma}}_i & \mathbf{O} \\ \mathbf{O} & \mathbf{O} \end{pmatrix} \begin{pmatrix} \tilde{\mathbf{U}}_i^T \\ \mathbf{R}_i^{sT} \end{pmatrix}, \tag{9}$$

where

$$\Sigma_i = \text{diag}(\lambda_1, \lambda_2, \dots, \lambda_{i-1}, \lambda_i, \lambda_{i+1}, \dots, \lambda_n)$$

hold singular values of S_i . Due to singularity, a significant jump, which signalizes the place where $\tilde{\Sigma}_i$ ends and from where the eigenvalues can be considered as zeros, can be observed. Practically, the place of jump is given by condition

$$\frac{\lambda_i}{\lambda_{i+1}} > 1e + 5.$$

When it is fulfilled, $\tilde{\Sigma}_i$ in (9) is determined as well as R_i^s . Finally R_i^r is given by (8), and the kernel of original matrix K_i is

$$R_i = Q_i \begin{pmatrix} R_i^r \\ R_i^s \end{pmatrix}.$$

4 Numerical experiments and results

In the previous section, we gave the assumption that the probability of bad choice of FNs is minimal. Now we are convinced that our assumption is right. Let us consider a uniformly meshed cube with n nodes in each direction. The singular set s is selected via several DOFs belonging to randomly chosen FNs. The quality of a number selected nodes is measured by the ratio of bad choices (nodes lying in the same line) to all possible combinations for a given number of FNs and the size of mesh n . It is not so surprising that the probability of bad choice decreases with increasing FNs for a fixed number of nodes per edge n , as we can see in Figure 3.

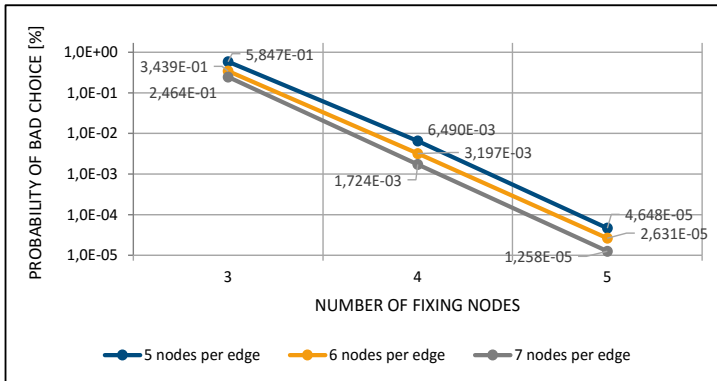


Fig. 3. Probability of bad choice of FNs for a various number of FNs.

Surprisingly enough, for a fixed number of FNs and a simultaneously enlarging mesh size (increasing parameter n), the probability of a bad choice decreases as well, see Figure 4.

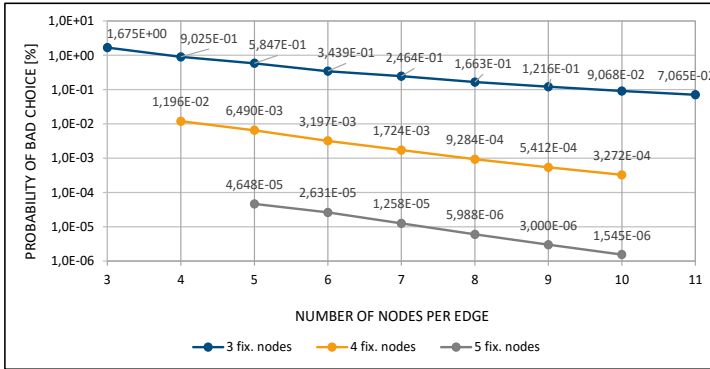


Fig. 4. Probability of bad choice of FNs for a various number of nodes per edge.

Lots of numerical experiments were made and the computed probabilities of a bad choice were confirmed.

5 Conclusion

We described the Total FETI method as an efficient method for massively parallel computations. Our new approach to the kernel detection of singular stiffness matrix was introduced and the power of this approach was shown in the last section about numerical experiments.

References

1. C. Farhat and F-X. Roux, An Unconventional Domain Decomposition Method for an Efficient Parallel Solution of Large-Scale Finite Element Systems, *SIAM Journal on Sci. and Stat. Computing*, vol. 13, pp. 379-396, <http://dx.doi.org/10.1137/0913020>, 1992.
2. Z. Dostál, D. Horák and R. Kučera, Total FETI - an easier implementable variant of the FETI method for numerical solution of elliptic PDE, *Comm. in Num. Methods in Engineering*, vol. 22, num. 12, pp. 1155-1162, doi: 10.1002/cnm.881, 2006.
3. T. Brzobohatý, Z. Dostál, T. Kozubek, P. Kovář and A. Markopoulos, Cholesky decomposition with fixing nodes to stable computation of a generalized inverse of the stiffness matrix of a floating structure, *International Journal for Num. Methods in Engineering*, vol. 88, pp. 493-509, doi: 10.1002/nme.3187, 2011.
4. Z. Dostál, T. Kozubek, A. Markopoulos and M. Menšík, Cholesky decomposition of a positive semidefinite matrix with known kernel, *Applied Mathematics and Computation*, vol. 217, num. 13, pp. 6067-6077, doi: 10.1016/j.amc.2010.12.069, 2011.
5. A. Suzuki and F.-X. Roux, A dissection solver with kernel detection for symmetric finite element matrices on shared memory computers, *International Journal for Num. Methods in Engineering*, 100(2): pp. 136-164, 2014.

Discrete Mathematics in Parallel Boundary Element Method

Michal Kravčenko

Department of Applied Mathematics, FEECS,
VŠB – Technical University of Ostrava, 17. listopadu 15,
708 33 Ostrava – Poruba, Czech Republic
michal.kravcenko@vsb.cz

Abstract. The paper touches the subject of connection between numerical and discrete mathematics. Namely, it shows that we can use cyclic decomposition of complete graphs to efficiently calculate solutions of PDEs using Boundary Element Method in parallel. The paper first describes domain decomposition techniques, then cyclic decomposition of complete graphs and lastly describes the properties of such a parallel solution on a Laplace problem in 3D.

Keywords: parallelism, cyclic graph decomposition, boundary element method, laplace.

1 Introduction

Discrete mathematics can offer useful tools to analyze discrete structures, such as those that arise in solving Partial Differential Equations (PDEs) using the Boundary Element Method (BEM). In particular, solving the problem 1 by BEM requires us to perform a variational reformulation of 1 and applying Green's theorems which yields the equation 2. With the knowledge of the fundamental solution $G(x, y) = \frac{1}{4\pi} \frac{1}{\|x-y\|}$ to the laplace problem in 3D, we can then approximate the unknown potentials $\frac{\partial u}{\partial n}(y)$ on Γ_D and $\frac{\partial u}{\partial n}(y)$ on Γ_N by a linear combination of basis functions to obtain an approximation of the boundary element equation 2. This approximation leads to solving a system of linear equations represented by very dense matrices.

$$\begin{cases} -\Delta u = f & \text{in } \Omega \subset \mathbb{R}^3 \\ u = g & \text{on } \Gamma_D \subset \partial\Omega \\ \frac{\partial u}{\partial n} = h & \text{on } \Gamma_N \subset \partial\Omega \end{cases} \quad (1)$$

Equation 1 represents a Laplace problem in 3D, where u is the unknown function, Ω is the problem domain, Γ_D denotes that part of the domain surface which admits Dirichlet boundary conditions and Γ_N is that part of the domain surface which admits Neumann boundary conditions, and where $\partial\Omega$ is the domain surface. For extensive and complete definition of function spaces and other conditions required for this formulation, please see [2].

$$\forall x \in \Omega : u(x) = \int_{\Omega} f(y) G(x, y) dy + \int_{\partial\Omega} \frac{\partial u}{\partial n}(y) G(x, y) - u(y) \frac{\partial G(x, y)}{\partial n(y)} dl(y) \tag{2}$$

Thus, to solve 2 on large problems it is necessary to accurately approximate the the underlying very dense matrices, lets denote them V, K . To achieve a good approximations of V, K it is often assumed that a pair of surface elements which are far from each other are influencing the solution in lesser extent than a pair of surface elements which are mutually closer. This suggests that the interaction of mutually far away elements can be approximated and the precision of such an approximation is proportional to the surface distance of those two elements. This leads, for example, to Adaptive Cross Approximation (ACA) techniques or Fast Multipole Method (FMM).

To parallelize the finding of solution to 1 we need to distribute the computation as evenly as possible among the processors, particularly in the case of very dense matrices. One such technique utilizes space-filling curves, but in this paper we describe another technique, based on cyclic graph decomposition, which was extensively described, for example, in [1], [3], [4].

2 Cyclic graph decomposition

To be able to perform a parallel matrix-vector multiplication Vx, Kx as efficiently as possible, it is required to divide the workload among the processors evenly. Assume that $\partial\Omega$ consists of triangles $T := \{t_1, t_2, \dots, t_k\}$ and that we split $\partial\Omega$ into p submeshes $\partial\Omega_1, \partial\Omega_2, \dots, \partial\Omega_p$, where p denotes the number of processors. Moreover, assume that this domain decomposition has the property that $\forall i \in \{1, 2, \dots, p\}, \partial\Omega_i$ is continuous, that is that it does not contain in its interior a triangle or a set of triangles belonging to a different $\partial\Omega_j$. Also assume that $\bigcup_{i=1}^p \partial\Omega_i = \partial\Omega$ and that $\partial\Omega_i \cup \partial\Omega_j = \emptyset$ for $i \neq j$. Domain decomposition with this property allows us to represent the matrices derived from equation 2 in a block form, where each such a matrix consists of p^2 blocks.

The task now is to distribute those p^2 blocks among the processors (p blocks per processor) so that the parallel computation of Vx, Kx is as efficient as possible. The algorithm which finds the proper block distribution is based on a cyclic graph decomposition of complete graphs. We would like to find a cyclic decomposition of complete graph on p vertices (where each vertex represents one submesh of $\partial\Omega$ and each edge represents the interaction of two submeshes). Moreover, the lesser the number of vertices in each component based on such a graph decomposition, the less memory is required to store the matrices (the number of submeshes required per processor is equal to the number of vertices in the cyclic decomposition). Furthermore, the less vertices in cyclic decomposition,

the less communication is required during the computation of Vx, Kx (the size of subvector of x which each processor needs for computation is proportional to the number of vertices in the cyclic decomposition, same applies to the collection of the partial result of Ax, Kx).

In Figure 1 you can see examples of block distributions based on good and bad cyclic graph decompositions, respectively. Both examples represent a matrix A divided into 7×7 blocks, where each block contains the index of processor which it belongs to.

For more details, please refer to [1], [3] and [4].

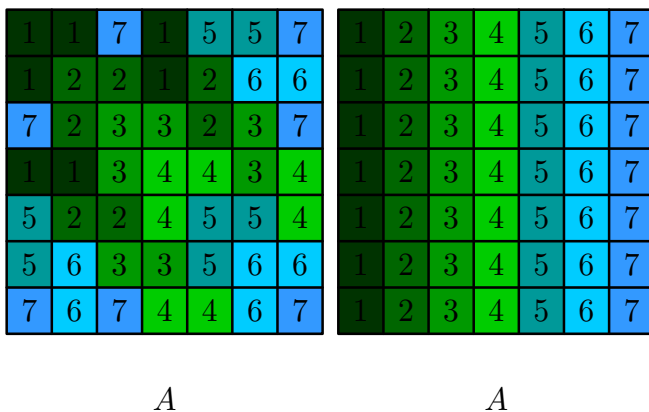


Fig. 1. On the left, you can see a block distribution based on a perfect cyclic graph decomposition, where each processor needs to know 3 out of 7 submeshes. On the right, you can see a trivial cyclic block distribution, where each processor needs to know all 7 submeshes.

3 Numerical results

In this section, we present the results of our experiments on assembling the dense matrix V, K with Ω being an L-shape (see Figure 3).

The tests were performed on the Salomon supercomputer on $1, 2, \dots, 8$ compute nodes, each capable of efficiently executing 24 threads. The implementation is part of the BEM4I library. The measured assembly times can be seen in Table 3.

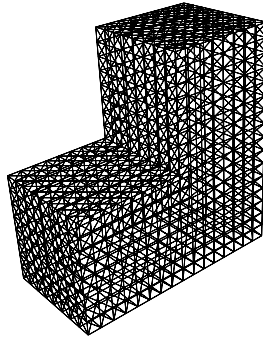


Fig. 2. Surface mesh of the example domain. This L-shape contains 258 048 surface elements and 129 026 surface nodes.

p	assembly (V) [s]	strong scal. (V) [%]	assembly (K) [s]	strong scal. (K) [%]
24	63.878	100.00	172.907	100.00
48	31.556	101.21	87.315	99.01
72	20.872	102.02	57.250	100.67
96	16.294	98.01	44.249	97.69
120	11.383	112.23	30.949	111.74
144	11.097	95.94	29.215	98.64
168	10.377	87.94	28.315	87.24
192	8.729	91.47	22.463	96.22

Table 1. This table shows the assembly times of matrices V, K derived from the discretization of Equation 2. As you can see, the parallelism based on the optimized cyclic graph decomposition yields very good strong scalability of the assembly times both of V and K .

4 Conclusions

The reader was presented with a very basic insight into the problem of solving Partial Differential Equations using the Boundary Element Method. It was argued that since the resulting system of linear equations have dense matrices, it is especially critical to think about the ways how to efficiently store those matrices and how to distribute them among the processors so the underlying problem can be solved in parallel. For matrix approximation, Adaptive Cross Approximation was mentioned. More importantly, a block representation of matrices was offered so they can be distributed easily among the processors. To calculate which block will belong to which processor, a cyclic graph decomposition of complete graphs was introduced and examples of good/bad block distributions were showcased.

Finally, it was shown that parallelization based on this approach (utilizing ACA and cyclic graph decomposition) yields good strong scalability.

References

1. D. Lukáš, P. Kovář, T. Kovářová, and M. Merta; *A Parallel Fast Boundary Element Method Using Cyclic Graph Decompositions*, Numerical Algorithms (IF 1.128), accepted.
2. Sadowská, M.; *Scalable Total BETI for 2D and 3D Contact Problems*, PhD thesis, VŠB-TU Ostrava, 2008. Supervisor RNDr. Jiří Bouchala, Ph.D., available at http://home1.vsb.cz/~sad015/publications/PhDThesis/disertacni_prace_ms.pdf.
3. Kravčenko, M.; *Parallel Matrix-vector Multiplication, its Memory Requirements and Optimizations*, WOFEX 2014 12th annual workshop, pp. 496 - 501. ISBN 978-80-248-3458-0.
4. Kravčenko, M.; *Optimization Techniques for Finding Approximations of Perfect Difference Sets*, WOFEX 2015 12th annual workshop, pp. 466 - 472. ISBN 978-80-248-3787-1.

The Minimization of The Maximal Out-degree in a Simple Graph

Matěj Krbeček, Petr Kovář, Michal Kravčenko, and Adam Silber

Department of Applied Mathematics, FEECS,
VŠB – Technical University of Ostrava, 17. listopadu 15,
708 33 Ostrava – Poruba, Czech Republic
{matej.krbecek, petr.kovar, michal.kravcenko, adam.silber}@vsb.cz

Abstract. In this paper we address the problem of the minimization of the maximal out-degree in a general simple graph. We continue on the previous paper [1] and we introduce a new polynomial time algorithm, which finds optimal orientation in a regular graph. This algorithm is based on finding a set of eulerian paths.

Furthermore, we show the construction of a graph G for which this heuristic algorithm does not work correctly. The Heuristic algorithm was introduced in a previous paper [1].

Key words: linear time algorithm, general simple graph, minimization, heuristic algorithm

1 Introduction

Recall [1], that the problem the minimization of the maximal out-degree in a general simple graph is based on a real problem. The minimization of the maximal number of boundaries, which a core supercomputers must process. If maximum out-degree is minimal, then we say that orientation of graph G is optimal. We denote this orientation $\Delta_{OPT}(G)$.

In the previous paper we showed several known results. For a planar graph G there exist an algorithm which finds optimal orientation in linear time $O(m)$, where m is the number of edges in graph G , ($m = |E(G)|$) [2]. In a general simple graph G (does not have multi-edges and loops) an optimal orientation can be found in $O(m^{3/2} \cdot \log(\Delta_i(G)))$ time, where $m = |E(G)|$ and $\Delta_i(G)$ is minimum value of maximum out-degree [3]. Then we introduced a heuristic algorithm which is faster than the general algorithm based augmenting path [1].

Though our heuristic algorithm finds minimum value of maximum out-degree in many graphs, we constructed a graph where the heuristics does not find optimal orientation of graph G . Now we show this construction of the graph G .

2 Counter-example

Note: the complete graph K_n with one edge removed we denote by K'_n .

© M. Krátký, J. Dvorský, P. Moravec (Eds.): WOFEX 2016, pp. 368–372.

VŠB – Technical University of Ostrava, FEECS, 2016, ISBN 978-80-248-3961-5.

We start with the 2-regular graph G_1 on four vertices (v_1, v_2, v_3 and v_4). First, we connect a graph K'_4 (blue bubble in the figure 1) to each vertex of the graph G_1 . Now exactly four vertex have not degree three. Just one in each a component K'_4 . A pair of these vertices connect edge among themselves. This will create a 3-regular graph G_2 . Because we start on an even number of vertices, therefore there will always be an even number of added components. In the second step we connect graph K'_5 (green bubble in the figure 1) to each vertices in the graph G_2 . For edges maintain regularity, again we add edge between two components K'_5 without one edge and and we obtain 4-regular graph G_3 .

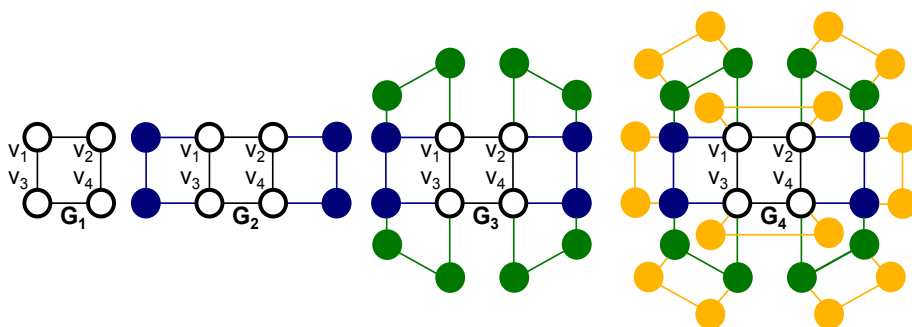


Fig. 1. Diagram of graph G

In the following steps we follow the same procedure. In the i -th step we connect a graph K'_{i+3} to each vertex in the graph G_i and add an edge between two components K'_{i+3} . This way we construct the r -regular graph G . Figure 1 shows diagram of graph G , where blue bubbles are K'_4 , green bubbles are K'_5 without one edge and yellow bubbles are K'_6 .

Now we orient the edges in the graph G using our heuristic algorithm. Recall that edge to orientate are chosen according the following three rules:

1. Choose all vertices $M_{out} \subseteq V(G)$ with smallest out-degree.
2. Choose all vertices $M_{act} \subseteq M_{out}$ with smallest actual-degree.
3. Choose any vertex $v_i \in M_{act}$, whose neighbor $v_j \in V(G)$ has the largest actual-degree. We orient edge $v_i v_j$ from v_i to v_j ,

where $|M_{akt}|$ is number of not-oriented edges in the current iteration. Because graph G is r -regular, on the begining we can choose any edge and this edge orientation. It may therefore happen, that we orientate edge from G_1 to the last added component K'_{i+3} . Next we orient edges in this component. In this

component, the edges may be oriented so that all vertices will have outgoing degree (each vertex gets exactly one outdegree in each iteration [1]), and the edge between two components K'_{i+3} will not be oriented. See 2 orientation can be same for all remaining edges. It is, we orient from all the vertices of graph G edge to last-added component K'_{i+3} . Edges of the K'_{i+3} are oriented so, that the edge between two adjacent K'_{i+3} is not oriented. Now, all vertices of graph G have one outgoing edge. This ends the first iteration.

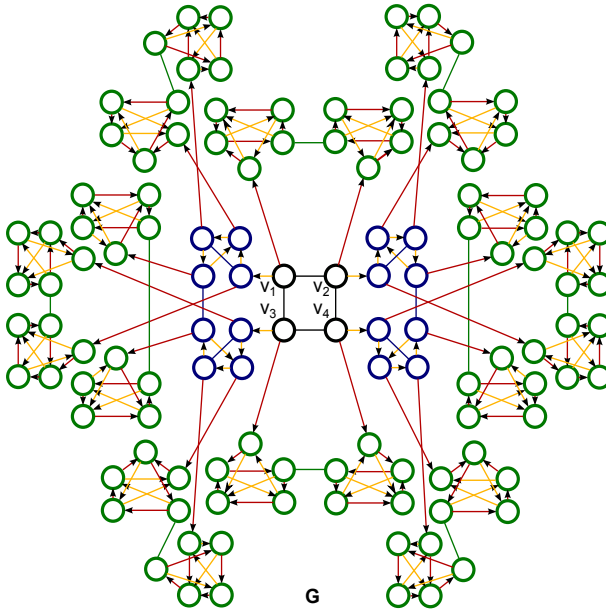


Fig. 2. Orientation of grap G

Because we oriented edges from the vertex v_1, v_2, v_3 and v_4 to different K'_{i+3} and we did not orient the edge between K'_{i+3} so, the vertex v_1, v_2, v_3 and v_4 can not have an incoming edge. We proceed in the second iteration in the same way as the in first iteration. But, now we orient the edge from all vertices to $K'_{(i-1)+3}$ (edges in K'_{i+3} are no longer of importance, because no edge can go from K'_{i+3} to the vertices v_1, v_2, v_3, v_4) and edges of $K'_{(i-1)+3}$ we orient so, that the edge between two adjacent $K'_{(i-1)+3}$ is not oriented. Thus, vertices v_1, v_2, v_3, v_4 does not have an incoming edge neither in second iteration. Suppose the algorithm continues in the same way. In the k -th orientation we orient the edge from all vertices to $K'_{(i-k)+3}$ and edges of $K'_{(i-k)+3}$ we orient so, that the edge between two adjacent $K'_{(i-k)+3}$ is not oriented. So, vertices v_1, v_2, v_3 and v_4 will have only one incoming edge, which they will gain in the last iteration. When we will orient the edges v_1v_2, v_2v_3, v_3v_4 and v_1v_4 .

Each edge contributes to the degree of the two vertices. Therefore minimum of maximum outdegree (the optimum) is $\Delta_{OPT}(G) = \frac{d(G)}{2}$, where $d(G)$ is average degree. $\Delta_{OPT}(G) = \frac{r}{2}$ for even-regular graphs. If r is odd, then half of the vertices has number of outgoing edges $\lceil \frac{r}{2} \rceil$ and half of the vertices has number of outgoing $\lceil \frac{r}{2} \rceil - 1$ by Eulers theorem.

Vertices v_1, v_2, v_3, v_4 have only one incoming edge in the graph G (orientation of graph G is on figure 2, red edges represent the frist iteration and yellow edges represent the second iteration), so the orientations of G is not optimal. Furthermore, we can miss the optimum adding more component K'_{i+3} by an arbitrarily large value.

Our the heuristic algorithm works well for non-regular graphs, but might not find the optimum in regular graphs. Therefore, we introduce a new polynomial time algorithm ($O(n)$, where n is number of edge of graph G) for r -regular graphs.

3 Algorithm for r-regular graphs

Consider an r -regular graph G . First, we assume that r is an even. In such a graph there exists an exists an Eulerian path, the algorithms to fing such path are well known. Some proof of the existence of an eulerian path includes an algorithm to find this path. We use this known algorithm.

In graph G , we find a set of edge-disjoint cycles which contain all vertices of G . We denote these cycles as C_1, C_2, \dots, C_n . Now we orient these edges arbitrarily. For example, we orient cycle C_1 clockwise. Now each vertex of the cycle has one outgoing edge and one incoming edge (Figure 3).

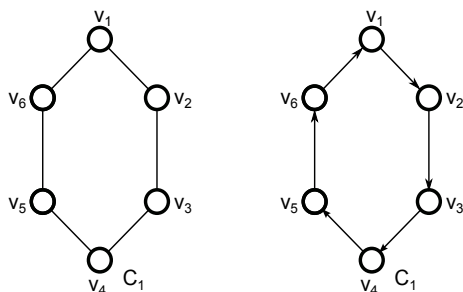


Fig. 3. Example of orientation cycle C_1

We orient the remaining cycles in some way and we join these cycles together. Now we have the oriented Eulerian trail. Furthermore each vertex of G has half

edges outgoing and half edges incoming. Thus, G has an optimal orientation.

If r is odd, then we use a well known trick. We add a new vertex v_{n+1} in to graph G and we join this vertex to all other vertices of odd degree of graph G . This way we create graph G' , which is even-regular. Now we use the procedure described above for even-regular graphs. Then we remove vertex v_{n+1} from graph G' . Because the vertex v_{n+1} had half edges outgoing and half edges incoming, so half vertices lost one outgoing edge and half vertices lost one incoming edge in a graph G . Now we have graph G oriented so that half vertices has number of outgoing degree $\lceil \frac{r}{2} \rceil$ and second half vertices has number of outgoing degree $\lceil \frac{r}{2} \rceil - 1$ (Figure 3). Thus, G has an optimal orientation.

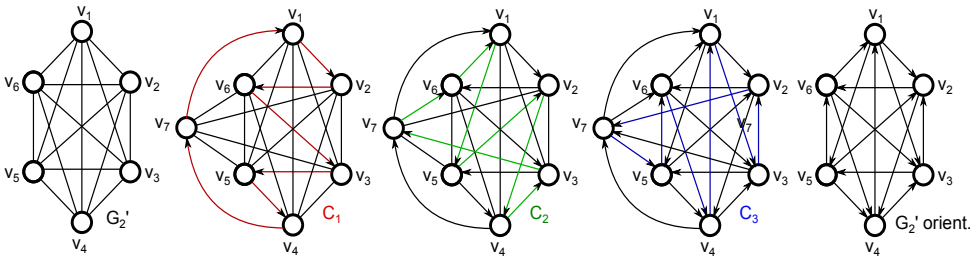


Fig. 4. Example of orientation odd-regular graph G .

4 References

1. M. Krbeček, M. Kravčenko, A. Silber. Optimization out-degree in planar and simple graphs, 2015, Ostrava, 472-478.
2. M. Chrobák, D. Eppstein. Planar orientations with Low Out-degree and Compaction of Adjacency Matrices, 1989, Theoretical Computer Science archive Volume 86 Issue 2, 243-266.
3. Y. Asahiro, E. Miyano, H. Ono, K. Zenmyo. Graph Orientation Algorithms to Minimize the Maximum Outdegree, 2006, In Proc. Twelfth Computing: The Australasian Theory Symposium (CATS2006), Hobart, Australia.

Bayesian Formulation of Image Segmentation Problem

Daniel Krpelík

Department of Applied Mathematics, FEECS,
VŠB – Technical University of Ostrava, 17. listopadu 15,
708 33 Ostrava – Poruba, Czech Republic
IT4Innovation, VŠB – Technical University of Ostrava, 17. listopadu 15,
708 33 Ostrava – Poruba, Czech Republic
daniel.krpelik@vsb.cz

Abstract. In this paper we will briefly introduce problem of image segmentation and its connections to probability theory. The amount of image data raises a demand for effective automatic algorithms for their analysis. Segmentation task is generally about discrimination of subsets of a general set. In case of image segmentation the task is to select image subsets corresponding with specified objects of interest. A spacial information is also coded into data in the case of images and has to be taken into account in order to acquire reasonable results.

Main aim of ongoing work is to develop a software solution for medical image analysis in order to improve the process of medical diagnosis. This paper includes a basic introduction to the segmentation problem and it's probabilistic formulation together with specific problem of assessment of eye orbit bone fractures as an example.

Keywords: Image segmentation, Bayesian inference

1 Introduction

Segmentation plays essential role in medical diagnosis. So far it is performed manually by medical specialist. It is a time consuming process even for 2-dimensional images. Time necessary for manual segmentation becomes unbearable in the case of spacial images and any sort of automatization would provide valuable help.

Medical imaging covers vast range of techniques. They differ in features they are able to capture and also the in cost and hazards of the image production. Computed tomography (CT) and Magnetic resonance imaging (MRI) are technologies which enables us to capture object's inside as a 3-dimensional image. Consequent analysis of such images introduces additional information in process of medical diagnosis.

A challenging task in medical image analysis is to select parts of images which belong to the specified anatomical organs (e.g. bones, lungs, hearth, liver etc.) in order to create a 3-dimensional model of corresponding organ for further

analysis. Color space of medical images (CT and MR) are levels of grey. That reduces the distinguishability between parts corresponding with different organs. Medical images are also subject to high noise which has to be either filtered or accounted in formulation of segmentation problem.

Statistics is a mathematical tool to describe variance within a set to assess differences among similar objects of interest. Statistics is used to describe two main common features of images in the problem of image analysis. One is variability among group of common depicted objects in order to recognize and classify them and the second are distortions in image due to imperfect technology of image capturing.

This work contributes to the project of developing software solution for medical image segmentation. The aim is to develop a High Performance Computing backed tool to assess internal morphology of a patient in order to provide additional information for medical doctors in the process of medical diagnosis. Although many software solutions have been already developed, the segmentation process is yet not fully solved nor automatized. Operating such softwares requires special training and is still time-consuming.

The article is organized as follows: In section 2 we will briefly state the image segmentation problem and a list of methods which are used for its solution. In section 3 we will introduce bayesian model which enables to express the discrimination criteria for segmentation. In section 4 we will present an example of utilization of segmentation in medical image analysis. The last chapter presents immediate pursuit for the coming year.

2 Image segmentation

The segmentation task is to create a subselection of general set Ω based on stated criteria.

In case of image segmentation Ω is often interpreted as the set of image pixels. Segmentation task then focuses on selecting certain subset of image which denotes an object of interest (e.g. persons in security footages or an organ of interest in case of medical data segmentation).

Common algorithms to deal with image segmentation problem are the following:

- **Fully manual segmentation** – An expert has to select segmented region or its boundary himself.
- **Threshold algorithm/watershed algorithm** – Select pixels with intensities within selected threshold or a connected region of such pixels in case of watershed.
- **Lloyd’s algorithm [1]** – Known as “k-means, k-nearest neighbours”. Similar to threshold, but able to automatically (iteratively) select threshold boundaries.
- **Expectation-maximization algorithm [2]** – Similar to Lloyd’s algorithm, but provides fuzzy segmentation. Concurrent postprocessing is required to provide sharp segmentation.

- **Active contour segmentation** [3] – Segmentation via evolution of parametrized subsets’s boundaries.
- **Level set segmentation** [4,5] – Variational formulation of segmentation problem. Region shape is coded as a function and problem is reformulated into problem of minimizing a functional.

Manual and watershed methods are based on active expert intervention. Rest of the methods require a specific description of a region to select which is time consuming task.

They may also be used as fully automated methods if we are to solve similar task of clustering i.e. instead of selecting a subset of original domain Ω we would aim to find a complete disjoint decomposition of domain Ω into $k \in \mathbb{N}$ regions. The specific formulation differs, but vaguely speaking we require that the elements (pixels) within same set are as similar as possible.

The drawback of such automatic algorithms is that the resulting decomposition may not correspond with original segmentation problem. This means that decomposition is either too general, and fail to distinguish sought object of interest from other objects, or too specific, and sought object of interest will be scattered among many regions. Both these incorrect results may be taken as intermediate results and passed by to another step in segmentation workflow, but there we face the same problem again.

3 Probability framework

Bayesian inference is statistical method for calculating conditional probabilities. It is based on Bayesian theorem (equation 1) and enables us to express posterior probability of hypothesis H conditioned upon evidence E .

$$P(H|E) \propto P(E|H) \cdot P(H), \quad (1)$$

where P denotes probability function and $P(A|B)$ denotes conditional probability of event A conditioned upon realization of event B . Element $P(E|H)$ is called likelihood function and element $P(H)$ is called prior probability function.

Conditional probability of evidence upon hypothesis is easier to construct opposed to the contrary, which is often hard to express.

In probability framework we may assign probability function $P(H|E)$ to any possible segmentation $H \subset \Omega$ (i.e. hypothesis is that pixels H belong to the sought object). The evidence E in this case is interpreted as captured image.

Using Bayesian theorem (equation 1) we decompose this probability into two terms:

- **Likelihood function** $P(E|H)$ denotes probability of capturing image E in case that H is correct segmentation,
- **Prior probability function** $P(H)$ summarizes our prior knowledge about objects of interest (e.g. shapes).

Given an ordering of subset segmentations based on probability a straightforward conclusion is to select the most probable one. This is sadly a complex optimization task but some of the methods mentioned in section 2 may be mounted to find an approximate solution.

Probability models are built based on statistical or machine learning methods. In both cases we require a set of correct (ground-truth) segmentations from which we are to extrude likelihood and prior probability functions.

4 Case study

Automated segmentation finds application in medical image processing. Segmentation is used to select subsets of medical images (sets of pixels or voxels) corresponding with internal structures (e.g. organs or their anatomical parts). Result of segmentation is consequently used to assess auxiliary biomarkers like sizes, shapes and topology, and provides valuable information in treatment decision process.

Implementation of fully automated methods is a challenging task and in case of medical image segmentation it often requires a set of correctly segmented cases. Therefore the first step is to create this test set for following machine learning process. Rest of the section describes a specific problem being solved by semi-automatic methodology.

Case study deals with assessing the extent of bone fractures of eye orbit (bone bordering eye). The main drawback is that this fracture cannot be segmented directly, because they are expressed differently (there may be a little crack in bone, bone may be shifted, tilted, replaced by eye tissue leaking from eye or air escaping from air cavity bellow etc.). This forces us to split analysis into multiphase process.

Bone itself cannot be segmented directly because of low image resolution compared to the magnitude of bone. Current workflow consists of segmenting eye tissue inside bone orbit together with possible leakages through fractures. A 3-dimensional model is created afterwards by the process described in [6] and this model is manually compared to the model of healthy (non-defective) counterpart.

Resulting model is then used to assess demanded biomarkers depicted in figure 1. In our case it is the extension of fracture (defective area in cm^2) or its ratio to the area of patient's eye bed (which is anatomical subset of eye orbit in between eye and air cavity bellow it). To assess these values another level of segmentation is performed.

In order to assess fracture size we need to localize it's boundary on reconstructed tissue model. This requires to manually identify few landmarks, based on visual comparison with non-defective object or original medical images. Using these landmarks the rest of the boundary may be reconstructed automatically by connecting shortest paths on reconstructed mesh. Similar process is adapted to reconstruct the eye bed with landmarks denoting eye bed boundary.

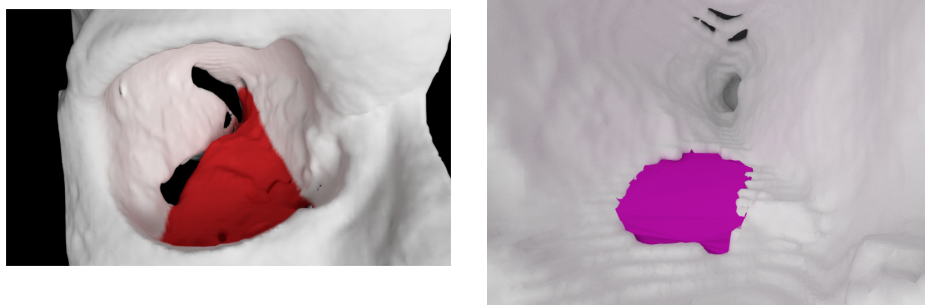


Fig. 1. Anatomical parts sought in medical images. Left image shows eye bed (red) on reconstructed skull of a healthy patient. Right image shows fracture (purple; part of the eye bed) reconstructed by the process described in article (view orientation is the same as in the left picture; it is zoomed inside the reconstructed tissue model).

This process still requires a lot of manual work, but less than fully manual segmentation. It consists of segmentation of 3-dimensional image and consequent segmentation of reconstructed mesh (landmark are placed in 3D modeling software environment). Medical experts cannot spend this much effort to analyze each patient not to mention time necessary in order to gain user skills with operation of implemented software. In order to utilize these information in medical practice an automated solution must be provided.

Recent work provided us with a test group of over 20 patients so far which we are to exploit in constructing probabilistic models mentioned in section 3.

5 Conclusion

We have introduced specific problem of medical image analysis which is currently being solved. Although a working solution has been developed, which is more efficient than preceding manual way, it still requires expert intervention. The cost is therefore the valuable time of medical expert, which might be better utilized elsewhere. Any human intervention in measuring process also introduces additional fundamental error in measuring process. We demand measuring process to be as stable as possible (i.e. measuring the same thing many times should provide same or at least very similar results). Solution for these problems is continuing automatization of image analysis problem.

The formulation of the segmentation problem and its connection to probability theory has been stated in section 2 and 3. Probability theory itself is natural way of describing data analysis problems because it covers variability in heterogeneous world from which we acquire data and also includes errors which may occur in data capturing process. Probability formulation seems to be necessary in order to automatize the segmentation algorithms. It depends on probability model induced via statistics and/or generally machine learning methodology.

The direct prosecution in this topic include analysis of probability distributions on shape and scene (consisting of more bodies) spaces. Shapes of sought objects and their relative position is the main feature used by human experts so it is only convenient to include it into segmentation framework.

Acknowledgement

This work was supported by The Ministry of Education, Youth and Sports from the National Programme of Sustainability (NPU II) project “IT4Innovations excellence in science – LQ1602” and from the Large Infrastructures for Research, Experimental Development and Innovations project “IT4Innovations National Supercomputing Center – LM2015070”. All CT images used in this paper were provided by The University Hospital in Ostrava.

References

1. S. Lloyd: Least squares quantization in PCM, in *IEEE Transactions on Information Theory*, vol. 28, no. 2, pp. 129-137, Mar 1982.
2. D. P. Dempster, N. M. Laird, D. B. Rubin: Maximum Likelihood from Incomplete Data via the EM Algorithm, *Journal of the Royal Statistical Society. Series B (Methodological)* 39, no. 1 (1977), pp. 1-38. <http://www.jstor.org/stable/2984875>.
3. M. Kass, A. Witkin, D. Terzopoulos: Snakes: Active contour models, *International Journal of Computer Vision*. Vol. 1, no. 4 (1988), pp. 321-331.
4. R. Malladi, J. A. Sethian, B. C. Vemuri: Shape Modeling with Front Propagation: A Level Set Approach, *IEEE Trans. on Pattern Analysis and Machine Intelligence*, 17, 2, pp. 158-175, 1995.
5. D. Cremers, M. Rousson, R. Deriche: A Review of Statistical Approaches to Level Set Segmentation: Integrating Color, Texture, Motion and Shape, *Int. J. Comput. Vision* 72, 2 (April 2007), pp. 195-215. DOI=<http://dx.doi.org/10.1007/s11263-006-8711-1>
6. M. Jaros: Reconstruction of the human bones from CT images and their visualization, *WOFEX 2015*, pp. 454-459

Domain Decomposition for Mixed Finite Elements in Elasticity

Lukáš Malý

Department of Applied Mathematics, FEECS,
VŠB – Technical University of Ostrava, 17. listopadu 15,
708 33 Ostrava – Poruba, Czech Republic
lukas.maly@vsb.cz

Abstract. Since the pure displacement formulations suffer from locking effects, mixed variational formulations are often used in field of linear elasticity. Nevertheless, the drawback of mixed finite element methods is their high number of degrees of freedom and ill-conditioning. We aim to propose an effective primal domain decomposition method, which is applicable for mixed problems of geometrically anisotropic linear elasticity. We follow the hybridized tangential-displacement normal-normal-stress formulation developed by Joachim Schöberl and Astrid Pechstein and apply the principles of primal domain decomposition methods. The main aim of student's final thesis is to develop an effective preconditioner accompanied by numerical experiments and provide a theoretical insight into preconditioning of mixed methods. Here we demonstrate the problem in a model setting and present achieved results, where we study the conditioning of the system.

1 Introduction

We consider the problem of linear elasticity [6] on a bounded Lipschitz domain $\Omega \subset \mathbb{R}^3$. We are interested in finding the displacement vector $\mathbf{u} = [u_1, u_2, u_3]^\top$ and the stress tensor $\underline{\sigma}$ subject to the assumptions of linear elasticity, volume forces \mathbf{f} , and boundary conditions, that are either the Dirichlet boundary condition, where the displacements are prescribed on Γ_D , or the Neumann boundary condition with known surface traction on Γ_N . Therefore, we solve the system

$$\left\{ \begin{array}{ll} \underline{\mathbf{A}} \underline{\sigma} - \underline{\varepsilon}(\mathbf{u}) = 0 & \text{in } \Omega, \\ -\operatorname{div} \underline{\sigma} = \mathbf{f} & \text{in } \Omega. \\ \mathbf{u} = \mathbf{u}_D & \text{on } \Gamma_D, \\ \underline{\sigma} \mathbf{n} = \mathbf{t}_N & \text{on } \Gamma_N, \end{array} \right. \quad (1)$$

where \mathbf{u}_D and \mathbf{t}_N are the prescribed Dirichlet and Neumann boundary conditions respectively, $\underline{\varepsilon}(\mathbf{u}) = \frac{1}{2} (\nabla \mathbf{u} + (\nabla \mathbf{u})^\top)$ is a symmetric strain tensor and $\underline{\mathbf{A}}$ is the compliance tensor, which implements Hooke's linear material law, the Young modulus and the Poisson ratio.

In our model problem we solve the system (1) on a plate-type geometry depicted in Fig. 1, where $L_x = L_y = 1$ and the thickness L_z varies, starting

from the cube, down to very thin plates. We fix all the vertical faces using zero Dirichlet boundary condition, and apply the Neumann boundary condition on the horizontal faces.

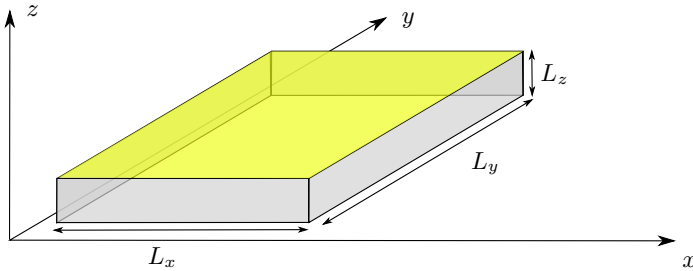


Fig. 1. Plate-type geometry with varying thickness Lz . The Neumann boundary conditions are prescribed on the top and bottom faces, the rest is fixed using the Dirichlet boundary conditions.

2 TD-NNS Mixed Formulation and Finite Elements

For the purpose of solving the problem on an anisotropic geometry, such as thin plate, we apply the TD-NNS mixed formulation introduced by Schöberl and Pechstein [5, 7], which does not suffer from locking effects.

In TD-NNS formulation the displacements are sought in the vector-valued space $\mathbf{H}(\mathbf{curl})$, while the stresses lie in the tensor-valued space $\underline{\mathbf{H}}(\mathbf{divdiv})$. Consider a discretization of the above domain Ω into hexahedral elements $\mathcal{T}_h = \bigcup\{T\}$ with a maximum mesh size h , then one may to approximate the mentioned infinite dimensional spaces using finite dimensional spaces

$$\begin{aligned} \mathbf{V}_h &:= \{ \mathbf{v} \in \mathbf{L}^2 : \mathbf{v}|_T \in \mathbf{P}^1 \forall T \in \mathcal{T}_h, \mathbf{v}_t \text{ continuous}, \mathbf{v}_t = 0 \text{ on } \Gamma_D \}, \\ \underline{\Sigma}_h &:= \{ \underline{\boldsymbol{\sigma}} \in \underline{\mathbf{L}}_{sym}^2 : \underline{\boldsymbol{\sigma}}|_T \in \underline{\mathbf{P}}^1 \forall T \in \mathcal{T}_h, \boldsymbol{\sigma}_{nn} \text{ continuous}, \boldsymbol{\sigma}_{nn} = 0 \text{ on } \Gamma_N \}, \end{aligned}$$

where for the displacements, the Nédélec tangential continuous elements are used, and for the stresses, the authors introduced normal-normal continuous finite elements. Therefore, the mixed TD-NNS formulation reads as: Find $\underline{\boldsymbol{\sigma}} \in \underline{\Sigma}_h, \mathbf{u} \in \mathbf{V}_h$ such that

$$\begin{aligned} \int_{\Omega} (\underline{\mathbf{A}} \underline{\boldsymbol{\sigma}}) : \underline{\boldsymbol{\tau}} \, d\mathbf{x} + \langle \mathbf{div} \underline{\boldsymbol{\tau}}, \mathbf{u} \rangle_V &= \int_{\Gamma_D} u_{D,n} \tau_{nn} \, ds & \forall \underline{\boldsymbol{\tau}} \in \underline{\Sigma}_0, \\ \langle \mathbf{div} \underline{\boldsymbol{\sigma}}, \mathbf{v} \rangle_V &= - \int_{\Omega} \mathbf{f} \cdot \mathbf{v} \, d\mathbf{x} + \int_{\Gamma_N} \mathbf{t}_{N,\tau} \cdot \mathbf{v}_{\tau} \, ds & \forall \mathbf{v} \in \mathbf{V}_h, \end{aligned}$$

with the duality product defined for appropriately smooth \mathbf{v} by

$$\begin{aligned} \langle \operatorname{div} \underline{\boldsymbol{\tau}}, \mathbf{v} \rangle_{V_0} &= \int_{\Omega} \operatorname{div} \underline{\boldsymbol{\tau}} \cdot \mathbf{v} \, d\mathbf{x} - \int_{\Gamma_D} \boldsymbol{\tau}_{n\tau} \mathbf{v}_{\tau} \, ds \\ &= - \int_{\Omega} \underline{\boldsymbol{\tau}} : \underline{\boldsymbol{\varepsilon}} \, d\mathbf{x} + \int_{\Gamma_N} \tau_{nn} v_n \, ds. \end{aligned}$$

We have implemented respective anisotropic hexahedral finite elements to approximate displacements and stresses within the TD-NNS formulation, see Fig. 2. To obtain stable finite elements, we need to have 2 degrees of freedom per each edge, 4 degrees of freedom per vertical face, and 2 bubble degrees of freedom per interior element as far as displacements are considered. Concerning stresses, we have 6 degrees of freedom per vertical face, 9 degrees of freedom per horizontal face, and 57 bubble degrees of freedom per element interior.

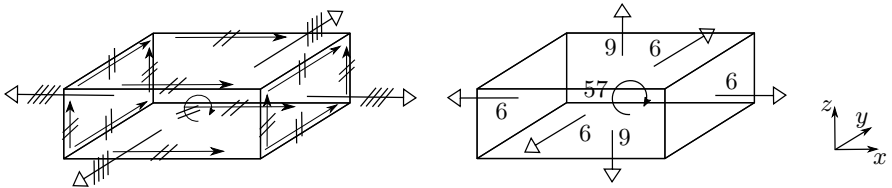


Fig. 2. Degrees of freedom for TD-NNS finite elements, left: displacement element, right: stress element. Black, white and curved arrows are used to denote edge, face and bubble degrees of freedom respectively.

Using the finite elements method, the original problem (1) finally leads to the following saddle point system of linear equations,

$$\begin{pmatrix} \mathbf{A} & \mathbf{B} \\ \mathbf{B}^T & \mathbf{0} \end{pmatrix} \begin{pmatrix} \boldsymbol{\sigma} \\ \mathbf{u} \end{pmatrix} = \begin{pmatrix} \mathbf{F}_1 \\ \mathbf{F}_2 \end{pmatrix}, \tag{2}$$

where \mathbf{A} represents Hooke’s law, and \mathbf{B}^T is related to the equilibrium of inner forces.

3 Domain Decomposition

Large number of unknowns is typical for most of mixed finite element methods and the TD-NNS is not an exception. As we have seen above, the numbers of degrees of freedom are much higher than for classical pure displacement formulations. Therefore we apply a method of domain decomposition, where the original domain Ω is decomposed into $N \times N$ non-overlapping subdomains Ω_i such that $\overline{\Omega} = \bigcup_{i=1}^{N \times N} \overline{\Omega}_i$. Furthermore, we define the skeleton (interface) as a union of the individual subdomain boundaries $\Gamma := \bigcup_{i=1}^{N \times N} \partial \Omega_i$. Concerning the plate-type

geometries we decompose the domain in two dimensions only, we cut in horizontal directions. The decomposition level is given by the maximal subdomain size denoted by H .

Primal domain decomposition method rely on re-sorting the linear system into parts related to subdomain interior degrees of freedom, denoted by index I , and parts related to skeleton degrees of freedom, denoted by Γ . When the system (2) is viewed as a single-matrix form denoted by $\mathbf{A}\mathbf{x} = \mathbf{b}$ the re-sorting translates the linear system into the following form,

$$\begin{pmatrix} \mathbf{A}^{II} & \mathbf{A}^{I\Gamma} \\ \mathbf{A}^{\Gamma I} & \mathbf{A}^{\Gamma\Gamma} \end{pmatrix} \begin{pmatrix} \mathbf{x}^I \\ \mathbf{x}^\Gamma \end{pmatrix} = \begin{pmatrix} \mathbf{b}^I \\ \mathbf{b}^\Gamma \end{pmatrix}. \quad (3)$$

To solve the system we use the method of Schur complement which is based on the LDL^\top -factorization. The method consists of three steps and proceeds as follows,

1. $\mathbf{A}^{II}\mathbf{v}^I = \mathbf{b}^I$,
2. $\mathbf{S}\mathbf{x}^\Gamma = \mathbf{b}^\Gamma - \mathbf{A}^{\Gamma I}\mathbf{v}^I$, $\mathbf{S} := \mathbf{A}^{\Gamma\Gamma} - \mathbf{A}^{\Gamma I}(\mathbf{A}^{II})^{-1}\mathbf{A}^{I\Gamma}$,
3. $\mathbf{A}^{II}\mathbf{w}^I = -\mathbf{A}^{I\Gamma}\mathbf{x}^\Gamma$,
 $\mathbf{x}^I = \mathbf{v}^I + \mathbf{w}^I$.

Matrix \mathbf{S} from the second step is Schur complement which stands for a global problem on the skeleton. Matrix \mathbf{A}^{II} is block-diagonal with respect to subdomains, thus the steps 1 and 3 are easy to parallelize. The construction of the Schur complement matrix or its application are the main bottlenecks of such algorithms, therefore we are further interested in finding some preconditioning for matrices arisen from the TD-NNS formulation of linear elasticity.

3.1 Preconditioning

The TD-NNS formulation for elasticity is stable also in case of very thin geometry, however the linear system is ill-conditioned and further investigation on preconditioning is needed.

Since the above three-step method is derived from the LDL^\top -factorization, it is favourable to use these factors also to explore an approximation of an inverse matrix. In the inverse

$$\mathbf{A}^{-1} = \begin{pmatrix} \mathbf{I} - (\mathbf{A}^{II})^{-1}\mathbf{A}^{I\Gamma} & \\ \mathbf{0} & \mathbf{I} \end{pmatrix} \begin{pmatrix} (\mathbf{A}^{II})^{-1} & \mathbf{0} \\ \mathbf{0} & \mathbf{S}^{-1} \end{pmatrix} \begin{pmatrix} \mathbf{I} & \mathbf{0} \\ -\mathbf{A}^{\Gamma I}(\mathbf{A}^{II})^{-1} & \mathbf{I} \end{pmatrix} \quad (4)$$

one needs to approximate the diagonal term, namely \mathbf{A}^{II} - and \mathbf{S} -inverses.

The authors of the TD-NNS formulation have already presented a FETI preconditioned method for elasticity in two dimensions [4], some preconditioner for different elasticity models are described in [8]. General techniques and essential tools can be found in [1].

4 Numerical Results

So far we have studied condition numbers of matrices within the TD-NNS formulation using the hexahedral elements described above. We study the original system (2) itself and also the sub-systems related to the domain decomposition, such as the Schur complement matrix S or the local system matrices A^{II} .

We solve the problem of linear elasticity on plate-type domain depicted in Fig. 1. The elasticity constants are set as follows. The Young modulus $E = 1$, the Poisson ratio $\nu = 0.285$ and the density $\rho = 2700$. The domain is discretized using the hexahedral element with only one element in z -direction (for thickness).

In Fig. 3 on the left, the condition number of matrix $K = B^T A^{-1} B$, which is exactly what we get when solving the system (2) for displacements u , is measured for different discretization levels h . The thickness is set to be $1, \frac{1}{2}, \frac{1}{4}$ and $\frac{1}{8}$. On the right, we study the Schur complement matrix obtained within the domain decomposition algorithm. We fix the ratio $\frac{H}{h}$ between the subdomain diameter and the discretization size for increasing number of subdomains $N \times N$. Both figures are in log log-scaling with highlighted quadratic dependency. All

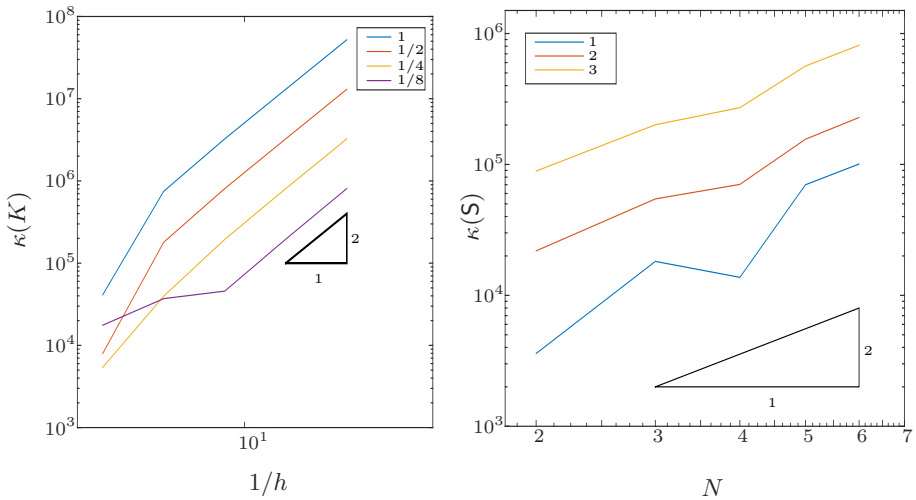


Fig. 3. Condition numbers, left: matrix K for different thicknesses of the plate with respect to the discretisation size h , right: matrix S for different ratio $\frac{H}{h}$ with respect to the number of subdomains N .

obtained results are consistent with known theory, see [8], since both systems have quadratic dependency. When one fixes the ratio $\frac{H}{h}$ and increases the number of subdomains, the Schur complement system depends on H . Theoretical bounds were observed also for such relatively small examples.

The further work on this topic will be dedicated to applications of individual matrix approximation approaches. We start with the easier ones, well-known

basic techniques, and then proceed to more sophisticated, similar to our previous work [3] to finally obtain a fine parallel preconditioner.

Acknowledgements

This work was supported by TA ČR from the project TA03010140, and by The Ministry of Education, Youth and Sports from the National Programme of Sustainability (NPU II) project IT4Innovations excellence in science - LQ1602 and from the Large Infrastructures for Research, Experimental Development and Innovations project IT4Innovations National Supercomputing Center LM2015070.

The author acknowledges the support of VŠB-Technical University of Ostrava under the grants SGS SP2016/113 and SGS SP2016/108.

Together with the colleagues a joint paper [2] giving the theory in details for 2-dimensional primal domain decomposition has been published in the impacted *Applications of Mathematics*. Talks presented the numerical results have already been given by the author at

- the SPOMECH workshop held in Ostrava on 13/11/2013,
- the Modelling conference held in Rožnov pod Radhoštěm on 6/6/2014.

Another talk has been presented by author's supervisor Dalibor Lukáš at

- the conference DD22 held in Lugano on 16/9/2013.

The author was supported by Moravian-Silesian region under the grant 02669/2014/RRC.

References

1. Bramble, J.H., Pasciak, J.E., Schatz, A.H.: The construction of preconditioners for elliptic problems by substructuring, *I. Math. Comp.* 47(175), 103–134 (1986)
2. D., L., J., B., P., V., L., M.: 2-dimensional primal domain decomposition theory in detail. *Application of Mathematics* 60(3), 265–283 (2015)
3. Maly, L.: Primal Domain Decomposition Methods and Boundary Elements. Diploma thesis, VSB-Technical University of Ostrava (2013)
4. Pechstein, A., Pechstein, C.: A FETI Method For A TDNNS Discretization of Plane Elasticity. *RICAM-Report* 11, 30 (2013), <http://www.sfb013.uni-linz.ac.at/index.php?id=reports> <http://www.ricam.oeaw.ac.at/publications/list/> <http://www.numa.uni-linz.ac.at/Publications/List/>
5. Pechstein, A., Schberl, J.: Tangential-displacement and normalnormal-stress continuous mixed finite elements for elasticity. *Mathematical Models and Methods in Applied Sciences* 21(08), 1761–1782 (2011), <http://www.worldscientific.com/doi/abs/10.1142/S0218202511005568>
6. Piaras, K.: Mechanics Lecture Notes. Available on-line at <http://homepages.engineering.auckland.ac.nz/pkel015/SolidMechanicsBooks> (2016), <http://homepages.engineering.auckland.ac.nz/pkel015/SolidMechanicsBooks>
7. Sinwel, A.: A New Family of Mixed Finite Elements for Elasticity. PhD thesis, Johannes Kepler University, Institute of Computational Mathematics (December 2008), <http://www.numa.uni-linz.ac.at/Teaching/PhD/Finished/sinwel>
8. Toselli, A., Widlund, O.: Domain Decomposition Methods - Algorithms and Theory, Springer Series in Computational Mathematics, vol. 34. Springer (2004)

Numerical Solution of Hartree-Fock Equations using the Inexact Restoration Method and Tensor Numerical Methods

Martin Mrovec

Department of Applied Mathematics, FEECS,
VŠB – Technical University of Ostrava, 17. listopadu 15,
708 33 Ostrava – Poruba, Czech Republic
`martin.mrovec@vsb.cz`

Abstract. The paper deals with solution of Hartree-Fock equations. It focuses on optimization approach using the inexact restoration method. Further tensor numerical methods, which can be used as an effective tool to store discretized basis functions, are also discussed. Algorithms are implemented in Matlab and are tested on simple molecule sets using Slater type orbital bases.

Keywords: Hartree-Fock equations, inexact restoration method, tensor numerical methods, basis functions

1 Introduction

Electronic structure calculations are some of the most time consuming tasks in the area of high performance computing. Despite the huge progress in recent years there still exist many challenges from a mathematical point of view. In this paper we show an implementation of the Hartree-Fock method using special techniques like the inexact restoration method ([1]) for solving an optimization problem and tensor numerical methods ([2]) used to store and numerically treat various types of atomic basis sets.

2 Hartree-Fock equations

A system of N electrons is described by the wave function

$$\psi(\mathbf{x}_1, \mathbf{x}_2, \dots, \mathbf{x}_N), \quad (1)$$

where \mathbf{x}_i is a vector of space coordinates x_i, y_i, z_i and the spin s_i of the i -th electron. This function is antisymmetric which means that by interchanging any two of its coordinates the function must change its sign, i.e.

$$\forall i, j \in \mathbb{N}, i \neq j : \psi(\dots, \mathbf{x}_i, \dots, \mathbf{x}_j, \dots) = -\psi(\dots, \mathbf{x}_j, \dots, \mathbf{x}_i, \dots). \quad (2)$$

Our wave function is obtained as a solution of the stationary Schroedinger equation

$$\hat{H}\psi = E\psi \quad (3)$$

with Hamiltonian

$$\hat{H} = \hat{T}_e + \hat{V}_{ee} + \hat{V}_{en} \tag{4}$$

where \hat{T}_e is a differential operator of kinetic energy, \hat{V}_{ee} is a potential representing the electron-electron electrostatic repulsion, \hat{V}_{en} is a potential representing the electron-nucleon electrostatic attraction. We search the smallest eigenvalue E representing the ground state energy and corresponding eigenfunction ψ . Due to the large number of variables ($3N$) the problem becomes intractable for standard discretization techniques. This phenomenon is usually called "The Curse of Dimensionality". The problem can be solved by using the Hartree-Fock (HF) approximation which transforms the original $3N$ dimensional problem to a system of N 3-dimensional equations (see [3]). Consider a closed shell system (a system without unpaired electrons) of $2N$ electrons. We can write the HF equations as

$$\forall k \in \{1, \dots, N\} :$$

$$\left(\hat{T} + \hat{V}_{en} + \hat{V}_H + \hat{V}_x \right) \phi_k(\mathbf{r}) = \lambda_k \phi_k(\mathbf{r}) \tag{5}$$

where ϕ_k is a one electron wave function (orbital) which depends only on spatial coordinates ($\mathbf{r} = (x, y, z)$), \hat{T}_e is a differential operator of kinetic energy (one electron), \hat{V}_H and \hat{V}_x are Hartree and exchange potentials that are integral operators (see [3]).

2.1 Discretization

Using a standard Galerkin approach we introduce an orthonormal basis set (e.g. plane wave basis or localized orbitals):

$$\phi_i(\mathbf{r}) = \sum_{j=1}^{N_b} c_{ji} \mu_j(\mathbf{r}) \tag{6}$$

where μ_j are suitable basis functions, $c_{ij} \in \mathbb{R}$ and N_b is the number of basis functions. Choosing μ_j as test functions and using a variational formulation we can rewrite the system (5) as a generalized eigenvalue problem

$$\begin{cases} \mathbf{F}(\mathbf{C}) \mathbf{C} = \mathbf{S} \mathbf{C} \mathbf{\Lambda}, \\ \mathbf{C}^T \mathbf{S} \mathbf{C} = \mathbf{I} \end{cases} \tag{7}$$

with coefficient matrix $\mathbf{C} \in \mathbb{R}^{N_b \times N}$, $(\mathbf{C})_{ij} = c_{ij}$, overlap matrix $\mathbf{S} \in \mathbb{R}^{N_b \times N_b}$, $(\mathbf{S})_{ij} = \int_{\mathbb{R}^3} \mu_i(\mathbf{r}) \mu_j(\mathbf{r}) d^3\mathbf{r}$, diagonal matrix $\mathbf{\Lambda} = \text{diag}(\lambda_1, \dots, \lambda_N)$ and Fock matrix $\mathbf{F} \in \mathbb{R}^{N_b \times N_b}$

$$\mathbf{F}(\mathbf{C}) = \mathbf{H} + \mathbf{J}(\mathbf{C}) + \mathbf{K}(\mathbf{C}) \tag{8}$$

where submatrices $\mathbf{H}, \mathbf{J}, \mathbf{K}$ represent discretized operators of (5) (see [4]). Unfortunately this problem is not linear, because to compute \mathbf{F} it is necessary to know matrix \mathbf{C} . However the system of equations can be solved iteratively until self-consistency is achieved (SCF) (see [3]), i.e.

$$\mathbf{F}(\mathbf{C}_{k-1}) \mathbf{C}_k = \mathbf{S} \mathbf{C}_k \mathbf{\Lambda} \tag{9}$$

(\mathbf{C}_0 is an arbitrary initial guess). To reach convergence one may use the DIIS iteration, where a new coefficient matrix is computed as a combination of previous iterations (see [5]). Another problem occurs in computation of \mathbf{F} itself. At each iteration of SCF we have to use precomputed coefficients

$$g_{ijkl} = \int_{\mathbb{R}^3} \int_{\mathbb{R}^3} \frac{\mu_i(\mathbf{r}) \mu_j(\mathbf{r}) \mu_k(\mathbf{r}') \mu_l(\mathbf{r}')}{\|\mathbf{r} - \mathbf{r}'\|} d^3\mathbf{r} d^3\mathbf{r}' \quad (10)$$

of so called two electron integrals (TEI). Analytical computation is possible only for special types of basis functions (Gaussians). Unfortunately the numerical computation is difficult because of singularities and number of discretization points needed to ensure required accuracy. Tensor numerical methods come with a smart solution of this problem and are discussed in next chapters.

2.2 Optimization approach

An alternative to the standard approach may be an optimization approach based on direct minimization of the energy functional. The Hartree-Fock energy functional can be written as

$$E(\mathbf{Z}) = \text{Trace}[2\mathbf{HZ} + (\mathbf{J}(\mathbf{Z}) + \mathbf{K}(\mathbf{Z}))\mathbf{Z}] \quad (11)$$

where matrix $\mathbf{Z} \in \mathbb{R}^{N_b \times N_b}$ is defined as $\mathbf{Z} := \mathbf{C}\mathbf{C}^T$. Using a substitution $\mathbf{X} = \mathbf{S}^{1/2}\mathbf{Z}\mathbf{S}^{1/2}$ we can write our problem as

$$\text{find } \min f(\mathbf{X}) \quad (12)$$

subject to

$$\mathbf{X} = \mathbf{X}^T, \quad (13)$$

$$\mathbf{X}\mathbf{X} = \mathbf{X}, \quad (14)$$

$$\text{Trace}(\mathbf{X}) = N, \quad (15)$$

which is a quadratically constrained quadratic programming (QCQP) problem. These constraints represent the number of electrons and the orthonormality of orbitals.

3 Inexact restoration method

To find a solution of Hartree-Fock equations we use the inexact restoration method (IRM, see [1]). It is an algorithm designed for solving optimization problems with equality constraints. The algorithm is based on two alternating steps. Given an iterate x_i that is not necessarily in the feasible set (set of points, that fulfill equality constraints) the first step (restoration phase) finds a point y_i , that is closer to the feasible set. Next in the optimality phase the lagrangian is minimized in the tangent set. These two steps are repeated until convergence. For solving the Hartree-Fock equations there exist methods to adapt the algorithm to our minimization problem (see [1]).

4 Basis functions

The TEI can be evaluated analytically only if we use the Gaussian type basis (GTO) in the form

$$\mu(x, y, z) = Cx^k y^l z^m e^{-\lambda(x^2+y^2+z^2)}, \quad k, l, m \in \mathbb{N} \cup \{0\} \tag{16}$$

with a normalization coefficient C . A major disadvantage of GTO is a poor behavior in the area around the atomic core. An alternative may be the Slater type basis (STO) which differs from GTO in the exponent (i.e. $e^{-\lambda\sqrt{x^2+y^2+z^2}}$ instead of $e^{-\lambda(x^2+y^2+z^2)}$). Unfortunately with Slater functions the TEI cannot be evaluated analytically so we have to find a numerical solution. Consider a finite cube-shaped computational box. If we use the equidistant grid (with step h and number of grid points in one dimension n), we can rewrite (10) as

$$b_{ijkl} \approx h^6 \langle \mathbf{G}_i \odot \mathbf{G}_j, \mathcal{P}_N * (\mathbf{G}_k \odot \mathbf{G}_l) \rangle \tag{17}$$

where $\mathbf{G}_i \in \mathbb{R}^{n \times n \times n}$ is so called 3D tensor containing a discretized basis function, \mathcal{P}_N is discretized Newton kernel $\frac{1}{\sqrt{x^2+y^2+z^2}}$, symbol $*$ denotes the discrete convolution, \odot is the Hadamard product and brackets $\langle \cdot, \cdot \rangle$ denote Frobenius type dot product (see [4]). If we look at the TEI, we can notice that the integrand has an infinite number of singularities. To resolve them we have to consider very fine grids (on the order of $10^4 - 10^6$ in one dimension). Storage requirements of such tensors and computational demands of mathematical operations are too high ($\mathcal{O}(n^3)$). However tensor numerical methods come with a solution.

4.1 Tensor Numerical methods

Similarly to the matrix singular value decomposition (SVD)

$$\mathbb{R}^{n \times n} \ni \mathbf{A} = \mathbf{U}\mathbf{S}\mathbf{V}^T = \sum_{i=1}^r \sigma_i \mathbf{u}_i \mathbf{v}_i^T, \tag{18}$$

where r is the rank of matrix \mathbf{A} , a d -dimensional tensor can be written in so called canonical format (see [4] and Figure 1):

$$\mathbf{A} = \sum_{k=1}^r \sigma_k \mathbf{a}_k^{(1)} \otimes \dots \otimes \mathbf{a}_k^{(d)}, \quad \mathbf{a}_k^{(\ell)} \in \mathbb{R}^{n_\ell}. \tag{19}$$

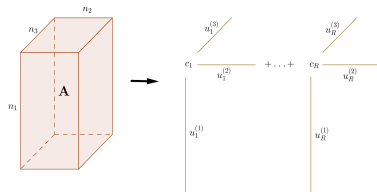


Fig. 1: Canonical representation of a given tensor \mathbf{A}

Storage costs of such tensor are d^n instead of n^3 and, e.g., computational complexity of the dot product is $d r_1 r_2 n$ (r_1, r_2 are canonical ranks of the two given tensors). Generally there does not exist a universal algorithm to find a canonical representation of a given tensor, but for some kinds of discretized functions (including $\frac{1}{\sqrt{x^2+y^2+z^2}}, e^{-\lambda\sqrt{x^2+y^2+z^2}}$) there exist special techniques for finding a good low-rank approximation (see [2]). We use one of those techniques (particularly the sinc approximation) to represent the STO functions in the canonical format. Assume that a function $u(x_1, \dots, x_d) = v\left(\sum_{i=1}^d x_i^2\right)$ can be written as an integral transformation

$$u(x_1, \dots, x_d) = v\left(\sum_{i=1}^d x_i^2\right) = \int_{\Omega} G(t) e^{\sum_{i=1}^d x_i^2 F(t)} dt, \quad \Omega \in \{\mathbb{R}, \mathbb{R}_+, [a, b]\} \quad (20)$$

where $G(t)$ and $F(t)$ are suitable functions. Using a sinc quadrature we obtain a fully separable rank- R approximation

$$u(x_1, \dots, x_d) \approx \sum_{j=1}^R \omega_j G(t_j) \prod_{i=1}^d e^{x_i^2 F(t_j)} \quad (21)$$

where ω_j are quadrature weights and t_j are quadrature points. For STO exponential function we use the following formula

$$e^{-2\alpha\sqrt{\sum_{i=1}^d x_i^2}} = \frac{\alpha}{\sqrt{\pi}} \int_{\mathbb{R}} e^{\left(-\frac{t}{2} - \frac{\alpha^2}{e^t}\right)} \cdot e^{-e^t \sum_{i=1}^d x_i^2} dt \quad (22)$$

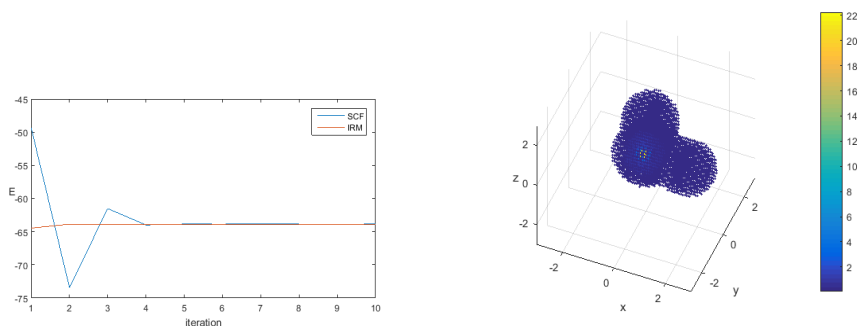
which represents a good approximation. Moreover it allows us to use an universal quadrature whose structure basically does not depend on α .

5 Implementation

We have implemented a Matlab Hartree-Fock solver that stores GTO and STO bases in the canonical format. After the pre-computing phase either IRM or the standard SCF approach can be used to find a solution. An important advantage of our implementation is the possibility of combining various basis function types in a single computation. Functions that describe inner electrons can be chosen as Slater type functions whereas valence electrons can be represented by Gaussian type functions that have lower computational complexity.

5.1 Results

Our implementation has been tested on selected simple molecules. Figure 2 shows the numerical solution of the ground state of the water molecule using a STO basis. In Figure 2a we can see the convergence history graph of the standard SCF approach and IRM. Figure 2b is an illustration of the ground state electronic charge density of the water molecule.



(a) Comparison of convergence of the ground state energy using IRM and SCF (b) Model of water molecule electronic charge density

Fig. 2: Computation of the ground state of the water molecule using STO basis

6 Conclusion

In this article we have presented our implementation of the Hartree-Fock method which includes Gaussian and Slater type basis functions. Our approach already allows us to use combinations of different type basis functions in a single computation which brings important advantages. In further research we want to focus on using tensor methods in the density functional theory (see [3]).

7 Acknowledgements

This work was supported by The Ministry of Education, Youth and Sports from the National Programme of Sustainability (NPU II) project "IT4Innovations excellence in science - LQ1602"

References

1. Francisco, J. B., Martnez, J. M., Martnez, L., Pisnitchenko, F.: Inexact restoration method for minimization problems arising in electronic structure calculations. *Computational Optimization and Applications*. 2011, DOI: 10.1007/s10589-010-9318-6. ISSN 0926-6003.
2. Khoromskij, B. N.: Introduction to Tensor Numerical Methods in Scientific Computing. Zuerich, 2011.
3. Saad, Y., Chelikowsky, J. R., Shontz, S. M.: Numerical Methods for Electronic Structure Calculations of Materials. *SIAM Review*. 2010, DOI: 10.1137/060651653. ISSN 0036-1445.
4. Khoromskij, B. N.: Tensor Numerical Methods for High-dimensional PDEs: Basic Theory and Initial Applications. Leipzig, 2014.
5. Pulay, P.: Convergence acceleration of iterative sequences. the case of scf iteration. *Chemical Physics Letters*. 1980, 73(2), 393-398. DOI: 10.1016/0009-2614(80)80396-4

Proximal Bundle Method for Constraint Nonlinear Optimization Problem

Nikola Plívová and Petr Beremlijski

Department of Applied Mathematics, FEECS,
VŠB – Technical University of Ostrava, 17. listopadu 15,
708 33 Ostrava – Poruba, Czech Republic
{nikola.plivova, petr.beremlijski}@vsb.cz

Abstract. In some optimization problems, e.g., in contact mechanics or also in contact problems with friction, the cost function is unfortunately nonsmooth and employing standard gradient or Newton methods is not straightforward. In this contribution we would like to describe the proximal bundle method. This method concerns clustering subgradients from every iteration step, thereby we can approximate Clarke generalized gradient of the cost function better. This allows us to implement stopping rule and to choose descent direction.

Keywords: nonsmooth optimization, Clarke calculus, proximal bundle method

1 Introduction

Consider the following problem

$$\begin{cases} \text{minimize} & f(x) \\ \text{subject to} & x \in \Omega, \end{cases} \quad (1)$$

which is nonlinear and constrained. When the objective function is continuously differentiable, we say, that f is smooth or also that f is in \mathbb{C}^1 . In this case, we can employ common methods (e.g. gradient method) to find solution. Unfortunately, our objective function is only locally Lipschitz on the feasible set $\Omega \subset \mathbb{R}^n$, therefore using mentioned methods approaches could lead to bad results. This is the main reason to prospect for another solver.

Optimization methods are habitually iterative. In the frame below, you can see some general basic iterative algorithm.

Step 0: (Initialization) Find a feasible starting point $x_1 \in \Omega$ and set $k = 1$.

Step 1: (Direction finding) Find a feasible descent direction $d_k \in \mathbb{R}^n$:

$$f(x_k + td_k) < f(x_k) \text{ and } x_k + td_k \in \Omega \text{ for some } t > 0.$$

Step 2: (Stopping criterion) If x_k is "close enough" to the required solution then STOP.

Step 3: (Line search) Find a step size $t_k > 0$ such that

$$t_k \approx \arg \min_{t>0} \{f(x_k + td_k)\} \text{ and } x_k + td_k \in \Omega$$

Step 4: (Updating) Set $x_{k+1} = x_k + t_k d_k, k = k + 1$ and go on to Step 1.

In a situation where f is in \mathbb{C}^1 , a descent direction (Step 1) is generated by exploiting gradients - because opposite direction to the gradient is the steepest descent one. Objective function nonsmoothness entails lots of obstacles. The hardest difficulty is just in seeking a right direction in Step 1, since the gradient doesn't exist at each point, so we cannot employ it outright. There are two classes of methods, that can solve this problem: subgradient method (for more information please see [1]) and bundle methods. Bundle methods are based on the idea, that we are able to acquire a function value and an appropriate subgradient value at every point. One of the methods belonging to this group is proximal bundle. You can learn something about this method in the following lines.

2 Proximal bundle method

2.1 Nonsmooth analysis - Clarke calculus

Before we come to the derivation of mentioned method, it is necessary to be familiar with the needful theory. Whereas we often use the term generalized gradient and subgradients, it is suitable to define them.

Definition 1. *Let the objective function $f : \mathbb{R}^n \rightarrow \mathbb{R}$ to be locally Lipschitz continuous (in \mathbb{R}^n). The generalized gradient of the objective function f at $x \in \mathbb{R}^n$ is the set*

$$\partial f(x) = \text{conv} \left\{ g \in \mathbb{R}^n \mid g = \lim_{i \rightarrow \infty} \nabla f(x_i), x_i \rightarrow x, x_i \notin \Omega_f \right\}, \tag{2}$$

where $\Omega_f = \{x \in \mathbb{R}^n, f \text{ is not differentiable in } x\}$.

Each element $g \in \partial f(x)$ is called the subgradient of the objective function f at x .

Theorem 1. *Let the objective function f to be continuously differentiable at x . Then*

$$\nabla f(x) = \{\partial f(x)\}. \tag{3}$$

To understand definition of the generalized gradient is not as onerous as it seems to be, but lets explain it on a simple example.

Example 1 (Generalized gradient). Find the generalized gradient of a given function f at $x = 0$, where

$$f(x) = |x - 1| + |x| + |x + 1|. \tag{4}$$

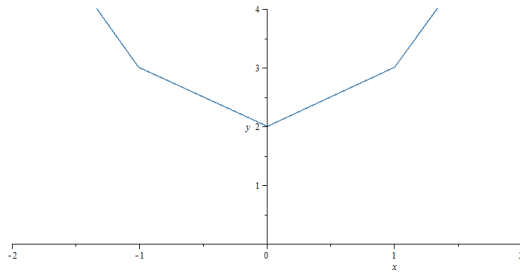


Fig. 1. Graph of function f .

Inasmuch as the function f is not smooth at $x = 0$, we have to use one-sided limits.

For

$$\left. \begin{array}{l} x_i \rightarrow 0^+ : g = 1 \\ x_i \rightarrow 0^- : g = -1 \end{array} \right\} \partial f(x) = \text{conv}\{-1, 1\}.$$

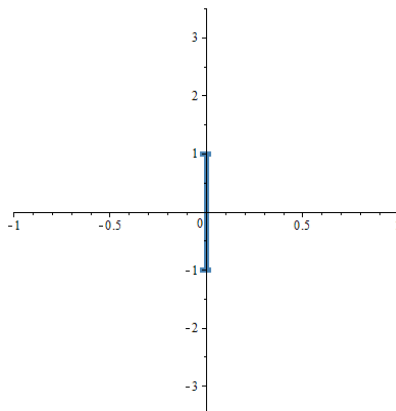


Fig. 2. Graph of the generalized gradient of f at $x = 0$.

The general gradient of f for all $x \in \mathbb{R}$ is

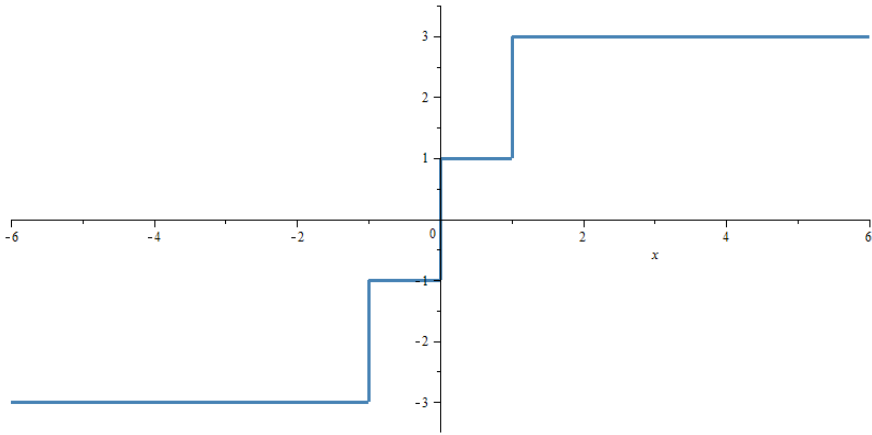


Fig. 3. Graph of the general gradient of f .

If you are interested in the theory of nonsmooth analysis, please, look into [1], [2] or [3]. More definitions, pictures and examples could be found here.

2.2 Derivation of the method

Contemplate the following nonlinear constrained optimization problem

$$\begin{cases} \text{minimize} & f(x), \\ \text{subject to} & Cx \leq b, \\ & x_{min} \leq x \leq x_{max}, \end{cases} \quad (5)$$

where the objective function is locally Lipschitz on \mathbb{R}^n , C is an constraint matrix, b is a right-handed vector and x_{max}, x_{min} are bound vectors. To make these notations simple we suppose, that the simple bounds x_{min}, x_{max} are included in the matrix C .

Direction finding

Our aim is to solve the problem

$$\begin{cases} \text{minimize} & f(x_k + d) - f(x_k), \\ \text{subject to} & x_k + d \in \Omega, \end{cases} \quad (6)$$

where d is the coveted descent direction.

Suppose that we have some starting point $x_1 \in \Omega$ and the current iteration point $x_k \in \Omega$. Lets define the linearisation in its recursive form

$$f_j^{k+1} = f_j^k + \left(g_j^f\right) (x_{k+1} - x_k) \text{ for all } j \in J_f^k, \quad (7)$$

where $J_f^k \subset \{1, \dots, k\}$ is the nonempty index set. Moreover, we employ this linearisation for polyhedral approximation of the objective function

$$\hat{f}_j^k = \max \{ \bar{f}_j(x) \mid j \in J_f^k \} \tag{8}$$

and then we can define improvement polyhedral function \hat{H}

$$\hat{H}^k(x) = \hat{f}^k(x) - f(x_k) \text{ for all } x \in \mathbb{R}^n. \tag{9}$$

By employing the proximal bundle idea ¹ and after series of adjustments, we can rewrite the whole problem into its dual form

$$\left\{ \begin{array}{l} \text{minimize} \quad \frac{1}{2u_k} \left\| \sum_{j \in J_f^k} \lambda_j g_j^k + \sum_{i \in I} \nu_i C_i \right\|^2 \\ \quad + \sum_{j \in J_f^k} \lambda_j \alpha_{f,j}^k + \sum_{i \in I} \nu_i \alpha_{C,i}^k \\ \text{subject to} \quad \sum_{j \in J_f^k} \lambda_j = 1 \\ \text{and} \quad \lambda, \nu \geq 0. \end{array} \right. \tag{10}$$

There is still one hidden but equally important problem in (10). Lets focus on the index set J_f^k . How to choose this set? The simplest way seems to be

$$J_f^k = \{1, \dots, k\}. \tag{11}$$

However, it is not true, because in every iteration step the index set will be enlarging which causes bigger and bigger memory requirements. We have to find another way.

In 1985, prof. Kiwiel presented the subgradient aggregation strategy. The idea is to aggregate the constraints made up by the previous subgradients. This strategy allows us to keep the quantity of constraints bounded. First, we need to scaled multipliers for all $j \in J_f^k$ by

$$\tilde{\lambda}_j^k = \begin{cases} \lambda_j^k / \lambda_f^k, & \text{if } \lambda_f^k > 0, \\ 1/|J_f^k|, & \text{if } \lambda_f^k = 0. \end{cases} \tag{12}$$

Now we are able to convey the aggregate subgradients by

$$\left(p_f^k, \tilde{f}_p^k, \tilde{\alpha}_{f,p}^k \right) = \sum_{j \in J_f^k} \tilde{\lambda}_j^k \left(g_j^k, f_j^k, \alpha_{f,j}^k \right) \tag{13}$$

and the aggregate linearisation by

$$\tilde{f}_p^k(x) = \tilde{f}_p^k + (p_f^k)^T (x - x_k). \tag{14}$$

¹ The idea of adding a penalty to be able to limit the step length.

Using stated equations we are able to rewrite problem (10) in suitable form for keeping the index set finite. Via restriction and dualization we obtain

$$\left\{ \begin{array}{l} \text{minimize} \quad \frac{1}{2u_k} \left\| \sum_{j \in J_f^k} \lambda_j g_j^k + \lambda_p p_f^{k-1} + \sum_{i \in I} \nu_i C_i \right\|^2 \\ \quad + \sum_{j \in J_f^k} \lambda_j \alpha_{f,j}^k + \lambda_p \alpha_{f,p}^k + \sum_{i \in I} \nu_i \alpha_{C,i}^k, \\ \text{subject to} \quad \sum_{j \in J_f^k} \lambda_j + \lambda_p = 1, \\ \text{and} \quad \lambda_j, \lambda_p, \nu \geq 0. \end{array} \right. \quad (15)$$

Line search

The descent direction $d_k = -\frac{1}{u_k} \left(\lambda_f^k p_f^k + \sum_{i \in I} \nu_i^k C_i \right)$ and the awaited decrease $v_k = \hat{f}(x_k + d_k) - f(x_k) < 0$ are known. But we don't know yet, how far we can go in direction d_k to enumerate next value x_{k+1} . Solution of this problem was presented by Krzysztof C. Kiwiel in 1990 in his work [4].

Weight update

One of the last but still very important question is the choice of weight update u_k . We cannot keep u_k invariable, because it could make some hassles (e.g. if the parameter u_k is large, values $|v_k|$ and $\|d_k\|$ will be very small and therefore all the steps will be taken as the serious ones and the decrease will be small).

This seemingly small difficulty was also solved by Krzysztof C. Kiwiel in 1990. Outcomes of his work can be found in this article [4].

3 Conclusion

In this work, the nonsmooth optimization problem with nonlinear constraints $Cx \leq b$ and with some simple bounds x_{min}, x_{max} was presented. As we stated at the beginning, algorithms for the nonsmooth optimization are used for example in contact problems with friction. To be able to solve some comprehensive problems, we are making efforts to improve our algorithm by adding a solver for linear constraints and to enhance line search.

References

1. Mäkelä, M. M., Neittaanmäki, P.: Nonsmooth Optimization, Analysis and Algorithms with Application to Optimal Control. World Scientific, Singapore, 90–137, (1992)
2. Zowe, J.: Nondifferentiable Optimization. University of Bayreuth, Germany, (1985)
3. Outrata, J., Kočvara, M., Zowe, J.: Nonsmooth Approach to Optimization Problems with Equilibrium Constraints, Nonconvex optimization and its applications. Kluwer Academic Publishers, (1998)
4. Kiwiel, K.C.: Proximity Control in Bundle Methods for Convex Nondifferentiable Minimization. Polish Academy of Science, Warsaw, (1990)

Time Series Similarity Measure using Dynamic Time Warping

Robert Skopal

Department of Applied Mathematics, FEECS,
VŠB – Technical University of Ostrava, 17. listopadu 15,
708 33 Ostrava – Poruba, Czech Republic
robert.skopal@vsb.cz

Abstract. Time series has become important data format in wide range of applications. One of the techniques used to analyze multiple time series is clustering. In order to be able to cluster time series one must be able to say how similar two time series are. Since metrics like for example Euclidean distance are not suitable for all real applications this paper presents the use of Dynamic Time Warping algorithm for similarity measure of univariate and multivariate time series which is then parallelized using OpenMP and tested on SALOMON cluster.

1 Introduction

Time series [1] classification is for long well known problem for example in the area of speech recognition [2]. From there it found usage in wide area of applications and earned great interest within the data mining community.

The key element for time series clustering is the ability to tell how similar two time series are [2]. The well know euclidean distance is not suitable in all situation because it cannot handle time dilatations which are presented in significant amount of applications. As a alternative which solves this issue the Dynamic Time Warping (DTW) was introduced.

In section 2 the theory behind DTW [4], [3] is described in details along with the algorithm for computation in 2.1. In section 3 and 3.3 the experimental results are presented.

2 Dynamic Time Warping

Let $X = x_1, x_2, \dots, x_n$ and $Y = y_1, y_2, \dots, y_m$ be two univariate or multivariate time series with lengths n and m respectively and assume that local dissimilarity function $f(x, y) \geq 0$ which is able to compare each pair of input series elements (x_i, y_j) is defined. Then $\hat{D} \in \mathbb{R}^{m \times n}$ denotes the cross distance matrix with elements $d(i, j) = f(x_i, y_j)$.

The core of DTW is the warping path (curve) which is a sequence of time indexes combinations defined as

$$\Phi(k) = (\Phi_x(k), \Phi_y(k)), k \in \{1, \dots, T\}$$

where

$$\Phi_x(k) \in \{1, \dots, n\} \text{ and } \Phi_y(k) \in \{1, \dots, m\}$$

are so called warping functions, that are responsible for remapping time indexes of X and Y .

The warping functions must meet following monotonicity constrains

$$\Phi_x(k + 1) \geq \Phi_x(k),$$

$$\Phi_y(k + 1) \geq \Phi_y(k)$$

and endpoint constrains

$$\Phi_x(1) = \Phi_y(1) = 0,$$

$$\Phi_x(T) = n, \Phi_y(T) = m.$$

The global dissimilarity is then defined as average accumulated distortion

$$d_{\Phi}(X, Y) = \sum_{k=1}^T \frac{f(\Phi_x(k), \Phi_y(k))m_{\Phi}(k)}{M_{\Phi}},$$

where M_{Φ} represents normalization constant, m_{Φ} weight coefficients and $f(\Phi_x(k), \Phi_y(k))$ local dissimilarity function applied on given warping curve Φ elements.

The DTW distance is then finally given as

$$DTW(X, Y) = \min_{\Phi} d_{\Phi}(X, Y),$$

where $DTW(X, Y)$ represents final distance between X and Y given as minimal global dissimilarity between all possible warping paths and $\hat{\Phi} = \underset{\Phi}{\operatorname{argmin}} d_{\Phi}(X, Y)$ is than optimal alignment.

2.1 Computation

The DTW can be easily computed using the cost matrix $D \in \mathbb{R}^{m+1 \times n+1}$, where each element $D(i, j)$ is defined as

$$D(i, j) = \hat{D}(i - 1, j - 1) + \min \begin{cases} D(i - 1, j) \\ D(i, j - 1) \\ D(i - 1, j - 1) \end{cases},$$

where $i \in \{2, \dots, m + 1\}$, $j \in \{2, \dots, n + 1\}$ and $\hat{D}(i - 1, j - 1)$ is the respective element in cross distance matrix \hat{D} . The first row and column id D is set to infinity and $D(0, 0) = 0$.

The DTW distance is than located at the position $D(m + 1, n + 1)$ and cheapest path from $D(0, 0)$ to $D(m + 1, n + 1)$ represents the optimal warping path. The path must meet the requirements of the warping functions.

3 Experiments

In this section the implementation of the DTW algorithm and results are being presented.

As an input the collection of 8000 randomly generated two-dimensional multivariate time series of the same size were used with 2D euclidean distance as a local dissimilarity function.

3.1 Implementation

The implementation of the MDTW was done in C++ using the C++11 standard. Parallelization was done using the OpenMP. Code was compiled using the Intel compiler 2016.01 with -O3 optimization and AVX-2 for most effective loops optimization and vectorization. The compact thread affinity was used for OpenMP threads.

3.2 Experimental setup

All computations were done on the single node of the SALOMON cluster containing 2x Intel Xeon E5-2680v3, 2.5GHz processors with 12 cores and 128GB, 5.3GB per core, DDR4@2133 MHz memory.

3.3 Results

Table 1 shows time performance of the MDTW implementation for different number of threads and number of input time series.

	OpenMP threads					
N	1	2	4	8	12	24
500	4.11	3.13	1.57	0.94	0.64	0.32
1000	16.48	12.51	6.29	3.81	2.53	1.28
2000	65.81	50.12	25.15	15.24	10.19	5.12
4000	262.72	200.21	100.59	60.92	40.58	20.36
8000	1088.59	803.93	402.05	201.01	134.09	80.12

Table 1: Time performance

Results are then visualized in Figure 1.

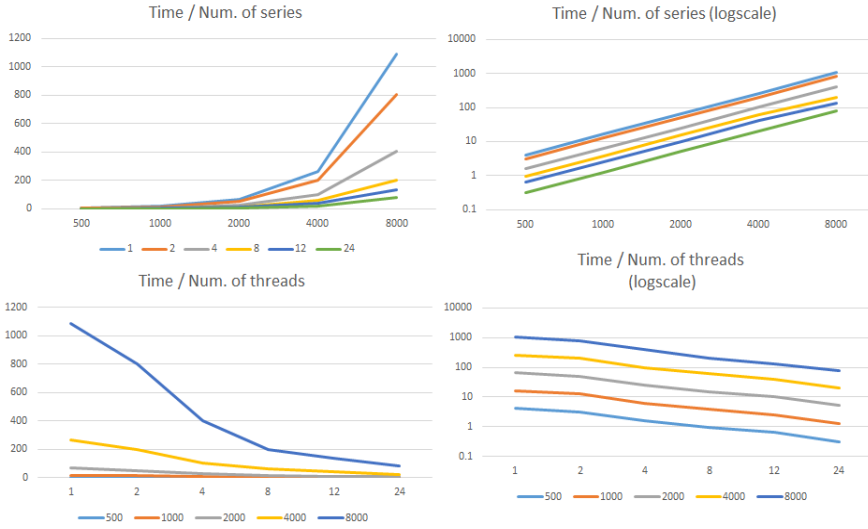


Fig. 1. Time performance

Table 2 shows speedup and efficiency of the MDTW implementation for different number of OpenMP threads and different number of input time series.

	OpenMP threads											
	N=1		N=2		N=4		N=8		N=12		N=24	
	S	E	S	E	S	E	S	E	S	E	S	E
500	1.00	1.00	1.31	0.66	2.62	0.65	4.37	0.55	6.42	0.54	12.84	0.54
1000	1.00	1.00	1.32	0.66	2.62	0.66	4.33	0.54	6.51	0.54	12.88	0.54
2000	1.00	1.00	1.31	0.66	2.62	0.65	4.32	0.54	6.46	0.54	12.85	0.54
4000	1.00	1.00	1.31	0.66	2.61	0.65	4.31	0.54	6.47	0.54	12.90	0.54
8000	1.00	1.00	1.35	0.68	2.71	0.68	5.42	0.68	8.12	0.68	13.59	0.57

Table 2: Scalability and efficiency based on num. of threads

Results are also visualized in Figure 2.

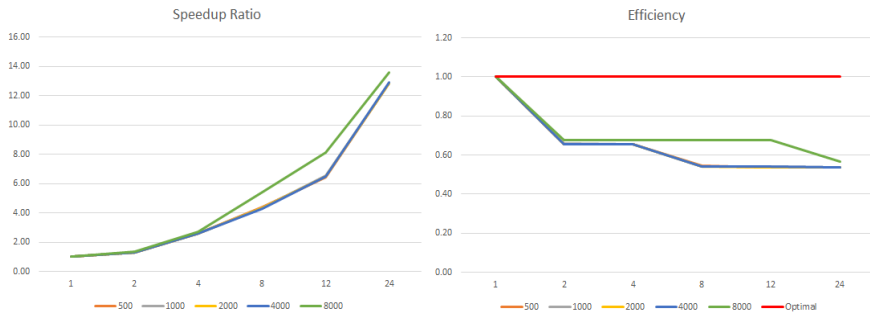


Fig. 2. Scalability and efficiency based on num. of threads

4 Conclusion

In this paper the Dynamic Time Warping algorithm for univariate and multivariate time series was presented. Algorithm was then implemented in C++ and parallelized using OpenMP and the performance was tested on SALOMON cluster for the generated collection of two-dimensional multivariate time series.

From Tables 1, 2 and Figures 1 and 2 can be seen that OpenMP implementation of DTW can perform very good for even large number of time series. The speedup is getting closer to linear function with increasing number of input time series and also parallel efficiency increases as expected.

The proposed implementation can be therefore further used in order to cluster large number of real time series.

Acknowledgement

This work was supported by The Ministry of Education, Youth and Sports from the National Programme of Sustainability (NPU II) project “IT4Innovations excellence in science - LQ1602”, from the Large Infrastructures for Research, Experimental Development and Innovations project “IT4Innovations National Supercomputing Center LM2015070” and co-financed by the internal grant agency of VB - Technical University of Ostrava, Czech Republic, under the projects no. SP2016/166 “HPC Usage for Analysis of Uncertain Time Series II” and no. SP2016/179 “HPC Usage for Transport Optimization based on Dynamic Routing II”.

References

1. Ch. Chatfield, *The Analysis of Time Series, An Introduction*. CRC Press LLC (2004)
2. T. W. Liao *Clustering of time series data - a survey*. Pattern recognition 38 (2005)
3. M. Muller *Information Retrieval for Music and Motion*. Springer (2007)
4. Ch. A. Ratanamahatana, E. Keogh, *Everything you know about Dynamic Time Warping is wrong*. Citeseer (2004)

Bayes Estimators of the Mixture of Failure Rate Model

Tien Thanh Thach^{1,2} and Radim Bris¹

¹Department of Applied Mathematics, FEECS,
VŠB – Technical University of Ostrava, 17. listopadu 15,
708 33 Ostrava – Poruba, Czech Republic

²Faculty of Mathematics and Statistics, Ton Duc Thang University, Department of
Statistics, Ho Chi Minh City, Vietnam
`radim.bris@vsb.cz`

Abstract. In this paper, we have obtained the Bayes estimators of the parameters and reliability characteristics of a mixture of failure rate using Lindley approximation under symmetric and asymmetric loss functions. The proposed estimators have been compared with the corresponding MLE based on simulated sample from the failure time distribution.

1 Introduction

Engineering systems, while in operation, are always subject to environmental stresses and shocks which may or may not alter the failure rate function of the system. Suppose p is the unknown probability that the system is able to bear these stresses and its failure model remains unaffected, and q is the probability of the complementary event. In such situations, a failure distribution is generally used to describe mathematically the failure rate on the system. To some extent, the solution to the proposed problem is attempted through the mixture of distributions (Mann et al. [1], Sinha [2], Lawless [3]). Let the failure rate function of the system be in either of the following two states (Sharma et al. [6]):

State 1: Initially it experiences a constant failure rate model and this model may (or may not) change with probability q ($p = 1 - q$).

State 2: If the stresses and shocks alter the failure rate model of the system with probability q , then it experiences a wear-out failure model. In comparison with Sharma et al. [6], this study brings distinctive generalization of the state by implementation of a new parameter, which enables to take into account also more general Weibull model.

2 Assumptions

Let p be the probability of the event A , that the system is able to bear the stresses and shocks and its failure pattern remains unaltered and $q = 1 - p$ be the probability of the complementary event A^c .

Further, let, the mixture of the failure rate function be

$$h(t) = p\lambda + (1 - p)\lambda t^k, \quad \lambda, k, t > 0, 0 < p < 1. \quad (1)$$

3 Characteristics of the life-time distribution

Using the well-known relationship

$$f(t) = h(t)e^{-\int_0^t h(x)dx} \tag{2}$$

and in view of equation (1), the p.d.f. of the life-time T is

$$f(t) = \begin{cases} (p\lambda + (1-p)\lambda t^k) e^{-(p\lambda t + \frac{\lambda(1-p)}{k+1}t^{k+1})}, & t > 0 \\ 0, & \text{otherwise.} \end{cases} \tag{3}$$

The reliability function is

$$R(t) = e^{-(p\lambda t + \frac{\lambda(1-p)}{k+1}t^{k+1})}, \quad t > 0. \tag{4}$$

The mean time to failure (MTTF) is given by

$$\mathbf{MTTF} = \mathbb{E}(T) = \int_0^\infty R(t)dt = \int_0^\infty e^{-(p\lambda t + \frac{\lambda(1-p)}{k+1}t^{k+1})}dt \tag{5}$$

This integral can be obtained by using some suitable numerical methods.

4 Estimation of parameters and reliability characteristics

Let t_1, \dots, t_n be the random failure times of n items under test whose failure time distribution is as given in equation (3). Then the likelihood function is

$$L = L(t_1, \dots, t_n | p, \lambda, k) = \lambda^n \left[\prod_{i=1}^n (p + (1-p)t_i^k) \right] e^{-\lambda \sum_{i=1}^n (pt_i + \frac{1-p}{k+1}t_i^{k+1})}. \tag{6}$$

4.1 Maximum likelihood estimation of the parameters

To find the MLE of $p, \lambda,$ and $k,$ we consider

$$l = \log(L) = n \log \lambda + \sum_{i=1}^n \log (p + (1-p)t_i^k) - \lambda \sum_{i=1}^n \left(pt_i + \frac{1-p}{k+1}t_i^{k+1} \right). \tag{7}$$

The maximum likelihood estimates of parameters of the mixture failure rate are given as solution of equations

$$\begin{cases} \sum_{i=1}^n \frac{1}{p + \frac{t_i^k}{1-t_i^k}} - \lambda \left(\sum_{i=1}^n t_i - \frac{1}{k+1} \sum_{i=1}^n t_i^{k+1} \right) = 0 \\ \frac{n}{\lambda} - \frac{1}{k+1} \sum_{i=1}^n t_i^{k+1} - p \left(\sum_{i=1}^n t_i - \frac{1}{k+1} \sum_{i=1}^n t_i^{k+1} \right) = 0 \\ \sum_{i=1}^n \frac{\log t_i}{1 - \left(\frac{1}{t_i^k} \right)^p} - \lambda \sum_{i=1}^n \left(\frac{\log t_i}{k+1} - \frac{1}{(k+1)^2} \right) t_i^{k+1} = 0 \end{cases} \tag{8}$$

which maybe solved using a iteration scheme.

By using the invariance property of MLE's, we get the estimators of $R(t), h(t)$ and MTTF.

5 Bayesian estimation of the parameters

In Bayesian estimation, we consider three types of loss functions. The first is the squared error loss (SEL) function,

$$L(\theta, \theta^*) \propto (\theta - \theta^*)^2 \tag{9}$$

where θ^* is an estimate of parameter θ . The Bayes estimator of θ under the SEL function is the value θ^* which minimizes $\mathbb{E}_\theta [(\theta - \theta^*)^2]$. It is

$$\theta_{BS}^* = \mathbb{E}_\theta [\theta] \tag{10}$$

where $\mathbb{E}_\theta(\cdot)$ denotes the posterior expectation with respect to the posterior density of θ .

The second is the LINEX loss function,

$$L(\theta, \theta^*) \propto e^{c(\theta^* - \theta)} - c(\theta^* - \theta) - 1, \quad c \neq 1. \tag{11}$$

The posterior expectation of the LINEX loss function is

$$\mathbb{E}_\theta [L(\theta, \theta^*)] \propto e^{c\theta^*} \mathbb{E}_\theta [e^{-c\theta}] - c(\theta^* - \mathbb{E}_\theta[\theta]) - 1. \tag{12}$$

The Bayes estimator of θ under the LINEX loss function is the value θ^* which minimizes (12). It is

$$\theta_{BL}^* = -\frac{1}{c} \log \{ \mathbb{E}_\theta [e^{-c\theta}] \} \tag{13}$$

provided that the expectation $\mathbb{E}_\theta [e^{-c\theta}]$ exists and is finite.

And the third is the general entropy loss (GEL) function,

$$L(\theta, \theta^*) \propto \left(\frac{\theta^*}{\theta} \right)^c - c \log \left(\frac{\theta^*}{\theta} \right) - 1. \tag{14}$$

The Bayes estimate relate to the general entropy loss is given as

$$\theta_{BE}^* = (\mathbb{E}_\theta [\theta^{-c}])^{-\frac{1}{c}} \tag{15}$$

provided that the expectation $\mathbb{E}_\theta [\theta^{-c}]$ exists and is finite.

The proposed priors for parameters p, λ , and k may be taken as

$$\pi(p) = \frac{1}{p}, \quad 0 < p < 1; \quad \pi(k) = \frac{1}{k}, \quad k > 0 \tag{16}$$

$$\pi(\lambda) = \frac{\alpha^\beta}{\Gamma(\beta)} \lambda^{\beta-1} e^{-\alpha\lambda}, \quad \lambda > 0, \alpha > 0, \beta > 0 \tag{17}$$

For all parameter, we assume independent priors. Then the joint prior distribution for p, λ , and k is

$$\pi(p, \lambda, k) = \frac{\alpha^\beta}{pk\Gamma(\beta)} \lambda^{\beta-1} e^{-\alpha\lambda}, \quad \lambda, k > 0, 0 < p < 1, \alpha > 0, \beta > 0. \tag{18}$$

In view of the prior in equation (18), the posterior distribution of p, λ , and k given t_1, \dots, t_n is given by

$$\pi(p, \lambda, k | t_1, \dots, t_n) = \frac{L(t_1, \dots, t_n | p, \lambda, k) \pi(\lambda, p, k)}{\int_0^{+\infty} \int_0^{+\infty} \int_0^1 L(t_1, \dots, t_n | p, \lambda, k) \pi(p, \lambda, k) dp d\lambda dk} \tag{19}$$

It may be noted here that the posterior distribution of (p, λ, k) takes a ratio form that involves an integration in the denominator and cannot be reduced to a closed form. Thus, we propose the use of Lindley’s approximation for obtaining the Bayes estimators of p, λ , and k and reliability characteristics. If n is sufficiently large, according to Lindley [9], any ratio of the integral of the form

$$I(t) = \mathbb{E} [u(\theta)] = \frac{\int_{(\theta_1, \theta_2, \theta_3)} u(\theta_1, \theta_2, \theta_3) e^{l(\theta_1, \theta_2, \theta_3) + \rho(\theta_1, \theta_2, \theta_3)} d(\theta_1, \theta_2, \theta_3)}{\int_{(\theta_1, \theta_2, \theta_3)} e^{l(\theta_1, \theta_2, \theta_3) + \rho(\theta_1, \theta_2, \theta_3)} d(\theta_1, \theta_2, \theta_3)} \tag{20}$$

where $u(\theta) = u(\theta_1, \theta_2, \theta_3)$ is a function of θ_1, θ_2 or θ_3 only, $l(\theta_1, \theta_2, \theta_3)$ is log of likelihood, $\rho(\theta_1, \theta_2, \theta_3)$ is log joint prior of θ_1, θ_2 and θ_3 , can be evaluated as

$$I(t) = u(\hat{\theta}_1, \hat{\theta}_2, \hat{\theta}_3) + (u_1 a_1 + u_2 a_2 + u_3 a_3 + a_4 + a_5) + \frac{1}{2} \left[A(u_1 \sigma_{11} + u_2 \sigma_{12} + u_3 \sigma_{13}) + B(u_1 \sigma_{21} + u_2 \sigma_{22} + u_3 \sigma_{23}) + C(u_1 \sigma_{31} + u_2 \sigma_{32} + u_3 \sigma_{33}) \right] \tag{21}$$

where $\hat{\theta}_1, \hat{\theta}_2$ and $\hat{\theta}_3$ are the MLE of θ_1, θ_2 and θ_3 respectively,

$$a_i = \rho_1 \sigma_{i1} + \rho_2 \sigma_{i2} + \rho_3 \sigma_{i3}, \quad i = 1, 2, 3 \tag{22}$$

$$a_4 = u_{12} \sigma_{12} + u_{13} \sigma_{13} + u_{23} \sigma_{23}; \quad a_5 = \frac{1}{2} (u_{11} \sigma_{11} + u_{22} \sigma_{22} + u_{33} \sigma_{33}) \tag{23}$$

$$A = \sigma_{11} l_{111} + 2\sigma_{12} l_{121} + 2\sigma_{13} l_{131} + 2\sigma_{23} l_{231} + \sigma_{22} l_{221} + \sigma_{33} l_{331} \tag{24}$$

$$B = \sigma_{11} l_{112} + 2\sigma_{12} l_{122} + 2\sigma_{13} l_{132} + 2\sigma_{23} l_{232} + \sigma_{22} l_{222} + \sigma_{33} l_{332} \tag{25}$$

$$C = \sigma_{11} l_{113} + 2\sigma_{12} l_{123} + 2\sigma_{13} l_{133} + 2\sigma_{23} l_{233} + \sigma_{22} l_{223} + \sigma_{33} l_{333} \tag{26}$$

and subscripts 1, 2, 3 on the right-hand sides refer to θ_1, θ_2 and θ_3 respectively and

$$\rho_i = \frac{\partial \rho}{\partial \theta_i}; \quad u_i = \frac{\partial u(\theta_1, \theta_2, \theta_3)}{\partial \theta_i}, \quad i = 1, 2, 3 \tag{27}$$

$$u_{ij} = \frac{\partial^2 u(\theta_1, \theta_2, \theta_3)}{\partial \theta_i \partial \theta_j}; \quad l_{ij} = \frac{\partial^2 l(\theta_1, \theta_2, \theta_3)}{\partial \theta_i \partial \theta_j}, \quad i, j = 1, 2, 3 \tag{28}$$

$$l_{ijk} = \frac{\partial^3 l(\theta_1, \theta_2, \theta_3)}{\partial \theta_i \partial \theta_j \partial \theta_k}, \quad i, j, k = 1, 2, 3 \tag{29}$$

and $\sigma_{ij} = (-l_{ij})^{-1}$, all evaluated at the MLE of parameters. Now we can obtain the values of the Bayes estimates of various parameters.

5.1 Under squared error loss function

1. If $u(\hat{p}, \hat{\lambda}, \hat{k}) = \hat{p}$ then

$$p_{BS}^* = \hat{p} - \frac{1}{\hat{p}}\sigma_{11} + \left(\frac{\beta - 1}{\hat{\lambda}} - \alpha\right)\sigma_{12} - \frac{1}{\hat{k}}\sigma_{13} + \frac{1}{2}(A\sigma_{11} + B\sigma_{21} + C\sigma_{31}) \quad (30)$$

2. If $u(\hat{p}, \hat{\lambda}, \hat{k}) = \hat{\lambda}$ then

$$\lambda_{BS}^* = \hat{\lambda} - \frac{1}{\hat{p}}\sigma_{21} + \left(\frac{\beta - 1}{\hat{\lambda}} - \alpha\right)\sigma_{22} - \frac{1}{\hat{k}}\sigma_{23} + \frac{1}{2}(A\sigma_{12} + B\sigma_{22} + C\sigma_{32}) \quad (31)$$

3. If $u(\hat{p}, \hat{\lambda}, \hat{k}) = \hat{k}$ then

$$k_{BS}^* = \hat{k} - \frac{1}{\hat{p}}\sigma_{31} + \left(\frac{\beta - 1}{\hat{\lambda}} - \alpha\right)\sigma_{32} - \frac{1}{\hat{k}}\sigma_{33} + \frac{1}{2}(A\sigma_{13} + B\sigma_{23} + C\sigma_{33}) \quad (32)$$

4. If $u(\hat{p}, \hat{\lambda}, \hat{k}) = e^{-\hat{\lambda}\left(\hat{p}t + \frac{(1-\hat{p})}{\hat{k}+1}t^{\hat{k}+1}\right)}$ then we get $R_{BS}^*(t)$ via equation (21).

5. If $u(\hat{p}, \hat{\lambda}, \hat{k}) = \hat{\lambda}\left(\hat{p} + (1 - \hat{p})t^{\hat{k}}\right)$ then we get $h_{BS}^*(t)$ via equation (21).

5.2 Under LINEX loss function

In this case, we do similarly to the SEL, but using the Bayes estimate form given in equation (13) instead.

5.3 Under general entropy loss function

In this case, we also do similarly to the SEL and LINEX, but using the Bayes estimate form given in equation (15) instead.

6 Simulation study

In this section, we perform a numerical study to compare the proposed estimates of $p, \lambda, k, R(t)$ and $h(t)$. Because the space restrictions, we only show the simulation under SEL. A sample of size $n = 30, 60$ and 100 was considered to represent relatively small, medium and large data set. The values of the parameters chosen were $p = 0.3, \lambda = 0.3$ and $k = 2$. Prior parameters α and β are arbitrary taken as 3.0 . The results of MLE and Bayes estimation are present in the Table 1, Fig.1 and Fig.2.

7 Conclusion

The performance of the proposed Bayes estimators via Lindley approximation has been compared to the maximum likelihood estimators. On the basis of these results, we may conclude that under square error loss function, the Bayes method can show better result than MLEs method to estimate the parameters and reliability characteristics of the mixture of failure rate model. When sample size is large enough, both methods give comparable results.

Table 1. MLE and Bayes estimates under SEL function

True	$p = 0.3, \lambda = 0.3, k = 2 (MTTF = 1.945675)$	
Estimate	MLE	Bayes
$n = 30$	$\hat{p} = 0.2292543 \hat{\lambda} = 0.3761959$ $\hat{k} = 2.0378268 \hat{MTTF} = 1.765466$	$p_{BS}^* = 0.301264 \lambda_{BS}^* = 0.349760$ $k_{BS}^* = 1.998313 \hat{MTTF}_{BS}^* = 1.772956$
$n = 60$	$\hat{p} = 0.2361298 \hat{\lambda} = 0.2990294$ $\hat{k} = 2.1173058 \hat{MTTF} = 1.908684$	$p_{BS}^* = 0.265241 \lambda_{BS}^* = 0.283132$ $k_{BS}^* = 2.127173 \hat{MTTF}_{BS}^* = 2.101174$
$n = 100$	$\hat{p} = 0.3214353 \hat{\lambda} = 0.3088706$ $\hat{k} = 2.0366736 \hat{MTTF} = 1.915936$	$p_{BS}^* = 0.3396956 \lambda_{BS}^* = 0.302008$ $k_{BS}^* = 2.033015 \hat{MTTF}_{BS}^* = 2.140842$

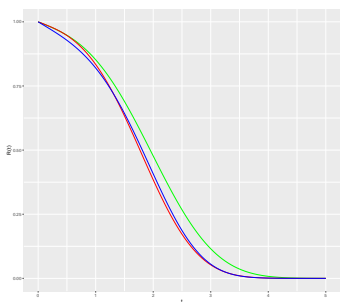


Fig. 1. Reliability functions under SEL function, $n = 30$

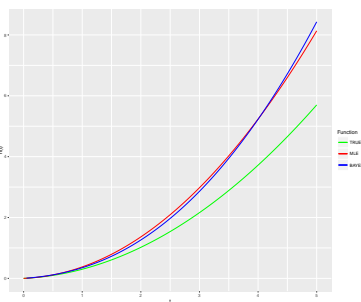


Fig. 2. Failure rate functions under SEL function, $n = 30$

References

1. Mann, N., Schaffer, E., Singpurwalla, N.: Methods for Statistical Analysis of Reliability and Life Data. Wiley. NY (1974)
2. Sinha, S. K.: Reliability and Life Testing. Wiley Eastern Ltd. USA (1986)
3. Lawless, J. F.: Statistical Models and Methods for Life-time Data. John Wiley and Sons. NY (1982)
4. Martz, H. F., Waller, R. A.: Bayesian Reliability Analysis. John Wiley and Sons. NY (1982)
5. Pandey, A., Singh, A., Zimmer, W. J.: Bayes estimation of the linear hazard-rate model. IEEE Trans. Reliab. 42 (1993)
6. Sharma, K. K., Krishna, H., Singh, B.: Bayes estimation of the mixture of hazard rate model. Reliability Engineering and System Safety. 42, 9–13 (1997)
7. Harris, C. M., Singpurwalla, N. D.: Life Distributions Derived from Stochastic Hazard Functions. IEEE Trans. Reliab. 17, 70–79 (1968)
8. Aslam, M., Kazmi, S. M. A., Ahmad, I., Shah, S. H.: Bayesian Estimation for Parameters of the Weibull Distribution. Sci.Int.(Lahore). 26(5), 1915-1920 (2014)
9. Lindley, D. V.: Approximate Bayes Methods. Bayesian Statistics, Valency (1980)

The Influence of Temperature on Chromatic and Polarization-mode Dispersion of the Optical Fiber

Lukas Bednarek

Department of Telecommunications, FEECS,
VŠB – Technical University of Ostrava, 17. listopadu 15,
708 33 Ostrava – Poruba, Czech Republic
lukas.bednarek@vsb.cz

Abstract. Generally, the influence of weather conditions on parameters of the optical fiber is a matter of long-term research. This article shows the primordial results of the measurement of the coefficient of chromatic dispersion, λ_0 , and values of polarization-mode dispersion. These data were evaluated according to the temperature around the optical fiber. Measurements were carried out on the roof of the building of N in the campus the VSB-Technical University of Ostrava during the period of 2 weeks. The results not only determine the dependence of these parameters on temperature, but results also show the progress of changes of parameters from the start of measurement to the end of the measurement.

Keywords: chromatic dispersion, polarization-mode dispersion, temperature, optical fiber

1 Introduction

The impact of weather on parameters of the optical fiber is a matter of long-term research. Primarily, this article focuses on the temperature around the optical fiber, but we can also see the progress of the measured values from the beginning to the end of the measurement in the graphs. The investigated parameters are the coefficient of chromatic dispersion, λ_0 (the wavelength, where chromatic dispersion is zero), and values of polarization-mode dispersion (PMD).

Generally, the dispersion indicates the extension of the pulse in the time domain after passing the optical signal through the optical fiber. Chromatic dispersion (CD) is the most affecting dispersion in single-mode optical fibers. CD consists of material dispersion, waveguide dispersion, and profile dispersion. Material dispersion is caused by the dependence of the refractive index of the core of the optical fiber (hence the speed of propagation of the beam) on the wavelength. The composition of the material of the fiber core may slightly affect this dispersion. Waveguide dispersion is caused by the different speed of light propagation in the core and cladding of the fiber. In cross section, selection of an appropriate profile of refractive index affects the dependence of the waveguide dispersion on the wavelength. The last compo-

ment of chromatic dispersion is profile dispersion. Dependence of profile of refractive index of core and cladding on the wavelength raises this dispersion. Profile dispersion manifests only at high transmission speeds. Material dispersion and profile dispersion can be partially compensate mutually.

The physical nature resulting from the theory of polarization of light to induces polarization-mode dispersion. Two orthogonal components which are horizontally polarized mode and vertically polarized mode spread the light in the optical fiber (in waveguide general). These components propagate by different speeds due to non-circularity of the optical fiber. So, the extension of the pulse is caused. Polarization-mode dispersion arises as the most restricting at transmission speeds of 40 Gbit/s and above.

The coefficient of the chromatic dispersion characterizes the size of chromatic dispersion. This coefficient indicates the change of group delay of signal t_g depending on the wavelength at passing through the optical fiber. The unit is ps/(nm*km), which means that the coefficient gives a value of pulse extension in ps, using a radiation source with a spectral width of 1 nm, and after passing through the fiber with the length of 1 km. This definition means that the value of the coefficient of chromatic dispersion, the spectral width of the radiation source and the length of optical fiber increase the extension of the pulse. The typical value of chromatic dispersion coefficient is 16-18 ps/(nm*km) at the wavelength of 1550 nm.

λ_0 is the wavelength at which the chromatic dispersion is zero. A typical value of the conventional optical fiber is 1300-1324 nm. The coefficient of chromatic dispersion is negative for the wavelengths less than λ_0 . For this reason, shorter wavelengths are delayed against longer wavelengths. This coefficient is positive for wavelengths greater than λ_0 , and it indicates that longer wavelengths are delayed against shorter wavelengths.

The size of polarization-mode dispersion is less than 1 ps for conventional fibers. The value is influenced by many external factors, for example, a length of optical fiber, bends, weather conditions, deformation of the optical fiber, etc.

2 Measurement procedure

Examined optical fiber consists of several welded optical fibers mutually. These fibers were located in one optical cable. The total length of the fiber was 14.9 km. The cable was placed along the edge of the roof of the building of N in the campus the VSB-Technical University of Ostrava. I realized these measurements in the period February 8 to 21, 2016.

Four temperature sensors which were located at the corners of the roof recorded temperature at a given location. Distribution of temperature sensors was chosen with regard to the changing conditions in different parts of the roof. Each sensor wrote temperature after 1 minute. Then, the average temperature value which was determined to be relevant was calculated from these values.

Measurements of the coefficient of chromatic dispersion and λ_0 were performed using the module of FTB-5800B from the company EXFO. This module uses the plat-

form of FTB-500 from the same company as a chassis. The radiation source is FLS-5800A, which is modulated, polarizable, and high-power super LED (SLED). The module uses the phase shift method for measuring chromatic dispersion. This method is the reference method of measurement, and its accuracy is in tenths ps. The measurements were done at wavelengths from 1520 to 1625 nm. The coefficient of chromatic dispersion for a wavelength of 1550 nm and the wavelength with zero chromatic dispersion were calculated from the results of the measurement. Repeated measurements were performed every 10 minutes.

The module FTB-5500B provides a measurement of the polarization-mode dispersion. The chassis and the radiation source are the same as for measurement of the CD. This module uses the general interferometric method of measurement GINTY. The measurements were carried out for C and L bands of the wavelengths. Measurement module evaluated the value of PMD subsequently. Repeated measurements were performed every 5 minutes.

3 Results

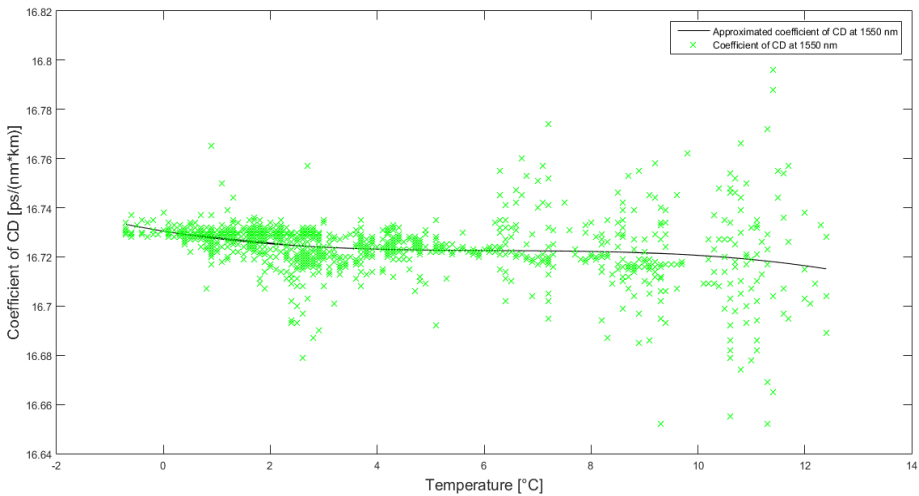


Fig. 1. Dependence of CD coefficient on temperature

Figure 1 shows the dependence of CD coefficient on the temperature at a wavelength of 1550 nm. The graph shows that the CD is more stable at lower temperatures. At a temperature above 6°C, the dispersion of the values is higher, however, the maximum difference is 0.15 ps/(nm*km). The variance of values increases with temperature further. The trend of CD decreases with increasing temperature.

In Figure 2, the graph shows the dependence of λ_0 on temperature. At temperature up to 5°C, the dispersion of the values is very low. Therefore, the wavelength with zero dispersion is very stable at low temperatures. The variance of values increases at the temperature above 5°C. The dispersion of measured values increases with increas-

ing temperature. The highest difference is at the temperature of 11°C, and the value is about 26 nm. Trend λ_0 is constant up to a temperature 8°C, then the wavelength with zero dispersion begins slightly decrease.

Figure 3 shows the dependence of the PMD on temperature. At first glance, the scatter of values is high. The maximum variance is 0.6 ps. High differences of values are determined by the influence of other factors at the same temperatures. Generally, the values of PMD are very low. Dependence of PMD on slight changes in the weather is much greater than in the case of the CD. Measurements were probably influenced by factors such as atmospheric precipitations, changes in atmospheric pressure, and higher strain at particular locations. However, the trend of values of PMD increases with increasing temperature.

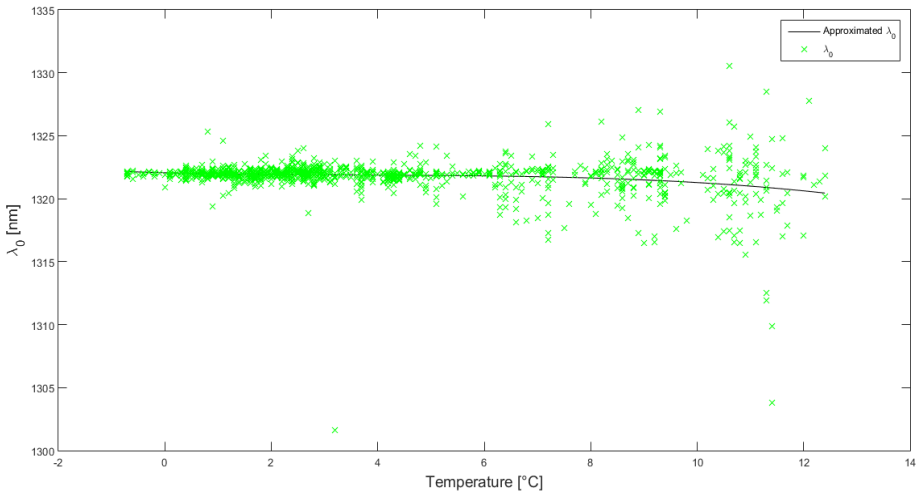


Fig. 2. Dependence of λ_0 on temperature

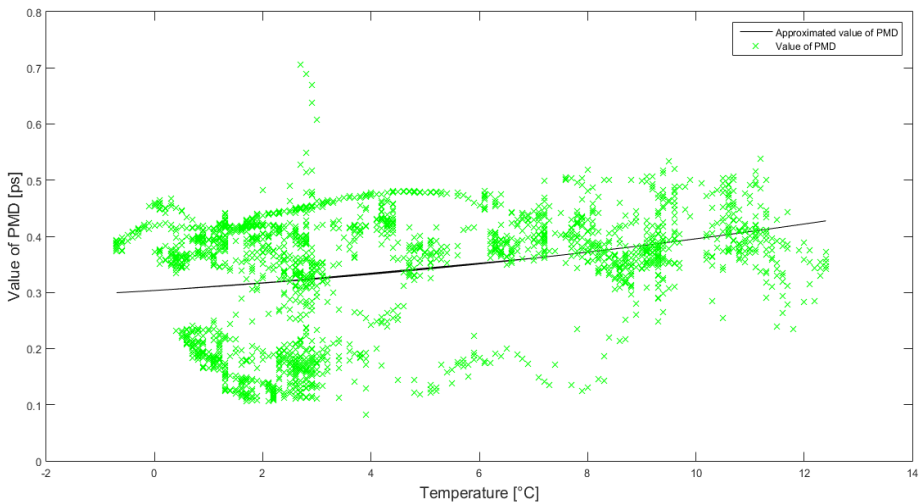


Fig. 3. Dependence of PMD values on temperature

Figure 4 shows the coefficient of the CD in the sequence of measured values from the beginning to the end of the measurement. The graph shows that the first 200 measurements had the large variance of values. It is given by very unstable weather because it was snowing, or the sun was shining, or the strong wind was blowing. In the following days, the weather was more stable, one day only slightly snowed, one day the sun was shining. However, the chart shows the recurrent decrease of values. These declines were mostly observed at night. The trend of CD was constant or slightly increasing throughout the measurement. Values started to decline from an 800th measurement.

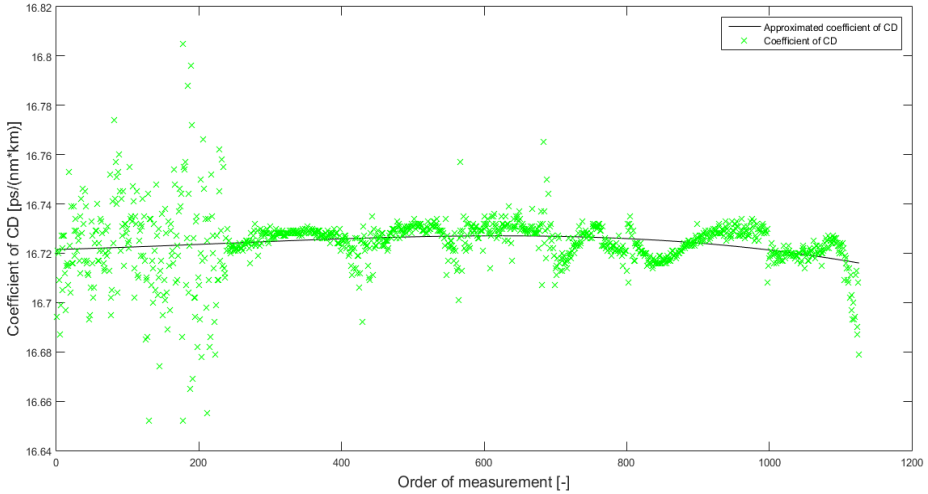


Fig. 4. Coefficient of CD depending on the order of measurement

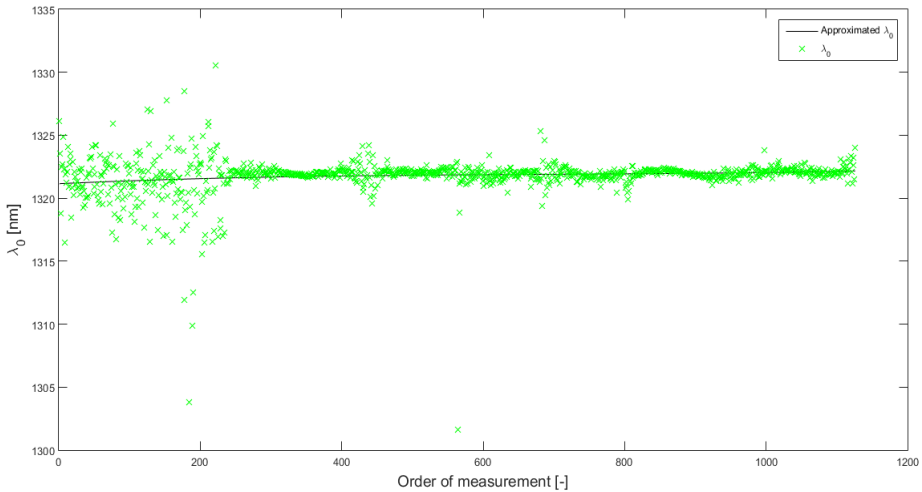


Fig. 5. λ_0 depending on the order of measurement

In figure 5, the graph shows the dependence of λ_0 on the sequence of measurement. The weather was very unstable during the first 200 measurements, so the variation of

values of the wavelength with zero dispersion is high. The weather was more stable in the following days, and therefore the measured values had very low dispersion. The falls of values are not as large as in the case of measuring the coefficient of CD. The approximated curve shows a slightly upward till the constant course of values.

Graph of the dependence of PMD values on time is not given here. As mentioned above, PMD values are very low and also very sensitive to minimal changes in the parameters of weather (temperature, atmospheric pressure, precipitation, etc.). From this reason, the graph of PMD values in depending on time have not credible value, since the values changed depending on the specific conditions at the time of measurement and for the next measurements were different. The approximated curve also showed no trend since it was increasing, decreasing, and constant in some sections measuring, however, no relationship was found.

4 Conclusion

The article dealt by the influence of temperature (and some other parameters of weather) on the chromatic dispersion and polarization-mode dispersion of the optical fiber. The presented results showed that determination of the effect of weather is a matter of long-term research. The temperature range was low since measurements were only carried out during two weeks. Other measurements of these dispersions are continuing in the summer months when temperatures are much higher. Then it will merge the measured results. Therefore, I can the more accurate determination of the influence of temperature and weather to dispersions of the optical fiber.

5 References

1. Vasinek V., Siska P., Bednarek L., Latal J., Koudelka P., Marcinka O., *Ageing of fiber optical devices* In: Next-Generation Optical Communication: Components, Sub-Systems, and Systems IV, 2015, DOI: 10.1117/12.2087165.
2. Bednarek L., Marcinka O., Perecar F., Papes M., Hajek L., Nedoma J., Vasinek V., *The aging process of optical couplers by gamma irradiation* In.: Photonic Fiber and Crystal Devices: Advances in Materials and Innovations in Device Applications IX, 2015, DOI: 10.1117/12.2187044
3. Perecar F., Marcinka O., Bednarek L., Lucki M., Liner A., Hajek L., Papes M., Jaros J., Vasinek V., *The impacts of ageing effects due to radiation burden on optical fiber couplers* In.: Photonic Fiber and Crystal Devices: Advances in Materials and Innovations in Device Applications IX, 2015, DOI: 10.1117/12.2187517
4. Vasinek V., Hajek L., Bednarek L., Vanderka A., Hlavinka T., Marcinka O., *Influence of gamma radiation on optical fibers and devices* In.: International Conference on Photonics Solutions 2015, 2015, DOI: 10.1117/12.2196372
5. Bednarek L., Hajek L., Vanderka A., Nedoma J., Fajkus M., Zboril O., Vasinek V., *The influence of thermal aging on the optical coupler*, published at the conference Photonic Fiber and Crystal Devices: Advances in Materials and Innovations in Device Applications X, San Diego (USA), August 2016

Qualitative Comparison of Video Codec Standards H.264 and H.265/HEVC for 4K Resolution

Jaroslav Frnda¹ and Erik Chromy²

¹Department of Telecommunications, FEECS,
VŠB – Technical University of Ostrava, 17. listopadu 15,
708 33 Ostrava – Poruba, Czech Republic

jaroslav.frnda@vsb.cz ²FEI – Slovak University of Technology, Ilkovicova 3, 812 19
Bratislava, Slovak Republic
chromy@ut.feituba.sk

Abstract. This paper deals with the analysis of compression efficiency for two well-known video codecs of MPEG family namely H.264 and H.265. Video codec H.264 is the most commonly used codec for TV broadcasting in Europe nowadays. H.265 is its successor offers better compression ratio but on the other hand, needs higher computational power. Objective video metrics were used for analyzing a video quality. Objective metrics calculated a score that represents offered quality of these two compression techniques. Several test scenarios were performed and obtained results allowed us to compare the level of quality for both video codecs.

Keywords: H.264/AVC, H.265/HEVC, SSIM, VQM

1 Introduction

In the last years video service has begun a majority part of all data transmitted via IP based network. However, this transition had to deal with some difficulties because packet networks based on IP protocol had not been designed to transfer real-time traffic. The video quality is affected by several parameters, especially resolution, bitrate, compression technique and finally transmission link imperfection.

The compression technology can be considered as one of the main factors that influence the video quality. Nowadays many new compression standards are being developed, e.g. H.265/HEVC or VP9. Because of this video quality assessment plays still a big role in the research area. Today some institutes and research teams deal with video quality evaluation but most of them focus on the FullHD resolutions [1], [6], [7]. By 2016, 4K television market share had increased greatly as prices fell dramatically during last two years. Many sports performances and new TV series are now available for end-users who have 4K TV with HEVC decoder. Because of this, paper describes impact of H.264/AVC and H.265/HEVC compression standards on the video quality for 4K resolution is measured and evaluated.

1.1 MPEG Compression Standards

MPEG, which stands for Moving Picture Experts Group, is the name of a family of standards used for coding audio-visual information (e.g. movies, video, music) in a digital compressed format.

H.264/AVC is currently the most used compression standard. It has been designed for a wide range of applications, ranging from video for mobile phones through web applications to TV broadcasting. Some of the feature enhancements in H.264/AVC standard over the earlier codecs are presented e.g. DCT algorithm works at 4x4 pixels instead of 8x8, color sampling is supported at 4:2:2 and 4:4:4, redundant pictures or flexible macroblock ordering. H.264/AVC also defines profiles and levels. There are several profiles currently defined: Baseline, Main, Extended and High which is adopted by Blu-ray Discs and digital TV broadcasting. Level is a specified set of constraints that indicate a degree of required decoder performance for a profile. For example, a level of support within a profile specifies the maximum picture resolution, frame rate, and bitrate that a decoder may use [1], [5].

The High Efficiency Video Coding (HEVC) standard is the most recent joint video project of the ITU-T Video Coding Experts Group (VCEG) and the ISO/IEC Moving Picture Experts Group (MPEG) standardization organizations, working together in a partnership known as the Joint Collaborative Team on Video Coding (JCT-VC). H.265/HEVC has the same basic structure as previous standards such as MPEG-2 Video and H.264/AVC. However, H.265/HEVC contains many incremental improvements such as [6], [8]:

- More flexible partitioning, from large to small partition sizes.
- Greater flexibility in prediction modes and transform block sizes.
- More sophisticated interpolation and deblocking filters.
- More sophisticated prediction and signaling of modes and motion vectors.
- Features to support efficient parallel processing.

The result is a video coding standard that can enable better compression, at the cost of potentially increased processing power. With H.265/HEVC, it should be possible to store or transmit video more efficiently than with earlier technologies such as H.264/AVC. This means that at the same picture size and quality HEVC video sequence should occupy less storage or transmission capacity than the equivalent H.264 video sequence. Secondly, at the same storage or transmission bandwidth, the quality and/or resolution of an HEVC video sequence should be higher than the corresponding H.264 video sequence [6], [7], [8].

1.2 Objective assessment methods

The video quality evaluation can be differentiated into objective and subjective assessment. The subjective assessment consists of the use of human observers

(people) who score the video quality. It is the most reliable way how to determine the video quality. The disadvantage of these methods is that they are time consuming and human resources are needed. Because of this fact, the objective methods are mostly used. They consist of the use of mathematical computational methods called “metrics” that produce values that score the video quality. The well-known and mostly used objective metrics are peak signal-to-noise ratio (PSNR), video quality metric (VQM) and structural similarity index (SSIM). First metric is the oldest one with worse adaption of human perception than metrics SSIM and VQM [2], [3], [4].

The SSIM metric measures three components, the luminance similarity, the contrast similarity and the structural similarity and combines them into one final value, which determines the quality of the test sequence. It is due to the human vision system that is highly specialized in extracting structural information from the viewing field and it is not specialized in extracting the errors. Owing to this factor, SSIM metric achieves good correlation with subjective impression. As an output is defined a score from 0 to 1 where 1 represents two identical pictures [1], [2].

The VQM metric computes the visibility of artefacts expressed in the DCT domain. The input of the metric is a pair of color image sequences, the reference one and the test one. Both sequences are cropped, then converted from the input color space to the YOZ color space, then transformed to blocked DCT and afterwards converted to units of local contrast. In the next step, the input sequences are subjected to temporal filtering, which implements the temporal part of the contrast sensitivity function. In the following step the contrast masking operation to the difference sequence is performed. Finally, the masked differences are weighted and pooled over all dimensions to yield summary measures of visual error. The output value of the VQM metric indicates the amount of distortion of the sequence, for no impairment the value is equal to zero and for rising level of impairment the output value rises [1], [5].

2 Measurements

Nowadays some free databases containing video sequences used for video quality evaluation are available. Many of them include video sequences in FullHD or 4K resolution in uncompressed form (.yuv) or compressed by H.264/AVC or H.265/HEVC standards. In our experiments four types of test sequences were used [9]:

- “Beauty”: Closeup on female face, hair waving around. Black background (Fig. 1).
- “Bosphorus”: Zoomed in luxury yacht, huge bridge on background. Panning right (Fig. 1).
- “Jockey”: Horse racing with camera panning to the left to follow.
- “ReadySteadyGo”: Horse racing track, riders getting ready for launch. The gates open and horses are running to the left.



Fig.1. Video sequence Beauty (left) and Bosphorus (right).

All sequences were in the 4K resolution (3840x2160) and 16:9 aspect ratio with 30 fps (frames per second). The length of these sequences was 600 frames, i.e. 20 seconds. The measurement procedure consists of following steps:

First, both sequences were downloaded from [9] in the uncompressed format (*.yuv) and used as the reference sequences. Afterwards, they were encoded to both MPEG compression standards, H.264/AVC and H.265/HEVC, using the x264 and x265 tool respectively. The target bitrates were in range from 2 Mbps to 30 Mbps, changed in 2 Mbps steps. The parameters of the encoded sequences were set to High Profile, Level 5.2 for H.264/AVC compression standard and Main Profile, Level 5.2 for H.265/HEVC compression standard. The GOP parameter was set to $N = 12$ and $M = 3$ which means that GOP length was 12 and two B frames between two successive P frames were stored. Finally, the quality between these sequences and the reference (uncompressed) sequence was compared and evaluated. This was done using the MSU Measuring Tool Pro version 3.0. SSIM and VQM objective metrics for the measurements were used.

3 Results

According to the graphs the H.265/HEVC compression standard yields better compression efficiency than H.264/AVC compression standard, at the same resolution and bitrate the compression quality of H.265/HEVC standard is better than H.264/AVC. Due to the limited space only a few graphs are listed below.

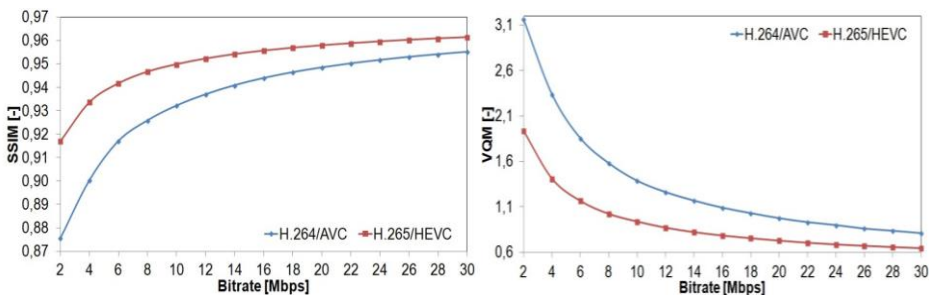


Fig.2. The relationship between video quality (SSIM – left and VQM - right) and bitrate of both compression standards for "Bosphorus" test sequence.

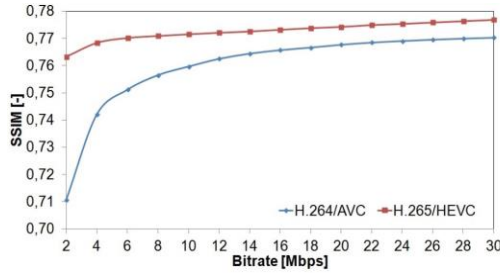


Fig.3. The relationship between video quality (SSIM) and bitrate of both compression standards for "Beauty" test sequence.

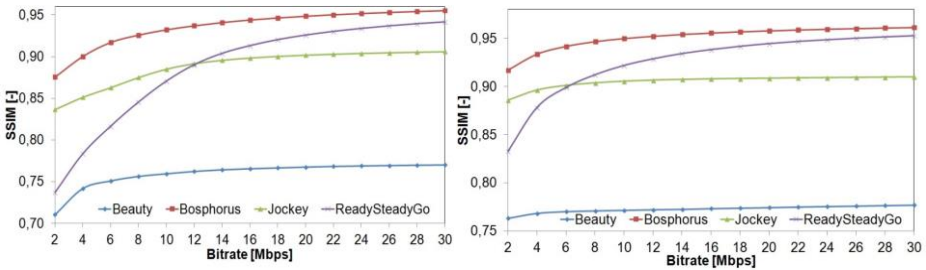


Fig.4. The relationship between video quality (SSIM) and bitrate of all test sequences for H.264 (left) and H.265 (right) compression standard.

Bigger difference in quality between these two compression standards is in lower bitrates, with increasing bitrate the quality of H.264/AVC standard approach the H.265/HEVC standard. The effectiveness of compression depends on the type of sequence. Figure 2, Fig. 3 and Fig. 4 show compression efficiency of both compression standards for various test sequences.

As it can be seen from the graphs, the compression efficiency depends on the types of test sequences. In consideration of measurements results we can say that:

- in sequences where is a slightly movement of one object on a static background as by "Bosphorus" sequence not only best quality is achieved but also settled, there is no big difference between quality by low and high bitrates
- in sequences where is a quick movement of more objects on a static background as by "ReadySteadyGo" sequence, only in higher bitrates very good quality is reached (not settled), there is a difference between quality by low and high bitrates

4 Conclusion

In this article the impact of H.264/AVC and H.265/HEVC compression standards on the video quality for 4K resolution was tested. According to the results, the H.265/HEVC compression standard yield better compression efficiency than

H.264/AVC compression standard. The bigger difference in quality between these two compression standards is in lower bitrates with increasing bitrate the quality of H.264/AVC standard approaches the H.265/HEVC standard. It can be also stated that the effectiveness of compression depends on the type of sequence.

Acknowledgements

This work was supported by the internal grant of Faculty of Electrical Engineering and Computer Science SGS No. SP2016/170.

Recent publications

1. J. Frnda, M. Voznak, L. Sevcik, *Impact of packet loss and delay variation on the quality of real-time video streaming*, In SPRINGER Telecommunication Systems, Volume 62, Issue 2, 2016, pp. 265-275. DOI: 10.1007/s11235-015-0037-2
2. J. Frnda, M. Voznak, L. Sevcik, P. Fazio, *Prediction Model of Triple play services for QoS Assessment in IP Based Networks*, In Journal of Networks, Vol. 10, No. 4, pp. 232-239, April 2015, DOI: 10.4304/jnw.10.4.232-239.
3. J. Frnda, M. Voznak, M. Hlozak, J. Slachta, J. Lin, *Application Tool for Prediction and Implementation of QoS in IP Based Network*, In SPRINGER Advances in Intelligent Systems and Computing AISC, Volume 370, 2015, pp. 143-154
4. J. Frnda, M. Voznak, L. Sevcik, *Network Performance QoS Prediction*, In SPRINGER Advances in Intelligent Systems and Computing AISC, Volume 297, 2014, pp. 165-174, DOI: 10.1007/978-3-319-07776-5_18
5. L. Sevcik, D. Uhrin, J. Frnda, M. Voznak, H. Toral-Cruz, M. Mikulec, S. Jakovlev, *Encryption for confidentiality of the network and influence of this to the quality of streaming video through network*, In Proc. SPIE. 9497, Mobile Multimedia/Image Processing, Security, and Applications 2015, DOI: 10.1117/12.2177555

Other references

6. Nguyen, T. and D. Marpe. *Objective Performance Evaluation of the HEVC Main Still Picture Profile*. IEEE Transactions on Circuits and Systems for Video Technology. 2013, pp. 1–8. ISSN 1051-8215. DOI: 10.1109/TCSVT.2014.2358000
7. Kim, I.-K., S. Lee, Y. Piao and J. CHen. *Coding efficiency comparison of new video coding standards: HEVC vs VP9 vs AVS2 video*. In: International Conference on Multimedia and Expo Workshops (ICMEW). Chengdu: IEEE, 2014, pp. 1–6. ISSN 1945-7871
8. G. J. Sullivan, J.-R. Ohm, W.-J. Han and T. Wiegand. *Overview of the High Efficiency Video Coding (HEVC) Standard*. IEEE Transactions on Circuits and Systems for Video Technology. 2012, Volume. 22, Issue. 12, pp. 1649–1668. ISSN 1051-8215. DOI: 10.1109/TCSVT.2012.2221191
9. Test sequences. ULTRA VIDEO GROUP. Available at: <http://ultravideo.cs.tut.fi/#testsequences>.

Optical Vehicle-to-vehicle (V2V) Communication: Analyze of Photometric Quantities DRL Jaguar XK

Peter Hajduk and Vladimir Vasinek

Department of Telecommunications, FEECS,
VŠB – Technical University of Ostrava, 17. listopadu 15,
708 33 Ostrava – Poruba, Czech Republic
{peter.hajduk.st2, vladimir.vasinek}@vsb.cz

Abstract. The article focuses on the implementation of vehicle to vehicle (V2V) communication technology in the field of road traffic safety, by way of light-emitting diodes (LED), which serve for the transmission of an optical signal within the range of the visible optical radiation (VLC). LED technology is nowadays used standardly in higher versions of car headlights and tail-lights, where it fulfills signaling functions as well as headlight functions. The future of V2V technology lies in the hybrid application of optical wireless communication which utilises LED sources on the side of the optical transmitter and a camera system (OCI, optical communication imaging sensor) on the side of the receiver, along with mobile technologies transmitting information about the state and character of the roadway. The authors of the work carried out research in the area of verifying the possibility of implementing the function of a DRL headlight in a Jaguar XK model 2011 in V2V communication, with the legislative demands for the specific function of the headlight in mind.

Keywords: Photometric quantity; VLC; Bias-Tee; V2V communication.

1 Introduction

Optical wireless data transfer between vehicles (V2V) is a new field of research, based on VLC technology. This technology is undergoing dynamic growth, as a result of the European Union's effort to react to the rapid increase in the frequency of road traffic accidents. The emphasis is put on raising active and passive safety, and therefore on the two basics of external automobile lighting – to see and be seen. The concept of road traffic safety is supported by research conducted by premier automotive manufacturers (BMW, Audi), where the applying of hybrid V2V communication is assumed. In this concept, mobile technologies transmit information about the roadway at greater distances (fog, rain), with OWC used for data transfer at shorter distances, about sudden changes in the roadway, when a quick response of the system >190ms (braking, change of direction) is important. Naturally, the utilisation of an optical V2V communication system opens up a series of problems. These include the necessity of integrating the modulator into the electronic control units of a headlight, as well as its placement in built-up and housing development areas. Another issue is the ful-

filling of legal regulations concerning the individual functions of a headlight, along with the homogeneity of a specific function determined by the car manufacturer.

2 Optical V2V communication system

Research in the field of optical communication between vehicles (V2V) is seeing expansion mainly in conjunction with the light-emitting LED diode for optical wireless communication (OWC). The optical source utilising the LED diode represents an appropriate OWC device for transmitting an optical signal within the visible spectrum of the VLC, with the possibility of modulating LED at high transmission speeds, with a long operational lifespan, effectiveness, and allowing automobile designers to create concepts typical for individual marques. This technology is commonly utilised in tail-lights, brake lights, headlights or in traffic signaling [1].

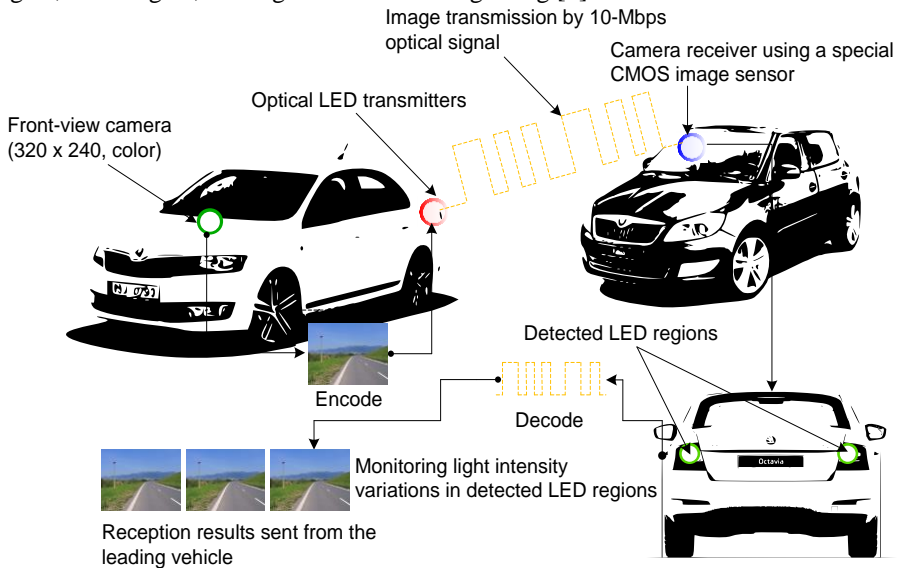


Fig. 1. Illustration of the optical V2V communication system.

The optical signal receiver in OWC automobile systems is comprised of a camera device utilising a special CMOS image sensor, referred to as a communication image sensor (OCI, optical communication image) [2]. The OCI uses so-called communication pixels (CPx), specialised for high-speed receiving of an optical signal. In addition to that, it contains an input circuit that reacts to intense light sources, e.g. LED, thus facilitating their detection. This means that the OWC technology uses a camera (an image sensor) providing non-crosstalk communication with multiple-access LED without a complex protocol and processing, preventing the mixing of an optical signal with noise, such as directly falling rays of sunlight. The applying of a camera system as a part of V2V communication also counts with the utilisation of camera systems, which are currently being used in the automotive industry for safety and comfort applications.

3 Optical V2V transmitter

The proposed concept of an optical transmitter within the context of the transfer concept is influenced by regulation ECE R 87, which is intended for the automotive industry and concerns the function of the DRL (daytime running lamp) daily lighting of a vehicle. Therefore, the optical transmitter factors in the decrease of optical radiation intensity in cases of applying advanced modulation formats, which could have transmission rate negative influence on the function of the headlight from a perspective of the lamp’s legality in road traffic.

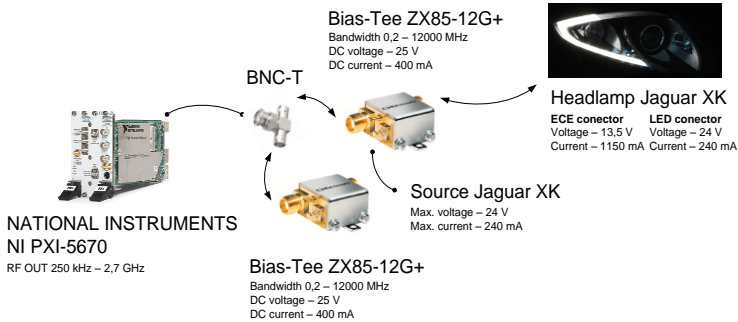


Fig. 2. Design concept of optical transmitter system DRL Jaguar XK model 2011.

The Bias-Tee ZX85-12G+ device in the proposed transmission system concept serves for the merging of an unidirectional signal on the DC port with the radio frequency signal on the RF port [3]. The combined RF+DC signal is used for setting the work point of the modulation of the individual LED segments of a DRL to a mean value of $I_{F(s)} = 240 \text{ mA}$. The DC port feed is implemented via the control electronics of the headlight.

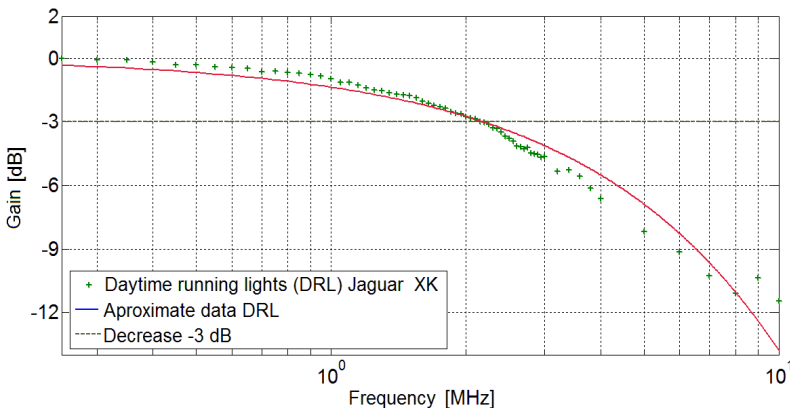


Fig. 3. Results of measurements optical output DRL Jaguar XK.

4 Measurement

For signal transmission, the optical transmission concept utilises a quadrature amplitudal modulation (64-QAM) with a carrier wave of 2 MHz, during which the maximum transfer speed achieved was 7,8 Mbit/s at a distance of 0,1 m between the detector and the DRL headlight of a Jaguar XK. The generating and subsequent analysis of the modulations was carried out with the use of the sophisticated LabVIEW software with the Modulation Toolkit library of functions. The software works with the hardware segment, with a PXI-5670 vector signal generator and PXI-5661 analyser.

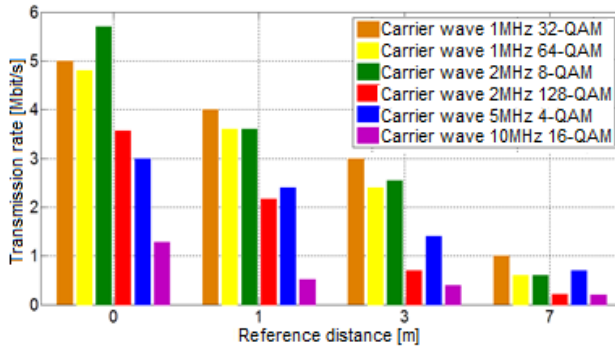


Fig. 4. Results of measurements transmission rate DRL Jaguar XK.

The analysis of the photometric quantities of a DRL headlight’s radiated optical radiation was carried out in an experimental testing room with the use of a goniophotometer device. The device is defined in the ECE 37 (Economic Commission for Europe) as a source with nominal geometric and photometric properties. The result of this measurement is a protocol of intensities in the measurement points and an isocandel map, which serve for the validation of the product.

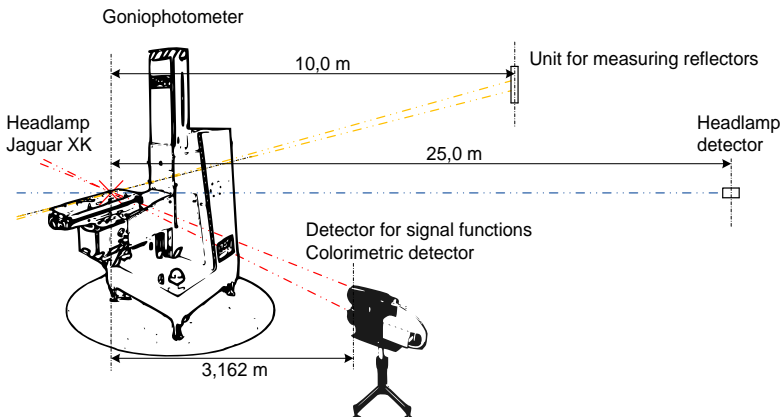


Fig. 5. Experimental lab for measurements of photometric values automotive headlamps and rear lamps.

The headlight of the Jaguar XK was positioned on a shifting arm of a goniophotometer device during photometric quantities analysis. Testing of the DRL daytime lighting proceeded at a maximum voltage of $U_F = 13,5 \text{ V}$ and environmental temperature of $T_a = 25 \text{ }^\circ\text{C}$. During testing, the shifting arm of the device turned the headlight itself under angles ranging from -20° to 20° on a horizontal axis and from -5° to 10° on a vertical axis. The detector for signal functions and the colorimetric detector were positioned at a referential distance of 3,162 m from the source of optical radiation, the unit for measuring reflections at a distance of 10 m and the headlight detector at a distance of 25 m. The individual detectors are positioned in a stationary manner. The optical centre of the headlight was determined before initiating the measurement process itself [4].

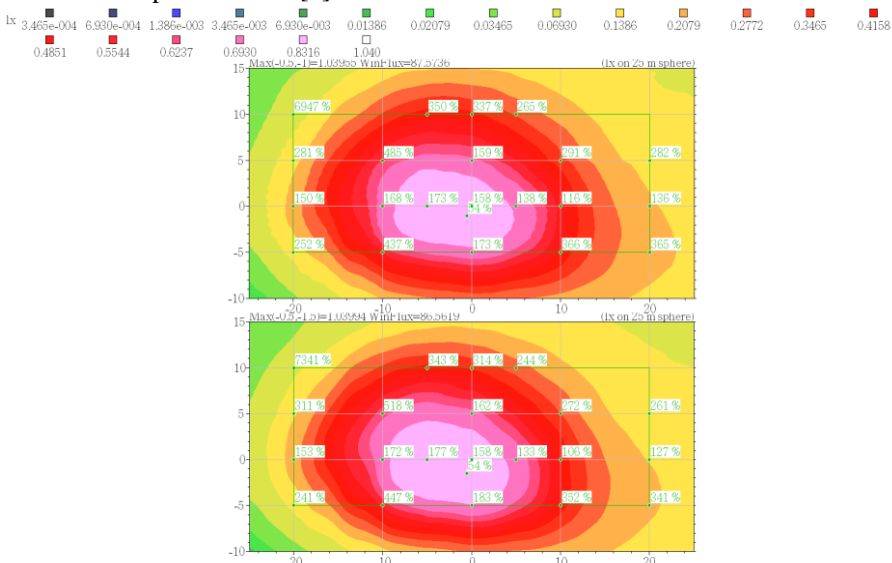


Fig. 6. Results of isocandel map and the protocol of intensities in the measurement points of the DRL.

Based on the resulting isocandel map and the protocol of intensities in the measurement points of the DRL headlight function, it is clear that the integrating of V2V optical communication by way of the advanced modulation format 64-QAM does not have a statistically significant impact on the photometric prediction, and therefore on the fulfilling of the ECE R 87 legal requirements. The evaluation of the DRL function fluctuates within the bounds of an acceptable variation, as defined by both the homologation institution and the headlight manufacturer, who adds a certain margin in the test points influenced production technology.

5 Conclusion

The goal of this article was to carry out an analysis on the feasibility of implementing a homologated headlight, intended for road traffic, in V2V communication as an opti-

cal transmitter in the transfer concept, with the use of advanced modulation formats. In our case, the headlight was that of an Jaguar XK, where the DRL function was used, with the original control electronics. Optical wireless communication achieved the maximum transfer speed of 7,8 Mbit/s, at a carrier frequency of 2 MHz and a modulation format of 64-QAM. The resultant analysis of the isocandel map and the protocol of intensities in the measurement points proves, that a headlight supplemented an active modulation system complies with the legislative regulation ECE R 87 pertaining to the function of DRL, and so the modified version of the headlight is eligible for implementation in road traffic.

6 References

1. TAKAI, Isamu, Tomohisa HARADA, Michinori ANDOH, Keita YASUTOMI, Keiichiro KAGAWA a Shoji KAWAHITO. Optical Vehicle-to-Vehicle Communication System Using LED Transmitter and Camera Receiver. IEEE Photonics Journal. 2014, vol. 6, issue 5, s. 1-14. DOI: 10.1109/jphot.2014.2352620.
2. M. S. Z. Sarker et al., "Design and implementation of a CMOS light pulse receiver cell array for spatial optical communications," Sensors, vol. 11, no. 2, pp. 2056–2076, Feb. 2011.
3. MINI-CIRCUITS. Coaxial Bias-Tee: ZX85-12G+. Brooklyn, NY. Dostupné z: <http://194.75.38.69/pdfs/ZX85-12G+.pdf>.
4. HAJDUK, Peter. *Study effect of LED modulation on photometric quantities and beam homogeneity from automotive lighting*. Ostrava, 2015. Master thesis. Vysoká škola báňská - Technická univerzita Ostrava - VŠB-TUO.

Classification of Different Turbulent Conditions for Propagation of Optical Laser Light Trough Laboratory Box

Lukas Hajek and Vladimir Vasinek

Department of Telecommunications, FEECS,
VŠB – Technical University of Ostrava, 17. listopadu 15,
708 33 Ostrava – Poruba, Czech Republic
{lukas.hajek, vladimir.vasinek}@vsb.cz

Abstract. The main aim of this article is a classification of turbulent environment in laboratory box for propagation of laser light. Current research of this problematic was focused on propagation of laser light through middle axis of laboratory box. Turbulent environment is created by use of mechanical fans blowing room air or hot air generated by heating devices. This paper is focused on study of turbulent environment by using ANSYS Fluent software for scaling the propagation path from maximum to minimum turbulent intensity. After finding of these boundary conditions the effect of turbulent flow on optical properties of propagated light is measured and evaluated.

Keywords: Flow, FSO, regression analysis, scintillation, simulation, turbulent intensity.

1 Introduction

Fiberless technology of information transmission using an optical signal known as a FSO (Free Space Optics) is very similar to the directional radio technology WiFi. Thanks to its advantages such as high data rate (up to $10 \text{ Gbit}\cdot\text{s}^{-1}$), safety of communication chain, unlicensed communication frequency band and range (about 5 km), this technology is very promised for the future. Already today it is advantageous to use FSO links wherever the buildup of fiber line is impossible or complicated.

As every technology, the FSO have some disadvantages. The one major is price and operation of FSO link. For the build of the optical channel between the transmitting and receiving station it is necessary to build line without any barriers because light waves in contrast to radio waves operate at wavelengths which are not able to pass through solid objects.

Another factor that plays role in the choice of the FSO link is the climatic conditions in the area. If the FSO link will be built in the area with big changes of atmosphere it is necessary to choose system with mechanism for elimination of turbulent effects. Because the turbulences can corrupt or totally interrupt data transmission. Turbulences in atmosphere have two characters of origin. They are formed on the

base of air flow at the boundary layer, when the flow changes direction thanks to structure of terrain, vegetation and buildings. Secondly, turbulences development is based on the changes of temperature gradient and they are formed when the hot air rise to the higher area of troposphere where mix with cold air. These turbulences zones are also called turbulence cells and affect beam by several ways, scintillation of optical beam on the detector or also receiving aperture of optical connection. The scintillation causes increase of the BER (Bit Error Ratio) of receiving data and it can lead to disturbing of information or to losing of connection.

The question is how to predict the atmosphere behavior or how to make the system which will be able to simulate this behavior. This system could be used for testing FSO resistance in the area.

Earlier and continuing works [6], [8], which dealt with the question of the using the ANSYS Fluent 15 simulating software in this area shown that it is possible to use this software for modeling turbulent flow without and with transmission of heat with certain accuracy. In other articles the simulation was made in area of ANSYS fluent to describe turbulence conditions in the testing device. For example, the article dealt with effect of turbulence behavior on the light polarizing functionality [2].

Similarly to previous work, there is also examined character of turbulent flow in the closed box. The difference is that the scintillation of voltage on the photo-detector of receiver is measured in this work and these results are compared with maximal values of turbulent intensity inside the box. On the basis of regress dependence between turbulence intensity and scintillation of voltage the characters of transfer are derived to transport between turbulent intensity and scintillation of voltage.

2 Measuring of optical scintillation

For measuring of optical intensity scintillation the workplace was constructed based on the figure 1:

- 1., 2., 3. represents input high-speed ventilator SUNON PMD1212PMB1-A,
- 4., 5., 6. represents output high-speed ventilator SUNON PMD1212PMB1-A,
- 7. high-speed photodetector Thorlabs PDA 10A-EC (200-1100 nm),
- 8. cylindrical Helium Neon laser (He-Ne). Melles Griot-25-LHP-151-230 (Class 3B laser, 15 mW, 633 nm, TEM₀₀),
- 9. oscilloscope Lecroy – 204 Xi.

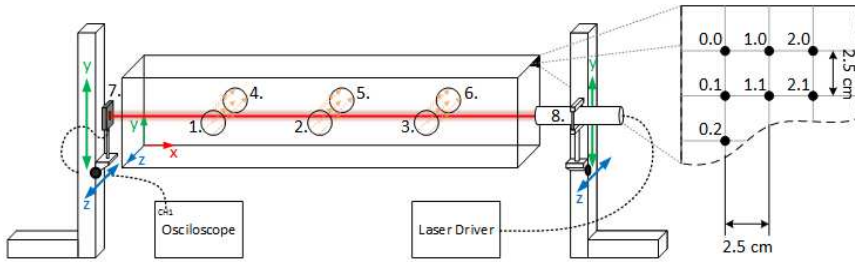


Fig. 1. Optical scintillation measurement using h high-speed photodetector.

Turbulences conditions in the optical box were formed using series of input and output ventilators. These ventilators were installed around 3 openings along the laser trajectory. Ahead of input of each ventilator the heating device was placed, which procured sucking heat air into the box which increases the influence of turbulences on the optical beam. The output ventilator is used to suck air from the box.

The temperature on input was during the measurement controlled using thermistor sensors. Each opening was set with 4 sensors whose values were averaged and then were used as output values of border conditions in the simulation.

The process of measuring is shown on the figure 1. in the side part. Thanks to manual mechanical shifts the detector and laser move on the axis y and axis z with the same step on the frontal surface of the laboratory box. The individual points formed matrix of points which were 2.5 cm far apart on both axis. Totally there were measured 324 points.

With high-speed detector the change (scintillation) of optical intensity transfer to voltage was examined on the oscilloscope. Specifically the mean value of standard deviation of voltage change on detector was measured. The mean value was calculated from 1000 samples from measurement this quantity.

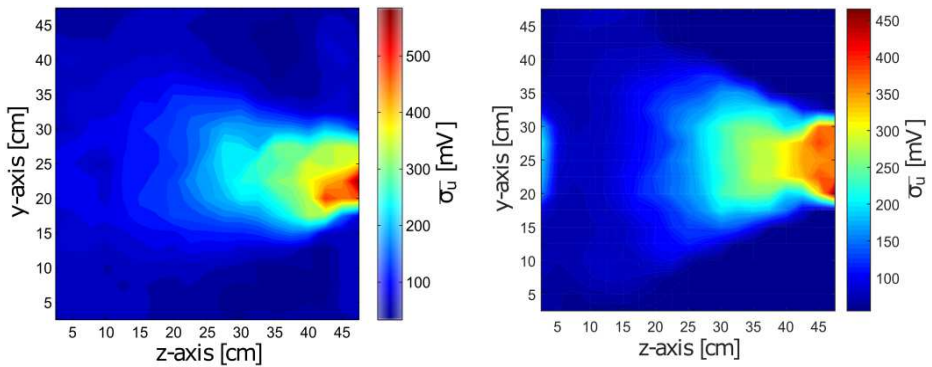
3 Comparison of results and CFD numerical simulation

Table 1. Comparison of regression and polynomial models.

Regression type	R-squared [%]		
	k-ε Standard	k-ε Realizable	k-ε RNG
Linear	67.503	42.074	49.579
Square root	70.665	50.413	58.813
Exponential	69.935	56.275	65.396
2 nd order	67.691	54.283	70.874
3 rd order	76.406	54.709	71.163
4 th order	76.917	54.912	71.889
5 th order	77.897	55.025	73.021

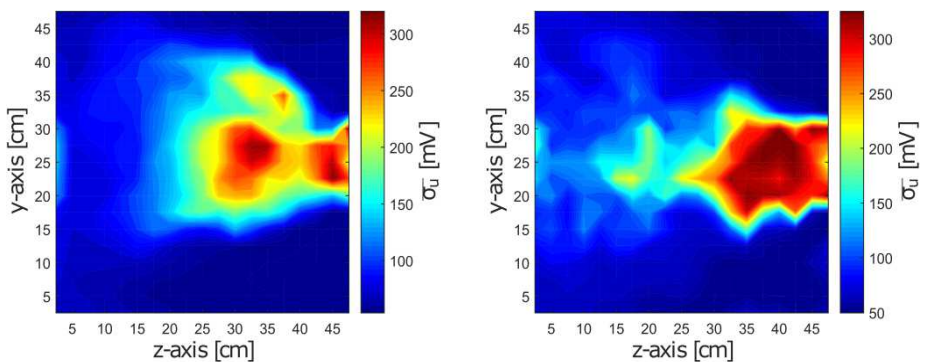
Now the question is how to evaluate two completely different parameters and find the relationship between simulation and real measurement. Possible answer could be finding conversion characteristics using regression analysis.

In Table 1. there are given individual results of regression analysis (linear, exponential and square root regression) of each model. The highest accuracy was attained for k- ϵ Standard using Square root regression and so it is possible describe up to 70.665 % of the measured data. Much higher accuracy has been achieved by fitting the data by polynomial of n^{th} degree. With increasing level of polynomial the accuracy increases. Approximately from 5th order the accuracy changed on the position of hundredths, so we chose 5th order of polynomial regression.



a) Result from measurement of voltage scintillation across laboratory box.

b) Conversion of results for k- ϵ Standard model according to 5th order polynomial regression.



c) Conversion of results for k- ϵ Realizable model according to exponential regression.

d) Conversion of results for k- ϵ RNG model according to 5th order polynomial regression.

Fig. 2. Color maps for real measurement and simulations.

The model k-ε Standard gained the best match again, after spacing by polynomial of 5th order this model describes up to 77.897 % of measured values. With this finding the conversion for each model was made. The conversion is based on final equations of exponential or polynomial regression models.

The following mathematical equation (eq. 1) corresponds to the conversion of turbulent intensity I to mean values of voltage scintillation for the model k-ε Standard by the polynomial of the 5th order:

$$\bar{\sigma}_u = 34.5484 + 2.22632 \cdot I - 0.0812137 \cdot I^2 + 0.001204 \cdot I^3 - 0.000005897 \cdot I^4 + 9.2868E - 9 \cdot I^5 \tag{1}$$

The equation 2. expresses final form set by exponential regression for model k-ε Realizable:

$$\bar{\sigma}_u = \exp (3.45433 + 0.0153505 \cdot I) \tag{2}$$

The accuracy of this regression was lower 56.275 %. The last equation 3. was obtained by spacing data by polynomial of the 5th level and it is able to describe the development of data from 73.021 %:

$$\bar{\sigma}_u = 12223.96 - 158.208 \cdot I + 8.13519 \cdot I^2 - 0.19903 \cdot I^3 - 0.0023194 \cdot I^4 - 0.00001020 \cdot I^5 \tag{3}$$

The following graphs 3. and 4. show the character of the voltage scintillation in cuts through the middle of the measured plane perpendicular to the y-axis and z-axis. From these graphs we can see that model k-ε Standard very realistically reproduces the measured data in both axes.

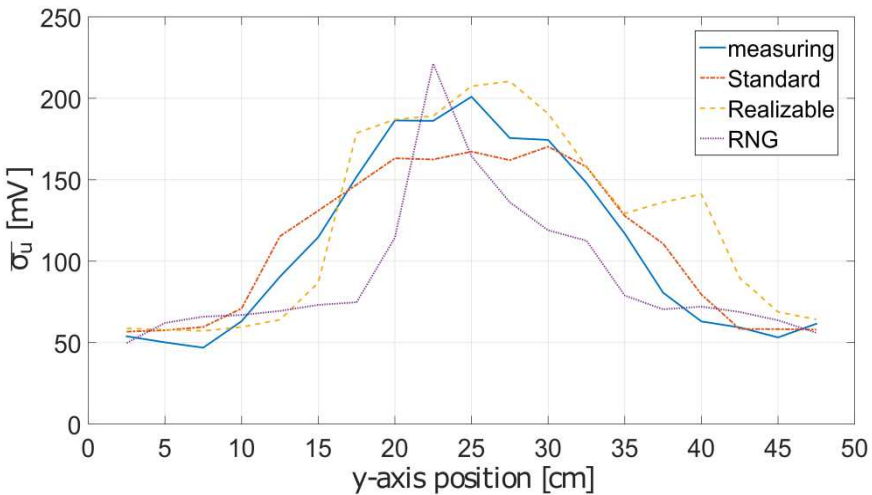


Fig. 3. Comparison of the measured values of the voltage scintillation to the calculated values in the middle of the box in a direction perpendicular to the z-axis for simulation and measured data.

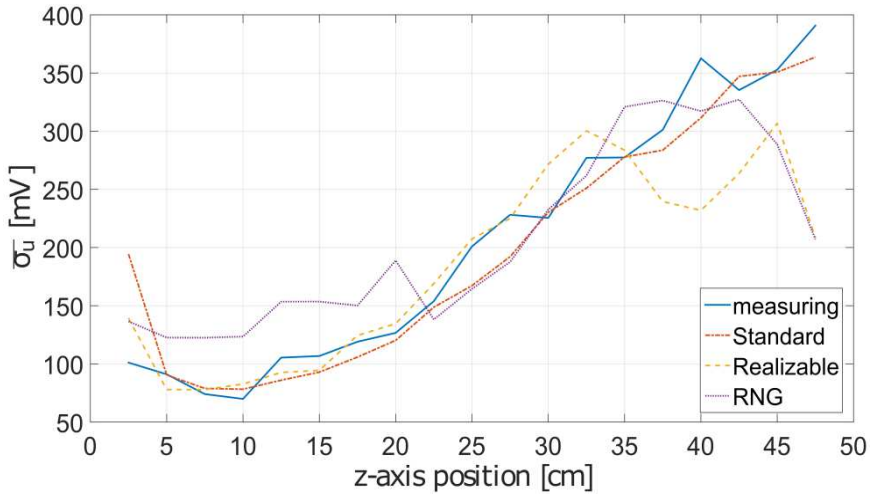


Fig. 4. Comparison of the measured values of the voltage scintillation to the calculated values in the middle of the box in a direction perpendicular to the y-axis for simulation and measured data.

The model k- ϵ Realizable corresponds well with the measured values in the direction perpendicular to the z-axis and y-axis but from 35 cm it noticeably deviates in both cases. The model k- ϵ RNG appears graphically as the worst for selected position of measurement. Especially in a direction perpendicular to the z-axis has a large differences in the increase/decrease of voltage scintillation.

4 Conclusion

The article which was aimed at qualifying turbulent intensity in the laboratory box was the first of this type of research. Based on measurements of voltage scintillation on the photodetector and simulation of turbulent intensity by using ANSYS Fluent 15 the area with maximal influence of turbulence in the box was found. The results of comparison are transfer characteristics of individual turbulent models which showed the best ability to describe the measured volume of data. The best results have been obtained for model k- ϵ Standard using of the 5th order polynomial regression function. This mathematical model is able to describe up to 77.897 % of data. Work in this area will be continue to refine the simulation models and will be measured with another arrangements of turbulent sources and the related change in the turbulent flow inside the laboratory box.

5 Acknowledgements

The research described in this article was undertaken thanks to the active support of the Ministry of Education, Youth and Sports of the Czech Republic through grant project no. CZ.1.07/2.3.00/20.0217 within the frame of the operation programme Education for competitiveness financed by the European Structural Funds and from the state budget of the Czech Republic. This article was also supported by project Technology Agency of the Czech Republic TA03020439 and TA04021263. The research has been partially supported by the projects no. SP2015/130, SP2015/182 and VI20152020008.

6 References

1. KOZUBKOVA, M. *Modeling of liquid flow: FLUENT, CFX*. Ostrava: VŠB - Technical University of Ostrava, 2008, vol. 1, pp. 153.
2. BLEJCHAR, T. *Turbulences–Flow modeling–CFX*. 1. vyd. Ostrava: VŠB - Technical University of Ostrava, 2010, vol. 1, pp. 262, ISBN 978-80-248-2606-6.
3. KOZUBKOVA, M. and S. DRABKOVA. *Numerical modeling of flow: FLUENT I*. Ostrava: VŠB - Technical University of Ostrava, 2003, vol. 1, pp. 115. ISBN 80-248-0525-1.
4. SAS IP, Inc. *ANSYS FLUENT: Theory Guide. Release 14.0*. Canonsburg, November 2011. Available: http://cdlab2.fluid.tuwien.ac.at/LEHRE/TURB/Fluent.Inc/v140/flu_th.pdf
5. *Optical wireless communications*. Editor Eric J Korevaar. Boston: SPIE, c1999, xiv, 128 s. ISBN 08-194-2993-7.
6. HAJEK, L., J. LATAL, M. BOJKO, R. POBORIL, P. KOUDELKA, J. VITASEK, P. SISKA, V. VASINEK. Modelling of airflow in a closed simulation box with regard to atmospheric optical link. *8th International Conference on Experimental Fluid Mechanics*. 2014, vol. 67. ISBN: 978-802605375-0. DOI: 10.1051/epjconf/20146702032.
7. LATAL, J., J. VITASEK, L. HAJEK, P. KOUDELKA, P. SISKA et al. Measurement of turbulences influence on the laser beam polarization state, *Proc. SPIE 9659, International Conference on Photonics Solutions*. doi:10.1117/12.2196261;
8. LATAL, J., M. BOJKO, J. VITASEK, P. KOUDELKA, P. SISKA, A. LINER, M. PAPES and V. VASINEK. Influence of thermal turbulences on the optical beam of atmospheric optical link. In: *36th International Conference on Telecommunications and Signal Processing (TSP)*. Roma: IEEE, 2013, pp. 138-143. ISBN: 978-1-4799-0402-0 DOI: 10.1109/TSP.2013.6613907.
9. VITASEK, J., J. LATAL, S. HEJDUK, J. BOCHEZA and P. KOUDELKA. Atmospheric turbulences in Free Space Optics channel. 2011, 34th International Conference on Telecommunications and Signal Processing, TSP 2011 - Proceedings , art. no. 6043763, 104-10. ISBN 978-145771411-5.

Utilization of Optical Fibers in Building Structures

David Hrubý

Department of Telecommunications, FEECS,
VŠB – Technical University of Ostrava, 17. listopadu 15,
708 33 Ostrava – Poruba, Czech Republic
david.hruby@vsb.cz

Abstract. This article describes my activities in third year at the Faculty of Electrical Engineering and Computer Science. It description measurement of insulation layers, publication activities, work on projects and next activity for department of Telecommunications.

1 Measurement of insulation layers

Optical fiber is in the case of using DTS understood as a distributed fiber sensor. Fiber optic DTS system is increasingly gaining ground in industrial use due to the properties of optical fibers and their low cost. One of the possible use of DTS is sensing the temperature profile of the different building insulating layers. Rock wool insulation is produced at high temperatures by defibering basalt or gabbro in a furnace and by forming these fibers into the mats or plates. Each insulating layer is usually measured using temperature probes. These probes allowed temperature measurement only in the place of their location makes it difficult to simply measure the temperature profile of the entire layer. DTS system solves the problem with multiple temperature sensing probes with separate terminals as one optical fiber can serve as many sensors across whole sensing area.

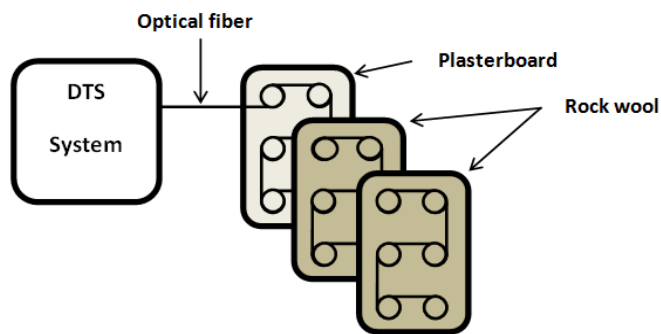


Fig. 1. Schematic diagram

It was necessary to prepare the sensory fiber-optic fields before the measurements of temperature changes among building insulating materials. In total, three fields with

dimensions of 2670 x 690 mm were made. Each sensory field contained 27 sensory rings that were placed in 9 rows and 3 columns. Spacing between the rings were 400 mm and each ring contained 3 m of fiber to ensure the accuracy of the measurement. DTS system with 50 m long G.651 launching fiber was connected to sensory field (Figure.1). All layers were covered a waterproof membrane (Figure.2).



Fig. 2. Placement of the third sensory layer and waterproof membrane

The overall progress of the measurement is shown in Figure 3. Values were read at 5 minute iterations for 37 hours. The whole measurements were performed in an air conditioned room. All measured values were processed and plotted using a script created in Matlab.

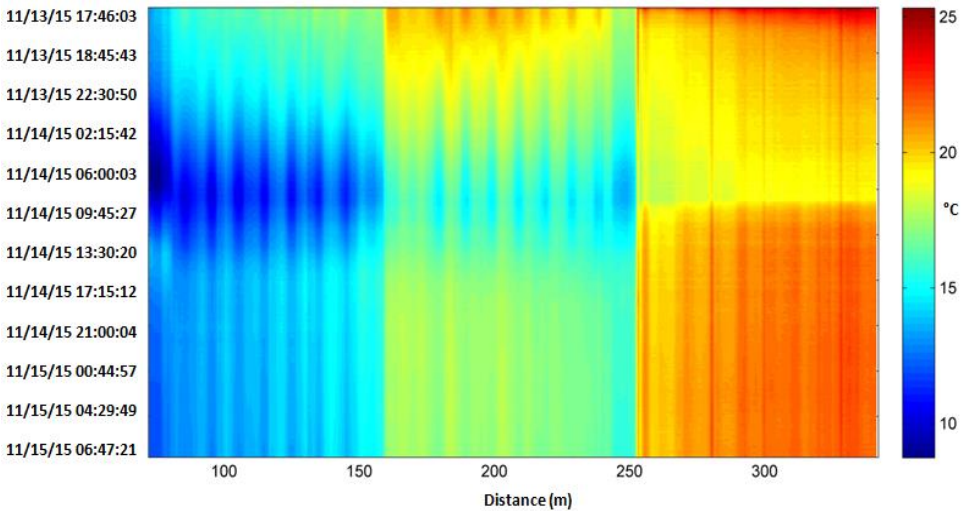


Fig. 3. The overall development of the temperature at the time in the measurement location

The overall graph (Fig. 3) shows the layout of the individual layers and the temperature distribution in these insulating layers. First sensory layer is located in the distance from 72 to 159 m, the second layer is in the range from 160 to 248 m, and the third layer is from 254 to 342 meters. The aim of this experimental measurement was to determine whether it is possible to measure the transmission of heat through the insulating layers formed by rock wool using fiber-optic DTS system. Measurements showed us that the DTS system is capable of such measurements. Furthermore, with the use of optical fiber as the sensor the whole surface among the insulation layers can be covered. The largest drop in temperature occurred approximately between 6:00 and 10:00 on November 14 the outside temperature was -2.9°C . Temperature of 8.7°C , 13.5°C and 17.2°C was measured at first, second and third sensory layer. Room temperature was 17.7°C . The temperature difference between the first and third sensory layer was around 8.5°C .

2 Publications during academic year

2.1 Concrete deflection measurement using fiber optic distributed strain system

Undesirable or excessive deformations of materials are phenomena which are unacceptable in construction, especially in supporting structures. These issues are currently monitored by electromechanical sensor in most cases. It is a classic technique when the sensor measures the material stress at the point of its installation. This paper deals with the concrete deflection measurement using fiber optic distributed strain system. This system uses optical fiber as a sensor and operates at the principle of measurement of Brillouin frequencies.

2.2 Temperature measurement inside metallic cable using distributed temperature system

In our work, we present the temperature distribution measurement inside the metallic cables using distributed temperature system. Within the cooperation with manufacturer of the metallic cables, optical fibers were implemented into these cables. The cables are double coated and the fibers are allocated between these coatings and also in the center of the cable. Thus we are able to measure the temperature inside the cable and also on the surface temperature along the whole cable length with spatial resolution 1 m during the cable heating.

3 Cooperation on projects

As part of my studies, I was actively involved in solving four projects, namely:

1. TA ČR - Intelligent modules for lighting and communication
2. TA ČR - Safety of optical transport networks and the development of opt. parts for electric power and electrical appliances
3. Studenstká grantová soutěž SP2016/149
4. Project PROSEED TG0101013
5. Project GUARDSENSE

4 Other activities for the department

In the winter semester, I was actively involved in ensure the teaching with the subject ZEL (Groundwork Electronics). In the summer semester, I taught courses TS (Telecommunication Networks). My Other activities were stocktaking on building N, CPIT and FEI and and on revisions of electrical devices for building FEI.

5 References

1. Papes, M., A. Liner, P. Koudelka, P. Siska, J. Cubik, S. Kepak, J. Jaros, V. Vasinek, F. Baldini, J. Homola and R. A. Lieberman, "*Detection and localization of building insulation faults using optical-fiber DTS system*," The International Society for Optical Engineering 8774, (2013)
2. LONG, D. *The Raman effect: a unified treatment of the theory of Raman scattering by molecules*. New York: Wiley, c2002, xxiv, 597 p. ISBN 0471490288-
3. BALL, David W. *Theory of Raman Spectroscopy*. *Spectroscopy* [online]. 2001, roč. 11, č. 16, 28 - 30 [cit. 2013-05-04]. ISSN 0887-6703. Available at: <http://www.spectroscopyonline.com/spectroscopy/data/articlestandard//spectroscopy/452001/1017/article.pdf>
4. KOUDELKA, P., J. LÁTAL, J. VITÁSEK, P. ŠIŠKA, J. HURTA, A. LÍNER a M. PÁPEŠ. *Implementation of Optical Meanders of the Optical-Fiber DTS System Based on Raman Stimulated Scattering into the Building Processes* [online]. 2012 [cit. 2013-05-01]. ISSN 1804-3119. Available at: <http://advances.utc.sk/index.php/AEEE/article/view/643>

Study of the Colour Correlated Temperature in PDMS Fiber Depending on the Concentration of the Luminophore and on the Distance from the Face of the Fiber

Jan Jargus

Department of Telecommunications, FEECS,
VŠB – Technical University of Ostrava, 17. listopadu 15,
708 33 Ostrava – Poruba, Czech Republic
jan.jargus.st@vsb.cz

Abstract. Silicone materials have many of excellent physical and chemical properties due to which find application in many industries. When we mix polydimethylsiloxane (PDMS) and luminophore, we get new material with other interesting properties. Last year, our team started to deal with this issue. This article is focused on the description of the initial measurements of the mixture PDMS and luminophore performed at our department.

1 Introduction

The silicone materials have use for various industrial applications. The main applications include production of solar panels, the production of LEDs, electronics, heat dissipation, automotive, aviation, cosmonautics, etc [1]. But our attention is focused on exploring the properties of a mixture of PDMS and luminophore. There are many kinds of luminophores and polydimethylsiloxanes, and we have begun to investigate the properties of a mixture of PDMS Sylgard 184 and luminophore with tradename U2, which is a cerium activated yttrium aluminum garnet $Y_3Al_5O_{12}:Ce$. We were interested in whether we can get from our mix with blue excitation LED white light with a desired colour correlated temperature. The first part of the article is focused on familiarization with the theme of colour correlated temperature (CCT). The equipment for measuring is shown in the next chapter and then experimental measurements are presented. Finally, the results of measurements of CCT mixture of PDMS and luminophore are summarized.

2 Colour correlated temperature

Light colour is a property of light evoking a visual perception, which is given spectral composition of light [2]. Colour correlated temperature (CCT) determines the colour of the light corresponding to the colour of a black body for a given temperature. In Figure 1 we can see the colour chart, wherein the black line in the middle diagram

determines the colour of a black body, depending on its temperature. In this diagram, T_C denotes CCT. White light is considered in a range of colour temperatures from about 2700K to 6500K.

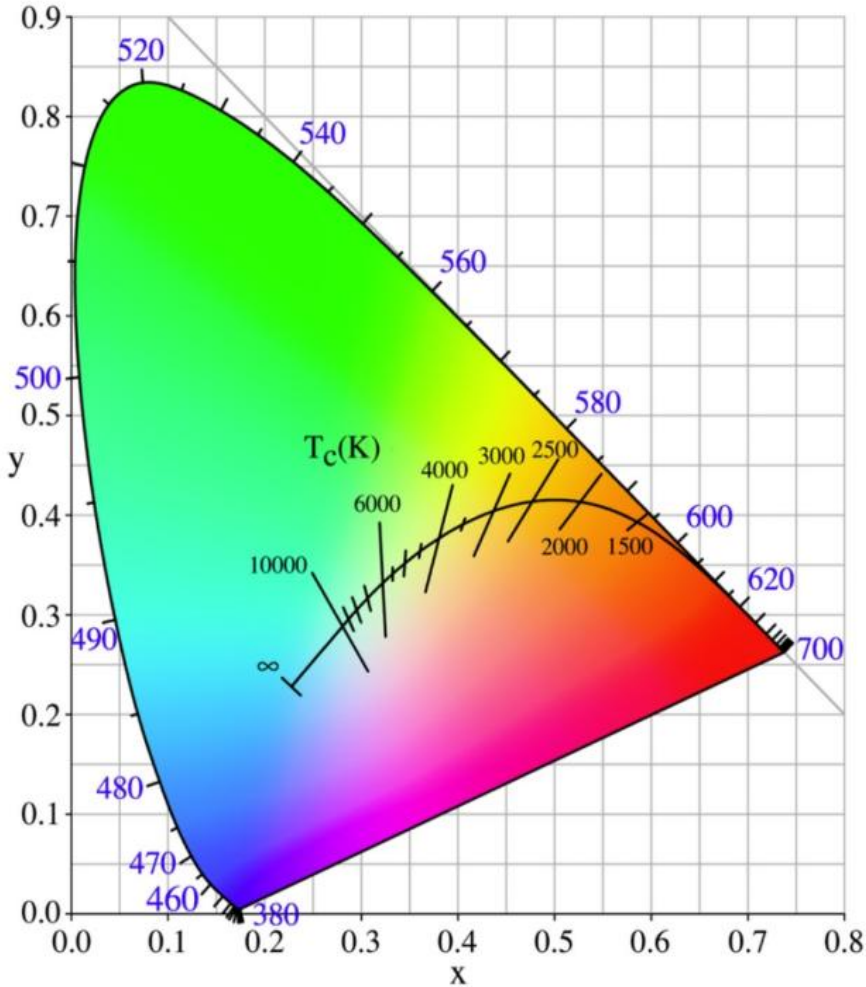


Figure 1. Colour chart of the colour correlated temperature

3 The equipment for measuring

Sylgard 184 was used, which was blended in a ratio of 1:10 with reagent. The mixture was stirred manually about 30 seconds and then 5 minutes on a shaker Vortex Genius 3 on speed 1. Then the mixture was placed in a refrigerator at 120min with temperature 280.5K to remove bubbles. Then the mixture was added by luminophore

Yttrium Aluminium Oxide: Cerium and four test-tubes samples with fixed ratios were created, as we can see in table 1.

Table 1. The values of the samples and the concentration of the luminophore

Sample	Diameter [mm]	PDMS [g]	Luminophore [g]	Ratio
1	14	10.005	0.100	1:100
2	14	10.002	0.050	1:200
3	14	10.007	0.033	1:300
4	14	10.008	0.025	1:400

Weight of luminophore have been weighing on the scale model TScale NHB-150 +. The mixture was subsequently 5h stirring and shaking on a rotary shaker and with a speed of 1 revolution for 4 min and with a longitudinal shaking of 5 cycles per second. For each sample was then measured dependence of the colour correlated temperature on the distance from the face of the PDMS fiber doped luminophore. While at the same time they were measured spectral characteristics. Scheme measurement is shown in Figure 2.

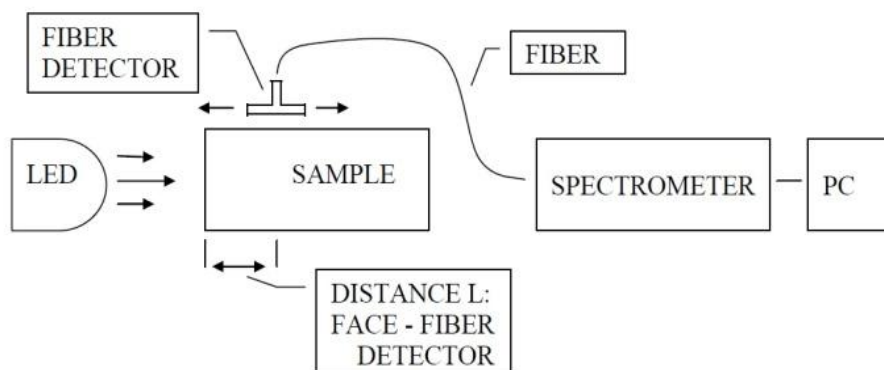


Figure 2. Measurement scheme

In the measuring assembly was used blue LED from company SQS with a maximum emission at a wavelength of 455nm, which was powered by a regulated voltage source STATRON - TYP 2229 with power voltage 12V. The spectrum and the colour correlated temperature of the samples was measured using a spectrometer Ocean Optics USB 4000. At the following figures, we can see some details of the measuring assembly.

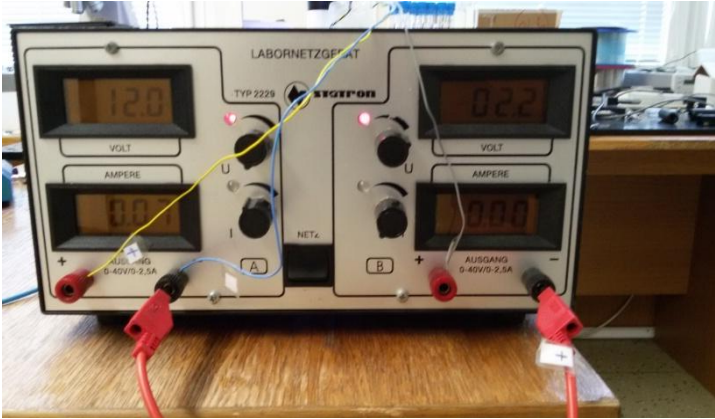


Figure 3. The regulated voltage source STATRON - TYP 2229

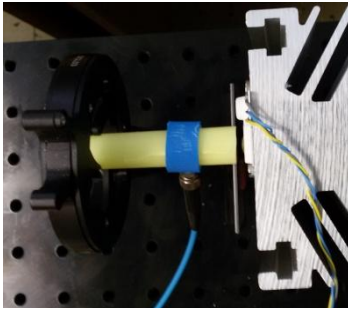


Figure 4. Measuring assembly with disabled power supply

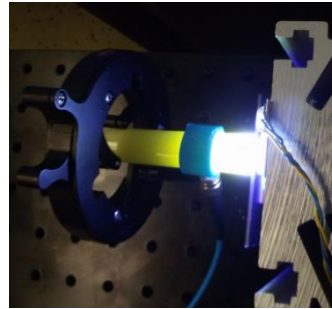


Figure 5. Measuring assembly with enabled power supply

4 The experimental measuring

Due to the structure of the measuring assembly, the measurements were carried out at a distance in range 7-17 mm from the face of the fiber in increments of 2 mm. Measurement results for the samples are in the following tables.

Table 2. The colour correlated temperature of the sample 1 for the distance L.

L [mm]	CCT [K]	L [mm]	CCT [K]
7	5296	13	4405
9	4855	15	4327
11	4582	17	4254

Table 3. The colour correlated temperature of the sample 2 for the distance L

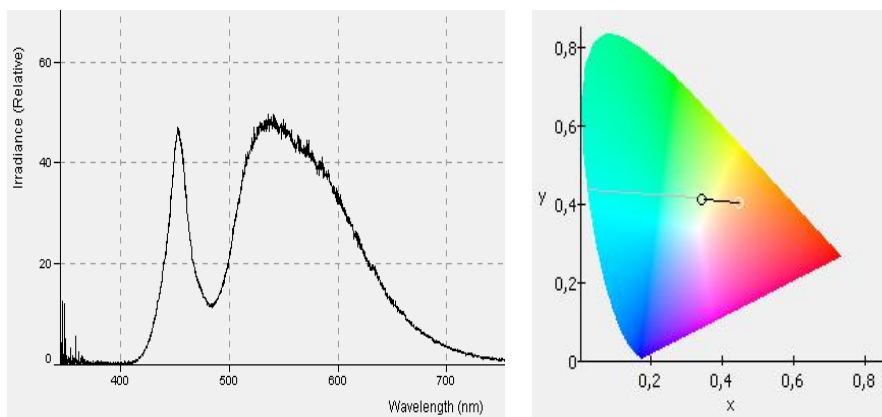
L [mm]	CCT [K]	L [mm]	CCT [K]
7	7019	13	4870
9	5773	15	4727
11	5071	17	4582

Table 4. The colour correlated temperature of the sample 3 for the distance L

L [mm]	CCT [K]	L [mm]	CCT [K]
7	undefined	13	106557
9	undefined	15	23258
11	undefined	17	16758

Table 5. The colour correlated temperature of the sample 4 for the distance L

L [mm]	CCT [K]	L [mm]	CCT [K]
7	undefined	13	undefined
9	undefined	15	undefined
11	undefined	17	undefined

**Figure 6.** The spectrum and the chromatic diagram for the sample 1 and L = 7 mm

5 Conclusion

This article dealt with the colour correlated temperature of the mixture of the PDMS and luminophor primarily. Importance use of silicone materials was mentioned in the beginning. Then theme of the colour correlated temperature was outlined. The description of the equipment for measuring and the preparing of the samples followed further. The results of measurements are content of the next chapter.

From the results obtained in tables 2-5 we can draw some conclusions. At first, we can see, that the samples with higher concentration of luminophor in PDMS have lower CCT. At second, CCT value depends on the distance L for each sample. And at third, while L increases, CCT value decreases. Good results CCT were obtained mainly for samples 1 and 2 in this arrangement of the measuring assembly.

However, research in this area will continue, because we want to measure not only the monolithic samples but also layered samples with other optical properties.

The research described in this article could be carried out thanks to the active support of the Ministry of Education of the Czech Republic within the projects no. SP2015/130, SP2015/182. This article was supported by projects Technology Agency of the Czech Republic TA03020439 and TA04021263. The research has been partially supported by the Ministry of Education, Youth and Sports of the Czech Republic through grant project no. CZ.1.07/2.3.00/20.0217 within the frame of the operation programme "Education for Competitiveness" financed by the European Structural Funds and from the state budget of the Czech Republic.

References

1. NORRIS, A., J. DEGROOT, F. NISHIDA, U. PERNISZ, N. KUSHIBIKI a T. OGAWA. Silicone Materials for Optical Applications. *DOW Corning* [online]. 2003 [cit. 2015-08-07]. Dostupné z: http://www.dowcorning.com.cn/zh_CN/content/publishedlit/75-1007-01_single.pdf
2. VRBOVÁ, M. a kol.: *Lasery a moderní optika*. Prometheus, 1. vydání, 1994, ISBN 80-85849-56-9

Study of the Incidence of External Influences on Optical Fiber Connectors

Tomáš Kajnar

Department of Telecommunications, FEECS,
VŠB – Technical University of Ostrava, 17. listopadu 15,
708 33 Ostrava – Poruba, Czech Republic
tomas.kajnar@vsb.cz

Abstract. This article describes my incidence of my third year at the Faculty of Electrical Engineering and Computer Science. It description my dissertation work, work on projects, publication activities and next activity for department of Telecommunications.

Keywords: optical connector, insert loss, return loss

1 Dissertation work

The head of my dissertation is prof. RNDr. Vladimír Vašínek, CSc. My work deal with the influence of external factors on various types optical connections. Has work tie follows on diploma work. The work deals with the long-term effects of temperature, humidity, water and other influences on optical connections. The most important parameters for monitoring the insertion loss and return loss, which arises mainly on optical connectors and mechanical couplings. Particular scheme measurement is shown Figure 1. and 2.

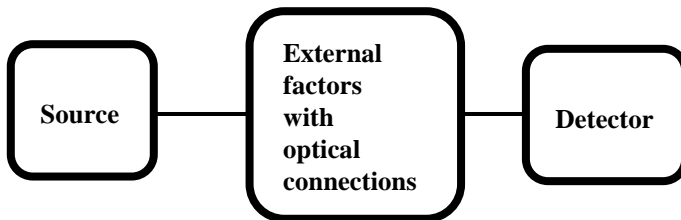


Fig. 1. The wiring diagram for the measurement of insertion loss

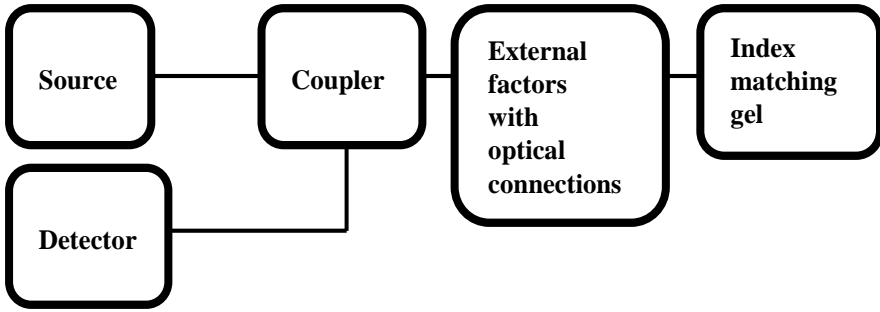


Fig. 2. The wiring diagram for the measurement of return loss

At measuring short - term temperature influence on optical fibre connector type SC, FC and E2000 with ferrule PC and APC was ascertained, that the return loss is dependent on the temperature and his dependence is for every type connector other and so, that the don't agree with parameters specified by the manufacturer. Changes loss is also dependent on the wavelength. Measurement was carried out at the wavelengths for single mode fiber at 1310 nm and 1550 nm. Evaluation was carried out followed by regression analysis and analysis of variance, as shown in Figure 3. and 4.

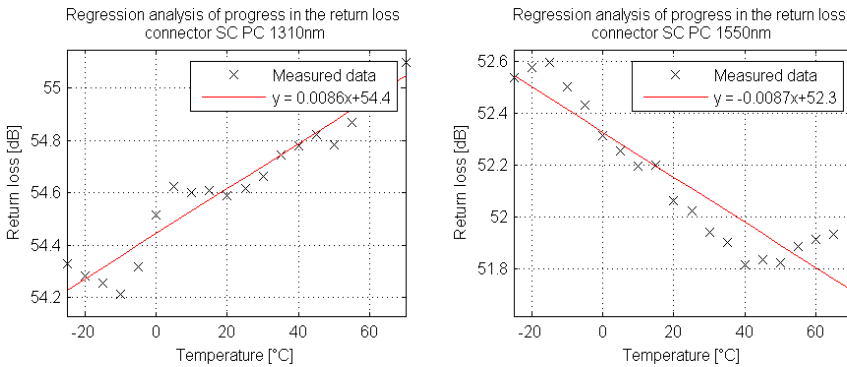


Fig. 3. The regression line for SC connector

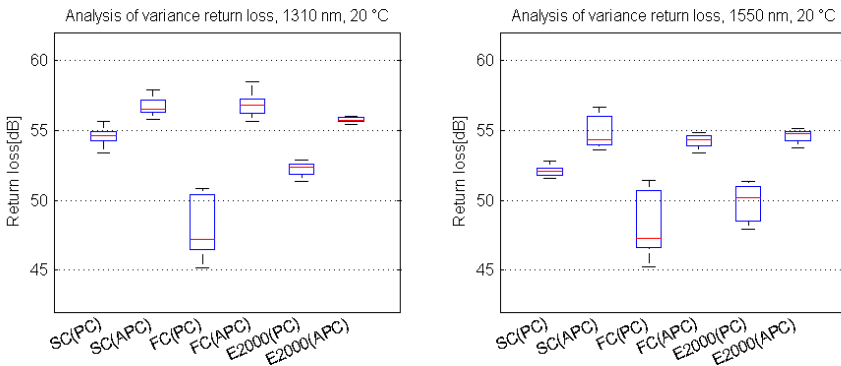


Fig. 4. Analysis of Variance of the measured data

Measuring the distilled water were carried out according to standard EN 61300-2-45. Duration of action of the water was 168 hours at 25 ° C. For measurements were used optical connectors SC, FC ferrule with a PC and APC, E2000 with APC and LC ferrule with ferrule PC, mechanical and optical coupling welds. Measurement of insertion loss was always carried out after 168 hours, when the joints are still in the water. They were then withdrawn and allowed to dry at 25 ° C for 24 hours. He was then again measured insertion loss. The average values of these measurements are recorded in Table 1. There were also observed front ferrule shown in Figure 5. In the form a thin film after drying the water, which leads to scattering of light and deterioration of attenuation.

Table 1. Change in Insertion Loss

	Reference		In the water		After drying	
SC (PC)	0,13	0,18	0,33	0,26	0,35	0,26
SC (APC)	0,35	0,36	1,33	1,12	1,38	1,13
FC (PC)	0,5	0,48	0,48	0,44	0,49	0,41
FC (APC)	0,81	0,65	0,6	0,64	0,7	0,69
LC (PC)	0,61	0,47	0,77	0,62	0,77	0,58
E2000 (APC)	0,62	0,48	0,4	0,42	0,41	0,34
Mechanical	0,43	0,31	1,22	1,21	1,7	1,58
Weld	0,42	0,4	0,87	0,74	0,42	0,33

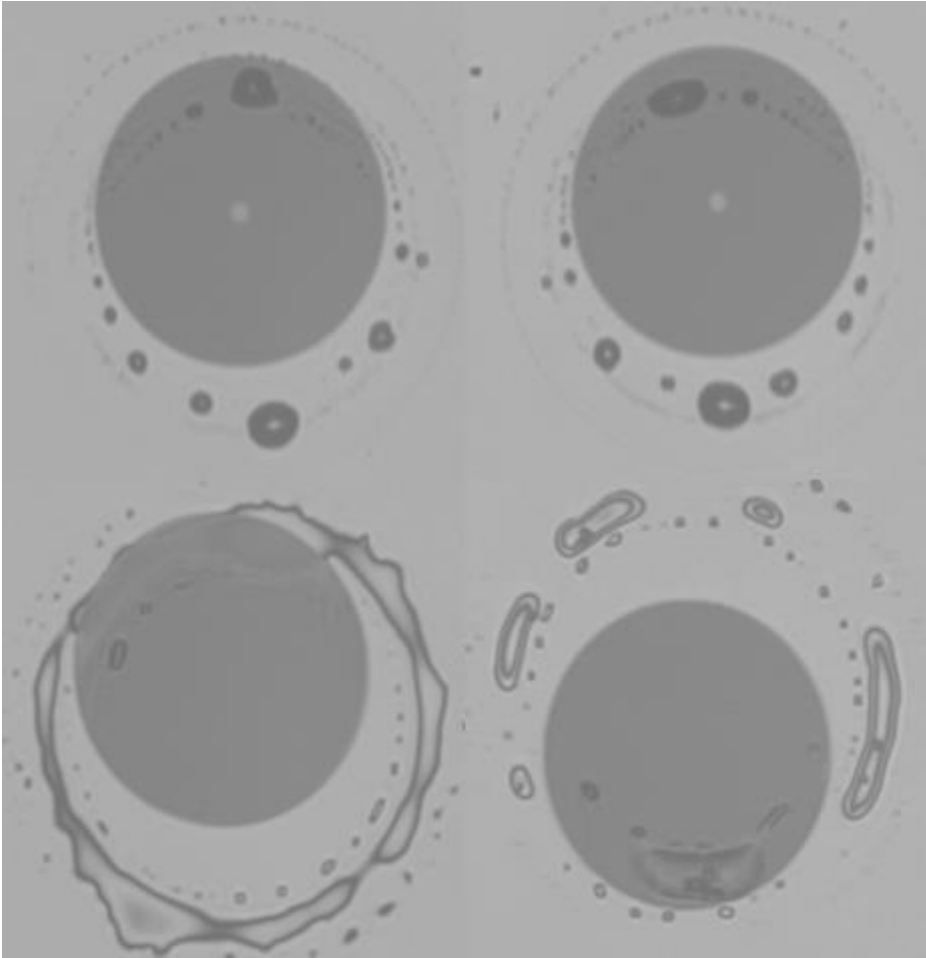


Fig. 5. The faces of the ferrule after drying

2 Publications during academic year

2.1 Measurement of the temperature distribution inside the power cable using distributed temperature system

The paper deal with temperature measurement by the help of DTS system rising on power cable at transit electric field.

3 Cooperation on projects

As part of my studies, I was actively involved in solving four projects, namely:

1. TA ČR - Intelligent modules for lighting and communication
2. TA ČR - Safety of optical transport networks and the development of opt. parts for electric power and electrical appliances
3. Studeňská grantová soutěž SP2016/149
4. Project GUARDSENSE

Below these projects belongs to cooperation in the design, build and measuring with next members, such as:

- Preparation of fiber for measuring ageing in Řež

Preparation of fiber and welding optical fiber pigtail on fiber for measuring influence radiation on aging fibers in nuclear research institute in Řež.
- Preparation of fiber and measuring ageing fiber influence to external conditions on the roof building N

Preparation of the fibers, their installation and measurement of various parameters affecting aging fibers by external influences
- Measuring mechanical and acoustic vibration in the tram tracks

Installation, supervision and measuring mechanical and acoustic vibration generated when passing tram.

4 Other activities for the department

In the winter semester, I was actively involved in ensure the teaching with the subject PSaM (Communication Systems and Media). In the summer semester, I taught courses TS (Telecommunication Networks). Further I'm involve on stocktaking on building N, CPIT and FEI and and on revisions of electrical devices for building FEI.

References

- [1] KAJNAR, Tomáš. Studium působení vnějších vlivů na optické konektory. Ostrava, 2013. pp. 53. Available at: https://dspace.vsb.cz/bitstream/handle/10084/98613/KAJ050_FEI_N2647_2601T013_2013.pdf?sequence=1. Diploma thesis. VSB-Technical university of Ostrava.
- [2] KIHARA, M., S. NAGASAWA a T. TANIFUJI. Return loss characteristics of optical fiber connectors. *Journal of Lightwave Technology*. 1996, vol. 14, iss. 9, pp. 1986-1991. DOI: 10.1109/50.536966.
- [3] KIHARA, M., S. NAGASAWA a T. TANIFUJI. Temperature dependence of return loss for optical fiber connectors with refractive index-matching material. *IEEE Photonics Technology Letters*. 1995, vol. 7, iss. 7, pp. 795-797. DOI: 10.1109/68.393209.

- [4] KIHARA, M., S. TOMITA a T. HAIBARA. Influence of Wavelength and Temperature Changes on Optical Performance of Fiber Joints With Small Gap. *IEEE Photonics Technology Letters*. 2006, vol. 18, iss. 20, pp. 2120-2122. DOI: 10.1109/LPT.2006.883256
- [5] RAO, R. a J.S. COOK. Erratum: High return loss connector design without using fibre contact or index matching. *Electronics Letters*. 1986, vol. 22, iss. 23, s. 1272-. DOI: 10.1049/el:19860872.
- [6] POBORIL, R., LATAL, J., KOUDELKA, P., VITASEK, J., SISKÁ, P., SKAPA, J., VASINEK, V., "A Concept of a Hybrid WDM/TDM Topology Using the Fabry-Perot Laser in the Optiwave Simulation Environment," *Advances in Electrical and Electronic Engineering*, vol. 9, iss. 4, pp. 167-178, 2011, ISSN 1804-3119.

Nondestructive Fiber-optical System for Measurement of Speed in Road Traffic

Jan Nedoma

Department of Telecommunications, FEECS,
VŠB – Technical University of Ostrava, 17. listopadu 15,
708 33 Ostrava – Poruba, Czech Republic
jan.nedoma@vsb.cz

Abstract. The article summarizes the progress of the two years of the author's study of the field of Communication technology. The topic of dissertation thesis is the Nondestructive fiber-optical system for measurement of speed in road traffic. The article summarizes activities at the Department of Telecommunications during the academic year 2015/2016, research and development activities related to the theses and research projects.

Keywords: interferometer, optical fiber, speed, thesis

1 Introduction

Allow me to introduce myself. My name is Jan Nedoma. I am studying full-time doctoral study at the Faculty of Electrical Engineering and Computer Science at the Technical University of Ostrava. My education program is called Computer Science, Communication Technology and Applied Mathematics and field of study is Communication Technology. Head of my dissertation thesis is professor Vladimir Vasinek. The theme of my thesis is entitled "*Nondestructive fiber-optical system for measurement of speed in road traffic*" and as the title implies, focuses on optoelectronics and optical communications. State doctoral exam I was passed on May 27, 2016.

2 Activities related to the dissertation thesis

Fiber optic sensors offer the attractive option to the existing sensor for measuring the vehicle speed in automobile traffic. My dissertation thesis describes the involvement of two interferometric sensor units including input-output components. This involvement forms a system to a measuring the vehicle speed. The interferometric sensors operate based on Mach-Zehnder interferometer. The sensors are constructed to detection of vibration from passing vehicles concerning sensing low frequency up to 3000 Hz. The sensor system processes the vibrational response, which detects the vehicle speed, in the time and frequency domains. A DFB laser, with a wavelength of 1550 nm and input power of 1-5 mW, is used as a radiative source. The optical receiver included PbSe detector. The solution provides very high sensitivity. Therefore, it belongs to the field of non-destructive sensors. It is not implemented into the road-

way necessary. Both units do not need the electrical power supply. The fiber-optic cables offer the possible connecting to the existing networks along roads too. The series repeating of a passage of vehicle was carried out for speeds from 10 kph to 55 kph. We monitored the speed using GPS. The highest relative difference of evaluated speed was 7.7 %, the smallest was 1.36 %. When recalculated on kph, the absolute error ranged in the tolerance ± 3 kph, which denotes segmental measuring systems in CZE. The resulting measuring scheme with is shown in figure 1.

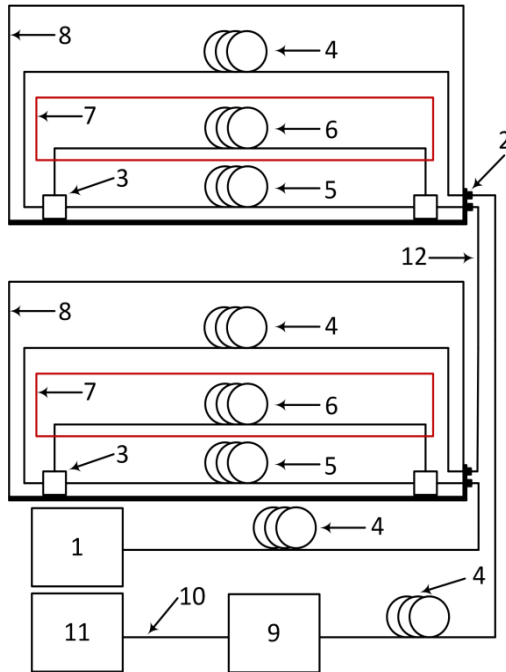


Fig. 1. Scheme for measurement of the speed of vehicles

List of referential marks (applies to Figures 1):

Laser radiation source (1), I/O interface (2), coupler (3), conventional optical fiber G.652D (4), measuring part of the interferometer (5), reference part of interferometer (6), dampening part of the reference arm (7), protective waterproof box (8), photodetector (or photodetector system) (9), coaxial cable (10), part of signal processing (11), conventional optical fiber for connection of the sensor units (12).

I tested DFB laser source (1) with values of the output power in the range 1 to 10 mW, sufficient stability, and coherence length. The conventional SM (single mode) fiber G.652.D represents patch cords (4) of sensor units. Test cable length was selected in the range from 1 to 250 m. The length of the patch cord (12), for connecting sensor units, was tested depending on the distance of the location of the units from one another in the range of 1 to 50 m. However, the minimum distance is 1 m due to the resolution of the evaluation software. Couplers (3) have the split ratio of

50:50 with a tolerance of $\pm 5\%$. Involvement of sensory units is a Mach-Zehnder type. The interferometer is connected and stored in a protective waterproof box (8), with respect to the greatest sensitivity on the low frequency, for detecting of the vibration response of cars. The photodetector (or photodetector system) (9) detects a signal which arises due to the interference of optical beams from the reference (6) and measuring (5) arms and converts it into a measurable electric current. A signal processing device (11) uses a high-pass filter with a cutoff frequency of 8 Hz for ensuring of zero offset voltage. The amplifier is 16-bit analog-to-digital converter with the sampling rate of 250 kS/s. Actual evaluation software handles signals in the time domain. The application displays the progress of the signal as a voltage versus time (amplitude spectrum of the input signal). Figure 2 shows experimental measurement of vehicle speed [1, 2, 3].



Fig. 2. Experimental measurement of vehicle speed

3 Projects

As part of my studies, I was actively involved in solving seven projects, namely:

1. TA ČR - Intelligent modules for lighting and communication
2. TA ČR - Safety of optical transport networks and the development of opt. parts for electric power and electrical appliances
3. TA ČR GAMA PP1 - PRE SEED fund VŠB Technical University of Ostrava
4. Project GUARDSENSE I - The modern structure of photonic sensors and new innovative principles for intrusion detection systems, integrity and protection of critical infrastructures

5. Project GUARDSENSE II - Comprehensive security and critical infrastructure facilities addressed fiber optic sensors using modern information systems
6. SGS SP2016/149 - New types of photonic systems
7. SGS SP2015/130 - Research on aging elements of optical networks

As an author, I participated in the drafting and submission of 4 projects for the organization with named Technology Agency of the Czech Republic (TA CR) and for the Ministry of Industry and Trade of the Czech Republic (MPO).

About my work on projects:

In project "*Intelligent modules for lighting and communication*" I conducted according to the assignment of laboratory measurements and individual evaluation of experiments, field measurements, I worked on the preparation of documents for publishing the results. In the project number 2 was my task to take part in the design layout of scientific researchers laboratories project and I participated in the research and development of fiber optic networks and systems, mostly in the form of measuring the impact of weather conditions on the transmission characteristics of optical cable/fiber, which are installed N building on the roof areas. Within a measurement, polygon parameters are measured attenuation, chromatic and polarization mode dispersion, changes in temperature over the length of testing circuits. Also, I conducted measurements of parameters of aging optical fibers. In project number 3 was my main task of improvement sensing of unit M-Z interferometer and implementation experimental tests in practice. Within the sensing unit, we arrived at the reduction both in terms of size or weight. There was also better arrangement the optical fibers both in terms of sensory or reference. The actual sensing unit was placed in a removable plastic cover with the appropriate interconnection systems. Functional prototype which we successfully presented in project TA CR GAMA PP1 is shown on figure 3.



Fig. 3. Final sensing unit with M-Z interferometer for project TA CR GAMA PP1

In project with number 4 and 5 my task was to help design a prototype implementation of Security plastic windows against foreign intrusion based on fiber optic interferometer. As part of this task, I also conducted experimental measurement function-

ality and output characteristics of the assembled prototype - optimization solutions engagement, measurement frequency range prototype sensitivity to vibration sensing of the environment and the ability to detect speech. Furthermore, in the study, I actively participated in the external measuring vibration response of the car and train. I also worked on the preparation of non-invasive probes for sensing of the core human functions. The resulting measuring scheme with the sensing probe is shown in figure 4.

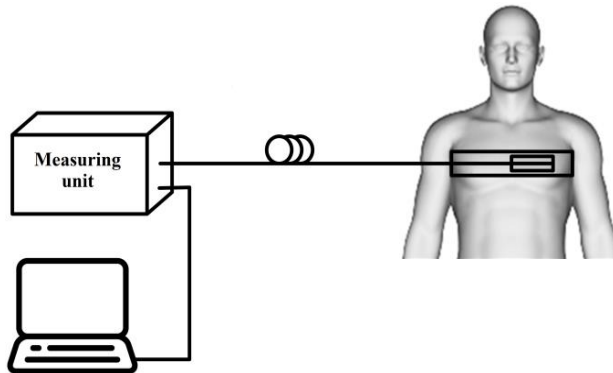


Fig. 4. Measuring scheme with the sensing probe

4 Publications activities

To date 7/2016, I mention a total of 13 accepted or published publications (conference proceedings or the reviewed journal). Also I have 3 publications under review in the reviewed journal. I am a member of the authors team which has a valid patent and utility model with entitled "*Fiber optic and a touch sensor for securing the selected area*". Also, I am a co-author of 3 patent and utility model applications, which are now under review. Among Applied outputs can include "*Software for the collection and processing of data Measured*" and functional sample "*Fiber-optic traffic monitor.*" Both are related to my dissertation.

5 Pedagogic part

In the winter semester, I was actively involved in ensuring the teaching with the subject ZEL (Groundwork Electronics). I also worked as supervision during exam tests. In the summer semester, I taught courses ÚDKT (Introduction to Communication Technologies) and OK II (Optical Communications II). In both cases, I led the complete teaching load exercise course - 4h per week. I also was a member of two cathedral commissions and helped in the final state exams. As an opponent, I've evaluated a bachelor thesis. As a leading bachelor thesis I led three topics (two topics were successfully vindicated).

6 Other activities at the Department of Telecommunications

I worked full-year presentation of the Department of Telecommunications. The proportion of work consisted mainly in the preparation and presentation of the presented subjects of the Department of Telecommunications Engineering at secondary schools, the building of FEI or open days. Furthermore, I was involved in preparing a presentation for the optical portion, preparation, and presentation of the optical laboratory and putting my whole program. With my colleagues we have prepared for students the laser maze (figure 5). Since March 2016, I became an employee at the Department of Telecommunications. My job position is called "*Assistant for science and research*". The job description is to work on projects and publishing activities. For my study results in the first year of study, I received an incentive grant of doctoral programs of the Technical University of Ostrava awarded for outstanding achievements in science and research.

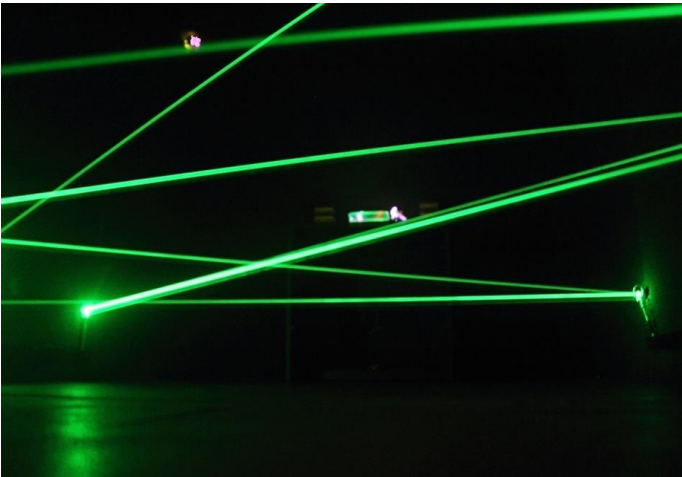


Fig. 5. Laser maze

References

- [1] LÓPEZ-HIGUERA, José Miguel. Handbook of optical fibre sensing technology. New York: Wiley, 2002. ISBN 0471820539.
- [2] Jan NEDOMA, Ondrej ZBORIL, Marcel FAJKUS, et al. Fiber optic system design for vehicle detection and analysis [online]. In: 98892D [cit. 2016-08-11]. DOI: 10.1117/12.2239549.
- [3] KRAUTER, K. G., G. F. JACOBSON, J. R. PATTERSON, J. H. NGUYEN a W. P. AMBROSE. Single-mode fiber, velocity interferometry. Review of Scientific Instruments [online]. 2011, 82(4), 045110- [cit. 2016-06-10]. DOI: 10.1063/1.3574797. ISSN 00346748.

Measurements of the Attenuation Constant of the Poly-dimethylsiloxane

Martin Novak

Department of Telecommunications, FEECS,
VŠB – Technical University of Ostrava, 17. listopadu 15,
708 33 Ostrava – Poruba, Czech Republic
martin.novak.st@vsb.cz

Abstract. The paper describes the measurement of attenuation cylindrical waveguides of polydimethylsiloxane and determines the attenuation constant in different parts of the sample. For the fabrication of samples was used two-component silicone gel with a commercial designation Sylgard 184. The work describes existing publications and teaching activities of my first doctoral studies 2015/2016.

Keywords: polydimethylsiloxane, PDMS, attenuation constant, glovebox

1 Introduction

Polydimethylsiloxane (PDMS) is a moderately viscous liquid. One of the main characteristics is the thermal stability, which is given due to Si-O bonds and by the high binding energy of 452 kJ/mol and the Si-CH₃ (Fig. 1). Regarding chemical composition, it is one of the cleanest silicone materials at all. Siloxanes have a high resistivity ($1,5 \cdot 10^{15} \Omega/\text{cm}$) and include electrical insulators. The dielectric strength is about 19 kV/mm, depending on the siloxane. Other features include resistance to chemicals, radiation, and UV radiation. It used in a wide range of industries e.g. in aerospace, medical, food industry, electronics, and automotive industries. The refractive index of PDMS is around 1.399 [-] for a wavelength of 1550 nm and the transmittance in the visible spectrum of 96 %. Regarding of the optical properties, PDMS is a fascinating material.

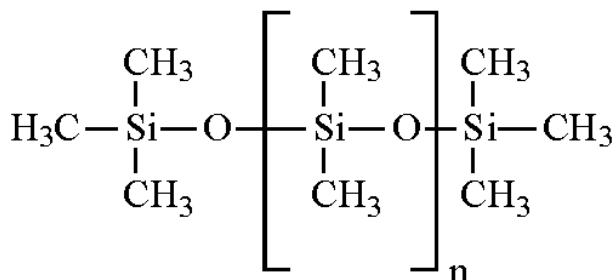


Fig. 1: The chemical composition of PDMS

Sample preparation and methods of measurement

For all the produced samples were used two-component elastomer Sylgard 184. The first component is a PDMS itself (A) and the second part is called curing agent (B). After adding the curing agent in a defined ratio (10:1) (A:B) may be a mixture of elevated temperature cured.

Recommended temperatures for curing are in the range 50-150 °C. This type of elastomer can be cured even at room temperature, but the whole process takes 48 hours. The higher the curing temperature, the faster the mixture is cured. Final blend dispensed in sterile tubes with a diameter of 5 mm and a length of 45 mm, thus providing the cylindrical structure of the waveguide. We defined two procedures connection PDMS and a curing agent (manually mixed or by the ultrasonic bath). Ultrasonic bath can effectively eliminate the bubbles, while by the manual mixing, it was necessary to let the bubbles disappear spontaneously during a particular period.

Assertions thus prepared samples was carried out in a temperature box at a constant temperature of $65 \text{ }^{\circ}\text{C} \pm 3 \text{ }^{\circ}\text{C}$. Considering the thermal resistance of the tubes was higher the temperature used; this implies the increased curing period about 60 minutes. The whole process of production of cylindrical waveguides is carried out under ambient conditions. The cured samples split into smaller samples 5 mm, in which further measurements realized. To calculate the decay constant it was necessary to determine the input power P_1 (the power directed into the waveguide) and the output power P_2 (measured on the output waveguide).

To create the measuring workplace I used optomechanical construction Thorlabs. Measuring workplace consists of the power adapter light (Light Emitting Diode (LED) with central wavelength 470 nm), the photodetector (Thorlabs S121C) and power meter (Thorlabs Power meter PM100D) and curtains made of an impermeable material with a defined opening. The photodetector was first measured performance behind the screen representing the input power coupled into the waveguide (P_1). Subsequently, between the diaphragm and the photodetector inserted sample of PDMS and measured output power (P_2). Measuring workplace shows Fig. 2.



Fig. 2: Picture of created measuring workplace

2 Results

The resulting waveforms represent the average value of the attenuation constant across all parts of 5 mm produced samples. For each method of mixing was made 20 samples. Manual mixing was carried out for 10 minutes and the time relaxes sample was 60 minutes so that air bubbles disappeared. Mixing for using ultrasound to proceed for 30 minutes with a frequency of 20 kHz. With this method, I did not need any relaxation time, because the ultrasound effectively broke the air bubbles. For manual mixing, dispersion values of the attenuation constants greater, but regarding the attenuation is a better quality sample. Using an ultrasonic bath ensures greater homogeneity of the entire sample, both components Sylgard 184 are better mixed. Using ultrasound decaying, molecular bonds polydimethylsiloxane, because there are an increase attenuation values tested samples.

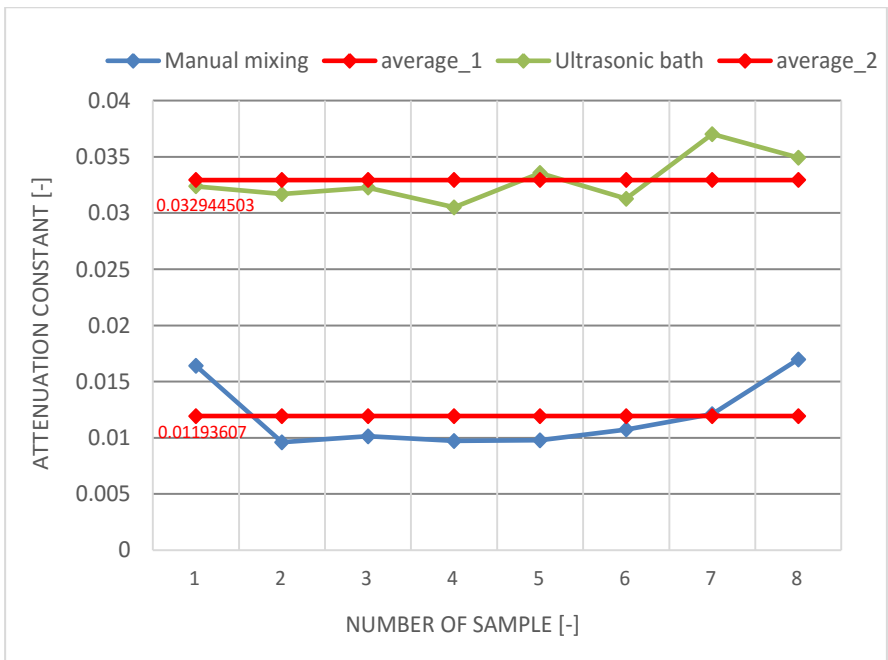


Fig. 3: Attenuation constant of the PDMS

3 Conclusion

Homogeneity of the waveguide is as important as the attenuation, so is important find a compromise between these two methods, or find another effective method of preparation. Even clean working environment plays a critical role in the design of the waveguide, therefore, was designed vacuum box which shown in Fig. 4.

The purity of the environment was ensured by the air purifier and ionizer, which effectively processes dust particles inside the vacuum box. The properties and behav-

ior of the PDMS can be influenced by the addition of impurities in the form of various micro and nanopowders. Using the vacuum box are eliminated potential health risks.



Fig. 4: Picture of created vacuum box

4 Projects

In the first year of doctoral studies, I was involved in solving three projects.

1. Project GUARDSENSE II – Comprehensive security and critical infrastructure facilities addressed fiber optic sensors using modern information systems
2. SGS SP2016/149 - New types of photonic systems
3. SGS SP2015/130 - Research on aging elements of optical networks

About my work on projects:

I participated in several measurements when we tried to implement a new type of sensor based on M-Z interferometer. This system used for detection of vehicles, and we can differentiate the type of vehicles (cars, trucks) according to the particular frequency. M-Z interferometer was also built in a plastic box, which serves as a safety element against intrusion by unauthorized persons. In this prototype, I conducted an extensive range of measurement, the measuring of the sensitivity of the system. I worked on developing a new type of sensor for monitoring vital signs (respiration, pulse). The sensor uses Bragg grating encapsulated in PDMS, which provides protection of the flexible sensor. The primary focus of my work was the development of novel photonic systems in PDMS. These are mainly cylindrical and planar structures with ingredients that are used to generate white light (Fig. 5).



Fig. 5: Created sample of PDMS which generated white light

5 References

1. Martinček I., Turek I., Tarjányi N., Effect of boundary on refractive index of PDMS. *Optical Materials Express*. 2014. DOI: 10.1364/OME.4.001997. ISSN 21593930.
2. Cai D.K., Neyer A., Kuckuk R., Heise H.M.b., Optical absorption in transparent PDMS materials applied for multimode waveguides fabrication. *Optical Materials*. 2008. DOI: 10.1016/j.optmat.2007.05.041. ISSN 09253467.
3. Hosseinzadeh A., Middlebrook C.T., a Mullins M.E., Optical waveguides using PDMS-metal oxide hybrid nanocomposites. In: *Proceedings of SPIE - The International Society for Optical Engineering*. 2015. DOI: 10.1117/12.2080582. ISBN 978-162841450-9. ISSN 0277786X.
4. Steckl A.J., Allen S.C., A nearly ideal phosphor-converted white light-emitting diode. *Applied Physics Letters*. 2008. DOI: 10.1063/1.2901378. ISSN 00036951.

A New Approach to Speech Quality Evaluation

Lukas Orcik¹, Miroslav Voznak¹, and Erik Chromy²

¹Department of Telecommunications, FEECS,
VŠB – Technical University of Ostrava, 17. listopadu 15,
708 33 Ostrava – Poruba, Czech Republic

²FEI – Slovak University of Technology, Ilkovicova 3, 812 19 Bratislava, Slovak
Republic

{lukas.orcik, miroslav.voznak}@vsb.cz, chromy@ut.fei.stuba.sk

Abstract. The paper presents a system for monitoring and assessment the speech quality in the IP telephony infrastructures using modular probes. The probes are placed at key nodes in the network where aggregating packet loss data. The system dynamically measures speech quality and results are collected on a central server. For data analysis we applied four-state Markov model for modeling the impact of network impairments on speech quality. Information about the speech quality are displayed in the form of automatically generated graphs and tables.

Keywords: Speech Quality, Network Probes

1 Introduction

The number of VoIP installations has grown rapidly in the past years. This trend is motivated by the numerous advantages the VoIP technology has and high availability of it due to the decreased purchase and management costs [1]. It has, however, its disadvantages as well, because it relies on the quality and the availability of Internet connection. The computer network is a dynamically changing eco-system. The main parameter, that changes in accordance to the network load is the packet loss. Therefore, it is essential to measure and predict the changes and events in the network and react accordingly to protect and preserve the high quality of service. In this paper, the mechanism of function of the information system, which is meant to predict and estimate the quality of call using numerous network probes, is described. Its main purpose is to allow for better understanding where and when the packet loss occurs. Using the mentioned probes dislocated in different places in the network, the information about the packet loss is collected and consecutively sent to the central server, where this data is stored and then sorted and preprocessed so that the neural network can process it. The output of the system is the MOS (Mean Opinion Score) estimation, which is then compared to the output of the ITU-T P.862 PESQ (Perceptual Evaluation of the Speech Quality), which serves as the reference value [3], [4], [5]. The aim of this paper is to present the generally system design that would allow the user to estimate the speech quality regardless of the signal being carried inside the RTP(Real-time Transport Protocol) packets themselves. This system effectively estimates the impact of the packet loss on the

speech quality and it can be integrated to any existing environment because it uses general network statistics and the information from the RTP headers.

2 State of the Art

There are several technologies that are capable of measuring the network characteristics [6]. However, they do not offer a complex data analysis nor data interpretation [7]. The correct understanding of how the network infrastructure works is essential for the optimization and security of the provided services [8]. The survey provided in [9] showed that the PESQ algorithm accommodates the effects of packet loss on speech quality better than the E-model, and is, therefore, better suited for the task making its estimation a sensible way for improving the precision of the estimation. The speech quality estimation system proposed in this article is an enhancement and generalization of the system proposed in [10].

The author in this paper uses 2-state Gilbert Model to generate the losses and tries to fit the observed packet sequence into the model. This, however, proves problematic for the networks with different packet loss distributions. Paper consists of two main parts. The first one is focused on the network probes design and the second one, where the information about the algorithms are discussed which are used in order to obtain the characteristics of packet loss and MOS. In case of the probe, the cornerstones consist of the measuring of packet loss in the real infrastructure and the data exchange between the probe and the server.

3 Design and Technology of the System

It works on the principle of autonomous probes which are placed at key nodes in the network and periodically carry out test calls to adjacent probes. Once the test call is made, measured data are sent to the server, they are analysed. Server side is based on the Zabbix [11] monitoring tool, which is enhanced by our algorithms for data collection. Server also allows to monitor individual probes and respond to potential failure. Users can easily monitor the quality of speech on different call routes and on the basis of this information they can optimize network flow, or edit voice codecs for VoIP traffic.

From the perspective of the technologies that were used in the implementation, it is again necessary to divide a whole system into two parts. Server uses a virtualized platform running on Zabbix monitoring system and it was necessary to implement a communication interface using the Python programming language. Detailed description of the interface itself and ongoing communication is then given in the following chapter.

Probe side will be developed on a specially modified OpenWRT [12] Linux distribution, which is suitable for low-cost and energy-saving devices. However, the most important parts of the probe are classes for communication with the server, applications

for control periodic processes and a test call generator itself. In addition, the probe includes classes for evaluation of speech quality and communication interface with other probes. As was already mentioned, the probes may be deployed in a network in many ways, allowing rapid expansion of the system and also gain a more accurate measurement.

3.1 Measuring

The main task of the measuring probes is the periodic measurement of the packet loss in distinct media paths. The measuring probes are both the origin and destination of the connection. The measurement consists of sending the RTP packets among the individual probes and observing how many of the packets reach the designated target. Many different scenarios can be simulated such as variable packet sizing, amount of data sent in one measuring cycle and timing measurements. Each measurement consists of the set of rules to follow and these rules are not dependent on the central server. The server can instruct the probe to conduct the measurement as well. All the collected data are stored locally on the probe and in regular time intervals they are sent to the central server for a permanent storage.

3.2 System Communications

The communication between the probes and the central server uses the following protocols.

JSON-RPC (JavaScript Object Notation – Remote Procedure Call protocol) interface [13] was selected for communication between the probe and the Zabbix server. It sends the string as a JSON object through HTTP (Hypertext Transfer Protocol) request. Operation and manipulation of data in this form is simple and this class can obtain information from Zabbix server in the form of instance parameters (items) that the server accepts. Whether they are active or passive, it is possible to add your items using this interface.

With this interface, it is first necessary to authenticate and encrypt communication using an asymmetric cryptography, the probe is signed and encrypted using the private key, the server owns the public one. Then SSH (Secure Shell) [14] tunnel is created and the JSON objects are transferred through it.

3.3 Packet loss measuring

The speech quality estimation is meant to be used with the basic characteristics of the IP networks - the packet loss, the one-way delay and jitter, it enables speech quality prediction. Each characteristic impacts the speech quality differently. Moreover, only the packet loss can be acquired by simple packet observation [15]. For jitter effect to be measured, the playout buffer needs to be employed. For the delay measurements the external source, such as RTCP(RTP Control Protocol), needs to be harnessed [16]. The entire estimation system is divided into several modules based on the functionality each

part implements. These parts are designed to simulate the effect of the above mentioned characteristics and to perform the necessary calculations for the system to work.

Playout Buffer Module

There is a simplistic implementation of the playout (or de-jitter) buffer functionalities in this module. The main purpose of this module is to prove the viability and the accuracy of the original assumption that the delay variations add to both the network loss and network delay impairments. The playout buffer implemented for the testing and measuring purposes is the fixed-length one with an unlimited data space (no early-arriving packets are discarded). Our algorithm is initialized with the first arriving packet in de-jitter buffer and is able to resynchronize the time scale after the sequence of five consecutive discards. Let T_0 and T_i be the actual arrival times of first and i -th arriving packet (in seconds from unix epoch) and t_0 and t_i be a timestamp in the RTP header of the respective packet (in milliseconds after recalculation using codec sampling frequency), then the ideal packet arrival time T'_i can be calculated:

$$T'_i = T_0 + t_i - t_0 \quad (1)$$

By using this ideal arrival time, the packet discard happens under this condition:

$$T_i - T'_i > S \quad (2)$$

where S is the playout buffer size in milliseconds. By discarding late on arrival packets the playout buffer increases the overall statistics of the network packet loss and their characteristics causing increase in speech quality deterioration. Moreover, the fixed length of the buffer adds to the overall packet delay, which is also used to calculate the effect of the delay.

3.4 Packet Loss Analyzer

The Packet Loss Analyzer converts the information about the network losses and playout buffer discards into five RFC 3611 compliant statistics [fried], which are described as follows.

Packet Loss Probability

Denoted as P_{PL} , the Packet Loss Probability is the overall percentage of the lost packets in relation to the total number of the packets sent (see eq. 3).

$$PPL = \frac{N_{LOST}}{N_{SENT}} [-] \quad (3)$$

where N_{LOST} is the number of lost packets and N_{SENT} the total number of RTP packets sent.

Packet Loss Probability in Burst

Denoted as P_{BPL} , the Packet Loss Probability in Burst is the overall percentage of packets lost in a burst (according the burst definition in RFC 3611) defined as stated in eq 4.

$$PBPL = \frac{N_{LOST_IN_BURST}}{N_{SENT}} [-] \quad (4)$$

where $N_{LOST_IN_BURST}$ is the number of packets lost in all bursts in a packet sequence.

Burst Density

Denoted as ρ , the Burst Density is the ratio of the number of lost packets in all burst periods and the total length of all bursts in a packet sequence (see eq.5).

$$\rho = \frac{N_{LOST}}{N_{BURST}} [-] \quad (5)$$

where N_{BURST} is the number of all packets lost in all bursts in a packet sequence.

4 Conclusion

Results of the research presented in this paper are a contribution to the field of speech quality assessment. The proposed algorithms based on four-state Markov. We have proved their correlation with PESQ and in Comparison with PESQ the used approach brings possibility to perform assessment in real time.

In this paper, the architecture of the complex system meant to measure and predict the quality of call was described. The measuring probes perform the measurement of packet loss, preprocess the data and consecutively send them to the central server, where the deeper analysis takes place. The results are presented to the user in a graphic manner. This system takes the observed network loss statistics compliant to those defined in RFC 3611 and perform the MOS_{LQE} .

References

1. Rezac, F., Voznak, M., Tomala, K., Voice Messaging System as a Form of Distribution of an Urgent Information, *Wireless Personal Communications*, Volume 85, Issue 1, pp. 63--76 (2015)
2. ITU-T, Recommendation P.862.1: Mapping function for transforming P.862 raw result scores to MOS_{LQO} . International Telecommunication Union (2004)
3. F.De Rango, M.Tropea, P.Fazio, S.Marano, Overview on VoIP: Subjective and Objective Measurement Methods, *Int. Journal of Computer Science and Network Security*, Volume 6, Issue 1, pp.140-153 (2006)
4. F. De Rango, P. Fazio, F. Scarcello, F. Conte, A new distributed application and network layer protocol for VoIP in mobile ad hoc networks, *Mobile Computing, IEEE Transactions on*, Volume 13, Issue 10, pp. 1536-1233 (2014)

5. Pocta, P., Holub, J., Mrvova, M., Impact of different Active-Speech-Ratios on PESQ's predictions in simulated VoIP environment, *Acta Acustica united with Acustica*, Volume 95, Issue 5, pp. 950--957 (2009)
6. Kadioglu, R., Dalveren, Y., Kara, A., Quality of service assessment: A case study on performance benchmarking of cellular network operators in Turkey, *Turkish Journal of Electrical Engineering and Computer Sciences*, Volume 23, Issue 2, pp. 548--559 (2015)
7. Sunder, D.S., Kushwaha, R.K., Evaluation of narrow band speech codecs for Ubiquitous Speech Collection and Analysis Systems. In *Proc. International Conference on Industrial Instrumentation and Control*, ICIC 2015, art. no. 7150718, pp. 93--98 (2015)
8. Raake, A., *Speech Quality of VoIP: Assessment and Prediction*. John Wiley & Sons, Chichester (2007)
9. Khan, H.A., Sun, L., Assessment of Speech Quality for VoIP Applications using PESQ and E-Model, *Advances in Communications, Computing, Networks and Security*, Volume 7, pp. 263--273 (2008)
10. Sun, L., Ifeachor, E.C., Voice quality prediction models and their application in VoIP networks, *IEEE Transactions on Multimedia*, Volume 8, Issue 4, pp. 809--820 (2006)
11. Rozhon, J., Rezac, F., Slachta, J., Voznak, M., Monitoring of Speech Quality in Full-Mesh Networks, *Communications in Computer and Information Science*, Volume 431, pp. 157--166 (2014)
12. OpenWRT - Wireless Freedom, <https://openwrt.org/>
13. Summerfield, M.: *Python in Practice: Create Better Programs Using Concurrency, Libraries, and Patterns*. Addison-Wesley Professional; 1 edition, Indiana (2013)
14. Barret, D. J., Silverman, R. E., Byrnes, R. G.: *SSH, The Secure Shell: The Definitive Guide*. O'Reilly Media; Second Edition edition, Sebastopol (2005)
15. Klucik, S., Chromy, E., Baronak, I., Model to Increase the Number of Output States of a Random Variable Using a Histogram Based PDF, *Wireless Personal Communications*, Volume 85, Issue 1, pp. 137--149 (2015)
16. Burget, R., Komosny, D., Ganeshan, K., Topology aware feedback transmission for real-time control protocol, *Journal of Network and Computer Applications*, Volume 35, Issue 2, pp. 723--730 (2012)

The Influence of Temperature Loading on the Optical Fiber Passive Components

Frantisek Perecar

Department of Telecommunications, FEECS,
VŠB – Technical University of Ostrava, 17. listopadu 15,
708 33 Ostrava – Poruba, Czech Republic
frantisek.perecar@vsb.cz

Abstract. The paper discusses about aging of the passive optical couplers and the passive optical splitters in their burdened high temperature. The article focuses on applied research and experimental development of resources for safety operation of optical networks in environment with higher temperature. It addresses issues of accelerated ageing of optical fiber components in their burdened with high temperature. How does temperature influence on optical network elements? It is necessary to specify the changes in the optical coupler and find out why these changes occur. This article is devoted to experimental measurement of the impact of temperature loading on the SM optical FBT coupler with 8 branches. Optical passive components were exposed to temperature 95°C for 433 hours. Measurements are focused on the parameters of geometry of optical beam. Graphical and mathematical detect changes in the dissemination of energy coupler after single doses of temperature loading are useful to understand the phenomenon of accelerated ageing elements of optical networks in environments with an higher temperature.

Keywords: FBT coupler, temperature loading, ageing, MFD, energy propagation

1 Introduction

Conventional lines and cables are slowly being replaced by fiber optic and conventional integrated circuits they are being replaced with optical integrated circuits. The signal is not transmitted by current, but by light volume. The optical fiber is used not only for data communication but also to a number of other applications such as sensors, fiber lasers and many others. Optical fibers have many advantages, they are non-electric, immune to RFI (Radio-Frequency Interference) and EMI (electromagnetic interference), have small weight and size, enable access to normally inaccessible areas, etc. After years of expansion of new fiber networks, there are new issues that in constructing nobody bothered with. As optical fibers and cables stored in the ground in the early 90's, still capable of trouble-free operation? When it's time for a generational change optical network infrastructure in order to prevent the degradation of optical networks, respectively, in order to avoid the total collapse of the network? When asked about accelerated aging of passive optical elements, we can be looked at the issue from several angles. The findings on the mechanism of aging

and finding, a reliable model that enables the prediction of evolution of the transmission characteristics of optical fibers and optical passive components in time, will have huge economic importance. This work refers to the analysis of changes in the parameters of optical fiber couplers, in particular geometry parameter of the optical beam - MFD (Mode Field Diameter). Stress of optical passive components can be individual or combined - temperature performance, gamma radiation, both accelerate naturally aging. Optical passive components are potentially resistant to higher temperatures. We are trying to find out if it is really so. By understanding the problems, we learn to maintain optical networks longer in good shape or even slow down the aging process.[1][2]

2 Thermal loading of optical couplers

The loading process with heat is carried at specialized department of Technical University of Ostrava. The accelerated aging occurs under conditions that comply with the conditions specified in datasheet optical components. Optical couplers are stressed by temperature so that the conditions correspond influences that threat real trouble-free operation of optical networks [3]. The simulation of the critical operating conditions is simulated in electric oven. Optical coupler with 8 output branches and an even split ratio of optical power is inserted into the pipe, which is placed on a metal substrate. Coupler is rotated regularly to ensure compliance with the homogeneity occurred burden on all sides. The temperature of stress is constant 95 ° C. Temperature of the oven surrounding is maintained at 23 °C. Temperature was chosen based on previous experiments which were tested resistance of the connector coupler FC/APC. Connectors show no signs of mechanical damage to the temperature of 98 ° C. At higher temperatures it leads to irreversible damage to. Plastic coating of optical coupler begins to melt. When heated, protection output coupler in the hardening process began to curl, which resulted in the bends with very small radius. The total period of load moment is 433 hours. Passive optical elements were loaded in three successive load cycles:

- 1st time stress - 142 hours,
- 2nd time stress - 126 hours,
- 3rd time stress - 165 hours.

After the results were obtained, we have determined that a more suitable procedure will exert continuous couplers. Parameter measurement will be done directly during loading, without the need for pulling out of the oven components investigated. For this to be feasible, the branches will be drawn out of the active thermal oven. Load of 95 °C leads to accelerated aging of coupler, since according to the datasheet coupler is working properly at temperatures ranging from -40 ° C to 85 ° C. For conversion of time burden within years in the standard operating conditions, we employ accelerated aging Arrhenius relations. Arrhenius relations show the calculation of operating time, based on the determination of the activation energy.

3 Experimental Measurement

For monitoring parameters was used a scanning slit system applied to the profile of the optical beam (Optical Scanning Slit Beam Profiler) from Thorlabs. BP109-IR device covers band from 700nm to 1800nm. As detection material is used Indium Gallium Arsenide compound - InGaAs. Foundation is mobile head, whose main component is a rotating drum with a photosensitive material intended solely to detect radiation in the infrared range. The device has an integrated Power Meter, which is not calibrated and can effectively suppress the noise level [6]. Software environment was covered by program Thorlabs Beam 6.0. The measurements were made on single-mode coupler with 8 output branches, manufactured by company Optokon. Coupler original conditions, conditions after the first loading, conditions after the second loading and conditions after third thermal loading finally were observed. The measurements were carried out at constant conditions (i.e. room temperature 23°C), at wavelengths 1303nm and 1553nm of CW laser. We used optical light source FLS-2100 manufactured by company EXFO. Output power was 2mW. We applied filter modes to restrict of wrong modes. This concept is filtering higher order modes. The distance was elected so that to the best visualize, describe defects arising after stress coupler. Energy propagation was measured at a distance of 1 cm from scanning slit on our machine. Scan rate was set at 12000Hz and target resolution 2.5 μ m

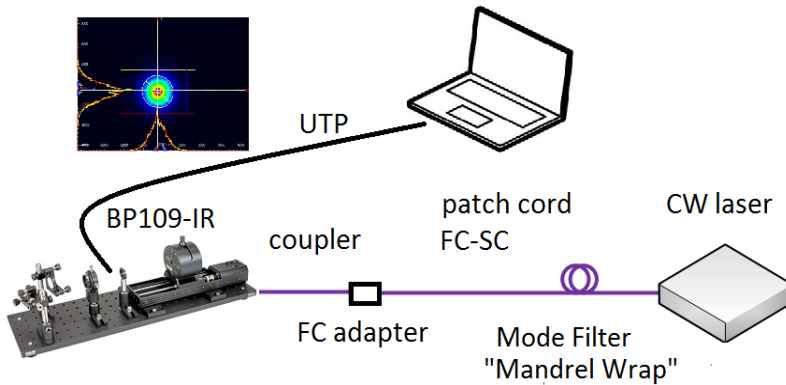


Fig. 1. Synoptic diagram visualization system for measuring an energy propagation of optical fiber coupler

The way of scanning slit is ideal for analyzing the shape of the beam which is close to Gaussian distribution. Measurement is relatively simple using IR-BP109, it is quick and transparent method to render the optical beam. This approach is not a standard method of measuring selected parameters, but it is the recommended method. This is a neat approach to the issue with a number of added features suitable for a more comprehensive investigation. It is a new effective way by which we can identify changes caused by different types of loads[4][5].

4 Results

As previously mentioned the size parameters were measured at a distance of 1 cm from scanning slit on our machine for various branches of the coupler. The effective values MFD_{eff} were obtained. The original values of parameters MFD_{eff} and values after thermal loading were compared with. The left part of table 1 is divided into eight branches of optical coupler. MFD_{eff} was obtained for axis x and axis y. The upper part of table is divided into 4 time steps of loading. Total time of burden was 433 hours. The measurements were carried out at a wavelength of 1310 nm and 1550 nm. Values devoted average values MFD_{eff} .

Table 1. : Average values of MFD for 1:8 coupler with even split ratio of optical power

MFD_{eff}	Time	0h		142h		268h		433h	
Branch	Axis / λ	1310	1550	1310	1550	1310	1550	1310	1550
1	X μm	2328	2391	2445	2532	2388	2236	2444	2409
	Y μm	2186	2329	2228	2275	2264	2085	2317	2156
2	X μm	2327	2388	2413	2402	2303	2330	2442	2522
	Y μm	2331	2294	2362	2486	2340	2271	2315	2368
3	X μm	2326	2405	2388	2485	2336	2519	2442	2523
	Y μm	2246	2384	2673	2497	2278	2522	2350	2325
4	X μm	2357	2386	2380	2416	2304	2315	2493	2778
	Y μm	2212	2363	2373	2383	2245	2330	2392	2436
5	X μm	2338	2172	2333	2591	2292	2400	2486	2557
	Y μm	2195	2319	2320	2332	2191	2382	2323	2493
6	X μm	2407	2523	2361	2473	2296	2412	2509	2599
	Y μm	2253	2429	2361	2393	2209	2342	2344	2565
7	X μm	2339	2416	2385	2381	2317	2393	2438	2490
	Y μm	2194	2317	2227	2256	2215	2325	2324	2454
8	X μm	2387	2404	2584	2418	2303	2374	2439	2534
	Y μm	2551	2378	2684	2288	2212	2221	2331	2461

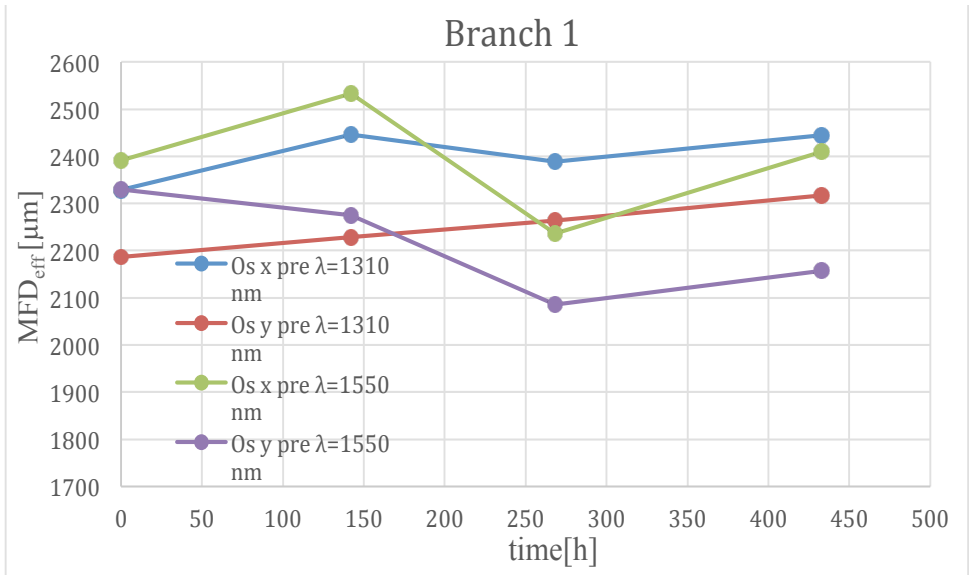


Fig. 2. The MFD_{eff} dependence of loading time

The graph (fig. 2) shows the results for the first branch passive optical fiber coupler. The x axis presents loading time and the y axis presents value of the parameter MFD_{eff} after that burdened. As we can see from the results obtained, the first signs of change have been demonstrated for first branch when after second dote of loading MFD_{eff} decreased (y axis at $\lambda = 1550$ nm). Remaining values due to thermal load reach constant values. From this we can conclude that loading period 433h is not long enough to changes were appeared. Therefore, the loading process continue.

Within measuring of parameters the width of the optical beam MFD_{eff} were found no significant changes the monitored parameters, when coupler was out of the temperature range declared by the manufacturer. Accelerated aging process is going on. It is expected that long-term continuous load will produce different results. and Research will continue until the time when the temperature load reflected on the measured parameters of optical fiber coupler.

5 Summary

The accelerated aging occurs under conditions that do not correspond to the datasets of optical passive components. Optical couplers have been loaded temperature so that it matches influences that compromise actual operation of optical networks. The aim of the experiment was to determine whether the temperature loading is able to impact negatively on observation element. After statistical processing of the values obtained, we have found that the thermal loading has minimal influence on measured parameters. As it was mentioned research will go on until there will occur some changes of the measured parameters. It is necessary to find out what influence has the ageing of optical elements, what and why changes occur and determine the way of reduction the ones.

References

- 1 DERICKSON, Dennis. *Fiber Optic Test and Measurement*. New Jersey: Prentice-Hall, Inc. 1998. ISBN 0135343305
- 2 SHUAI, Ci-jun, Ji-an DUAN a Jue ZHONG. Effect of technological parameters on optical performance of fiber coupler. In: *Journal of Central South University of Technology*. 2007, s. 370-373. DOI: 10.1007/s11771-007-0073-5. ISSN 1005-9784
- 3 LI, Junhui, Jinchao DANG, Ning ZHANG, Xinzhan WANG a et al. High and low temperature life experiments of Y waveguide multifunctional integrated optical devices. *Zhongguo Guanxing Jishu Xuebao/Journal of Chinese Inertial Technology*. 2014, (22), 109-113. DOI: 10.13695/j.cnki.12-1222/o3.2014.01.022. ISSN 10056734
- 4 Arrhenius. *NIST/SEMATECH e-Handbook of Statistical Methods*, 2012
Dostupné z: <http://www.itl.nist.gov/div898/handbook/apr/section1/apr151.htm>
- 5 BAYLE, Franck, Adamantios, METTAS. *Temperature Acceleration Models in Reliability Predictions: Justification & Improvements*. In: Reliability and Maintainability Symposium, San Diego. 2010 IEEE.
Dostupné z: http://www.reliasoft.com/pubs/2010_RAMS_temperature_acceleration_models.pdf
- 6 THORLABS. *Thorlabs Beam, Beam Analyzing Software, BP104-UV, -VIS, -IR, -IR2, BP109-UV, -VIS, -IR, -IR2 Operation Manual*. 2011.

Aging of Optical Fibers due to Radiation of High Optical Performance

Radek Pobořil

Department of Telecommunications, FEECS,
VŠB – Technical University of Ostrava, 17. listopadu 15,
708 33 Ostrava – Poruba, Czech Republic
radek.poboril@gmail.com

Abstract. The aim of this article is to familiarize readers with the issue of aging of optical fibers. Optical fibers as such are considered to be very durable. However, each material is aging and losing its properties. In the first chapter we will briefly describe the laser system for delivering optical energy. In the following part we will focus on the actual aging of the optical fiber, measuring the attenuation change with the real-time method. Finally, the results will be discussed.

Keywords: EDFA, erbium, optical amplifier, optical fibers

1 Introduction

Nowadays, optical fibers belong among the most important telecommunication elements generally. Even though they are very resistant to various influences of the surrounding environment acting on them, they succumb to the influence of time. Each material is subject to the change of their structure. This degradation can manifest itself by gradual or abrupt changes in material parameters. In case of optical fibers we talk primarily about material change of the fiber itself, i.e. silicon dioxide [1],[2].

These changes may affect the basic parameters of the optical fiber: attenuation, dispersion, resistance to bending. But more complex parameters, such as normalized frequency or mode structure of the fiber, can be affected as well [3].

Therefore, the whole purpose of this research is to prove that fibers age, and to elaborate a research not only in fibers but also in optical components. Optical communications have countless benefits, but all of them come at a price. The question of how long the used components and fibers are able to withstand is economically very important [4].

2 Power system setup

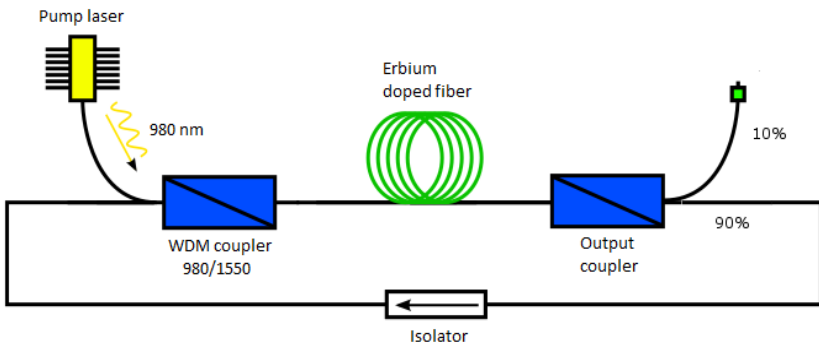
The aim of this connection is to create a fiber laser emitting at the wavelength of 1550 nm with the highest output power possible. Given that fiber lasers are quite expensive, it was a clear choice for us to design and subsequently construct it on our own.

The following chapters will gradually describe the laser design, including two stages formed by EDFA amplifiers.

2.1 The first stage – an erbium-doped fiber laser

At first we have constructed an erbium-doped fiber amplifier FiberCore IsoGain I-6.

Light of the wavelength of 1550 nm is generated in the erbium-doped fiber. Then it is supplied with energy using a laser diode at the wavelength of 978 nm. The delivered light output is 600 mW. The following figure shows a connection where the gained light of the 980nm wavelength is delivered through the 1550/980nm wave coupler, followed by a 6-metre erbium-doped fiber. The fiber is then connected to a divider with the ratio of 90 to 10%. The output of the 10% of power is used as the output portion of the whole first stage. The 90% output is connected to an isolator that is connected to the input of the 1550/980 nm WDM coupler, which makes it a loop. It is therefore a laser with a circular resonator. The output coupler was chosen out of many ratios for achieving the maximum output power. The length of the doped fiber was simulated in the Optiwave program and in the software by the provider of the fiber. This theory was subsequently verified experimentally. The output power of the first stage was 75.85 mW.



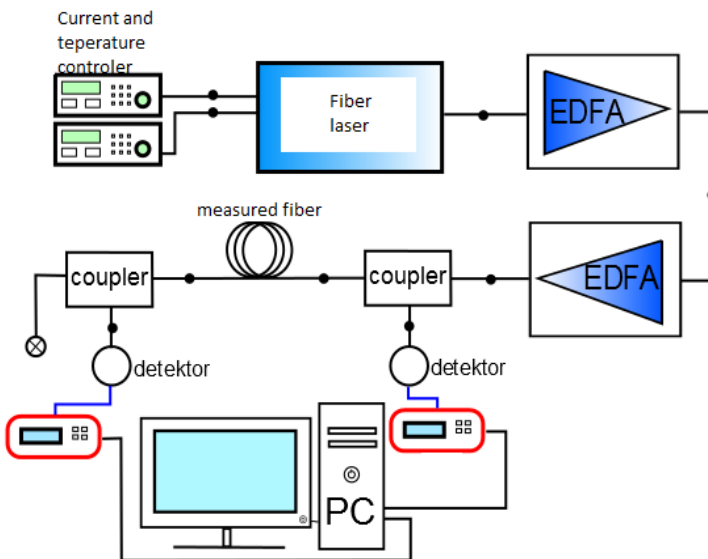
2.2 The second and the third stage – EDFA amplifiers

In the second and the third stage we used standard EDFA amplifiers in as minimized connection as possible. The figure shows the connection. In both cases we used the power supply equal to the diode output power of 500mW. The wavelength was 980 nm.

For supplying the erbium-doped fiber with the gained light we used a 980/1550 nm coupler with an integrated isolator. The integrated isolator prevents the light from returning to the pumping and signal path in the wrong direction. For the first amplifier we used the fiber Liekki ER110-4/125 with the length of 40 cm. Such short length was used because of the high absorption of the material at 110dB. For the second amplifier we used the standard doped fiber IsoGain I-6 with the length of 10 m. With the Leikki fiber it was possible to shift the wavelength from 1550 to 1559 nm.

3 Measuring attenuation variations of the optical fiber

Measuring attenuation variations of the optical fiber was performed by the real-time measurement method. The whole method is based on a suitable location of two measuring power meters. The created laser was connected to a spool of optical fiber of the length of approximately 1.5 km. Before and behind the spool there were power splitters that led 1% of the power to the power meter. This enabled us to perform measurement that lasted continuously for 20 days. During this measurement we have collected more than 1M of values. The following figure describes a connection of the measuring system.



The results are shown in the following chart. There are attenuations from input and output power measured before and behind the fiber. The graph shows a slight rise of the attenuation. Significant variations in measurement are mainly due to temperature instability in the room, which was caused by the fact that it was not possible to allocate the laboratory only for this experiment.

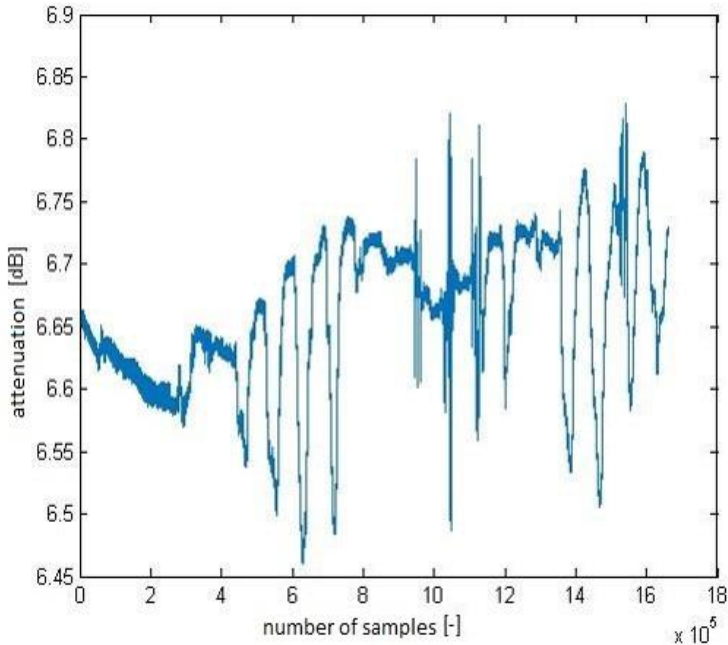


Fig. 1. Distribution of attenuation per the number of measured samples

In the second part of the measurement we also investigated geometrical distribution of the optical beam in the fiber. For this purposes we used a profilometer by Thorlabs. The measurement was repeated 20 times and all results were identical. It was expected that a sufficiently high performance of the laser would result in damage of the fiber and in subsequent deformation of the mode guided in the fiber. This deformation would be caused by disruption of ties among the molecules of silicon dioxide, which would lead to local changes in refractive index. The refractive index would change due to reaction of residual impurities in the fiber to sufficient performance. If the refractive index changed, normalized frequency together with mode structure would change as well. Unfortunately, these conclusions could not be confirmed due to insufficient laser power.

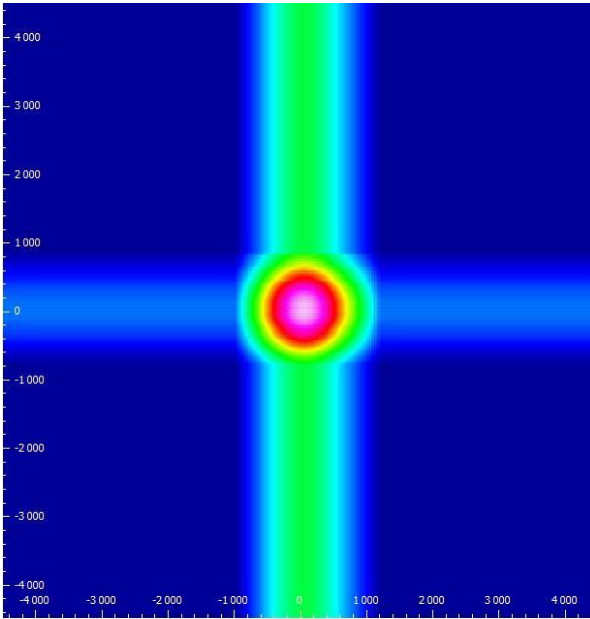


Fig. 2. Profile of the beam at the fiber output before the application of high performance

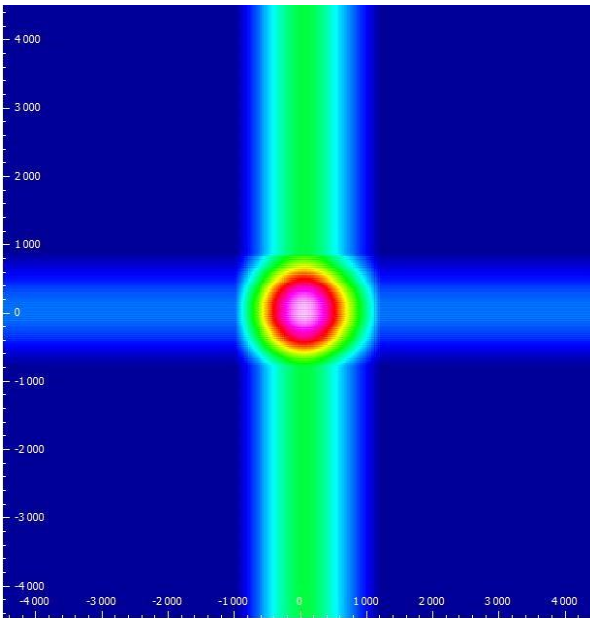


Fig. 3. Profile of the beam at the fiber output after the application of high performance

4 Conclusion

Results of the whole measurement show that radiation of high optical performance influences optical fibers. However, it is necessary to note that the whole experiment is at its beginnings and further conclusions may vary. It will definitely be necessary to increase the optical power in order to observe more considerable changes. If there is damage to the fiber to such an extent that the geometric shape of the mode in the fiber is disrupted, it will be necessary to use a pulse laser. Another suggestion for improving the measurement is to ensure better conditions, particularly in terms of temperature. It is necessary to keep stable environment because temperature change has a great impact on the stability of the whole laser system. The next measurement will be focused also on Brillouin frequencies that are extremely sensitive to any changes to the structure of an optical fiber.

References

- [1] KOZAK, M., B. JAUMARD and L. BOHAC. On Regenerator Placement in Loss-less Optical Burst Switching Networks. In: *36th International Conference on Telecommunications and Signal Processing*. Piscataway: IEEE, 2013, pp. 311-315. ISBN 978-1-4799-0403-7.
- [2] RAMASWAMI, R., K. N. SIVARAJAN and G. H. SASAKI. *Optical Networks: A Practical Perspective*. 3rd ed. Amsterdam: Morgan Kaufmann, 2009, xxxiv, Morgan Kaufmann series in networking. ISBN 978-0-12-374092-2.
- [3] BECKER, P., N. OLSSON and J. SIMPSON. *Erbium-Doped Fiber Amplifiers: Fundamentals and Technology*. San Diego: Academic Press, 1999, xv, ISBN 01-208-4590-3.
- [4] KOROSHETZ J., B. BRICKEEN, S. FAHR, A. RAPAPORT and M. BASS, Athermal emission in Yb,Er:glass. In: *Optics Express*, Vol. 15, pp. 11530-11535, 2007.

Broadband over Visible Light: High Power Wideband Bias-T Solution

Tomas Stratil¹, Petr Koudelka¹, Radek Martinek², and Vladimir Vasinek¹

¹Department of Telecommunications, FEECS,
VŠB – Technical University of Ostrava, 17. listopadu 15,
708 33 Ostrava – Poruba, Czech Republic

{tomas.stratil, petr.koudelka, vladimir.vasinek}@vsb.cz
²Department of Cybernetics and Biomedical Engineering, FEECS,
VŠB – Technical University of Ostrava, 17. listopadu 15,
708 33 Ostrava – Poruba, Czech Republic
radek.martinek@vsb.cz

Abstract. Broadband over Visible Light (BVL) is a new trend in research that combines technological principles of VLC during duplex communication between the source of optical radiation and the receiver on the side of the user and utilization of a chipset of the technology Broadband over Power Line (BPL), including provision of connectivity on power conductors. The use of the technology Bias-T proves to be a highly efficient concept of the VLC modulator. The article deals with the design of a high power broadband Bias-T allowing the use of the BVL technology at large SMD LED matrices or matrices containing power LED. The designed Bias-T was created and its functionality verified using a network analyzer.

Keywords: VLC, Visible Light Communication, Bias-T

1 Introduction

Broadband over Visible Light (BVL) is a new research direction based essentially on VLC technology. Again, it is intended to utilize the visible spectrum of optical radiation as a communication direction to the end user (download) and to utilize the infra-red spectrum of optical radiation (940 nm) in the reverse communication direction (upload). Moreover, compared to the VLC concept, in the case of BVL, it is intended to use the chipset of the Broadband over Power Line (BPL) technology, which, inter alia, allows the use of the OFDM MQAM modulation format at the number of 1,536 sub-carriers in the frequency range from 2 MHz to 34 MHz (IEEE 1901, for example chipset DS2). The BVL technology should, by its nature, enable transmission speed of 100 Mbps. Additionally, the BVL technology provides connectivity over power conductors in an efficient way.

2 High Power Wideband Bias-T

For the proper interconnection of the BPL and VLC technologies in the form of the resulting BVL technology, it is necessary, inter alia, to choose a suitable

concept of the modulator. A concept based on Bias-T is the current trend in the technological solutions of the VLC modulator [6]. This modulator concept is based on the so-called feeding switch point, which is commonly used in the RF technology. The commonly available Bias-T, designed primarily for the RF technology, allows adjustment of the operating point on the LI curve of the used LED (LED matrices) at the maximum values of $I_{DCmax} = 400 \text{ mA}$ and $U_{DCmax} = 25 \text{ V}$ for the band from 0.2 MHz to 12 GHz. There are also Bias-T options that are able to handle higher current loads, defined by the maximum values of $I_{DCmax} = 1.5 \text{ A}$ and $U_{DCmax} = 30 \text{ V}$ for the band from 10 MHz to 2.8 GHz.

As already mentioned, currently, there are performance options that are capable of a higher current load characterized by the parameter I_{DCmax} . Nevertheless, these performance options of Bias-T are on the DC side restricted by the parameter U_{DCmax} and the lower limit of the frequency band. It is obvious that the available Bias-T's are designed primarily for the RF technology and, in their intended usage as modulators for the BVL technology, it is necessary to make certain changes to their design.

The first changes to the Bias-T design for the BVL technology must be based on the required frequency band of the BPL technology chipset based on standard IEEE 1901, which corresponds to 90 % of the current solutions. This standard defines the lower frequency $f_{min} = 2 \text{ MHz}$. The reason is a frequency reserve for the possibility of simultaneous usage of the narrow band technology Power Line Communication (PLC), [1]. At present, the available solutions to performance Bias-T's are defined by the lower frequency f_{min} , which range around the values of 10 MHz.

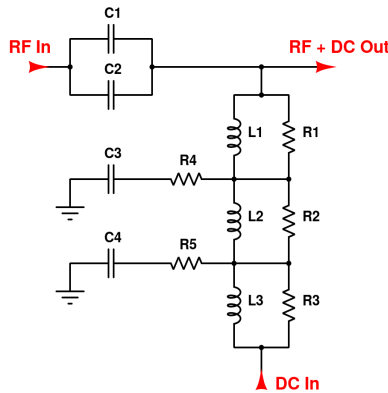


Fig. 1: Design of high power wideband Bias-T for Broadband over Visible Light

Other changes, when designing Bias-T for the BVL technology, must reflect the changes in the lighting technology. The recent trend in the lighting technology is to reduce the current value of the operating point I_{DC} while increasing

the value of the operating point voltage U_{DC} . For example, conventional light intended for public lighting having the performance of 80 W (Thor) defines its driver operating point in the form of $I_{DC} = 700$ mA and $U_{DC} = 112$ V. On the other hand, the area of indoor lighting, point light having the performance of 40 W (Philips Fortimo), defines its driver operating point in the form of $I_{DC} = 700$ mA and $U_{DC} = 62$ V. It must be noted that maintaining the original power solution in the form of a driver is always considered in the entire BVL concept. Currently available solutions to performance Bias-T's are able to handle high current loads ($I_{DCmax} = 1.5$ A) without any problems, but the low value of voltage on the DC input ($U_{DCmax} = 30$ V) is a considerably limiting factor.

2.1 Basic Function and Design Bias-T

Bias-T for VLC can be thought of as a feeding switch point in the RF technology which allows connection of a DC signal component in order to determine the operating point of LED (I_{bias}) on the basis of the LI curve and an AC component containing the information transmitted. As for this concept, the most suitable modulation formats are the ones based on keying the carrier. The combination of high performance on the DC side and the required frequency bandwidth is a major obstacle when designing Bias-T. In case of using Bias-T as a modulator of a BVL system, different parameters than with the RF technology must be considered at the designing stage. In our case, the emphasis is placed on high frequencies in units or tens of GHz, but the bandwidth of 1-250 MHz is fully sufficient [1]. The lower frequency range is fully sufficient for the concept of a BVL system.

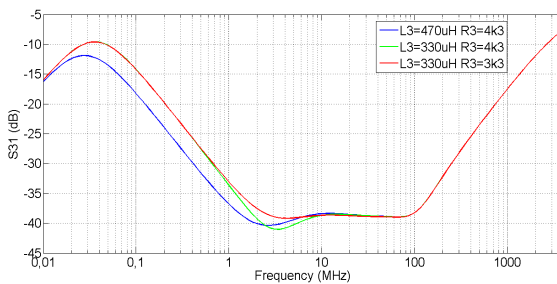


Fig. 2: Simulation results for different values of parallel resistor R3 and coil L3

Very important parameters include maximum current I_{DCmax} and maximum voltage U_{DCmax} , which Bias-T can manage, because the performance of optical radiation sources in lighting technology vary from tens to hundreds of Watts. It is not possible to construct a Bias-T for such high values of I_{DCmax} only on the basis of one coil in terms of requirements for a high inductance value. Current load distribution into multiple branches at the expense of deterioration of S parameters is a more appropriate method, which is not critical in the case

of a BVL concept. In the case of this article, Bias-T with the parameters of $I_{DCmax} = 1$ A and $U_{DCmax} = 150$ V at the minimum frequency bandwidth B_{min} of 100 MHz was considered.

2.2 Simulation

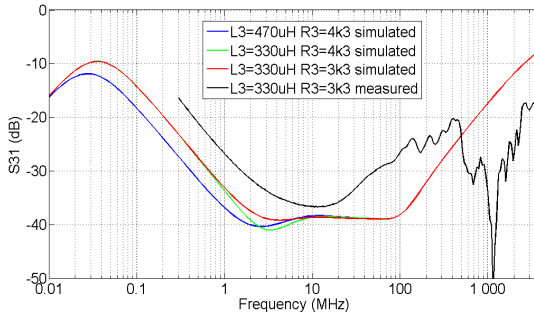
Figure 1 shows the final design scheme of the intended Bias-T. When designing, a number of components that would allow implementation in the SMD form were taken into consideration. The proposed Bias-T was designed for the target values $I_{DCmax} = 1$ A and $U_{DCmax} = 150$ V at the lower frequency $f_{min} = 2$ MHz and at the current minimum bandwidth of B_{min} of 100 MHz. These parameters of the designed Bias-T would allow usage of the BPL technology chipset working in the frequency band of 2–34 MHz enabling the transmission speed of 100 Mbps (OFDM 16QAM).

Two capacitors connected parallel to each other were used for blocking the DC component. These capacitors are labelled C1 and C2 in the diagram in Fig. 1. The final value 54 nF corresponds to the frequency of 29.47 kHz. Reason is filtering out possible PWM signal for control DC power on DC input by LED driver. Standard frequency PWM signal for control DC power has 400–500 Hz range. Coil L1 dampens lower frequencies around the value of 33.86 kHz. In contrast, coil L2 dampens lower frequencies around the value of 1.06 MHz. These values are only theoretical for an ideal circuit [2]. The parallel resistors R1, R2 and R3 with coils are used for smoothing of insulation characteristics defined as parameter S31. Simulations were conducted for the individual values of the parallel resistor R1 and coil L3 and they are compared graphically in Fig. 2.

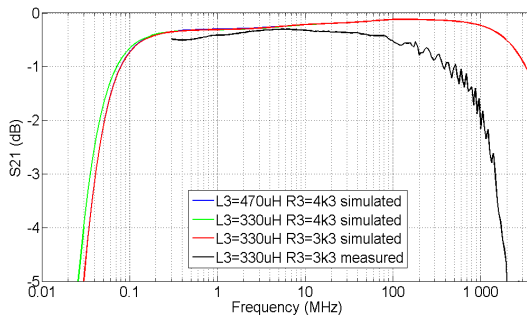
The higher resistance value of the parallel combination of R1, R2 and R3 connected to a coil increases deepening of insulation characteristics S31. Parameter S31 defines how much the signal from the DC input to the RF + DC output is damped. An equal characteristic across the entire length of the bandwidth is an ideal state. A configuration with the resistance of $R3 = 3.3$ k Ω and $L3 = 330$ μ H was used for the real implementation. A real solution contaminates the circuit with undesired parasitic effects from the connectors, printed circuit board designs, etc.

2.3 Measurement

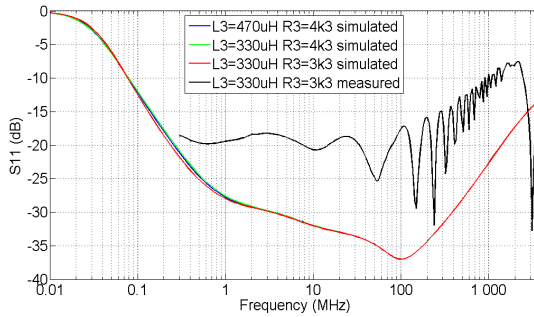
Measurement of S parameters of the final Bias-T prototype according to Fig. 1 was conducted using a Network analyzer Rhode-Schwarz ZVB4 [3]. Based on the comparison of the simulation results and the final measured values, we can say that real results approximate to the results of the simulations. Parameter S31 achieves the lowest values from 1.6 MHz to 105 MHz, Fig. 3(a). Parameter S21 that indicates signal insertion loss from the RF input to the RF + DC output. According to the measurements, there is a decrease by level 3 dB to the frequency 100 MHz, Fig. 3(b). S11 determines return loss for the RF input, Fig. 3(c). For frequencies higher than 100 MHz, Bias-T moves into resonance.



(a)



(b)



(c)

Fig. 3: Result of simulation and measurement (a) S_{31} (b) S_{21} and (c) S_{11}

3 Conclusion

The objective of this article was to carry out the design and implementation of a high power broadband Bias-T allowing the use of the BVL technology at large SMD LED matrices or matrices containing power LED. In our case, it was a professional point light Philips Fortimo LED DLM 3000 44 W/840 containing

a matrix of blue SMD LED. The total electric power of the point light in the operating point was 40 W. The designed modulator based on Bias-T enables usage at the intended maximum values of operating points $I_{DCmax} = 1$ A and $U_{DCmax} = 150$ V. When used with the professional point light Philips Fortimo LED DLM 3000 44 W/840, the modulator was loaded with operating point $I_{DC} = 700$ mA and $U_{DC} = 62$ V.

Results are published in: 2016 IEEE 17th Annual Wireless and Microwave Technology Conference (WAMICON), DOI: 10.1109/WAMICON.2016.7483841 and 10th International Symposium on Communication Systems, Networks and Digital Signal Processing 2016 (CSNDSP).

References

1. MLYNEK, P., J. MISUREC, M. KOUTNY, R. FUJDIK and T. JEDLICKA. Analysis and Experimental Evaluation of Power Line Transmission Parameters for Power Line Communication. *Measurement Science Review*. 2015, vol. 15, iss. 2, pp. 64–71. ISSN 1335-8871. DOI: 10.1515/msr-2015-0010.
2. BAYLIS, C., L. DUNLEAVY and W. CLAUSEN. Design of bias tees for a pulsed-bias, pulsed-RF test system using accurate component models. *Microwave Journal*. 2006, vol. 49, iss. 10, pp. 68–90. ISSN 0192-6225.
3. KIM, N.-T. Ultra-wideband bias-tee design using distributed network synthesis. *IEICE Electronics Express*. 2013, vol. 10, no. 15, pp. 1–8. ISSN 1349-2543. DOI: 10.1587/elex.10.20130472.
4. LATAL, J., P. KOUDELKA, V. VASINEK, F. DOSTAL and K. SOKANSKY. Possible use of power LEDs for lighting and communication. *Przegląd Elektrotechniczny*. 2011, vol. 87, iss. 4, pp. 25–28. ISSN: 0033-2097.
5. KOUDELKA, P., J. LATAL, V. VASINEK, F. DOSTAL and K. SOKANSKY. Research of power LEDs for mobile communication. *Przegląd Elektrotechniczny*. 2011, vol. 87, iss. 4, pp. 1–4. ISSN: 0033-2097.
6. KOUDELKA, P., P. HANULAK, J. JAROS, M. PAPES, J. LATAL, P. SISKÁ and V. VASINEK. Study of LED modulation effect on the photometric quantities and beam homogeneity of automotive lighting. In: *2nd International Conference on Photonics Solutions*. Hua Hin: SPIE, 2015. ISBN 978-162841875-0. DOI: 10.1117/12.2196299.

Quality Comparison of Streaming Video and Streaming Encrypted Video using Objective Methods

Lukas Sevcik¹, Miroslav Voznak¹, and Erik Chromy²

¹Department of Telecommunications, FEECS,
VŠB – Technical University of Ostrava, 17. listopadu 15,
708 33 Ostrava – Poruba, Czech Republic

²FEI – Slovak University of Technology, Ilkovicova 3, 812 19 Bratislava, Slovak
Republic
lukassefosevcik@gmail.com

Abstract. Nowadays, transmission of triple play services over internet, mainly video is very popular. It is necessary to bring information about factors that influence the video quality. The aim of this paper is the quality assessment of the video using objective methods. We use SSIM and VQM metrics.

First task is to compare quality of transmission video with encrypted video. We use IPsec tunnel which provide protection as encryption or authentication. We use two types of ciphers – AES and 3DES with hash function SHA.

Next goal is to compare quality of video with packet loss. We evaluate impact of encryption and packet loss for two types of video formats for two types of videos – static and dynamic. Measurements are performing for two resolutions.

Keywords: quality of service, encryption, packet loss, AES, 3DES

1 Methodology

1.1 Video quality evaluation

The process of measuring packet loss is shown in the Fig.1. Our testing scenarios reflect the situation that can actually happen in the network. Especially the mobile networks, capable of using IP architecture like UMTS and LTE, reach high values of packet loss [1]. We used Linux tool called Netem for the purpose of settings of our scenarios. Netem provides Network Emulation functionality for testing protocols by emulating the properties of wide area networks. The current version emulates variable delay, loss, duplication and re-ordering [2].



Fig. 1. Measurement procedure

We create network with IPsec tunnel on the second part of our measurement. IPsec using Diffie hellman algorithm. It uses ESP and AH header. We use authentication with share password (ISAKMP). We compare symmetric ciphers – AES and 3DES. We use hash function SHA. Topology is shown in the Fig. 2.

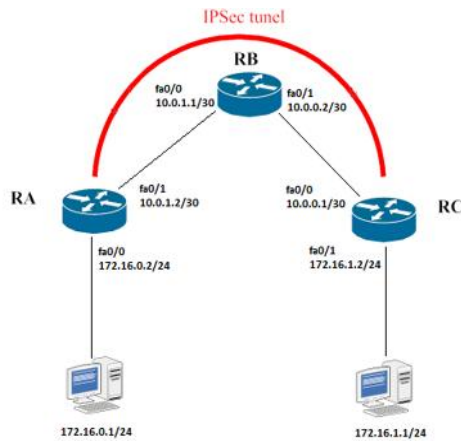


Fig. 2. Topology with IPsec technology

To evaluate the quality we adopted methods SSIM and VQM. SSIM correlates better with the perception of the human eye [3], [4]. Video records were assessed by using MSU VQM Tool. As a first step, we created a stream in the VLC Player. As for the video content, streaming process RTP/UDP/IP method with MPEG 2(TS) and H.264(MP4) was used. The video stream was broadcasted on the local computer interface. We captured and saved the stream to the local disk by using another VLC Player. We saved this transfer video and tagged it as the original video.

2 Results

2.1 Packet Loss

The results of the measurements verified our prediction that not only the type of video codec has a degradation impact on video quality. On the other hand, video resolution was not proven as a significant parameter of video robustness.

Performed experiments demonstrated that the video compression type is the most important factor affecting video quality. Compression rate of video codec H.264 (MPEG-4 Part 10) is higher, nevertheless its robustness against packet loss is lower than the older MPEG-2. According to the results of the static video measurements, which are listed in Table 1, there is no significant difference between the resolutions used. We detected a slight decrease in higher resolution. During the static scene, where changes were very slow, mainly the P and B frames contained approximately the same information regardless of the resolution used [4].

We tested dynamic video sequence with high bitrate. High bitrate means lot of information contain in I, B and P frames and its loss causes significant degradation of video quality. This sequence achieved worse results than the static video. Again, the differences between the used resolutions were small. All the GOP frames contain more information, so packet loss influences more the picture reconstruction. That is the reason why dynamic video is generally more sensitive to data loss [4], [5].

2.2 IPsec

The chosen codec has important impact on quality of video encrypted by using IPsec. The produced stream by H264 codec requires lower bandwidth than MPEG2 codec, therefore the CPU of router executing encryption is less occupied in case of H264 than MPEG2 and moreover the load on network interfaces is lower if H264 is used. We observed the most significant degradation in case of dynamic video where differences between H264 and MPEG2 are greatest.

Table 1. Comparison of AES256 and 3DES encryption - HD resolution

	MPEG 2		H 264	
	3DES	AES256	3DES	AES256
Static video	0.862	0.874	0.945	0.941
High rate dynamic	0.521	0.515	0.852	0.835

Table 2. Comparison of AES256 and 3DES encryption - Full HD resolution

	MPEG 2		H 264	
	3DES	AES256	3DES	AES256
Static video	0.656	0.658	0.939	0.941
High rate dynamic	0.358	0.312	0.698	0.708

The tables 1 and 2 show differences in quality of transmission video between AES256 and 3DES. Whereas results of assessment by SSIM method are depicted in Table 1 and 2, results achieved by VQM method are listed in Table 3 for HD and in Table 4 for Full HD video.

Table 3. Comparison of encryption of HD video

Type of video	AES256		3DES	
	MPEG-2	MPEG-4	MPEG-2	MPEG-4
Static video	5.75	2.15	5.6	1.89
High rate dynamic	11.12	8.75	12.43	7.86

Table 4. Comparison of encryption of Full HD video

Type of video	AES256		3DES	
	MPEG-2	MPEG-4	MPEG-2	MPEG-4
Static video	12.58	2.051	12.15	2.21
High rate dynamic	17.15	11.12	16.85	12.91

The aim of this paper was compare impact of packet loss and encryption on video quality. Our results show that H264 codec achieves better results for encryption, but worse results for packet loss.

3 Conclusion

Security is a highly discussed topic nowadays, and protocols such as IPsec, VPN/SSL and SRTP are becoming more and more frequently used to secure the content of voice or video, so computational mathematical models should handle this new situation.

The aim of this work was to bring a detailed view of the performance of video streaming over an IP-based network. We compared quality of video with packet loss and encryption, too. The measured results showed the relation between the video codec type and bitrate to the final video quality. It showed differences between encryption ciphers and compare quality of security transmission of video.

Our future works in security will focus on impact of other kind of encryption video. We want focus on technologies MPLS VPN and OpenVPN.

References:

1. Chan, M.CH., Ramjee, R.:TCP/IP Performance over 3G Wireless Links with Rate and Delay Variation. In SPRINGER. Wireless Networks, Volume 11, 2005, pp. 81-97, DOI 10.1007/s11276-004-4748-7

2. Netem. Linux Foundation. Available at: <http://www.linuxfoundation.org/collaborate/workgroups/networking/netem>
3. Loke, H.M., Ong, P.E., Lin, W., Lu, Z., Yao, S.: Comparison of Video Quality Metrics on Multimedia Videos. In: IEEE International Conference on Image Processing, 2006. Atlanta: IEEE, 2006, pp. 457-460. ISBN 1-4244-0480-0. DOI: 10.1109/ICIP.2006.312492
4. Uhrina, M., Hlubik, J., Vaculik, M.: Correlation Between Objective and Subjective Methods Used for Video Quality Evaluation, In Journal Advances in Electrical and Electronic Engineering, Volume 11, Number 2, December 2013, ISSN: 1804-3119
5. Uhrina, M., Hlubik, J., Vaculik, M.: Impact of Compression on the Video Quality. In Journal Advances in Electrical and Electronic Engineering, Volume 10, Number 4, December 2012, ISSN: 1804-3119
6. Bovik, A.: Handbook of image and video processing. 2nd ed. Burlington: Elsevier Academic Press, 2005, xv, 1372 s. ISBN 01-211-9792-1

My Papers:

- J. Frnda, L. Sevcik, M. Uhrina, M. Voznak, *Network Degradation Effects on Different Codec Types and Characteristics of Video Streaming*, In Journal Advances in Electrical and Electronic Engineering, Vol. 12, Issue 4, pp. 368-376, (**SCOPUS, SJR=0.239**) DOI:10.15598/aeec.v12i4.1218
- M. Uhrina, J. Frnda, L. Sevcik, M. Vaculik, Impact of H.264/AVC and H.265/HEVC Compression Standards on the Video Quality for 4K Resolution, In Journal Advances in Electrical and Electronic Engineering, Vol. 12, Issue 4, pp. 377-383, (SCOPUS, SJR=0.239) DOI: 10.15598/aeec.v12i4.1216
- J. Frnda, M. Voznak, L. Sevcik, Impact of packet loss and delay variation on the quality of real-time video streaming, In SPRINGER Telecommunication Systems , 17 April 2015, DOI 10.1007/s11235-015-0037-2 , pre-published, SCIE, IF=1.163 (2013)
- J. Frnda, M. Voznak, L. Sevcik, P. Fazio, Prediction Model of Triple play services for QoS Assessment in IP Based Networks, In Journal of Networks, Vol. 10, No. 4, pp. 232-239, April 2015, DOI 10.4304/jnw.10.4.232-239 SCOPUS, SJR=0.316 (2013)
- L. Sevcik, D. Uhrin, J. Frnda, M. Voznak, H. Toral-Cruz, M. Mikulec, S. Jakovlev, Encryption for confidentiality of the network and influence of this to the quality of streaming video through network, In Proc. SPIE. 9497, Mobile Multimedia/Image Processing, Security, and Applications 2015, 94970A, Baltimore, Maryland, USA. (May 21, 2015) doi:10.1117/12.2177555 WoS, SCOPUS, SJR=0.203 (2014)
- M. Voznak, M. Prokes, L. Sevcik, J. Frnda, H. Toral-Cruz, S. Jakovlev, P. Fazio, M. Mehic, M. Mikulec, Vulnerabilities in GSM technology and feasibility of selected attacks, In Proc. SPIE 9456, Sensors, and Command, Control, Communications, and Intelligence (C3I) Technologies for Homeland Security, Defense, and Law Enforcement XIV, 94560T, Baltimore, Maryland, USA. (May 23, 2015) doi: 10.1117/12.2177111 WoS, SCOPUS, SJR=0.203 (2014)
- L. Sevcik, M. Voznak, J. Frnda, QoE Prediction Model for Multimedia Services in IP Network Applying Queuing Policy, International Symposium on Performance

- Evaluation of Computer and Telecommunication Systems, July 6-10, 2014, Monterey, CA, USA, ISBN 1-56555-354-3, pp. 593-598. (SCOPUS , IEEE-Xplore)
- J. Frnda, M. Voznak, L. Sevcik, Network Performance QoS Prediction, In SPRINGER Advances in Intelligent Systems and Computing AISC, Volume 297, 2014, pp. 165-174, DOI 10.1007/978-3-319-07776-5_18 (SCOPUS, SJR=0.135)
 - L. Sevcik, K. Tomala, J. Frnda, M. Voznak, QoS of Triple Play Services in LTE Networks, In SPRINGER Advances in Intelligent Systems and Computing AISC, Volume 298, 2014, pp. 25-33, 10.1007/978-3-319-07773-4_3 (SCOPUS, SJR=0.135)
 - J. Chun-Wei Lin, L. Yang, P. Fournier-Viger, J. FRNDA, L. SEVCIK, M. VOZNAK, An Evolutionary Algorithm to Mine High-Utility Itemsets, In Journal Advances in Electrical and Electronic Engineering, Vol. 13, Issue 4, (SCOPUS, SJR=0.239) DOI:10.15598/aeec.v13i4.1471
 - M. Uhrina, J. Frnda, L. Ševčík, M. Vaculík, The impact of GOP pattern and packet loss on the video quality of H. 264/AVC compression standard, In Advances in Neural Networks, Fuzzy Systems and Artificial Intelligence, ISSN: 1790-5109 ISBN: 978-960-474-379-7
 - J. Frnda, M. Voznak, L. Sevcik, Impact of packet loss and delay variation on the quality of real-time video streaming, In SPRINGER Telecommunication Systems , Volume 62, Issue 2, 2016, pp. 265-275. DOI 10.1007/s11235-015- 0037-2. SCIE, IF 0.822 (2015/Q3), SJR 0.0566 (2015/Q2)
 - J.C.-W. Lin, W. Gan, P. Fournier-Viger, L Yang, Q. Liu, J. Frnda, L. Sevcik, M. Voznak, High Utility-Itemset Mining and Privacy-Preserving Utility Mining, In ELSEVIER : Perspectives in Science , Vol. 7, March 2016, pp. 74-80. DOI: 10.1016/j.pisc.2015.11.013
 - T.-Y. Wu, J.C.-W. Lin, C.-M. Chen, Y.-M. Tseng, J. Frnda, L. Sevcik, M. Voznak, A brief review of revocable ID-based public key cryptosystem, In ELSEVIER : Perspectives in Science , Vol. 7, March 2016, pp. 81-86. DOI: 10.1016/j.pisc.2015.11.014

IoT LoRa Gateway on System for Embedded Devices

Jiri Slachta and Miroslav Voznak

Department of Telecommunications, FEECS,
VŠB – Technical University of Ostrava, 17. listopadu 15,
708 33 Ostrava – Poruba, Czech Republic
{jiri.slachta, miroslav.voznak}@vsb.cz

Abstract. In these days there is undergoing massive adoption of Internet of Things in almost every place. Delivered functionality from this technology comprises of different variants of sensors of any kind (from light detectors, energy metering to mobile devices, cars or even the whole houses) delivering the data through the radio layer to cloud-based centers which provides their remote control and management in the form of SaaS (Software as a Service). Since this technology is about having control over the obtained data it is important to keep in mind issues of personal security, sensor security and privacy issues in general. This article focuses on the detailed aspects of the creation of IoT gateway prototype based on OpenWrt platform in the mostly used use-case by ISP's.

Keywords: LoRa, LoRaWAN, IoT, OpenWrt, embedded devices

1 Introduction

Nowadays there is a tendency to deploy intensively sensor networks in which information and communication systems meets new challenges. In the light of the difficulties, these systems are invisibly embedded into the environment as a completely transparent, infrastructure role. The paradigm of Internet of Things (IoT) leads to providing the whole infrastructure mainly because of the simplicity of the usage of service: from deploying sensors, easiness of user interface controlling the sensors to regular payments for IoT services as an IaaS and SaaS (Infrastructure and Software as a Service). Mostly this centralized, operator solution is not usually the most modifiable and the most secure since the data from sensors are decrypted at the end of infrastructure. A solution that would provide the possibility to build the infrastructure at low cost or decentralized solution would lead to higher variability and modularity itself. Cloud computing and data analysis try to obtain the most valuable commodity, the data from users. In this article, we are focusing on extending the existing platform to operator solution with the proposal of the movement to the decentralized variant.

In order to reduce costs for maintaining communication systems, both physical devices and services running on them, many companies make decision on moving the service infrastructure to cloud service providers. Nevertheless, during the movement of infrastructure to third party several questions might arise.

Services in cloud infrastructure were designed to be used for everyone, but they usually lack the broad configurability. In addition to these issues the security questions has to be resolved, since the infrastructure is not under the control. During the years of development, a platform to address the mentioned issues has been created [4], [5]. Among desired characteristics belongs an easy integration of such device into almost any computer network. In mid of 2011, a new project (BESIP) was established under strong support of the CESNET association (Association of Czech universities and Academy of Science), aiming on a robust and secure VoIP telephony infrastructure with additional key components, that makes this solution easily adaptable and configurable even without the deep knowledge of the technologies used by the components. It also aims to be a scalable solution with unified configuration in mind[4]. The given name BESIP has had to be changed to BEESIP (The Bright Efficient Embedded Solution for IP Telephony) because registration of our BESIP trademark was rejected by the Czech Industrial Property Office due to the same existing trademark in field of public transport.

2 Creation of IoT gateway

2.1 BeeSIP platform and architecture

One of the biggest challenges during BEESIP development was to create or modify any existing Linux distribution to serve our expectations. We needed to create an environment that would be fully customizable to any purpose and also to be easily maintainable through the time the BEESIP would be developed. The advantage of portability to any platform was also welcomed. The choice of Linux distribution we wanted to modify fell on OpenWrt Linux distribution. The reason why we chose that system was the approach for building firmware, the toolchain, cross-compiler and all applications are downloaded, patched and built by scratch. This means that OpenWrt does not contain any source code, it does only have its build system with templates, patches and Makefiles with procedures how to build a system and its packages for targeted device. This approach allows us to create custom procedures for build system and packages that can be modified at any stage.

A simplified view on BEESIP architecture is depicted in Fig.1 which describes how the architecture is designed. The first block, the build system, is a wrapper on the top of the OpenWrt build system. It is designed for easy creation of firmware images within the single text file which describes what should be built for specific architecture and device we are targeting on. The secondary part of BEESIP is the OpenWrt Linux distribution which uses packages that provides desired functionality. In this case to provide modules from packages that serves as PBX, monitoring system, security system, management system and the core connecting modules among themselves.

The architecture of BEESIP system focused primarily on providing multimedia services, such as VoIP telephony. Administrators of this services have to

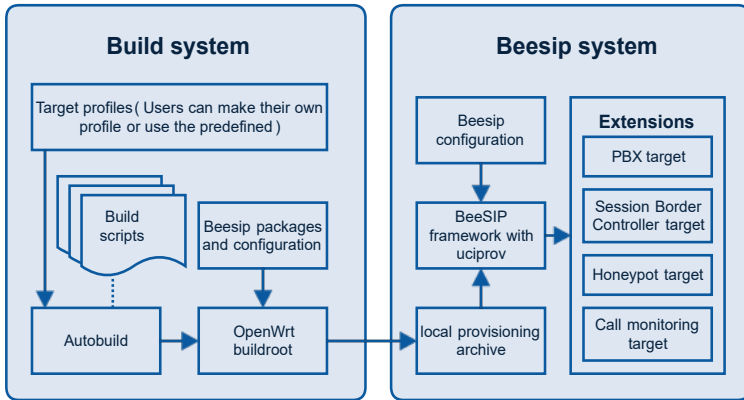


Fig. 1. BeeSIP architecture.

ensure if the content is delivered reliably, securely and the data should also follow given quality parameters as well. In the beginning of the project the first version of monitoring system was proposed [6].

2.2 Build system

Before the concept of BEESIP system is described, it is necessary to introduce the build system which reduces the building procedure into one script call. As said above, BEESIP is based on GNU/Linux distribution OpenWrt which is built on top of the OpenWrt Buildroot. Buildroot is a set of Makefiles and files that allows to compile cross-compilation toolchain and to generate by that toolchain resulting cross-compiled applications into a root filesystem image to be used in the targeting device. Cross-compilation toolchain is compiled by host compilation system which is provided by any GNU/Linux distribution.

In the beginning of BEESIP development we met issues that were holding us back. We could not test all changes immediately, we had to recompile all code and generate images nearly always when we ported new application, modified post installation scripts or when cross-compilation toolchain has changed. Also, the system behaves differently during testing if it is new root filesystem image, or modified root filesystem that has been run more than once. At least those issues led us to create an easy interface that will ease the creation, automation and functional testing for system images.

BEESIP build system is a set of scripts, Makefiles and definition files that make an easy interface to OpenWrt Buildroot. We can consider the main Makefile to be as a core of the BEESIP build system. It performs all atomic operations with OpenWrt Buildroot, works with source code management systems (to update/revert/any operation with local copies of OpenWrt source codes), patches OpenWrt Buildroot and executes images as virtual machines. Those commands might be used by any user or by autobuild scripts, which will be described after. On the top of the core Makefile is autobuild.sh script. This script calls all atomic

operations within more complex parameterized operations whose variables are defined in specific target files. Those target files are user defined and on the basis of those files are configuration files for OpenWrt Buildroot created. Once we have configuration files the system images could be created by calling `auto-build.sh` script with command `build` and parameter containing the name of the target file. The following simplified example shows, how to create target file.

2.3 Configuration provisioning

The impetus for development of provisioning tool arose during the period when firmware images created by BEESIP build system were deployed to computers, routers and wireless access points. Those machines were not configured for target networks, which were supposed to be deployed on. Because the target configuration does not depend on a person which builds the system, but on the network administrator, then configuration should lay outside of a BEESIP firmware image. The target configuration could be stored on a server designated within an URI in a variable from TXT record which is obtained from static URL provided by BEESIP build system. This solution is replicable for any protocol which allows distribution that kind of information (LLDP, DHCP or any other else). If a device knows where to obtain configuration from, then it can obtain configuration data from ordinary transport protocols designated in provisioning URI. The benefits that BEESIP draws from OpenWrt builds upon the UCI configuration system which is based on plain text configuration files with firmly defined structure. During the development of any application or any system the developers needs the ease up the process of deployment of applications and its configuration, thus the UCI provisioning tool was developed, known under abbreviation *uciprov*.

2.4 Extending existing platform by adding IoT module

In the networks used for Internet of Things there are three main choices used for obtaining the data from sensors - existing mobile networks (LTE, GSM), SigFox and Lora Technology. In this article the creation of LoraWAN gateway is described.

LoRa Technology is primarily designed to provide LP-WAN network with features needed to support low-cost, low-powered and secure bi-directional communication for Internet of Things and machine-to-machine communication on large scale and area. Such networks are usually described as LP-WAN networks. LoRaWAN standard specifies the network architecture to a star-of-stars topology. Gateways represents a transparent bridge relaying messages between end-devices and a central network server in the backend.

During the development of LoRaWAN stack on BeeSIP platform several alternative implementations have been released. Due to the complications in porting the packet forwarder to OpenWrt platform, the development of Lora server, as the main component of the LoRa network, stopped and the main development focus was on the packet forwarder as a transparent bridge for relaying messages.

Fig. 2 depicts the architecture of LoRaWAN network, in which as a Network Server was used LoRa Server[1] and as a bridge between packet forwarder and Network server was used LoRa Gateway Bridge [2].

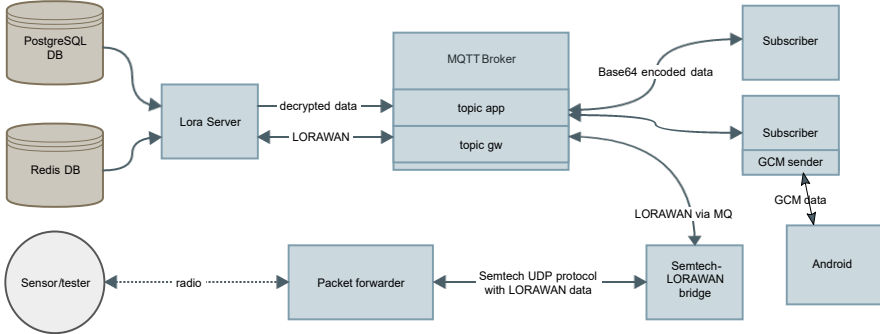


Fig. 2. Current architecture of LoraWAN network.

The packet forwarder, which communicates directly with the sensors, forwards the LoRaWAN data encapsulated in Semtech JSON UDP protocol.

The main difficulties for this application lies in:

- porting the following software:
 - HAL driver **libloragw**,
 - library for interfacing SPI/I2C devices **libmpsse**,
 - packet forwarder.
- optimization of the software functionality on non-supported OS.

With all prerequisites implemented in ported packages for desired OpenWrt platform we can create custom target for the build system of BeeSIP. Following code describes the creation of it.

```
$(eval $(call BeesipDefaults,x86_32))

OWRT_NAME=chaos_calmer
TARGET_NAME=iot_${(BEESIP_VERSION)}-${(TARGET_CPU)}
OWRT_IMG_PROFILE=Generic
BEESIP_PACKAGES+=\
    kmod-usb-serial-ftdi=y libmpsse=y libftdi=y packet-forwarder=y
```

After the creation the target file the build system is able to build the factory image for the targeted device. With all prerequisites inside the system image the device is able to communicate with LoRa Gateway Bridge[2] directly with straightforward configuration.

```
"gateway_conf": {
```

```

"gateway_ID": "AA555A0000000000",
"server_address": "IP address of LoRa Gateway Bridge",
...
}

```

The contribution of this work lies in the proposal of creation custom gateway in the overall concept of the LoRaWAN network on the OpenWrt/Beesip platform which can help networkers, researchers and developers to easily deploy the adaptable solution to any network with the full benefits of OpenWrt/BeeSIP platform.

3 Conclusion

This paper describes several ideas for Internet of Things on the BeeSIP system which is based on one of the popular Linux distributions for the embedded devices. The developed system is fully adaptable, and each component is reusable on any other Linux distribution.

Described solution realizes elements of operator infrastructure of LoRa Network which are not suitable for local infrastructure at the customer level (e.g. family houses). Even if someone would think about deployment of this solution, the complexity of it is excessive. Despite the fact, that network operators enforce their solution centralized, the current development of this project moves the Network Server (Lora Server) at the level of packet-forwarder. With server-to-server integration along with the provisioning configuration makes the solution decentralized from the data-layer and possibly centralized from the configuration-layer to keep the customer data at his level. Also the extensibility of the BeeSIP platform can be easily used for creation of gateway using sensors on multiple technologies and protocols.

References

1. Orne Brocaar, Project Lora Server, Repository with image and source codes, Available on URL: <https://github.com/brocaar/loraserver>
2. Orne Brocaar, Project Lora Gateway Bridge, Repository with image and source codes, Available on URL: <https://github.com/brocaar/lora-gateway-bridge>
3. Jiri Slachta, Project BeeSIP, Repository with image and source codes, Available on URL: <https://bitbucket.org/liptel/beesip>
4. M. Voznak, J. Slachta, L. Macura L and K. Tomala, "Advanced solution of SIP communication server with a new approach to management," *Telecommunication Systems*, 9 p., 2014 (Article in Press).
5. M. Voznak, J. Slachta L. Macura, "Development of advanced concept of voice communication server on embedded platform," *International Journal of Mathematical Models and Methods in Applied Sciences*, vol. 7, no. 2, 2013, pp. 103-110.
6. M. Voznak, K. Tomala, J. Vychodil, J. Slachta, "Advanced concept of voice communication server on embedded platform," *Przegląd Elektrotechniczny*, vol. 89, no. 2 B, 2013, pp. 228-233.

Design of Multilayer Neural Network for Speaker Identification

Jaromir Tovarek¹, Miroslav Voznak¹, and Erik Chromy²

¹Department of Telecommunications, FEECS,

VŠB – Technical University of Ostrava, 17. listopadu 15,

708 33 Ostrava – Poruba, Czech Republic

{jaromir.tovarek, miroslav.voznak}@vsb.cz ²Department of Telecommunications,

Faculty of Electrical Engineering and Information Technology, Slovak University of

Technology, Ilkovicova 3, 812 19 Bratislava, Slovak Republic

erik.chromy@stuba.sk

Abstract. This article discusses the impact of multilayer neural network parameters for speaker identification. The main task of speaker identification is to find a specific person in the known set of speakers. It means that the voice of an unknown speaker (wanted person) belongs to a group of reference speakers from the voice database. One of the requests was to develop the text-independent system, which means to classify wanted person regardless of content and language. Multilayer neural network has been used for speaker identification in this research. Artificial neural network (ANN) needs to set parameters like activation function of neurons, steepness of activation functions, learning rate, the maximum number of iterations and a number of neurons in the hidden and output layers. ANN accuracy and validation time are directly influenced by the parameter settings. Different roles require different settings. Identification accuracy and ANN validation time were evaluated with the same input data but different parameter settings. The goal was to find parameters for the neural network with the highest precision and shortest validation time. Input data of neural networks are a Mel-frequency cepstral coefficients (MFCC). These parameters describe the properties of the vocal tract. Audio samples were recorded for all speakers in a laboratory environment. Training, testing and validation data set were split into 70, 15 and 15 %. The result of the research described in this article is different parameter setting for the multilayer neural network for four speakers.

Keywords: Accuracy, ANN, MFCC, Speaker identification, Validation time

1 Introduction

The human voice is often used for speaker recognition in biometrics. This group includes fingerprints, hand geometry, genetic structure, retina, handwriting and many others. Compared with techniques that use magnetic cards, keys, badges, codes and passwords learned by heart, biometric characteristics should be more reliable, unmistakable in some cases. This fact stems from the uniqueness of each person's biometric.

Biometric characteristics are divided into two groups. Physiological biometrics uses characteristics that are almost unchanged throughout human life. Exceptions are caused bodily injury or surgery. This group includes mentioned fingerprints, retina, genetic

structure and the like. The second group consists of behavioral biometrics that characterizes human behavior in a particular situation. It includes voice, heartbeat, handwriting or signature. Recognizing humans based on behavioral characteristics is much more complex problems, such as fingerprint recognition. Behavioral characteristics are relatively quite affected by human mood and an environment. This fact is the main reason that fingerprint is a standard application in biometrics while there is no reliable and secure way for speaker recognition in all possible situations. Speaker recognition system with higher level of reliability requires several conditions:

- Speaker should not attempt to change his voice.
- The conditions for recording the speech signal, and the processing techniques are known and can be affected.
- Speech for training system has been recording similar conditions as speech signal speaker recognition.
- Verification threshold must be set for each application separately (regarding security requirements).

The accuracy of the system can be increased also with following restrictions:

- The speaker must voluntary cooperate with the system.
- Limit fraudsters use sophisticated tools to penetrate.
- Limitation of the content (number of words) for the speaker recognition.

Biometric identification based on the human voice consists of three main steps. The process begins with the biometric sample (recording of speech), followed by a speech processing (features extraction). The final step is the classification of the speaker. This article discusses how to optimize the parameters of the neural network, based on the speaker verification accuracy. [1]

2 Methods

2.1 Inputs

Speech of four adult objects (26 - 28 aged) was recorded for our experiment. The recordings were made in the laboratory without background noise. The database consists of 40 recordings (10 recordings each object). Each object spoke different content. The duration of recording per user was circa 20 seconds. The speech signal was recorded as a waveform audio file format with 8 kHz frequency and 32-bit sampling. [1]

2.2 Pre-Processing

The next step was prior to processing of speech recordings. Pre-processing consists of four phases show in Fig. 1: removing DC component (takes no useful information and can be for further processing interference), pre-emphasis (used to compensate frequency characteristics), segmentation (speech signal is unsteady, so it needs to be divided into smaller 25 ms frames) and smoothing function (remove sharp transitions between frames). [2]

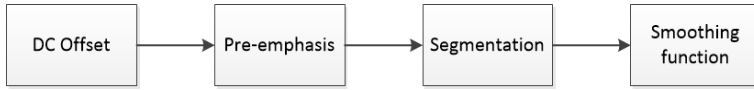


Fig. 1. Pre-Processing diagram of speech signal.

2.3 Speech Processing

Many parameters are used for speech parameterization. The most commonly used are the cepstral coefficients for their excellent performance.

Human hearing is non-linear. This feature is compensated by triangular filters with nonlinear frequency distribution (Eq. 1). Mel filter bank is used in calculating the Mel-Frequency Cepstral Coefficients (MFCC), which are defined by Eq. 2 and the process of cepstral analysis is shown in Fig. 2. Besides frequency scaling, MFCC also meet the following requirements: robustness - parameters do not change over time, significance - clearly define the parameters of the speaker (vocal tract), practicality - relatively fast calculation. [2]

$$f_m = 2595 \log \left(1 + \frac{f}{700} \right), \tag{1}$$

where f is the frequency in hertz scale and f_m is frequency in mel scale.

$$c_m(j) = \sum_{i=1}^{M^*} \log y_m(i) \cos \left(\frac{\pi j}{M^*} (i - 0,5) \right), \text{ for } j = 0, 1, \dots, M, \tag{2}$$

where $y_m(i)$ is the filter response, M^* represents a number of bands in the filter bank, and M is the number of cepstral coefficients. We used 13 coefficients, which represents voiceprint of one segment pre-processed from speaker recordings.



Fig. 2. Block diagram of Mel-Frequency Cepstral Coefficients algorithm.

2.4 Classification

As mentioned above, the final step in the process of speaker recognition is classification. We used feedforward multilayer neural network with backpropagation. The network consisted of three layers (input, hidden and output layer). The number of neurons in the input layer is determined by the number of extracted parameters for a given speech segment. The number of output layer neurons is determined by the number of reference

speakers from a closed set. The number of neurons in the hidden layer was gradually adjusted in the range of 5 to 15. For the activation functions were used: sigmoid, symmetric sigmoid, a stepwise linear approximation of sigmoid. Effect of the activation function steepness on accuracy has been investigated only marginally. Backpropagation method is based on seeking the minimum of cross-entropy error function E defined in Eq. 3, where y_j is real and o_j is required response of j^{th} neuron of output layer. Equation 4 defines the changes of weights. [3], [4], [5]

$$E = \frac{1}{2} \sum_{i=1}^p \sum_{j=1}^m [y_j \ln(o_j) + (1 - y_j) \ln(1 - o_j)], \quad (3)$$

$$\Delta w_i = -\eta \frac{\partial E}{\partial w_i} + \mu \Delta w'_i, \quad (4)$$

where η is the learning coefficient, coefficient μ influence changes weights from the previous step in the interval $\langle 0, 1 \rangle$, $\Delta w'_i$ change synaptic weights from the previous step.

3 Results

The aim of this research was to identify the best settings of feedforward ANN with backpropagation for speaker identification in a closed set of speakers (objects). A set of objects consists of four adult males aged 26-28 years. Network parameters were selected based on the classification accuracy of validation data and validation time. Results are shown in Tab. 1. Choice of four activation functions was the first step of the experiment, mentioned in Sec. 2.4. Validation time exhibits minimal changes for different activation functions. This parameter is not considered in further analysis. [1]

Table 1. Validation accuracy and validation time for different activation function.

Activation function	sigmoid	sigmoid stepwise	sigmoid symmetric (tanh)	sigmoid symmetric stepwise
Accuracy [%]	good (74–78)	worst (66–76)	best (80–85)	good (76–79)
Validation time [s]	0.0274	0.0265	0.0275	0.0272

The test of activation function steepness was also executed. Influence of steepness was marginal. Steepness parameter λ was set on default value 0.5.

Second part of the experiment. The aim was increasing the number of neurons in the hidden layer. Verification accuracy, cross-entropy error and number of epochs required for training are shown in Tab 2. Training was stopped after 6 epochs without decreased cross-entropy error (stop rule).

One of the prerequisites is increasing accuracy of verification in a larger number of neurons, but the theory of the neural network says about the accuracy limits of the network. Therefore, we expect stagnation of precision with increased number of neurons. The measured values are shown in Fig. 3 below. The curve shows that the best setup of

Table 2. The accuracy of verification due to the number of neurons in the hidden layer.

Number of neurons in hidden layer	5	6	7	8	9	10	11	12	13	14	15
Epoch [-]	40	33	58	72	61	67	50	73	55	71	49
Cross-entropy [-]	0.174	0.154	0.126	0.123	0.118	0.115	0.122	0.113	0.106	0.111	0.123
Accuracy [%]	67.4	71.5	74.3	78.1	79.1	81.1	78.7	79.8	82.1	81.4	80.3

ANN provides 10 neurons in the hidden layer. In our case, the ANN with a larger number of neurons does not increase verification accuracy (fluctuation of 1-2 percent). On the other hand, expansion of the network structure means an increase in computational complexity.

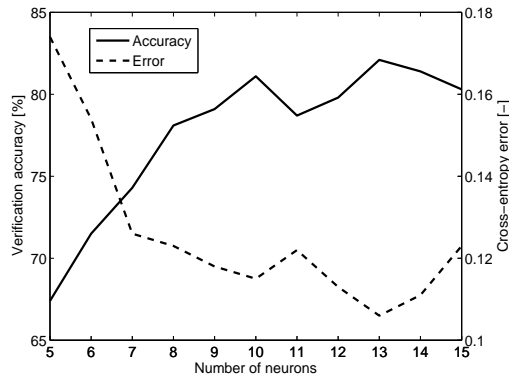
**Fig. 3.** Precision and error rate of feedforward neural network for a different number of neurons in the hidden layer.

Table 3 shows the confusion matrix for ANN with 10 neurons in the hidden layer and symmetric sigmoid activation function with 0.5 steepness. Classes represent individual speakers (objects). Output classes represent the real output of the classifier. The required outputs are represented by target class. Highlighted values indicate recognition accuracy of each speaker (1-4) and the overall average accuracy (81.1 %). Speaker number one was the best recognizable with an accuracy of 87.4 %.

4 Conclusion and Discussion

The aim of our experiment was to verify the accuracy of speaker recognition using feedforward backpropagation neural network. As expected, it was found the correlation between the structural setting of the network and its accuracy. The input of neural network represents 13 MFCC calculated for each speech segment. Next step of the ex-

Table 3. Validation confusion matrix.

Output class	1	146 20.1 %	8 1.1 %	15 2.1 %	11 1.5 %	81.1 %
	2	3 0.4 %	131 18.0 %	4 0.6 %	3 0.4 %	92.9 %
	3	9 1.2 %	14 1.9 %	132 18.2 %	26 3.6 %	72.9 %
	4	9 1.2 %	13 1.8 %	22 3.0 %	180 24.8 %	80.4 %
		87.4 %	78.9 %	76.3 %	81.8 %	81.1 %
		1	2	3	4	
		Target class				

periment was testing different activation functions and a different number of neurons in the hidden layer.

The ANN classification accuracy represents successfully recognized speech segments of speakers (13 MFCC). Results bring approximately 81 % of precision for all of the speakers. These results were achieved by setting symmetrical sigmoid activation function with steepness 0.5 and the 10 neurons in the hidden layer. Improvement of the method can be achieved by removing voiceless segments of speech. We can predict that voiceless segments are not significant regarding speaker recognition. Due to the real application, it is appropriate to consider score over the entire recording. The final decision about the identity of the speaker is also simpler because we consider the close dataset of speakers. Speaker recognition system has to choose the one with the highest score. Future work will focus on the verification results in an increased number of speakers, where we expect similar results.

References

1. Tovarek, J., Partila, P., Rozhon, J., Voznak, M., Skapa, J., Uhrin, D., Chmelikova, Z. Optimization of multilayer neural network parameters for speaker recognition. Proceedings of SPIE - The International Society for Optical Engineering, 9850, 2016, DOI:10.1117/12.2223545
2. Partila, P., Voznak, M., Tovarek, J. Pattern Recognition Methods and Features Selection for Speech Emotion Recognition System. Scientific World Journal, 2015, DOI: 10.1155/2015/573068
3. Tovarek, J., Partila, P., Voznak, M., Mikulec, M., Mehic, M. Detection of Cardiac Activity Changes from Human Speech. Proceedings of SPIE - The International Society for Optical Engineering, 9496, 2015, DOI: 10.1117/12.2177282
4. Partila, P., Tovarek, J., Voznak, M., Safarik, J. Classification Methods Accuracy for Speech Emotion Recognition System. In: Springer Advances in Intelligent Systems and Computing AISC, Vol. 289, 2014, pp. 439–447, DOI: 10.1007/978-3-319-07401-6_44
5. Partila, P., Tovarek, J., Frnda, J., Voznak, M., Penhaker, M., Peterek, T. Emotional Impact on Neurological Characteristics and Human Speech. In: Springer Advances in Intelligent Systems and Computing AISC, Volume 298, 2014, pp. 527–533, DOI: 10.1007/978-3-319-07773-4_52

Czech Database of Real Speech Emotions

Dominik Uhrin¹ and Erik Chromy²

¹Department of Telecommunications, FEECS,
VŠB – Technical University of Ostrava, 17. listopadu 15,
708 33 Ostrava – Poruba, Czech Republic
dominik.uhrin@vsb.cz

²FEI – Slovak University of Technology, Ilkovicova 3, 812 19 Bratislava, Slovak
Republic
chromy@ut.feituba.sk

Abstract. In last year we dealt with enlargement of Czech speech emotion database and modification of evaluation tool. Our aim was to create export part of evaluation tool for easier export of data after evaluation of recordings; and also to eliminate improper and have more suitable sound recordings for training and testing systems of speech emotion recognition. These systems are able to detect human emotions in his voice. Detection of emotional state of human is useful in the security forces and emergency call service and the evaluation of the psychological state is the key factor for successful intervention. A quality database of sound recordings is very important for the creation of emotion recognition systems. There is lot of quality databases with acted emotions. It means that the recordings contain simulated emotions, not real. Our research aims at creating a database of the Czech emotional recordings of real human speech. Collecting sound samples to the database is only one of the tasks. Another one, no less important, is to evaluate the significance of recordings from the perspective of emotional states. The design of a methodology for evaluating emotional recordings credibility is described in this article. The results describe the advantages and applicability of the developed method.

Keywords: Emotion, Evaluation, Real emotion, Emotion database, Speech

1 Introduction

The speech is one of the most developed methods for information exchange between people. Therefore, in the last few years, developers, scientists and companies are trying to make the interaction between people and smart devices as natural as possible. Today smart devices offer voice and gesture control. It not only allows a user to give orders to execute something but also device has built-in sensors which can detect and record some parameters relevant not only for emotional and physical detection. Of course, an option for emotional and physical state detection is still developing, but use of emotion classifier can achieve it. In our case, we are using speech to detect the emotional state of the human. Speech offers a whole range of information which can be extracted with high accuracy. From this information, we can determine speaker age, gender, actual emotional state, speech deviations, etc. [1]. Emotion is a complex phenomenon which also includes experience. In general, emotion can be defined as a

change of psychological status which is triggered during achieving of some aim. We distinguish positive or negative emotion. Speech information extraction and its analysis can be used in different fields. For example in call centers (not only emergency), in government sectors like police, fire department and mainly military forces, create most emotional pressure on their employees. In order to create emotion recognition system, speech emotion samples are needed to train it. Nowadays a lot of emotional recordings databases exist, but a significant number of databases are based on simulated emotions by actors, not on real life emotions. Actors are mostly pronouncing same sentences and it guarantees the identical context of recordings. These recordings are more efficient for training emotion classifier but do not guarantee better results compare to real emotion. Here are some most known and recent emotion recordings databases: Humane [2], Emotional Prosody Speech and Transcripts, Danish Emotional Speech Corpus, Berlin Emotional Speech Database [3], Serbian Emotional Speech Database [4].

2 Design and Implementation

In this chapter, we will describe steps which were necessary to take, in order to find suitable recordings, process and evaluate them and then assess of results of evaluation.

2.1 Creation of Sample Database

The first step of the creation of speech emotion database, which contains emotions from real life situations that are not played by actors, is necessary to collect a lot of hours of raw sound recordings of radio and TV show broadcastings. To find records which include real emotion is very hard because people who are part of the show can pretend their emotional state, in which case we cannot talk about the real emotions. So there can be a situation. We have emphasized the process of picking right sound recordings. The preparation process of sound samples for evaluation was hard and also took long. It was necessary to handle a lot of hours of recordings and cut it into little chunks, so they could be evaluated correctly. Some of the recordings have been available on the official web pages archives of radio stations. Some of the television show broadcastings were downloaded from video share portal like Youtube (we used only sound track of video). All the emotion samples had to meet specific conditions set by authors. Each sample of database has the unique name. The name has to meet these three parameters. The first one is state of the emotion, which we think sample contains. We created database only for five emotion states because of the rest of states (boredom, disgust) it is difficult to find real emotion recordings or it is hard to recognize it. The second parameter is order number and last one is the gender of the speaker on sound recordings. The first iteration of speech database involved only four kinds of emotion, namely anger, happiness, sadness and neutral emotion [7]. Later in the second iteration, the fear was added as fifth emotion. The first iteration had around 200 samples and in the second iteration were added more than 200 recordings [7]. So the current number of samples in the database is 444. As an output format for database samples have been used waveform audio file. For audio files, we set these

parameters: 16-bit PCM (Pulse Code Modulation) coding, mono channel and sample frequency at the level of 16 kHz. For editing and cutting off source recordings, we used software Audacity.

2.2 Evaluation Tool

Next step in the building of emotion database was the creation of the tool for evaluation of database samples from which emotion database have been created after evaluation. We have chosen subjective method for evaluation. Subjective methods represent using of people to evaluate a few samples. The web page constitutes evaluation tool as a direct tool for evaluation connected with MySQL database for saving results of subjective evaluation. The web page consists of four pages. Invitation page, here in the background, the algorithm for newly added samples runs. We implemented load_file_list (\$directory, \$recursive) function which return list of files saved in sample directory. We used db_lookup(\$file) function for control if files from sample directory are included in the database. Next, if the database does not contain information about newly added samples, information are automatically written to the database using table1_insert(\$file_name) and table2_insert(\$file_name). The second page is evaluation page. It is the core of evaluating tool. It consists of html5 audio player for playing database sound samples and rollout menu for selection of state of emotion. A subject just plays recording selected by the algorithm and subsequently choose emotion in rollout menu by its decision. A result is sent to and saved in MySQL database. So first function counter_load() loads order number for next sample. Function generate_sample (\$count) loads sample for function audio(\$file1,\$directory_audio) which allows to play it. Then function mysql_query(\$query) updates table information and last one counter_update(\$count) save new order value in database. The last two pages of the tool are a termination and an error page. Beside web page tool also consist of MySQL database. As it was mentioned above, the database was used to save results of subjective evaluation. The database includes two connected tables. These tables are shown in figure 1.

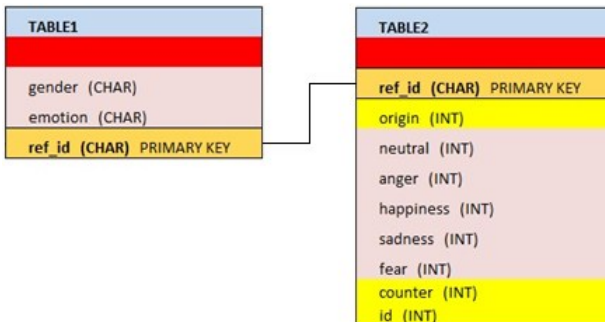


Fig. 1. The structure of MySQL database tables

The first table is dedicated to information about individual emotion samples. Ref_id column represents a unique name for a sample. The second table is dedicated to information about evaluation. The meaning of first one, ref_id, is same as in table one. Origin column represents how many times have been selected same emotion by sub-

ject for a sample as was originally selected by the authors during the process of creating database samples. The last two columns, counter and id are auxiliary variables. For connecting web page to the MySQL was used typical script `mysql_connect($host, $login, $pass)` and `mysql_select_db($db_name, $connection_active)`. The web page also logically contains scripts to perform queries by using `mysql_query()` with SELECT or UPDATE queries. The web pages are also using POST and GET forms to obtain data from previous page loads. For playing samples we used html5 audio player which we implemented in `audio($file,$directory_audio)` function. Using html5 audio player is much easier to implement and it is built-in part of a web browser.

2.3 Export Database Data Files

When all the database samples are evaluated a sufficient number of times, assessment data have to be extracted and analyzed. For this case, we prepared export web page which is also part of the evaluation tool. The web page is able to export database data in two forms. The short version exports `ref_id`, value of veracity, the level of veracity, the gender of a speaker and final emotion of sample. The full version of the database contains all the data from database table 2 and also information from short version table. Mentioned data can be downloaded in a form of Microsoft Excel, LibreOffice Spreadsheet and comma-separated-value file format. Also, the web page allows a user to download chosen sound files packed in a zip archive. A user has to select emotion or emotions of samples, choose a gender of a speaker in sample and range of veracity, lower and upper limit. The web page not only allows a user to export data but also enables him to display the short version table. In order to export or list data from the database, we had to implement a couple of functions. First two important functions are `mysql_query_list_data($low, $high, $gender, $selected_emotion)` and `mysql_query_database_data($low,$high,$gender,$selected_emotion)`. These two functions allow to perform MySQL queries and they return a result to create a short version and a full version table data. The first mentioned is used not only for export but also for displaying. Next function `table_write_output($result)` use output from `mysql_query_list_data($low, $high, $gender, $selected_emotion)` and display a short version table on the web page using HTML tags. Finally when we have had functions to get data from database we implemented function called `export_data($result, $low, $high, $data_kind, $data_format)`. It is the function which allows exporting of four kinds of files in plain text, Excel, Libre Spreadsheet and comma-separated-value formats. Last important function is for download sound samples in zip package, named `file_to_zip_download($result,$low,$high,$directory_audio,$selected_emotion)`. [8]

3 Results

The evaluation of database samples was made by subjects whose were represented by students in the age range from 18 to 26 years. Selection rate of each emotion kind for random sample shows table 1. After sample evaluation, it was necessary to assess results of sample evaluation. For each sample from the database, it was important to determine the assessment in percentage and final emotion which is based on this rate.

Table 1. probability of what was emotion selected.

<i>Emotion</i>	<i>Probability for one sample (%)</i>
Neutral	37,2
Anger	34
Happiness	12,6
Sadness	12,4
Fear	3,8

After we had implemented determining of veracity value, we had an idea to estimate a level of veracity for each sample. We defined three levels of veracity: low, medium, high. The low level has a range from 0 to 80 percent and represents samples that are not adequately validated or it is harder for a subject to determine emotional state. The medium level range is from 80 – 90 percent and samples in this range are suitable for training of the neural classifier. And the last one the high level has a range from 90 up to 100 percent is useful for learning of the neural classifier. Three final emotion databases have been created based on percentage range of these three levels. During the creation of process, emotion state of these samples have been subjectively selected by the authors, but after the process of evaluation, emotion state of some emotion samples have been changed in dependence on the assessment outputs. The first database with the high veracity of samples has the average value of veracity at 98.63 percent. It is suitable for learning of neural emotion classifier. This classifier is developing by colleague Mr. Partila at our university [1],[5],[6]. The second database of samples with medium veracity has the average value of veracity at 85.80 percent is also suitable for the neural classifier to verify its learning skills. And the last database of emotion samples with the low level of veracity has the average veracity value 59.57 percent is formed by samples that contain mixed emotions. This emotion database should be assessed more times to determine an emotional state of samples more precisely. Figure 2 shows a difference in count of individual levels of veracity within one emotional state. In the case of neutral emotion, it is almost exponential decrease. The same thing occurs when we look at happiness, sadness and fear. Number of fear samples is low, because it is hard to find real fear recordings.

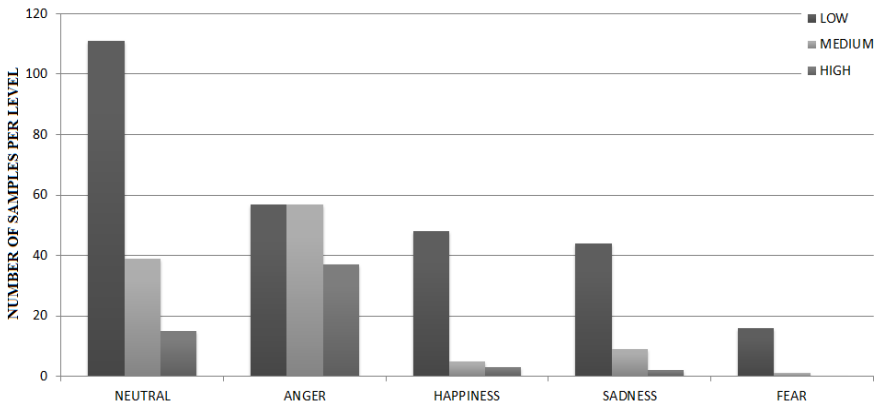


Fig. 2: Number of samples per emotion state and also per veracity level

4 Conclusion

The aim of this paper was to bring view on how to build real emotion database which can be used for further development of emotion recognition field. Our goal was to enlarge speech emotion database and also modify evaluation tool. In this second iteration, we added more than 200 samples and the final number of recordings in all three databases is 444. We repaired some bugs from previous iteration and modify code to make it more effective and precise. We had to analyze evaluation results, so we implemented export page to make this analysis automatically. Results of analysis can be exported in four different file formats. Base on the analysis and our decision, we divided the database into three smaller final emotion databases. This was done in first iteration [7], but percentage range for the levels has been changed. The idea of all this was to create the basis for an open database of real emotions in a way that any subject could access database and have the option to insert samples that will be evaluated. For a possible future development, the tool has to be modified for inserting samples with strictly defined parameters, for automatic sending of results of sample assessment and the tool should be publically accessible.

5 References

1. P. Partila, M. Voznak, "Speech Emotions Recognition Using 2-D Neural Classifier", *Nostradamus 2013: Prediction, Modeling and Analysis of Complex Systems*, Springer International Publishing, 2013, Pages 221-231.
2. D. Ververidis, C. Kotropoulos, "A review of emotional speech databases", *Proc. Panhellenic Conference on Informatics (PCI)*. 2003, Pages 560-574.
3. F. Burkhardt, A. Paeschke, M. Rolfes, W. Sendlmeier, B. Weiss, "A Database of German Emotional Speech", *Interspeech 2005 – Eurospeech, 9th European Conference on Speech Communication and Technology*, September 2003, Pages. 1517–1520.
4. S.T. Jovičić, Z. Kašić, M. Đorđević, M. Rajković, "Serbian emotional speech database: design, processing and evaluation", *9th Conference Speech and Computer, SPECOM 2004*, St. Petersburg, Russia, Pages 77–81.
5. M. Voznak, P. Partila, M. Mehic, S. Jakovlev, "Recognizing Emotions from Human Speech Using 2-D Neural Classifier and Influence the Selection of Input Parameters on its Accuracy", *21st Telecommunications Forum Telfor*, art no. 6716272, November 2013, Pages 482-485.
6. P. Partila, M. Voznak, M. Mikulec, J. Zdralek, "Fundamental frequency extraction method using central clipping and its importance for the classification of emotional state", *Advances in Electrical and Electronic Engineering*, Volume 10, Issue 4, 2012, Pages 270-275.
7. Uhrin D., Partila P., Voznak M., Chmelikova Z., Hlozak M. and Orcik L., "Design and implementation of Czech database of speech emotions", *22nd Telecommunications Forum Telfor (TELFOR)*, Belgrade, 2014, Pages 529-532.
8. Uhrin D., Chmelikova Z., Tovarek. J., Partila P., Voznak M., "One approach to design of speech emotion database", In *Proc. SPIE 9850, Machine Intelligence and Bio-inspired Computation: Theory and Applications X*, 98500B, 2016.

Common Issues with Simulation of Antenna Systems in COMSOL Multiphysics

Zdeněk Urban, Lukáš Wežranowski, and Lubomír Ivánek

Department of Electrical Engineering, FEECS,
VŠB – Technical University of Ostrava, 17. listopadu 15,
708 33 Ostrava – Poruba, Czech Republic
{zdenek.urban, lukas.wezranovski, lubomir.ivanek}@vsb.cz

Abstract. This paper deals with most common issues, with which the user of COMSOL Multiphysics and RF module may encounter. The purpose of RF module in the mentioned software are shortly shown in this paper. Some basic advices for users are mentioned here. Also, very short examples of two antenna simulations are in this paper. First of the examples is the magnetic loop antenna, the second one is the rectangular patch, both with complex optimization and with referring to instructions guides.

Keywords: COMSOL Multiphysics, RF module, iteration, simulation, optimization, PML, antenna system, magnetic loop antenna, patch antenna.

1 RF module - most common issues and very basic guidance

RF module is the most important part of COMSOL Multiphysics. Compared to traditional electromagnetic modeling, we can antenna systems, simulating antenna environment and mostly for every application of radio & frequency problems. So, we can quickly and accurately simulating electromagnetic wave propagation and resonant behavior. Engineers are able to compute electromagnetic field distributions, transmission, reflection, impedance, Q-factors, S-parameters, and power dissipation. Simulation offers the benefits of lower cost combine also extend model to include effects such as temperature rise, structural deformations, and fluid flow.

At first is the most important exactly know what we want to achieve. If we use the popular trial and error method, in most cases this lead only to waste of the time. This is caused by the complexity of the COMSOL Multiphysics software. The better way is to read the guides and examine tutorials to every step of the draft of antenna system.

Entering parameters by the section Definition – parameters is the best way how to avoid many mistakes. The user can creates as many variables as he wants. This can greatly facilitate and streamline work. In the next work, this way of work allows to use a lot of variables and refer to them, and no need to change everything by manually retyping.

Computing power

Software COMSOL is very expensive to computing power. The more precise specification of the problem and determine more precisely the limitation calculation significantly reduces the calculation time. For example if the user has some mistakes in the expression it is better for him when the error occurs already after 2 hours than after 3 days

With right adjustment the calculation may converge faster like this in Fig. 1 (left side), optimization is performed in 5 steps and the calculation goes relatively steeply to the target. One step can be done in about 7 iterations.

If the values are set wrong, the calculation may not converge - Fig. 1 (right side). That means the first step is not finished. If the number of iterations is not limited, the calculations still running and for example after 3 days not coming to the end.

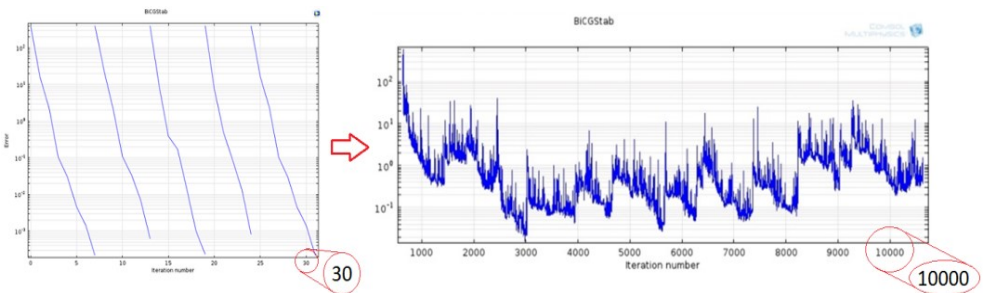


Figure 1. Comparison of right and wrong convergence in one case.

As we can see in the Figure 1, it is one same model but one the parameter settings is right and the other not. In this case the model on the left was calculated about 2 hours, on the right side was calculated about 3 days. After this time, user shut down the calculating process manually.

Instructions for this issue can be only that user must beware to the input data. If this issue happens, it can be only detected by the signaling of the calculation, because it is regularly repeating.

Proper MESH

Correct mesh building of the model is one of the most important steps this setting can have a fatal consequences to the calculation power.

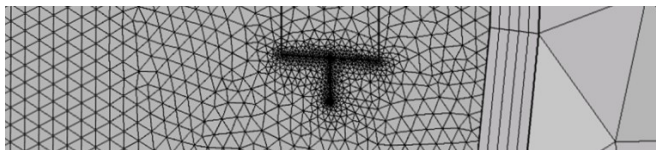


Figure 2. Different levels of meshing the model.

With the settings of maximum element size (minimum element size) we can set the size of mesh. In the COMSOL guide is recommended to use, for the air material, size

less than $0,2x$ lambda. This provision is important, it serves for simplify the calculations in places where it is not needed and use more complicated mesh to parts what we need perfectly calculate like in Fig. 2. In this figure we can see different meshes, on the antenna it is more accurate, and in the air around antenna it is less accurate and least accurate it is on the PML layer.

PML layer

PML (Perfectly matched layer) must be set up in every models, which use the radio frequency waves.

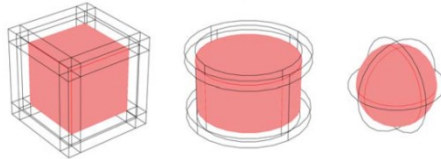


Figure 3. Various types of PML layers. [1]

Shortened and simplified, this layer made an impenetrable wall to RF waves. This layer must be set properly around the simulated model. There is 3 ways how general to set up this layer - see Figure 3. If user don't set this layer properly, radio waves will spread to the infinity. Shortly, that means the simulation will never finish.

Lumped port

Other problem with which users frequently encounter is the properly set lumped port. This issue relates only to active models with the input power. Lumped port is the input power port.

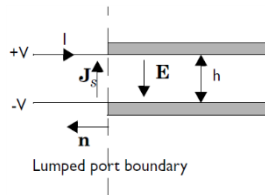


Figure 4. The lumped port scheme. [1]

There is one very important rule for the lumped ports: the excitation point must be similar to excitation transmission lines. This means that the gap, between the electric poles, must be smaller than the wavelength. Then it is possible to define the electric field and voltage. Also, user must set up right the direction of radiation. If the direction will be set up badly the simulation can interrupt. But in the worst case, the simulation will be completed, but not correctly. The user then may not even recognize the error and then he will also work with poor outcome.

Continuous data validation

If the user have very big model and wants to simulate it properly it is more than recommended to calculate the single steps. For example if we calculate the optimization by the $\text{abs}(S_{11})$, at the same time (just for the checking) give in the table also the

value S11dB, the gain of the antenna, impedance of the lumped port etc. Then in the graph we get more precisely information's about how the model behaves. After checking we know if the values are even real and then we can seamlessly run the final calculation.

This was only some of the issues and basic advices, for the more information we recommend to see [1],[2] or the COMSOL Multiphysics RF module user guide.

2 Magnetic loop antenna

One of the successful example of COMSOL using is MLA (magnetic loop antenna). The antenna is the simple circle made of copper rod. Antenna is used mostly by radio amateurs. This antenna is also used in the electrically noisy environments, because it is immune to the electrical part of the radio waves. This is why it is called magnetic loop.

From the Figure 5. is clear that the air and PML layer is around the antenna. The PML is at proper distance from the antenna, this can be derived from a wavelength. Step by step guide how to build and simulate this antenna is available [1],[7].

With modelling this antenna was a little issue as mentioned above, about the lumped port, because antenna shape is round.

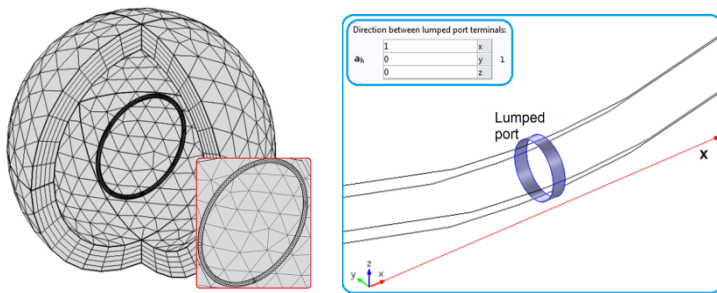


Figure 5. Meshing & lumped port. [1]

Therefore, it is not clear how to be placed radiating areas. In the Fig. 5 the radiation of the lumped port copying the axis X. This is good solution, every else ends with error or worse with the bad result.

The antenna simulation time was about half an hour. The computing time of the optimization it is always depends on the frequency step. The time scattering, there may be from minutes to the days or weeks, this is also depends on the user PC.

As we can see in the Figure 6, the model was successfully simulated, on the electric field in the left we can see the how energy flows and spreads to the body of the antenna. This is useful when checking whether the model is correct, because if it is not correct, the energy wouldn't spread at all.

Another graphs are just informative and it is final graphs of the simulated model. Only the optimization graph is important, because from this graph can user specify which frequency is best for the antenna. Optimization module is one of the biggest part of COMSOL Multiphysics and we can optimize every antenna value.

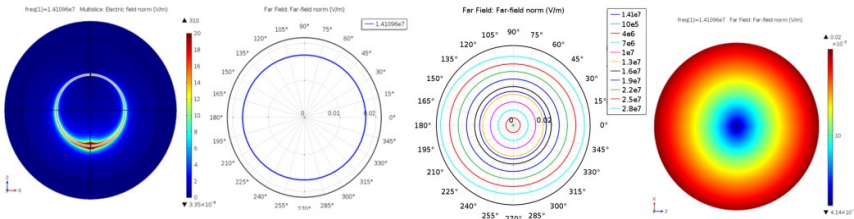


Figure 6. Electrical field, polar graph, frequency optimization graph and 3D radiation pattern of MLA. [1]

3 Patch antenna

The patch antenna is newer antenna then MLA. The patch antenna itself is quite successful and it is used in the mobile devices. It is primarily made from PCB and it is very small device. It can be used for MIMO technology.

In the Figure 7 is the meshing of the one and two patch antennas on the PCB board. As you can imagine this is much more consuming the computing power, because there is many small elements.

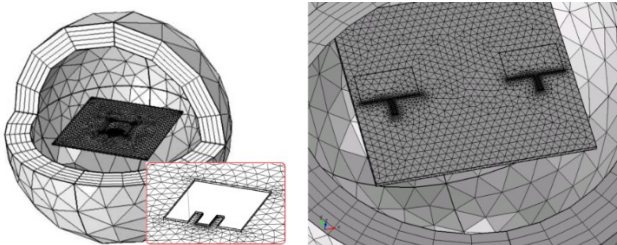


Figure 7. One patch antenna (left side). Two patch antennas for MIMO (right side). [2]

There was many issues especially with the optimization. In the COMSOL software is the primarily 4 methods of optimization. For example in the Figure 8 to optimize frequency. This topic is well described here [3].

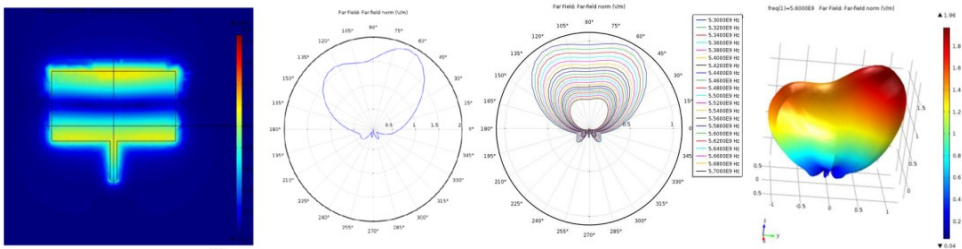


Figure 8. Electrical field, polar graph, frequency optimization graph and 3D radiation pattern of patch antenna. [2]

As regards to MIMO technology of patch antennas, there is a big issue about energy flow between antenna circuits. If there is system of 3x3 patch antennas and only one is used to radiation, there is leakage phenomenon to another patch antennas. Because of this problem it must be carefully designed and also optimized the whole antenna system [2].

4 CONCLUSION

In this paper was described only some of the issues and basic advices for the starting user of COMSOL Multiphysics RF module. Of course there is much more of issues what we don't mention. Many of the another issues are described here [1],[2]. And there is also completely guides to build the above mentioned antennas [7].

The COMSOL Multiphysics is indeed one of the most comprehensive simulation software, which are now available on the market. Using this program can be designed any physical problems from electrical engineering, mechanics and chemistry to liquids and various other tasks. The advantage is also that each sector can freely connect and thus create a unique system for processing and simulation of multiphysics problems.

But in this versatility and great strength of the program is also a big problem. The program is very complicated and for a complete layman absolutely impossible to do some more complicated model in it. It is therefore necessary to properly acquainted with the program in detail and go through all the options. For the full mastery of the complete program with all modules will need to practice a length of several years.

5 References

- [1] URBAN, Zdeněk. *MLA Antenna Simulation in COMSOL Multiphysics®*. Ostrava, 2015. Diploma thesis. VŠB-TU Ostrava. Supervisor Ing. Marek Dvorský, Ph.D., URL: <http://hdl.handle.net/10084/108561>
- [2] WEŽRANOVSKI, Lukáš. *Design antenna technology 3 x 3*. Ostrava, 2015. Disertation thesis. Supervisor Doc. Ing. Ivánek, Csc.
- [3] WEŽRANOVSKI, Lukáš, Lubomír IVÁNEK, Zdeněk URBAN a Yahia ZAKARIA. Patch antenna optimization in COMSOL Multiphysics, *ELEKTRO 2016, Štrbské pleso Slovakia*
- [4] WEŽRANOVSKI, Lukáš, Lubomír IVÁNEK, Zdeněk URBAN a Yahia ZAKARIA, *Optimization of Antenna System for MIMO Technology*, IITI-2016, Sochi Russia
- [5] COMSOL. *Introduction to RF Module* [online]. 2012, 1.5. Available from: <http://www.lmn.pub.ro/~daniel/ElectromagneticModelingDoctoral/Books/COMSOL4.3/rf/IntroductionToRFModule.pdf>
- [6] COMSOL. *RF Module User`s Guide v4.3*. [online]. 2012, 1.5. Available from: <https://is.muni.cz/el/1431/podzim2013/F7061/um/RFModuleUsersGuide.pdf>

Testing FSO-WDM Communication Systems and Real Measurements Modulation Formats for FSO with using USRP

Ales Vanderka

Department of Telecommunications, FEECS,
VŠB – Technical University of Ostrava, 17. listopadu 15,
708 33 Ostrava – Poruba, Czech Republic
ales.vanderka@vsb.cz

Abstract. In this article the author's team deals with using Wavelength Division Multiplexing (WDM) for Free Space Optical (FSO) Communications. In FSO communication occurs due to the influence of atmospheric effect (attenuation, and fluctuation the received power signal, influence turbulence) and the WDM channels suffers from interchannel crosstalk. There is considered only the one direction. The behavior FSO link was tested for one or eight channels. Furthermore, the paper deals concept of deploying Software Defined Radio (SDR) for laser beam modulation in FSO. We performed a variety of tests in order to determine the resistance of modulation formats to simulated atmospheric effects with the aid of the Error Vector Magnitude (EVM) and Modulation Error Ratio (MER) parameters. This tests of atmospheric effects were achieved by using a plexiglass box.

Keywords: FSO, USRP, WDM, modulation formats, turbulences.

1 The influence of turbulences on the optical beam

Turbulent flow is based on the turbulent cells that have different size, temperature and density, they are unstable in time (they arise, change and disappear). According to the size of optical beam we can divide turbulent cells into three categories: light beam is smaller, bigger or same as the turbulent cell. The refraction arise here, it is caused by the change of the refractive index between turbulent cells. The optical beam leaves the turbulent cell at different angle than is the entrance angle. This leads to the fluctuation of the received power on the receiver and fluctuation of the coherent wave phase. If the optical beam has smaller diameter than that of the turbulent cell it releases into deflection of the entire optical beam from its path. The optical beam leave the turbulent cell at different angel then is the entrance angel.

The amplitude and frequency of scintillation depends on the cell size compared to the size of the optical beams. With the increasing light frequency the amplitude and frequency of scintillations increases. For the flat wave in the environment with low turbulences and for the concrete receiver, the scintillating dispersion can be expressed by this relation:

$$\alpha_{\text{sin}} = 2\sqrt{23,17 \cdot \left(\frac{2\pi \cdot 10^9}{\lambda}\right)^7 \cdot C_n^2 \cdot L^{11}} \quad [\text{dB}], \tag{3}$$

where λ is transmission wavelength [nm], L is the length of the transmission channel [m], C_n^2 is structural parameter of the refractive index [$\text{m}^{-2/3}$].

2 Results

Design and testing of FSO communications were performed in OptiSystem 14 from Optiwave. Most of the set value correspond already realized singel-channel connection in the area of VSB TUO where head are 1400 m far away. The baud rate is set to 1,25 Gbps.

The schema of simulation connection is shown on the Fig. 1. The transmitting part is formed by CW laser with an output of 50 mW at the wavelength in the C band. Pseudo-random bit sequence PRBS generator generates a signal for Pulse generator module (NRZ, RZ, BPSK and QAM). This modulated signal is transmitted to Mach-zehnder Modulator MZ which uses the electrical component to modulating optical signal from CW laser. Next, there is WDM multiplexer in-stalled that combines all the channels into one fiber. The light is liberated from the fiber in the head and it is transmitted under the beam angle of 2 mrad with the help of optic in the head.

For FSO the parameters of the transmitting head was set on 8cm and of receiving head on 20 cm. The attenuation of route is chosen for the route in slightly polluted environment of 4.6 dB. During the simulation the FSO channel is affect-ed by many atmospheric effects, turbulences and fog have the biggest impact. Turbulences were simulated with the changing the structural parameter of the refractive index. The structural parameter of the refractive index was set ac-cording to real values which can occur in the atmosphere $C_n^2=10^{-17}-10^{-12}$. Next we focused on the impact of the fog at-tenuation on the connection with 1 and 8 active channels which were modulated by different modulating format.

In the receiving optic, the optical signal is tied to the optical fiber where is divided by the WDM demultiplexer to 8 chan-nels.

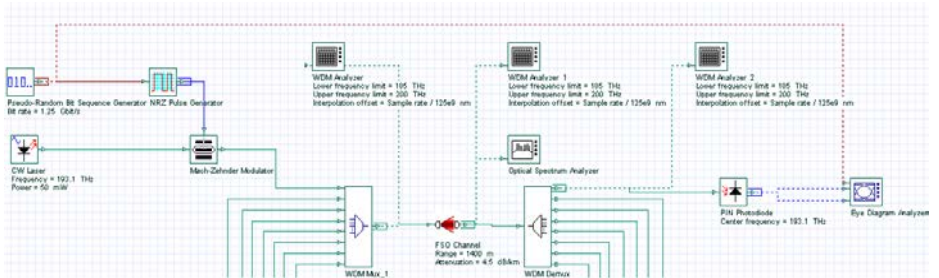


Figure 1: A diagram of the experimental set-up of OptiSystem 14.

Firstly, the impact of fog (attenuation of channel) to channel error rate was examined at WDM FSO. There were compared situations when only one channel works and when 8 channels were in the function. At the modulation NRZ we can see that increase of the number of lines has significant effect on the error rate. The line in this configuration with this modulation would work to the attenuation of $\text{dB}\cdot\text{km}^{-1}$ if the border reliability will be error rate of 10^{-9} . The error rate for the RZ modulation with one and 8 channels is similar. At this modulation the transmit would be reliable to the attenuation of $6.25 \text{ dB}\cdot\text{km}^{-1}$. At the QAM modulation, the error rate increase with the increasing number of channels. But this modulation was more resistant to increasing attenuation where the connection was reliable to the attenuation of $7.8 \text{ dB}\cdot\text{km}^{-1}$. The BPSK modulation was tested last. The curve overlap but the error rate also increases a little bit. With this modulation format the connection would be reliable to the attenuation of 9 dB . The detailed comparison of all simulations are on the Fig.2. We can see that modulation formats NRZ and RZ are comparable during the whole simulation. To the connect attenuation of $3.5 \text{ dB}\cdot\text{km}^{-1}$ the best modulation format was QAM. After this value the best format was BPSK.

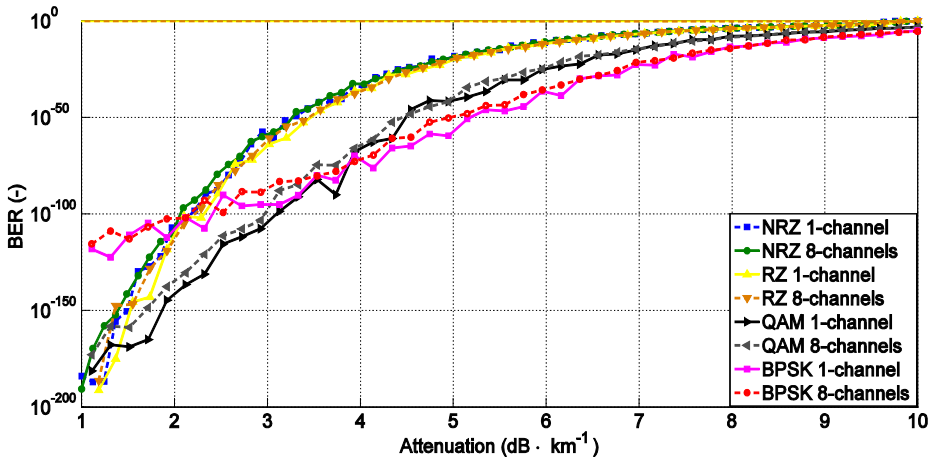


Figure 2: Comparison of the modulation formats NRZ, RZ, QAM and BPSK depending on attenuation.

Next, we made the simulation of the turbulence impact in atmosphere to the error rate of WDM FSO connection depending on number of channels and modulation formats NRZ, RZ, BPSK and QAM. To eliminate random errors the simulation was done for ten times and final values were averaged (Fig. 3). We can see comparison of the modulation formats NRZ, RZ, QAM and BPSK. The BPSK has the smaller error rate in the whole area C_n^2 . The next best format was QAM. The similar results have the modulation format NRZ and RZ. The better was NRZ format.

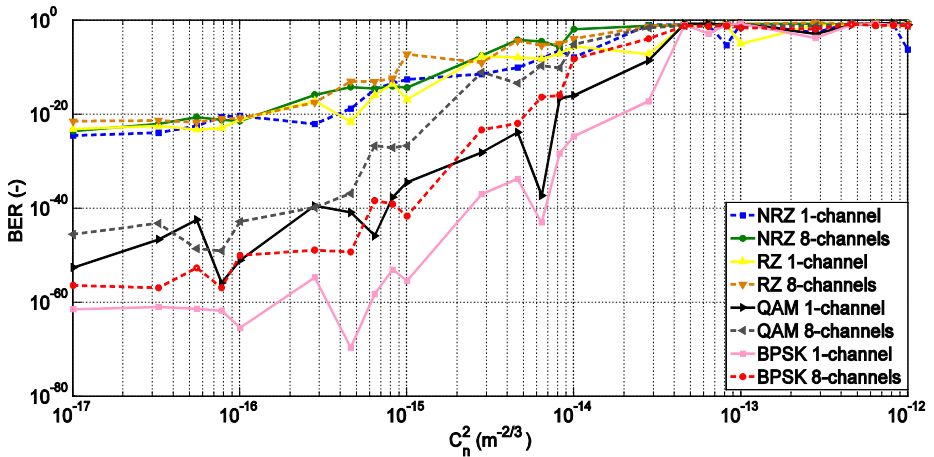


Figure 3: Comparison of the modulation formats NRZ, RZ, QAM and BPSK depending on C_n^2 .

3 Testing modulation PSK modulation formats

For our experiments we put together the apparatus shown in Fig. 4. It was comprised of a measurement box made from plexiglass 2.5 m long, 0.5 m high and 0.5 m wide, with 120 mm openings on all sides (separated from each other by 625 mm), to position ventilators or allow air conduction. To generate thermal turbulences, CTH-5000 Empire fan heaters with the following specifications were used: 2 kW power, hot air temperature $\sim 48\text{ }^\circ\text{C}$, and convection speed = $3.5\text{ m}\cdot\text{s}^{-1}$. For our experiments many different scenarios were set by changing position of Hot-Air ventilator along one side of laboratory box. With this arrangement, a warm air stream could be generated to change the local refractive index parameter in the measurement box.

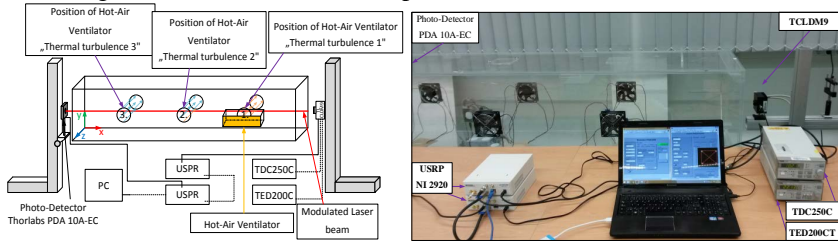


Figure 4. A diagram of the experimental set-up and real set experiment.

The application that was created in the LabVIEW recorded the parameters MER and EVM during each measurement: the box without turbulences, with air stream turbulences and with Hot-Air ventilator in position 1, 2 and 3. Figure 5 shows the changes of the EVM parameter for different modulation formats with respect to the type of measurement and positions of the Hot-Air ventilator. The EVM parameter is the comparison of actual measured values of amplitude and phase with reference val-

ues. For the BPSK modulation, the EVM has a similar value to that of the 8-PSK modulation with the Hot-Air ventilator placed close to the emitting laser diode. It is notable that placing the Hot-Air ventilator solely in position 1 mostly affected the modulated optical beam. The next parameter was MER, which represents the modulation error from ideal position of the given symbol to the actual position. The MER was uniform when the Hot-Air ventilator was in the middle of the box.

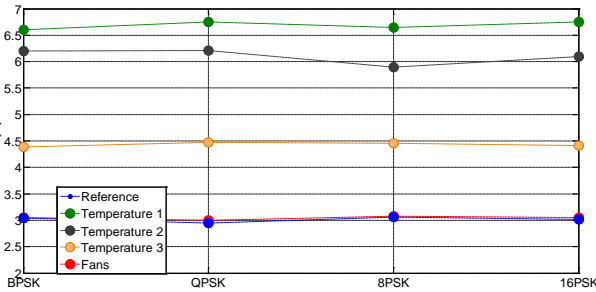


Figure 5. Comparison of EVM for modulation formats based upon different configurations of measurement.

Figure 6 shows the measurement of the EVM for the modulated laser beam with BPSK modulation format and its dependence on influences of simulated atmospheric effects in the form of thermal turbulence for all three Hot-Air ventilator positions in the box. For this experiment 1000 samples were collected. The blue curve defines the measured value of the EVM for the reference measurement of the BPSK modulation, which is around 3%. The green curve was measured for position 2 and defines the measured value of the EVM parameter for the BPSK modulation, which is in the 4% to 14% range.

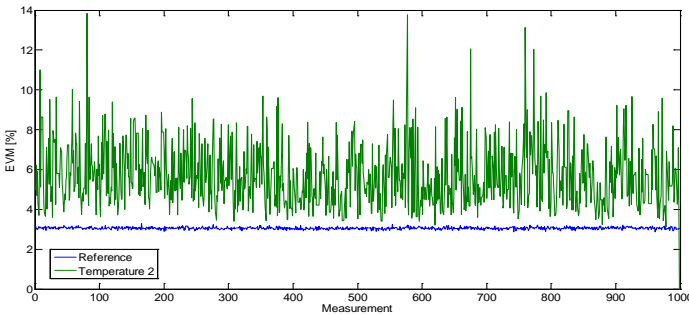


Figure 6. The BPSK modulation by thermal turbulences for 1000 samples of the EVM.

4 CONCLUSION

In this article the FSO connection was simulated in combination with WDM. Two main factors influencing quality of transmission were examined here. One of these factor was progressively increasing attenuation which should simulate increasing number of aerosol particles in the atmosphere. Another factor was increasing structural refractive index that simulated increasing turbulences in the atmosphere. We compared the error rate of BER for 1 and 8 active channels. Results of all simulations lead

to conclusion that the number of active channel have an impact to the error rate of individual channels. At one active channel the error rate is smaller than at 8 active channels which is also caused by mishearing on WDM demultiplexer. The difference in the error rate between 1 and 8 active channels was bigger at simulation of turbulences in atmosphere than at simulation of fog.

The BPSK modulation reached the best results in simulations. The second bet was QAM modulation. The NRZ and RZ modulation had the worst results from all tested modulating formats. The BPSK reaches good BER to the attenuation of $9 \text{ dB} \cdot \text{km}^{-1}$, the QAM modulation to $7.8 \text{ dB} \cdot \text{km}^{-1}$ and for modulation NRZ and RZ the value is $6.3 \text{ dB} \cdot \text{km}^{-1}$. During turbulences the best choice is again the BPSK modulation where at using 8-wave multiplex reaches good error rate to value $C_n^2=9.5 \cdot 10^{-23}$. With using more lines on the FSO connection the transmitter rate increases a lot that is in the same time redeemed by bigger error rate of connection for fixed transmitter powers. We can compensated this by the installing EDFA amplifier in front of the FSO channel and so the transmitter power of connection increases and the error rate is smaller

In the second part of measured values and experimental results indicated that the BPSK format provides the best conditions or resistance against simulated atmospheric effects. Nevertheless it is necessary to emphasize that the BPSK modulation scheme transmits fewer symbols than those of the higher modulation formats.

5 References

1. VANDERKA, A., L. Hajek, J. Latal, J. Vitasek and P. Koudelka. Design, simulation and testing of the OOK NRZ modulation format for free space optic communication in a simulation box. *Advances in Electrical and Electronic Engineering*. 2014, vol. 12, iss. 6, pp. 604-616. ISSN 13361376. DOI: 10.15598/aeec.v12i6.1255.
2. LATAL, J., Vanderka, A., J. Vitasek, P. Koudelka. P. Siska, A. Liner and V. Vasinek. Experimental measurement of thermal turbulence effects on modulated optical beam in the laboratory. In: *OptoElectronics and Communication Conference*. Melbourne: 2014, pp. 455-457. ISBN: 978-192210721-3.
3. VANDERKA, A., L. Hajek, J. Latal, J. Vitasek, S. Hejduk and V. Vasinek. Testing resistance modulation formats for FSO communication in turbulent environment, with used simulation box. In: *SPIE Laser Communication and Propagation through the Atmosphere and Oceans IV*. San Diego: 2015, no. 96140S. ISBN: 978-162841780-7. DOI: 10.1117/12.2180335.
4. HAJEK, L., J. Vitasek. A. Vanderka, J. Latal, F. Perecar and V. Vasinek. Statistical prediction of the atmospheric behavior for free space optical link. In: *SPIE Laser Communication and Propagation through the Atmosphere and Oceans IV*. San Diego: 2015, no. 96140V. ISBN: 978-162841780-7. DOI: 10.1117/12.2180338.
5. VANDERKA, A., J. Latal, L. Hajek, J. Vitasek, P. Koudelka, R. Martinek, V. Vasinek and H. Nazeran. Utilization of Software Defined Radio for Laser Beam Modulation of OWC by Influence of Simulated Atmospheric Phenomena. In: *ICTON 2016*.
6. VANDERKA, A., L. Hajek, J. Latal, J. Vitasek, S. Hejduk and V. Vasinek. Testing FSO WDM communication system in simulation software optiwave OptiSystem in different atmospheric environments. In: *SPIE Laser Communication and Propagation through the Atmosphere and Oceans V*. San Diego: 2016,

Path Loss Models in Urban and Rural Terrain for Wireless Communication

Yahia Zakaria and Lubomír Ivánek

Department of Electrical Engineering, FEECS,
VŠB – Technical University of Ostrava, 17. listopadu 15,
708 33 Ostrava – Poruba, Czech Republic
{yahia.salem.st, lubomir.ivanek}@vsb.cz

Abstract. The main goal of this research is to analyze the behavior of channel propagation models of wireless communication systems. There are different types of propagation models that can precisely calculate the path loss in all types of terrain. In this research various propagation models (COST 231 Wal-fisch-Ikegami (W-I) Model, Ericsson Model and Stanford University Interim (SUI) Model) are analyzed and compared. These propagation models have been proposed for different receiver antenna heights in urban and rural environments. It was noticed from the results of the path loss estimation for 2 m, 7 m and 14 m receiver antenna heights in urban environment that COST 231 (W-I) model showed the lowest path loss results (138 dB in 2 m, 7 m and 14 m receiver antenna heights) as compared with the other models in urban environment. On the contrary, SUI model showed the highest path loss result (166 dB in 2 m receiver antenna height) as compared with the other models in the same environment. The purpose of my dissertation is to select and refine a model suitable for use in environments typical of urban and suburban and rural area in Egypt. WiFi technology is the most appropriate for verification models through measurement. In this band we can reduce the adverse influence of other entities disturbance of their equipment.

Keywords: Terrain; Stanford University Interim (SUI) Model; COST 231 Wal-fisch-Ikegami (W-I) Model; Urban area; Rural area.

1 Introduction

The electromagnetic waves usually can not directly reach the receiver due to many obstacles that block the line of sight path. The travelled signal from transmitter to receiver over a lot of reflection path is called multipath propagation which always causes fluctuations in the receiver signal's phase and amplitude [3]. The propagation models are mathematical tools used by engineers and scientists to plan and optimize wireless communication systems.

They are developed to predict the loss of signal strength or coverage in a particular location. Moreover, path loss can be defined as the ratio of the transmitted to received power, usually expressed as the following form in decibels, [2]:

$$PL(d) = PL(d_0) + 10n \log_{10}(d / d_0) \quad (1)$$

Where, d is the distance; d_0 is the reference point at 1km; n is the path loss exponent.

Finding an accurate propagation model for propagation losses is a leading issue that will give us the best path loss prediction when designing a wireless communication network. Path loss calculation is one of the major factor that we have to estimate. For wireless communication system, the system should have the ability to predict the accurateness of the radio propagation behavior. Therefore, it is very important to find out a suitable propagation model for all types of the environments to provide guidelines for cell planning of wireless communication systems.

For more details about COST 231 (W-I), Ericsson and SUI models see [5],[6],[7],[8].

Cost 231 is elementary propagation model. It is based on the Okumura propagation model. This model gives a graphical expression for path loss between the receiving and the transmitting antenna for a frequency range between 200 MHz and 1920 MHz.

Ericsson model is Ericsson's implementation of Hata model. In this model the modification of model parameters is possible according to propagation environment.

SUI model was developed by Stanford University. SUI model parameters depend on terrain type divided into three groups: hilly terrain with moderate to heavy tree densities with biggest path loss; mostly flat terrain with moderate to heavy tree densities or hilly terrain with light tree densities; mostly flat terrain with light tree densities where path loss is minimal.

We decided to investigate differences in that result when calculating the path loss using several models. We adjusted the various parameters such as: Transmitter antenna height, Mobile transmitter power, Correction for shadowing, Base station transmitter power, Receiver antenna height. An example of this calculation is in the next chapter for three selected models.

2 Analysis and results

Results for 2 m and 14 m receiver antenna heights, Fig. 1 and Fig. 2 show the path loss in urban area.

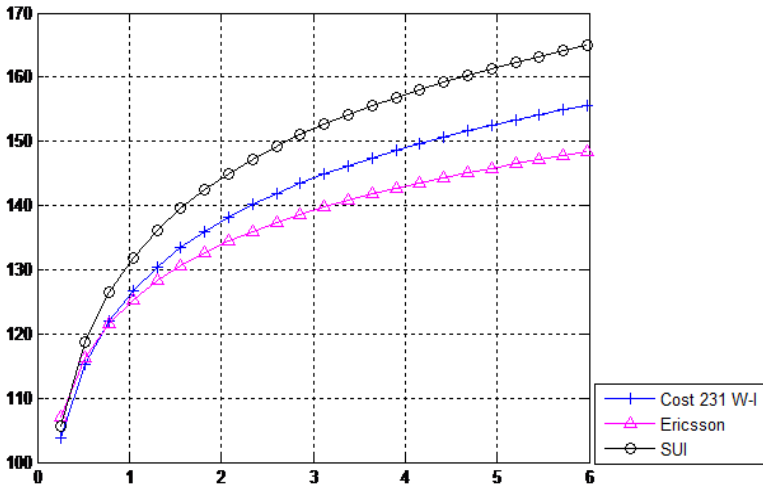


Fig. 1. Path Loss for 2 m Receiver Antenna Height in Urban Environment

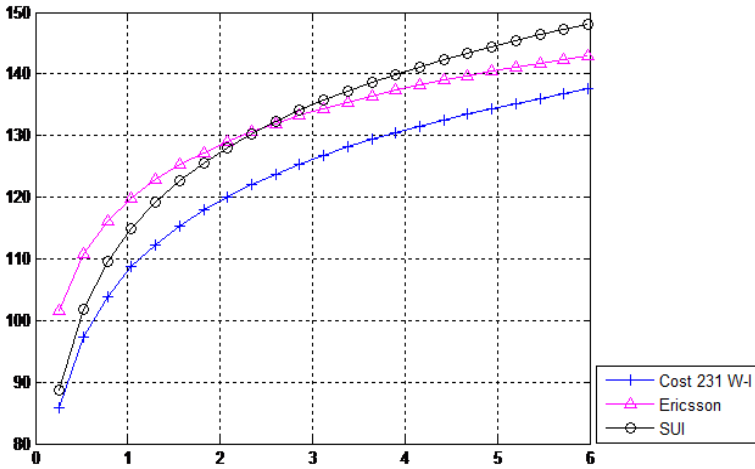


Fig. 2. Path Loss for 14 m Receiver Antenna Height in Urban Environment

Also, Fig. 3 and Fig. 4 show the results for the described propagation models in rural area

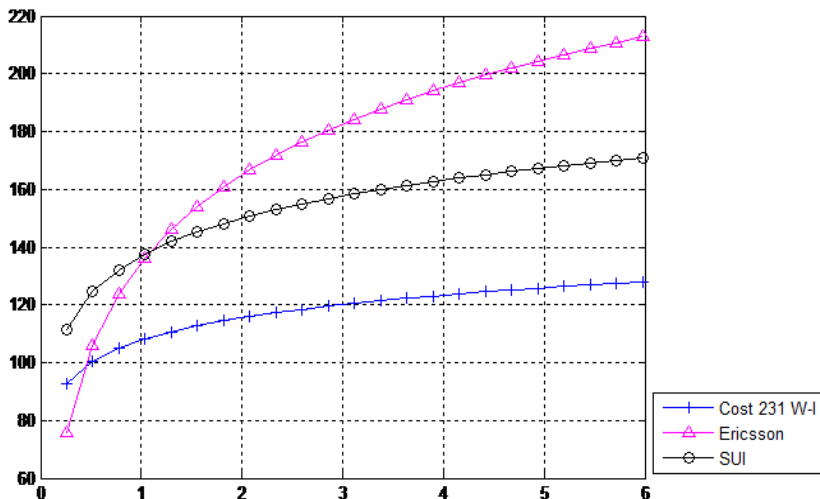


Fig. 3. Path Loss for 2 m Receiver Antenna Height in Rural Environment

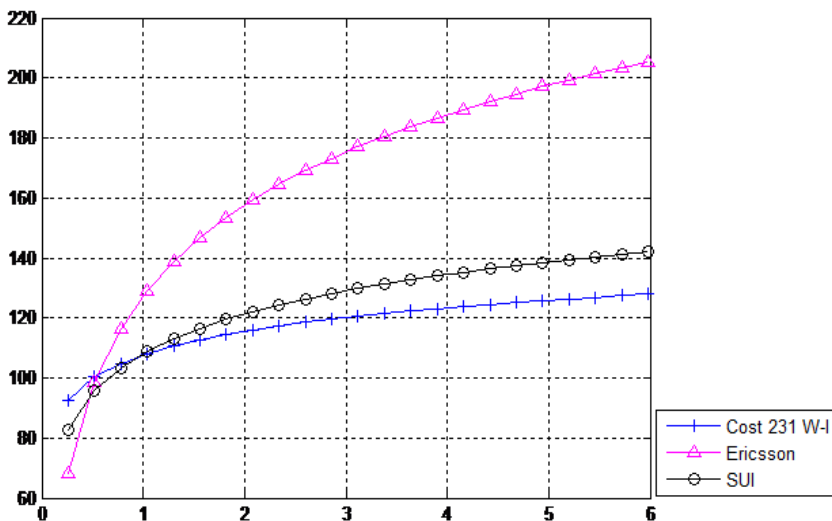


Fig. 4. Path Loss for 14 m Receiver Antenna Height in Rural Environment

On the x-axis is plotted the distance between the transmitting and receiving antenna (km). On the y-axis is path loss (dB).

The following table shows values of the parameters which were applied at this research.

Table 1. Parameters of Research

Parameters	Values
Transmitter antenna height	26 m
Mobile transmitter power	31 dBm
Correction for shadowing	10.7 dB
Base station transmitter power	44 dBm
Receiver antenna height	2 m, 14 m

The results analysis of rural environments are shown in the following Figure 5.

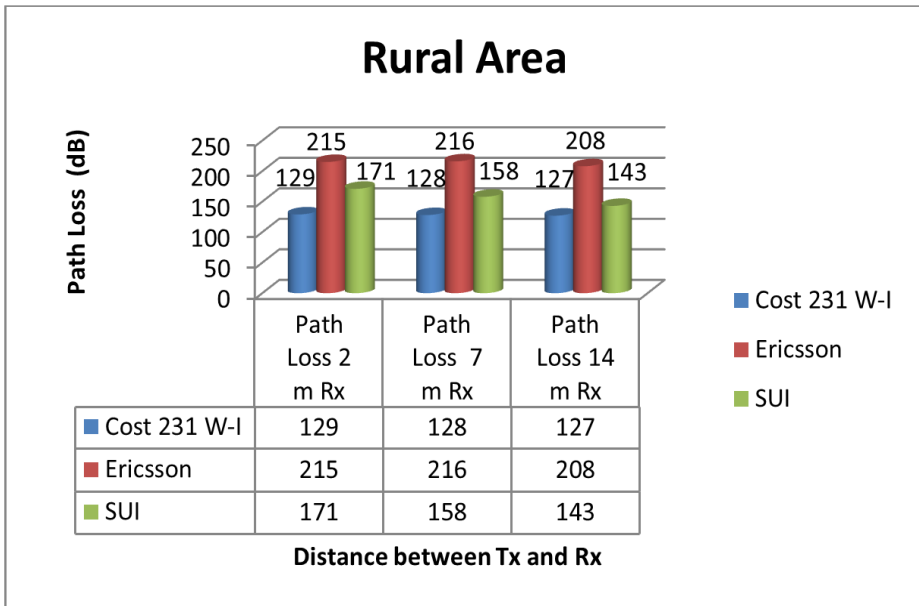


Fig. 5. Analysis of the results in Rural Environment

3 Conclusion

It was obvious from the results of the path loss estimation for 2 m and 14 m receiver antenna heights in urban environment that SUI model showed the highest path loss result (166 dB in 2 m receiver antenna height) as compared with the other models in urban environment. The results testify the assumption that the path loss decreases with increasing height of the antenna.

4 Acknowledgement

This research is supported by the project SP 2016/143 "Research of antenna systems; effectiveness and diagnostics of electric drives with harmonic power; reliability of the

supply of electric traction; issue data anomalies." The authors would like to express their thanks to the members of Department of Electrical Engineering at VSB - Technical University of Ostrava for their valuable instructions and support.

5 References

1. Zakaria, Y, Ivanek, L. "Propagation Modelling of Path Loss Models for Wireless Communication in Urban and Rural Environments at 1800 GSM Frequency Band", *Advances of Electrical and Electronics Engineering*, 2016.
2. Zakaria, Y, Ivanek, L, Urban, Z. "Suggested Model for Wireless Communication in Suburban Environments with Estimation of Different Channel Models" *The eleventh International Conference ELEKTRO 2016, Štrbsk Pleso - High Tatras, May 16th-18th, 2016.*
3. Rappaport, T.S., "Wireless Communications", Prentice-Hall, Upper Saddle River, New Jersey, Ch. 3 and 4, 1996.
4. V.S. Abhayawardhana, I.J. Wassell, D. Crosby, M.P. Sellars, M.G. Brown "Comparison of empirical propagation path loss models for fixed wireless access systems" *Vehicular Technology Conference*, vol. 1, pp. 73 – 77, 2005.
5. M. Didarul Alam, S. Chowdhury, et al., "Performance Evaluation of Different Frequency Bands of WiMAX and Their Selection Procedure," *International Journal of Advanced Science and Technology*, vol. 62, pp. 1-18, 2014.
6. J. Milanovic, S. Rimac-Drlje, K. Bejuk, "Comparison of propagation model accuracy for WiMAX on 3.5GHz," *14th IEEE International conference on electronic circuits and systems, Morocco*, pp. 111-114, 2007.
7. Simic I. Igor, Stanic I., and Zmic B., "Minimax LS Algorithm for Automatic Propagation Model Tuning," *Proceeding of the 9th Telecommunications Forum (TELFOR 2001)*, Belgrade, November 2001.
8. V. Erceg, K V S Hari, et al., "Channel models for fixed wireless applications," *tech. rep., IEEE 802.16 Broadband wireless access working group*, Jan 2001.

Optoelectronic Elements Made from Polydimethylsiloxane

Ondřej Zbořil

Department of Telecommunications, FEECS,
VŠB – Technical University of Ostrava, 17. listopadu 15,
708 33 Ostrava – Poruba, Czech Republic
ondrej.zboril@gmail.com

Abstract. This article describes the progress of the third year of the author's study of the field of Communication technology. The article summarizes author's activities at the Department of Telecommunications during the academic year 2015/2016, research and development activities, work on projects and other activities in which the author participated.

Keywords: optical fiber, microlens, polydimethylsiloxane, waveguide

1 Introduction

I am studying full-time doctoral study at the Faculty of Electrical Engineering and Computer Science at the Technical University of Ostrava. My study program is called Computer Science, Communication technology and Applied Mathematics and field of study is Communication Technology. My dissertation thesis is focused on elements made from polydimethylsiloxane and my tutor is Professor Vašínek. This article summarizes the third year of study.

2 Dissertation work

My dissertation deals with elements made of polydimethylsiloxane. First it is necessary to handle the production of simple elements of polydimethylsiloxane and master these manufacturing processes.

In the past year, I've created several different elements of PDMS. Some of them are included in the patent proceeding, or they'll be dealt with in other articles. This article deals with the production of optical lenses of PDMS at the end of the optical fiber.

In telecommunications and sensor is a very important suitable coupling of optical fibers with other elements such as the radiation source, photodetector, or other components. To improve the coupling is advisable to use a focusing system, but sometimes it's for basic application unnecessarily complicated, expensive, or when there is not a place for a system of lenses and other components. Further, there are problems with the symmetry and the centering components that significantly reduces the possibility of coupling, which requires precision work.

There is the possibility of using microlenses made at the end of the optical fiber. There are two categories where we can assign such microlenses. Intrinsic, wherein the lens is part of the fibers itself and extrinsic, wherein the lens is a separate microcomponent.

To prepare the microlenses is several ways, such as heating (electric arc or laser), photo-polymerization, by chemical treatment of the surface fibers by hydro fluoride, glue finished lens on the end of the thread, etc., or a combination.

The method of heating is preferred in processing speed, but there is a great loss due to deformation of the core. Photopolymerization takes a few minutes and provides good reproducibility, at a cost reduced resistance connection of the optical fiber and the polymer. Chemical treatment is a time-consuming process, but it will solve the transmission loss.

This article deals with another method when on the end of the optical fiber is applied the little dose of polydimethylsiloxane (PDMS) and this is subsequently cured by high temperature. This is a relatively fast process, however, these microlenses are susceptible to mechanical damage of the thread end, which often results in their separation from the fiber end. It was made a series of micro lenses on the end of optical fibers (Fig 1.). These microlenses are for use Visible light communication (VLC), as behind the focal length of the lens increases the numerical aperture as compared to conventional optical fiber. Other possible applications of the optical fiber microlens is a fiber-optic probe, which benefits from its small size and the possibility of focusing the optical beam on a very small area to test in place of the focal length.

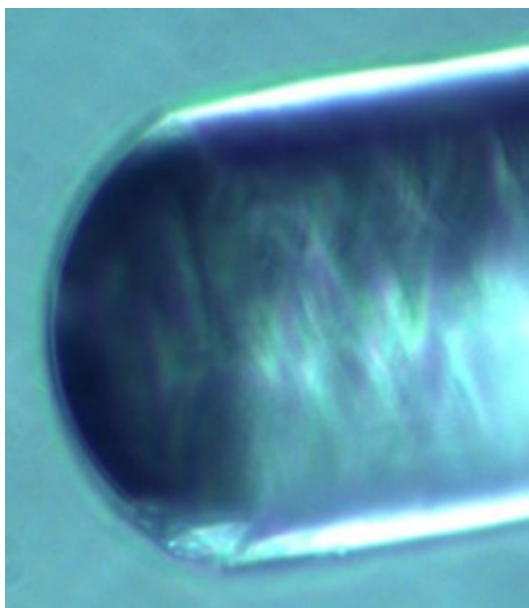


Fig. 1. Experimental PDMS microlens on the end of optical fiber

To produce lenses is required mount for an optical fiber with micro displacement (Fig2). Holder is shifted to a plastic rod which is wetted in PDMS. Against this stick with PDMS slowly approaches the end of the optical fiber which is fixed in a holder on the micro displacement. Everything is checked under a microscope. End of the fiber is wetted with the PDMS droplet to stick and then again moves away from the end of the fiber rod with the dose PDMS. In the end is the end of the optical fiber cured by high temperature.

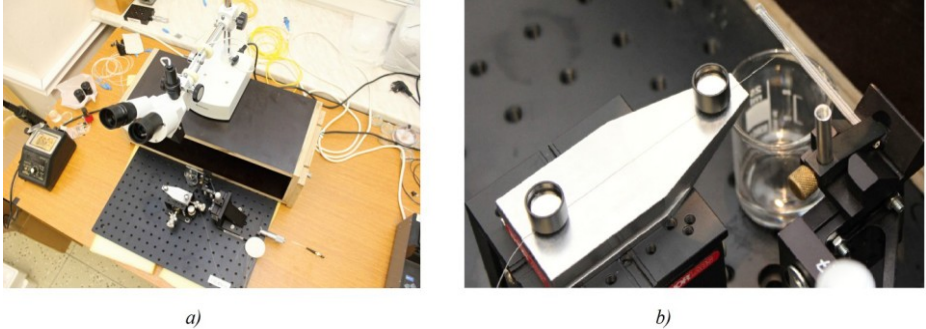


Fig. 2. a) Workplace with microscope b) Detail of holder with micro displacement

Optical fibers with PDMS micro lens have a larger radiation angle in comparison with the conventional clean end of the optical fiber. This difference can be seen on Figure 3 for optical fiber type 50/125 μm and Figure 4 fiber type 62.5/125 μm .

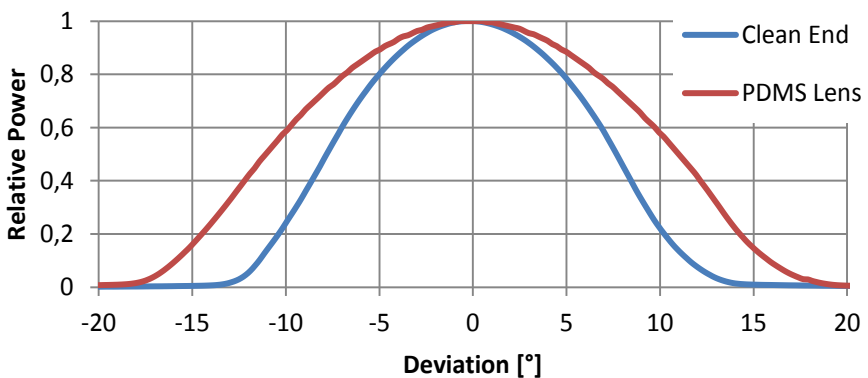


Fig. 3. Radiation angle of the optical fiber 50/125 μm

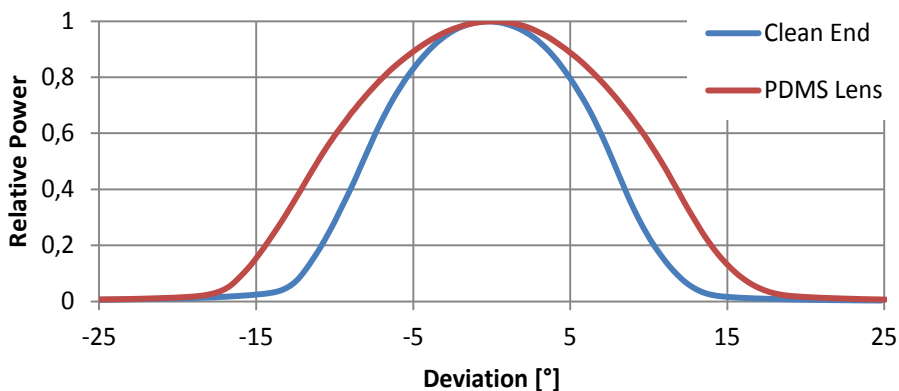


Fig. 4. Radiation angle of the optical fiber 62.5/125 μm

I plan to measure other parameters and also to verify the usability of the PDMS micro lenses. Everything will be summarized in a more comprehensive article that I would like to present at the international conference.

3 Cooperation on projects

I was actively involved in solving on two projects under the auspices of the Technology Agency of the Czech Republic. I also participated in project GUARDSENSE under the auspices of the Ministry of Interior.

- TA ČR - Intelligent modules for lighting and communication
- TA ČR - Safety of optical transport networks and the development of opt. parts for electric power and electrical appliances
- Project GUARDSENSE

Participation on these projects includes activities as designing, building and measuring, such as:

- Measuring mechanical and acoustic vibration for the security of space assets via fiber-optic interferometer

I participated in the production of a prototype measurement units built into a plastic window. The unit serves as the detector against external intrusion. The prototype functionality has been tested, also the frequency range and sensitivity. The results of this work have resulted in valid patent and conference article, which I presented at the conference in Brussels.



Fig. 5. Window prototype

- Measuring mechanical vibration for traffic monitoring via fiber-optic interferometer

Installation and measuring mechanical vibration generated when passing cars around. The result of this work was the conference article presented at the conference in Brussels, where I was the co-author.

- Preparation of fiber and measuring ageing fiber influence to external conditions on the roof building N

Measurement of various parameters affecting the aging of optical fibers by external influences. We measured the parameters for each week. The measured data were compared so we can see the influence of the temperature etc.

4 Publications during academic year

As co-author, I participated in the creation of valid patent. This patent was the result of the successful experiment of the securing area using an optical fiber placed inside the plastic window. The patent is named "Fiber-optic interferometer for the security of space assets" and I have a share of 20% on it. I was involved in prototype design, measuring data and verifying its functionality. Furthermore, I was processing the part of the patent application. We are also working on another two patents. They are at this moment at the patent lawyer.

I'm the author of the article "Sensitivity distribution of a vibration sensor based on Mach-Zehnder interferometer designed inside a window system". I'm also the co-author of the articles "Fiber optic system design for vehicle detection and analysis", "Effect of the geometric deformations on the Brillouin scattering in the standard single-mode optical fiber" and "Fiber optic interferometer as a security element". We were at the conference in Brussels with those articles.

5 Pedagogic part

In the winter semester, I was actively involved in ensuring the practical tutorials in Communication Systems and Media (PSaM). In the summer semester, I was helping with teaching Logical Circuits (LO). I was also helping at final exams.

I was opponent for bachelor thesis. I also listed the three bachelor thesis and students has already signed on these topics. I was a clerk / registrar for final state examination for two days, same as last two years.

6 Other activities at the Department of Telecommunications

I represented the Department of Telecommunications and the faculty at secondary schools or the building of faculty. I was involved in preparing a presentation for the optical portion, preparation and presentation of the optical laboratory and putting the whole program.

7 References

1. NORRIS, A., J. DEGROOT, F. NISHIDA, U. PERNISZ, N. KUSHIBIKI a T. OGAWA. *Silicone Materials for Optical Applications*. DOW Corning [online]. 2003. Available from: http://www.dowcorning.com.cn/zh_CN/content/publishedlit/75-1007-01_single.pdf
2. GHATAK,A., THYAGARAJAN,K.: *Introduction to fiber optics*. Cambridge University Press, 1998, ISBN 0-521-577853
3. MÉNDEZ, Alexis, T MORSE. *Specialty optical fibers handbook*. Oxford: Academic Press, 2007, xlii, 798 p.

Detection of Human Silhouette in Depth Maps using HOG Algorithm

Rafał Gasz

Department of Computer Science, FEECS,
VŠB – Technical University of Ostrava, 17. listopadu 15,
708 33 Ostrava – Poruba, Czech Republic
Faculty of Electrical Engineering, Automatic Control and Computer Science, Opole
University of Technology, ul. Prószkowska 76, 45-758 Opole, Poland
rafal.gasz.st@vsb.cz, r.gasz@po.opole.pl

Abstract. In this paper the author presents a proposal of identifying the shape of human silhouette on obtained depth maps. In order to detect the shape of silhouette the author implements the HOG algorithm with appropriately defined SVG descriptor, which is a known solution of this research task used to identify the silhouettes using RGB images.

1 Introduction

Depth map is an image containing a projection of point cloud onto a plane, the equation of which can be freely selected, which enables the observation of projection of a given scene from different perspectives. Most often selected plane is the one that passes through the image-recording object, perpendicular to the optical axis which allows the comparison of real image with a depth map. In practical applications, the most commonly accepted agreement is that projections of points located at great distance are marked with darker color, and points located closer are marked with a brighter color. There are a number of methods to estimate the depth map: with the use of two or more digital cameras, devices that use structured light or TOF type cameras [1, 2, 3].

The principles of operation of TOF type systems is based on measuring the time between the moment of sending the light impulse by the transmitter, and the detector sensing the impulse reflected from obstacle. The farther away the object the distance of which is measured is located, the longer the propagation time of the impulse. Generating steep slope waveforms with a short duration is difficult in practical use (most suitable for it are lasers), and therefore they are replaced with sinusoidal signal and receiver calculates the phase difference of transmitted and reflected signal. The use of sinusoidal waveforms allows you to build a system operating with different types of transmitters. The flaw of this solution is method of noise reduction, wherein the phase difference of signals is calculated by integrating over time, which leads to a delay in the estimation of depth map or the blur associated with camera movement. Surfaces

strongly absorbing infrared radiation might not be properly reconstructed. TOF devices operate at low resolutions, which can lead to a situation in which the calculated position of a pixel located at the edge of the object will be significantly changing over time. The asset of TOF type cameras is operating in real-time resulting from lack of complicated numerical calculations required to obtain 3D information and very little influence of scene differentiation or lighting conditions on the accuracy and density of depth map [1, 3, 5].

Another group of systems for estimating depth map are devices whose operating principle is based on the properties of structured light. Such system includes illuminator that mostly emits light of infrared range with a defined structure and a camera recording light of the same range. Optionally, RGB camera is used, which allows overlaying reconstructed point cloud on the real image and displaying 3D structure. An example of such a device is Kinect from Microsoft. Light emitted by the infrared illuminator is characterized by a special structure that is unique to pixel position, and with the knowledge of relative positions of illuminator and sensor it allows to explicitly determine the spatial position of the given point. For this purpose, the same relationships are used as in the case of a stereo-vision system – e.g. Triangulation [4, 5, 6].

2 Human silhouette recognition algorithm

There are many algorithms used for tasks of human body parts identification in RGB images. The most popular are the ones recognizing human face, facial expressions, etc. Algorithms of this type are toned down in many phone applications for taking pictures. These algorithms are based on a number of predefined properties which a human face is characterized by. Let us take up a different task, namely detecting the shape of human body/silhouette on pictures.

Detection of people in RGB images is a difficult task due to their diverse appearance and a wide variability of poses in which people may be (sitting, standing, running, walking, etc.). In order to accomplish the task it is necessary to have a solid set of functions that will allow the identification of human form/shape, even in crowded environments and in difficult lighting conditions. Analysis of the existing algorithms for the detection of various forms of the human body shows that Histogram of Oriented Gradients (HOG) descriptor provides excellent performance in relation to other existing function sets. The proposed descriptors resemble edge orientation histograms - they are calculated on a dense grid of evenly spaced and used cells covering local normalization of contrast to enhance the efficiency and effectiveness of the algorithm [3, 4, 5].

HOD descriptor has several key advantages over other mathematical descriptions. Because it works on local pixels, it is fixed to the geometric and photometric transformations, with the exception of object orientation. Such changes do not appear only in larger spatial regions. In addition, the quality of spatial sampling is strong thanks to the local photometric normalization and allows individual body movement of pedestrians, which is to be ignored as long as it remains more or less in vertical position.

This descriptor is therefore particularly suited for the detection of human image [2, 3]. What is more, a detailed analysis of the effects of different implementation options concerning detector efficiency is performed, taking “Pedestrian Detection” (detection of the most often visible people in more or less vertical poses) as a test case. [1].

To facilitate the operation and to improve the speed, the HOG algorithm uses a linear SVM descriptor as a base classifier throughout the study. The new detectors provide essentially perfect scores on the test set of people. SVM classifier is the most popular in this type of tasks because in addition to performing linear classification, SVMs can effectively carry out non-linear classifications, using so-called “Kernel trick”, meaning mapping their entry into the high-dimensional space.

3 Detection of human silhouette in depth maps

Theoretical discourse described in earlier chapters about creating depth maps and detection algorithms of human body in images aimed to identify the current state of literature in this area in order to propose an efficient algorithm for recognizing the shape of people in depth maps.

In research conducted by the author, the device used for creating depth maps was Kinect One sensor from Microsoft, which creates depth maps in resolution of 512x424 px with a range of 4,5 – 5 m. After analyzing the literature, author decided to draw from existing human silhouette recognition algorithms known from the analysis of RGB images and implement the algorithm HOG together with SVG classifier developed for needs of this task.

Studies described in the article were conducted in laboratory conditions with good lighting conditions. Each time, the author subjected pair of images to analysis and shape detection: RGB image and depth map – performed at the same time. Fig.1. shows an example of pair of images subjected to analysis.



Fig. 1. RGB image to the left and depth map to the right

Then, as shown in Fig. 1, the images were analyzed in the developed program, in which described earlier algorithms for detecting shape of human body were implemented.



Fig. 2. The result of the program: silhouette detected in the RGB picture and depth on the map



Fig. 3. The result of the program: silhouette detected in the RGB picture and depth on the map



Fig. 4. The result of the program: silhouette detected in the RGB picture and depth on the map - image taken from a distance

After performing several series of analyzes in which different results were obtained, from very good to unacceptable, it was estimated that developed program with implemented algorithms for the analysis of shape in RGB images fulfills its role well also in depth maps. Initial disappointing results were caused by poor selection of values in classifier teaching.

Good results bring more questions and doubts: whether the algorithm can cope well if the image contains a number of people, can it handle diverse backgrounds and different positions of people. In order to answer these questions, another series of subsequent analysis was performed, the results of which are shown in Figures 5 and 6.

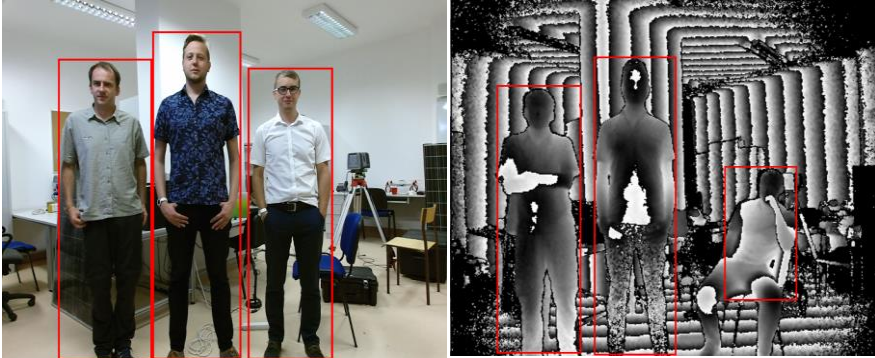


Fig. 5. The result of the program: detected more silhouettes

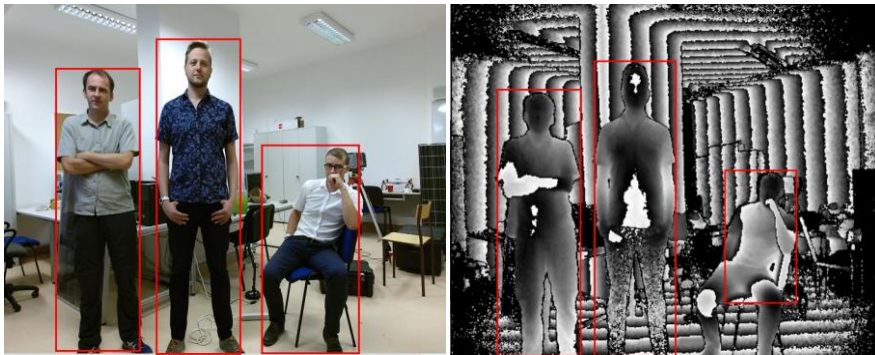


Fig. 6. The result of the program: detected silhouettes of people standing, there was a problem with the identification of the silhouette of the person sitting

After conducting additional analyzes it can be stated that program developed detects well in depth maps and also handles greater number of silhouette shapes appearing in the picture. However, it has a problem with identifying the shape of silhouette of a sitting person. At the current level of research the author is not able to determine the cause of this situation.

4 Conclusions

The article describes the problem of identifying human silhouette in depth maps. In order to accomplish this task, the author made the implementation of HOG algorithm together with SVG classifier. In the first phase of research it was decided to see whether such a solution will give effects – the results were satisfying. With the pro-

gress of research the author noticed other problems that can be subjected to analysis, such as: increasing the number of people in images, changing the position of body alignment, etc. At the current stage of research, the author can conclude that proposed solutions give good results in the identification of standing silhouettes, but faces problem with a different silhouette alignment. Further research on this subject will aim to develop universal algorithm to identify the shapes of the human silhouette in a variety of alignments, as well as other (non-laboratory) conditions with varying lighting conditions.

References

1. Castaneda V., Novab N.: Time-of-Flight and Kinect Imaging, Kinect Programming for Computer Vision, Technische Universität München, 2011
2. Dalal N., Triggs B.: Histograms of Oriented Gradients for Human Detection, <http://lear.inrialpes.fr/people/triggs/pubs/Dalal-cvpr05.pdf>
3. Ben-Hur A., Horn D., Siegelmann H.: Support vector clustering, *Journal of Machine Learning Research*, 2/2011
4. Nanni L., Lumini A. Dominio F., Zanuttigh P.: Effective and precise face detection based on color and depth data, *Applied Computing and Informatics*, 2014
5. Burgin, W., Pantofaru, C., Smart, W.D.: Using depth information to improve face detection, In: *Proceedings of the 6th ACM/IEEE International Conference on Human-Robot Interaction*, 2011
6. Hg R.I., Jasek P., Rofidal C., Nasrollahi K., Moeslund T.B., Tranchet G.: An RGB-D database using Microsoft's Kinect for Windows for face detection, In: *Eighth International Conference on Signal Image Technology and Internet Based Systems*, 2012

Microsoft Kinect Measurement Accuracy for Different Shapes of Objects

Jakub Osuchowski and Sławomir Szymocha

Opole University of Technology, Faculty of Electrical Engineering, Automatic Control and Computer Science, ul. Prószkowska 76, 45-758 Opole, Poland
jakub.osuchowski@gmail.com, slawomir.szymocha@doktorant.po.edu.pl

Abstract. In this paper author examines the Microsoft Kinect measurement accuracy. A method for receiving point clouds from Microsoft Kinect sensor is shown. The depth information from the MS Kinect is converted to a point cloud using Point Cloud Library. For point cloud filtering the voxelized grid approach was applied. Moreover the Ransac method was employed for plane segmentation and Euclidean cluster extraction for cluster detection. Microsoft Kinect construction, capabilities, functions and some point cloud processing methods have also been presented.

Keywords: Microsoft Kinect, point cloud, primitives, measurement

1 Introduction

Microsoft Kinect is an input device and gaming controller for the Microsoft Xbox. Originally this device was combined with the 3D human motion capture algorithm to provide interaction between users and game. Players do not need to hold any other devices and they are able to control characters or menus in the game. The first-generation Kinect was introduced in November 2010 and a version for Windows was released on February 2012. Microsoft released the Kinect software development kit for Windows 7 on June 16, this SDK was meant to allow developers to write Kinecting apps in C++/CLI, C#, or Visual Basic. The Kinect is a low cost sensor which consists of many components. The main parts of the sensor are RGB camera, infra-red (IR) camera, infra-red illuminator and microphone. The Kinect can easily synchronize color and depth images [1–3]. Recently, the Kinect sensor has increasingly been used in 3D modeling of the environment [1]. Nowadays, the 3D modeling process is widely used in the fields such as industrial quality control, civil engineering, robotics etc. Depending on the type of application scanner parameters such as accuracy, measurement rate or range are the most important factors in the process of choosing the scanning system. However, there is a great demand for low-cost systems, e.g. Microsoft Kinect, which can be used in many professional applications [1, 4]. The new Mi-

Microsoft Kinect v2 has a ranging system based on a time-of-flight (TOF) technology instead of triangulation-based scanning. This system indirectly measures the time it takes for infra-red pulses to travel from the IR illuminator to the IR sensor after returning from the target surface. Kinect v2 has also better depth resolution, higher camera resolution and frame rate than the previous version [4, 5]. The range of the virtual environment that can be reproduced in a single scan using a Kinect v2 sensor is limited to few meters. The device works properly in the distance range of 0.5m and 4.5m [4, 6].

The main question is how accurate are scans from Microsoft Kinect for different shapes of objects.

2 Point clouds acquisition and processing

The test stand designed for this study consists of the table, the rear wall and the set of different objects. For testing were selected two cubes, two cylinders and two spheres (Fig. 1).



Fig. 1. The test stand

Scans were taken from a distance of 1.5m for each object separately. The depth information from the IR camera was converted to a point cloud using Point Cloud Library (PCL) where each point represents the 3D position in the world coordinates. PCL contains numerous state-of-the-art algorithms for e.g. filtering, feature estimation as well as drivers for the most diffused 3D sensors [7, 8].

Two example point clouds received from the Microsoft Kinect during the study are shown in Fig. 2.



Fig. 2. Two examples of point clouds

The next step in this study was to detect clusters and cylinders in the received point cloud using PCL. At the beginning, the implemented algorithm reduces the number of points (filtering the point cloud) with the use of the voxelized grid approach. Next, the algorithm finds and segments the individual object point clusters lying on the plane. During this process the Random Sample Consensus (RANSAC) method was used. A clustering method subdivides an unorganized point cloud model P into smaller parts so that the overall processing time for P is significantly reduced. A simple data clustering approach, in the Euclidean sense, can be implemented making use of the 3D grid subdivision of the space using fixed width boxes, or more specifically, the octree data structure. More generally, the Kd-tree structure is used to find the nearest neighbors [8,9].

Subsequently, a primitive shapes were fit to the detected point clusters using Trimble Realworks. Primitives and point clusters are shown in Fig. 3 ,4 and 5.



Fig. 3. Large and small cuboid point clouds with fitting objects (primitives)

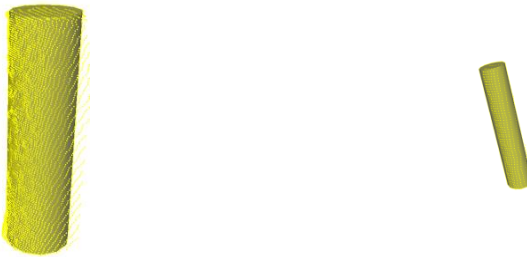


Fig. 4. Large and small cylinder point clouds with fitting objects (primitives)



Fig. 5. Large and small sphere point clouds with fitting objects (primitives)

Received primitives have been included into original point clouds to check how their fit. The whole point clouds received from Microsoft Kinect with selected fitting primitives are shown in Fig. 6.

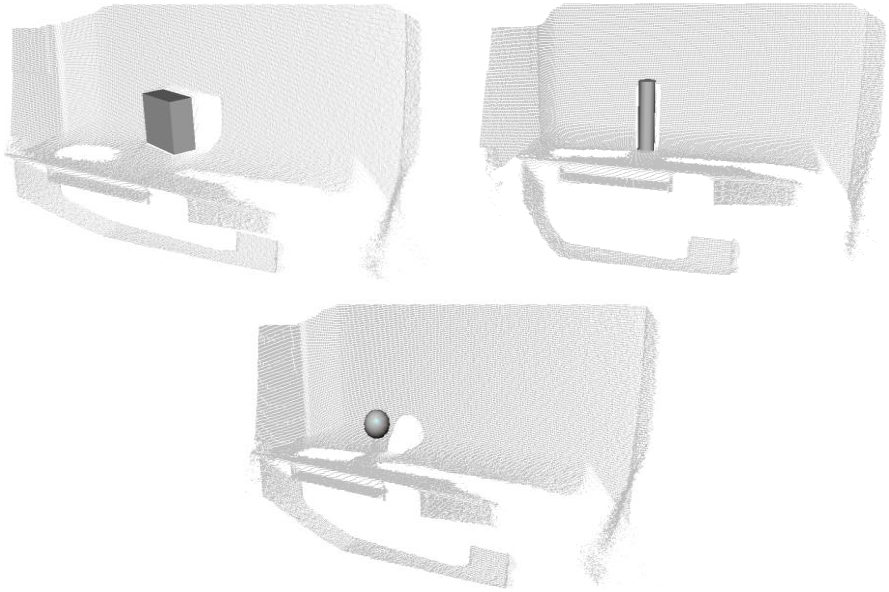


Fig. 6. Three examples of whole point clouds with fitting objects (primitives)

As can be seen in Fig. 6. generated primitives well replace the original parts of the point cloud and it is hard to detect any major imperfections. Using this method the whole point cloud can be divided into smaller parts (clusters and primitives), which can be subjects to further analysis. This approach has several advantages: shortening the processing time for specific object, allows to export selected fragments and it enables multi-threaded operation.

3 Measurement and results comparison

All the objects were measured and all received primitives have been exported to AutoCAD (DWG). Subsequently, in AutoCAD program all primitives have been dimensioned. Summary of test results is presented in table 1.

Table 1. Measurement results

Object	Dimension	Measured dimensions	Dimensions received in the study	Difference	Relative difference [%]
Large Cuboid	Height	272mm	262,7mm	9,3mm	3,42
	Width	324mm	314,2mm	9,8mm	3,02
	Depth	95mm	128,1mm	33,1mm	34,84
	Calculated Volume	8372160 mm ³	10573417,55 mm ³	2201257,55 mm ³	26,29

Small Cuboid	Height	108mm	110,8mm	2,8mm	2,59
	Width	53,7mm	53,7mm	0mm	0,00
	Depth	35,2mm	98,9mm	63,7mm	180,97
	Calculated Volume	204145,92 mm ³	588451,044 mm ³	384305,124 mm ³	188,25
Large Cylinder	Height	308,5mm	319,1mm	10,6mm	3,44
	Diameter	113,4mm	97,4mm	16mm	14,11
	Calculated Volume	3115811,38 mm ³	2377577,05 mm ³	738234,33 mm ³	23,69
Small Cylinder	Height	223mm	216,6mm	6,4mm	2,87
	Diameter	50mm	43mm	7mm	14,00
	Calculated Volume	437859,48 mm ³	314546,78 mm ³	123312,7 mm ³	28,16
Large Sphere	Diameter	153mm	144mm	9mm	5,88
	Calculated Volume	1875309,33 mm ³	1563457,57 mm ³	311851,76 mm ³	16,63
Small Sphere	Diameter	100mm	88,8mm	11,2mm	11,20
	Calculated Volume	523598,78 mm ³	366638,04 mm ³	156960,74 mm ³	29,98

As can be seen in table 1 a scans from Microsoft Kinect quite good represent scanning objects. It should be noted that dimensions which are perpendicular to the scanning direction (height, width) have at most 3,44% relative difference. Dimensions which are parallel to scanning direction have sometimes almost 181% of relative difference (mostly for small objects). This may be caused by the fact that scans from Microsoft Kinect have quite week resolution and they are characterized by high noise. Quite big factor is also the shape of the object. It should be highlight that great importance has the scan angle and the location of the objects. Good results could be achieve if the whole point cloud scene was created from the assembly of several scans from different angles. It should be assumed that this method has for the moment quite weak measurement capabilities. Change of the segmentation and fitting algorithm could make a difference but the weak point of the method is scanning noise and low density of point clouds. This possible could be improve be by changing the infrared illuminator in Microsoft Kinect or usage of polarized light algorithm [10].

What is most important all objects ware good recognized and quite good fits into primitives. This indicates that this method can be successfully used in damage detection, failure detection and some other industry control fields.

4 Conclusion

The point cloud processing and receiving from Microsoft Kinect have been done. The studies show that the accuracy of MS Kinect is on average level. The software have not any problem with the objects detection and primitives fitting. Conducted studies confirm usefulness and considerable potential of Microsoft Kinect in some engineering fields. Presented processing methods can be used in many fields, such as: power engineering (to find failures or other problems), robotic (to find obstacles), industry control (to truck down defective products), etc.

References

1. Difilippo N. M., Jouaneh M. K.: Characterization of Different Microsoft Kinect Sensor Models, *IEEE Sensors Journal*, vol. 15, 2015
2. Han J., Shao L., Xu D., Shotton J.: Enhanced computer vision with Microsoft Kinect sensor: A review, *IEEE Transactions on Cybernetics*, vol. 43, 2013
3. Thumbunpeng P., Ruchanurucks M., Khongma A.: Surface area calculation using Kinect's filtered point cloud with an application of burn care, 2013 *IEEE International Conference on Robotics and Biomimetics, ROBIO 2013*, 2013
4. Gonzalez-Jorge H., Rodriguez-Gonzalvez P., Martinez-Sanchez J., Gonzalez-Aguilera D., Arias P., Gesto M., Diaz-Vilarino L.: Metrological comparison between Kinect i and Kinect II sensors, *Measurement: Journal of the International Measurement Confederation*, vol. 70, 2015
5. Corti A., Giancola S., Mainetti G., Sala R.: A metrological characterization of the Kinect V2 time-of-flight camera, *Robotics and Autonomous Systems*, vol. 75, 2016
6. Hisahara H., Hane S., Takemura H., Chin Y., Ogitsu T., Mizoguchi H.: 3D Point Cloud-Based Virtual Environment for Safe Testing of Robot Control Programs: Measurement Range Expansion through Linking of Multiple Kinect v2 Sensors, 2015 *6th International Conference on Intelligent Systems, Modelling and Simulation*, 2015
7. Munaro M., Rusu R. B., Menegatti E.: 3D robot perception with Point Cloud Library, *Robotics and Autonomous Systems*, 2016
8. Rusu R. B., Cousins S.: 3D is here: Point Cloud Library (PCL), *Proceedings - IEEE International Conference on Robotics and Automation*, 2011
9. Euclidean Cluster Extraction, 2016. [Online]. Available: http://www.pointclouds.org/documentation/tutorials/cluster_extraction.php. [Accessed: 04-06-2016]
10. Hardesty L., Making 3-D imaging 1,000 times better, MIT News Office, [Online]. Available: <http://news.mit.edu/2015/algorithms-boost-3-d-imaging-resolution-1000-times-1201>. [Accessed: 03-06-2016]

The Use of Glass with PDLC Film in Active Dimming Systems

Sławomir Szymocha and Jakub Osuchowski

Opole University of Technology, Faculty of Electrical Engineering, Automatic Control and Computer Science, ul. Prószkowska 76, 45-758 Opole, Poland
slawomir.szymocha@doktorant.po.edu.pl, jakub.osuchowski@gmail.com

Abstract. In the paper the author proposes active dimming system for objects, which is based on the liquid crystals technology. The adjustment of the light permeability to set value is possible as a result of the change in voltage. The author based his system on the PLC driver and regulated DC power supply.

1 Introduction

The technology of regulated dimming was defined by Profesor Claesa Granqvista in 1980. He described the phenomena that enabled to alter light permeability properties of the structure, however the process was electrically controlled. [SM08] He used the term of "smart windows", which is related to the general technology regarding windows. Currently, there are many alternative definitions characterizing this technology: " IQ glass", " magic glass" "privacy glass". Nevertheless, a fundamental property of this technology has not changed and it is the electrically adjustable light transmission of the modified glass. The use of this technology allows to change the climate conditions in the building and control the light energy entering into the interior.

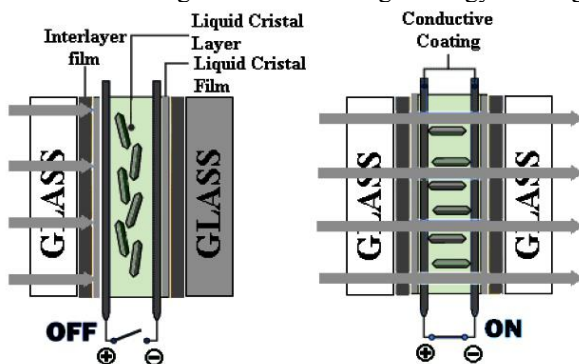


Fig. 1. PDLC film – how it works [OM06]

The author in his test installation used dimmable glaze based on technology PDLC. (Fig. 1) Change in light transmission occurs after the change of the voltage supplied to the film. Along with the voltage increase, the light transmission increases as well due to bigger number of crystals released from the hardened mass. The crystals are arranged horizontally thus allowing the passage of the sunlight into the interior . The whole process must be monitored by the control module and the voltage measuring module validating the obtained effect. This is due to uneven distribution of the crystals in comparison to voltage.

2 Control system of the dynamic dimming

The author has built a test system controlling the climate conditions in the building. (Fig. 2) System enabled control of airing, lighting, ventilation and heating. In order to increase the ability of regulation of the energy entering into the the building, the control unit of the glazing with the PDLC film was used. The film should be distributed between two panes of glass to regulate the amount of light radiation entering into the building during the process of dimming. The lack of regulation of solar energy entering through glazing of large size may result in the increase of internal temperature over 40 ° C. This dramatically increases the costs of building maintenance. Conventional solutions such as blinds or curtains do not offer the ability of full adjustment of the amount of heat and solar energy entering into the building. Once mounted blinds may only change its position and inclination angle in relation to the facade, however they cannot change its light permeability properties.

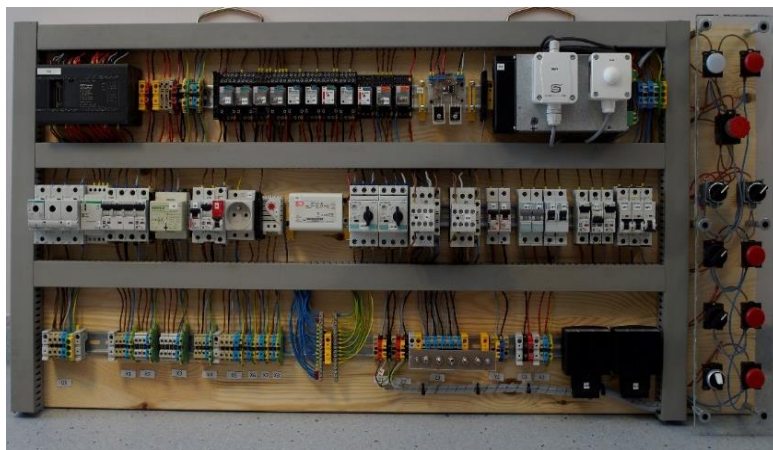


Fig. 2. The control system [SZ15]

The control process is performed by using many mechanical elements and as a result it increases the possibility of the damage. Mechanical elements such as rollers and gears are often damaged, poorly maintained engines in the section of the outdoor blinds frequently overheat, thus forcing their replacement with the new ones.

Driver PLC was using analog output for the management of regulated DC-DC converter. (Fig. 3) The voltage applied on the analog output was scaled proportionally to the output resolution from 0 to 10 V. By changing the level of the analog output signal of PLC driver, the converter was regulating voltage applied to tap changer, which was output supplying glass panes covered with PDLC film.

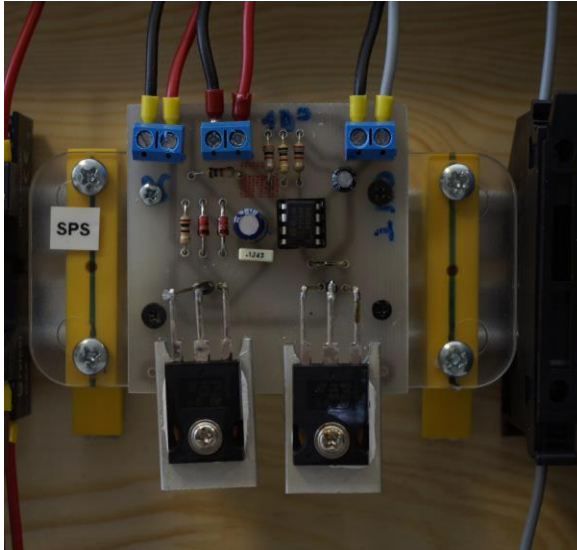


Fig. 3. DC-DC converter [SZ15]

The transition of the light permeability of tested glass pane followed the change of voltage in the range of 0 to 42 V DC. The residual voltage reflected the maximum level of glass dimming, in this state the crystals in the film remained in the form of hard, transparent gel. In response to increase in voltage, crystals had been slowly released resulting in an increase in the light permeability. During the process of release, crystals had adopted horizontal position letting the light radiation pass. The maximum saturation was observed at a voltage of about 37 V DC. (Fig. 4).



Fig. 4. Transparency adjustment [SZ15]

The process was repeated ten times and during the tests it was observed that the saturation of the crystals at a given voltage is not always the same. It was necessary to adjust supplying voltage around 1.2 V DC. This is connected with the random harden-

ing of the substance containing the crystals. The author has set as a quality criterion of the adjustment level of dimming to set parameters. The effect of the uneven saturation of glass covered with foil was reduced by the regular measuring of the light power. Light power sensor was placed behind the windscreen in order to measure the amount of solar energy entering into the interior. (Fig. 5) The measurement value in analog form has been transferred to the PLC driver in order to compare with the set value.

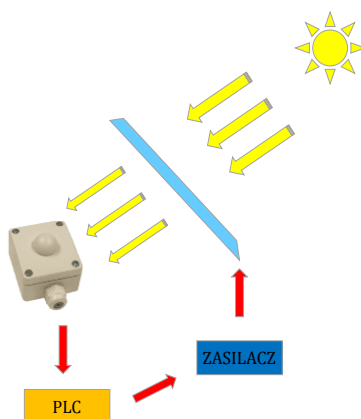


Fig. 5. A schematic diagram of the control system of light permeability [SZ15]

When the value has not complied with the set value, the PLC driver made a correction and changed the value of the analog output. DC-DC converter changes the voltage proportionally to the value received from the analog controller and remeasurement follows the correction. Permissible deviation accounted for 1% of the set value. Control measurement took place at an interval of 10 minutes. Sensor HFTM-U with the PT-1000 probe was used in order to check the difference of heating of the closed space in relation to the amount of solar radiation passing through the glass. The sensor was mounted inside a closed box supplied with the light energy passing through the glass covered with PDLC film. The difference of 10.3°C was recorded, nevertheless the measurement was only illustrative due to the lack of possibility to create specific conditions of a real object in the laboratory. Tests performed on a real object throughout the whole year are considered by the author as necessary.

4 Conclusions

The technology of glass with "IQ layers" is very promising in terms of its implementation on a large scale. However, current costs allow its use only in selected applications. Electrochromic glass are successfully used in aircraft and public buildings, unfortunately due to long duration of saturation, it is not suitable for fast changes in the state of permeability from a full dimming to full brightness. When it comes to glass panes with a large surface, it is necessary to divide them into smaller active sectors and it is related to uneven coverage of the dimming layer on a large surfaces.

Glass covered with PDLC films solves many of the problems of aforementioned technology. [LCP15] The change from full dimming to full permeability is obtained around 0.4 seconds. The number of cycles can be counted in millions and furthermore, it can be applied onto existing glass surfaces. However, its main disadvantage is the necessity to maintain the stability of the power supply for durable dimming effects.

The author focused on the potential use of PDLC film technology in order to control the dimming in the interiors with the possibility of the dynamic change of value. In addition, the control unit regulating the level of isolation was built into the system controlling the climate.

The use of PDLC film can be regarded as desirable due to the possibility of fast installation and option of controlling. By controlling the light transmission, the indoor temperature might be successfully regulated in the range few degrees depending on the conditions. In order to fully use the advantages of this technology, it is necessary to connect system controlling the isolation with the systems controlling air conditioning, ventilation, lighting and the presence of people inside the building. Centralizing control of all systems will allow a much better adjustment of the conditions inside the building and a large costs reduction.

References

- [SM08] Schwartz M.: Smart Materials, CRC Press, 2008.
- [SWI] Michałowski T.: “Szkło o zmiennej przezierności”, <http://www.swiat-szkla.pl/wydawnictwo/7236-szklo-o-zmiennej-przeziernosci.html>, access : 26.06.2016
- [SZ15] Szymocha S.: “Projekt i realizacja autonomicznego systemu zarządzania szklarnią, opartego na sterowniku PLC”, master’s thesis, Opole, 2015.
- [LCP15] Thakur V., Kessler M.: Liquid Crystalline Polymers, Volume 1–Structure and Chemistry, Springer, 2015.

Renewable Energy Integrated Microgrid for Rural Electrification and Productive use

Muhammad Taheruzzaman

BTU-Brandenburg Technical University Cottbus
taher.tum@gmail.com

Abstract. Electric power crisis is one of the major problems in developing countries, and Bangladesh is one of them. The breach between demand and supply is increasing disturbingly. Yet 52 % of the total population has no access to electricity in Bangladesh, and 75 % of them are the rural and isolated community. This paper addresses the renewable energy integrated small-scale power system for rural electrification in the developing countries like Bangladesh. This paper also concentrates on optimal design, sizing, and planning of distributed generation sources. Investigating the optimum design and sizing of generation unit for reliable and cost effective operation of microgrid; four different configurations including only biomass generator, biomass, PV/wind mix system, and further planning the main grid can also connect take into account. Lastly, technical and economic feasibility and optimization compared for both standalone and grid connected system for the community based electrification.

Keywords: DC Microgrid (DC-MG), solar home system (SHS), renewable energy, rural electrification.

1 Introduction

The global energy system trends have been struggling against global warming petrifyingly since surface temperature is also rising, the transition of energy system transform to a fully sustainable based local renewable sources would be a great solution to protect the environment. To increase about 124 % of renewable energy and 209% of biofuel by 2020, cut off half of greenhouse gasses by 2050 [1]. At present, 1.2 billion of total global population, which means around 20 % of total population have no access to electricity, South Asian countries accounts for 37% of the world's population without access to electricity [2]. The gap between demand and supply is increasing petrifyingly, due to high population growth in Bangladesh, the demand of electrical power increases and number of people are living in energy poverty, despite a continued positive efforts experienced for electrification across all over the Bangladesh [3]. Approximately less than 60 % of the overall population in the

developing countries have access to electricity, whereas urban electrification 80 % and about 15-25 % of rural areas are electrified. support rural electrification efforts by the respective country governments including use of renewable energy technologies including PV, wind, and biomass. Despite the continuous efforts of the international community and governments throughout the world, the pace of rural electrification in many developing countries is still very slow [4]. Rural electrification typically poses more challenges than urban electrification in terms of policy, finance, and institutional setup because of its distinct features. While the initial solution for rural electrification can be spreading the main grid by extending the transmission line, but some instance not technically and economically possible [5]. It is commonly agreed that to meet the present demand is the burden for natural gas and other conventional fossil fuels, integration of local renewable sources such as solar PV, small wind turbine (SWT), and biomass would be the alternate source of energy. Furthermore, the isolated and remote areas, RES distributed sources are being significantly recognized as cost-effective sources [6]. The remote areas, higher transmission line losses, and higher cost of transmission lines are encouraging to use of distributed renewable energy. With declining the cost of PV and increasing the performance of small wind turbine (SWT), in addition to improvement of the technologies including control system, and storage system, standalone renewable integrated system significantly enhances its stride [7]. Due to geographical location country like Bangladesh is blessed to generates PV and wind energy based electricity, unremitting deterioration of the prices and soft loan arrangement by state owned organization Infrastructure and Development Company Limited (IDCOL) of Bangladesh already installed 3.2 million solar home system (SHS) by 2014 and extent the number of 6 million by 2017 through installing 50,000 SHS each month [8].

2 System Description

The community based μ -grid consisting of small scale biomass-fueled generator, distributed micro generation unit including PV system, and small wind turbine (SWT). The distributed micro generation sources are being well popular in the developing eventually in the isolated community from the utility network. For enhancing rural electrification and access to electricity μ -grid would be the best possible solution. The concept of community based μ -grid which acknowledges integrating distributed μ -generator sources to the low voltage (LV) distributed network [9]. The proposed system where PV system is considered as several solar home systems (SHSs) connected to the system as distributed μ -generation sources and defined as prosumers¹, SWT and biomass fueled generator shows in fig.1 . The choice of generator is driven by the need and local conditions at the target to end user, keeping in mind that the system integration should have a good balance of being most efficient, reliable, cost-effective, socially beneficial, least polluting and sustainable in

¹ Solar home system (SHS) integrated microgrid; where SHS act as feed electricity into the microgrid and consumer electricity as well

the long run. In developing countries hybrid renewable integrated system have a particular strong relevance in improving the quality of life, especially among rural communities. The electric load in the system considered in DC, including households' appliances, irrigation pumps, rice husking machine, cold storage refrigeration system. The biomass-fueled generator is the primary main source of energy and SHS and wind turbine used for an additional source for electricity to meet the base load of the system, and utilize the use of cost free fuels.

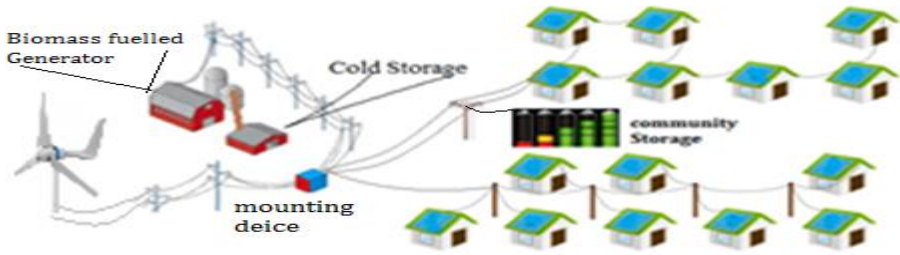


Fig. 1. Proposed Community based DC-MG

3 Model Assumption and Input

3.1 Electric Load

The fig.1, representation of a hypothetical load profile of a community in Bangladesh. The proposed system, the community households consumed 70 kWh per day with maximum peak 15 kW at the evening. The demand data is synthetic and 5% day to day variation considered, and Homer tool randomly inducements the daily perturbation factor in the very hour. Bangladesh is a tropical country as winter demand is comparatively lower than the other seasons.

3.2 Productive Usable Load

The productive load considered as Irrigation pump operates between 7:00 to 11:00 each day from October to March. A small size community based cold storage working for 24 hours a day with the capacity of .8 kW and a rice husking mills peak load 1.3 kW and operates 8 hours a day except the weekend. Total consumption including households and productive loads 36,885 kWh per year.

3.3 Local Renewable Potential

The solar irradiation profile of kaptai, Chittagong (26°26' N, 96°16' E) assume for this work. Solar radiation data is taken from the NASA surface metrology and solar

energy². The proposed location monthly average solar radiation 4.63 kWh/m²/day. The monthly average wind energy 5.79 m/s respectively. Biomass combustion has 68-79 % efficiency depending on fuel moisture content, and combustor design, and combustion operation [10]. The community food waste, crops, leafs, and animal manure to generate biogas that landfill avoided which reduces methane potential damage the atmosphere [11]. The local cows and buffalos roughly produced 10 kg/day, and approximately 60 % of Agricultural residues, 30 % of animal waste and poultry and 10 % of others average biomass production. The average biomass production = 2.04 tons/day.

3.4 Community Based Battery Storage System

The proposed system where comply the meet the load and supply, a community based battery storage is recommended. As the distribution system defined as 12 V, the battery nominal voltage 12 V has considered as the terminal voltage. The nominal capacity of each battery assumes 1 kWh, and maximum capacity 80 Ah. Initial state of charge 100% and minimum charge 40% considered for the system optimization.

4 Result and Comparison of various cases

In this section, four difference cases according to system configurations for analyze all assumptions and constrains for the favorable optimal design option for MG planning as shows in table 1. The first case assumes as an isolated network system fed by a biomass generator. However, the system capital investment is very high installation, operation and maintenance cost, though the fuel cost not so expensive as compare to other traditional fossil fuel such as diesel or furnace oil system. In case-2 the system configures along with number of SHS, SWT, and biomass fueled generator, while case-1 only biomass dependent system, and case-3 is also mixed fuel based configuration but number of SHS increases from 20 to 25 (i.e. PV system capacity increases to 2.5 kW). The case-3 configuration mainly instigates from bottom up swarm electrification concept, where the surplus electricity can be supply to the new users without interrupting present participants. Finally, case-4 assumes similar to case-3 but operates grid connected mode, and the MG system operation adopt to purchase electricity from the grid and sell back surplus unit to the grid. Designing and planning of optimal MG system for rural electrification different configuration taking into account. The main objectives of these interpretation finding the least-cost, self-dependent system, effective use of biomass and other renewable sources for renewable contribution.

² HOMER Analysis <https://analysis.nrel.gov/homer/>.

Table 1: Summary of different configurations for optimal studies

Cases	Description of various scheme
case-1	Biomass fueled generator
case-2	Renewable mixed: Biomass generator, SWT, SHSs
case-3	renewable mixed: increase capacity of PV
case-4	Grid Connected with DC-MG: allow purchase and sellback

The first configuration (case-1) consists of only a 15 kW biomass generator which operates 6423 hours and produces 38,791 kWh per year. The produced electricity is not only meeting the total demand of community loads including households but also productive use, and 139 kWh of excess electricity produces. The precise design can be optimized with 12 battery integrate within the system. While case-2, renewable mixed system cogitates along with 10 kW biomass generator, 2.0 kW PV (i.e. 20 SHS), 2 SWT (turbine capacity 1 kW each). The mixed fuel system all together produces 38,440 kWh per year, alone biomass generator produces 31,000 kWh by operates 4852 hours every year, aside the 20 SHSs and 2 SWT produces 3,197 kWh, and 4,274 kWh respectively. The total production of electricity for case-2 shows in fig. 2(a), and the PV system and SWT operates roughly 4400 hours and 4700 hours respectively per year for each case.

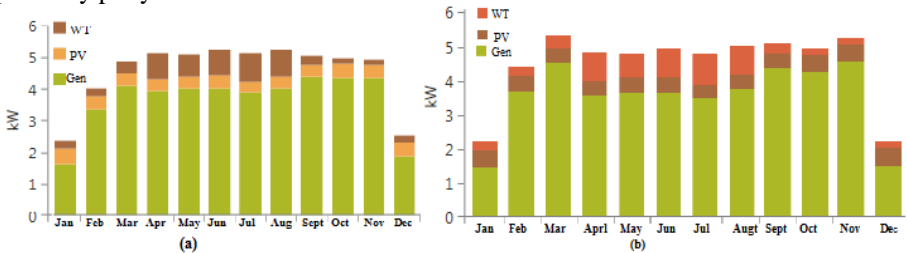


Fig. 2. Electricity Production in MG (a) case-2 and (b) case-3

The renewable mixed fuel MG in case-3 configures along 10 kW biomass generator, 2.5 kW PV system (25 SHS system), and 2 kW SWT, where the biomass generator operates 4791 hours and generates 31,657 kWh, and SWT produces same as previous configuration 4,274 kWh per year. As the number of SHS has considered in case-3, production increases to 3,990 kWh. In case-3 total production 39,921, kWh per year by the renewable mixed fuel system, the biomass, wind energy, and PV contributes 78%, 9%, and 13% individually shows in figure 2(b).

In case-4 consisting also of 2.5 kW PV (25 SHSs), 2 SWT, and capacity of biomass generator similar as the previous cases 10kW. Among all together these sources produce 51,148 kWh per year; while 6.5 % by PV, 8.5% by SWT, 72% by the generator, and 13% from grid purchase shows in fig. 3(2), and the system surplus electricity can be selling back to the grid shows in fig.3(b). The case wise comparison among various cases precisely present in table 2, biomass generator fuel consumptions and operational hours for different cases present in table 3.

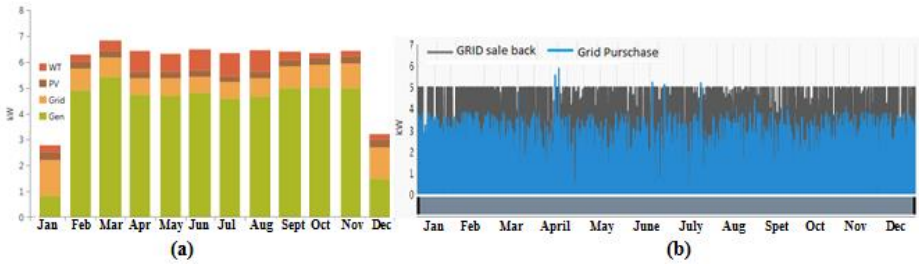


Fig. 3. Case - 4 (a) electricity Production (b) Average monthly grid purchase and sell back

The case-3 and case-4 are the most economical possible solution for optimal configuration. However, among all the configurations holds over 85% of renewable penetration, case-4 (grid extension cost of capital not considered) is one of the cheapest as the NPC, Levelized cost of economic (LCOE), and operating costs are comparatively lower than any other cases of the configuration shown in table 4. However, the LCOE is higher in case-1 and case-2 because of large capital cost. It has shown case-1 is grip the largest cost components.

Table 2: Optimal configuration of various cases

Component	Case-1	Case-2	Case-3	Case-4
Biomass generator [kWh/year]	38,791	31,000	31,657	36,879
PV system	0	3,197	3990	3,197
SWT	0	4274	4274	4,274
Grid	0	0	0	6,798
Total electricity	38,791	38,440	39,931	51,148
Renewable fraction [%]	100	100	100	86
Excess electricity (kWh/year)	139	0	1789	0
Number of battery	12	10	8	5

Table 3: Case-wise comparison of biomass generator

Biomass generator	Case-1	Case-2	Case-3	Case-4
Number of operation hours [hour]	6423	4852	4791	3726
Fuel consumption [tons/year]	22.4	17.6	29.89	17.62

Table 4: Comparison of cost constrains for various cases

Economic Constrains	Case-1	Case-2	Case-3	Case-4
Net Present value [\$]	106,303	103,235	91,737	63,377
LCOE [\$/kWh]	0.203	0.113	0.113	0.091
Operating cost [\$/year]	7,364	8,394	4,551	2,731

5 Conclusion

An acceptable amount of power generation in a sustainable way is an important issue for rapidly increasing population and economic development in the low-income and developing countries. Renewable energy can play an effective role to meet energy demand. Since it is an agrarian country, biomass is one of the potential renewable energy sources in Bangladesh. Agricultural crop residues, residual waste, woods, and animal manure are the major sources of biomass energy in the remote areas country.

In this paper has determined the potential of biomass that operates various ranges of generator fueled by the available local biomass, focuses the optimal design and compare different feasible configuration that complies the local biomass potential. The studies also determine the opportunism of other sources including solar PV and wind energy, and the renewable integrated system would be the ultimate solution for the electricity access into the rural community. The investigation also focuses the break-even point of grid connected system, technical and economic feasibility of the proposed standalone DC-MG configuration care case -2 and case-3. If grid connected is available, then (case-4) is the most economically promising solution. In addition, SHS also illustrate in this paper which also one of the emerging technology in Bangladesh. The social context in Bangladesh stimulate house-owns SHSs, the excess electricity can be stored in the community based battery storage, and shares among other end-users. The SSHs are the prosumers, end users and productive loads are consumers in the DC-MG system.

It is to be noted renewable mix more need to study as a consequence of higher investment costs and replacement costs. The government of Bangladesh may introduce the feed-in tariffs to encourage more renewable penetration for present and future electricity demand, and significant role in the renewable integration. Finally, 10 kW biomass-fueled generator, 20 SHS, and 2 SWT is the optimal solution for the 50 households and other community based productive usable load. .

References

1. T. Boden, G. Marland and R. Andres, "Global, Regional, and National Fossil-Fuel CO₂ Emissions. Carbon Dioxide Information Analysis Center, Oak Ridge National Laboratory,," U.S. Department of Energy, , Oak Ridge, Tenn., U.S.A, 2010.
2. D. Palit, "Solar energy programs for rural electrification: Experiences and lessons," *Elsvier: Energy for sustainable development* , no. 17, p. 270–279 , 2013.
3. IEA, "World Energy Outlook 2013," International Energy Agency, 2013. [Online]. Available: <http://dx.doi.org/10.1787/weo-2013-en>. [Accessed 12 March 2016].
4. C. Paul, "Infrastructure, rural electrification and development.," *Energy for Development* , no. 15, pp. 304-312, 2011.
5. M. Fadaee; M. Radzi, "Multi-objective optimization of a stand-alone hybrid renewable energy system by using evolutionary algorithms: a review," in *Renewable Sustainable Energy Rev*, 16, 2012.
6. H. Omar and B. Kankar, "Optimal planning and design of a renewable energy based supply system for microgrids," *Renewable energy* , vol. 45, pp. 7-15 , 2012 .

7. IRENA (International Renewable Energy Agency), "International off-grid renewable energy conference: key findings and recommendations," 2013. [Online]. Available: www.irena.org/DocumentDownloads/Publications/IOREC_Key%20Findings%20and%20Recommendations.pdf.
8. R. Kempener, O. Lavagne d'Ortigue, D. Saygin; et. al., "Off grid Renewable Energy System: Status and Methodological Status," IRENA (International Renewable Energy Agency), Bonn, Germany , 2015
9. D. Pudjianto. G. Strbac; et.al., "Investigation of Regulatory Commercial, Economic and Environmental issues in microgrids," International conference on future power systems, 2005.
10. D. Hall and R. Overend, "Biomass Combustion," in *Biomass regenerable Energy*, Jhon Wiley and sons Ltd., 1987, pp. 2003-219.
11. Cogenco, " Dalika combined heat and power," [Online]. Available: http://www.cogenco.com/uk-cogenco/ressources/documents/1/44419,Cannington-Cold-Stores_Cogenco.pdf. [Accessed 01 Feb 2016].

Author Index

- Ćosić, Rajko, 342
- Bailová, Michaela, 324
Baleja, Richard, 1, 61
Barteček, Martin, 212
Bednarek, Lukas, 408
Běloch, Michal, 330
Beremlijski, Petr, 391
Béřeš, Michal, 336
Bos, Petr, 1
Bris, Radim, 402
Buček, Petr, 218
Burianek, Tomas, 223
- Cab, Lukas, 146
- Domesová, Simona, 347
Dong, Chau Si Thien, 79
- Foltyn, Ladislav, 353
Frnda, Jaroslav, 414
Fulneček, Jan, 7
- Gasz, Rafał, 532
Gono, Radomir, 19, 25, 73
- Hajduk, Peter, 420
Hajek, Lukas, 426
Hajovsky, Jiri, 85
Hanusek, Tomáš, 13
Hanzelka, Jiří, 229
Hawliczek, Petr, 19
Hendrych, Jakub, 235
Holý, Branislav, 241
Hrabal, Josef, 247
Hrabuška, Radek, 158
Hrubý, David, 433
Hrubý, Tomáš, 122
- Chamrád, Petr, 91
Chromy, Erik, 414, 460, 484, 496, 502
- Ivánek, Lubomír, 508, 520
- Janoušek, Jan, 254
Januška, Peter, 97
Jargus, Jan, 437
Jirůtková, Pavla, 357
- Kajnar, Tomáš, 443
Kocman, Stanislav, 122
Kojecký, Lumír, 260
Koudelka, Petr, 478
Koutný, Martin, 103
Kovář, Petr, 368
Kral, Martin, 25
Krátký, Michal, 319
Kravčenko, Michal, 363, 368
Krbeček, Matěj, 368
Kroczek, Lukáš, 266
Kročil, Josef, 164
Krpelík, Daniel, 373
Kubalík, Petr, 31
Kubicek, Jan, 170
Kuncicky, Radim, 270
- Leonowicz, Zbigniew, 73
- Mach, Veleslav, 7, 73
Malý, Lukáš, 379
Marcincin, Oliver, 37
Markopoulos, Alexandros, 357
Martinek, Radek, 478
Mikolajek, Martin, 176
Mozdřen, Tomáš, 43
Mrovec, Martin, 385
- Nedoma, Jan, 449
Ney, Michal, 110
Novak, Martin, 455
Novák, Tomáš, 1, 61
Novosád, Ladislav, 49
Nowaková, Jana, 182
- Ondraczka, Tomas, 188
Orcik, Lukas, 460
Osuchowski, Jakub, 538, 544
Otýpka, Jan, 116
- Pečínka, Pavel, 122
Perecar, Frantisek, 466
Petrtyl, Ondrej, 128
Plaček, Jiří, 55
Platoš, Jan, 306
Plívová, Nikola, 391
Pobořil, Radek, 472
- Sevcik, Lukas, 484

Silber, Adam, 368
Simonik, Petr, 146
Skopal, Robert, 397
Slachta, Jiri, 490
Sokanský, Karel, 1, 61
Stratil, Tomas, 478
Szymocha, Sławomir, 538, 544

Špaček, Michal, 67
Štrba, Radoslav, 276
Šurkovský, Martin, 282
Švecová, Lucie, 194

Taheruzzaman, Muhammad, 549
Takac, Jiri, 152
Thach, Tien Thanh, 402
Tien, Dung Vo, 73
Tomaszek, Lukas, 288
Tovarek, Jaromir, 496
Tran, Thinh Cong, 134

Uher, Vojtěch, 294
Uhrin, Dominik, 502
Urban, Zdeněk, 508
Urbanczyk, Tomas, 200

Vanderka, Ales, 514
Vantuch, Tomas, 300
Vasínek, Vladimír, 420, 426, 478
Vašínek, Michal, 306
Venclíkova, Marketa, 206
Vo, Hau Huu, 140
Voznak, Miroslav, 460, 484, 490, 496

Weżranowski, Lukáš, 508

Zakaria, Yahia, 520
Zatloukal, Filip, 312
Zbořil, Ondřej, 526
Zwierzyna, Martin, 319

Editors: Michal Krátký, Jiří Dvorský, Pavel Moravec
Dept. of Computer Science
VŠB – Technical University of Ostrava

Title: WOFEX 2016

Place, year, edition: Ostrava, 2016, 1st

Page count: 575

Edit: VŠB – Technical University of Ostrava,
17. listopadu 15, 708 33 Ostrava-Poruba
Czech Republic

Impression: 200

Not for sale.

ISBN 978-80-248-3961-5